# DEMYSTIFYING THE INFRARED EMISSION OF TYPE-1 AGNS FROM $z \sim 0$ TO $z \sim 6$

by

Jianwei Lyu



A Dissertation Submitted to the Faculty of the

DEPARTMENT OF ASTRONOMY

In Partial Fulfillment of the Requirements
For the Degree of

DOCTOR OF PHILOSOPHY
WITH A MAJOR IN ASTRONOMY AND ASTROPHYSICS

In the Graduate College

THE UNIVERSITY OF ARIZONA

2020

THE UNIVERSITY OF ARIZONA
GRADUATE COLLEGE

As members of the Dissertation Committee, we certify that we have read the dissertation prepared by: Jianwei Lyu, titled: Demystifying the Infrared Emission of Type-1 AGNs from z~0 to z~6

and recommend that it be accepted as fulfilling the dissertation requirement for the Degree of Doctor of Philosophy.

George H. Rieke — Date: Dec 18, 2019

Xiaohui Fan — Date: Dec 18, 2019

Richard Green — Date: Dec 18, 2019

Eiichi Egami — Date: Dec 18, 2019

Peter Behroozi — Date: Dec 18, 2019

Final approval and acceptance of this dissertation is contingent upon the candidate's submission of the final copies of the dissertation to the Graduate College.

I hereby certify that I have read this dissertation prepared under my direction and recommend that it be accepted as fulfilling the dissertation requirement.

George H. Rieke — Date: Dec 18, 2019
Dissertation Committee Chair
Department of Astronomy

# ACKNOWLEDGMENTS

"Every journey starts with just one step." When I was a eight-year-old kid, excitedly pointing my hand-made telescope (with plastic lens and paper tubes) to the Moon but only saw the strong chromatic aberration, I never expected that one day I would travel to the other side of the Earth to conduct serious astronomy research and publish meaningful results. As finishing up this thesis to mark the end of my journey as a PhD student, my mind flashed back to various moments that so many people have helped me to get this far.

First I must thank my parents and two sisters, who have encouraged me to pursue my interest since childhood and done everything possible to support me. Although none of them can get what I have researched out, I dedicate this thesis to them.

Then, of course, I would like to express my deep gratitude to my advisor, George Rieke, for his terrific mentorship and support. George has a very sharp mind, many unique ideas and a great sense of humor, which have guided me through many difficult times in research. While serving as a very responsive and friendly mentor, he has also provided me a high degree of freedom to explore my own ideas, without which a thesis like this would not be possible. George is the role model for a PhD advisor and a great (and very interesting) astronomer and I am so fortunate to be his student during these years.

I would like to thank all the current and past members of my mentoring committee, including Xiaohui Fan, Richard Green, Eiichi Egami, Peter Behroozi and Dan Stark. They have always been nice to talk with me on various topics and offer helps. I also thank many other local scientific staff and/or post-docs, e.g., Gurtina Besla, Robert Kennicutt, Paul Smith, Alberts Stacey, Kevin Hainline, Feige Wang, Jinyi Yang, Robert Nikutta, Huanian Zhang, for their career advises and/or science discussions.

I want to express my great gratitude to Michelle Cournoyer and many other supporting staff at Steward Observatory for all their hard work, which keeps the department running smoothly and supports my graduate study here.

Thanks to my officemates, including Rixin Li, Jennifer Kadowaki, Michael Hammer and Christine O'Donnell, for the happy years that we spent together. Our people and office (SO #341) are the best in the whole department!

# DEDICATION

For my parents and sisters, who have continously supported me in various ways since the beginning of my memory.

# TABLE OF CONTENTS

LIST OF FIGURES . . . . . **10**

LIST OF TABLES . . . . . **15**

ABSTRACT . . . . . **17**

CHAPTER 1. BACKGROUND AND MOTIVATIONS . . . . . **18**
1.1. Why Care about AGN IR Emission? . . . . . 18
1.1.1. Interpretation of the AGN Phenomena . . . . . 18
1.1.2. Identification of the AGN Population . . . . . 20
1.1.3. Study of the BH-Galaxy Evolution . . . . . 21
1.1.4. Some Other Applications . . . . . 24
1.2. Unresolved Empirical SED Studies . . . . . 25
1.2.1. Quasars and Seyfert Nuclei at Low-redshift . . . . . 26
1.2.2. High-redshift AGNs . . . . . 28
1.3. Spatially and Temporally Resolved Studies . . . . . 30
1.3.1. IR Images and Spectra from Single Telescopes . . . . . 30
1.3.2. Interferometry Observations . . . . . 32
1.3.3. IR Continuum Variability . . . . . 34
1.3.4. Dust Reverberation Mapping . . . . . 36
1.4. Modeling Efforts . . . . . 37
1.4.1. Phenomenological Models . . . . . 38
1.4.2. Theoretical Models . . . . . 41
1.4.3. SED Models for Composite Galaxies . . . . . 42
1.5. Thesis Aim and Overview . . . . . 44

CHAPTER 2. DUST-DEFICIENT PALOMAR-GREEN QUASARS AND THE DIVERSITY OF AGN INTRINSIC IR EMISSION . . . . . **48**
2.1. Introduction . . . . . 49
2.2. Data . . . . . 51
2.2.1. Data Compilation . . . . . 51
2.2.2. Photometric Variability . . . . . 53
2.3. The IR SED Templates for AGNs . . . . . 55
2.3.1. Normal Quasars . . . . . 55
2.3.2. Dust-Deficient Quasars . . . . . 57
2.3.3. Are the HDD and WDD Templates Bona Fide? . . . . . 60
2.4. SED Decomposition of PG Quasars . . . . . 63
2.5. Results . . . . . 65
2.5.1. Quality of the SED Reproduction . . . . . 67
2.5.2. Identification of the HDD and WDD Quasars . . . . . 71
2.5.3. Host Galaxy Contamination . . . . . 73

TABLE OF CONTENTS—*Continued*

2.6. Discussion . . . 78
2.6.1. The Diversity of Infrared Colors of PG Quasars . . . 78
2.6.2. Characteristics of the Dust-deficient PG Quasars . . . 83
2.6.3. Are the High-$z$ Dust-deficient Quasars Abnormal in Terms of Their SEDs? . . . 87
2.6.4. Does the HDD Quasar Fraction Evolve with Redshift? . . . 95
2.6.5. Dust-deficient Quasars: What is the Cause? . . . 100
2.7. Summary . . . 104

CHAPTER 3. THE INTRINSIC FAR-INFRARED CONTINUA OF TYPE-1 QUASARS **108**
3.1. Introduction . . . 108
3.2. Energy Balance . . . 112
3.2.1. Rationale . . . 112
3.2.2. Template for AGN Soft X-Ray/UV/Optical Emission . . . 113
3.2.3. Energy Budget Calculations . . . 114
3.2.4. Analysis and Results . . . 117
3.3. Decomposition of the Quasar IR SEDs . . . 120
3.3.1. The $f_{\rm AGN,\,MIR}$–$f_{\rm AGN,\,TIR}$ Relation . . . 120
3.3.2. Using the Mid-IR Aromatic Features to Trace the SF Contribution to the Quasar Far-IR Emission . . . 122
3.3.3. Testing Alternative AGN "Intrinsic" IR Templates . . . 128
3.4. Discussion . . . 133
3.4.1. Does the Normal Quasar IR Template Apply to Other Populations of Type-1 AGNs? . . . 133
3.4.2. Implications for the Obscuring Structure . . . 135
3.5. Summary . . . 139

CHAPTER 4. POLAR DUST, NUCLEAR OBSCURATION AND IR SED DIVERSITY IN TYPE-1 AGNS . . . **142**
4.1. Introduction . . . 142
4.2. A Semi-empirical SED Model for Reddened Type-1 AGNs . . . 147
4.2.1. Accretion Disk and Dusty Torus . . . 147
4.2.2. Extended Polar Dust Component . . . 148
4.2.3. Reddened Type-1 SEDs from the Model . . . 153
4.2.4. Model Validation with Observations of NGC 3783 . . . 156
4.2.5. The Degeneracy of Models Constrained Only by the AGN SED . . . 158
4.3. Reproducing the SEDs of Low-$z$ Seyfert Nuclei . . . 160
4.3.1. Sample and Data . . . 160
4.3.2. SED Fitting Method . . . 163
4.3.3. Fitting the IR SEDs of Individual Objects . . . 167
4.3.4. Testing the Reddened AGN Templates with Composite SEDs . . . 169
4.4. Characterizing the AGN Polar Dust Emission . . . 173
4.4.1. SED Features . . . 173

TABLE OF CONTENTS—*Continued*


4.4.2. Observed Size . . . 175
4.4.3. The Prevalence of AGNs with Strong Polar Dust Emission . . . 177
4.4.4. Comparison with Mid-IR Morphology-based Polar Dust Identification . . . 180
4.4.5. Type-2 AGNs . . . 181
4.5. High-$z$ Type-1 AGNs with Peculiar SED Features . . . 181
4.5.1. Extremely Red Quasars . . . 182
4.5.2. AGNs with Mid-IR Warm-excess Emission . . . 182
4.5.3. Hot Dust-obscured Galaxies . . . 185
4.6. Discussion . . . 188
4.6.1. Interpreting the AGN Mid-IR Emission . . . 189
4.6.2. Dust-covering Factor of Type-1 AGNs . . . 190
4.6.3. AGN X-ray Obscuration and Polar Dust Optical Depth . . . 192
4.6.4. AGN Structures and Unification . . . 194
4.6.5. The Diverse Dust Environments of AGNs . . . 197
4.7. Summary and Conclusions . . . 199

CHAPTER 5. MID-IR VARIABILITY AND DUST REVERBERATION MAPPING OF LOW-$z$ QUASARS . . . **204**
5.1. Introduction . . . 205
5.2. Photometric Data and Light Curves . . . 207
5.2.1. Data Ensemble . . . 207
5.2.2. Construction and Evaluation of the Light Curves . . . 214
5.2.3. Converting the Mid-IR Measurements at $\lambda > 10$ $\mu$m for Comparison 222
5.3. Reverberation Analysis Methods . . . 224
5.3.1. Constraining the Optical Continuum Variability . . . 225
5.3.2. Retrieving Dust Reverberation Signals . . . 226
5.3.3. Detecting the Time Lags . . . 228
5.4. Results . . . 233
5.4.1. Mid-IR Variability and Dust Reverberation Signals . . . 233
5.4.2. The IR Time Lag – AGN Luminosity Correlation . . . 236
5.4.3. PG Quasar Variability at 10–25 $\mu$m . . . 242
5.4.4. AGN Variability at 22–24 $\mu$m in a Larger Sample . . . 243
5.5. Discussion . . . 250
5.5.1. The Origin of AGN Mid-IR Variability . . . 250
5.5.2. Constraints on the Torus Properties . . . 257
5.5.3. Relation between Dusty Torus and Broad-line Regions . . . 263
5.6. Summary . . . 266

CHAPTER 6. THE CONTRIBUTION OF HOST GALAXIES TO THE INFRARED ENERGY OUTPUT OF $z \gtrsim 5.0$ QUASARS . . . **271**
6.1. Introduction . . . 271
6.2. Selection of SED Templates . . . 274

TABLE OF CONTENTS—*Continued*


6.2.1. Host Galaxy Template: Why Haro 11? . . . 274
6.2.2. AGN Continuum Template . . . 277
6.2.3. Fitting Procedure . . . 279
6.3. Tests of the Templates . . . 280
6.3.1. Template Fits for High-$z$ Galaxies . . . 280
6.3.2. Template Fits for High-$z$ Quasars . . . 282
6.3.3. SED Fitting with Well-measured High-$z$ Quasars . . . 283
6.4. AGN and Host Galaxy Decomposition for Quasars at $z \gtrsim 5$ . . . 288
6.5. Discussion . . . 296
6.5.1. Heating Sources for the Infrared Energy Output . . . 296
6.5.2. Are AGN Host Galaxies at $z \gtrsim 5$ Low-metallicity? . . . 297
6.5.3. The Star Formation Rates of Quasars at $z \gtrsim 5$ . . . 299
6.5.4. AGN Luminosity . . . 302
6.5.5. Implications for BH-galaxy Evolution . . . 304
6.6. Summary . . . 307

CHAPTER 7. SUMMARY AND OUTLOOK . . . **310**
7.1. Summary of Key Results . . . 310
7.2. Ongoing and Future Work . . . 312

APPENDIX A. THE AGN INTRINSIC SED TEMPLATES . . . **317**

APPENDIX B. PURE STAR-FORMING GALAXIES IN THE GOALS SAMPLE . . . **318**

APPENDIX C. THE EFFECTS OF OPTICAL THICKNESS . . . **320**

APPENDIX D. SAMPLE AND DATA COMPILATION FOR LOW-$z$ SEYFERT-1 NUCLEI **324**
D.1. AGNs with HSR SED Observations . . . 324
D.2. The SDSS-*Spitzer*/IRS Type-1 AGNs . . . 325
D.3. IR Light Curves from WISE/NEOWISE . . . 326

APPENDIX E. PHOTOMETRIC STABILITY OF OPTICAL TRANSIENT SURVEYS AND *WISE*/*NEOWISE* MISSION . . . **328**
E.1. Optical Data from CRTS and ASAS-SN . . . 328
E.2. Mid-IR from *WISE*/NEOWISE . . . 329

APPENDIX F. A SIMPLE MODEL FOR RELATING TIME LAGS TO THE TORUS STRUCTURES . . . **334**

APPENDIX G. A REVISIT OF THE KOSHIDA ET AL. SAMPLE . . . **337**
G.1. SED Analysis . . . 337
G.2. Time Lag Measurements . . . 339

TABLE OF CONTENTS—*Continued*

APPENDIX H. TEMPLATES FOR DWARF GALAXIES . . . . . **341**
H.1. Sample and Infrared Data . . . . . 341
H.2. SED Modeling and Template Construction . . . . . 342
H.3. Features of Low-metallicity Galaxy Templates . . . . . 343

APPENDIX I. STAR FORMATION IN DWARF GALAXIES . . . . . **348**
I.1. Star Formation Determination . . . . . 348
I.1.1. Star Formation Law of Haro 11 . . . . . 351

REFERENCES . . . . . **356**

# LIST OF FIGURES

FIGURE 1.1. The evolving picture of AGN circumnuclear dust . . . 19
FIGURE 1.2. The many facets of AGN obscuration . . . 20
FIGURE 1.3. Composite SEDs with different AGN contributions . . . 21
FIGURE 1.4. Mid-IR color-color diagram for AGN Selection . . . 22
FIGURE 1.5. Galaxy growth via gas-rich major mergers . . . 23
FIGURE 1.6. Growth of galaxies and their black holes . . . 24
FIGURE 1.7. SED decomposition examples . . . 25
FIGURE 1.8. Comparison of nuclear SED of Seyfert nuclei and quasars . . . 27
FIGURE 1.9. SEDs of unobscured type-1 quasars . . . 28
FIGURE 1.10. Example high-$z$ type-1 AGNs with abnormal SED features . . . 29
FIGURE 1.11. Contour plot of the 12.5 $\mu$m image overlied on the [O III]image of NGC 1068 . . . 31
FIGURE 1.12. Torus size measured from near-IR interferometry instruments as a function of AGN luminosity . . . 33
FIGURE 1.13. Example Seyfert nuclei with detected mid-IR polar dust emission . . . 34
FIGURE 1.14. AGN torus in NGC 1068 as resolved by ALMA . . . 35
FIGURE 1.15. Radii of torus inner edge and the broad line region as a function of AGN V-band luminosity . . . 38
FIGURE 1.16. Setup of a typical torus model . . . 40
FIGURE 1.17. Model spectra from the Nenkova et al. (2008b) CLUMPY torus model 40
FIGURE 1.18. AGN torus could be a dynamical radiatively-driven "fountain" . . . 43
FIGURE 1.19. AGN torus as a natural result of AGN feedback that evacuates gas in the polar regions . . . 44
FIGURE 1.20. Synthetic SEDs of Type-1 AGN produced by Calistro Rivera et al. (2016) AGNfitter code . . . 45

FIGURE 2.1. Example *WISE* $W1, W2$ band light curves for a few PG quasars. . . . 54
FIGURE 2.2. SED templates for hot-dust-deficient (HDD) and warm-dust-deficient (WDD) AGNs . . . 58
FIGURE 2.3. *Akari*+*Spitzer*/IRS combined infrared spectra for example normal, WDD and HDD quasars . . . 61
FIGURE 2.4. Mock SEDs of quasars . . . 62
FIGURE 2.5. SED decomposition results and the residual plots for the PG sample 68
FIGURE 2.5. SED decomposition results and the residual plots for the PG sample 69
FIGURE 2.5. SED decomposition results and the residual plots for the PG sample 70
FIGURE 2.6. SED decomposition of quasars with ambiguous classifications . . . 74
FIGURE 2.7. Comparison of the host galaxy stellar emission to the total quasar light in observed $H$ band, $F_{\rm star,\,H}/F_{\rm quasar,\,H}$, based on image decomposition and that from SED decomposition. . . . 76
FIGURE 2.8. Comparison of imaging and SED deconvolution results for normal quasars and using the Assef et al. (2010) AGN template. . . . 77

LIST OF FIGURES—*Continued*

FIGURE 2.9. Comparison of the star formation rates derived through our fitting of the FIR SEDs with those in Shi et al. (2014) from the 11.3 $\mu$maromatic feature strength. . . . . 79
FIGURE 2.10. Infrared color distribution of the 87 PG quasars and various SEDs of normal and dust-deficient quasars . . . . . 80
FIGURE 2.11. Distributions of AGN luminosities and black hole masses of 87 PG quasars . . . . . 85
FIGURE 2.12. Fractions of dust-deficient quasars as a function of AGN luminosity. 86
FIGURE 2.13. Distributions of AGN luminosities ($L_{\rm AGN}$) and 10 $\mu$msilicate strength ($S_{10}$) for normal, WDD and HDD quasars. . . . . 87
FIGURE 2.14. A check of $z \gtrsim 5$ dust-poor quasars . . . . . 89
FIGURE 2.15. The SEDs of hot-dust-deficient and warm-dust-deficient quasars at high and intermediate redshifts. . . . . 92
FIGURE 2.16. Comparison of the stacked SED of $z \gtrsim 5$ *Herschel* non-detected quasars in Leipski et al. (2014) with the normal AGN template, the WDD template, and the HDD template. . . . . 93
FIGURE 2.17. Comparison of the mean SEDs of three classes of hot-dust-poor quasars in Hao et al. 2010 with the composite SEDs of the normal AGN template or the HDD AGN template. . . . . 95
FIGURE 2.18. Host galaxy contribution vs. AGN luminosity from the SED model. 97
FIGURE 2.19. The Hao et al. (2010) selection of hot-dust-poor quasars applied to the PG sample. . . . . 99
FIGURE 2.20. Schematic demonstration of the torus geometry of normal, WDD and HDD quasars. . . . . 104

FIGURE 3.1. Examples of proposed empirical AGN SED templates, normalized at 3.0 $\mu$m. . . . . 110
FIGURE 3.2. Mock infrared SEDs of galaxies with different mixing of the Elvis AGN template and the $\log(L_{\rm IR}/L_{\odot}) = 11.25$ Rieke et al. (2009) template. . . 121
FIGURE 3.3. Comparisons of the luminosity conversion factors for the 11.3 $\mu$maromatic feature to the 8–1000 $\mu$mIR emission in Dale & Helou (2002) templates and Rieke et al. (2009) templates. . . . . 124
FIGURE 3.4. Relation between the derived host galaxy infrared luminosities with the $\chi^2$ selected Rieke et al. (2009) template luminosities. . . . . 127
FIGURE 3.5. Comparison of the 11.3 $\mu$maromatic feature flux measured from the mid-IR spectra and that from the SED model . . . . . 129
FIGURE 3.6. Reproduction of the Symeonidis et al. (2016) far-IR AGN template . 131
FIGURE 3.7. Equivalent width of the 11.3 $\mu$mfeature as a function of AGN contribution to the total infrared luminosity, $f_{\rm AGN,TIR}$ for the 57 normal quasars in the PG sample . . . . . 133
FIGURE 3.8. Comparison of the AGN templates for quasars and Seyfert galaxies. 135
FIGURE 3.9. Dust component decomposition of the three empirical AGN templates 138

LIST OF FIGURES—*Continued*

FIGURE 4.1. Illustration for the weak geometry effects on the optically-thin IR emission . . . 154
FIGURE 4.2. The influence of model parameters on the output SEDs . . . 156
FIGURE 4.3. Model fitting to the optical-to-IR SED of NGC 3783 . . . 159
FIGURE 4.4. Comparisons of different stellar templates . . . 165
FIGURE 4.5. Model fitting for low-$z$ Seyfert-1 nuclei with the reddened AGN model 168
FIGURE 4.5. Model fitting for low-$z$ Seyfert-1 nuclei with reddened AGN model (continued.) . . . 169
FIGURE 4.6. individual and composite SEDs of the SDSS-*Spitzer*/IRS Seyfert-1 AGN sample . . . 170
FIGURE 4.7. Mid-IR spectra, UV-to-MIR SEDs and reddened AGN model fittings for normal, dust-deficient and warm-excess AGNs in the SDSS-*Spitzer*/IRS Seyfert-1 sample . . . 172
FIGURE 4.8. The integrated IR emission SED of the polar dust component and the corresponding contributions from different processes . . . 174
FIGURE 4.9. Comparison of the IR SED template for the AGN polar dust emission and the intrinsic normal AGM template . . . 176
FIGURE 4.10. Extinction curve of the suggested AGN polar dust and classical ISM dust . . . 177
FIGURE 4.11. Radial profiles of the dust temperature of the extended dust component with different optical depth . . . 178
FIGURE 4.12. Reddened AGN model fitting to the median SEDs of extremely red quasars . . . 183
FIGURE 4.13. Reddened AGN model fittings to the mid-IR warm-excess AGNs reported in Xu et al. (2015b) . . . 184
FIGURE 4.14. Reproduction of the median SED of hot-dust-obscured AGNs with our reddened AGN model . . . 186
FIGURE 4.15. SEDs and the best-fit model of low-$z$ candidate hot-dust-obscured AGNs. . . . 188
FIGURE 4.16. The AGN mid-to-optical luminosity ratio as a function of optical depth of the extended dust component . . . 191
FIGURE 4.17. the distribution of gas column density and polar dust optical depth of the low-$z$ Seyfert-1 and the high-$z$ reddened populations . . . 193
FIGURE 4.18. Schematic drawing for the dust environment around a typical Seyfert-like nuclei . . . 196
FIGURE 4.19. Schematic drawings for the different dust environment around an AGN and the corresponding SEDs . . . 198

FIGURE 5.1. Time coverage and wavelength sampling of time-series datasets used 209
FIGURE 5.2. Comparisons of the best-fit DRW model parameters for ASAS-SN and CRTS light curves . . . 217
FIGURE 5.3. Example optical light curves of PG quasars . . . 218
FIGURE 5.4. DRW damping timescale as a function of AGN bolometric luminosity 226

LIST OF FIGURES—*Continued*

FIGURE 5.5. Representative optical and mid-IR light curves and corresponding DRW and time-lag fits of PG quasars . . . 229
FIGURE 5.6. Cross-correlation functions between the optical and IR light curves of example PG quasars . . . 230
FIGURE 5.7. Comparison of mid-IR time lags between the results from $\chi^2$ fittings and cross-correlation analysis . . . 231
FIGURE 5.8. Comparison of the normal, WDD and HDD AGN templates developed in Lyu et al. (2017) . . . 239
FIGURE 5.9. Dust time lags between the *WISE* mid-IR band and optical band light curves plotted against the AGN luminosity for PG quasars . . . 240
FIGURE 5.10. Distribution of variability significance $S_{i,j}$ between different 24 $\mu m$ measurements in all 139 quasars . . . 245
FIGURE 5.11. Multi-band IR and optical light curves of the radio-quiet PG 1535+547 (left) and the blazar PG 1226+023 (right) . . . 249
FIGURE 5.12. The flux boosting factor as a function of observing angle for different Lorentz factors ($\gamma$=5, 10, 20, 100). . . . 251
FIGURE 5.13. Sketch of the main AGN structures related to the AGN optical and mid-IR continuum variabilities . . . 254
FIGURE 5.14. The distribution of variation amplitudes and time lags for normal (grey), WDD (green) and HDD (red) quasars . . . 263
FIGURE 5.15. Comparison of the infrared light lags in the *WISE* W1 band ($\sim$ 3.4 $\mu m$) from this work and the broad emission line lags of 17 PG quasars from Kaspi et al. (2000) . . . 267

FIGURE 6.1. *Spitzer* and HST images of Haro 11 . . . 276
FIGURE 6.2. SED Comparsion of Haro 11 and normal SFGs . . . 281
FIGURE 6.3. Comparison of $z \sim 2$ galaxy SED with normal SFG templates . . . 282
FIGURE 6.4. Model fittings of the stacked SEDs in Leipski et al. (2014) . . . 284
FIGURE 6.5. SED decompositions for 5 $z \gtrsim 5$ quasars with best far-IR SED constraints . . . 287
FIGURE 6.5. SED decompositions for 5 $z \gtrsim 5$ quasars with best far-IR SED constraints . . . 288
FIGURE 6.6. Two-component SED decompositions of 69 $z \gtrsim 5$ quasars . . . 290
FIGURE 6.6. Two-component SED decompositions of 69 $z \gtrsim 5$ quasars . . . 291
FIGURE 6.7. Comparison of AGN luminosities derived from mag(1450Å) and infrared SED fits. . . . 303
FIGURE 6.8. The IR luminosity of the star-formation component $L_{\rm SF,IR}$ versus the total AGN luminosity $L_{\rm AGN}$ for quasars at different redshifts . . . 305

FIGURE 7.1. Flux density profile of the AGN polar dust emission based on Lyu & Rieke (2018) model . . . 313
FIGURE 7.2. AGN mid-IR color-color selection and variablity search . . . 315
FIGURE 7.3. Simulated JWST/NIRSpec spectrum for a quasar at $z \sim 6$ . . . 316

LIST OF FIGURES—*Continued*

FIGURE C.1. The output SEds of images of a single dusty cloud plus the accretion disk emission viewing from different angles . . . . . 321
FIGURE C.2. The output SEDs of systems with different numbers of dusty clumps with optical depth $\tau_V = 1, 5, 10, 50$, heated by the accretion disk emission observed from different lines of sight . . . . . 322
FIGURE C.3. Demonstration on the effect of clumpiness . . . . . 323

FIGURE E.1. Optical light curves of 15 optical spectrophotometric standard stars . 330
FIGURE E.2. *WISE* W1 (left) and W2 (right) light curves of 14 IR calibration standard stars . . . . . 332

FIGURE F.1. The geometry of a dusty shell with a radius $r$ from the origin (accretion disk) and a half opening angle $\Omega_{TOR}$ . . . . . 334

FIGURE G.1. SED best-fit results for the Seyfert-1 nuclei studied in Koshida et al. (2014) . . . . . 338
FIGURE G.2. AGN luminosity estimation comparison between SED fitting and V-band photometry from Koshida et al. (2014) . . . . . 338
FIGURE G.3. K-band time lag comparison between our model and the Koshida et al. (2014) method . . . . . 339

FIGURE H.1. IR SEDs of the 19 DGS galaxies . . . . . 345
FIGURE H.2. Full IR SEDs of the 19 DGS galaxies with good *Spitzer*/IRS spectra 346
FIGURE H.3. Family of full IR SEDs of the 19 DGS galaxies, normalized at rest-frame 14 $\mu$m . . . . . 347

FIGURE I.1. Comparison of star formation rates (SFRs) from the total infrared luminosity (8-1000 $\mu$m) and those from GALEX FUV + MIPS 24 $\mu$m . . . . 351
FIGURE I.2. Histogram of the ratio between the 24$\mu$m-based SFR and $L_{IR}$-based SFR of dwarf galaxies. . . . . 354

# LIST OF TABLES

TABLE 2.1. PG quasars used to derive the templates . . . 59
TABLE 2.2. SED decomposition results for the 87 Palmor-Green quasars . . . 66
TABLE 2.2. SED decomposition results for the 87 Palmor-Green quasars . . . 67
TABLE 2.3. Dust-deficient Quasars in $z < 0.5$ PG sample . . . 72
TABLE 2.3. Dust-deficient Quasars in $z < 0.5$ PG sample . . . 73
TABLE 2.4. K-S probabilities of the HDD and WDD quasars against normal quasars 88
TABLE 2.5. Dust-deficient Quasars at $z$=0.5-6 . . . 90
TABLE 2.5. Dust-deficient Quasars at $z$=0.5-6 . . . 91

TABLE 3.1. Fraction of Short-$\lambda$ Luminosity Reradiated in the Infrared of Representative AGN Templates . . . 115
TABLE 3.2. Host Galaxy IR Properties of the 24 Palomar–Green Quasars . . . 126
TABLE 3.3. Dust Components for the Quasar Intrinsic AGN IR Emission . . . 137

TABLE 4.1. DUSTY model setup . . . 155
TABLE 4.2. Suggested model parameters for NGC 3783 . . . 158
TABLE 4.3. List of the Low-redshift Seyfert-1 Nuclei . . . 162
TABLE 4.3. List of the Low-redshift Seyfert-1 Nuclei . . . 164
TABLE 4.4. Candidate AGNs with Significant Polar Dust Emission . . . 179
TABLE 4.5. Suggested Model Parameters for Hot Dust-Obscured Galaxies . . . 187

TABLE 5.1. Time-series datasets used in this work . . . 208
TABLE 5.2. Quasar flux measurements at 24 $\mu$m and the variability results . . . 213
TABLE 5.2. Quasar flux measurements at 24 $\mu$m and the variability results . . . 215
TABLE 5.3. Summary of Available Data and Basic Variability Properties . . . 220
TABLE 5.3. Summary of Available Data and Basic Variability Properties . . . 221
TABLE 5.3. Summary of Available Data and Basic Variability Properties . . . 223
TABLE 5.4. Summary of the Mid-IR Reverberation Properties . . . 234
TABLE 5.4. Summary of the Mid-IR Reverberation Properties . . . 235
TABLE 5.4. Summary of the Mid-IR Reverberation Properties . . . 237
TABLE 5.5. PG quasar variability at 12 and 22 $\mu$m . . . 244
TABLE 5.6. Results of Linear Regression of Lag-Luminosity Relation . . . 258
TABLE 5.7. Parameters related to the torus radial density profiles . . . 262
TABLE 5.8. K-S probabilities of the HDD and WDD quasars against normal quasars 264
TABLE 5.9. Time lag comparison of BLR and mid-IR dust for 12 PG quasars . . . 265

TABLE 6.1. Comparisons of galaxy templates used to fit $z > 4$ galaxies . . . 283
TABLE 6.2. SED decomposition results for $z \gtrsim 5$ 5 quasars with well-measured SEDs . . . 288
TABLE 6.3. SED decomposition results for $z \gtrsim 5.0$ 69 quasars (*sample-A*) . . . 293
TABLE 6.3. SED decomposition results for $z \gtrsim 5.0$ 69 quasars (*sample-A*) . . . 294
TABLE 6.4. SED decomposition results for $z \gtrsim 5.0$ 33 quasars (*sample-B*) . . . 295

LIST OF TABLES—*Continued*

TABLE 6.5. SED decomposition results for the stacked quasar SEDs . . . . . 297
TABLE 6.6. Estimation of a typical host galaxy mass . . . . . 307

TABLE A.1. AGN Intrinsic Templates . . . . . 317

TABLE B.1. Properties of 101 SFGs in the GOALS sample . . . . . 319

TABLE E.1. Measurements of Optical Standard Stars . . . . . 329
TABLE E.2. Measurements of Mid-IR Standard Stars . . . . . 331
TABLE E.2. Measurements of Mid-IR Standard Stars . . . . . 333

TABLE G.1. New Time Lag Measurements of the Koshida et al. (2014) Seyfert-1 Sample . . . . . 340

TABLE H.1. Low-metallicity Galaxies Used to Derive the Templates . . . . . 344

TABLE I.1. The star formation rates of the dwarf galaxies . . . . . 350
TABLE I.1. The star formation rates of the dwarf galaxies . . . . . 352
TABLE I.2. Star Formation Rate of Haro 11 . . . . . 353

# ABSTRACT

The accretion of supermassive black holes (SMBHs) is accompanied by large columns of dusty gas connected to the host galaxy interstellar medium, resulting in significant emission in the infrared (IR) spectral range ($\lambda$ $\sim$1–1000 $\mu$m). IR observations of these systems provide a wealth of information to reveal the physics of active galactic nuclei (AGN) and its role in galaxy evolution. In this thesis, I present a systematic study to characterize and decipher the IR emission of Type-1 AGNs over very broad ranges of luminosity ($L_{\rm AGN,bol} \sim 10^8$–$10^{14}$ $L_\odot$) and redshift ($z$ $\sim$0–6) from different perspectives: (1) we have demonstrated that the intrinsic IR SEDs of type-1 quasars at $z$ $\sim$0–6 have variations from hot-/warm-dust-deficient populations to the normal population and characterized the similar AGN-heated far-IR SEDs among different AGN populations; (2) By adding UV-optical obscuration and IR-reprocessed emission of an extended distribution of large dust grains to the intrinsic AGN templates, we have successfully reconciled the IR behaviors of all major populations of type-1 AGNs, including the strong polar dust emission found in several Seyfert-1 nuclei by mid-IR interferometry observations and the large SED variations among local Seyfert-1 nuclei, normal blue quasars, extremely red quasars at $z$ $\sim$2–3, AGNs with mid-IR excess emission at $z$ $\sim$0.7–2, hot-dust-obscured galaxies at $z$ $\sim$1.5–4, and dust-free quasars at $z \sim 6$, which provided critical insights on how the diverse AGN dust environment can be reflected by the different IR SED shapes; (3) With an innovative usage of the time-series data from asteroid/supernova-hunting surveys, we have developed the first mid-IR dust reverberation survey of quasars and put several important constraints on the AGN torus structures and supported the unification model; (4) Based on an accurate knowledge of galaxy and AGN IR emission, we have shown the far-IR properties of quasar host galaxies at $z$ $\sim$5–6 should be similar to the low-metallicity starbursting galaxy Haro 11 and studied the quasar star formation rates and typical stellar masss when the Universe is only $\sim$1 Gyr old.

# CHAPTER 1
# BACKGROUND AND MOTIVATIONS

The IR window ($\lambda$ ~1–1000 $\mu m$) provides important diagnostic features to interpret various active galactic nuclei (AGN) phenomena, search for obscured (and unobscured) AGNs, and probe the role of AGN in galaxy evolution. Since the discovery of the IR emission at 2–10 $\mu$m in the first quasar 3C 273 by Johnson (1964); Low & Johnson (1965), substantial progress has been made to characterize and understand the IR behavior of these accreting supermassive black holes (SMBHs) over very wide ranges of luminosity and redshift (up to the most distant quasar at $z = 7.5$; Venemans et al. 2017).

In this Chapter, after highlighting the importance of AGN IR study in Section 1.1, I give a brief overview of past and recent representative efforts to address and understand the AGN IR properties in Section 1.2–1.4. Section 1.5 introduces the major goals and organization of this thesis.

## 1.1 Why Care about AGN IR Emission?

### 1.1.1 Interpretation of the AGN Phenomena

The AGN unification scheme suggests that the great diversity of AGN classes can be reconciled into the same structure with different observing angles (Antonucci, 1993; Urry & Padovani, 1995). The central engine is powered by an accreting SMBH ($\sim 10^6$–$10^8$ $M_\odot$) with accretion disk that produces strong emission peaked in the UV-optical band (so called "big blue bump"). Surrounding the accretion disk is an optically thick circumnuclear dusty structure which can obscure the broad-line emission from the high-velocity clouds near the accretion disk (aka, the broad-line regions) for inclined observing angles (left panel in Figure 1.1). As the result of energy balance, this dust structure produces strong emission in the IR band with a large range of dust temperatures (so called "IR bump"). Given its great importance, very intensive efforts have been spent to constrain the AGN near- to mid-IR emission in terms to characterize the SED shape (e.g., Rieke 1978; Sanders et al.

1989; Alonso-Herrero et al. 2003), explore its possible evolution with AGN properties (e.g., Maiolino et al. 2007; Jun & Im 2013) and infer the underlying dust compositions or structures (e.g., Alonso-Herrero et al. 2011; Mor & Netzer 2012a; Xie et al. 2014).

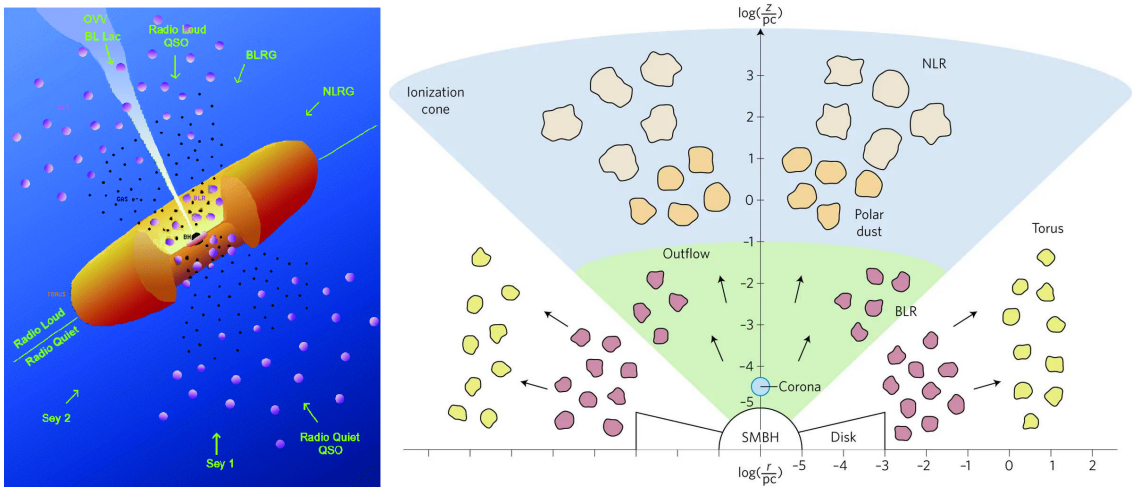


Figure 1.1 A comparison of the classical unification picture with a doughnut-like smooth torus (Antonucci, 1993) and one of the latest proposals of AGN structures featuring clumpy torus and polar dust (Ramos Almeida & Ricci, 2017).

With spatially-resolved IR observations (see discussions in Section 1.3), the classical torus picture (left panel in Figure 1.1) is gradually evolving into a more complex one (e.g., right panel in Figure 1.1). It appears that the dust along the polar direction, for example, dust in the narrow-line regions and/or outflows, can also obscure the nuclei and produce significant IR emission (e.g., Raban et al., 2009; Hönig et al., 2013). Such behaviors seem to be common across a wide redshift range and could be related with the AGN feedback to the galaxy (Lyu & Rieke, 2018).

In fact, obscuration happens on diverse physical scales (e.g., see reviews by Bianchi et al. 2012; Hickox & Alexander 2018; see Figure 1.2), which can also influence the AGN IR behaviors. For example, Goulding et al. (2012) found the strong mid-IR silicate absorptions in Compton-thick AGNs are typically associated with edge-on disk galaxies or mergers.

IR observations provide clues on the build-ups of the SMBHs. For example, on the scales of the whole galaxy, there is relatively weak relation between the AGN luminosity

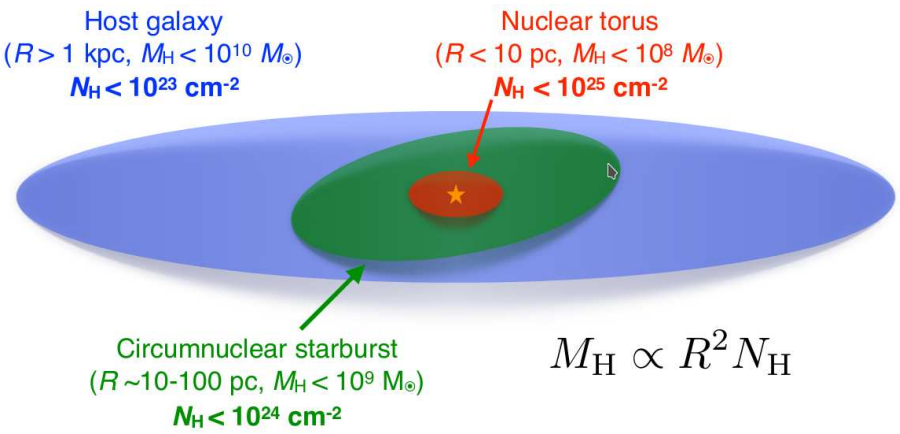


Figure 1.2 A schematic drawing of the different scales of AGN obscuration for a Milky-Way like galaxy. Figure adopted from Hickox & Alexander (2018).

and star formation rate (traced by far-IR emission) for AGNs with moderate luminosities (e.g., Rosario et al. 2012). However, these relationships become tighter at small spatial scales (e.g., Diamond-Stanic & Rieke 2012), indicating that the accreting SMBHs are typically located in a starburst disk on $< 10^2$ pc scales that can provide gas to feed their growth. Evidence of AGN inflows/outflows on such scales has been revealed with submm observations by ALMA, demonstrating the active connections between the circumnuclear torus and the host galaxy ISM (see Section 1.3).

### 1.1.2 Identification of the AGN Population

A complete census of luminous AGN activity is critical to constrain the build-up of SMBHs as a function of cosmic time which can have critical impacts on galaxy evolution. However, due to the large gas and dust surrounding the nuclei, the majority of the AGN population is obscured. Although deep X-ray imaging is frequently used to search for obscured AGNs, the sample is incomplete especially for the Compton-thick objects at high-$z$ (e.g., Del Moro et al. 2016).

Luckily, the opacity of dust grains is a strong function of wavelength: in the IR, the extinction is expected to be at least two orders of magnitude less than that in the optical, making the AGN dust emission, especially in the mid-IR, little affected by obscuration. Meanwhile, regardless of the type of a galaxy, the Rayleigh Jeans tail of the stellar

emission and galaxy dust emission from H II regions always produce a SED minimum at 4–5 $\mu m$, which is in striking contrast with the AGN whose hot and warm dust emission peaks at these wavelengths. In other words, from the change of the mid-IR emission SED, we can identify the existence of AGN, as demonstrated in Figure 1.3. Taking advantage of these features, large sample of AGNs can be picked out with multi-band mid-IR color selections with survey data from e.g., *Spitzer*/IRAC and *WISE* (e.g., Stern et al. 2005; Alonso-Herrero et al. 2006; Mateos et al. 2012; Assef et al. 2013; see Figure 1.4).

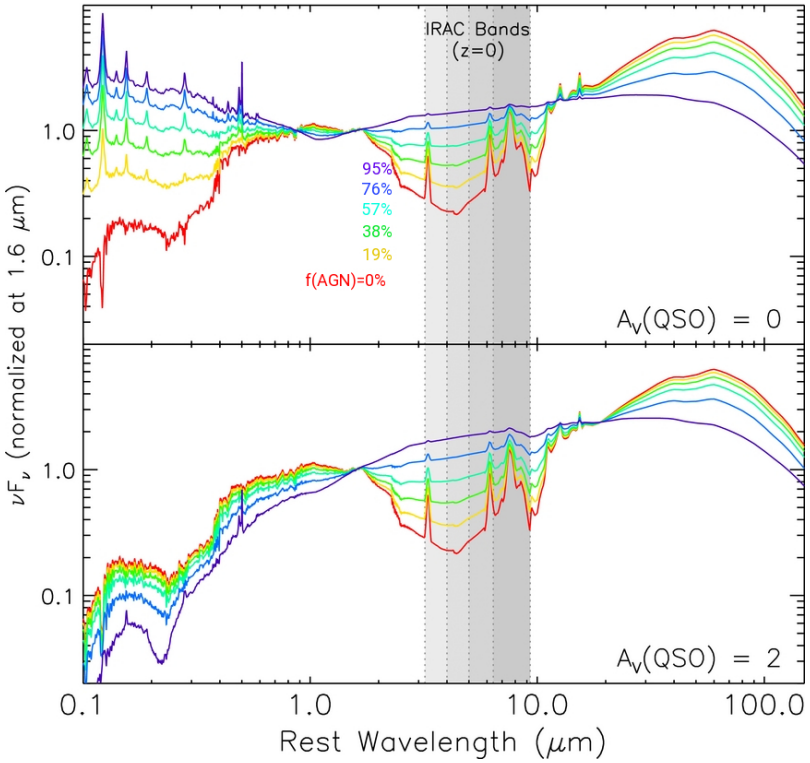


Figure 1.3 Mock composite SEDs with different level of AGN contribution in unobscured case (top panel) and obscured case (bottom panel). The AGN contributions are normalized at 1–10 $\mu m$ of the total emission and the corresponding composite SEDs are shown with different colors. Figure adopted from Donley et al. (2012).

### 1.1.3 Study of the BH-Galaxy Evolution

The discovery of tight correlations between BH mass and host galaxy properties indicate the possible co-evolution of SMBHs and their host galaxies (Kormendy & Ho, 2013, and references therein). One possible mechanism to establish such correlations is through

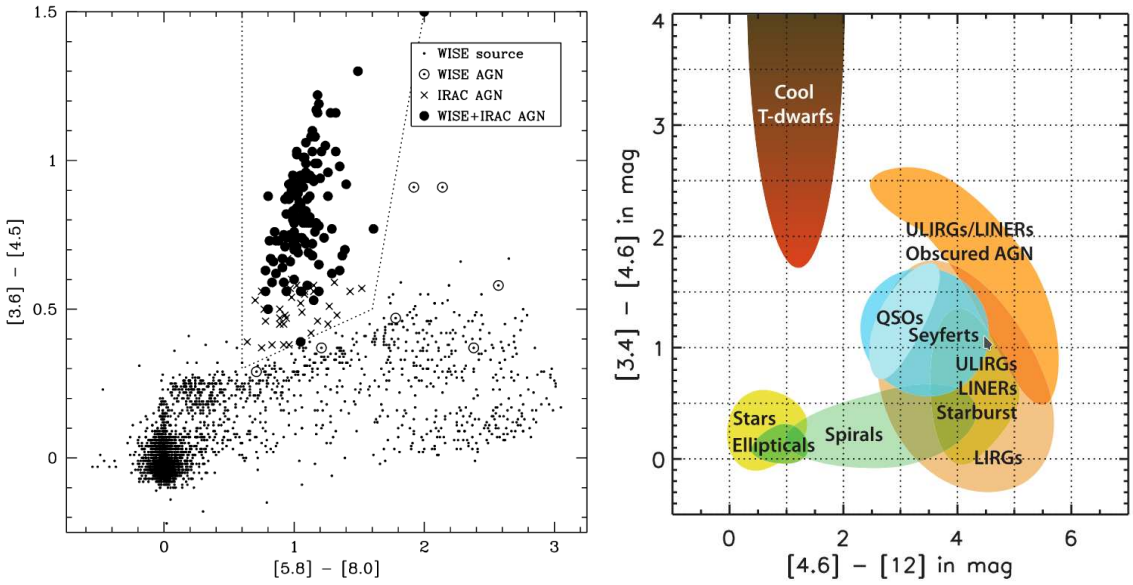


Figure 1.4 IRAC color-color diagram of WISE-selected sources in the COSMOS field (left; Stern et al. 2012) and WISE color-color diagram with the locations of different types of objects (right; Wright et al. 2010)

merging of gas-rich galaxies in which starbursts, quasars, SMBH growth and the formation of red, elliptical galaxies are connected via an evolutionary sequence (e.g., Sanders et al. 1988a; Alexander & Hickox 2012; see Figure 1.5). In this picture, the changes of host galaxy star formation intensity, AGN luminosity and the obscuration level of the central engine should change the observed SED, especially the IR part, of the system.

Many researchers have exploited IR photometric measurements from *Herschel* surveys to search for correlations between the phases of intensive host and black hole growth that finally established the local scaling relations. Since the AGN torus SED peaks in the mid-IR ($\sim$3–20 $\mu m$) and the host star-forming dust emission generally peaks in the far-IR ($\sim$50–70 $\mu m$), the rest-frame far-IR luminosity is frequently assumed to be dominated by the host galaxy and thus used to trace the star formation rates. Figure 1.6 presents a summary of average far-IR luminosities for AGN at different luminosities and redshifts from the review by Lutz (2014). For moderately luminous AGNs at $z < 0.8$, there is no strong evidence for the dependence of SFR on AGN luminosity. But the positive correlation becomes clear for high-luminosity ones ($L_{\rm AGN} \gtrsim 10^{44}\ L_{\odot}$). At $0.8 < z < 2.5$, there is no significant SFR variations for AGNs with a wide range of luminosity but a trend for the

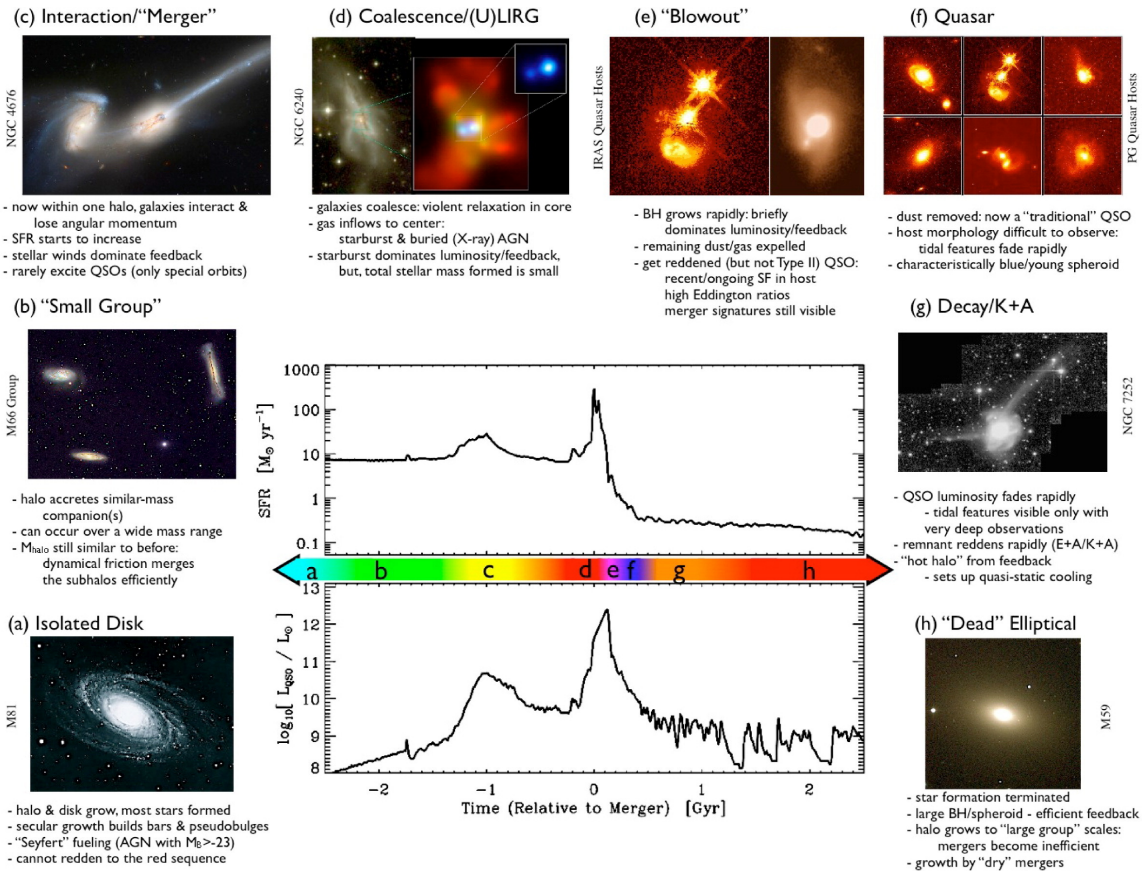


Figure 1.5 Schematic outline of different phases of galaxies under the merger-driven evolutionary scenario. Figure adopted from Hopkins et al. (2008).

increasing SFR with redshift. Powerful $z > 2$ quasars are found to have very active star formations in their host galaxies on average. These results indicate that the BH feeding and star formation are connected by the common gas reservoir and supply over a long galaxy evolution timescale (see review by Lutz, 2014, and references therein).

Detailed analysis of the IR emission helps us to capture the status and growth of the SMBH as well as the host galaxy (e.g., Bongiorno et al., 2007, 2012; Xu et al., 2015b; Lyu et al., 2016; Collinson et al., 2017). With the observational SED constraints and the knowledge of the dust emission of the AGN and galaxy components, we can measure the host galaxy properties (e.g., star formation rate, stellar mass) and AGN luminosity for individual objects from detailed SED decompositions. Some examples are demonstrated in Figure 1.7. With a careful selection of correct templates, the stellar masses constrained

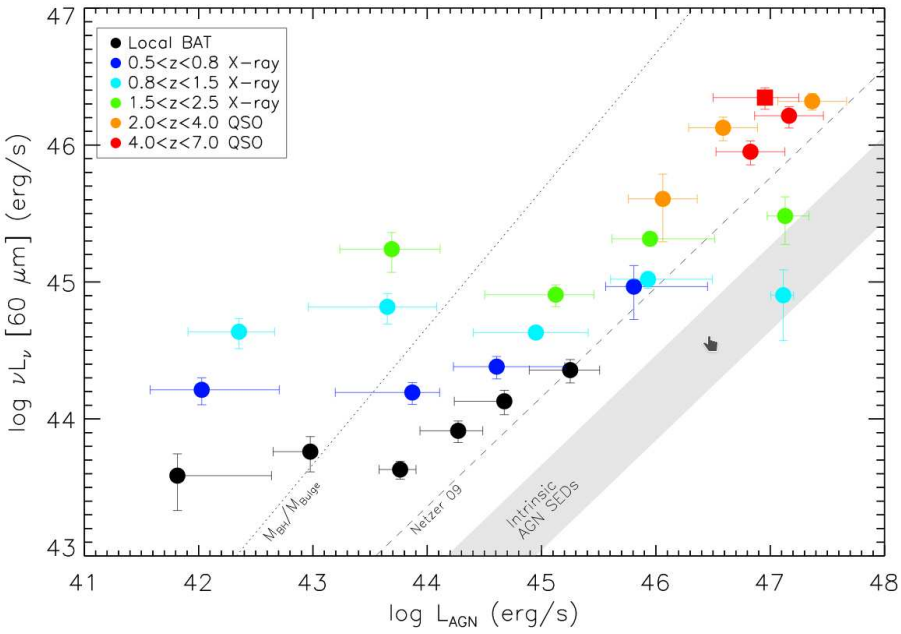


Figure 1.6 The relation of average observed rest-frame far-IR emission (which is assumed to be dominated by the AGN host galaxy) and the bolometric AGN luminosity for objects at different redshifts. Figure adopted from Lutz (2014).

from such SED decompositions are in excellent consistency with the measurements from detailed image decompositions with HST near-IR images, and the SFRs from SED analysis also generally agree with the values from the aromatic (PAH) features in the mid-IR spectra (Lyu et al., 2017; Lyu & Rieke, 2017). From the dust mass measurements, we can approximate the gas mass assuming some gas-to-dust relation (e.g., Shangguan et al., 2018).

### 1.1.4 Some Other Applications

Besides the great importances for the study of AGNs and their host galaxies mentioned above, constraints on the AGN IR properties can be used to measure the Hubble constant. In fact, the dust torus inner radius is determined by the dust sublimation and has a strong linear relation with the square-root of AGN luminosity. Once the torus size can be measured by the dust reverberation technique (see introduction in Section 1.3.4), the AGN luminosity distance can be inferred. Such works have been presented in e.g., Yoshii et al.

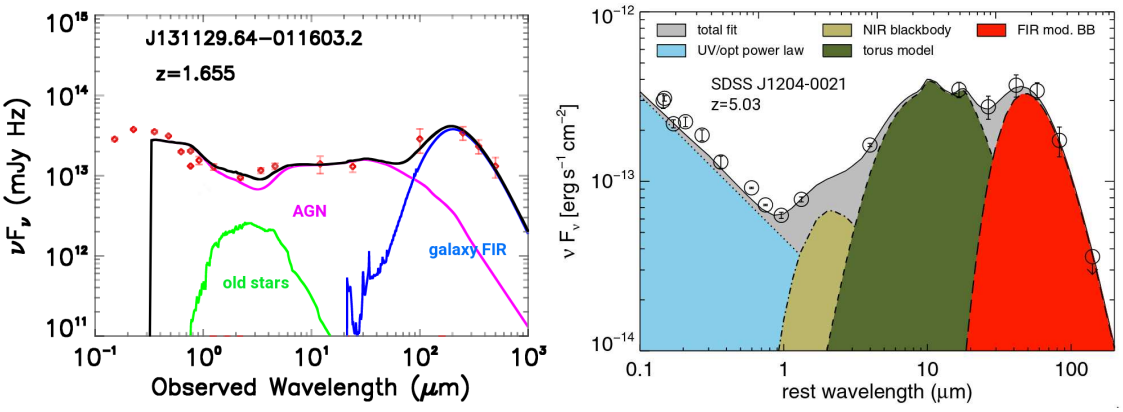


Figure 1.7 SED decomposition examples to retrieve host galaxy properties. The left panel shows the SED of a type-1 AGN at $z = 1.655$ and the corresponding fits of an empirical SEd model (AGN+old_stars+galaxy_IR) from Xu et al. (2015b). The right panel is the SED of an unobscured quasar at $z = 5.03$ with fitting results of an analytical SED model from Leipski et al. (2014).

(2014), finding a $H_0 = 73$ km s$^{-1}$ Mpc$^{-1}$ consistent with the standard estimates.

IR emission of AGNs also provides clues for the properties and evolution of dust grain particles in very extreme environments. For example, Li et al. (2008a) suggested the broadened 10 $\mu m$ silicate emission profile in AGN compared with the Galactic ISM is a result of porous dust formed via grain coagulation in the dense circumnuclear environment of the AGN; Xie et al. (2014) showed clear evidence of crystalline silicate features with mid-IR spectra of some AGNs, which can be interpreted as newly formed dust in the gas near the AGN.

## 1.2 Unresolved Empirical SED Studies

The dust grains in the AGN circumnuclear structures absorb the UV-optical photons from the central engine and re-radiate the energy into the IR bands. Over the last 10–15 years, with the launches of major IR space telescopes (e.g., *Spitzer*, *Herschel*, WISE), photometric surveys and pointed observations enable statistical (and mostly unresolved) characterizations of the IR properties of galaxies and AGNs from the local Universe to the epoch of reionization age and reveal some common patterns as well as large diversities.

### 1.2.1 Quasars and Seyfert Nuclei at Low-redshift

Based on data collected by ground-based telescopes, Rieke (1978) presented the near- to mid-IR ($\sim$1–10 $\mu m$) SEDs of 54 Seyfert galaxies and established the common existence of a strong IR excess emission that was roughly consistent with dust in the gas surrounding the nuclei. By combining the ground-based optical data with UV and IR data from space-based facilities International Ultraviolet Explorer (IUE) and the Infrared Astronomical Satellite (IRAS), Edelson & Malkan (1986) studied the SEDs of AGNs at $\lambda$ $\sim$0.1–100 $\mu m$ and showed the typical appearance of the 3–5 $\mu$m IR bump in both Seyfert galaxies and quasars. Sanders et al. (1989) reported measurements of 109 quasars and further increased the SED wavelength coverage at 0.0003–60000 $\mu m$ ($10^{10}$–$10^{18}$ Hz), showing the similar SED shapes for most objects. These authors also shown that this typical SED can be reproduced by combining the emission from a hot accretion disk at shorter wavelengths and heated dust at longer wavelengths.

Elvis et al. (1994) presented the first quasar SED templates over radio to 10 keV X-ray with attempts to remove the host galaxy stellar contamination and foreground extinction. The average SEDs of radio-loud and radio-quiet quasars were found to be remarkably similar from the X-ray to the far-IR bands, featuring two SED bumps in the UV-optical bands and IR bands separated at a local minimum at $\lambda \sim 1.3$ $\mu m$ (see Figure 1.8). Later studies of the average quasar SED with better data and/or large sample reported strikingly similar results from the UV to the mid-IR bands, regardless of the sample selection (e.g., Richards et al., 2006; Shang et al., 2011; Krawczyk et al., 2013; Scott & Stewart, 2014) (see Figure 1.9). Such a result provides support for the similar structures of various AGN (continuum light emitting) components for most quasars. In the far-IR/submm bands, the situations are less clear with a large SED dispersion reported in the literature (see discussions in Lyu & Rieke, 2017, and references therein).

Because of the low AGN luminosity of Seyfert nuclei, the contamination of host galaxy emission is typically significant so that the shape of AGN-heated SED of Seyfert galaxies is difficult to characterize. For very nearby targets, the galaxy contamination in the SED can be reduced by obtaining high spatial resolution data (sub-arcsec or arcsec) over a wide

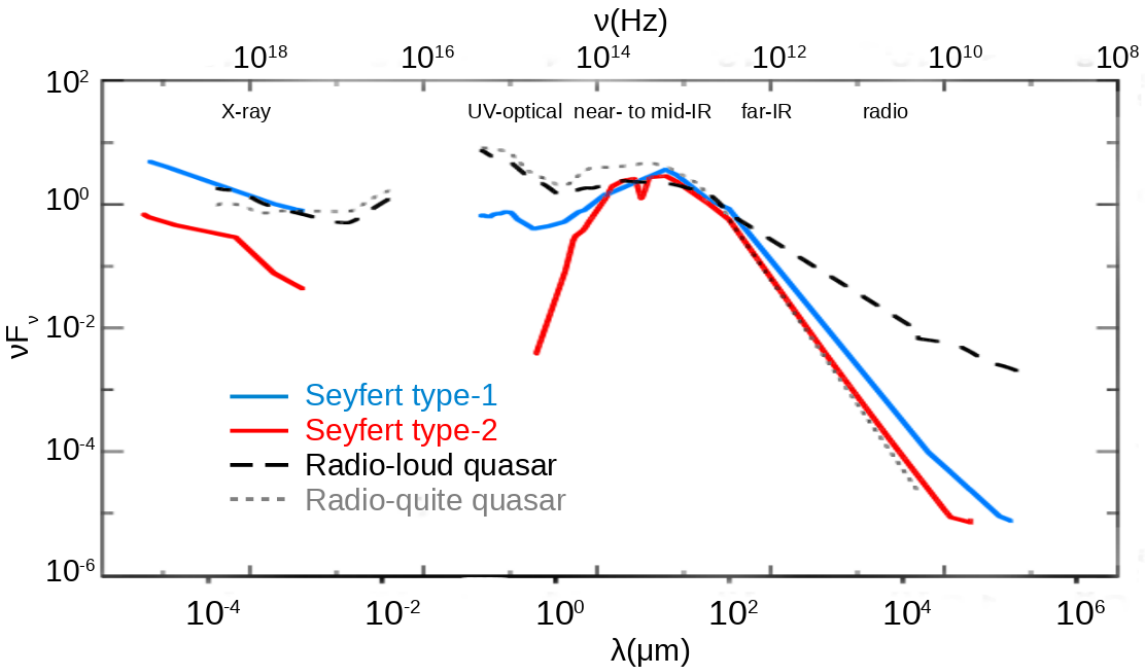


Figure 1.8 Comparison of the SEDs of Seyfert type-1 (red), type-2 (blue) nuclei from Prieto et al. (2010) and radio-loud (dash-line), radio-quiet (dots) quasars from Elvis et al. (1994).

range of wavelengths (e.g., Alonso-Herrero et al., 2003; Prieto et al., 2010). In Figure 1.8, we also present SED templates for the Seyfert type-1 and type-2 AGNs from Prieto et al. (2010). The IR SED shape at $\lambda \gtrsim 2\ \mu m$ is similar for both Seyfert types. The SED of Seyfert type-2 nuclei presents a sharp decay from 2 $\mu m$ to the optical wavelengths while type-1 shows a decay shortward of 2 $\mu m$ but recovers quickly at $\lambda \lesssim 1\ \mu m$ with the appearance of the UV-optical big blue bump. Such SED differences are consistent with the nuclear obscuration by a compact torus in type-2 AGNs Antonucci (1993).

Some resemblance exists of the averaged SEDs between Seyfert nuclei and quasars: all of them feature a strong IR bump with most energy released at 2–100 $\mu$m and comparable width. However, compared with the quasar templates in Elvis et al. (1994), the average SED of Seyfert-1 nuclei in Prieto et al. (2010) has relatively weaker and redder UV-optical continuum emission with a steeply rising power-law SED from near- to mid-IR bands. In contrast with quasars, Seyfert-2 SEDs have a rapidly dropping near-IR emission, very little UV-optical emission and weaker X-ray emission. These differences can be explained if the

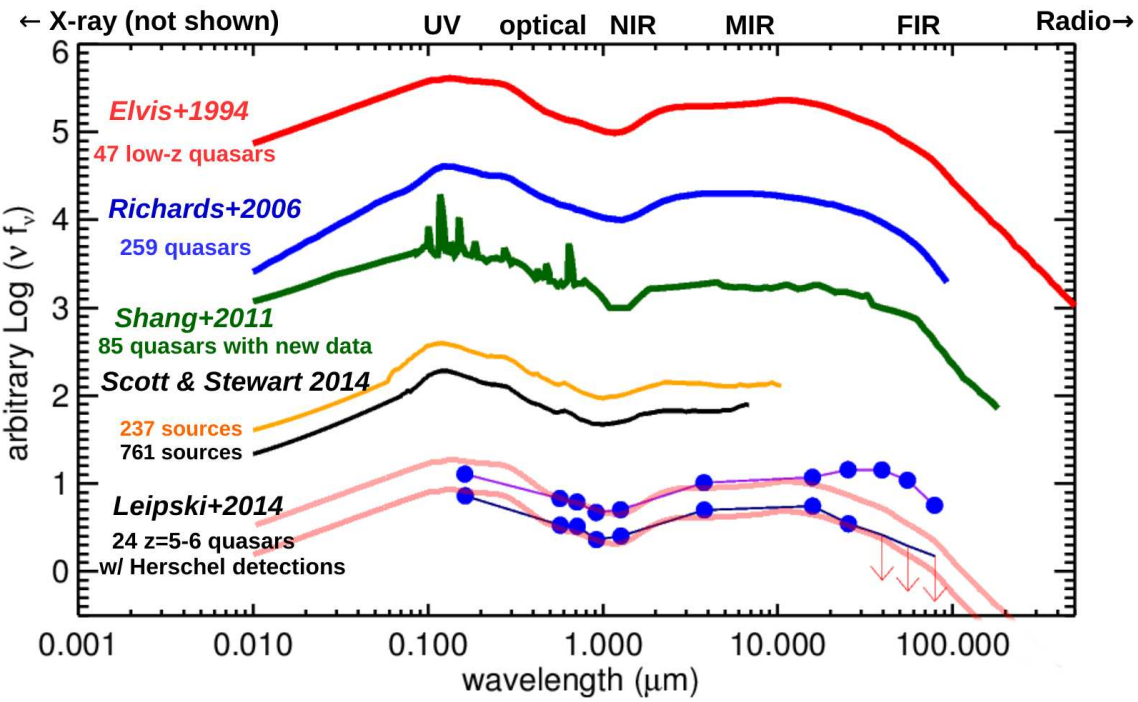


Figure 1.9 Comparison of empirical average SED templates derived for type-1 quasars from Elvis et al. (1994), Richards et al. (2006), Shang et al. (2011) and Scott & Stewart (2014) as well as the average SEDs composed for $z \sim$5–6.5 quasars with *Herschel* detections from Leipski et al. (2014).

obscuration level of the central engine increases gradually from quasars to Seyfert-1 nuclei and then to Seyfert-2 nuclei.

### 1.2.2 High-redshift AGNs

With the multi-wavelength data collected from large and/or deep sky surveys with e.g., *Chandra*, XMM-*Newton*, GALEX, SDSS, 2MASS, UKIDSS, *WISE*, *Spitzer*, *Herschel*, AGN SED construction for statistical samples at high-$z$ has became possible. The SEDs at $\lambda \lesssim 24\ \mu m$ for unreddened type-1 quasars up to $z \sim 3$ are found to be well described by the Elvis et al. (1994)-like AGN template, no matter if the parent sample is optically selected (e.g., Krawczyk et al., 2013), or combined with mid-IR selection (e.g., Richards et al., 2006), or X-ray selected (e.g., Elvis et al., 2012). Even at $z \gtrsim$5–6, most of the spectroscopically confirmed quasars have the similar Elvis-like SEDs of low-$z$ objects at $z \sim 0$ (e.g., Jiang et al., 2006; Wang et al., 2008b; Leipski et al., 2014). Little variations on the

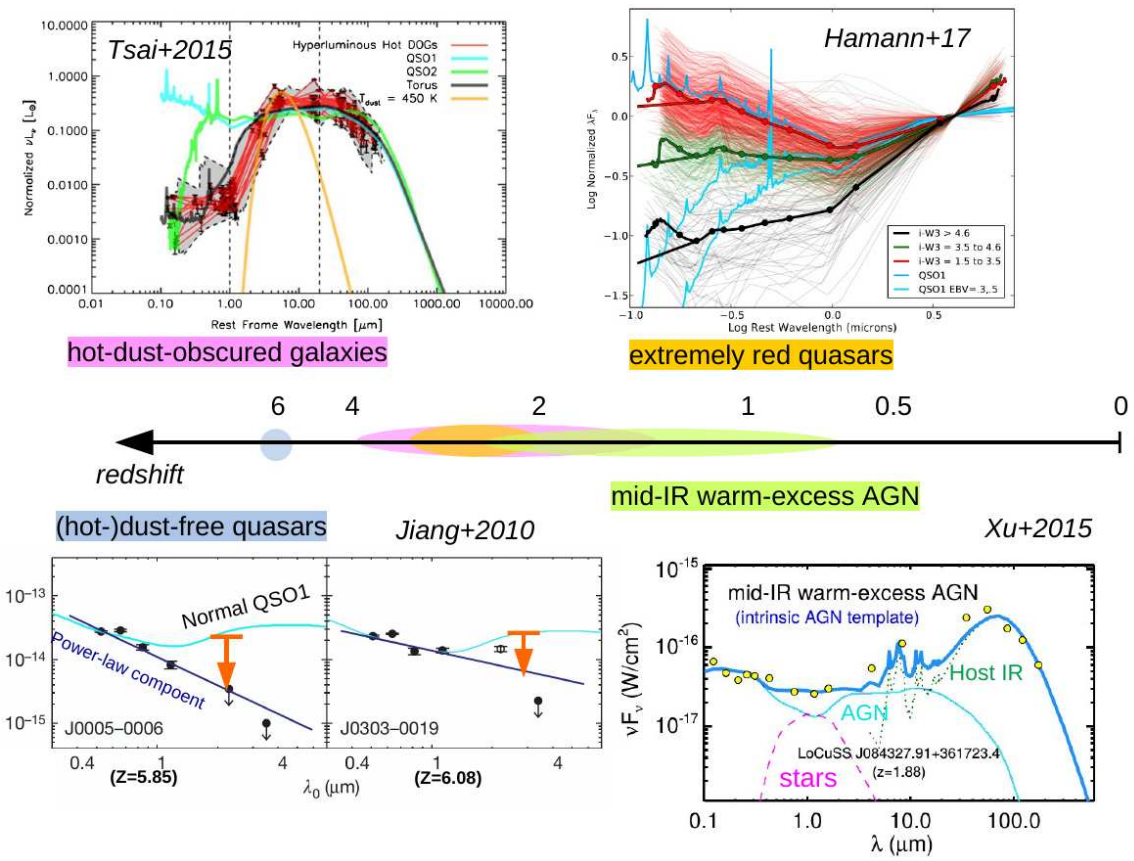


Figure 1.10 Example high-$z$ type-1 AGNs with abnormal SED features, including dust-free quasars from Jiang et al. (2010), hot-dust-obscured galaxies from Tsai et al. (2015), extremely red quasars from Hamann et al. (2017) and mid-IR warm-excess AGNs from Xu et al. (2015b).

mean AGN SED shape of quasars have been found across broad ranges of luminosity and redshift (e.g., Wang et al., 2008b; Elvis et al., 2012; Hao et al., 2014).

However, large variations of type-1 AGN SEDs have been revealed among individual objects or some specific population with dedicated selection criteria. Some examples are shown in Figure 1.10: Jiang et al. (2010) have reported the non-detection of the hot dust emission for two $z \sim 6$ quasars whose UV–to–mid-IR SEDs can be matched by a single power-law; Eisenhardt et al. (2012) and Wu et al. (2012) identified a population of very luminous IR galaxies hosting broad-line AGNs obscured by hot dust at $z \sim$1.5–4, namely hot-dust-obscured galaxies or hot DOGs with a peculiar SED featuring very strong hot dust emission; from the SDSS Baryon Oscillation Sky Survey and WISE survey, Ross et al.

(2015) found a population of extremely red type-1 quasars at $z \sim$2–3, whose SEDs cannot be reproduced by reddening the normal blue quasar template with the commonly used SMC-like extinction curve (Hamann et al., 2017); Xu et al. (2015b) investigated the behaviors of the Elvis-like AGN template at $z \sim$0.5–2: although it worked for most objects, there are some cases presenting strong mid-IR excess emission that cannot be reproduced by the empirical SED model. We are still lacking an understanding of the physical reasons behind these SED variations.

## 1.3 Spatially and Temporally Resolved Studies

Targeted high-spatial-resolution investigations of nearest AGNs have been carried out with IR telescopes from the ground, making detailed study of the size, morphology, column density and dynamics of the AGN obscuring structures and their relation with the host ISM possible. Time-resolved analysis, especially the dust reverberation mapping, also offers many critical constraints on the AGN circumnuclear structures.

### 1.3.1 IR Images and Spectra from Single Telescopes

Near-IR high-resolution images from HST and ground-based 10-meter telescopes with AO reveal evidence for large-scale dust filaments crossing the center of nearby AGNs, which can obscure the nuclei given a large optical depth and/or a weak AGN (e.g., Prieto et al., 2005, 2010, 2014). In addition, there is evidence that the nuclear dust filaments run from kpc distance to the central few pc, providing evidence on how the ISM materials are transported to feed the BH (e.g., Prieto et al., 2005).

A lot of progress has also been made in the mid-IR bands. The existence of extended dust over 50 pc has been reported in the type-2 AGN NGC 1068 in 1990s (Braatz et al., 1993; Cameron et al., 1993; Bock et al., 2000) (see Figure 1.11). Similar behaviors are also found in other type-2 AGNs like Cygnus A (Radomski et al., 2002), Circinus (Packham et al., 2005; Reunanen et al., 2010), NGC 1386 (Reunanen et al., 2010), IC 5063 and MCG-3-34-64 (Hönig et al., 2010), as well as type-1 AGN NGC 4151 (Radomski et al., 2003). In general, the mid-IR extended emission traces the narrow-line regions or has identi-

cal location as outflows. Recently, Asmus et al. (2014, 2016) presented a survey of 149 AGNs with ground-based 10-m telescope mid-IR imaging observations. 21 of these objects have extended mid-IR emission on single-dish images. In 18 objects, the extended MIR emission aligns with the position angle of the system axis, as established by [O III], radio, polarization, or maser-based measurements.

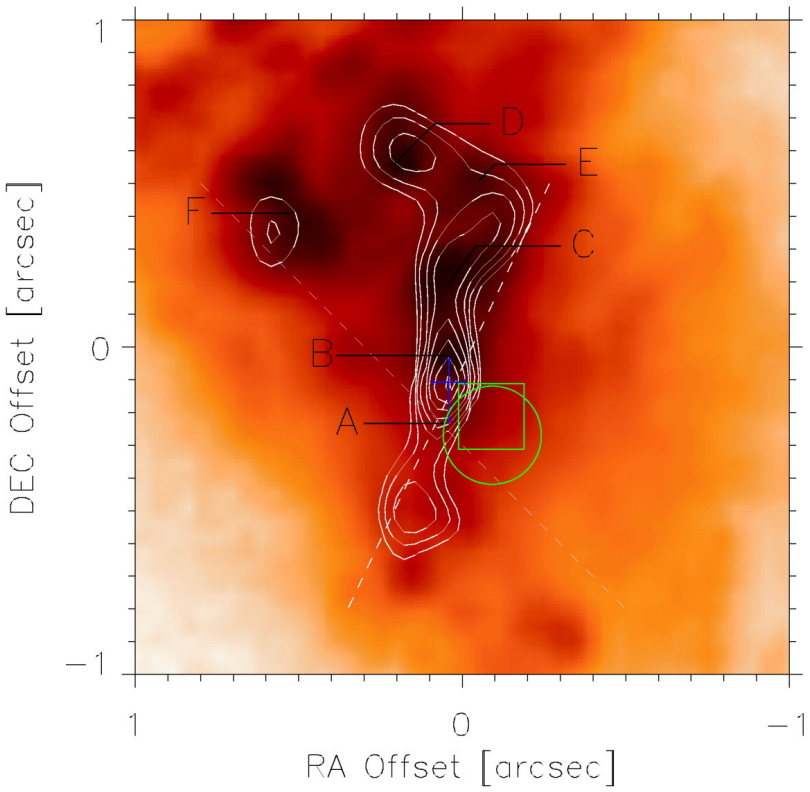


Figure 1.11 For NGC 1068, its mid-IR emission at 12.5 $\mu$m has an extended morphology (white contours) that is co-spatial with the optical [O III] emission (background image). The location of the central engine inferred from UV polarimetry is indicated as blue cross. The green square and circle denote the AGN location indicated at near-IR and mid-IR. Figure from Bock et al. (2000).

García-González et al. (2016) and Lutz et al. (2016) studied the size of the far-IR emitting regions of Seyfert nuclei and quasars with *Herschel* observations, finding that the extended far-IR emission is due to host star formation.

### 1.3.2 Interferometry Observations

By coherently combining the light from the same object observed by different telescopes/receivers, the AGN dusty structures can be studied via the long-baseline interferometry. Within the last $\sim$ 15 years, about 50 AGNs have been observed in the near- or mid-IR with the relevant instruments on the Very Large Telescope Interferometer (VLTI, maximum baseline $\sim$ 130m ) on Paranal in Chile and the Keck Interferometer (KI, maximum baseline $\sim$ 85m) on Mauna Kea in US and offer constraints on the dust size and morphology. In the sub-millimeter (submm) bands, the Atacama Large Millimeter Array (ALMA) enables high-resolution ($\sim$0.02 arcsec at $\lambda > 400\ \mu m$) investigations of the morphology, column density and dynamics of obscuring structures in nearby AGNs. Below is a summary of some key results.

*Near-IR Bands* With KI and AMBER at VLTI, the continuum emission of the dust sublimation region has been marginally resolved around 10 nearby AGNs in K-band and the sizes show a relatively tight correlation with $L_{\rm AGN}^{1/2}$ (Swain et al., 2003; Kishimoto et al., 2011a, 2013; Weigelt et al., 2012). Compared with the sizes obtained from dust reverberation mapping, the IR interferometry inferred sizes are slightly larger, which have been used as a probe for the hot dust radial distribution (Kishimoto et al., 2011a). The second-generation near-IR interferometer GRAVITY at VLTI significantly improved sensitivity and coverage and new hot dust measurements of 8 AGNs have been recently reported (GRAVITY Collaboration et al., 2019), as shown in Figure 1.12. Finally, the possible K-band dust size change of NGC 4151 over a timescale of $\sim$6 years has been explored for NGC 4151 with multi-epoch near-IR interferometry observations (Pott et al., 2010; Kishimoto et al., 2013), which provide tentative evidence for the destruction and reformation of the innermost dust structure.

*Mid-IR Bands* For the cooler dust, the AGN mid-IR ($N$ band with $\lambda \sim 8$–$13\ \mu m$) sizes constrained with MIDI at VLTI have a large scatter around the $R$–$L^{1/2}$ relation (e.g., Kishimoto et al., 2011a), indicating the intrinsic differences in their dust structures. In fact, there is a strong evidence for a polar-elongated dust component, instead of the ex-

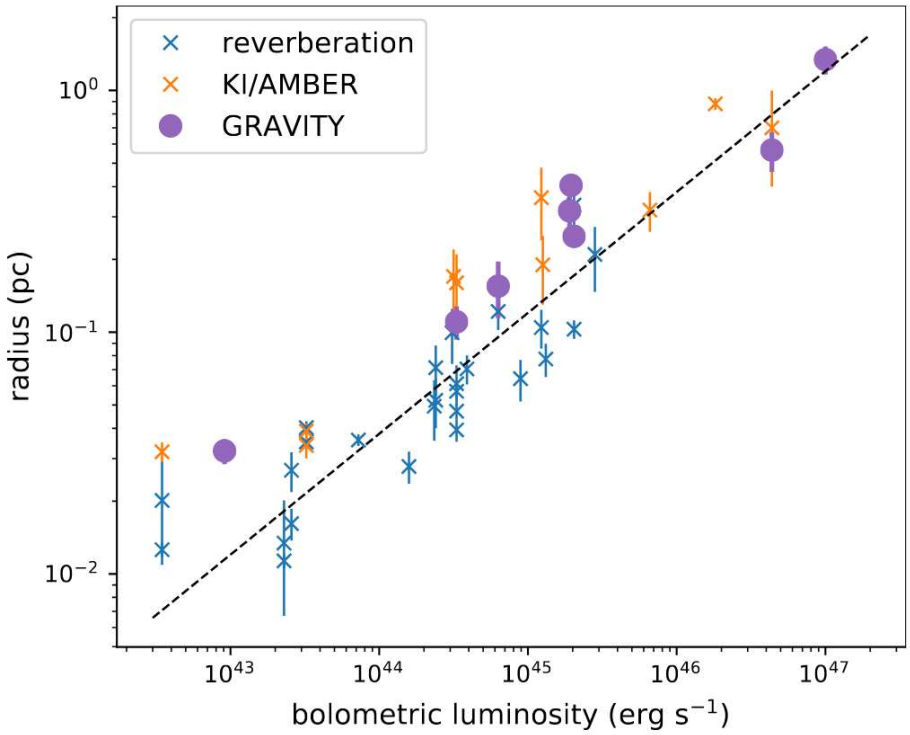


Figure 1.12 Torus size measured from near-IR interferometry instruments as a function of AGN luminosity. Figure from GRAVITY Collaboration et al. (2019).

pected equatorial torus-like structures, that could dominate the AGN mid-IR emission (e.g., Hönig et al., 2012, 2013; Tristram et al., 2014) (see examples in Figure 1.13). Such behaviors have been detected in both type-2 (e.g., NGC 1068, Circinus galaxy, NGC 424; see López-Gonzaga et al. 2016 and references therein) and type-1 (NGC 3783, NGC 5506 and ESO 323-G77; Hönig et al. 2013; López-Gonzaga et al. 2016; Leftley et al. 2018), indicating the common existence of a warm polar dust component at (sub)-ten parsec scales at least for the nearby AGNs.

*Sub-mm Bands* Due to the quickly dropping SED in the submm bands and the possible contamination of the jet, a direct detection of the torus dust submm emission with ALMA is not an easy task (e.g., see discussions in Pasetto et al., 2019). In fact, NGC 1068 is the only AGN so far with reported torus dust continuum emission that spans $\sim 4 \times 7$ pc$^2$ (e.g., García-Burillo et al., 2016; Gallimore et al., 2016). Typically, gas emission lines from the torus warm molecular gas, such as CO, HCO+ and HCN, are used to trace the

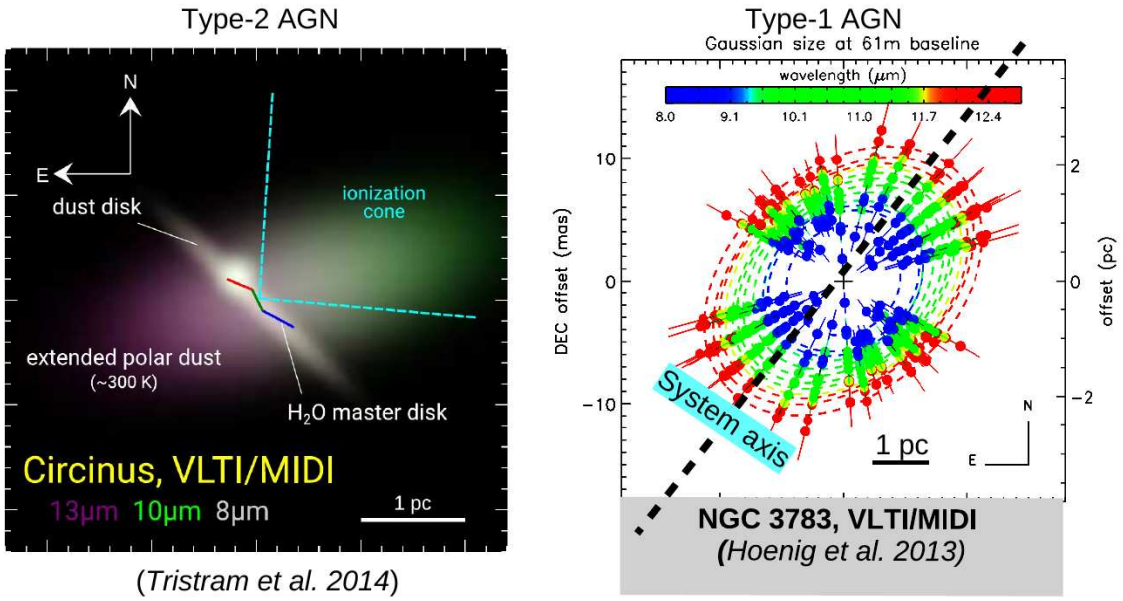


Figure 1.13 Example Seyfert galaxies with detected mid-IR polar dust emission. Figures are modified based on the original versions in Tristram et al. (2014) and Hönig et al. (2013).

torus morphology and dynamics. For the central 2″of NGC 1068, the dust and molecular torus is found to extend at 7-10 parsec with $M_{\rm gas} \sim 10^5\ M_\odot$ and $M_{\rm dust} \sim 1600\ M_\odot$ and it is located in a circumnuclear disk with recent star formation activity at 300×200 pc (e.g., Gallimore et al., 2016; Imanishi et al., 2018). The dynamics of NGC 1068 molecular gas is found to be rotating but highly inhomogeneous with large velocity dispersions (e.g., Imanishi et al. 2018; see Figure 1.14), possible linked to the outflows on scales 50 pc to 400 pc from the AGN (García-Burillo et al., 2014). Similar studies have been applied for other AGNs with a range of reported torus size (∼5–30 pc), mass ($\sim 10^6$–$10^7\ M_\odot$) and dynamics (rotating, inflows, outflows) (e.g., Izumi et al., 2018; Alonso-Herrero et al., 2018, 2019; Combes et al., 2019).

### 1.3.3 IR Continuum Variability

IR variability of Seyfert galaxies has been investigated as early as 1970s (Pacholczyk, 1971; Penston, 1973; O'Dell et al., 1978; Rieke, 1978). Rieke & Lebofsky (1981) reported the declining IR variability amplitudes of NGC 4151 as a function of wavelength

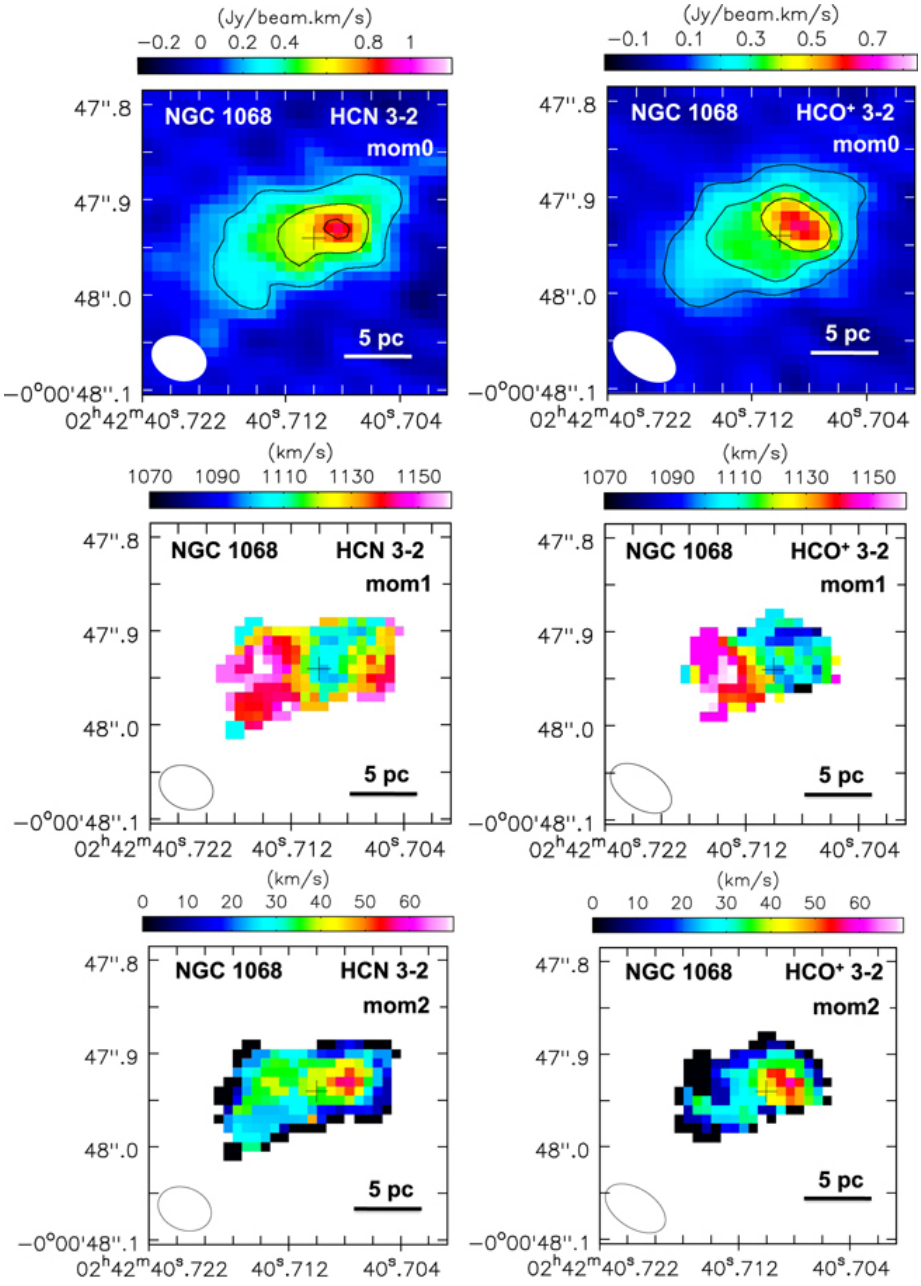


Figure 1.14 ALMA observations of NGC 1068 reveal a compact rotating molecular structure with inhomogeneous morphology and large velocity dispersions. Figure from Imanishi et al. (2018).

and demonstrated the dust thermal origin of its AGN IR emission. Later work by e.g., Clavel et al. (1989) revealed that the near-IR variability of Fairall 9 is consistent with being delayed response of the dust structures to the AGN optical-UV emission variability and initiated the study of AGN torus structure via the dust reverberation mapping technique (to be discussed in the next section). Neugebauer & Matthews (1999) presented a 25-year monitoring of the 1–10 $\mu m$ continuum emission of 25 quasars and showed the correlated variations in all bands. Variability at 10 $\mu m$ has been detected in seven radio-loud quasars and in only one radio-quite quasar, indicating that the mid-IR energy output of radio-quite quasars is very unlikely dominated by nonthermal emission. With the amplitude information of variations in these bands, Neugebauer & Matthews (1999) also inferred the sizes of the dust distribution.

With the advent of space-based IR telescopes like *Spitzer* and *WISE*, high-precision mid-IR photometry was made possible, which has greatly pushed the progresses of this field. Vazquez et al. (2015) reported the first mid-IR dust reverberation study at 3.6 and 4.5 $\mu m$ for a reddened type-1 AGN in NGC 6418. With multi-epoch *Spitzer*/IRAC photometry of the $\sim$ 9 sq. deg. Decadal IRAC Bootes Survey, Kozłowski et al. (2016) characterized the ensemble mid-IR variability of $\sim$ 1500 AGNs with single power-law structure functions (SF) and provided evidence for the more extended emission regions of the IR emission than that of the optical emission. Thanks to the large sky coverage of the *WISE*/*NEOWISE* mission, mid-IR variability study has been able to be extended for specific AGN populations like radio-loud narrow-line Seyfert galaxies (e.g., Jiang et al., 2012) and changing-look quasars (e.g., Sheng et al., 2017) and has revealed many critical constraints on the properties of such objects. The time-series mid-IR data from *WISE*/*NEOWISE* also has fostered the search of obscured quasars (e.g., Assef et al., 2018) and changing look quasars (e.g., Yang et al., 2018).

### 1.3.4 Dust Reverberation Mapping

Since light speed is limited, when the optical emission of the BH accretion disk varies, it takes some time for the signals to arrive at the torus. As a result, the IR light curve of an AGN presents a time lag relative to its optical light curve, which can be used to infer the

geometry of the circumnuclear dust distribution. The delayed IR variation signals have been noted as early as 1970-1980 for NGC 4151 (Penston et al., 1971) and a few other Seyfert-1 nuclei (Lebofsky & Rieke, 1980).

Clavel et al. (1989) presented the first near-IR dust time lag measurement of the type-1 AGN nucleus Fairall 9 with data obtained over a period of 10 yr. Later work by Barvainis (1992) proposed a detailed model for dust heating by the central optical/UV source and matched the spectral and temporal behaviors of the infrared light, showing the dust reverberation was indeed a valid explanation. Similar works have been carried out for other AGNs and the inferred near-IR dust emission sizes follow a $R \propto L_{\rm AGN}^{1/2}$ relation, demonstrating the similar dust sublimation temperature in all these sources (e.g., Oknyanskij & Horne, 2001; Glass, 2004; Suganuma et al., 2006; Lira et al., 2011; Koshida et al., 2014; Pozo Nuñez et al., 2014; Ramolla et al., 2018; Mandal et al., 2018; Minezaki et al., 2019). As shown in Figure 1.15, Minezaki et al. (2019) presented a most recent $K$-band radius-luminosity relation for the innermost dust tori for Seyfert galaxies and quasars over four orders of magnitude in luminosity, indicating the common existence of a dust structure around the AGN. In addition, the inferred K-band torus sizes are systematically larger than the broad line regions, supporting the classical AGN unification (e.g., Suganuma et al., 2006; Koshida et al., 2014; Minezaki et al., 2019).

Besides the constraining torus size, long-term variations of the dust-reverberation lags for a few AGNs (NGC 4151, Mrk 590) have also been studied (Koshida et al., 2009, 2014; Kokubo & Minezaki, 2019) and the changes of the inferred dust emission sizes as a function of time have been interpreted as the torus structure evolution due to AGN optical variability (but see Schnülle et al. 2015). With the first spectroscopic dust reverberation study, Landt et al. (2019) recently showed the similar spectral shape at $\lambda \gtrsim 1\ \mu m$ of NGC 5548 and suggested that both the IR emission and variations are dominated by the same dust component.

## 1.4 Modeling Efforts

Given the critical role of AGN IR emission and the ample observational constraints, various ad-hoc and theoretical models have been developed to either match the IR observations

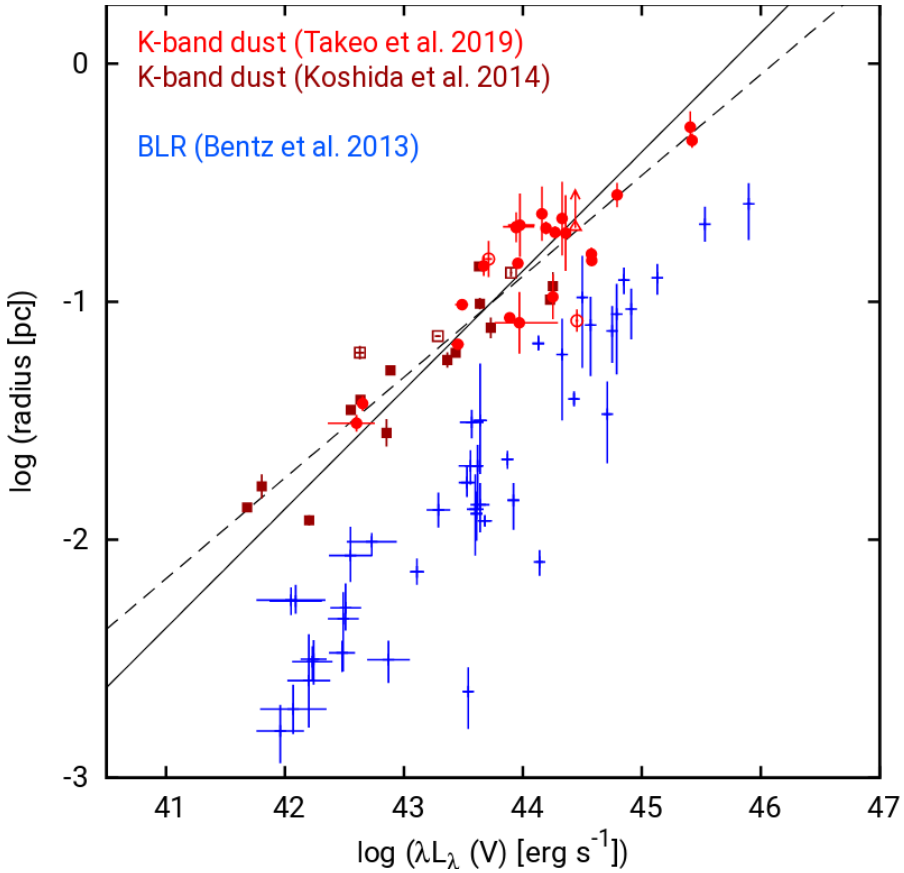


Figure 1.15 Radii of the dust torus innermost region and the broad line region as a function of AGN V-band luminosity. Figure adaped from Minezaki et al. (2019).

or to obtain physical understandings of the corresponding obscuring structures.

### 1.4.1 Phenomenological Models

Many ad hoc models with dust radiative transfer calculations have been constructed to produce the IR SED and/or images of the AGN circumnuclear dust structures at different wavelengths. Depending on the assumption of the torus dust distribution, they can be broadly classified in to continuous (or smooth) torus models (e.g., Pier & Krolik, 1992; Granato & Danese, 1994; Efstathiou & Rowan-Robinson, 1995; Dullemond & van Bemmel, 2005; Fritz et al., 2006; Jud et al., 2017), torus clumpy models (e.g., Rowan-Robinson, 1995; Heymann & Siebenmorgen, 2012; Stalevski et al., 2012; Hönig et al., 2006; Dullemond & van Bemmel 2005; Schartmann et al., 2008; Nenkova et al., 2008a,b), or hybrid (clumpy+smooth) torus

models (e.g., Siebenmorgen et al., 2015; Stalevski et al., 2016). Motivated by the discovery of AGN mid-IR polar dust, a few new models incorporating a polar dust component to match the morphology information have been developed (e.g., Hönig & Kishimoto, 2017; Stalevski et al., 2017, 2019).

Figure 1.16 provides a summary of the key parameters of the dust distribution typically assumed in these ad hoc torus models. All of them assume the dust distribution is axisymmetric and the size of the torus inner wall is determined by dust sublimation. In addition, other key parameters include the torus outer radii, the dust density profile (radial and angular directions) and the opening angle. For clumpy dust distribution, more parameters are introduced to describe the column density of individual clumps, the filling factor and/or the fraction of dust in the clumps (for hybrid models). In terms of dust grain properties, most of these models adopt the classical silicate-graphite dust mixture with normal grain size distribution in the ISM of the Milky Way, but variations with large dust grains or different grain species have been also considered (e.g., Schartmann et al., 2008; Hönig & Kishimoto, 2017). With the introduction of central source radiation (whose SED is typically assumed to be a broken power-law and the emission anisotropy is considered in some cases, such as Stalevski et al. 2016), dust radiative transfer calculations are carried out and the SEDs (and images) are produced for different parameter values. Some example torus model spectra are shown in Figure 1.17.

The model SEDs produced by these models have been widely adopted to fit the IR observations with SED decomposition techniques, aiming to put constraints on the AGN circumnuclear dust structures (e.g., Ramos Almeida et al., 2009, 2011), infer host galaxy properties (e.g., Leipski et al., 2014; Ciesla et al., 2015), or even identify the AGN existence (e.g., Leja et al., 2018). However, the strong degeneracy in these models and their parameter spaces greatly undermines the validity of the final results, especially for the constraints on AGN torus. Under the same parameter grids, Feltre et al. (2012) compared the smooth torus model by Fritz et al. (2006) and the clumpy torus model by Nenkova et al. (2008a). They showed that the most of the model SED differences come from the model assumptions (e.g., primary source, dust compositions) rather than from the dust distribution (smooth or clumpy) and ambiguities are common for deciding which model better

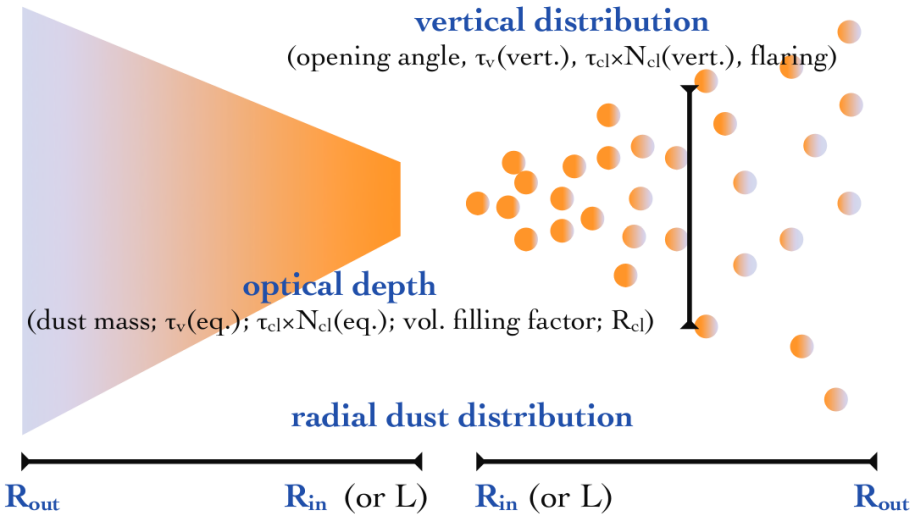


Figure 1.16 The sketch of typical setup of a torus model in a smooth (left) and clumpy (right) case. Figure is from Hönig et al. (2013).

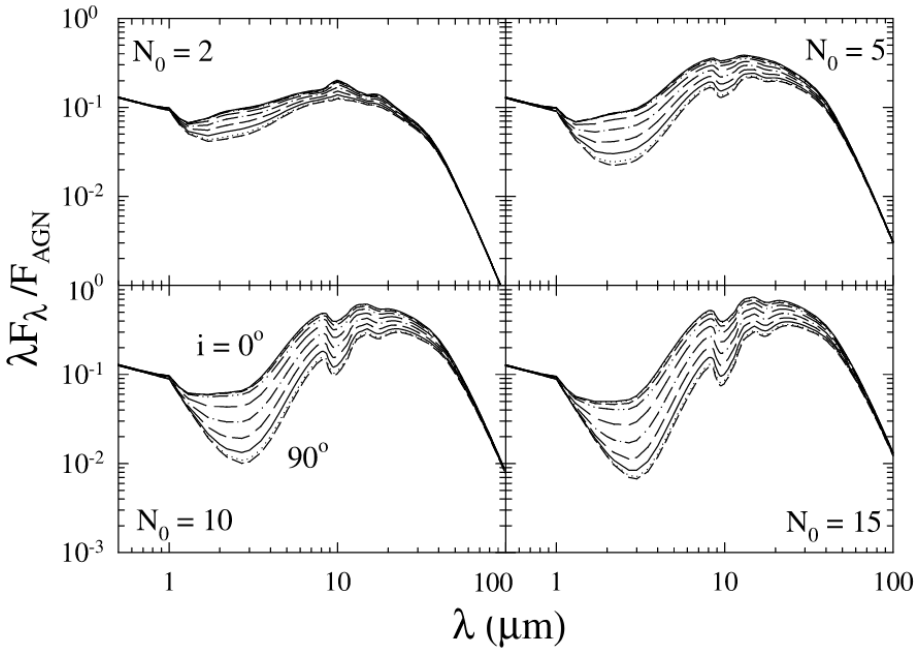


Figure 1.17 Example clumpy torus continnum spectra as a function of inclination angle (*i*) for different assumptions of the total number of clouds along a radial equatorial ray. Other parameters are fixed. Figure adopted from Nenkova et al. (2008b)

matches the SED observations. González-Martín et al. (2019a,b) discussed how to discriminate six popular torus models and explored if the model parameters can be robustly constrained from observations. Although their differences can be revealed from synthetic IR spectra, but the performance to match real data (i.e., *Spitzer*/IRS spectra of 110 AGNs) is quite limited. In fact, none of them can produce good fits for $\gtrsim 50\%$ of the sample and large residuals always exist irrespective of the model used. The only relatively well-constrained parameter is the total dust mass, which is actually trivial given its strong correlation with AGN IR luminosity.

### 1.4.2 Theoretical Models

To address the formation, stability, shape and evolution of the torus, many theoretical models have been developed by realizing physical processes such as cloud motions and collisions, dust radiation pressure, star-formation driven turbulence, supernova explosions, AGN and stellar feedback (e.g., Krolik & Begelman, 1988; Beckert & Duschl, 2004; Vollmer et al., 2008; Wada et al., 2009; Wada, 2012; Wada et al., 2016; Hönig, 2019). Compared to the above phenomenological models that generally ignore the connection between the torus and its surrounding, theoretical models provide more realistic descriptions of the circumnuclear dust structures and provide physical insights (see reviews by e.g., Netzer 2015).

A recent example model is presented in Wada et al. (2016), who have studied the structures and dynamics of molecular, atomic, and ionized gases around a low-luminosity AGN with a small black hole ($2 \times 10^6\ M_\odot$) with 3D radiation-hydrodynamic simulations. This model includes AGN outflows driven mainly by the radiation pressure of dust and X-ray heating, and stellar feedback with the energy released from supernovae in a circumnuclear gas disk near the equatorial plane. As demonstrated by these authors, the circulation of gas inflows and outflows results in a radiatively-driven "fountain" and forms a geometrically thick disk dominated by dense molecular gas that spans the scale of a few to tens of parsecs, which can provide the typical AGN obscuration. In addition, the AGN ionization cone is composed of bipolar outflows of inhomogeneous, diffuse ionized gas surrounded by a geometrically thick atomic gas, which can explain the mid-IR polar dust emission discovered by interferometry observations. The resulting SED of such a model can also

match the observed SED of the Circinus galaxy with a large inclination angle. Figure 1.18 shows the face-on and edge-on gas density distribution in one such model in Wada et al. (2016).

With the advent of zoom-in refinement techniques, the origin and evolution of AGN obscuration has been explored by hydrodynamic simulations of the interaction of feedback from AGN and the galactic multiphase ISM (Hopkins et al., 2012, 2016; Trebitsch et al., 2019). For example, Hopkins et al. (2016) investigated BH accretion and feedback in gas-rich environment at radii $\sim 0.1$–$100$ pc around a black hole with quasar-like luminosity. With an explicit treatment of SF and stellar feedback, the host ISM is turbulent and inhomogeneous with a morphology described in the upper panels of Figure 1.19. After introducing the AGN feedback (high-velocity winds from the central engine), the gas (and dust) in the polar region is evacuated by the AGN winds, resulting in a full unobscured view of the BH accretion disk, and self-consistently producing a torus-like morphology (lower-right panel in Figure 1.19). The gas column density of this structure spans from $\sim 10^{22}$–$10^{26}$ cm$^{-2}$, consistent with typical measurements of AGN X-ray obscuration (e.g., Ricci et al., 2017b).

### 1.4.3 SED Models for Composite Galaxies

In most cases, host galaxy emission contaminates the AGN-heated IR emission, so that proper models to reproduce or match the composite galaxy SEDs are typically desired. For most such SED models, different components (stellar emission, host galaxy IR emission, AGN) are treated separately and linearly combined. Some public available codes include, e.g., SED3FIT (Berta et al., 2013), CIGALE (Boquien et al., 2019), AGNfitter (Calistro Rivera et al., 2016) and Prospector-$\alpha$ (Leja et al., 2018), whose AGN component is commonly adopted from one of the torus phenomenological models. Due to the very large number of free parameters, Bayesian inference is commonly used to decide the final fitting results (see example in Figure 1.20). Simpler SED models based on empirical templates are also available, such as DecompIR (Mullaney et al., 2011) and DeblendIRS (Hernán-Caballero et al., 2015). Finally, some models have incorporated dust radiative transfer calculations to study if the AGN could heat the surrounding interstellar medium

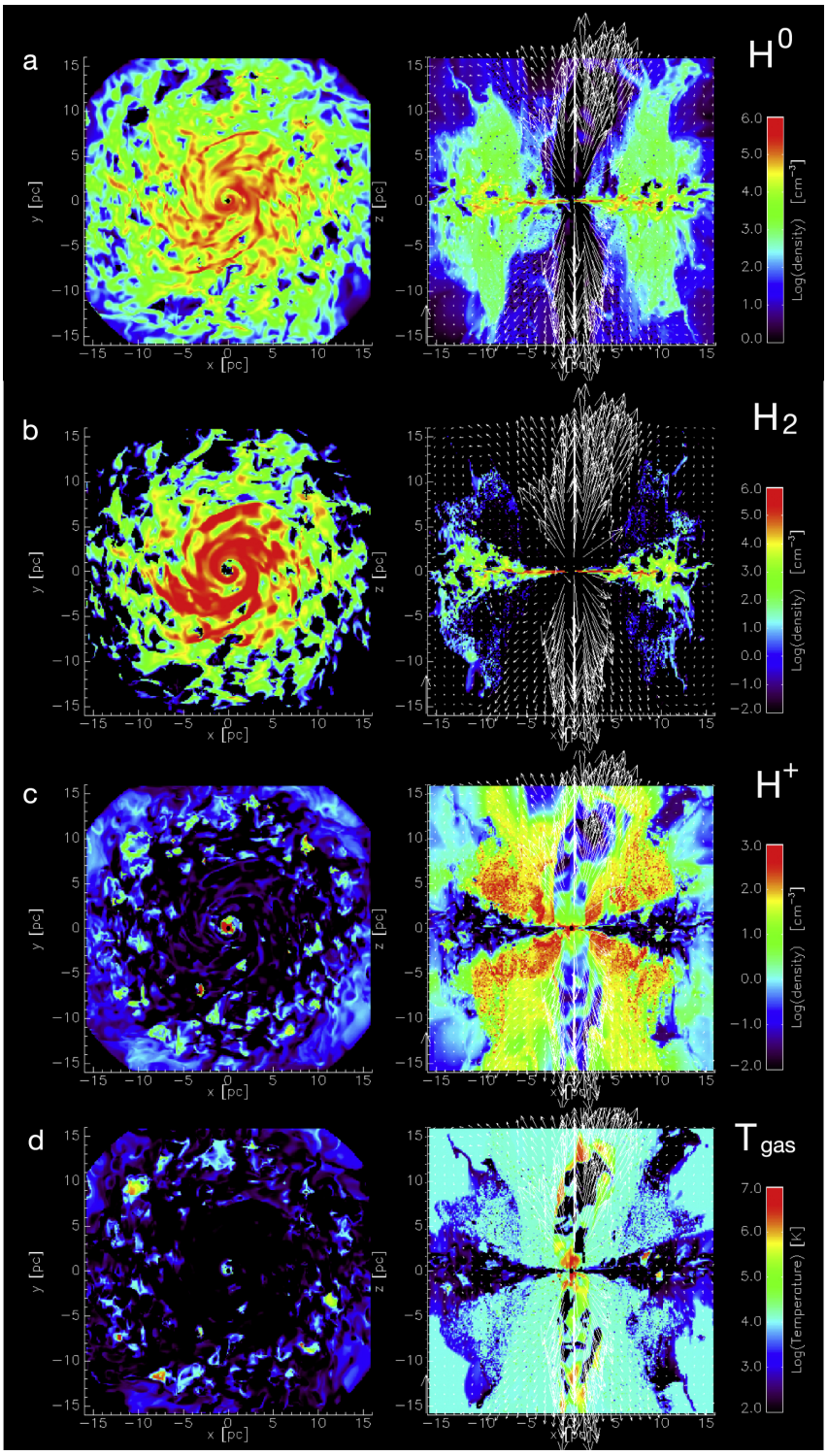


Figure 1.18 The AGN torus-like structures can be a dynamical radiatively-driven "fountain". Morphology of atomic gas ($H^0$), molecular gas ($H_2$), ionized gas ($H^+$) and gas temperature ($T_{gas}$) is presented from the top to the bottom. The left panels are face-on views and the right ones are edge-on views. Color represents gas density or temperature (red for the highest and black for the lowest). Figure from Wada et al. (2016).

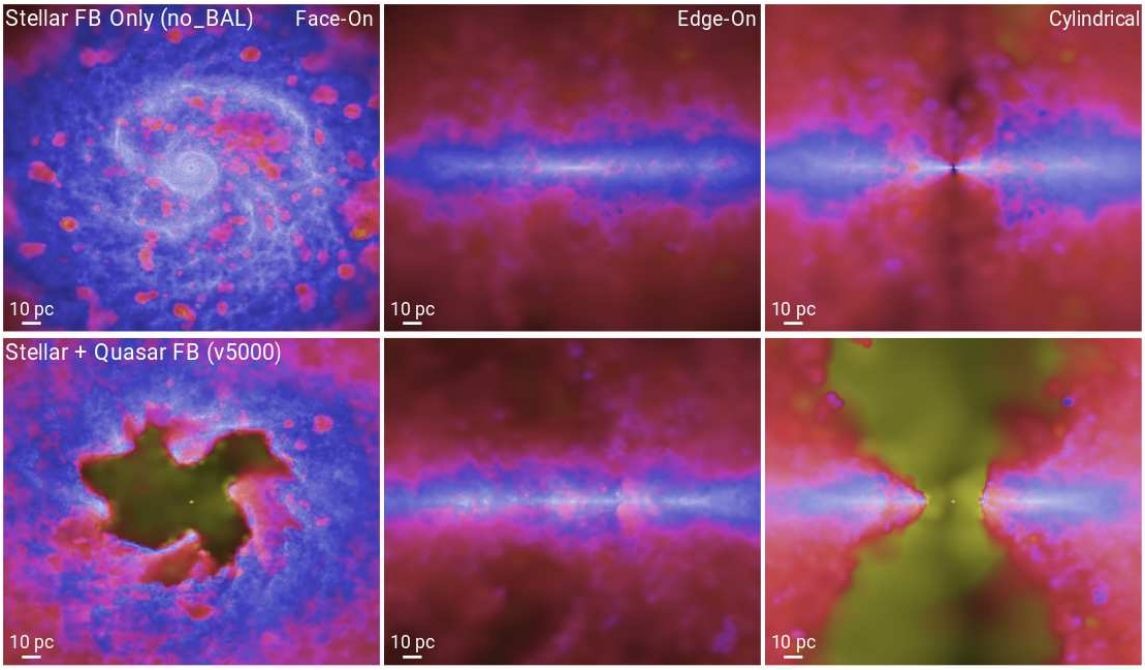


Figure 1.19 Morphology of circumnuclear gas in face-on (left), side-on (middle) and cylindrical projects for a simulated galaxy with stellar, but no AGN feedback (top) and the same simulation with AGN feedback (bottom). Brightness represents projected gas density (increasing with density) and color represents gas temperature (blue for $T \lesssim 1000$ K molecular gas and yellow for $T \gtrsim 10^6$ K hot gas. Figure from Hopkins et al. (2016).

(Schneider et al., 2015; Roebuck et al., 2016).

## 1.5 Thesis Aim and Overview

As seen above, the study of AGN IR emission has a long ($> 50$ yr) history. During the past two decades, a lot of progress has been achieved owing to the advent of major IR space telescopes and the increasing capability of high spatial resolution studies with IR telescopes on the ground. However, due to the complicated nature of this topic, the interpretations are quite ambiguous in many cases and we still lack a clear picture on how to reconcile the manifold observations.

The major goal of this thesis is to obtain general insights into the dust environment of type-1 AGNs with different luminosities ($L_{\rm AGN,bol} \sim 10^8$–$10^{13}\ L_\odot$) and redshifts ($z \sim$0–6). As a result, I conduct comparative SED analysis of low-$z$ AGNs to high-$z$ objects to understand their differences, develop empirical templates and new models to reconcile

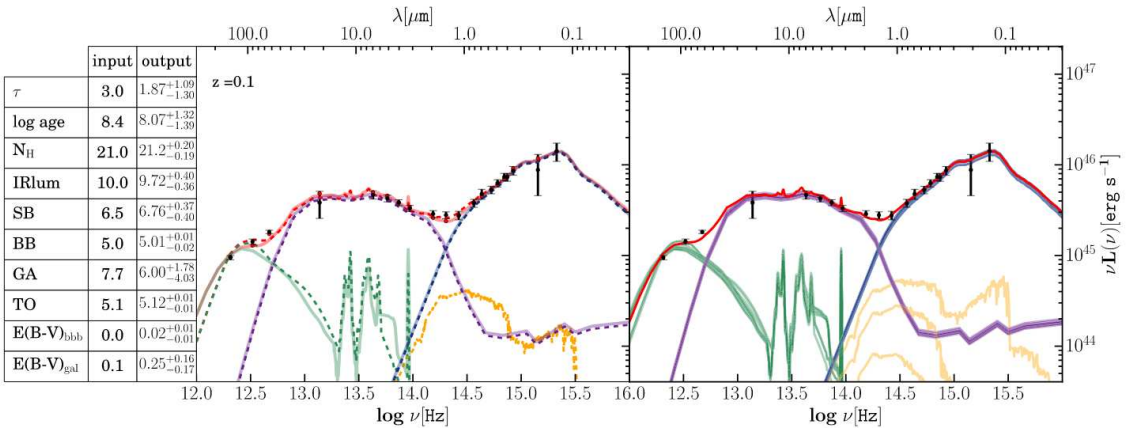


Figure 1.20 Synthetic SEDs of Type-1 AGN produced by the AGNfitter code from Calistro Rivera et al. (2016). The green and orange lines represent templates of the star-busrt and host galaxy stellar templates. The purple and blue lines stand for the torus dust emission and accretion disk emission. See the original paper for details.

the IR SED variations and relevant spatially-resolved observations, and carry out time-resolved study with multi-wavelength and multi-epoch data to put constraints on the spatial structures of the dust. This thesis is organized as follows:

In Chapter 2, we present a study on the intrinsic IR SEDs of type-1 quasars by detailed optical-to-IR SED decompositions of the low-$z$ Palomar-Green (PG) quasar sample and construct corresponding empirical AGN templates. We show that the quasar intrinsic IR SEDs, from $z \sim 0$ to $z \sim 6$, can be described by three basic types: the normal (Elvis-like), the warm-dust-deficient (WDD), and the hot-dust-deficient (HDD) AGNs. The appearance of these dust-deficient behaviors is found to be correlated with different AGN properties and can be explained by the change of circumnuclear torus structures.

Chapter 3 investigates the properties of AGN-heated far-IR emission by comparing representative AGN templates in the literature critically. We show that the Elvis-like version with a minor correction is the most preferred choice for AGN intrinsic IR SED shape based on an energy balance argument and detailed SED analysis. Despite the variations in the shorter wavelengths, different types of AGNs share similar far-IR intrinsic IR SED shapes at $\lambda \gtrsim 25\ \mu m$. We argue that this result is naturally expected due to the nature of optically thin emission in the far-IR. These results support the existence of compact AGN-heated dusty structures below sub-kiloparsec scales in the submm, rather than strong ISM

heating at kpc scales.

By introducing polar dust obscuration and the corresponding IR-reprocessed emission of large grains to our intrinsic AGN templates, Chapter 4 presents a successful effort to reconcile the dust emission of all major populations of type-1 AGNs in the Universe, including local Seyfert-1 nuclei, normal blue quasars, extremely red quasars at $z \sim$2–3, AGNs with mid-IR excess emission at $z \sim$0.7–2, hot-dust-obscured galaxies at $z \sim$ 1.5–4 and dust-free quasars at $z \sim 6$. It is highly likely that the AGN-heated dust environment of type-1 AGNs, regardless of their luminosities and redshifts, is composed of two components: a compact torus ($\lesssim$10 pc) with properties mainly determined by the BH accretion process, and an extended polar dust component ($r \sim$ 0.1–1 kpc) possibly shaped by AGN and/or galaxy feedback.

In Chapter 5, we demonstrate how to conduct mid-IR dust RM survey of bright quasars with the public time-domain data collected from asteroid/supernova-hunting surveys and provide such an analysis on 87 PG quasars. Convincing mid-IR dust time-lags have been detected in the WISE W1 ($\sim$ 3.4 $\mu$m) and W2 ($\sim$ 4.5 $\mu$m) bands in $\sim$70% of the sample and they are proportional to the square root of the AGN luminosity. Combined with previous K-band ($\sim$ 2.2 $\mu$m) RM results in the literature, we have provided the first wavelength-dependent torus dust size measurements and estimated the corresponding (projected) dust surface density. With multi-epoch *Spitzer* data and the later *WISE* photometry, we also study the AGN IR variability at 10–24 $\mu$m and provide further constraints on the torus structures as well as unification picture of radio-loud AGN.

With the knowledge of AGN intrinsic and galaxy IR emission, Chapter 6 proposes a simple two-free-parameter model (AGN+galaxy) to investigate the IR SEDs of all $z \sim 5$ with *Herschel* observations. We establish that the host galaxy far-IR emission of these systems is similar to Haro 11, a compact, moderately low-metallicity and star-bursting galaxy, rather than any other low-$z$ normal star-forming galaxies. The quasar host galaxies at $z \sim$5–6.5 are found to have very large variations of SFRs, ranging from $\lesssim$10 $M_{\odot}$/yr to $\sim$ 4000 $M_{\odot}$/yr but their average star formation infrared luminosity and average AGN luminosity follow the correlation defined by quasars at $z < 2.6$. We also provide the first estimation of the stellar mass of typical $z \sim$5–6 quasar host galaxies to be $< M_{*} > \sim$(3–

5)$\times 10^{11}$ $M_{\odot}$, enough to establish an average BH-galaxy mass ratio $M_{\rm BH}/M_{*}$ $\sim$0.1–1% consistent with the local relation.

Chapter 7 gives a summary of the key results of this thesis and provides a glimpse of related on-going and future projects.

CHAPTER 2

# DUST-DEFICIENT PALOMAR-GREEN QUASARS AND THE DIVERSITY OF AGN INTRINSIC IR EMISSION

To elucidate the intrinsic broadband infrared (IR) emission properties of active galactic nuclei (AGNs), we analyze the spectral energy distributions (SEDs) of 87 $z \lesssim 0.5$ Palomar-Green (PG) quasars. While the Elvis AGN template with a moderate far-IR correction can reasonably match the SEDs of the AGN components in $\sim 60\%$ of the sample (and is superior to alternatives such as that by Assef), it fails on two quasar populations: (1) hot-dust-deficient (HDD) quasars that show very weak emission thoroughly from the near-IR to the far-IR, and (2) warm-dust-deficient (WDD) quasars that have similar hot dust emission as normal quasars but are relatively faint in the mid- and far-IR. After building composite AGN templates for these dust-deficient quasars, we successfully fit the 0.3-500 $\mu$m SEDs of the PG sample with the appropriate AGN template, an infrared template of a star-forming galaxy, and a host galaxy stellar template. 20 HDD and 12 WDD quasars are identified from the SED decomposition, including seven ambiguous cases. Compared with normal quasars, the HDD quasars have AGNs with relatively low Eddington ratios and the fraction of WDD quasars increases with AGN luminosity. Moreover, both the HDD and WDD quasar populations show relatively stronger mid-IR silicate emission. Virtually identical SED properties are also found in some quasars from $z = 0.5$ to 6. We propose a conceptual model to demonstrate that the observed dust deficiency of quasars can result from a change of structures of the circumnuclear tori that can occur at any cosmic epoch. [1]

[1] A version of this chapter originally appeared as a published paper in the Astrophysical Journal (Lyu et al., 2017). All the works described here was carried out by me, with help from coauthor George Rieke and Yong Shi.

## 2.1 Introduction

The intrinsic UV to mid-IR spectral energy distributions (SEDs) of active galactic nuclei (AGNs) seem universal. Albeit large SED variations are seen among individual quasars, after removing the contamination from the host galaxies and the extinction caused by dust, and averaging the measurements of a sample of reasonable size, the mean SEDs of luminous AGNs are remarkably similar (e.g., Elvis et al., 1994; Richards et al., 2006; Shang et al., 2011). Two broad and prominent bumps dominate the UV-to-infrared SED – one in the optical-UV (known as the Big Blue Bump), contributed mainly by the thermal emission from the gas in an accretion disk, and another in the near- to mid-IR, dominated by the emission of dust heated by optical through soft X-ray photons (e.g., Rieke, 1978; Barvainis, 1987; Neugebauer et al., 1987; Sanders et al., 1989; Elvis et al., 1994). An inflection around 1.25 $\mu$m separates these two bumps, as a result of dust sublimation at a temperature of $\sim$ 1800 K (e.g., Barvainis, 1987). The mean AGN SEDs of quasars show little variation across a broad luminosity range as well as redshift (e.g., Wang et al., 2008b; Elvis et al., 2012; Hao et al., 2014; Lyu et al., 2016), suggesting that these massive black hole accreting systems and their nearby surroundings share similar properties (e.g., Scott & Stewart, 2014). Most importantly, the dusty obscuration structure, typically traced by the near- to mid-IR emission and termed as a 'torus,' lay the foundation for AGN unification (e.g., Antonucci 1993; see the recent review by Netzer 2015), and its formation is a vital part of the make-up of a quasar (e.g., Sanders et al., 1988b; King, 2003; Di Matteo et al., 2005; Hopkins et al., 2005, 2012; Vollmer et al., 2008).

Given the great importance of the AGN torus, it would be intriguing to look for quasars with abnormal IR SED features that could be potentially linked with the structure of the torus and its evolution. Jiang et al. (2010) reported the non-detection of hot dust emission from AGNs for two $z \gtrsim 5$ quasars, claiming they are likely to be the first-generation quasars in a dust-free environment. Hao et al. (2010, 2011) reported a population of "hot-dust-poor" quasars at moderate redshift and argued that there is a higher fraction at these redshifts compared to nearby quasars. Others have explored the redshift evolution of this special population of quasars based on large sky surveys but found contradictory results

(Mor & Netzer, 2012a; Jun & Im, 2013). Due to the limited observations at high redshift, the identifications of these quasars have been based on simple color selections, which is unlikely to be completely accurate. Meanwhile, since the mid-IR to far-IR infrared SEDs of these dust-deficient quasars are unknown, we lack a complete picture of the dust distribution in these systems.

A simple characterization of the torus is provided by the dust-covering factor, which is typically quantified by the relative luminosity between the torus and the accretion disk emission (e.g., Maiolino et al., 2007). In a number of papers, the mid-IR to optical luminosity ratios of quasars are found to reduce with increasing AGN luminosity (e.g., Maiolino et al. 2007; Treister et al. 2008; Mor & Trakhtenbrot 2011; Calderone et al. 2012; Gu 2013; Ma & Wang 2013; Roseboom et al. 2013), which is typically viewed as support for the model that the torus recedes as the luminosity increases (e.g., Lawrence, 1991; Simpson, 2005; Assef et al., 2013). In contrast, Richards et al. (2006) show that the mid-IR parts of the AGN SEDs are similar, but the most luminous quasars are much brighter at mid-IR bands compared with the least optically luminous quasars (see also, e.g., Edelson & Malkan 1986; Krawczyk et al. 2013). Meanwhile, others have reported that the fraction of quasars with weak hot dust emission was generally independent of the AGN luminosity (Hao et al., 2010, 2011; Mor & Netzer, 2012a). These apparent discrepancies again demonstrate our limited knowledge of quasars with weak dust emission as well as of the connection between the weak dust emission and AGN properties.

This work reports on the dust-deficient quasars among 87 $z < 0.5$ Palomar-Green (PG) quasars from the Palomar Bright Quasar Survey (Schmidt & Green, 1983; Boroson & Green, 1992). The PG sample is representative of bright optical-selected quasars and has been a cornerstone for quasar studies in the past 40 years. Thanks to the ample multiband observations made previously, we can calibrate the host galaxy properties derived from SED analysis with other independent methods and reveal the intrinsic AGN infrared emission. We will use SED decomposition to explore how well the classical AGN spectral template fits the behavior of these low-redshift AGNs and to identify any with a deficiency of hot or warm dust emission. The distributions of various AGN properties, such as AGN luminosities, black hole masses, and Eddington ratios, will be compared between the dust-deficient

quasar population and the normal quasar population. Finally, we will make comparative studies of the PG sample with the high-redshift results (e.g., Hao et al., 2010, 2011; Jiang et al., 2010; Leipski et al., 2014) and discuss the nature of the dust-deficient quasars in general.

The paper is organized as follows. A description of the data collection and the issue of AGN variability is provided in Section 2.2. We present the infrared SED templates for normal quasars as well as dust-deficient quasars in Section 6.2. Section 2.4 introduces the SED decomposition method. Section 2.5 contains the results from the SED analysis. We discuss the diversity of AGN infrared intrinsic emission, the characteristics of the dust-deficient quasars, as well as similar quasars found at high-$z$ in Section 3.4. A summary is given in Section 6.6.

Throughout this paper, we adopt the cosmology $\Omega_m = 0.27$, $\Omega_\Lambda = 0.73$ and $H_0 = 71\mathrm{km\ s^{-1}Mpc^{-1}}$.

## 2.2 Data

### 2.2.1 Data Compilation

To construct the IR SEDs of the 87 PG quasars, we compiled mid-IR to far-IR photometry measured by *Spitzer*/MIPS at 24, 70, and 160 $\mu$m (Shi et al., 2014), and far-IR and sub-millimeter photometry observed by Herschel PACS and SPIRE at 70, 100, 160, 250, 350, 500 $\mu$m (Petric et al., 2015). We also gathered the near-IR photometry at $J$ (1.24 $\mu$m), $H$ (1.66 $\mu$m), and $K_s$ (2.16 $\mu$m) from the 2 Micron All Sky Survey (2MASS; Skrutskie et al. 2006) and the UKIRT Infrared Deep Sky Survey (UKIDSS; Lawrence et al. 2007), and mid-IR photometry at $W1$ (3.4 $\mu$m), $W2$ (4.6 $\mu$m), $W3$ (12 $\mu$m), and $W4$ (22 $\mu$m) from the AllWISE program (Wright et al. 2010). Since we are going to compare the host galaxy stellar emission retrieved from SED decomposition with that from image analysis, particular attention has been paid to the selection of photometry data with appropriate apertures to include the whole light (AGN plus the host galaxy) of the quasar and reduce possible contamination. We used the Standard Photometry with isophotal apertures based on the $K_s$ 20 mag/arcsec$^2$ elliptical isophote from the 2MASS extended source catalog if the quasar

light profile is not identified to be a single point-spread-function by 2MASS. The *Wide-field Infrared Survey Explorer* (*WISE*) $W1$ and $W2$ bands can also be contaminated by the stellar emission. If a quasar has been identified as an extended object by 2MASS and the *WISE W1*/*W2* aperture photometry flux is larger than that based on the default profile-fit photometry optimized for point sources, we chose the *WISE W1*/*W2* band scaled-2MASS-aperture photometry with the largest aperture as long as no other source was included. UKIDSS has observed 29 PG quasars from our sample up to its Data Release 10. Compared with 2MASS, the UKIDSS data has a smaller time gap with the *WISE* data, reducing the effect on the SED due to long-term IR variability. However, UKIDSS used a 2.0 arcsec diameter aperture to record the quasar flux (Dye et al., 2006). We only use the UKIDSS data when the quasar is a 2MASS point source.[2] For 2MASS point-source PG quasars without the complete UKIDSS near-IR data, we used the profile-fit photometry in the 2MASS catalog. The *WISE W3* and *W4* band profile-fit photometry was adopted for all the PG quasars.

For the UV-optical data, the Galaxy Evolution Explorer (GALEX; Martin et al. 2005) has observed these PG quasars with far-UV (0.15 $\mu$m) detections for 72 of them and near-UV (0.23 $\mu$m) detections for 78 in GALEX Release 7 (Bianchi et al., 2014). We have archival optical $u$ (0.35 $\mu$m), $g$ (0.48 $\mu$m), $r$ (0.62 $\mu$m), $i$ (0.76 $\mu$m), and $z$ (0.91 $\mu$m) observations for 75 of our quasars from the Sloan Digital Sky Survey (SDSS; York et al. 2000a) Data Release 12 (Alam et al., 2015). We adopted the SDSS Model Magnitude, `modelMag`, to account for the optical emission of both resolved and unresolved objects. For quasars without SDSS or GALEX observations, we complete their SEDs with literature data[3] with the aid of the *NASA/IPAC Extragalactic Database* (NED) and the VizieR service

[2]We replaced the 2MASS data with the UKIDSS data for the following quasars: PG 0003+158, PG 0026+129, PG 0043+039, PG 1001+054, PG 1049−005, PG 1103−006, PG 1151+117, PG 1211+143, PG 1216+069, PG 1307+085, PG 1309+355, PG 1552+085, PG 1612+261, PG 2251+113, and PG 2308+098. Although PG 1004+130 is also a 2MASS point source that was matched in the UKIDSS catalog, we removed it from the list due to its lack of the UKIDSS $K$-band observation.

[3]Broadband 1450 Å continuum flux for PG 0844+349, PG 0953+414, and PG 0804+761 (Kaspi et al., 2005); CIV continuum flux (0.15 $\mu$m) for PG 1535+547 and PG 2308+098 (Baskin & Laor, 2005); broadband 1350 Å and 5500 Å continuum flux for PG 1416−129 (Labita et al., 2006; Hamilton et al., 2008); *XMM-Newton* 0.21-0.29 $\mu$m UV measurements for PG 0844+349, PG 0953+414, PG 1126−041, PG 1352+183, PG 1535+547, and PG 1626+554 (Brocksopp et al., 2006; Ballo et al., 2008; Gallo et al., 2011; Giustini et al., 2011; Page et al., 2012); interpolated 0.25 $\mu$m flux from published data for PG 0838+770 and PG 0804+761 (Steffen et al., 2006); integrated Johnson $B$ (0.44 $\mu$m) and I (0.88 $\mu$m) band flux for PG

(Ochsenbein et al., 2000).

We compared the SED composed by us with the observed SED data of 27 PG quasars presented in Elvis et al. (1994)[4]. The optical-to-near-IR SED shapes of these quasars do not show substantial changes over a timescale of ∼20 years. The mid- to far-IR SEDs of 16 of these quasars show a clear drop in the most recent data, which is due to the smaller beam sizes and higher sensitivities of *Spitzer*, *WISE*, and *Herschel* compared with those of the *Infrared Astronomical Satellite* (*IRAS*) whose data product was used in Elvis et al. (1994).

### 2.2.2 Photometric Variability

Since the photometric data used in this work were taken at various times spanning ∼ 20 years, AGN variability could be a potential factor to produce unphysical SED features between different data sets. Various programs of quasar monitoring have demonstrated that the variability deceases at longer wavelengths (e.g., Cutri et al., 1985; Neugebauer et al., 1989; di Clemente et al., 1996; de Vries et al., 2005). Although the UV variability of some quasars can be as large as ∼2-3 mag (e.g., Paltani & Courvoisier, 1994; Wheatley et al., 2008; Welsh et al., 2011), the optical variability amplitudes are typically at 0.2-1.5 mag (e.g. Giveon et al., 1999; de Vries et al., 2005), and the near-IR bands only at ∼0.2-0.3 mag (e.g., Enya et al., 2002a,b). For example, in the heterogeneous sample of ∼ 200 quasars observed by Enya et al. (2002a,b), excluding blazars, only 23 exceeded 0.1 dex in variation and only 5 exceeded 0.2 dex. This sample had disproportionate numbers of AGNs expected to vary, such as radio-loud ones. More relevant to our study, Neugebauer et al. (1989) reported on a comprehensive study of near infrared variability of PG quasars. Only 6 of 108 sources in their study varied by more than 0.15 mag and only 3 sources varied by

0838+770, PG 1126−041, and PG 1613+658 (Surace et al., 2001); Broadband 5100 Å continuum flux for PG 1700+518 (Kaspi et al., 2000); Johnson R photometry for PG 1700+518 (Carini et al., 2007); Johnson $B$, $V$, $R$, $I$ photometry for PG 1302−102 and PG 0804+761 (Ojha et al., 2009); Johnson $V$ band from the original PG Catalog for PG 1011−040, PG 1310−108 (Green et al., 1986); $B$ (∼ 0.44 $\mu$m), $V$ (∼ 0.55 $\mu$m), $g'$ (∼ 0.48 $\mu$m), or $r'$ (∼ 0.63 $\mu$m) photometry for PG 1048−090, PG 1149−110, PG 1435−067 from the AAVSO Photometric All Sky Survey (Henden et al., 2016); DENIS $I$-band (0.89 $\mu$m) photometry for PG 1011−040, PG 1310−108 (Paturel et al., 2003).

[4]We only focus on the quasars in the UVSX sample that have been analyzed in detail (Table 1A in Elvis et al. 1994)

more than 0.25 mag (0.1 dex). Of the 32 quasars that will be classified as being deficient in warm or hot dust by us (see section 2.5.2), 28 quasars were included in their study; only one (PG 0049+171) varied by more than 0.15 mag (= 0.06 dex). A longer baseline can be studied by comparing the photometry in Neugebauer et al. (1989) with 2MASS and UKIDSS photometry. However, differences in the measured fluxes could also be due to instrumental changes (i.e., aperture photometer versus array camera), so we can only identify *candidates* PG 1048−090, PG 1115+407, PG 1216+069, PG 1307+085, PG 1426+015, and PG 1617+175. For PG 1115+407 and PG 1426+015, the host galaxies are comparable in brightness to the AGNs (McLeod & Rieke 1994, Veilleux et al. 2009 respectively), so the evidence for variations is ambiguous, since different measurement strategies could include more or less of the host galaxy in the signal. PG 1226+023 (3C273) is one of the few blazars in the PG sample (Massaro et al., 2015). None of the changes are larger than 0.25 dex, even over the 25 year baseline represented by these measurements.

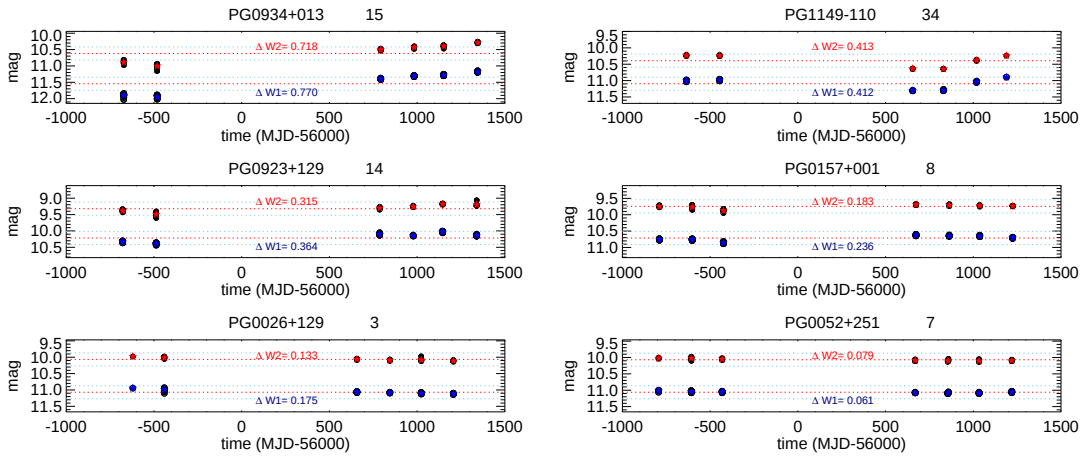


Figure 2.1 Example *WISE* $W1$ (3.4 $\mu$m, blue), $W2$ (4.6 $\mu$m, red) band light curves for a few PG quasars. The variability amplitudes are indicated as $\Delta W1$ and $\Delta W2$ in each plot. We denote the *ALLWISE* photometry value as red dotted lines with $\pm 0.15$ mag deviations for reference as blue dotted lines. We suggest $\Delta W1$ or $\Delta W2 > 0.3$ mag as strong variable signals.

To explore the longer-wavelength infrared variability of these quasars, we collected the $W1$ and $W2$ band observations from the WISE (Wright et al., 2010) and newly released data from the Near-Earth Object *WISE* Reactivation mission (*NEOWISE-R*; Mainzer et al. 2014). During a time period of five years (2010-2016), each quasar was observed for

five to seven epochs with 10-20 individual exposures in a single epoch. To reduce the systematic uncertainties, we average the photometric values during an epoch, after removing exposures with poor quality.[5] Figure 2.1 presents example *WISE* light curves for a few PG quasars with different variability amplitudes. For the mid-IR (3.4-4.6 $\mu$m) light curves probed by *WISE*, $\gtrsim$ 80 of the PG quasars have W1 or W2 variability amplitudes smaller than $\sim$ 0.4 mag. For a few extreme cases (e.g., PG 0003+199, PG 0934+013, PG 1534+580, PG 2304+042), the variability can be as large as $\sim$0.6-0.7 mag. Neugebauer & Matthews (1999) studied the mid-IR (3.7 and 10 $\mu$m) light curves of 25 PG quasars in 1974-1998, and reported similar variability amplitudes. Runnoe et al. (2012b) compared the *ALLWISE* $W3$ and $W4$ magnitudes with synthetic values derived from *Spitzer*/IRS spectra for 22 PG quasars in our sample and reported less than 0.2 mag variability amplitudes (i.e., less than 0.1 dex) over a period of four to five years. For these reasons, there could be a non-physical shift between the *WISE* and 2MASS data in a small number of cases. However, the influence is still within 0.2 dex.

Since the separation of the host galaxy and the AGN is mostly dependent on the near- and mid-IR for the great majority of cases, we conclude that the differing SED behavior we find below is not significantly influenced by variability over the time span for the various measurements.

## 2.3 The IR SED Templates for AGNs

### 2.3.1 Normal Quasars

After subtracting the near-IR and far-IR emission from host galaxies, a number of common dust features emerge in AGN SEDs. One such feature is hot dust emission peaked at $\sim$ 2 $\mu$m (e.g., Sanders et al., 1989; Elvis et al., 1994; Richards et al., 2006), which originates from the innermost region of the torus (e.g., Netzer et al., 2007). Another major feature is a relatively flat continuum that spans $\lambda$ $\sim$3-20 $\mu$m with silicate emission at $\sim$ 10 and $\sim$ 18 $\mu$m, contributed by the warm dust emission from the torus (e.g., Fritz et al., 2006;

[5] e.g., being influenced by the moon light or contaminated by halos due to nearby bright stars. See: http://wise2.ipac.caltech.edu/docs/release/allsky/expsup/sec2_4b.html

Nenkova et al., 2008a). The mid-IR emission of AGNs is strongly correlated with the hard X-ray flux (e.g., Lutz et al., 2004; Horst et al., 2006; Asmus et al., 2015; Mateos et al., 2015), further suggesting the similar SED properties of most luminous AGNs. In the far-IR, although the contamination from the host galaxy can become severe in many cases, the SED of AGNs is believed to drop quickly (e.g., Deo et al., 2009).

Elvis et al. (1994) built an AGN SED template based on a sample of both optically selected and radio-selected quasars that have strong X-ray emission and are optically blue. Although a number of these quasars were not detected by *IRAS* due to the limited sensitivity, the far-IR SED of Elvis et al. (1994) agrees remarkably well with later work (e.g., Richards et al., 2006; Shang et al., 2011). In Elvis et al. (1994), the host galaxy IR contribution of the AGN SED was not corrected since the dispersion of the mean template of spiral galaxies used then was too large to be useful. The lack of understanding of the galaxy IR SED was mitigated by later work (e.g., Rieke et al. 2009; Rujopakarn et al. 2011, 2013): for the same IR luminosity surface density, the IR SEDs of star-forming galaxies are similar. Based on the correlation between the 11.3 $\mu$m aromatic feature strength and the infrared colors, Xu et al. (2015b) removed the IR contribution from star formation in the Elvis et al. (1994) template. The validity of this updated AGN template to fit the UV-to-IR SED of high-redshift quasars has been demonstrated in Xu et al. (2015b) and Lyu et al. (2016).

Based on an iterative algorithm to derive the SED templates of $\sim 10^4$ AGNs at $z \sim$0-5.6, Assef et al. (2010) reported an AGN empirical template with a much deeper 1 $\mu$m inflection (or stronger hot dust emission) than the Richards et al. (2006) AGN template. Assef et al. (2010) suggested that the Elvis et al. (1994)-like AGN templates intrinsically have considerable amounts of host stellar contamination in the near-IR. We disagree with this argument. For the most luminous quasars at $z \gtrsim 5$, where the host galaxy contamination can be ignored, the Elvis et al. (1994)-like AGN templates match the observed UV-to-mid-IR SEDs well in most cases (e.g., Jiang et al., 2007, 2010; Wang et al., 2008b; Lyu et al., 2016). In Section 2.5.3, we will show that the Assef et al. (2010) AGN template systematically overestimates the host stellar emission in fitting normal PG quasars with HST image decomposition results as an independent calibrator.

Recently, some authors have claimed that the intrinsic AGN IR SED should contain much more far-IR emission, even compared with the far-IR uncorrected Elvis et al. (1994) template (e.g., Kirkpatrick et al., 2015; Symeonidis et al., 2016). The derivations of these templates are highly dependent on the detection of mid-IR spectral features related to host galaxy star formation and on use of appropriate SED templates for star forming galaxies to relate these features to the far IR emission. In fact, if we make a mock quasar SED by combining the Rieke et al. (2009) $\log(L_{\rm IR}/L_{\odot}) = 11.25$ star-formation galaxy template and Elvis et al. (1994) AGN template, when the host galaxy contribution is only $\sim 10\%$ in the mid-IR, the galaxy still contributes $\sim 50\%$ of the total IR (8-1000 $\mu$m) luminosity of the system. Given the limited signal-to-noise of the *Spitzer*/IRS spectra, the uncertainties in extrapolating to the far infrared make the derived quasar SEDs highly uncertain.

We will use the modified Elvis et al. (1994) AGN template by Xu et al. (2015b) to represent the intrinsic AGN SED for normal quasars in this paper.

### 2.3.2 Dust-Deficient Quasars

PG quasars with weak near- and mid-infrared emission were first noted in the early 1990s (Barvainis, 1990; McDowell et al., 1992) and later by Hao et al. (2011). In this paper, we use the classical Elvis et al. (1994) quasar template as a standard ruler to look for abnormal quasars in the near-IR or the mid-IR bands. Elvis et al. (1994) reported that the dispersion of quasar SEDs has a 68 percentile distribution within a factor of two to three of the mean throughout. Thus, we adopt a near- or mid-IR SED deviation from the normal quasar template by $\gtrsim 0.3$ dex to look for quasars with persuasive evidence of weak emission.

After visually inspecting the SEDs, we found a population of PG quasars with a deficiency of hot dust emission and very weak far-IR emission. However, host galaxy contamination in the near-IR (due to stellar emission) and the far-IR (due to star formation in HII regions) can make the identification of these quasars difficult. Therefore, we postulate that there is an intrinsic hot-dust-deficient (hereafter HDD) SED and make a template by averaging the SEDs of quasars that clearly present a deficiency of hot dust emission and do not have strong host galaxy contamination in their SEDs. After a detailed inspection of the observed SEDs of the whole sample, we ended up with four purest examples of HDD

quasars: PG 0026+129, PG 0049+171, PG 1121+422, and PG 1626+554. Normalized at 1.25 $\mu$m, their IR SEDs look quite similar, as shown in the left panel of Figure 2.2. Three of the four are not detected in the far-IR and one – PG 0039+171 – is not much above the SPIRE confusion noise (Nguyen et al., 2010). Their infrared emission is not likely to be strongly contaminated by radio synchrotron emission considering the small value of radio loudness (see Table 2.1). Therefore, as found in Xu et al. (2015b), we scale a blackbody of 118 K and with a wavelength-dependent emissivity proportional to $\lambda^{-1.5}$ to match the HDD template at $\lambda < 100$ $\mu$m. The optical SEDs of these four quasars show some variation but the SED obtained by averaging the individual quasar measurements is still similar to that of normal quasars. Thus, we assume the same average SED as that of normal quasars for the HDD template at $\lambda < 1.0$ $\mu$m.

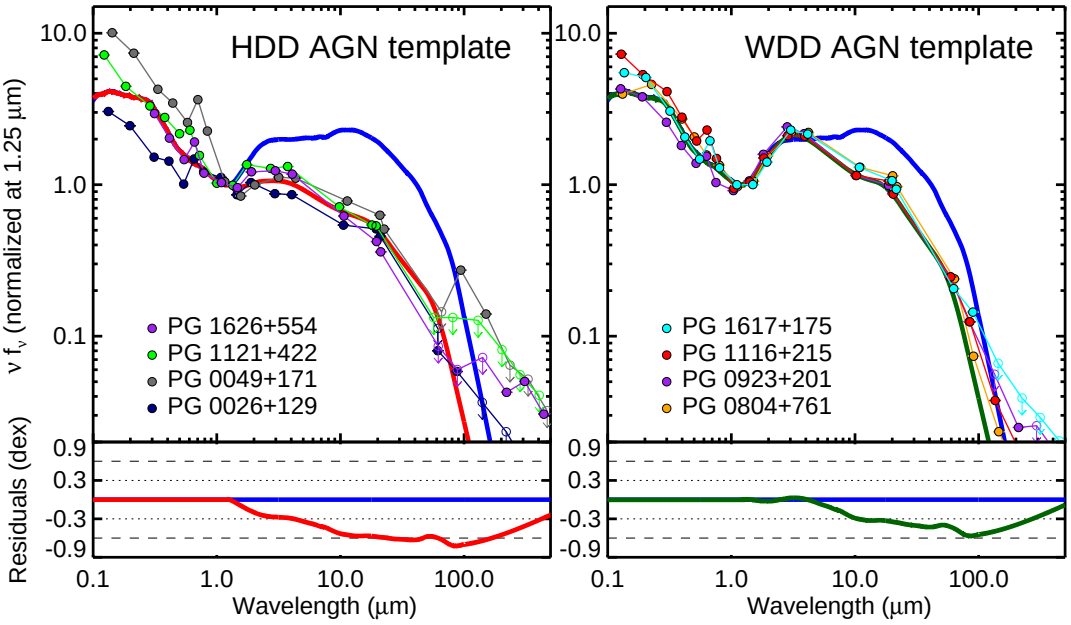


Figure 2.2 Comparison of the hot-dust-deficient (HDD) AGN template (left panel, red solid line) and the warm-dust-deficient (WDD) template (right panel, green solid line) to the normal Elvis et al. (1994) AGN template (far-IR corrected by Xu et al. 2015b; blue solid line). We also show the SEDs of the four PG quasars that are used to derive each template.

A standard procedure for making an AGN template should include the subtraction of the host galaxy contribution in the near-IR (e.g., Elvis et al., 1994; Richards et al., 2006; Shang et al., 2011). Nevertheless, the host galaxy contamination in these four HDD

Table 2.1. PG quasars used to derive the templates

| Source (1) | $z$ (2) | $f_{\rm nucleus,\ H}$ (3) | Reference (4) | Variability (5) | $R$ (6) |
|---|---|---|---|---|---|
| | | HDD template | | | |
| PG 0026+129 | 0.14 | 0.80 | 1 | N | 1.08 |
| PG 0049+171 | 0.06 | – | – | N | 0.32 |
| PG 1121+422 | 0.23 | 0.93 | 2 | N | 0.10 |
| PG 1626+544 | 0.13 | 0.72 | 1 | N | 0.11 |
| | | WDD template | | | |
| PG 0804+761 | 0.11 | 0.90 | 3 | N | 0.60 |
| PG 0923+201 | 0.19 | 0.77 | 1 | N | 1.74 |
| PG 1116+215 | 0.18 | 0.95 | 1 | N | 0.72 |
| PG 1617+175 | 0.11 | 0.89 | 1 | Y | 0.72 |

Note. — Column (1): object name; column (2): redshift; column (3): the contribution of the PSF component in the observed $H$ band from the HST image decomposition; column (4): references for HST image decomposition results: 1-Veilleux et al. (2009); 2-McLeod & McLeod (2001); 3-Guyon et al. (2006). column (5): if the quasar shows strong near-IR variability; column (6): radio loudness, taken from Petric et al. (2015).

quasars is small. For the three quasars with HST images, the quasar light substantially outshines the stellar emission in the near-IR (see Table 2.1). The other quasar, PG 0049+171, is not resolved in the 2MASS images despite its low redshift. It is barely resolved in $V$ band by Smith et al. (1986), who concluded that the host galaxy is two magnitudes fainter than the quasar at this wavelength. Its optical to near-IR colors are bluer than or identical to classical quasars, suggesting that the near-IR emission is not significantly boosted by the host galaxy. As a result, we conclude that the near-IR host galaxy stellar contamination for these four quasars is too small to have any visible influence on the derived HDD AGN template.

In addition, we have found that there are a number of quasars whose SEDs cannot be fitted adequately by either the normal or HDD templates, or by any combination of

them. Their near-IR SEDs present the typical bump peaked at $\sim 2.0$ $\mu$m, but they drop quickly at $\lambda > 5.0$ $\mu$m. In other words, hot dust emission is present in these quasars, but their mid-IR emission is relatively weak compared with normal quasars. Host galaxy contamination would not produce this type of SED, and should be small in any case as shown in Table 2.1. We combine the IR SEDs of four such quasars, PG 0804+761, PG 0923+201, PG 0953+414, PG 1116+215, and make a composite SED similarly to the HDD template (right panel of Figure 2.2). These four quasars all have small radio loudnesses and weak near-IR variability. We will describe this SED as the warm-dust-deficient (WDD) AGN template from now on.

We can confirm the distinct features of the three AGN SED templates for normal quasars, HDD quasars and WDD quasars by the *Akari* and *Spitzer*/IRS infrared spectra of example quasars, as shown in Figure 2.3. PG 0003+158, PG 1259+593, and PG 1103−006 were selected because their redshifts ($z > 0.43$) allow *Akari* spectra to cover the near-IR band ($\sim 1.7$ $\mu$m). The differences among normal, WDD and HDD quasars are due to the dust continuum, not any emission features like aromatic bands or silicate features. With the same UV-optical luminosity, the HDD AGN template has only ∼40% of the emission of the normal AGN template at 1.25-1000 $\mu$m. For the WDD AGN template, this value is ∼70%.

### 2.3.3 Are the HDD and WDD Templates Bona Fide?

An artificial SED similar to that of quasars with weak infrared emission could result if there is a strong contribution from the population of old stars in the host galaxy, which would peak near 1 micron and fill in the typical minimum near that wavelength in the normal (Elvis) quasar SED. In this subsection, we check if the HDD and WDD templates could be derived from the combination of normal quasar SED and stellar template.

In the top panel of Figure 2.4, we combine the Elvis et al. (1994) AGN template with a single stellar population template for 13 Gyr old stars from Bruzual & Charlot (2003) to explore the SEDs of normal quasars with different stellar contamination in the near-IR (as indicated by the AGN light fraction in the near-IR, $f_{\mathrm{AGN,1.25\ \mu m}}$). As the stellar emission in the near-IR increases, the prominence of the near-IR dust spectral bump gradually

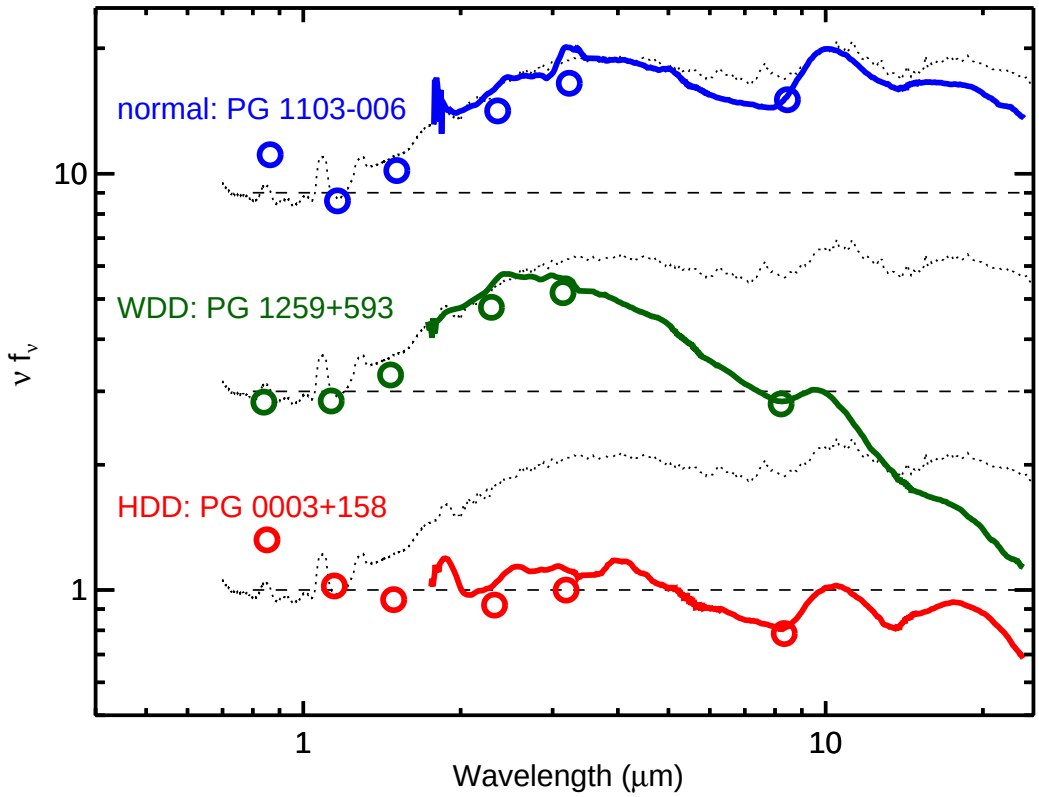


Figure 2.3 *Akari*+*Spitzer*/IRS combined infrared spectra for three PG quasars: the normal quasar PG 1103−006 (blue), the WDD quasar PG 1259+593 (green), and the HDD quasar PG 0003+158 (red). We also show the 2MASS ($J$, $H$, $K_s$) and *WISE* ($W1$, $W2$, $W3$) photometry for each quasar as open circles. We normalize each quasar IR spectrum and the corresponding template at 1.25 $\mu$m with respect to the dashed reference line. The dotted lines are the spectral templates for normal quasars, in which we join the 5-30 $\mu$m quasar template by Hao et al. (2007) and 1-10 $\mu$m quasar template by Hernán-Caballero et al. (2016) at 6.7 $\mu$m.

decreases. However, we also see a change of the optical slope away from that of normal quasars. As shown in Section 2.3.2, the HDD quasars share similar optical colors as other local quasars. Meanwhile, compared with the composite SEDs, the HDD template has relatively weaker emission in the mid-IR. For these reasons, we conclude that the HDD quasar template cannot be produced by a normal quasar template plus stellar emission in the near-IR. A similar argument can also be found in Hao et al. (2010, 2011).

We also investigate if the HDD quasar template is a result of the combination of the WDD quasar template and an old stellar population template. As shown in the right panel

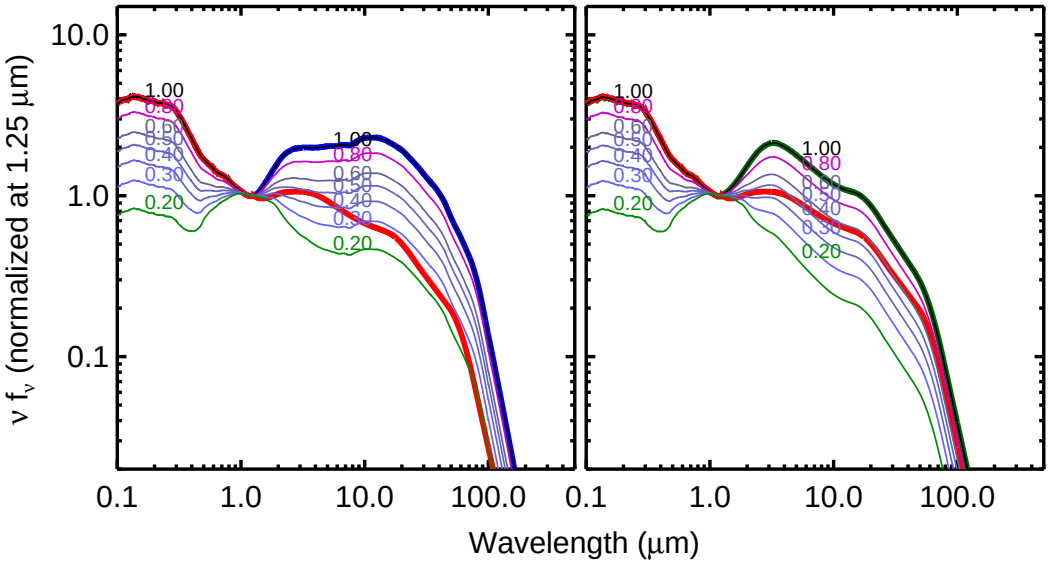


Figure 2.4 Mock SEDs of quasars. The left panel presents the composite SEDs of the Elvis AGN template and an old stellar population template, with the numbers indicating the fraction of the AGN contribution at 1.25 $\mu$m. The normal AGN template is shown as the red line. The right panel shows the composite SEDs of the WDD AGN template and an old stellar population template. The WDD AGN template is denoted as the green line. In both panels, the HDD template is shown as the blue thick line.

of Figure 2.4, though the $f_{\rm AGN,1.25\ \mu m}$=0.40-0.50 composite SEDs resemble the WDD template in the infrared, their optical colors differ from the WDD quasars (see the right panel of Figure 2.2). Additionally, we expect the stellar contributions to both HDD and WDD templates to be low (see the previous Subsection). As a result, we conclude that the HDD and WDD templates represent two different groups of quasars, rather than the results of different stellar near-IR contaminations.

The WDD AGN template is distinguished from the normal AGN template by its very weak mid-IR and far-IR emission. Normalized at 1.25 $\mu$m, the former has only $\sim$ 45% of the total infrared luminosity (8-1000 $\mu$m) of the latter. As stated in Appendix C of Xu et al. (2015b), the IR modified Elvis et al. (1994) AGN template provides a limiting case for the maximum plausible FIR contribution from star formation in a quasar. Given the consistent star formation rates (SFRs) based on the IR luminosities of the host galaxies and the mid-IR 11.3 $\mu$m aromatic feature strengths (see Section 2.5.3), we have no reason

to suggest that the intrinsic AGN emission of normal quasars could be as low as the case of the WDD AGN template. In other words, although sharing a similar hot dust emission feature, the normal AGN template and the WDD AGN template reflect two populations of quasars with distinct mid- to far-IR emission properties.

## 2.4 SED Decomposition of PG Quasars

We now use the three AGN SED templates to fit the behavior of the full set of 87 PG quasars.

The wide wavelength range covered by the photometry of PG quasars enables accurate SED decomposition of the emission from the AGN and the host galaxy. SED fitting methods using multiple components have been developed and demonstrated in a number of works (e.g., Bongiorno et al., 2007, 2012; Pozzi et al., 2010; Lusso et al., 2011; Xu et al., 2015b). The decomposition depends on the large differences in the behavior of the optical to near-IR SEDs of the stellar and AGN emission. As summarized in the Introduction, the AGN SED shows two broad maxima separated by a dip at $\sim 1.25$ $\mu$m. Meanwhile, the galaxy emission is a result of multiple stellar populations with different star formation histories. For the nearby massive galaxies, the stellar SEDs generally peak at $\sim 1$ $\mu$m, dominated by the emission from stars in old stellar populations, and drop quickly as a Rayleigh-Jeans tail toward the mid-IR. Examples of using a galaxy plus AGN component to decompose the optical-near-IR quasar SEDs can be seen in e.g., Bongiorno et al. (2007, 2012); Pozzi et al. (2010), and Lusso et al. (2011). For the mid-IR and far-IR emission of a quasar, both AGN and galaxy will contribute some emission by dust. With proper consideration of templates used to represent the intrinsic AGN emission and the host dust emission, separation of the contributions from these two are possible (e.g., Dale et al., 2014; Xu et al., 2015b; Lyu et al., 2016)

We model the 0.5-500 $\mu$m SED of each PG quasar with a combination of three components.

1. *AGN component with possible extinction*: As stated in Section 2.3.1, we select the AGN intrinsic template developed based on Elvis et al. (1994) by Xu et al. (2015b)

(see their Appendix C) to represent the AGN emission for normal quasars. This normal AGN template will be combined with the HDD or WDD AGN template to characterize the possible transitional infrared SEDs between the normal cases and dust-deficient cases, while keeping the SED of the UV-optical emission unchanged. To take into account the obscuration caused by dust in the AGN ambient regions as well as the host galaxy, we assume that the AGN component is reddened by an SMC-like ($\lambda < 1$ $\mu$m) plus MW-like ($\lambda > 1$ $\mu$m) composite extinction curve, as in Xu et al. (2015b). Such a combination is proposed based on the statistical study of quasar UV-optical extinction based on SDSS (Hopkins et al., 2004) and the lack of knowledge of the AGN near- to mid-IR extinction curves.

2. *IR emission of a luminous infrared galaxy*: Many PG quasar host galaxies are found to have SFRs ~10-100 $M_{\odot}\mathrm{yr}^{-1}$ (based on the strength of 11.3 $\mu$m aromatic feature, see Shi et al., 2014), which roughly puts them in the LIRG ($L_{\mathrm{IR}} > 10^{11}$ $L_{\odot}$) category. We adopt the templates in Rieke et al. (2009) with $\log_{10} L_{\mathrm{IR}}$=9.75-12.00. In Rieke et al. (2009), the shape of the infrared SED of nearby galaxies is found to be dependent on their infrared luminosity. We will pick the one that best fits the far-IR SED of the quasar in combination with the other components, without imposing a luminosity constraint.

3. *Stellar emission of an old stellar population*: We use the stellar SEDs from Bruzual & Charlot (2003) with a Salpeter initial mass function, Padova evolutionary tracks, and solar metallicity. Considering the similarity between the SEDs for a range of ages, we pick one single stellar population template for each quasar with an age of 0.5 Gyr, 1.6 Gyr, 7.2 Gyr, or 13 Gyr, to represent the overall SED properties of the stellar emission that contributes to the near-IR emission (in most cases, any differences in the optical and UV stellar SEDs are overwhelmed by the emission by the quasars).

Our SED model can be summarized by the following equation

$$f_{\mathrm{quasar}} = \left(c_1 f_{\mathrm{AGN,norm.}} + c_2 f_{\mathrm{AGN,defi.}}\right) e^{-c_3 (A_\lambda / A_{\mathrm{V}})} + c_4 f_{\mathrm{gal.,stars}} + c_5 f_{\mathrm{gal.,dust}} \quad ,$$

where $(A_\lambda/A_V)$ is the normalized extinction curve, and $f_{\rm AGN,norm.}$, $f_{\rm AGN,defi.}$, $f_{\rm gal.,stars}$, $f_{\rm gal.,dust}$ are the SED templates for normal AGN, HDD or WDD AGN, stellar emission, and galaxy infrared emission. There are five normalizing factors, denoted as $c_1, c_2, c_3, c_4, c_5$. With the selection of the stellar templates and galaxy IR templates, there are seven free parameters in total. The modeled photometry will be computed by convolving the corresponding filter with the modeled SED. Since the multiband photometry includes a large set of data with a diverse level of relative uncertainty, to reflect the overall SED shape rather than focusing on a few data points with the smallest uncertainties, we give the same weight to all data points in $\nu$-$\nu f_\nu$ space during the fitting. We will use the classical definition of the $\chi^2$ statistic to evaluate the goodness of the fitting at first, and then check the residuals of the points with large $\chi^2$ values in detail.

## 2.5 Results

The SED fitting results for the 87 PG quasars are described in Figure 2.5 and Table 2.2. As introduced briefly in Section 2.2.2, the AGN variability potentially embedded in different data sets could introduce some offset from the intrinsic SED ($\sim$ 1 dex in the UV, $\sim$0.1-0.2 dex in the near-IR). As a result, the UV-optical SEDs are hard to interpret. We will mainly focus on the reproduction of the overall shape of the SED, and the host galaxy contribution to the near-IR and far-IR.

Table 2.2. SED decomposition results for the 87 Palmor-Green quasars

| ID (1) | Source (2) | $z$ (3) | Type (4) | $f_{\rm HDD/WDD}$ (5) | $f_{\rm Stellar}$ (6) | $F_{\rm star,\,H}/F_{\rm quasar,\,H}$ (7) | $L_{\rm IR}/10^{11}L_{\odot}$ (8) | $f_{\rm host}$ (9) | $L_{\rm AGN}/10^{11}L_{\odot}$ (10) | SFR (11) |
|---|---|---|---|---|---|---|---|---|---|---|
| 0 | PG 0003+158 | 0.45 | HDD | 1.00 | 0.00 | 0.00 | 9.95 | 0.05 | 68.76 | 8.7 |
| 1 | PG 0003+199 | 0.03 | – | 0.00 | 0.56 | 0.48 | 0.33 | 0.06 | 2.22 | 0.4 |
| 2 | PG 0007+106 | 0.09 | – | 0.00 | 0.44 | 0.38 | 2.02 | 0.24 | 11.11 | 8.5 |
| 3 | PG 0026+129 | 0.14 | HDD | 0.81 | 0.11 | 0.10 | 1.62 | 0.00 | 11.81 | 0.0 |
| 4 | PG 0043+039 | 0.38 | HDD? | 0.84 | 0.17 | 0.18 | 10.40 | 0.35 | 49.50 | 62.2 |
| 5 | PG 0049+171 | 0.06 | HDD | 1.00 | 0.00 | 0.00 | 0.22 | 0.12 | 1.42 | 0.4 |
| 6 | PG 0050+124 | 0.06 | – | 0.00 | 0.52 | 0.40 | 6.66 | 0.44 | 26.92 | 51.1 |
| 7 | PG 0052+251 | 0.16 | HDD | 0.57 | 0.10 | 0.09 | 3.37 | 0.21 | 19.49 | 12.0 |
| 8 | PG 0157+001 | 0.16 | – | 0.00 | 0.12 | 0.10 | 25.35 | 0.69 | 56.82 | 303.4 |
| 9 | PG 0804+761 | 0.10 | WDD | 1.00 | 0.00 | 0.00 | 3.19 | 0.04 | 22.34 | 2.1 |
| 10 | PG 0838+770 | 0.13 | – | 0.00 | 0.52 | 0.47 | 2.66 | 0.49 | 9.91 | 22.5 |
| 11 | PG 0844+349 | 0.06 | HDD? | 0.70 | 0.40 | 0.36 | 0.62 | 0.23 | 3.49 | 2.4 |
| 12 | PG 0921+525 | 0.04 | – | 0.00 | 0.56 | 0.47 | 0.22 | 0.11 | 1.45 | 0.4 |
| 13 | PG 0923+201 | 0.19 | WDD | 1.00 | 0.00 | 0.00 | 3.39 | 0.09 | 22.59 | 5.0 |
| 14 | PG 0923+129 | 0.03 | – | 0.00 | 0.82 | 0.77 | 0.40 | 0.54 | 1.33 | 3.7 |
| 15 | PG 0934+013 | 0.05 | – | 0.00 | 0.64 | 0.58 | 0.40 | 0.62 | 1.10 | 4.3 |
| 16 | PG 0947+396 | 0.21 | – | 0.00 | 0.02 | 0.02 | 6.71 | 0.29 | 34.75 | 33.5 |
| 17 | PG 0953+414 | 0.24 | WDD | 1.00 | 0.00 | 0.00 | 7.31 | 0.00 | 53.24 | 0.0 |
| 18 | PG 1001+054 | 0.16 | – | 0.00 | 0.31 | 0.29 | 2.15 | 0.04 | 14.99 | 1.6 |
| 19 | PG 1004+130 | 0.24 | – | 0.00 | 0.37 | 0.36 | 8.87 | 0.16 | 54.24 | 24.6 |
| 20 | PG 1011−040 | 0.06 | HDD | 0.75 | 0.42 | 0.39 | 0.60 | 0.47 | 2.31 | 4.8 |
| 21 | PG 1012+008 | 0.19 | – | 0.00 | 0.50 | 0.48 | 3.76 | 0.24 | 20.82 | 15.6 |
| 22 | PG 1022+519 | 0.05 | HDD? | 0.63 | 0.61 | 0.58 | 0.30 | 0.65 | 0.77 | 3.3 |
| 23 | PG 1048+342 | 0.17 | – | 0.00 | 0.56 | 0.54 | 2.05 | 0.43 | 8.53 | 15.2 |
| 24 | PG 1048−090 | 0.34 | WDD | 1.00 | 0.00 | 0.00 | 6.08 | 0.06 | 41.46 | 6.7 |
| 25 | PG 1049−005 | 0.36 | – | 0.00 | 0.00 | 0.00 | 30.49 | 0.31 | 152.93 | 164.0 |
| 26 | PG 1100+772 | 0.31 | HDD | 0.67 | 0.00 | 0.00 | 11.87 | 0.32 | 58.76 | 65.7 |
| 27 | PG 1103−006 | 0.43 | – | 0.00 | 0.10 | 0.11 | 13.13 | 0.00 | 95.56 | 0.0 |
| 28 | PG 1114+445 | 0.14 | – | 0.00 | 0.05 | 0.04 | 4.04 | 0.03 | 28.58 | 2.0 |
| 29 | PG 1115+407 | 0.15 | HDD | 0.71 | 0.04 | 0.04 | 3.70 | 0.60 | 10.81 | 38.3 |
| 30 | PG 1116+215 | 0.18 | WDD | 1.00 | 0.00 | 0.00 | 7.23 | 0.00 | 52.60 | 0.0 |
| 31 | PG 1119+120 | 0.05 | – | 0.00 | 0.43 | 0.37 | 0.90 | 0.40 | 3.96 | 6.2 |
| 32 | PG 1121+422 | 0.23 | HDD | 1.00 | 0.00 | 0.00 | 1.73 | 0.00 | 12.62 | 0.0 |
| 33 | PG 1126−041 | 0.06 | – | 0.00 | 0.48 | 0.42 | 1.76 | 0.34 | 8.46 | 10.4 |
| 34 | PG 1149−110 | 0.05 | – | 0.00 | 0.82 | 0.78 | 0.53 | 0.56 | 1.69 | 5.2 |
| 35 | PG 1151+117 | 0.18 | – | 0.00 | 0.27 | 0.25 | 1.77 | 0.00 | 12.85 | 0.0 |
| 36 | PG 1202+281 | 0.17 | – | 0.00 | 0.01 | 0.01 | 3.36 | 0.26 | 18.10 | 15.2 |
| 37 | PG 1211+143 | 0.09 | – | 0.00 | 0.22 | 0.18 | 2.57 | 0.00 | 18.72 | 0.0 |
| 38 | PG 1216+069 | 0.33 | HDD | 1.00 | 0.13 | 0.14 | 5.55 | 0.00 | 40.38 | 0.0 |
| 39 | PG 1226+023 | 0.16 | WDD | 1.00 | 0.00 | 0.00 | 30.11 | 0.21 | 173.72 | 108.0 |
| 40 | PG 1229+204 | 0.06 | – | 0.00 | 0.61 | 0.56 | 0.90 | 0.29 | 4.66 | 4.5 |
| 41 | PG 1244+026 | 0.05 | – | 0.00 | 0.31 | 0.26 | 0.37 | 0.42 | 1.53 | 2.7 |
| 42 | PG 1259+593 | 0.47 | WDD | 1.00 | 0.00 | 0.00 | 16.16 | 0.00 | 117.63 | 0.0 |
| 43 | PG 1302−102 | 0.29 | HDD | 0.76 | 0.00 | 0.00 | 14.82 | 0.33 | 72.63 | 83.7 |
| 44 | PG 1307+085 | 0.16 | HDD | 0.00 | 0.26 | 0.23 | 2.79 | 0.01 | 20.18 | 0.3 |
| 45 | PG 1309+355 | 0.18 | – | 0.00 | 0.19 | 0.18 | 5.47 | 0.12 | 34.95 | 11.5 |
| 46 | PG 1310−108 | 0.04 | – | 0.00 | 0.45 | 0.37 | 0.20 | 0.20 | 1.18 | 0.7 |
| 47 | PG 1322+659 | 0.17 | – | 0.00 | 0.21 | 0.19 | 3.53 | 0.28 | 18.65 | 16.8 |
| 48 | PG 1341+258 | 0.09 | HDD? | 0.43 | 0.56 | 0.53 | 0.62 | 0.35 | 2.95 | 3.7 |
| 49 | PG 1351+236 | 0.05 | – | 0.00 | 0.89 | 0.86 | 0.63 | 0.79 | 0.98 | 8.6 |
| 50 | PG 1351+640 | 0.09 | – | 0.00 | 0.06 | 0.04 | 4.55 | 0.35 | 21.64 | 27.2 |
| 51 | PG 1352+183 | 0.16 | – | 0.00 | 0.31 | 0.29 | 1.63 | 0.00 | 11.84 | 0.0 |
| 52 | PG 1354+213 | 0.30 | – | 0.00 | 0.00 | 0.00 | 5.65 | 0.19 | 33.33 | 18.6 |
| 53 | PG 1402+261 | 0.16 | – | 0.00 | 0.00 | 0.00 | 6.79 | 0.24 | 37.39 | 28.6 |
| 54 | PG 1404+226 | 0.10 | HDD? | 0.49 | 0.38 | 0.34 | 0.64 | 0.33 | 3.11 | 3.6 |
| 55 | PG 1411+442 | 0.09 | – | 0.00 | 0.46 | 0.40 | 2.06 | 0.03 | 14.58 | 1.0 |
| 56 | PG 1415+451 | 0.11 | – | 0.00 | 0.64 | 0.61 | 1.61 | 0.34 | 7.69 | 9.5 |

Table 2.2 (cont'd)

| ID (1) | Source (2) | $z$ (3) | Type (4) | $f_{\rm HDD/WDD}$ (5) | $f_{\rm Stellar}$ (6) | $F_{\rm star,\,H}/F_{\rm quasar,\,H}$ (7) | $L_{\rm IR}/10^{11}L_{\odot}$ (8) | $f_{\rm host}$ (9) | $L_{\rm AGN}/10^{11}L_{\odot}$ (10) | SFR (11) |
|---|---|---|---|---|---|---|---|---|---|---|
| 57 | PG 1416−129 | 0.13 | – | 0.00 | 0.36 | 0.32 | 0.89 | 0.16 | 5.46 | 2.4 |
| 58 | PG 1425+267 | 0.37 | – | 0.00 | 0.14 | 0.14 | 13.00 | 0.21 | 75.05 | 46.5 |
| 59 | PG 1426+015 | 0.09 | – | 0.00 | 0.46 | 0.40 | 2.86 | 0.18 | 17.18 | 8.7 |
| 60 | PG 1427+480 | 0.22 | – | 0.00 | 0.19 | 0.18 | 3.94 | 0.32 | 19.40 | 22.0 |
| 61 | PG 1435−067 | 0.13 | HDD | 0.67 | 0.03 | 0.03 | 1.14 | 0.02 | 8.07 | 0.5 |
| 62 | PG 1440+356 | 0.08 | – | 0.00 | 0.58 | 0.53 | 2.92 | 0.50 | 10.64 | 25.2 |
| 63 | PG 1444+407 | 0.27 | – | 0.00 | 0.01 | 0.01 | 9.36 | 0.07 | 63.43 | 11.2 |
| 64 | PG 1448+273 | 0.06 | – | 0.00 | 0.63 | 0.57 | 0.74 | 0.31 | 3.75 | 3.9 |
| 65 | PG 1501+106 | 0.04 | – | 0.00 | 0.44 | 0.37 | 0.67 | 0.30 | 3.41 | 3.5 |
| 66 | PG 1512+370 | 0.37 | – | 0.00 | 0.05 | 0.05 | 9.43 | 0.03 | 66.95 | 4.1 |
| 67 | PG 1519+226 | 0.14 | – | 0.00 | 0.07 | 0.06 | 2.37 | 0.15 | 14.67 | 6.2 |
| 68 | PG 1534+580 | 0.03 | – | 0.00 | 0.55 | 0.48 | 0.22 | 0.24 | 1.24 | 0.9 |
| 69 | PG 1535+547 | 0.04 | – | 0.00 | 0.37 | 0.29 | 0.18 | 0.16 | 1.10 | 0.5 |
| 70 | PG 1543+489 | 0.40 | – | 0.00 | 0.00 | 0.00 | 41.26 | 0.45 | 165.92 | 319.3 |
| 71 | PG 1545+210 | 0.27 | WDD | 1.00 | 0.19 | 0.19 | 4.17 | 0.00 | 30.29 | 0.1 |
| 72 | PG 1552+085 | 0.12 | HDD? | 0.67 | 0.25 | 0.22 | 0.86 | 0.11 | 5.51 | 1.7 |
| 73 | PG 1612+261 | 0.13 | – | 0.00 | 0.17 | 0.15 | 3.47 | 0.40 | 15.15 | 24.1 |
| 74 | PG 1613+658 | 0.13 | – | 0.00 | 0.56 | 0.52 | 8.49 | 0.42 | 35.89 | 61.6 |
| 75 | PG 1617+175 | 0.11 | WDD | 1.00 | 0.00 | 0.00 | 1.19 | 0.05 | 8.28 | 1.0 |
| 76 | PG 1626+554 | 0.13 | HDD | 1.00 | 0.03 | 0.02 | 0.77 | 0.00 | 5.61 | 0.0 |
| 77 | PG 1700+518 | 0.28 | – | 0.00 | 0.09 | 0.09 | 33.94 | 0.26 | 181.59 | 155.5 |
| 78 | PG 1704+608 | 0.37 | – | 0.00 | 0.25 | 0.26 | 32.05 | 0.19 | 189.74 | 103.5 |
| 79 | PG 2112+059 | 0.47 | – | 0.00 | 0.20 | 0.21 | 37.35 | 0.05 | 257.26 | 34.8 |
| 80 | PG 2130+099 | 0.06 | – | 0.00 | 0.34 | 0.29 | 1.99 | 0.25 | 10.92 | 8.5 |
| 81 | PG 2209+184 | 0.07 | HDD? | 0.80 | 0.72 | 0.70 | 0.37 | 0.43 | 1.54 | 2.8 |
| 82 | PG 2214+139 | 0.07 | WDD | 1.00 | 0.52 | 0.47 | 0.74 | 0.13 | 4.68 | 1.6 |
| 83 | PG 2233+134 | 0.32 | – | 0.00 | 0.00 | 0.00 | 11.03 | 0.11 | 71.29 | 21.3 |
| 84 | PG 2251+113 | 0.32 | WDD | 1.00 | 0.37 | 0.37 | 7.24 | 0.07 | 49.18 | 8.3 |
| 85 | PG 2304+042 | 0.04 | – | 0.00 | 0.91 | 0.89 | 0.07 | 0.02 | 0.51 | 0.0 |
| 86 | PG 2308+098 | 0.43 | HDD | 0.88 | 0.00 | 0.00 | 9.22 | 0.00 | 67.13 | 0.0 |

Note. — Column (2): object name; column (3): redshift; column (4): identification of HDD and WDD; column (5): the relative contribution of the HDD template (for HDD quasars) or the WDD template (for WDD quasars) to the AGN emission at rest-frame 1.25 $\mu$m; column (6): the contribution fraction of the stellar template to the total quasar emission at rest-frame 1.25 $\mu$m; column (7): the host galaxy contribution to the total quasar light in observed $H$ band from SED decomposition; column (8): the total infrared luminosity (8-1000 $\mu$m) of the object; column (9): the host SF template fraction for $L_{\rm IR}$; column (10): the bolometric luminosity of the AGN. We adopted $L_{\rm AGN} = 5.29 L_{\rm IR,AGN} = 5.29 L_{\rm IR}(1 - f_{\rm host})$ for all the quasars; column (11): the derived star formation rate based on $L_{\rm IR,host} = L_{\rm IR} f_{\rm host}$ following the Kennicutt (1998) star-formation law.

### 2.5.1 Quality of the SED Reproduction

The optical-to-far-IR SEDs of most PG quasars studied in this work have been well reproduced by our model. The fitting residuals of the 0.5-100 $\mu$m SEDs of all 87 quasars are less than 0.3 dex (see the residual panels in Figure 2.5). For nearly all cases where the far-IR emission is strong, the fit selected a host galaxy template of luminosity $10^{11}$-$10^{12}$ $L_{\odot}$ as expected. The fitted extinction levels are small, usually zero. In 72 of the 87 cases the reduced $\chi^2$ is $< 3$ and only 11 have $\chi^2 > 5$. The HDD template is required by 20 quasars to best reproduce the SED. Twelve quasars required the WDD template to be included in the

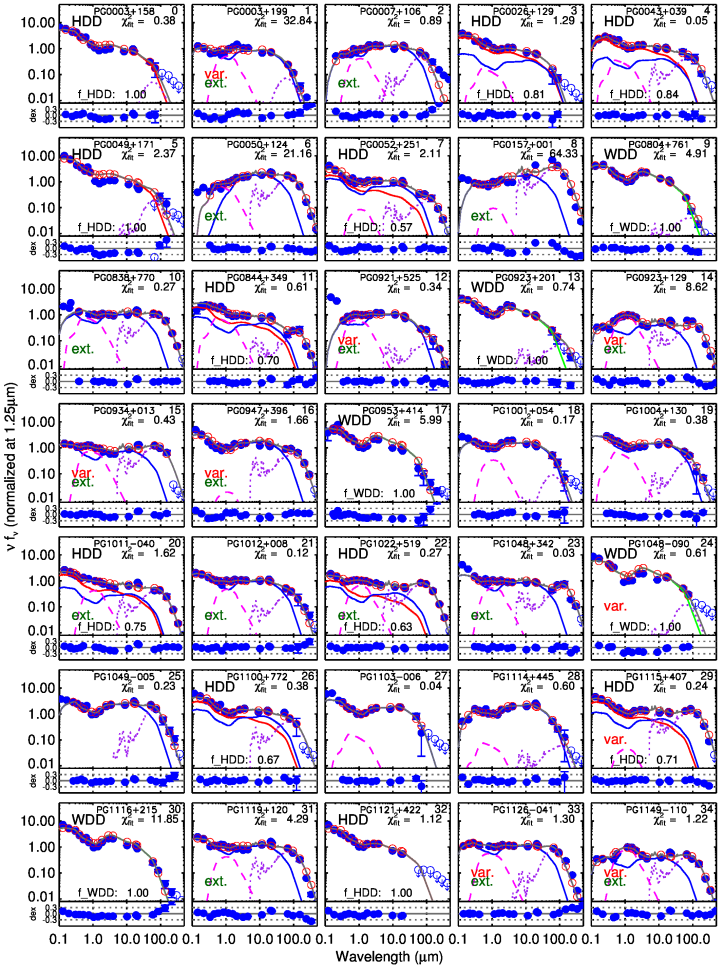


Figure 2.5 SED decomposition results (upper panels) and the residual plots (lower panels) for the PG sample. Data points are shown as blue dots (detection) and open circles with arrows (non-detection). The AGN components of the SED model are shown as solid lines: blue – the normal AGN template; green – the WDD AGN template; red – the HDD AGN template. The stellar template and the far-IR star formation template of the host galaxy are shown as magenta dashed lines and purple dotted lines, respectively. The final composite model SED is shown as the dark gray line, with the modeled points (convolved with the corresponding photometry filters) as open red circles. We also indicate the quasar type in the upper left corner of each figure. The fractional contribution of the HDD/WDD template in the AGN component at 1.25 $\mu$m is indicated as $f_{\rm HDD}$, $f_{\rm WDD}$, respectively. We use var. (red) to indicate quasars with infrared varability according to the *WISE* light curves or literature near-IR data (see Section 2.2.2) and ext. (green) to indicate quasars that are not identified as point sources in the 2MASS images (see Section 2.2.1).

model. We comment on the fitted SEDs and discuss some notable discrepancies between observations and model results below.

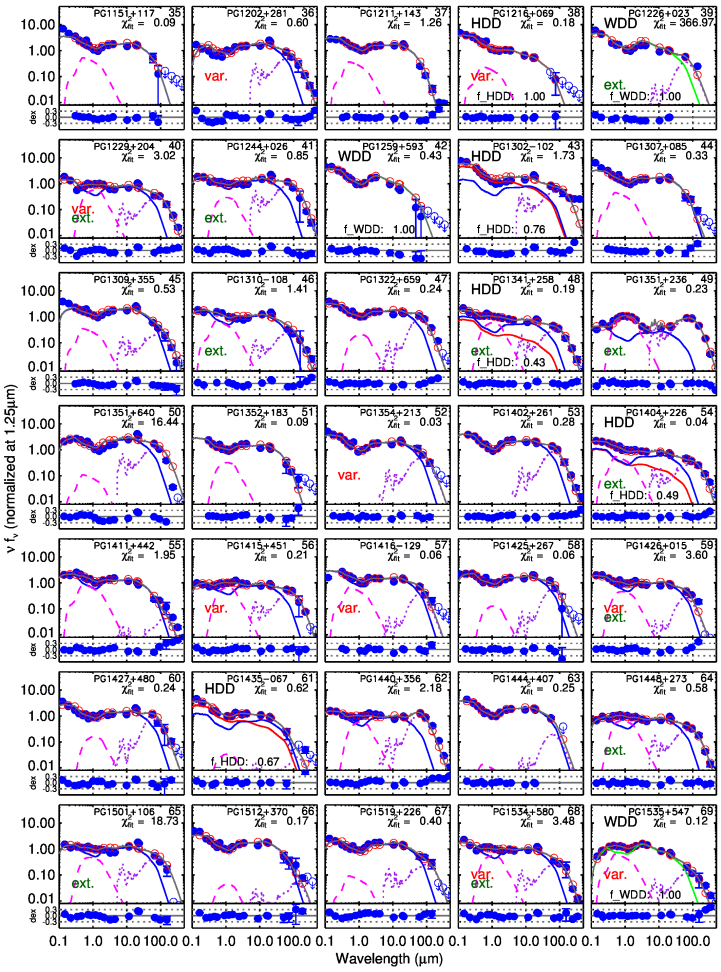


Figure 2.5 (continued.) SED decomposition results (upper panels) and the residual plots (lower panels) for the PG sample.

In the optical/UV bands, a few quasars show broadband excess emission if we normalize the model SED to the observed near-IR data points (e.g., PG 0003+158 and PG 0049+171). This behavior can be explained by contamination from AGN optical variability or the emission of young stellar populations in the AGN host galaxies. As shown in Giveon et al. (1999), the most variable quasars become bluer when they are brighter. For the second possibility, even a relatively small population of young stars can change the color of the host galaxy since their emitting power is very strong. In the UV band (0.1-0.3 $\mu$m), we see some moderate flux excess above the AGN templates in a few cases (e.g., PG 0921+525), which might arise from UV emission by very young stars.

With the combination of the normal, WDD, and HDD AGN templates with a stellar

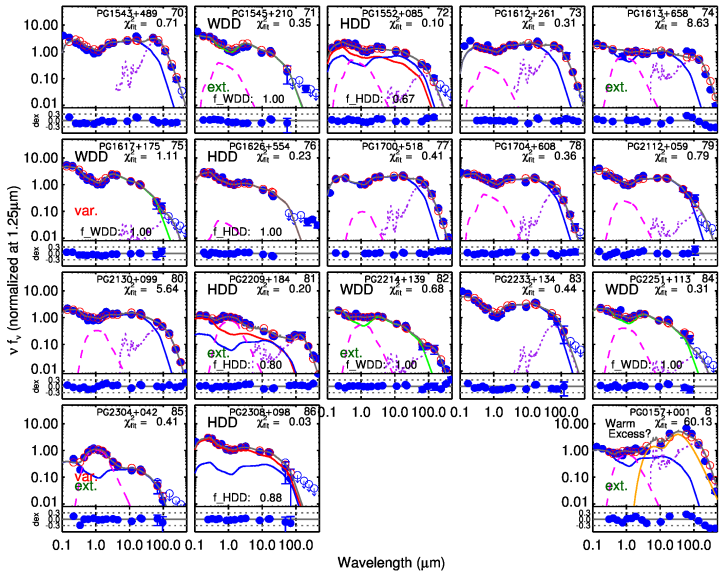


Figure 2.5 (continued.) SED decomposition results (upper panels) and the residual plots (lower panels) for the PG sample. In the final SED plot, we show the model fitting with a warm infrared component (orange solid line) for PG 017+001.

template, the near-IR to mid-IR SEDs of all quasars are reasonably reproduced. The template selections for some quasars (e.g., PG 1001+054 and PG 2251+113) are ambiguous, since some transition among these three populations of AGN are possible. Notably, PG 0157+001 has an exceptionally strong mid- to far-IR excess (20-100 $\mu$m). PG 0923+129 and PG 1613+658 also show warm excess with a moderate strength. We will discuss these quasars later.

The far-IR SEDs of most quasars are fitted with our model, suggesting that their dust emissivities lie between normal galaxies ($\beta$=0.7-1, Rieke et al. 2009) and typical AGNs ($\beta$=1.5 for large grains, as assumed in Xu et al. 2015b and this work). However, we find 12 quasars that show a much slower drop of the far-IR emission: PG 0003+199, PG 0007+106, PG 0947+396, PG 0953+414, PG 1116+215, PG 1211+143, PG 1302−102, PG 1341+258, PG 1411+442, PG 1426+015, PG 1535+547, and PG 2214+139. Only two of them – PG 1211+143 and PG 1302−102 – are radio-loud, in which case synchrotron emission may have a substantial influence on the far-IR slope. The reasons for the different dust emissivity of the other quasars are unknown.

### 2.5.2 Identification of the HDD and WDD Quasars

Based on the SED decomposition with different AGN templates, we identify 13 confirmed HDD quasars and another 7 candidate HDD quasars. For the 10 confirmed HDD quasars with image decomposition results, the stellar contribution in the observed $H$-band is less than 30%. The $\chi^2$ of the fit with the HDD template is at least a factor of two better than that with the normal AGN template only (see Table 2.3). Additionally, the HDD template model fits yield stellar near-IR contributions roughly consistent with the image decomposition results. For another four HDD quasars without image decomposition data, the host galaxy contamination is low. According to our fits, the near-IR AGN luminosities of these quasars are mainly contributed ($> 85\%$) by the HDD AGN component, suggesting the dominant HDD behavior. In addition, they have the same blue optical colors as the pure AGN template. Besides PG 1011+772, all the confirmed HDD quasars have not been resolved in 2MASS images, suggesting their weak host galaxy contamination in the near-IR. For PG 1011+772, we confirmed its HDD character because of a strong deficiency (with the peak discrepancy $> 0.3$ dex) of the near- to mid-IR emission if the normal AGN template is used.

The identifications of hot dust deficiency are less secure for the HDD candidate quasars. We show the comparison of fitting results with various AGN templates in Figure 2.6. For PG 0043+039, PG 0844+349, PG 1341+258, and PG 1404+226, the mid- to far-IR SEDs are better produced by the introduction of the HDD AGN template with reduced $\chi^2$ values. However, the host galaxy contribution in the near-IR seems to be strong ($\sim$30-50%), and these four quasars present relatively flat slopes in the optical. For PG 1022+519, PG 1552+085, and PG 2209+184, their dust deficiency is revealed by the overestimated mid-IR emission from the normal AGN template, however, whether they should be picked as HDD or WDD quasars is a question. Consequently, we suggest the HDD quasar fraction in this PG sample is 15%-23%.

The number of identified WDD quasars in the PG sample is 15 with 12 confirmed cases and three candidates. All confirmed WDD quasars show weak mid-infrared emission and a clear hot dust emission peak at $\sim$3 $\mu$m. As stated below, there are three HDD candidates

Table 2.3. Dust-deficient Quasars in $z < 0.5$ PG sample

| ID (1) | Source (2) | $z$ (3) | $f_{\rm nucleus,\ H}$ (4) | Reference (5) | Extended? (6) | $\chi^2_{0.5\text{-}30\mu\rm m}$ (7) |
|---|---|---|---|---|---|---|
| | | | HDD Quasars | | | |
| 0 | 0003+158 | 0.45 | – (1.00) | 0 | N | 1.8 (13.2) |
| 3 | 0026+129* | 0.14 | 0.80 (0.64) | 1 | N | 1.5 (22.2) |
| 5 | 0049+171* | 0.06 | – (1.00) | – | N | 9.4 (53.1) |
| 7 | 0052+251 | 0.16 | – (0.91) | – | N | 2.7 (11.3) |
| 20 | 1011−040 | 0.06 | – (0.61) | – | Y | 10.7 (34.1) |
| 26 | 1100+772 | 0.31 | 0.78 (1.00) | 4 | N | 0.3 (4.5) |
| 29 | 1115+407 | 0.15 | – (0.96) | – | N | 3.1 (12.2) |
| 32 | 1121+422* | 0.23 | 0.93 (1.00) | 2 | N | 0.4 (11.1) |
| 38 | 1216+069 | 0.33 | 0.91 (0.95) | 4 | N | 1.2 (15.7) |
| 43 | 1302−102 | 0.29 | 0.81 (1.00) | 1 | N | 10.9 (20.3) |
| 61 | 1435−067 | 0.13 | 0.73 (0.97) | 1 | N | 0.4 (6.6) |
| 76 | 1626+544* | 0.13 | 0.72 (0.98) | 1 | N | 0.5 (10.8) |
| 86 | 2308+098 | 0.43 | – (0.87) | – | N | 0.5 (5.2) |
| 4 | 0043+039? | 0.38 | – (0.92) | – | N | 0.32 (0.62) |
| 11 | 0844+349? | 0.06 | 0.40 (0.40) | 1 | N | 7.00 (12.6) |
| 22 | 1022+519? | 0.05 | – (0.32) | – | Y | 0.7 (2.8) |
| 48 | 1341+258? | 0.09 | – (0.47) | – | Y | 0.6 (1.2) |
| 54 | 1404+226? | 0.10 | – (0.66) | – | Y | 0.4 (1.2) |
| 72 | 1552+085? | 0.12 | – (0.29) | – | N | 0.3 (1.4) |
| 81 | 2209+184? | 0.07 | – (0.75) | – | Y | 1.5 (7.0) |
| | | | WDD Quasars | | | |

that may be WDD candidates as well. Given these numbers, we estimate the WDD quasar fraction in the PG sample ∼14-17%.

Table 2.3 (cont'd)

| ID (1) | Source (2) | $z$ (3) | $f_{\rm nucleus,\ H}$ (4) | Reference (5) | Extended? (6) | $\chi^2_{0.5\text{-}30\mu\rm m}$ (7) |
|---|---|---|---|---|---|---|
| 9 | 0804+761* | 0.11 | 0.90 (1.00) | 3 | N | 18.7 (152.8) |
| 13 | 0923+201* | 0.19 | 0.77 (1.00) | 1 | N | 2.5 (16.9) |
| 17 | 0953+414 | 0.24 | – (1.00) | – | N | 16.3 (18.5) |
| 24 | 1048−090 | 0.34 | – (1.00) | – | N | 2.7 (5.2) |
| 30 | 1116+215* | 0.18 | 0.95 (1.00) | 1 | N | 46.0 (171.7) |
| 39 | 1226+023 | 0.16 | – (1.00) | – | Y | 947.4 (1740.6) |
| 42 | 1259+593 | 0.47 | 0.94 (1.00) | 4 | N | 1.4 (8.4) |
| 69 | 1535+547 | 0.04 | – (0.37) | – | Y | 2.1 (5.2) |
| 71 | 1545+210 | 0.27 | – (0.81) | – | N | 3.5 (9.6) |
| 75 | 1617+175* | 0.11 | 0.89 (1.00) | 1 | N | 2.6 (63.4) |
| 82 | 2214+139 | 0.07 | 0.47 (0.63) | 1 | Y | 2.1 (37.6 |
| 84 | 2251+113 | 0.32 | 0.94 (0.66) | 1 | N | 1.0 (3.6) |
| 22 | 1022+519? | 0.05 | – (0.61) | – | Y | 0.6 (2.8) |
| 72 | 1552+085? | 0.12 | – (0.41) | – | N | 0.4 (1.4) |
| 81 | 2209+184? | 0.07 | – (0.72) | – | Y | 1.2 (7.0) |

Note. — Column (1): object id; column (2): object name ("PG" is omitted). We denote the ambiguous cases with "?", and the quasars used to derive the template with '*'. ; column (3): redshift; column (4): the contribution of PSF component in the observed $H$ band from the HST image decomposition with the same quantity based on the SED decomposition in the brackets; column (5): references for HST image decomposition results: 1-Veilleux et al. (2009); 2-McLeod & McLeod (2001); 3-Guyon et al. (2006); 4-Shang et al. (2011); column (6): whether the object is picked out as an extended source by 2MASS; column (7): the $\chi^2$ values for data points in the rest-frame 0.5-30 $\mu$m range, the numbers outside and inside the brackets corresponding to the fitting with the dust-deficient template and the fitting with the classical AGN template only.

### 2.5.3 Host Galaxy Contamination

To test if the three SED templates introduced in Section 6.2 are convincing representatives for the infrared emission coming from the AGN component in these PG quasars, we compare the strength of the AGN host galaxy emission deduced from the SED decomposition with that from other independent methods.

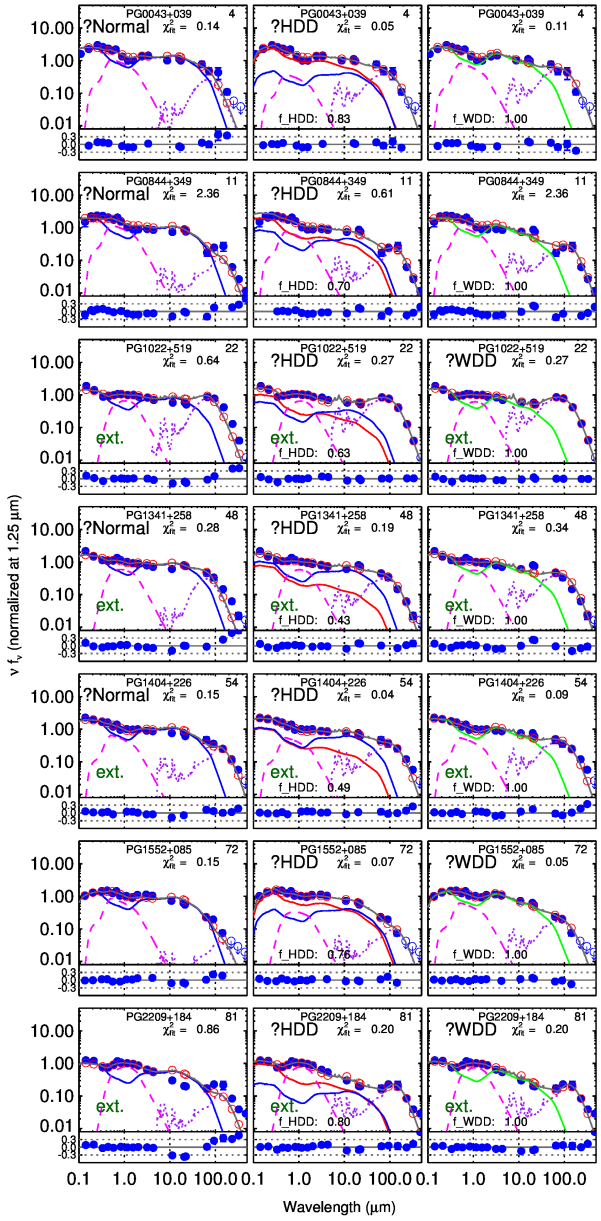


Figure 2.6 SED decomposition of quasars with ambiguous classifications with normal AGN model (left), HDD AGN model (middle) and WDD model (right). The meanings of the lines and the symbols are the same as Figure 2.5.

*Near-IR Stellar Emission* Detailed morphology decomposition of quasars can be applied on deep and high-resolution image observations in the near-IR (e.g., McLeod & McLeod, 2001; Guyon et al., 2006; Veilleux et al., 2009). By comparing the magnitudes of the AGN and the host components, we can calculate the host galaxy fraction at given bands. A similar host galaxy fraction can also be derived from the SED decomposition model. We

can compare the host galaxy fractions from these two methods to check the validity of our model.

Based on the SED decomposition, we computed the host galaxy contribution to the total quasar emission in the observed frame $H$-band, $F_{\rm star,\,H}/F_{\rm quasar,\,H}$. Figure 2.7 shows the comparison of the literature results on the host light fraction of 44 PG quasars retrieved from HST/ground-AO image decomposition (McLeod & McLeod, 2001; Hamilton et al., 2002; Marble et al., 2003; Guyon et al., 2006; Hamilton et al., 2008; Veilleux et al., 2009)[6] with our results based on the SED model. For the majority of these quasars, the host galaxy contributions derived from the SED decomposition and image decomposition are consistent, with an offset of less than 20%.

However, it seems the correlation disappears in the bottom-left corner of Figure 2.7: when the relative contribution of the near-IR stellar light is small (as indicated by the low $F_{\rm star,\,H}/F_{\rm quasar,\,H}$ values from image decomposition), our SED model underestimated – or even failed to identify – the host galaxy emission compared with the HST image decomposition. This is a known systematic bias of such SED models (see Section 5.3.1 in Xu et al. 2015b). Meanwhile, we note that the image decomposition technique suffers a number of systematics. For example, Kim et al. (2008) found that the flux of the host galaxy can be easily overestimated from image decompositions when $F_{\rm star,\,H}/F_{\rm quasar,\,H} \lesssim 0.5$ due to realistic PSF mismatches. It is likely that the systematics and uncertainties present in both AGN-host decomposition methods contribute to the discrepancies. However, the cases with weak host stellar emission are also the ones where the identification of HDD behavior is least likely affected.

Given the fact that our SED decomposition gives consistent results on the near-IR host stellar contamination with that based on the 2D image decompositions, the stellar emission contribution is not likely to lead to any incorrect identifications of HDD or WDD quasars.

With the $H$-band image decomposition results for 28 normal PG quasars, we can also test the validity of the Assef et al. (2010) AGN template to represent the AGN emission. In Figure 2.8, we compare the relative observed-frame $H$-band stellar emission strength derived from the SED model with the Assef et al. (2010) AGN template with the image

[6] See Zhang et al. (2016) for a summary of the image decomposition results of PG quasars in the literature.

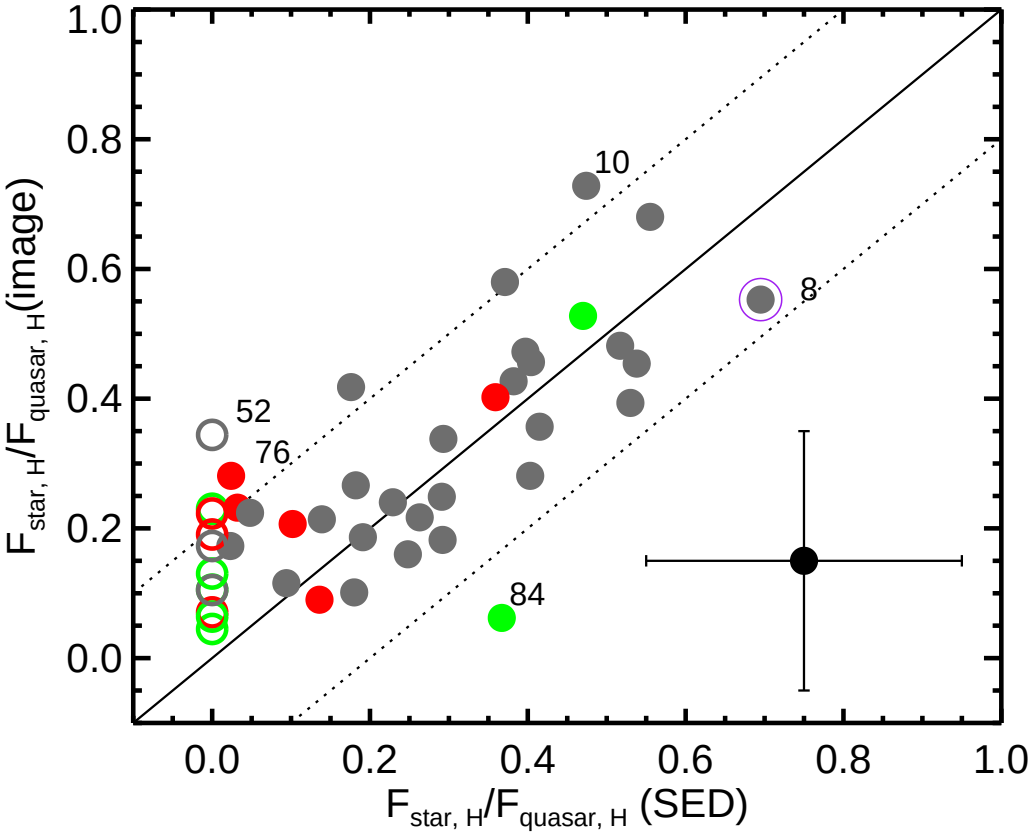


Figure 2.7 Comparison of the host galaxy stellar emission to the total quasar light in observed $H$ band, $F_{\rm star,\,H}/F_{\rm quasar,\,H}$, based on image decomposition and that from SED decomposition. We show the 1:1 relation and $\pm 0.2$ value deviations as solid and dotted black lines. Normal, WDD, and HDD quasars are indicated by gray, green, and red colors. Empty circles indicate that the SED decomposition yielded a near zero host contribution in the corresponding bands. PG 0157+001 (#8, as indicated with a purple circle) has a consistent host galaxy contribution from the SED decomposition and HST results if a warm excess component is introduced (see Section 2.6.1).

decomposition results. It is clear that the Assef et al. (2010) template model overestimates the stellar contamination for these quasars, suggesting that the much stronger 1 $\mu$m dip of the Assef et al. (2010) is unphysical. In other words, the Elvis et al. (1994)-like templates are preferred over the Assef et al. (2010) template to represent the AGN intrinsic near-IR emission of normal quasars.

*Mid- to Far-IR Dust Emission* The bolometric infrared luminosity of a galaxy is believed to be dominated by the dust thermal emission heated by hot, young stars, providing a mea-

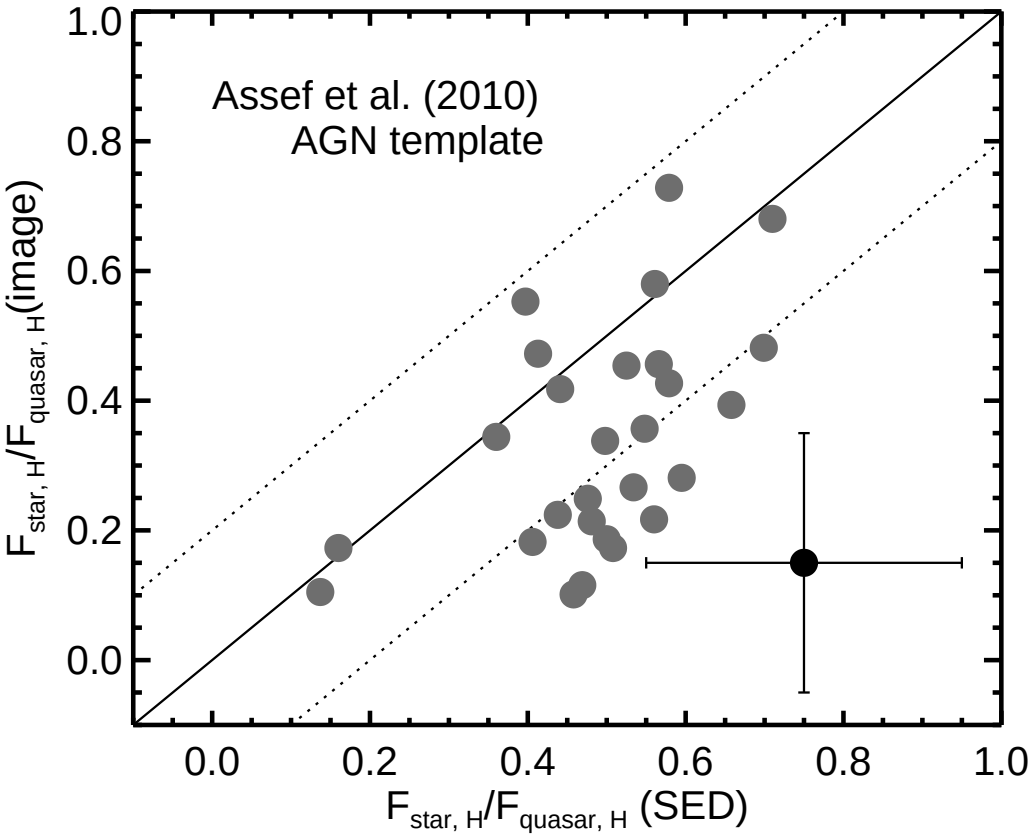


Figure 2.8 Comparison of imaging and SED deconvolution results for normal quasars and using the Assef et al. (2010) AGN template. The symbols and axes have the same meanings as in Figure 2.7.

sure of the SFR (e.g., Kennicutt, 1998). To calibrate the infrared emission of the quasar host galaxies, we can compare the SFRs based on the IR luminosities of the host galaxies from the SED decompositions with the SFRs based on another independent method. For quasars, the 11.3 $\mu$m aromatic feature is perhaps the only plausible spectroscopic star formation indicator where the AGN influence is negligible (Diamond-Stanic & Rieke, 2010; Esquej et al., 2014; Alonso-Herrero et al., 2014). Assuming the Kennicutt (1998) law, we compare the IR-derived SFRs with the SFR measurements based on the 11.3 $\mu$m aromatic feature strength by Shi et al. (2014) in Figure 2.9. The SFR results for the majority of PG quasars are consistent[7]. There is an indication that the SFRs based on the aromatic feature

[7]Among the three outlier quasars, PG 1216+069 (#38) and PG 2308+098 (#86) have low signal-to-noise spectra, which make the spectral measurements uncertain. PG 1259+593 (#42) shows a very broad and

are lower than the IR-derived SFRs when the SFRs are low (e.g., SFR $\lesssim 10\ M_{\odot}\mathrm{yr}^{-1}$). This could be due to (1) the difficulty of measuring the aromatic features when the AGN dominates the *Spitzer*/IRS infrared spectra; (2) that the 11.3 $\mu$m aromatic feature strength is reduced by the prominent AGN emission in luminous quasars; (3) the possible dust far-IR emission heated by old stars (e.g., Devereux & Eales, 1989; Popescu et al., 2002) in quasar host galaxies. Nevertheless, for the science goals of this paper, such deviations are only a secondary effect. At high SFRs, where the fits are best-constrained, there is no evidence for such a shift in the calibration. Thus, we suggest the infrared emission of the host galaxies is properly retrieved from our model.

The consistent SFR results with both of the methods in Figure 2.9 show that both the WDD and normal AGN templates are being applied appropriately. For the same near-IR luminosities, the WDD AGN template produces $\sim 45\%$ of the total infrared luminosity (8-1000 $\mu$m) of the normal AGN template. As there is no necessity to shift the positions of the normal quasars to match the 1:1 line in Figure 2.9, we can conclude that the WDD template is not the best choice to represent the intrinsic IR emission of normal quasars.

## 2.6 Discussion

### 2.6.1 The Diversity of Infrared Colors of PG Quasars

With the three AGN templates (Section 6.2) and our SED model (Section 2.4), we can explain the diversity of the near- to mid-IR colors of the PG quasars. For a normal AGN, the infrared SED is characterized by a quick upturn from the 1.25 $\mu$m inflection and a broad mid-infrared plateau in $\lambda$-$\nu f_{\nu}$ space from $\sim$3-20 $\mu$m. The relative strengths of these SED features can be found by normalizing the corresponding peak flux by the flux at the 1.25 $\mu$m inflection. As shown in Figure 2.2, a $\gtrsim 0.3$ dex deviation from the classical AGN template starts at $\sim 3.0$ $\mu$m for the HDD templates and at $\sim 10.0$ $\mu$m for the WDD template. As a result, we propose to use luminosities at 3.0 and 10 $\mu$m to reflect the

prominent silicate feature. The two Gaussian functions used to fit the silicate profile are widely separated, producing a local dip at $\sim 11$ $\mu$m (see the online Figure 1 of Shi et al. 2014) that is unphysical. As a result, for PG 1258+593, the equivalent width of the 11.3 $\mu$m aromatic feature above such a silicate feature continuum could be overestimated.

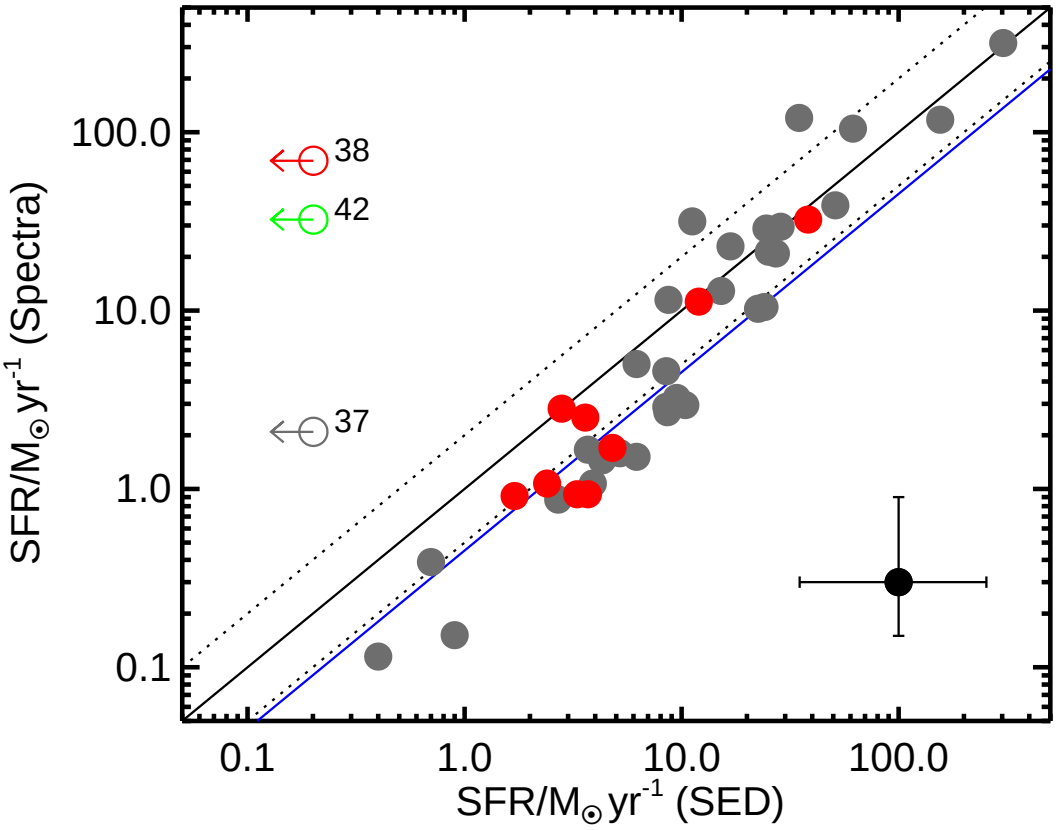


Figure 2.9 Comparison of the star formation rates derived through our fitting of the FIR SEDs with those in Shi et al. (2014) from the 11.3 $\mu$m aromatic feature strength. Normal, WDD, HDD quasars are shown as gray, green, and red dots, respectively. Open circles with a leftside arrow indicate that the quasars do not have sufficiently strong host galaxy contributions in the far-IR to derive a meaningful SFR (we arbitrarily set their SFRs = 0.2 $M_\odot$yr$^{-1}$ to plot these quasars in the figure). We show the 1:1 relation and its 0.3 dex deviations as solid and dotted black lines. The blue line denotes that the SFRs from SED decomposition for normal quasars should be increased by 2.2 times if the WDD template is adopted to represent the AGN intrinsic emission, resulting in a 0.34 dex offset from the 1:1 relation.

relative strengths of the hot and warm dust. For the Elvis template, we have

- intrinsic hot dust peak:

$$\lambda f_{\mathrm{normal},\lambda}[3.0\mu\mathrm{m}/1.25\mu\mathrm{m}] = 1.98 \ ;$$

- intrinsic warm dust peak:

$$\lambda f_{\mathrm{normal},\lambda}[10.0\mu\mathrm{m}/1.25\mu\mathrm{m}] = 2.29 \ .$$

We derive the observed quasar SED continuum by logarithmic interpolation on the UV-to-IR photometry and calculate the corresponding color $\lambda f_\lambda[3.0\mu\mathrm{m}/1.25\mu\mathrm{m}]$, and $\lambda f_\lambda[10.0\mu\mathrm{m}/1.25\mu\mathrm{m}]$. In Figure 2.10, we present the color distribution of all 87 PG quasars as well as their individual continuum SEDs.

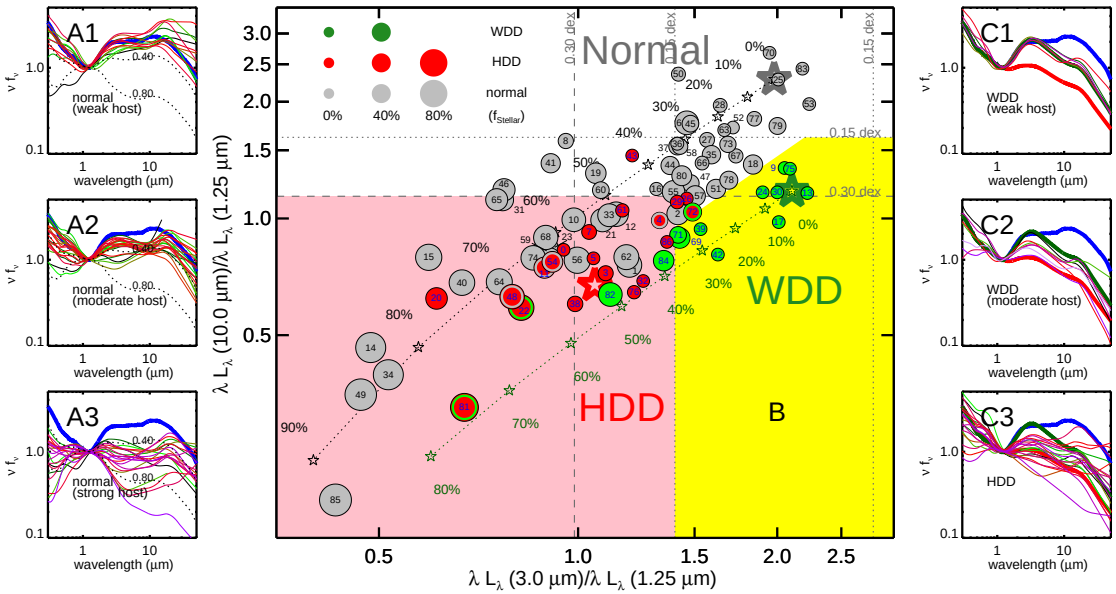


Figure 2.10 Infrared color distribution of the 87 PG quasars (Panel B) and various SEDs of normal quasars (Panels A1, A2, A3) and dust-deficient quasars (Panels C1, C2, C3). In panel B, the shaded regions denote quasars with different infrared properties. The colors of the templates for normal, WDD, and HDD quasars are plotted as black, green, and red big five-pointed stars. We also show the locations of normal and WDD quasars with different levels of host galaxy contributions as small five-pointed stars connected with dotted lines. Individual quasars are shown as dots with the sizes determined by the stellar near-IR contribution from the SED fittings. We denote the ambiguous cases with thick circles inside the dots. Panels A1, A2, A3 show the SEDs of individual normal quasars with 10.0/1.25 colors deviating from the Elvis template (red thick line) $< 0.15$ dex, 0.15-0.30 dex, $> 0.30$ dex, respectively. Panels C1 and C2 present the SEDs of all WDD quasars (green dots in panel B). Panel C3 shows the SEDs of all HDD quasars (red dots in panel B).

The most obvious feature of panel B in Figure 2.10 is that most quasars are distributed along the diagonal direction with changes of both apparent hot and warm dust emission. Such a diagonal distribution is mainly caused by the increasing near-IR contamination from the host stellar emission. For a normal quasar, as the host galaxy contribution increases, the position in Figure 2.10 is shifted to the lower left corner. To demonstrate

this, we combine the normal (Elvis) AGN template with a single old stellar population template, and calculate the colors of the composite SED as a function of the galaxy contribution in the near-IR (shown as small five-pointed stars connected with the dotted gray line in Figure 2.10). As expected, all normal quasars are randomly distributed along this normal quasar color line, and their galaxy contributions in the near-IR from the individual SED decompositions are roughly consistent with the model line. From panels A1, A2, to A3, as the apparent warm dust emission decreases, we see a systematic decrease of the optical slope for the normal quasars. The observed SEDs in these panels are also roughly consistent with the mock quasar SEDs using a combination of the normal AGN template and old stellar template with different relative strengths.

As Figure 2.10 shows, the colors of the HDD PG quasars typically deviate from the Elvis template by more than $-0.15$ dex for $\lambda f_{\mathrm{normal},\lambda}[3.0\mu\mathrm{m}/1.25\mu\mathrm{m}]$ and $-0.3$ dex for $\lambda f_{\mathrm{normal},\lambda}[10.0\mu\mathrm{m}/1.25\mu\mathrm{m}]$ (see Figure 2.2). Thus, we denote an HDD region in Figure 2.10 as

- apparent hot dust strength:

$$\lambda f_{\lambda}[3.0\mu\mathrm{m}/1.25\mu\mathrm{m}] < 1.40\ (-0.15\ \mathrm{dex})\ ,$$

- apparent warm dust strength:

$$\lambda f_{\lambda}[10.0\mu\mathrm{m}/1.25\mu\mathrm{m}] < 1.14\ (-0.30\ \mathrm{dex})\ .$$

A large number of normal quasars are also located in the HDD region. The cause of this contamination can be identified from Panels C3 and A3. HDD quasars have a blue UV-optical continuum similar to the AGN template, while normal quasars in the same region show strong galaxy contamination in the optical and near-IR.

In the lower-right region of Figure 2.10 are the WDD quasars, with the $\lambda f_{\mathrm{normal},\lambda}[3.0\mu\mathrm{m}/1.25\mu\mathrm{m}]$ color within $-0.15$ dex of the classical AGN, but $\lambda f_{\mathrm{normal},\lambda}[10.0\mu\mathrm{m}/1.25\mu\mathrm{m}]$ deviation greater than 0.15 dex. We can define a WDD region, where

- apparent hot dust strength:

$$\lambda f_{\lambda}[3.0\mu\mathrm{m}/1.25\mu\mathrm{m}] > 1.40\ (-0.15\ \mathrm{dex})\ ,$$

- apparent warm dust strength:

$$\lambda f_\lambda[10.0\mu\mathrm{m}/1.25\mu\mathrm{m}] < 1.62\ (-0.15\ \mathrm{dex})\ ,$$

- diagonal direction cut:

$$\log_{10}(\lambda f_\lambda[10.0\mu\mathrm{m}/1.25\mu\mathrm{m}]) > 1.98\log_{10}(\lambda f_\lambda[3.0\mu\mathrm{m}/1.25\mu\mathrm{m}]) - 0.39\ .$$

The third cut along the diagonal direction is based on the mock SED mixing galaxy and AGN templates. The contamination of normal quasars in this WDD region is quite low. We also see an increasing host galaxy contribution along the diagonal direction in the central panel, consistent with the prediction from the mock SEDs composed of the WDD template and a near-IR stellar template. The increasing host contribution among WDD quasars can also be seen in panel C1 ($\lambda f_\lambda[10.0\mu\mathrm{m}/1.25\mu\mathrm{m}] < 0.30$ dex of the Elvis template) and panel C2 ($\lambda f_\lambda[10.0\mu\mathrm{m}/1.25\mu\mathrm{m}] > 0.30$ dex of the Elvis template), for which the decrease of apparent warm dust emission is caused by the stronger host galaxy contamination at 1.25 $\mu$m. This behavior emphasizes the risk of host galaxy contamination in any purely photometric means to identify HDD quasars. However, it appears that such simple methods may work reasonably well for WDD objects, though there is still a mixture of normal quasars in their color space in the figure.

Broad IR spectral features may also influence the infrared colors of quasars. On average, type 1 quasars have moderate silicate emission at $\sim$ 10 $\mu$m with strength[8] $\sim$0.20 (e.g., Hao et al., 2007), which corresponds to 0.08 dex of the local continuum. This is much smaller compared to the 0.3 dex difference we picked to separate the HDD quasars. However, for individual quasars, the 10 $\mu$m silicate feature strength can be very large, in which cases its influence should be considered.

A number of normal quasars above the normal quasar color line present a smooth SED gradually peaked at the mid-infrared, e.g., PG 0157+001, PG 0934+013, PG 1119+120,

[8] The silicate strength is defined as

$$S_{10} = \ln\left(\frac{I_{\lambda*,\mathrm{obs}}}{I_{\lambda*,\mathrm{cont}}}\right),$$

where $\lambda*$ is the wavelength of the 10 $\mu$m silicate feature peak, $I_{\lambda*,\mathrm{obs}}$ and $I_{\lambda*,\mathrm{cont}}$ are the corresponding observed and continuum intensities, respectively.

PG 1244+026, PG 1310−108, PG 1351+640, PG 1501+106. Our best fitted model underpredicts the emission at 20-100 $\mu$m, suggesting a warm excess. Similar behavior has also been found for type-1 AGN at $z \sim$0.3-3 (Xu et al., 2015b; Kirkpatrick et al., 2015) as well as the low-luminosity AGNs in nearby Seyfert galaxies (e.g., Ho, 1999, 2008; Prieto et al., 2010). One possibility to generate this component is a very compact ($\lesssim$1 pc) starbursting disk in the nucleus of the galaxy (Thompson et al., 2005; Ballantyne, 2008). In most cases, our test fitting with an additional warm component following Xu et al. (2015b) hardly improved the $\chi^2$, suggesting that even if the warm-excesses are present, their contribution should be moderate. Another possibility is the additional IR-processed AGN emission by dust either in the galactic interstellar medium (e.g., Schneider et al., 2015; Roebuck et al., 2016) or in the polar region of the nucleus (e.g., Raban et al., 2009; Hönig et al., 2012, 2013; Tristram et al., 2014; Asmus et al., 2016; López-Gonzaga et al., 2016). For PG 0157+001, it could also be its strong shocks (e.g., Leipski et al., 2006), which may break up the surrounding dust into much smaller grains and boost the mid-IR emission.

### 2.6.2 Characteristics of the Dust-deficient PG Quasars

To judge if the dust-deficient population has special AGN properties, we compare the distributions of the black hole masses, AGN luminosities, as well as Eddington ratios between the dust-deficient quasars and normal quasars, as shown in Figure 2.11. We collect the black hole mass measurements from Peterson et al. (2004); Vestergaard & Peterson (2006), and Denney et al. (2010) with a virial factor from Woo et al. (2010). The AGN luminosities are derived from the AGN templates with the normalization from our SED decomposition results. Although the HDD population has identical luminous AGNs and massive black holes compared to the normal quasar population, its members have lower Eddington ratios ($f_{\rm Edd} = L_{\rm AGN}/L_{\rm Edd} \lesssim 0.1$) compared with normal quasars ($f_{\rm Edd,\ normal}$=0.1-1). The Kolmogorov-Smirnov (K-S) test yields a probability of only $\sim 0.025$ that the Eddington ratios of the HDD quasars are drawn from the same distribution as those of normal quasars. Additionally, we note the most HDD PG quasar, PG 0049+171, has the lowest Eddington ratio among the confirmed HDD quasars. All these observations suggest the

hot dust deficiency is possibly linked to the AGN Eddington ratio. Compared with normal quasars, the WDD quasars have higher AGN luminosities with a K-S probability of $\sim$0.057 that the parameter is drawn from the same distributions as for normal quasars. For both HDD and WDD quasar populations, their black hole masses do not show strong differences compared with the normal quasar population. We also explore if the dust deficiency is related to the quasar radio loudnesses, which was defined and measured by Kellermann et al. (1989). The fractions of radio-loud quasars among the HDD, WDD, and normal sample are quite similar (12%, 20%, 16%, respectively), suggesting the radio properties may not influence the dust deficiency.

We now explore whether the fraction of dust-deficient quasars is dependent on AGN luminosity. In Figure 2.12, we show the number fraction of dust-deficient quasars compared with normal quasars in three luminosity bins, $\log(L_{\rm AGN}/L_{\odot}) = [10.5, 11.5], [11.5, 12.5], [12.5, 13.5]$. The ambiguous cases for the HDD and WDD quasars are removed in the analysis. We can see the HDD quasar fraction is not sensitive to AGN luminosity, confirming similar conclusions reached by Hao et al. (2010, 2011) and Mor & Trakhtenbrot (2011). In contrast, the fraction of WDD quasars shows a clear boost with increasing AGN luminosity, which is generally consistent with the anti-correlation between the IR-optical luminosity ratio and AGN luminosity, as found by many authors (e.g., Maiolino et al., 2007; Roseboom et al., 2013; Mateos et al., 2016).

Results from previous studies on the relation between the hot dust deficiency and AGN properties are contradictory. Jiang et al. (2010); Jun & Im (2013) suggested that the quasars with weak hot dust emission tend to have relatively low black hole masses ($M_{\rm BH} \sim 10^8\ M_{\odot}$), and high Eddington ratios. On the contrary, Hao et al. (2010); Mor & Trakhtenbrot (2011) argued that the hot-dust-poor quasars are identical to normal quasars in $M_{\rm BH}$ and $f_{\rm Edd}$. We firstly note that all these studies focus on the very luminous quasars, with Hao et al. (2010); Mor & Trakhtenbrot (2011); Jun & Im (2013) at $L_{\rm AGN} \gtrsim 10^{12}\ L_{\odot}$ and Jiang et al. (2010) at $L_{\rm AGN} \gtrsim 10^{13}\ L_{\odot}$. As argued in Section 4.5, there is a bias toward more efficient dust-deficient quasar identification at higher AGN luminosity (also at higher redshift) using an optical-to-NIR color selection (e.g., Jiang et al. 2010; Jun & Im 2013). The AGN luminosities of the 87 PG quasars range from $10^{10.5}$ to $10^{13.5}\ L_{\odot}$. Since the

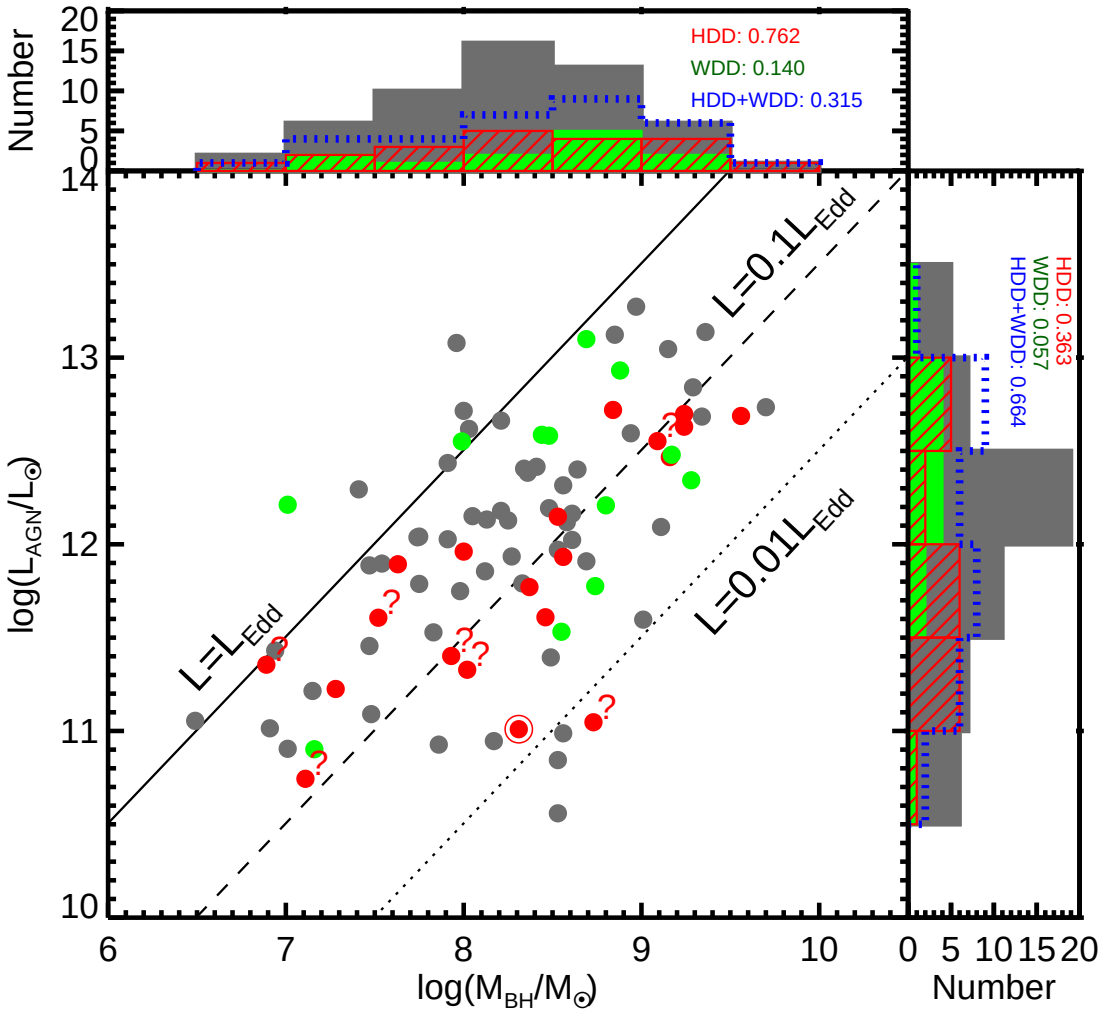


Figure 2.11 Distributions of AGN luminosities and black hole masses of 87 PG quasars color encoded by their infrared properties: gray for normal quasars, green for WDD quasars, and red for HDD quasars. We indicate the ambiguous HDD quasars with question marks and the most HDD quasar, PG 0049+171, with a red circle. The histograms of the properties of normal (gray shaded), WDD (green shaded), HDD (red crossed), and WDD+HDD (blue dotted line) quasars are shown on the corresponding sides. The K-S probabilities of the dust-deficient quasar samples against the normal quasar sample for the corresponding quantities are also presented.

Eddington ratios of AGN are positively correlated with their bolometric luminosities (e.g., Lusso et al., 2012), we are probing the dust deficiency in the weak accretion state of the black hole, different from previous studies.

The silicate feature is an important diagnostic of the dust structure around the AGN. In Figure 2.13, we investigate the strength of this feature, $S_{10}$, for different types of quasars

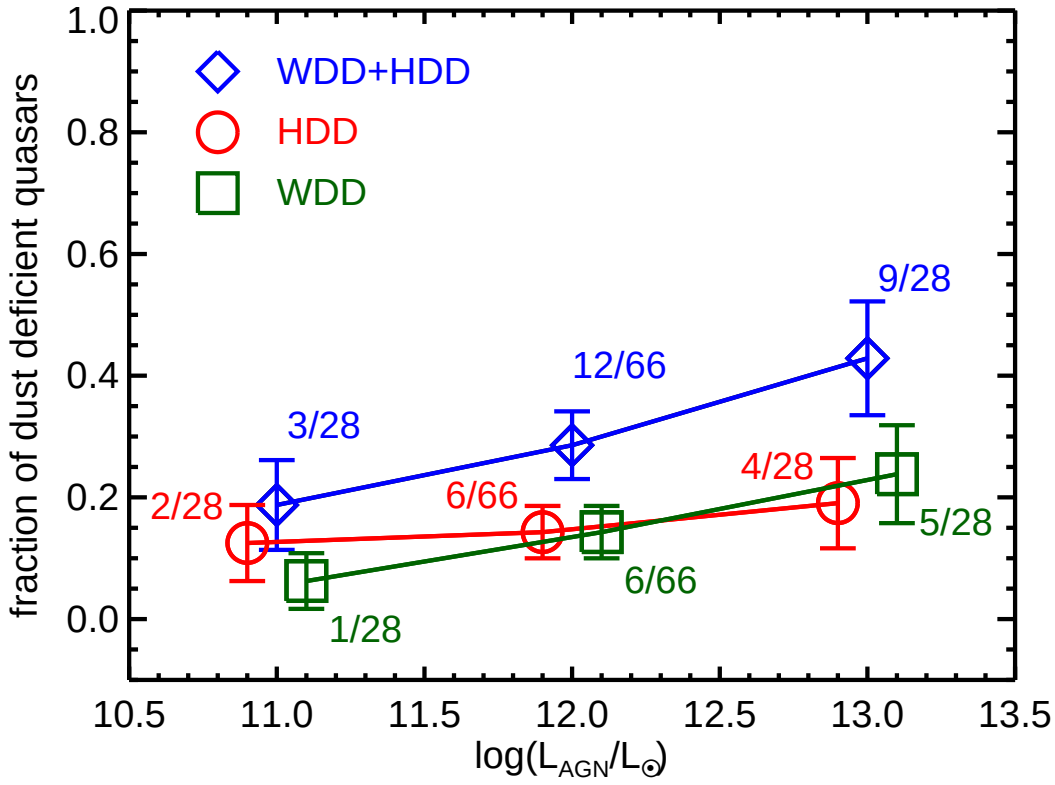


Figure 2.12 Fractions of dust-deficient quasars as a function of AGN luminosity. We denote the numbers of the dust-deficient quasars and the normal quasars in each luminosity bin. For clarity, data points for HDD and WDD populations are arbitrarily shifted on the X-axis.

compared with the AGN luminosity. The silicate measurements are adopted from Shi et al. (2014). We do not find any strong dependence of the silicate emission strength on the AGN luminosity, as seen by, e.g., Maiolino et al. (2007), which is possibly due to the limited dynamical range of the AGN luminosities of the PG sample. Meanwhile, the two dust-deficient populations peak at stronger silicate emission compared with the normal quasar population with K-S probabilities $< 0.01$ of being drawn from the same distribution.

The K-S probabilities of the AGN properties discussed in this section are summarized in Table 5.8. We caution that the PG sample is known to be incomplete (e.g., Jester et al., 2005) and the sample size is relatively small. Statistical studies on a much larger sample with a similar rich set of multiband observations are needed to solidify these arguments.

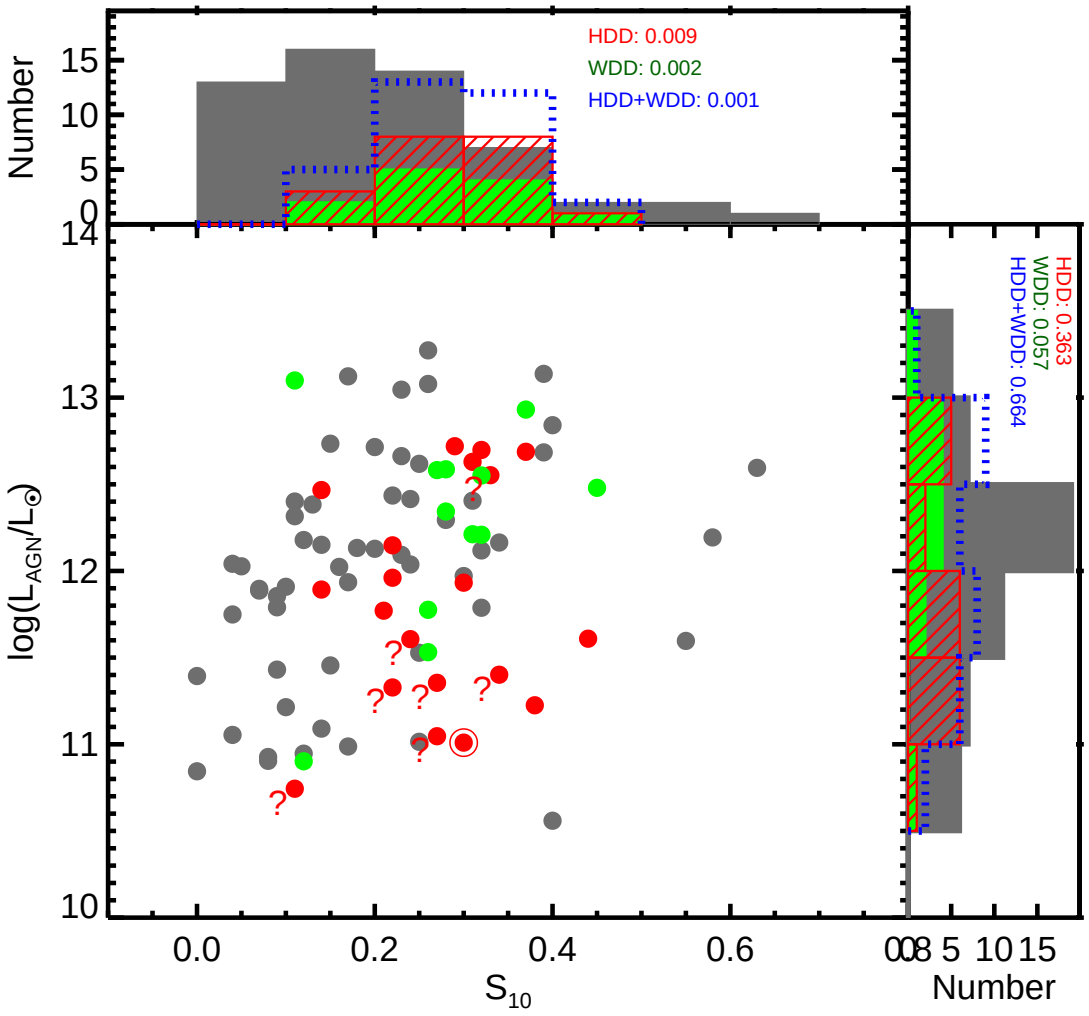


Figure 2.13 Distributions of AGN luminosities ($L_{\rm AGN}$) and 10 $\mu$m silicate strength ($S_{10}$) for normal, WDD and HDD quasars. Symbols and styles are the same as Figure 2.11.

### 2.6.3 Are the High-$z$ Dust-deficient Quasars Abnormal in Terms of Their SEDs?

$z \gtrsim 5$ Jiang et al. (2010) suggested that the two $z \sim 6$ quasars, J0005−0006 and J0303−0019, are dust-free due to their exceptionally low rest-frame 3.5 $\mu$m to 5,100 Å luminosity ratios. In the upper panel of Figure 2.14, we plot the near-IR to optical ratios as a function of luminosity for the $z > 5$ sample with the photometry data in Leipski et al. (2014) and the $z < 0.5$ PG quasars. The 11 $z > 5$ quasars with a dearth of hot dust emission (see Leipski et al. 2014, Lyu et al. 2016) are distributed around the value for the HDD AGN template. In the lower panel of the same figure, we compare the SEDs of three extreme

Table 2.4. K-S probabilities of the HDD and WDD quasars against normal quasars

| Property | HDD | WDD | HDD+WDD |
|---|---|---|---|
| $L_{\rm AGN}$ | 0.363 | **0.057**$^*$ | 0.664 |
| $M_{\rm BH}$ | 0.762 | 0.140 | 0.315 |
| $L_{\rm AGN}/L_{\rm Edd}$ | **0.025** | 0.688 | **0.074** |
| $S_{10}$ | **0.009** | **0.002** | **0.001** |

$^*$We indicate significant differences in bold.

cases: SDSS J0005−0006, SDSS J0303−0019, and SDSS J1411+1217, to the HDD AGN template as well as the SED of the most extreme HDD PG quasar PG 0049+171. We can see the SEDs of SDSS J0005−0006 and SDSS J1411+1217 are quite similar to that of PG 0049+171, suggesting that the latter could be a counterpart to the most dust-poor quasars at $z \sim 6$. Additionally, the *Spitzer*/IRAC 3.6 $\mu$m band (rest-frame 5100 $\AA$) is possibly contaminated by the optical H$\beta$ and [N II] emission lines at $z \sim 6$, thus a very low rest-frame 3.5 $\mu$m to 5,100 $\AA$ ratio may result. Therefore, the overall SEDs of the $z \sim 6$ hot-dust-free quasars resemble the HDD template, given the possible variation of the UV/optical slopes and emission line contaminations.

Besides the three extreme HDD $z \sim 6$ quasars above, Leipski et al. (2014) also suggested another eight HDD candidates (see also Lyu et al. 2016), as listed in Table 2.5 . We show their rest-frame SEDs in the top-left panel of Figure 2.15. These $z \gtrsim 5$ quasar SEDs are matched by our HDD AGN template reasonably well. At $z \gtrsim 5$, we also identified 10 WDD quasars from the Leipski et al. (2014) sample (as also listed in Table 2.5). Their SEDs present a strong near-IR hot dust emission bump but are weak in the mid-IR, as indicated by faint emission or even non-detections in the *Herschel* PACS 70 $\mu$m bands (the top-right panel in Figure 2.15). As argued in Lyu et al. (2016), the host galaxies of these quasars are likely to have a strong contribution to the mid-IR SEDs, due to their low-metallicity and compact starbursting properties. We expect that the mid-IR emission contributed by the AGN is smaller than the rest-frame mid-IR data points indicate. The number fraction of the $z \gtrsim 5$ WDD quasars in Leipski et al. (2014) is $\sim 14\%$.

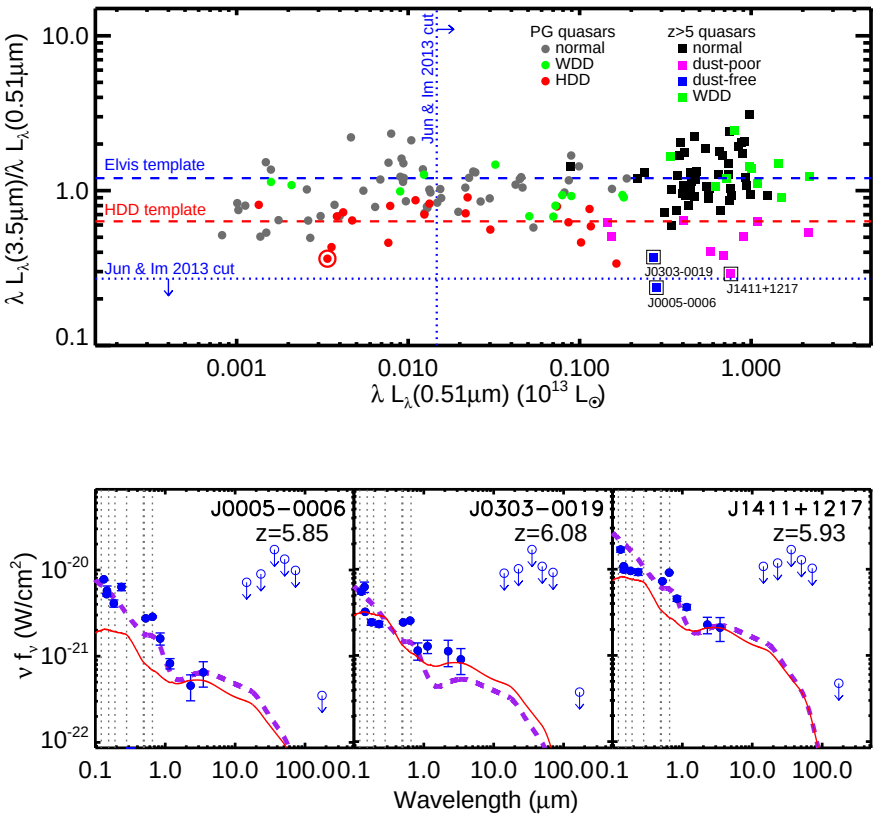


Figure 2.14 Upper panel: the 3.5 $\mu$m-to-0.51 $\mu$m (rest wavelengths) luminosity ratio as a function of the optical luminosity at 0.51 $\mu$m for PG quasars (dots) and $z \gtrsim 5$ quasars (squares). We use the PG quasar continuum SED based on this work and updated photometry of $z \gtrsim 5$ quasars (Leipski et al., 2014) to derive the corresponding quantities. $[\lambda L_\lambda(3.5\mu\mathrm{m})]/[\lambda L_\lambda(0.51\mu\mathrm{m})] = 0.5$ is denoted as the dotted line. The 3.5 $\mu$m-to-0.51 $\mu$m luminosity ratio for the most HDD quasar PG 0049+171 (marked with a red open circle) is shown as the dashed red line. For PG quasars, the gray, green, red colors represent normal, WDD, and HDD quasars. For $z \gtrsim 5$ quasars, the blue color represents the two hot-dust-free quasars in Jiang et al. (2010), the magenta represents the other hot-dust-poor quasars as suggested by Leipski et al. (2014), and the green represents the WDD quasars listed in Table 2.5. The three (possibly) hot-dust-free quasars, SDSS J005−0006, SDSS J0303-0019 and J1411+1217, are marked with black open squares. Lower panel: SEDs of the three (possibly) hot-dust-free quasars at $z \sim 6$. Observational data points are shown as blue dots (detection) and open circles with arrows (upper limit). We also scale the HDD template (red line) to the near-IR data points ($\lambda \sim$2-3 $\mu$m), and show the SED of the possible host galaxy observed at that redshift (red line). Comparisons with the SED of PG 0049+171 (purple dashed line) that has an extreme deficiency of hot dust emission are also included. We also indicate the locations of strong UV-optical lines, i.e., Ly$\alpha$, $C_{IV}$, $C_{III]}$, H$\beta$, H$\alpha$ (from left to right), as vertical dotted lines.

Table 2.5. Dust-deficient Quasars at $z$=0.5-6

| Source (1) | $z$ (2) | Type (3) |
|---|---|---|
| $z \gtrsim 5$ quasars in Leipski et al. (2014) | | |
| SDSS J001714.67−100055.4 | 5.01 | WDD |
| SDSS J073103.12+445949.4 | 5.01 | WDD |
| SDSS J081827.40+172251.8 | 6.00 | WDD |
| SDSS J104845.05+463718.3 | 6.23 | WDD |
| SDSS J114816.64+525150.3 | 6.43 | WDD |
| SDSS J122146.42+444528.0 | 5.19 | WDD |
| SDSS J125051.93+313021.9 | 6.13 | WDD |
| SDSS J142325.92+130300.7 | 5.08 | WDD |
| SDSS J162626.50+275132.4 | 5.30 | WDD |
| SDSS J211928.32+102906.6 | 5.18 | WDD |
| SDSS J000552.34−000655.8* | 5.85 | HDD |
| SDSS J013326.84+010637.7 | 5.30 | HDD |
| SDSS J023137.65−072854.5 | 5.41 | HDD |
| SDSS J030331.40−001912.9* | 6.08 | HDD |
| SDSS J083643.85+005453.3 | 5.81 | HDD |
| SDSS J114657.79+403708.7 | 5.01 | HDD |
| SDSS J120823.82+001027.7 | 5.27 | HDD |
| SDSS J124247.91+521306.8 | 5.05 | HDD |
| SDSS J141111.29+121737.4* | 5.93 | HDD |
| SDSS J222845.14−075755.2 | 5.14 | HDD |
| WFS J2245+0024 | 5.17 | HDD |

Table 2.5 (cont'd)

| Source (1) | $z$ (2) | Type (3) |
|---|---|---|
| AGN with MIPS 24 $\mu$m Flux $>$ 1 mJy in Xu et al. (2015b) | | |
| LoCuSS J131107.34−012857.9 | 0.92 | WDD |
| LoCuSS J164116.66+463946.3 | 1.13 | WDD |
| LoCuSS J163950.35+463327.1 | 2.09 | WDD |
| LoCuSS J024725.09−033807.9 | 2.42 | WDD |
| LoCuSS J090021.93+210803.9 | 0.70 | HDD |
| LoCuSS J164025.01+464449.2 | 0.54 | HDD |
| LoCuSS J024851.43−032249.3 | 0.30 | HDD |
| AGN with MIPS 24 $\mu$m Flux $<$ 1 mJy ** | | |
| LoCuSS J010720.40+005435.2 | 1.47 | HDD |
| LoCuSS J084218.48+362504.1 | 2.24 | HDD |
| LoCuSS J084258.80+361444.2 | 2.50 | HDD |
| LoCuSS J015208.74+010823.6 | 0.56 | HDD |
| LoCuSS J015202.95+010445.3 | 1.05 | HDD |

*The most extreme HDD quasars at $z \sim 6$.

**The data of LoCuSS AGN with $f_{24\ \mu\mathrm{m}} < 1$ mJy is provided by L. Xu (2016, private communication).

As shown by Leipski et al. (2014), the stacked SED of 33 *Herschel* non-detected $z \gtrsim 5$ quasars is not matched optimally with the classical AGN template (also see Lyu et al. 2016). With the AGN templates derived in this work, we find the average SED of the far-IR non-detected $z > 5$ quasars lies between the WDD and HDD AGN templates, as seen in Figure 2.16. Combining our previous work (Lyu et al., 2016) with the discussion in this section, we can conclude that the SEDs of the luminous quasars at $z \gtrsim 5$ can be characterized by the normal AGN template, WDD template, and HDD template derived from the $z < 0.5$ PG quasars. In other words, there is no indication of strong evolution of AGN infrared SEDs at $z \gtrsim 5$.

*$z \sim$0.5-2.5* For the majority of AGNs with *Spitzer*/MIPS 24 $\mu$m flux density $> 1$ mJy in the Local Cluster Substructure Survey (LoCuSS[9]), Xu et al. (2015b) presented accurate

[9] http://www.sr.bham.ac.uk/locuss/

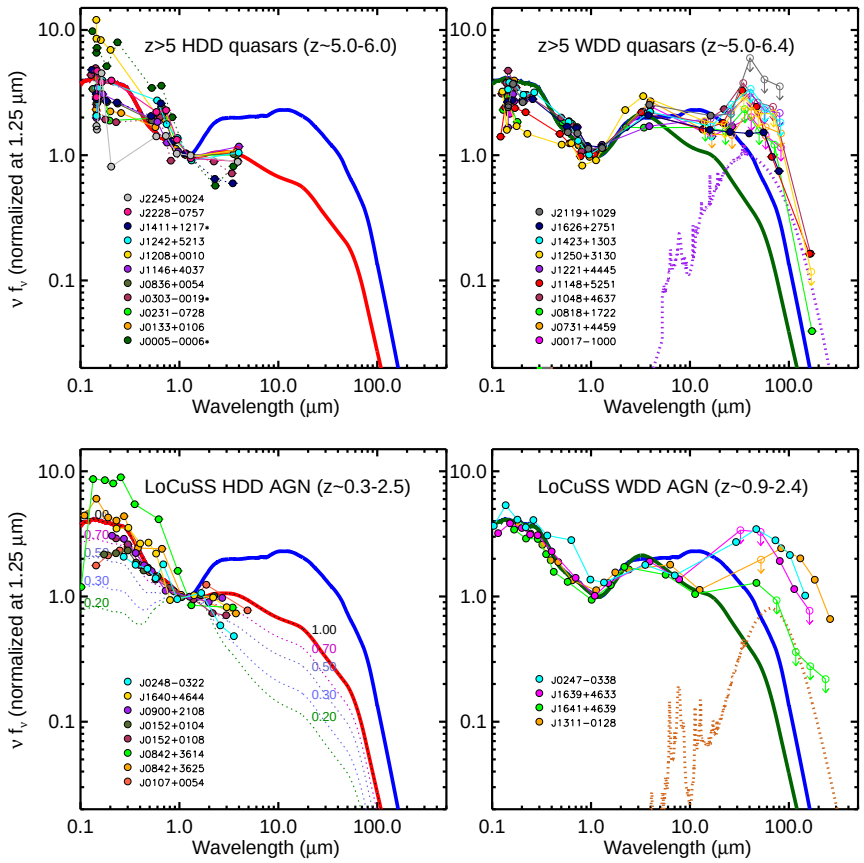


Figure 2.15 The SEDs of hot-dust-deficient and warm-dust-deficient quasars at high and intermediate redshifts. We also show the normal Elvis et al. (1994) AGN template (far-IR corrected; blue solid line), the HDD template (red solid line) and the WDD template (green solid line) in corresponding panels. In the top-left panel, we denote the three most HDD quasars at $z \sim 6$, J0005−0006, J0303−0019, and J1411+1217, with '*' and use dotted lines to connect the SED data points. Compared with the very luminous $z \gtrsim 5$ quasars, the LoCuSS AGNs are not bright and near-IR stellar contamination in the SED is still possible. As a result, we also show composite quasar SEDs composed of the HDD template and an old stellar population template (dotted lines with numbers to denote the host galaxy contribution at 1.25 $\mu$m) in the bottom-left panel. In the right panels, we also plot the IR SEDs of most possible kinds of host galaxies: a low-metallicity, compact, starbursting galaxy as represented by Haro 11 for $z \gtrsim 5$ quasars (Lyu et al. 2016; the purple dotted line in the top-right panel); a normal star-forming galaxy as represented by the Rieke et al. (2009) $\log(L_{\rm IR}/L_{\odot}) = 11.5$ galaxy template for $z \sim 2$ AGN (Xu et al. 2015b; the orange dotted line in the bottom-right panel).

decompositions with the same normal AGN template used in this work. We also searched for HDD and WDD quasars in this survey. Eight LoCuSS quasars with redshifts of 0.3-2.5 show indications of weak hot dust emission (see Table 2.5 and the bottom-left panel of

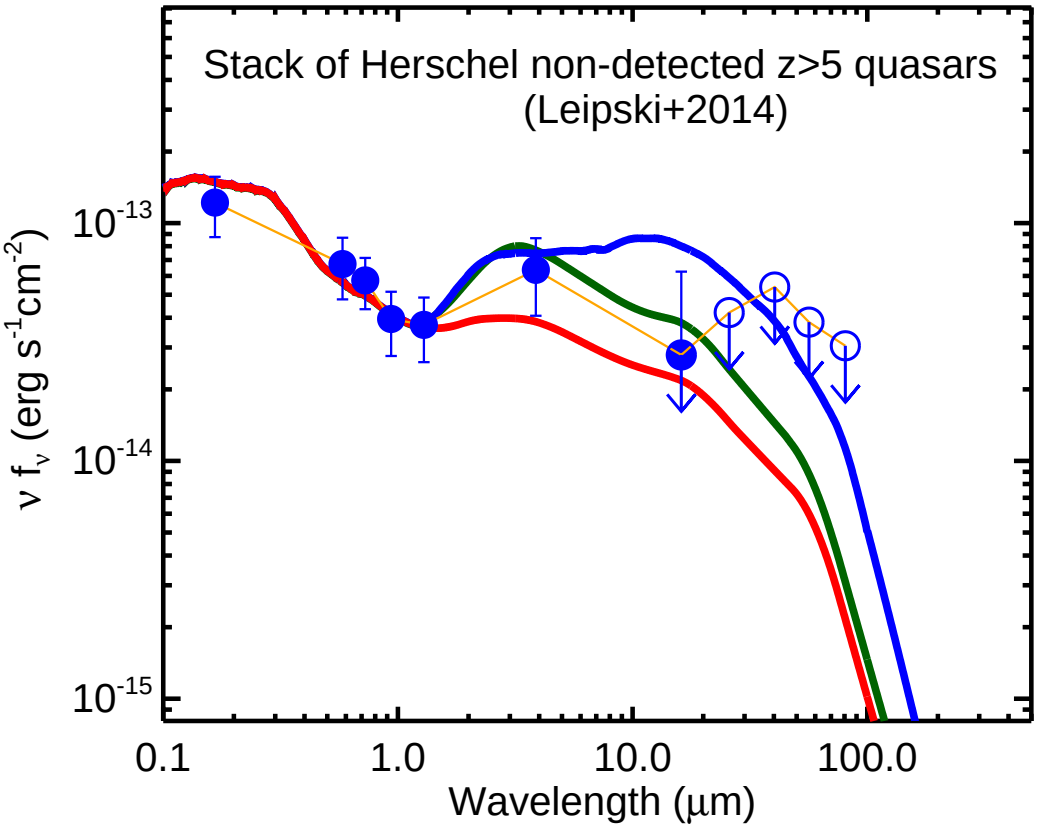


Figure 2.16 Comparison of the stacked SED of $z \gtrsim 5$ *Herschel* non-detected quasars in Leipski et al. (2014) with the normal Elvis et al. (1994) AGN template (far-IR corrected; blue solid line), the WDD template (green solid line), and the HDD template (red solid line).

Figure 2.15). Besides J084218.48+362504.1, all the rest of these LoCuSS HDD quasars are not detected by *Herschel*, indicating their weak far-IR emission. The variation of the SEDs of these quasars can be easily explained by adding an old stellar component to the HDD template. Thus we again confirm that similar HDD quasars are also seen at intermediate redshifts. We also find four WDD quasars at $z$=0.9-2.4 in the LoCuSS type-1 AGN sample (see Table 2.5 and the bottom-right panel of Figure 2.15). Although the observed far-IR emission is high (due to the host galaxy star-formation), the 0.1-10.0 $\mu$m SEDs of these AGNs show a clear SED turnover at 3 $\mu$m and are matched well by the WDD AGN template. Similarly to the situation at $z \gtrsim 5$, no evidence among the LoCuSS sample indicates the AGN SEDs at $z$=0.5-2.5 differ from those in the PG sample.

Hao et al. (2010, 2011) reported the discovery of hot-dust-poor (HDP) quasars at $z$=0.1-3 in the XMM-*COSMOS* sample (Elvis et al., 2012), the *Spitzer*+SDSS selected sample (Richards et al., 2006), and the Elvis et al. (1994) sample. These quasars are identified by their special combination of optical (0.3-1 $\mu$m) and near-IR (1-3 $\mu$m) slopes ($\alpha_{\rm opt}$ and $\alpha_{\rm NIR}$, respectively), and are further grouped into three classes based on the locations in a $\alpha_{\rm opt}$-$\alpha_{\rm NIR}$ plot (see details in Hao et al. 2010). We compare our AGN templates to the mean SEDs of the three classes of HDP quasars derived from the XMM-*COSMOS* sample (Hao et al., 2010) in Figure 2.17. Since the majority of HDP quasars in Hao et al. (2010) are at $z$=1-3, their mid-IR SEDs (3-10 $\mu$m) are poorly constrained by the MIPS 24 $\mu$m and IRAC 8 $\mu$m photometry. Thus we limit the comparison to $\lambda < 3$ $\mu$m. Firstly, we find that all three HDP templates prefer the HDD AGN template to represent their AGN component. As shown in the upper panels of Figure 2.17, if the normal AGN template is assumed, a strong contribution of the host galaxy is required to match the IR SEDs of these quasars ($f_{\rm host,1.25} \sim 0.6$ for class I, $f_{\rm host,1.25} \sim 0.8$ for class II and class III), leaving a strong underestimation of the UV-optical observed SED. Adding an extremely strong young stellar contribution to match such an SED deficiency is unlikely to be a reasonable solution. In contrast, if the AGN components in class I HDP quasars are represented by the HDD template, the host galaxy contamination in the near-IR would be small ($f_{\rm host,1.25} \sim 0.20$). The difference between the UV-optical SED of class I HDP quasars and the HDD AGN template can be completely mitigated by introducing moderate extinction to the AGN component. For the class II and class III HDP quasars, if a strong host galaxy contribution ($f_{\rm host,1.25}$ ~0.6-0.7) is added, the HDD AGN template can also recover the HDP SEDs reasonably well. As a result, we do not find that the HDP quasars presented by Hao et al. (2010, 2011) are atypical compared to the PG sample.

In summary, quasars with weak hot dust emission at $z$=0.5-2.5 do not have significantly different SEDs compared with the dust-deficient quasars in the PG sample, if AGN extinction and the possible host galaxy near-IR contamination are considered.

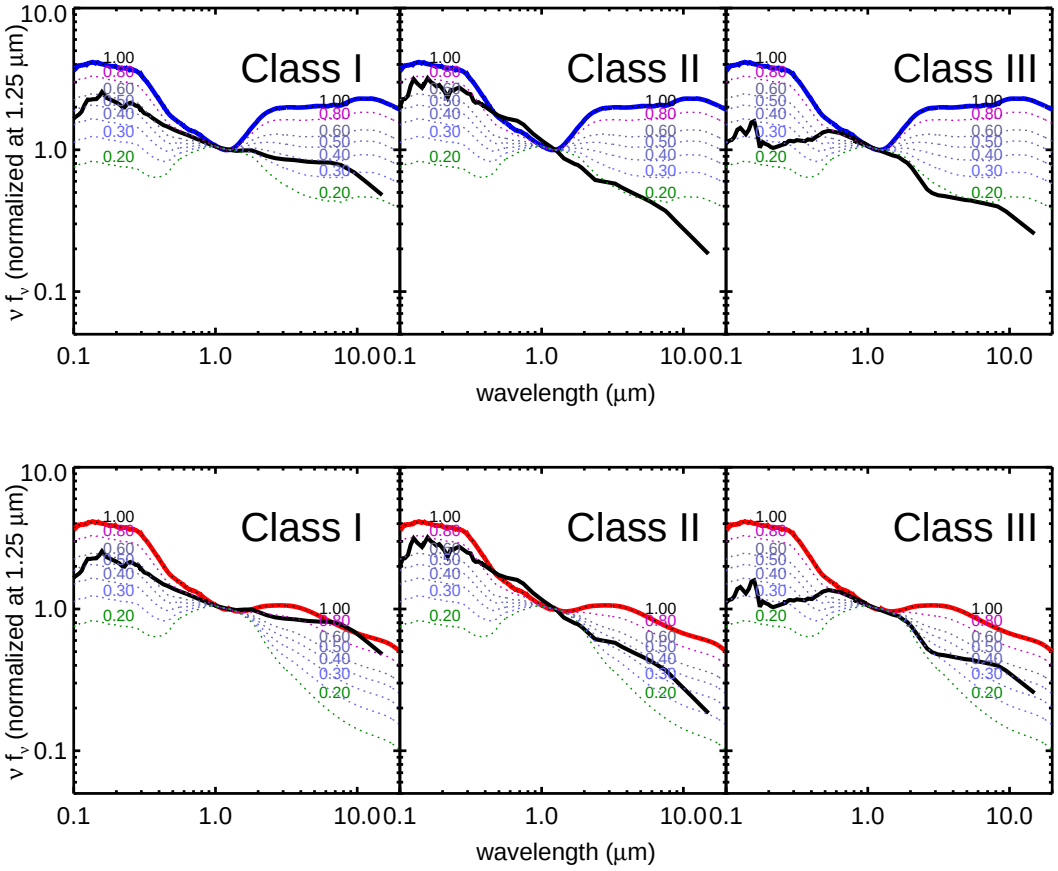


Figure 2.17 Comparison of the mean SEDs of three classes of hot-dust-poor quasars in Hao et al. 2010 (black lines) with the composite SEDs of the normal AGN template (blue lines in the upper panels) or the HDD AGN template (red lines in the lower panels). We also show the mock SEDs of the AGN templates with an old stellar population template as dotted lines with the numbers indicating the fraction of AGN contribution at 1.25 $\mu$m.

### 2.6.4 Does the HDD Quasar Fraction Evolve with Redshift?

*Bias Due to the Parent Sample* The HDD fractions are subject to the selection criteria of the parent sample. For the MIPS 24 $\mu$m $>$ 1 mJy complete type-1 LoCuSS AGN sample (Xu et al., 2015b), we only identify 3 out of 107 quasars to be HDD, making the HDD fraction only $\sim$ 3%. For the 19 quasars identified by other means (e.g., SDSS) in the same field but with MIPS 24 $\mu$m $<$ 1 mJy and relatively complete infrared SED observations, 5 quasars are HDD, making an HDD fraction $\sim$ 26%. Because the LoCuSS type-1 quasars were selected on 24 $\mu$m flux density, they are biased against quasars with weak infrared emission. A similar effect for near-IR color selection is also seen in the $z < 0.3$ 2MASS

sample in Shi et al. (2014), where no HDD quasars have been found. The 2MASS sample is characterized by a red AGN population with $J-K_s > 2$ (Cutri et al., 2001; Smith et al., 2002), while the HDD quasars tend to have $J-K_s$ ~1.0-1.5.

A luminosity bias of the parent sample may also produce specious evolution of the HDD fraction. As shown in Section 2.6.1, strong near-IR SED contamination by host galaxy stellar emission can mimic hot dust deficiency in normal quasars. In Figure 2.18, we combine the Elvis AGN template and an elliptical galaxy template to explore the host galaxy fraction $f_{\rm host}$ as a function of AGN luminosity. The host galaxy mass is assumed to be $10^{11.5}\ M_{\odot}$, which is likely to be the maximum value for most quasars (e.g., Reines & Volonteri, 2015; Bongiorno et al., 2016). We convert the stellar mass to the near-IR luminosity, adopting the mass to light ratio for local field galaxies (Bell et al., 2003). We can see at $\log(L_{\rm AGN}/L_{\odot}) > 13$, the host galaxy contamination at the optical bands as well as the near-IR to mid-IR bands is negligible (with $f_{\rm host} < 0.05$), so the simple two color identification adopted in Jiang et al. 2010 should be good enough to pick out dust-deficient quasars. At $12 < \log(L_{\rm AGN}/L_{\odot}) < 13$, we see a gradual increase of $f_{\rm host}$. Below $\log(L_{\rm AGN}/L_{\odot}) = 12$, the host galaxy contamination increases rapidly from $f_{\rm host} \sim 10\%$, in which case the identification of HDD quasars becomes very difficult.

In the upper panel of Figure 2.14, we show the $L_{0.51\ \mu{\rm m}} > 10^{44.73}$ erg s$^{-1}$ cut in Jun & Im 2013. For the same HDD quasar criteria ($\lambda f_{\lambda}[3.5\mu{\rm m}/0.51\mu{\rm m}] < 0.64$), no PG quasars are selected above the luminosity cut. A large number of dust-deficient PG quasars are still hidden in this simple selection. In contrast, similar HDD quasars at $z \gtrsim 5$ are easily identified. As we observe more luminous quasars at higher redshift, this color selection becomes more productive. As a result, we will get an increasing HDD quasar fraction even if the real value is constant. Nevertheless, for the samples in Jiang et al. (2010) ($L_{\rm AGN} \sim 10^{13}\ L_{\odot}$), Jun & Im (2013) ($L_{\rm AGN} > 10^{12}\ L_{\odot}$), and Mor & Trakhtenbrot (2011) ($L_{\rm AGN} > 10^{12}\ L_{\odot}$), the values of $f_{\rm host}$ at 0.51, 2.30, 3.10 $\mu$m are smaller than 10%. In other words, the host galaxy contribution has very limited impact on the dust-deficient quasar selection in these papers.

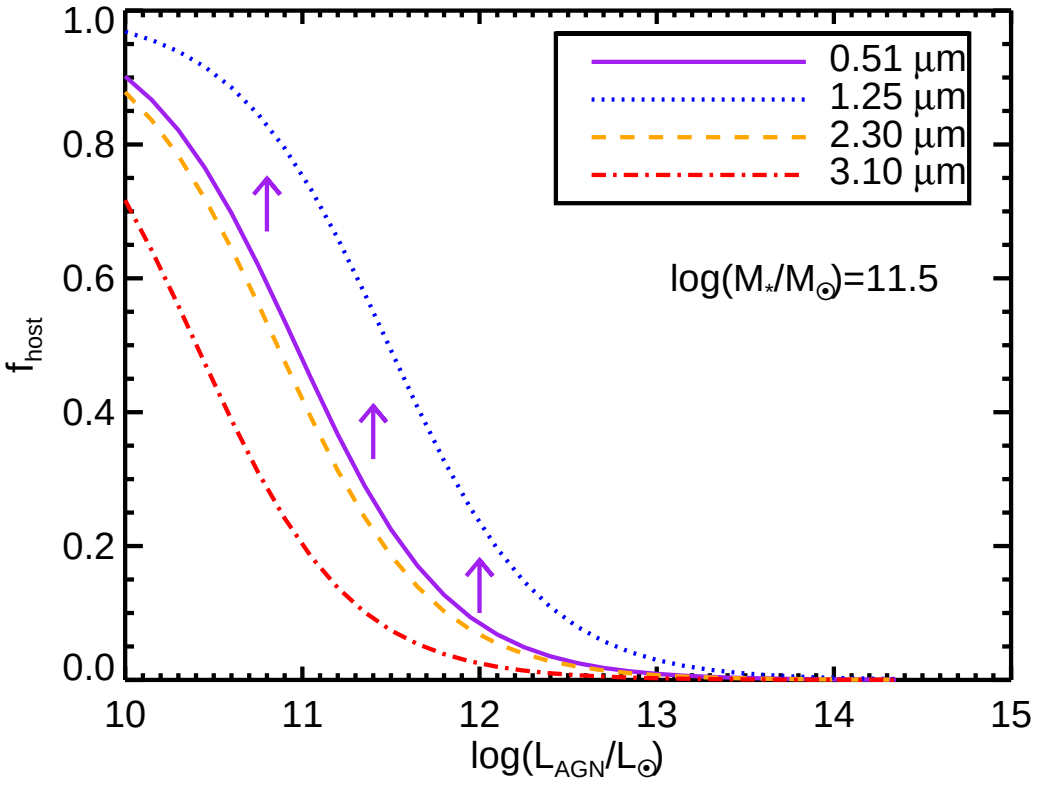


Figure 2.18 Host galaxy contribution vs. AGN luminosity from the SED model. We assume $10^{11.5}$ $M_{\odot}$ as the maximum possible host galaxy mass and adopt the mass to light ratio for local field galaxies (Bell et al., 2003). The arrows indicate the possible shift of the host galaxy fraction $f_{\rm host}$ if the galaxy contains young stellar populations. See the text for details.

*Bias Due to the Selection Methods* Different selection criteria are another important reason for the discrepancies in the HDD fractions in the literature. Hao et al. (2010) introduced the AGN-galaxy mixing diagram, which takes account of both host galaxy contamination and quasar reddening, to search for dust-deficient quasars. Following Hao et al. (2010, 2011), we fit power laws ($\nu F_{\nu} \propto \nu^{\alpha}$) at 0.3-1 $\mu$m and 1-3 $\mu$m to derive an optical slope ($\alpha_{\rm OPT}$) and an NIR slope ($\alpha_{\rm NIR}$) for each quasar in the PG sample, and show their distribution in the AGN-galaxy mixing diagram as Figure 2.19. For the HDD PG quasars, four out of the seven ambiguous cases, PG 0043+039,PG 1022+519, PG 1341+258, and PG 2209+184 locate below the AGN-galaxy mixing curve. Meanwhile, six other HDD PG quasars have deviations of $\alpha_{\rm OPT}$ and $\alpha_{\rm NIR}$ within the $1\sigma$ dispersion of the Elvis et al.

(1994) sample. HDD quasars like PG 1100+772, PG 1121+422, PG 1115+407, PG 1216+069, PG 1302−102, and PG 1626+554 are not revealed by the stringent selection. Besides PG 1011−040, the remaining HDD PG quasars are grouped into class I, suggesting the Hao et al. (2010) selection only recovers $\sim 50\%$ of the HDD quasars identified through SED decomposition. Additionally, the near-IR SEDs of class II and class III HDP quasars selected from this diagram are likely dominated by host galaxy emission, making the identification of the real dust-deficient quasars ambiguous.

Mor & Trakhtenbrot (2011) defined the dust-covering factor as the ratio between the luminosities of dust emission at 2-35 $\mu$m and the AGN power-law component, $C_{\rm HD} = L_{\rm dust,2\text{-}35\mu m}/L_{\rm AGN,power\text{-}law}$, to look for quasars with low dust-covering. They also apply a luminosity cut at rest-frame 3000 $\AA$, $L_{0.3} > 10^{45}$ erg s$^{-1}$ to remove quasars with possible strong host contamination. As demonstrated in their Figure 3, normal quasars have $C_{\rm HD}$ peaked around 0.23, and low dust-covering quasars have $C_{\rm HD}$ = 0.1-0.13. These values are consistent with our Elvis normal AGN template and HDD template. The 15-20% fraction in Mor & Trakhtenbrot (2011) is also similar to our value for HDD quasars (15-23%). However, since they did not study the IR SED shapes, the Mor & Trakhtenbrot (2011) low dust-covering quasar sample is not guaranteed to be purely HDD-like quasars.

Jun & Im (2013) required the luminosity ratio $L_{2.3}/L_{0.51} < 0.32$ to define HDD quasars, whereas the HDD AGN template we derived based on the PG sample has $L_{2.3}/L_{0.51} = 0.63$. Only the extreme HDD PG 0049+171 has a $L_{2.3}/L_{0.51} \sim 0.34$. As a result, Jun & Im (2013) only looked at the extreme HDD and rare quasars. These quasars may be extremely optically blue HDD quasars (as is the case for PG 0049+171).

*the HDD Quasar Fraction* Richards et al. (2009) showed that optical-only selection would miss 50% of the whole type 1 quasar sample (their Figure 9). As a rough estimation, the 20% HDD fraction in the PG sample should translate into about 10% in a complete sample to similar luminosity. This value is similar to HDP quasar fraction of the XMM-COSMOS AGN sample and the SDSS-*Spitzer* sample for AGN with $\log(L_{\rm AGN}/L_{\odot}) > 12$ ($z \sim$0.5-4, Hao et al. 2010, 2011), whose host stellar contamination is negligible.

In the Leipski et al. (2014) $z \gtrsim 5$ sample (selected by blue colors in the rest optical

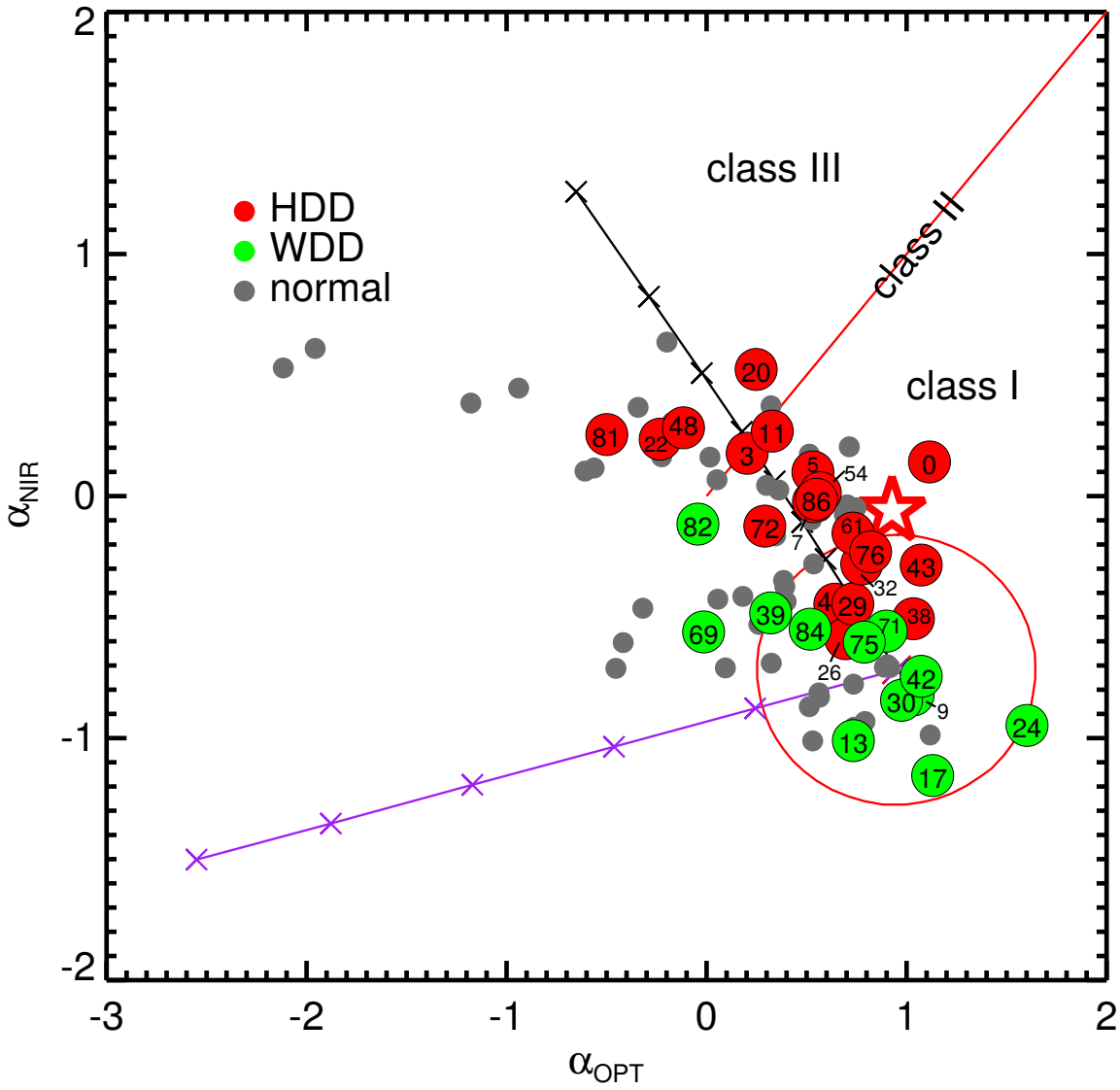


Figure 2.19 The Hao et al. (2010) selection of hot-dust-poor quasars applied to the PG sample. The red circle shows the Elvis et al. (1994) mean AGN SED and the $1\sigma$ dispersion of the Elvis et al. (1994) samples. The black line is a mixing curve of the AGN template and the galaxy template (Spi4 in the SWIRE library, see Figure 1 of Hao et al. 2010). The purple line shows the reddening vector for the Elvis et al. (1994) template. The straight solid line shows where $\alpha_{\rm OPT} = \alpha_{\rm NIR}$. The big red dots are selected HDD PG quasars. We also show the position of the HDD AGN template on this diagram as the red five-pointed star.

bands), the fraction of dust-deficient quasars is $11/69 \sim 16\%$, which is identical to that of our PG sample (optically selected). As shown in Figure 2.15, the SEDs of $z \gtrsim 5$ HDD quasars are similar to our HDD AGN template, suggesting a similar incidence of HDD AGNs. The luminosities of these quasars are very high ($L_{\rm AGN} \sim 10^{13}\ L_{\odot}$, Lyu et al. 2016),

so that the host galaxy stellar contamination can be ignored. However, most of these $z \gtrsim 5$ quasars are selected from SDSS and it is well-known that such a quasar sample could have very low completeness (e.g., McGreer et al., 2013). As a result, we should be cautious in comparing the $z \gtrsim 5$ sample to the intermediate-redshift or low-redshift results directly.

Hao et al. (2010) argued that the fraction of HDP AGNs shows a jump from $z < 2$ to $2 < z < 3.5$. Nevertheless, at $z < 2$, there is a large number of AGN with $\log(L_{\rm AGN}/L_{\odot}) < 12$ (Figure 2 in Elvis et al. 2012, assuming $L_{\rm AGN} \approx 50\nu L_{\nu}[2\ {\rm keV}]$). As shown above, the Hao et al. (2010) selection may miss a large number of HDD quasars with strong near-IR host galaxy contamination. As a result, we do not think the redshift evolution of the HDP quasar fraction in the XMM-COSMOS sample (Hao et al., 2010) is convincing since the degeneracy between the AGN luminosity and redshift was not considered. In agreement, in the subsequent paper by Hao et al. (2011), no detectable redshift evolution of the HDP quasar fraction was reported. For the Richards et al. (2006) SDSS-Spitzer sample studied in the second paper (Hao et al., 2011), the vast majority of AGNs have $\log(L_{\rm AGN}/L_{\odot}) > 12$ and therefore are bright enough that the host galaxies do not confuse the identification of hot-dust-poor quasars.

In summary, the HDD fraction of quasars from an optical sample is about 15-20%, with no strong evidence for redshift evolution. A purely NIR-selected quasar sample could miss a large number of HDD quasars due to their abnormal IR SEDs. In a complete sample, either selected by optical-IR techniques or by X-ray emission, the HDD fraction is around 10%.

### 2.6.5 Dust-deficient Quasars: What is the Cause?

The standard unified model of active nuclei (e.g., Urry & Padovani, 1995) suggests that the accretion disk lies within the central hole of a circumnuclear torus that is optically thick in the optical and near infrared; the torus is in turn surrounded by cold interstellar clouds. Within the main body of the torus, where much of the dust is shielded from direct illumination by the central source, the temperature decreases with increasing radius and the resulting SEDs are complex and depend on radiative transfer and viewing angle (e.g., Fritz et al., 2006). With this classical picture, several possibilities have been proposed in

the literature to explain the dust-deficient behavior of AGNs.

For example, Haas et al. (2003) proposed that quasars with weak near-IR and mid-IR emission might arise due to reduced optical-UV emission from the accretion disk, reducing the energy to be absorbed by the hot dust. However, we find that the UV/optical SEDs of the HDD quasars are similar to those of normal quasars, and their luminosities are not low (also see, e.g., Hao et al. 2010, 2011; Jiang et al. 2010; Mor & Netzer 2012a; Jun & Im 2013), contrary to this hypothesis.

Jiang et al. (2010) suggested that the $z \sim 6$ extremely IR-weak quasars could be the first-generation of quasars that live in a dust-free medium and hence do not have the torus structure. However, as we have shown, similar quasars can also be found in the nearby Universe (Section 4.5) and there is no evidence for strong redshift evolution of the fraction of HDD quasars (Section 2.6.4). Additionally, considering that quasars are already metal-rich (Nagao et al., 2006, 2012; Jiang et al., 2007; Juarez et al., 2009) at $z \sim$5-6, and very dusty quasars already exist at $z \sim 7$ (Barnett et al., 2015), a significant population of dust-free quasars at $z \sim 6$ would be surprising.

On the other hand, Kawakatu & Ohsuga (2011) argued that the weak near-IR dust emission of quasars is associated with a super Eddington ratio and stated that the IR-weak quasars in Jiang et al. (2010) have super Eddington ratios as a support for this model. However, we note that accurate Eddington ratios are hard to get for these quasars because of their lowest luminosities among quasars with UV to far-IR SED constraints at $z \gtrsim 5$ (Lyu et al., 2016) and the uncertainties in the calibration of the black hole mass estimators at high redshifts (e.g., see review by Shen, 2013). More importantly, our analysis of the HDD quasars suggests the opposite: the deficiency of hot dust emission is more easily seen in quasars with low accretion rates.

The receding torus model (e.g., Lawrence, 1991; Simpson, 2005; Assef et al., 2013) has been frequently invoked to explain the decrease in the infrared-to-optical luminosity ratios of quasars with increasing AGN luminosity (e.g., Maiolino et al., 2007; Roseboom et al., 2013; Mateos et al., 2016). The classical picture assumes the torus has an approximately constant scale height (e.g., Lawrence, 1991). The size of the inner wall of the torus is determined by the dust sublimation radius, $R_{\rm sub,0} \propto L_{\rm AGN,UV}^{0.5} T_{\rm sub}^{-2.8} a^{-0.5}$, where $T_{\rm sub}$ is the

dust sublimation temperature and $a$ is the dust grain size (e.g., Barvainis, 1987). With increasing AGN luminosity $L_{\rm AGN,UV}$, $R_{\rm sub}$ will grow, increasing the solid angle through which energy from the central engine can escape. As shown in Section 2.6.2, the fraction of WDD quasars grows with increasing AGN luminosity, seemingly consistent with this prediction.

However, the relatively stronger silicate emission feature observed in the WDD quasars (see Section 2.6.2) may be inconsistent with the assumption of a constant scale height for the torus. The silicate emission arises from warm dust relatively far from the central engine and of moderate optical depth (e.g., Fritz et al., 2006; Nenkova et al., 2008a). If the torus scale height were constant, with the receding of the torus we should observe similar silicate emission strength due to the identical structure of the warm dust emission region. In fact, we can explain the stronger silicate emission of dust-deficient quasars if the scale height of the warm dust above the torus mid-plane is reduced and the tori intercept less energy from their accretion disks (reducing the mid-IR continuum, while the outermost zones responsible for the silicate emission are relatively unchanged). Observations show the hydrogen column density for high-luminosity AGNs is lower than that for low-luminosity AGNs (e.g., Ueda et al., 2003; Barger et al., 2005; La Franca et al., 2005; Akylas et al., 2006), also favoring a smaller torus scale height with increasing AGN luminosity.

Finally, we propose a schematic model for the torus geometry evolution to explain the observed behavior of dust-deficient quasars through modifications in the standard model. As pointed out by, e.g., Stalevski et al. 2016, if the torus structure is not changed, the AGN luminosity alone does not modify the IR SED shape of the torus. Consequently, we focus on the geometry of the torus, not on the self-similar scale expansion of various structures with increasing AGN luminosity. In cartoon A of Figure 2.20, we picture the key components of our model. Heated by the UV-optical emission from the nucleus, the dust that makes up the torus assumes a temperature gradient as a function of distance to the accretion disk, resulting in a distribution of cold dust, warm dust and hot dust. Due to gravity, the dusty structures (e.g., clumpy clouds or a smooth distribution) have a higher density closer to the accretion disk and torus equatorial plane. In the innermost region of the torus, since the emission from the black hole accretion disk is anisotropic (e.g., Netzer,

1987), the dust grains sublimate and form a concave structure for the hot dust emission region (Kawaguchi & Mori, 2010). Following Kawaguchi & Mori (2010), we also assume the innermost region of the hot dust emission region is connected with the outermost region of the accretion disk. In the zoom-in plot of the inner region of the torus (panel A1), we show the concave part of the host dust emission is truncated at $\theta_{\rm min}$ and $\theta_{\rm max}$, controlled by the thickness of the torus and the thickness of the accretion disk, respectively.

For WDD quasars, an increase of AGN luminosity results in a smaller torus scale height or larger opening angle, reducing the volume of the warm dust emission region (cartoon B in Figure 2.20) and causing its output to drop. This reduction may be enhanced according to the suggestion by Hönig & Beckert (2007), that dust clouds at large torus scale heights would be destroyed by their exposure to the increased AGN luminosity. However, the structure of the innermost range of the hot dust emission region is identical to that of normal quasars due to a constant $\theta_{\rm max}$. Thus, there is little change in hot dust emission.

The HDD quasars tend to have lower Eddington ratios. For the outer part of the accretion disk, where gas pressure provides most of the vertical support, the scale height $h \propto (L/L_{\rm Edd})^{-0.7}$ (e.g., Krolik, 1999). Consequently, the hot dust emission region has a reduced $\theta_{\rm max}$ and smaller dust density with increasing $h$ (cartoon C in Figure 2.20). In addition, the projection of hot dust emission in the polar direction is less effective due to the relatively high skewness of the dust sublimation surface. As a result, we will not observe much hot dust emission. We may also expect that the cloud density in the warm dust emission region is decreased or that the opening angle of warm dust emission is increased, which would explain the observed stronger silicate emission (see Section 2.6.2) as well as the weak mid-IR emission.

In brief, we suggest that the observed deficiency of emission by warm and hot dust in some quasars can result from modifications of the torus structure: (1) WDD quasars can arise from an increase in the torus opening angle and the resulting reduction in the volume of warm dust; and (2) HDD quasars can arise from the increase of the accretion disk thickness for quasars with relatively low Eddington ratios, and the accompanying adjustment in the geometry of the regions dominating hot dust emission.

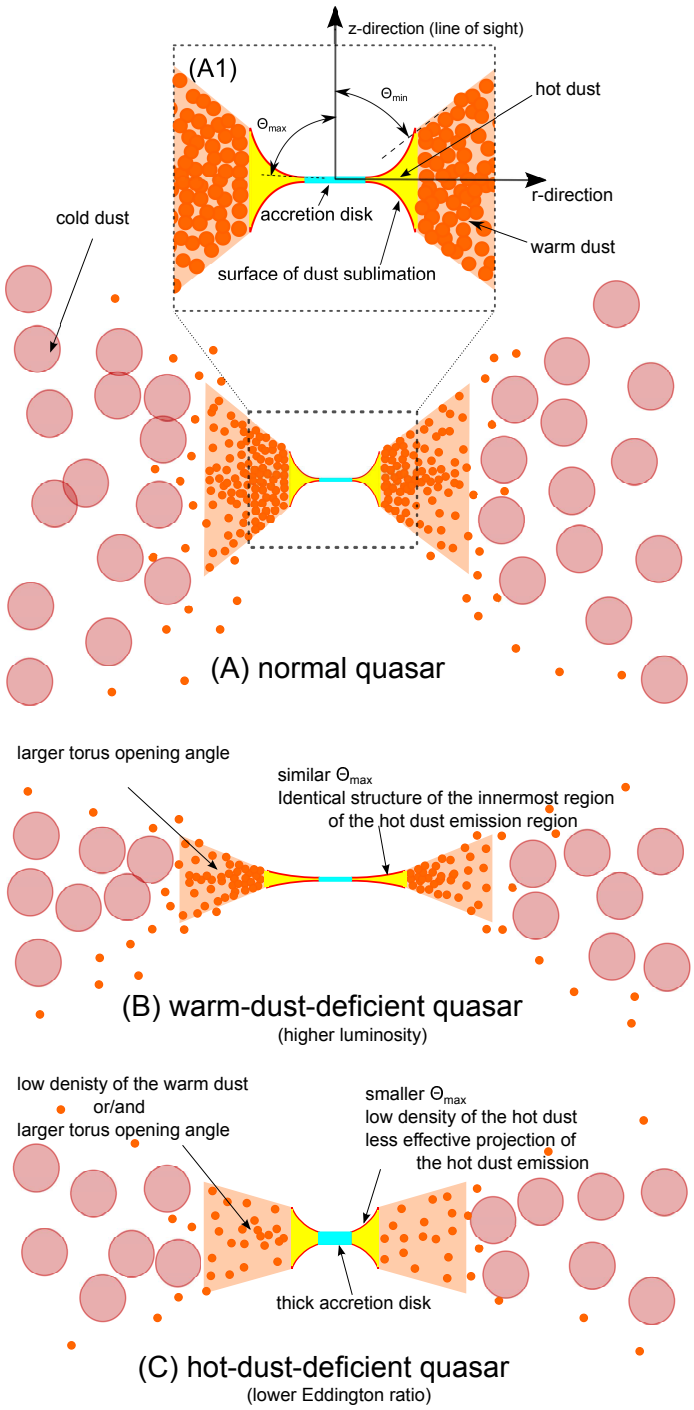


Figure 2.20 Schematic demonstration of the torus geometry of normal, WDD and HDD quasars. The shape of each component is exaggerated to reflect its distinct features. See the text for details.

## 2.7 Summary

Elvis et al. (1994) proposed what has become the classic template for quasar SEDs, shown

since to be appropriate for the majority of luminous AGNs. However, a minority of objects seem to depart from this standard in the infrared (e.g., Hao et al., 2010, 2011; Jiang et al., 2010). We have studied the AGN infrared SED variations in an archetypical optically selected sample composed of 87 $z < 0.5$ PG quasars. The optical to far-IR SEDs of these quasars were investigated with the aid of a three-component model including the AGN emission, the host galaxy stellar emission, and the host galaxy infrared emission powered by star formation. The host galaxy properties derived from the SED decomposition are consistent with those determined through other methods: the stellar contributions in the near-IR band based on the SED analysis are similar to the values derived from image decompositions on the high-resolution images obtained by HST or ground-based adaptive optics; and the infrared luminosities of the host galaxies yield SFRs consistent with the strength of the mid-IR 11.3 $\mu$m aromatic features. Our SED model fits generally have residuals within 0.3 dex of the observed SEDs at 0.2-500 $\mu$m and reproduce the 0.5-70 $\mu$m region especially well. The principal results can be summarized as follows.

1. The intrinsic infrared SEDs of the PG quasars cannot be represented by one single SED template. Normal quasars occupy $\sim 60\%$ of the sample and their AGN SEDs can be described by the Elvis et al. (1994) template reasonably well. In comparison, the AGN template derived by Assef et al. (2010) appears to have too deep a minimum near 1.0 $\mu$m, as indicated by the overestimate of host galaxy brightness using it in SED deconvolution.

2. There is a substantial fraction ($\sim$30-40%) of abnormal quasars with weak infrared emission in the PG sample, which have often been overlooked by previous studies. These IR-weak quasars can be classified into two populations with distinct SED properties.

3. The hot-dust-deficient (HDD) quasars are characterized by a deficiency of dust emission at $\lambda > 2$ $\mu$m. The AGN SEDs of these quasars do not have the typical hot dust emission peaked at $\sim 2$ $\mu$m and present very weak warm and cold dust emission. In the PG sample, they contribute $\sim$15-23% of the total population.

4. The warm-dust-deficient (WDD) quasars have a similar near-IR SED bump peaked at $\sim 2.0$ $\mu$m as is the case for normal quasars but have a very quick drop in the mid-IR. The fraction of the WDD quasars in the PG sample is $\sim$ 14-17%.

5. Compared with normal quasars, the HDD quasars are similar in terms of AGN luminosities and black hole masses, but they tend to have lower Eddington ratios with a K-S probability of $\sim$0.025 of being drawn from the same distribution. We also find that the HDD quasar fraction is not luminosity dependent, consistent with previous work by Hao et al. (2010, 2011) and Mor & Netzer (2012a). These HDD objects account for roughly 10% of quasar samples selected on the basis of bolometric luminosity.

6. The WDD quasars do not differ from normal quasars in Eddington ratio, but their fraction increases with AGN luminosity. The decreased mid-IR to optical luminosity ratios of quasars with increasing AGN luminosity (as found by, e.g., Maiolino et al. 2007; Treister et al. 2008; Mor & Trakhtenbrot 2011; Calderone et al. 2012; Ma & Wang 2013; Gu 2013; Roseboom et al. 2013) may be mostly contributed by the more frequent appearance of WDD quasars.

7. Compared with normal quasars, both WDD and HDD quasars tend to have stronger silicate emission features at $\sim 10$ $\mu$m, which can be explained by a reduced scale height of the warm dust above the equatorial plane of the circumnuclear torus.

8. The high-$z$ dust-free or dust-poor quasars found by, e.g., Jiang et al. (2010), Hao et al. (2010) share similar SEDs to the HDD quasars in the PG sample. WDD quasars are also seen at $z = 0.5 \sim 6$. Although the near- to mid-infrared SEDs of high-$z$ quasars vary to some degree, they show no obvious difference from the archetypal PG sample.

9. Considering biases in the parent sample and the selection methods, there is no evidence for a strong cosmic evolution of the dust-deficient quasars. Instead, we suggest that observed dust-deficient behavior of quasars is caused by a change of the torus structure controlled by AGN luminosity and Eddington ratio.

We thank Richard Green and the anonymous referee for helpful suggestions and Lei Xu for sharing the data of the LoCuSS *Spitzer*/MIPS AGN sample. This work was supported by NASA grants NNX13AD82G and 1255094. This publication has made use of data products from the *Wide-field Infrared Survey Explorer*, which is a joint project of the University of California, Los Angeles, and the Jet Propulsion Laboratory/California Institute of Technology, funded by the National Aeronautics and Space Administration. This publication also makes use of data products from NEOWISE, which is a project of the Jet Propulsion Laboratory/California Institute of Technology, funded by the Planetary Science Division of the National Aeronautics and Space Administration. This publication makes use of data products from the Two Micron All Sky Survey, which is a joint project of the University of Massachusetts and the Infrared Processing and Analysis Center/California Institute of Technology, funded by the National Aeronautics and Space Administration and the National Science Foundation. This work is also based in part on data obtained as part of the UKIRT Infrared Deep Sky Survey. We acknowledge the use of the NASA/IPAC Extragalactic Database (NED) which is operated by the Jet Propulsion Laboratory, California Institute of Technology, under contract with the National Aeronautics and Space Administration. This work has also made use of the VizieR catalog access tool, CDS, Strasbourg, France.

CHAPTER 3

# THE INTRINSIC FAR-INFRARED CONTINUA OF TYPE-1 QUASARS

The range of currently proposed active galactic nucleus (AGN) far-infrared templates results in uncertainties in retrieving host galaxy information from infrared observations and also undermines constraints on the outer part of the AGN torus. We discuss how to test and reconcile these templates. Physically, the fraction of the intrinsic AGN IR-processed luminosity compared with that from the central engine should be consistent with the dust-covering factor. In addition, besides reproducing the composite spectral energy distributions (SEDs) of quasars, a correct AGN IR template combined with an accurate library of star-forming galaxy templates should be able to reproduce the IR properties of the host galaxies, such as the luminosity-dependent SED shapes and aromatic feature strengths. We develop tests based on these expected behaviors and find that the shape of the AGN intrinsic far-IR emission drops off rapidly starting at $\sim 20$ $\mu$m and can be matched by an Elvis et al.-like template with a minor modification. Despite the variations in the near- to mid-IR bands, AGNs in quasars and Seyfert galaxies have remarkably similar intrinsic far-IR SEDs at $\lambda \sim$ 20-100 $\mu$m, suggesting a similar emission character of the outermost region of the circumnuclear torus. The variations of the intrinsic AGN IR SEDs among the type-1 quasar population can be explained by the changing relative strengths of four major dust components with similar characteristic temperatures, and there is evidence for compact AGN-heated dusty structures at sub-kiloparsec scales in the far-IR. [1]

## 3.1 Introduction

The infrared (IR) emission of quasars opens an invaluable window to study the nature of the central active galactic nuclei (AGNs) as well as their host galaxies. It is now

[1] A version of this chapter originally appeared as a published paper in the Astrophysical Journal (Lyu & Rieke, 2017). George Rieke contributed the calculations for the energy budget argument and all the remaining work was carried out by me, with the help from the coauthor George Rieke.

widely accepted that the AGN is powered by gas accretion onto the black hole and a substantial fraction of such accretion-released energy is absorbed by the surrounding dusty structures and re-emitted in the infrared (e.g., Rieke 1978; Neugebauer et al. 1986). In the past $\sim$ 30 years, with the launch and operation of each major space-based IR telescope, many papers have appeared with the goal of characterizing the IR spectral energy distributions (SEDs) of these systems, using data of improved quality and/or larger samples (e.g., Neugebauer et al. 1986; Sanders et al. 1989; Elvis et al. 1994 with the *Infrared Astronomical Satellite* in 1980s; e.g., Polletta et al. 2000; Haas et al. 2000, 2003; Alonso-Herrero et al. 2003 with the *Infrared Space Observatory* in 1990s; e.g., Richards et al. 2006; Polletta et al. 2007; Netzer et al. 2007; Shang et al. 2011; Mullaney et al. 2011; Mor & Netzer 2012a with the *Spitzer Space Telescope* in 2003-2009, e.g., Petric et al. 2015; García-González et al. 2016 with the *Herschel Space Observatory* in 2009-2013, and, e.g., Mor & Trakhtenbrot 2011; Petric et al. 2015 with the *Wide-field Infrared Survey Explorer* in the post-2010). Nonetheless, these intensive efforts have unexpectedly ended in significant disagreements about the appropriate template, especially for the far-IR (e.g., from 20 to 1000 $\mu$m). This can be seen in Figure 3.1, where we provide a partial summary of the AGN empirical IR templates in the literature.

The possible different levels of contamination from the IR light emitted by the host galaxies could underlie the broad distribution of the far-IR SEDs among different templates. Several groups have attempted to remove this contamination from the AGN template (e.g., Netzer et al., 2007; Mullaney et al., 2011; Kirkpatrick et al., 2015; Xu et al., 2015b; Symeonidis et al., 2016). However, there is still no consensus. These AGN "intrinsic" IR templates range from (1) the minimalist far-infrared output derived by Netzer et al. (2007) by subtracting a starburst-dominated ULIRG template from the average quasar IR SED under the assumption that the vast majority of the 50–100 $\mu$m emission is due to star formation, to (2) versions with substantially more far-infrared emission obtained, for example, by Kirkpatrick et al. (2015) who fitted the data with a combination of a galaxy mid-infrared spectrum, a power law in the same region for the AGN, and two black bodies at longer wavelengths. Most recently, based on a similar low-$z$ sample of optically selected bright quasars, Symeonidis et al. (2016) reported an "intrinsic" AGN IR tem-

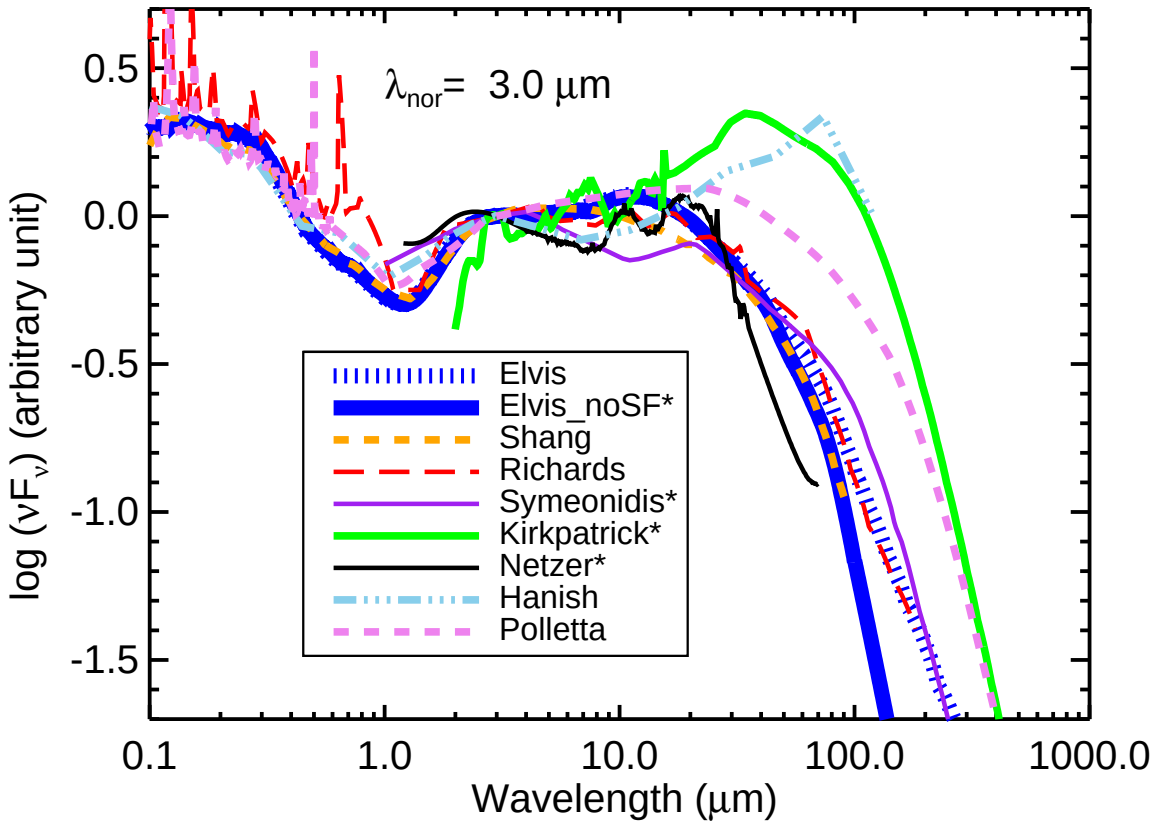


Figure 3.1 Examples of proposed empirical AGN SED templates, normalized at 3.0 $\mu$m. The nine versions are Elvis et al. (1994) based partly on the Palomar-Green (PG) sample; the same with a far-infrared star-forming component removed (Elvis_noSF) by Xu et al. (2015b); Richards et al. (2006) based on 259 quasars; the radio-quiet quasar template in Shang et al. (2011); the star-formation-corrected AGN template based on the radio-quiet PG sample proposed by Symeonidis et al. (2016); AGN3 from Kirkpatrick et al. (2015) with star formation removed by subtracting the suitably normalized SFG2 from the same source; Netzer et al. (2007) with star formation subtraction in the far-IR; that proposed by Hanish et al. (2013); and the QSO1 template from Polletta et al. (2007). We plot those templates with efforts to remove the star-formation contamination as solid lines and marked them with '*' in the legend.

plate with more far-IR emission than that predicted by the classic quasar template from Elvis et al. (1994), where the latter did not even correct the contamination by host galaxy star formation.

The importance of identifying the correct far-IR behavior of AGNs cannot be overstated. As pointed out by Lutz (2014) and Netzer (2015), theoretical torus models have too much freedom to distribute dust in ways that may not reflect the real situations. In

fact, given the wide range of observational results on AGN IR SEDs, no convincing observational tests can be made for these model templates in the far-IR. Determining which type of far-IR behavior is appropriate (or whether there is a broad range) will therefore have a direct impact on models of AGN tori, especially on their relation to the surrounding interstellar material. To measure the IR star formation rates (SFRs) of quasar host galaxies, a proper handling of the AGN far-IR contribution is critical. A number of papers have analyzed the quasar IR SEDs with a combination of the SED library from some torus model and templates/models for the host galaxies, and derived the host SFRs from the IR luminosities of the latter component (e.g., Delvecchio et al., 2014; Leipski et al., 2014; Dong & Wu, 2016; Netzer et al., 2016). However, since none of the torus models have been observationally well constrained in the far-IR, the accuracy of the SFR measurements is not always guaranteed, even if the fitting residuals are tiny. Recently, there have been concerns regarding whether the AGN contributes substantially to the heating of the surrounding interstellar medium (ISM; Schneider et al. 2015; Roebuck et al. 2016; Symeonidis 2017). The validity of such studies also rests on the knowledge of the complete SED of the intrinsic AGN IR emission.

As shown by our previous work (Lyu et al., 2017), it is clear that one single AGN IR template does not apply to all the type-1 quasar population ($L_{\rm AGN} \gtrsim 10^{11} L_{\odot}$). Additionally, similar SED variations of the intrinsic AGN IR emission are seen among quasars from $z \sim$0 to $z \sim$6, suggesting that such behavior is common. Following that work, this paper examines the intrinsic far-IR SEDs of AGNs in detail with the focus mainly on the type-1 quasar population. Firstly, an energy balance argument is applied to test some proposed AGN SED templates in Section 3.2. Then we present an in-depth analysis of the far-IR emission of the Palomar–Green (PG) quasars based on the study of Lyu et al. (2017), clarify several issues regarding the derivation of a correct intrinsic AGN far-IR SED, and determine our preferred template in Section 3.3. In Section 3.4, we discuss whether the AGN far-IR intrinsic template based on quasars is applicable to other kinds of AGNs, as well as some implications for the obscuring structure from our results. A summary is given in Section 6.6. We provide the intrinsic templates for type-1 quasars in Appendix A.

## 3.2 Energy Balance

### 3.2.1 Rationale

Luminous AGNs are believed to be powered by gas accretion onto the central supermassive black holes (Salpeter, 1964; Lynden-Bell, 1969; Shields, 1978). Various processes associated directly with such central engines dominate the X-ray to the optical far-red energy output of these systems. The continuum emission of the central engine should drop substantially at $\lambda \gtrsim 1$ $\mu$m as suggested from multiple theoretical studies (e.g., Kawaguchi et al., 2001; Cao, 2009; Liu et al., 2012) and confirmed by observations (Kishimoto et al., 2008). Under the precepts of AGN unification (e.g., Antonucci 1993; see the recent review by Netzer 2015), the central engine is surrounded by equatorial optically thick dusty structures that cause the nuclear photons to escape preferentially along the polar direction. Meanwhile, the energy of those "blocked" photons is absorbed by dust and reradiated into the near infrared to 10 $\mu$m (and almost certainly beyond to at least $\sim$ 100 $\mu$m) as a result of energy balance.

For a type-1 AGN viewed face-on, the SED crossover between the direct (intrinsic) emission from the accretion disk and the IR-processed emission by the dust obscuration is close to the spectral minimum at $\sim$ 1.3 $\mu$m. This basic hypothesis for the source emission was first suggested by SEDs (Rieke, 1978), then by detailed decomposition into spectral components demonstrating a reduction in the amplitude of the variability as one goes further into the infrared (Rieke & Lebofsky, 1981; Cutri et al., 1985; Neugebauer et al., 1989; Neugebauer & Matthews, 1999). It has been firmly established through reverberation mapping, which shows time lags in the infrared response to variations in the optical–ultraviolet output by roughly the time expected if the reradiating dust is at the distance from the nucleus where it is heated close to its sublimation temperature (e.g., Koshida et al., 2014; Gandhi et al., 2015; Lira et al., 2015; Pozo Nuñez et al., 2015; Schnülle et al., 2015).

If the infrared emission of quasars is reradiated energy absorbed from the central engine and accretion disk, a corollary is that the infrared luminosity must be less than that of the central source, or more accurately, less than the energy absorbed from the central

source. The geometry of the torus is often estimated by comparing the energy emitted by the central engine at wavelengths $<$1.3 $\mu$m with that emitted in the infrared, presuming that the central engine emits isotropically and that the infrared emission is dominated by energy absorbed in the torus. This approach is supported not only by the rapidly declining emission from the accretion disk going from the optical into the near-IR, but also by the low levels of absorption by silicate-rich interstellar dust in the red and near-IR (e.g., Corrales et al., 2016). Therefore, it is the optical blue, UV, and X-ray that are most effective in providing the energy input to the dust that obscures the nucleus. The portion of the total accretion disk emission that is reprocessed into the infrared is represented by the luminosity of the system between 1.3 and 1000 um, as seen in a type-1 AGN, that is $f_{\rm R} = L_{\rm dust}/L_{\rm accr.disk}$. When the dust is optically thick, $f_{\rm R}$ can be interpreted as the covering factor for the torus, $f_c$. As discussed in Section 3.2.4, a more accurate way to interpret $f_{\rm R}$ needs to take account of possible anisotropies in the accretion disk radiation and of radiative transfer in the torus (e.g., Runnoe et al., 2013; Stalevski et al., 2016).

As will be shown below, a number of recently proposed AGN SED templates with strong far-IR emission fail the requirements of energy balance between the accretion disk and the infrared luminosity.

### 3.2.2 Template for AGN Soft X-Ray/UV/Optical Emission

Since Elvis et al. (1994) published their SED template for unobscured type-1 (broad-line) quasars, there have been multiple studies that have confirmed the uncanny accuracy of this work (e.g., Richards et al., 2006; Shang et al., 2011; Runnoe et al., 2012c; Hanish et al., 2013; Scott & Stewart, 2014; Lyu et al., 2017). As a result, we can take the intrinsic SED of a type-1 quasar to be well-understood from the soft X-ray to $\sim$ 10 $\mu$m. Lusso et al. (2013) show that the torus is probably optically thin to X-rays more energetic than $\sim$ 1 keV, so they should not be included in this energy budget argument. Consequently, we can avoid concerns that the Elvis template may be biased toward being X-ray bright (Marconi et al., 2004).

The properties of AGNs show possible trends in SED behaviors from the most luminous quasars to the much less luminous low-ionization nuclear emission-line region

(LINERs) galaxies (Ho, 1999, 2008). However, the Elvis et al. (1994) template has been developed on quasars with $L_{\rm AGN} \gtrsim 10^{11}\ L_{\odot}$ and all the following templates are also based on AGN samples with similar luminosity ranges. Thus, we adopt the Elvis et al. (1994) template to represent the accretion disk emission where some other template does not cover the soft X-ray to optical bands.

### 3.2.3 Energy Budget Calculations

Table 3.1 summarizes the sample properties, approaches to synthesize template SEDs, and calculations of the energy budgets for the proposed AGN templates listed below. Nearly every template needs some adjustment or extension for these energy budget determinations. Because the luminosity is a free parameter, we have normalized the results so the luminosity between 1.3 $\mu$m and 1 keV is set to 1. As a result, the tabulated infrared luminosities indicate directly the reradiated fraction of the emission of the central engine.

**Elvis et al. (1994)**: the procedure is most straightforward in the case of the Elvis et al. (1994) template. Table 3.1 shows two results, the first for the original form and the second for the star-formation-removed version from Xu et al. (2015b).

**Richards et al. (2006)**: it was necessary to fill out this template for frequencies $\log(\nu)$ above 17 and below 12.5; this was done by joining on sections of the original Elvis template.

**Shang et al. (2011)**: this work updated the Elvis et al. (1994) SED with data from HST, *FUSE*, *Spitzer*, *Chandra*, and *XMM*. The silicate emission features in the mid-IR were reproduced thanks to the spectral data from *Spitzer*/IRS. Although the Elvis et al. (1994) SED was based on IRAS far-IR data with many upper limits, these two SED templates agreed remarkably well in the far-IR. There is no need to adjust this template.

**Symeonidis et al. (2016)**: this template was completed for wavelengths short of 0.4 $\mu$m by joining on an original Elvis template. The far-infrared behavior is similar to that of the Polletta template, but the lower fraction of reradiated luminosity results because the template is relatively bright in the 0.3–1.3 $\mu$m range (see Figure 3.1).

**Kirkpatrick et al. (2015)**: these templates were built according to the dominance of the AGN continuum contribution in mid-IR spectra from a study of 343 (ultra)luminous in-

Table 3.1. Fraction of Short-$\lambda$ Luminosity Reradiated in the Infrared of Representative AGN Templates

| Template | $\lambda$ Range | Sample Characteristics | $N$ | Stack Method | SF Cor.? | Correction Base | $f_R$ |
|---|---|---|---|---|---|---|---|
| (1) | (2) | (3) | (4) | (5) | (6) | (7) | (8) |
| Elvis | X-ray to Radio | optical-blue, X-ray bright quasars | 29 | Kaplan–Meier Mean, $\lambda_{nor} = 1.25\ \mu$m | N | – | $\geq$0.55 |
| Elvis_noSF | X-ray to Radio | optical-blue, X-ray bright quasars | 29 | Kaplan-Meier Mean, $\lambda_{nor} = 1.25\ \mu$m | Y | relation between 11.3 aromatic features and the IR 50-25 $\mu$m flux ratio of both quasars and SFGs | $\geq$0.53 |
| Richards | X-ray to Radio | mid-IR and optical color-selected quasars | 259 | Gap repair, luminosity matched | N | – | $\geq$0.65 |
| Shang | X-ray to Radio | UV/optical bright quasars | 27 | Median Mean, $\lambda_{nor} = 0.42\ \mu$m | N | – | $\geq$0.64 |
| Symeonidis | 0.4-500 $\mu$m | radio-quiet PG quasars | 47 | Arithmetic Mean, $\lambda_{nor} = 20\ \mu$m | Y | Matching the 11.3 aromatic feature-derived SFR with the SFG templates IR luminosity | $\geq$0.56 |
| Kirkpatrick AGN1 | 2-1000 $\mu$m | $z \sim$0.80 (U)LIRGs w/ AGN dominated (100%) mid-IR spectra | 22 | Median Mean, normalized by the 5-15 $\mu$m luminosity | Y | Decomposition of the mid-IR spectra | $\geq$0.70-0.78 |
| Kirkpatrick AGN2 | 2-1000 $\mu$m | $z \sim$1.03 (U)LIRGs w/ AGN dominated (93%) mid-IR spectra | 23 | Median Mean, normalized by the 5-15 $\mu$m luminosity | Y | Decomposition of the mid-IR spectra | $\geq$1.12-1.02 |
| Kirkpatrick AGN3 | 2-1000 $\mu$m | $z \sim$1.65 (U)LIRGs w/ AGN dominated (94%) mid-IR spectra | 21 | Median Mean, normalized by the 5-15 $\mu$m luminosity | Y | Decomposition of the mid-IR spectra | $\geq$0.80-0.85 |
| Kirkpatrick AGN4 | 2-1000 $\mu$m | $z \sim$1.96 (U)LIRGs w/ AGN dominated (93%) mid-IR spectra | 31 | Median Mean, normalized by the 5-15 $\mu$m luminosity | Y | Decomposition of the mid-IR spectra | $\geq$1.34-1.26 |
| Netzer | 1.2-70 $\mu$m | PG quasars, missing very high-luminosity objects | 29 | Arithmetic Mean, $\lambda_{nor} = 6\ \mu$m | Y | Assuming the 50-100 $\mu$m emission of the IR-weak and IR-strong quasar template is due to star formation | $\geq$0.46 |
| Hanish | 0.1-100 $\mu$m | SDSS spectroscopically selected quasars without strong optical reddening | 301 | Median Mean, normalized by the 0.2-1.0 $\mu$m luminosity | N | – | $\geq$0.91 |
| Polletta QSO1 | X-ray to mid-IR | Optically selected, spectroscopically confirmed type-1 quasars from SDSS | 35 | Mean weighted by luminosity, $\lambda_{nor} =$ 1.0 $\mu$m | N | – | $\geq$0.74 |

Note. — Column (4): the size of the sample from which the template was derived; Column (8): IR-processed light fraction of the template. $f_R = L_{dust}/L_{accr.\ disk}$. We calculate the 1 keV–1.25 $\mu$m luminosity of the AGN template as $L_{accr.\ disk}$ and the 1.25–1000 $\mu$m luminosity as $L_{dust}$. For the Kirkpatrick templates, we show the results for normalizing to the Elvis template between 2 and 10 $\mu$m and then at 12 $\mu$m.

frared galaxies at $z$=0.3–2.8, without constraints on the AGN types. Since the Kirkpatrick templates are only given for 2–1000 $\mu$m, to estimate the strength of the intrinsic disk accretion emission, we need to combine them with the Elvis template at shorter wavelengths with proper scalings. To do so, we forced the total luminosity between 2 and 10 $\mu$m to be the same, and then added the Elvis template luminosity between 1.3 and 2 $\mu$m to the reradiated total for the Kirkpatrick et al. (2015) template. Their sample probably includes some fraction of obscured or type-2 AGNs. Under the unified theory of AGNs, we expect these objects to have identical intrinsic X-ray/UV/optical and infrared reradiated SEDs to type-1 objects. However, if they have strong mid-infrared extinction, the normalization at 2–10 $\mu$m could underestimate the nuclear emission. Nevertheless, considering the lack of strong silicate absorption features in the Kirkpatrick AGN templates, such extinction is unlikely to be significant (e.g., Shi et al., 2006; Hatziminaoglou et al., 2015). In addition, the rough agreement of the continuum in these templates with the Elvis one between 2 and 10 $\mu$m supports the normalization we have adopted to obtain an estimate of the X-ray/UV/optical luminoisty. Finally, it is believed that the Kirkpatrick templates may have a significant contamination from star formation in the host galaxy (see the AGN template in their Figure 13). We therefore subtracted their star forming template SFG2 until the long wavelength cutoff of the remaining SED fell similarly to the Elvis template, i.e., we attributed as much as possible of the far-infrared flux to star formation (see Figure 3.1 for an illustration). The maximal nature of this adjustment is clear since it made the resulting AGN-only template go negative at wavelengths longer than 400 $\mu$m. The two other star forming templates in Kirkpatrick et al. (2015) are very similar in the far-infrared and using one of them would not have yielded any significant differences.

**Netzer et al. (2007)**: since this template does not remove host galaxy emission in the near-IR, we replace it with the Elvis template at $\lambda < 3.0$ $\mu$m, where no spectral features exist and the host galaxy contamination is negligible. We also believe the SED rise starting at $\lambda \sim 50$ $\mu$m is non-physical, so we completed the template with a Rayleigh–Jeans tail with a wavelength-dependent emissivity proportional to $\lambda^{-1.5}$ at $\lambda > 40$ $\mu$m.

**Hanish et al. (2013)**: the template was completed for wavelengths shorter than 0.1 $\mu$m and longer than 120 $\mu$m by joining on segments of the original Elvis template. The

possibility of the far-infrared peak in the template arising through star formation is mentioned by the authors, but there has been no attempt to correct for it. It is therefore not surprising that there might be a significant far-infrared component not associated with the central engine.

**Polletta et al. (2007)**: this template was completed for wavelengths short of 0.1 $\mu$m with the Elvis template. There is no explicit step in the assembly of the Polletta templates to remove a star-formation-powered component in the far-infrared, so it would not be surprising if there is a significant one.

### 3.2.4 Analysis and Results

Assuming the standard AGN unification point of view that type-2 AGNs are the same as type-1 AGNs but obscured by dust, a dust-covering factor can be obtained from the relative fraction of type-2 (obscured) to type-1 (unobscured) objects. Schmitt et al. (2001) found that 70% of their far-IR-selected sample of 88 Seyfert galaxies are obscured. Since this sample is IR-selected, this value is probably biased high. Based on the optical spectra of SDSS galaxies, Hao et al. (2005b) show that Seyfert 1 and Seyfert 2 galaxies have comparable numbers at low luminosity, while Seyfert 1 galaxies outnumber Seyfert 2 galaxies by a factor of two to four at high luminosity. Reyes et al. (2008) reported a type-2 quasar fraction in the SDSS sample within the range of $\sim$ 0.5–0.6. Considering the decreasing dust-covering factor with increasing AGN luminosity as first noted by Lawrence (1991) and confirmed by later works (e.g., Maiolino et al. 2007), plus the discussion in Stalevski et al. (2016), we adopt 0.65 as an upper limit for the dust-covering factor ($f_c$) in luminous AGNs.

Comparison of the value of the dust-covering factor with the ratio of the AGN infrared to optical–UV–X-ray luminosities is not straightforward because of anisotropies in the radiation field of the central engine. Stalevski et al. (2016) computed a grid of SEDs emitted by the dusty structures and studied how the relation between the covering fraction and the reradiated luminosity changes with different parameter values for the torus. When the accretion disk and the obscuring torus both emit isotropically, the IR-processed light fraction is a perfect proxy for the dust-covering factor with a one-to-one relation between

these two quantities. In the more realistic case of anisotropic accretion disk emission and a torus that is optically thick in the mid-IR, their simulations suggest that these two quantities are in agreement at ∼0.65. They also provide polynomial fits to allow estimation of the expected values away from 0.65. Although somewhat bright in the mid-infrared and faint in the far-infrared, the Stalevski et al. (2016) model SEDs still match reasonably well relative to the Elvis et al. (1994)-like observational AGN template, suggesting their results are appropriate for our study. We have compared with the model results for $\tau_{9.7}$ of 3–10 since the resulting SEDs roughly match the templates. The corresponding upper limit to the ratio of reradiated to central engine luminosity (a.k.a. $f_{\rm R}$) is then $\sim 0.75$.

The templates from Elvis et al. (1994), Symeonidis et al. (2016), and Netzer et al. (2007) satisfy the upper limit for energy balance between the output of the central engine and the luminosity reradiated in the infrared. It appears that the quasar templates by Hanish et al. (2013) contain too much far-IR emission, possibly due to the contamination from the host galaxy star formation. The Polletta et al. (2007) template is also only marginally consistent with this constraint. Although the exact values of the IR-processed light fractions of the Kirkpatrick et al. (2015) templates have relatively large uncertainties, they are still more luminous in the infrared than expected. Consequently, from the perspective of energy balance, we suggest the Kirkpatrick et al. (2015) templates are unlikely to represent the intrinsic far-IR emission for common type-1 AGNs. One way to make these latter three template families more consistent with energy balance is if their soft X-ray emission is significantly stronger than indicated by the AGN templates. The energy balance argument is difficult to apply to other AGN types because their intrinsic X-ray/UV SEDs are hard to determine. In the case of the Kirkpatrick et al. (2015) templates, we would underestimate the available X-ray/UV luminosity only if there are enough obscured AGNs in the sample to suppress the mid-IR spectrum where we have normalized the Elvis template.

To reassure ourselves of the credibility of the energy balance arguments above, we have examined the behavior of NGC 4151, since (1) its UV continuum has been derived in detail (Alexander et al., 1999), (2) its flux variations have been exceptionally well monitored (e.g., Lyuty & Doroshenko, 1999; Doroshenko et al., 2001), and (3) its infrared SED is very well determined (e.g., Rieke & Lebofsky, 1981; McAlary et al., 1983; Deo et al.,

2009; García-González et al., 2016). The energy balance test on this archetypal type-1 AGN seems to fail at very first glance: even if we take the UV continuum toward the upper range as derived by Alexander et al. (1999), the infrared luminosity is too large to be consistent with energy balance by 20% or more if we analyze the comparison for the simple case of isotropic emission. However, this conclusion is fallacious. Considering the diverse physical scales of the panchromatic emission and the time variability of the accretion disk emission, energy balance for a given AGN may not hold at a given time; the infrared output, particularly at the longer wavelengths, represents a time average of the input UV luminosity. If we normalize the Alexander et al. (1999) continuum to the average *U*-band brightness from 1968 through 2000 (Lyuty & Doroshenko, 1999; Doroshenko et al., 2001) - a factor of 1.62 higher than at the time of their study - ratios of $\sim$ 85% can be obtained but still with a UV continuum toward the upper range allowed (Alexander et al., 1999). This value is consistent with the escape fraction of 15.7% derived by Alonso-Herrero et al. (2011). Rather than raising the UV to the maximum allowed, another solution would be to increase the soft X-ray flux. However, since most of the energy is produced in the blue and UV, a substantial boost (by a factor of $\sim$3) would be necessary to make a significant difference in the energy balance. Besides the variability correction, we also need to consider the anisotropic nature of the accretion disk emission. If we analyze the results as in the models of Stalevski et al. (2016), the values become consistent with more probable fits to the UV continuum (Alexander et al., 1999) and without increasing the soft X-rays. As illustrated by this example, it is critical to apply the energy balance test on a time-averaged SED. (In fact, this requirement is satisfied by the construction of the AGN template.) The case of NGC 4151 also shows that the models by Stalevski et al. (2016) are appropriate to yield consistent energy balance results.

Finally, our emphasis has been the intrinsic AGN SED: the spectrum emitted by the central engine and circumnuclear torus that together appear to constitute a typical active nucleus. It is possible that an AGN heats the surrounding ISM, producing an additional emission component (e.g., Roebuck et al., 2016). Because the extent of this heating will depend on parameters such as the relative orientation of the circumnuclear torus and the host galaxy and on the amount of interstellar material in the host, the emission will differ

significantly from one AGN to another and is likely to be insignificant in many cases. We therefore do not consider it to be part of the intrinsic SED, although it is an interesting phenomenon that should yield additional insights to AGN behavior.

## 3.3 Decomposition of the Quasar IR SEDs

We illustrate some issues in deriving intrinsic AGN IR SEDs by extending the discussion in Lyu et al. (2017) on the infrared SEDs of PG quasars.

### 3.3.1 The $f_{\rm AGN,\,MIR}$–$f_{\rm AGN,\,TIR}$ Relation

The mid-IR spectral window preserves a lot of useful information about the star-forming activities in AGN host galaxies. With the aid of mid-IR spectral decompositions or measurements of the aromatic feaures, many authors have tried to remove the host galaxy contamination in the AGN far-IR emission (e.g., Mullaney et al., 2011; Kirkpatrick et al., 2012, 2015; Xu et al., 2015b; Symeonidis et al., 2016).

However, as suggested in Section 3.1 of Lyu et al. (2017), the host contribution in the infrared 8–1000 $\mu$m range could be underestimated by merely focusing on the mid-IR spectral features. This argument is based on the different IR SED behaviors of the AGN and the host galaxy: the IR output of an AGN is peaked in the mid-IR but drops quickly in the far-IR, while the galaxy emission is relatively weak in the mid-IR but strong in the far-IR. We illustrate this issue in Figure 3.2, which shows a series of mock galaxy SEDs derived by changing the relative contributions of the SF-corrected Elvis et al. (1994) template (Xu et al., 2015b) and a $\log(L_{\rm IR}/L_{\odot}) = 11.25$ Rieke et al. (2009) star-forming template. While the continua shapes of the 5–10 $\mu$m SEDs and the relative strengths of the aromatic features change drastically with the AGN contribution in the mid-IR, there is little modification in the far-IR. The zoom-in panel shows how the relative AGN contribution in the 8–1000 $\mu$m, $f_{\rm TIR}$, changes with that in the mid-IR (5–40 $\mu$m), $f_{\rm MIR}$. The host galaxy still contributes $\sim$50% of the 8–1000 $\mu$m luminosity of the composite SED when the AGN provides 90% of the mid-IR emission. This result qualitatively matches the trend between the AGN relative contribution in the mid-IR emission and that in the total IR emission of

the infrared luminous galaxies, as observationally determined by Kirkpatrick et al. (2015, Section 5).

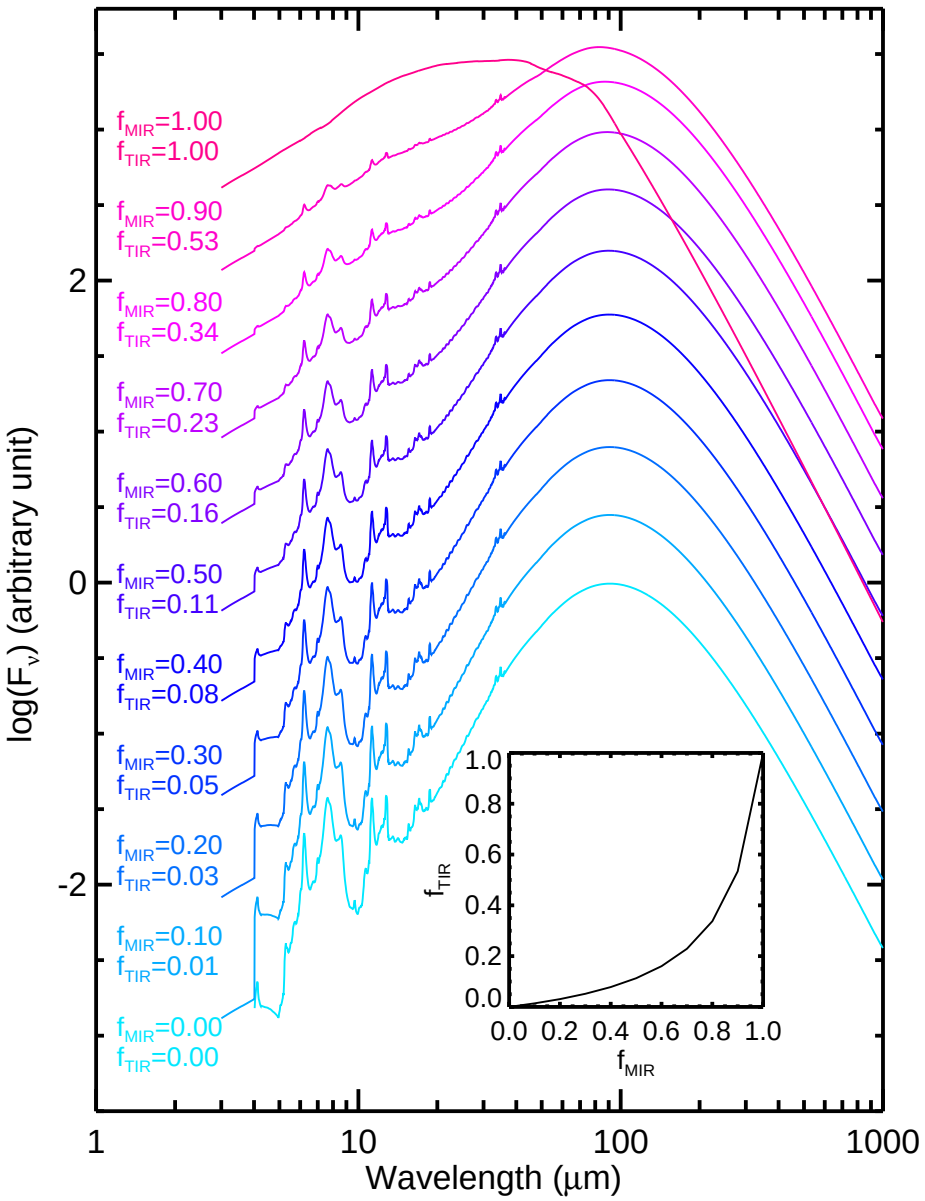


Figure 3.2 Mock infrared SEDs of galaxies with different mixing of the Elvis AGN template and the $\log(L_{\rm IR}/L_{\odot}) = 11.25$ Rieke et al. (2009) template. The AGN contributions in the mid-IR ($f_{\rm MIR}$) and total-IR ($f_{\rm TIR}$) are denoted on the left side of each SED. The zoom-in panel shows the relation between $f(\rm AGN)_{\rm MIR}$ and $f(\rm AGN)_{\rm TIR}$ in the mock SEDs.

For removing the host galaxy far-IR contribution based on relatively low S/N mid-IR spectra, such non-linear relations between $f_{\rm AGN,\,MIR}$ and $f_{\rm AGN,\,TIR}$ could cause an over-

estimation of the intrinsic AGN emission. In other words, although the mid-IR star formation feature may not be detected due to the low quality of the mid-IR data, substantial far-IR host galaxy contamination is still possible. This effect could be one of the reasons behind the strong far-IR emission in the Kirkpatrick et al. (2015) AGN templates. In addition, since their derivation was based on LIRGs and ULIRGs, there may be a selection bias toward cases where the AGN may be heating the galactic ISM, as suggested by Kirkpatrick et al. (2015) and Roebuck et al. (2016). Nonetheless, this situation is also subject to the energy balance constraint, which we have found to be an issue for these templates. In comparison, the study by Mullaney et al. (2011) simultaneously fitted the mid-IR spectra and the far-IR photometry of their X-ray selected sample, resulting in a far-IR AGN SED shape similar to the SF-corrected Elvis et al. (1994) template (see Section 3.4.1).

### 3.3.2 Using the Mid-IR Aromatic Features to Trace the SF Contribution to the Quasar Far-IR Emission

The 11.3 $\mu$m aromatic feature strength seems to be the only SFR-related spectral feature that is not strongly contaminated or influenced by the AGN (e.g., Diamond-Stanic & Rieke, 2010; Esquej et al., 2014; Alonso-Herrero et al., 2014). By matching the observed aromatic strength with a library of star-forming galaxy (SFG) templates, Shi et al. (2007, 2014) have constrained the host galaxy IR luminosities in quasars and these results have been used to derive the intrinsic AGN IR templates (Xu et al., 2015b; Symeonidis et al., 2016).

With the mid-IR spectrum of good quality as an essential prerequisite, the key to correctly gauge the galaxy contribution to the quasar far-IR emission is the luminosity conversion factor between the aromatic features and the galaxy far-IR emission, which is dependent on the selection of the SFG template. Additionally, there is a possibility that some of the feature excitation is provided by the AGN. These two issues are addressed in this section. Finally, we note that the measurements of the aromatic features can have significant biases due to the method to quantify the mid-IR dust emission continuum: typically, the spectral decomposition approach (e.g., *PAHFIT*) with a model of several different dust

components yields a factor of $\sim 2$ larger value of the 11.3 $\mu$m aromatic flux compared to the "interpolation continuum" approach of fitting some smooth function (e.g., spline or power law) to anchor points without strong aromatic emission (e.g., Smith et al., 2007b). We will utilize the results from spectral decomposition similar to *PAHFIT* in Shi et al. (2014), except in Section 3.3.3.

*Choosing the Proper Star-Forming Galaxy Templates* Many IR templates for SFGs are available in the literature (e.g., Chary & Elbaz 2001; Dale & Helou 2002; Lagache et al. 2003, 2004; Siebenmorgen & Krügel 2007; Rieke et al. 2009; see a review in Casey et al. 2014, as well as Ciesla et al. 2014). A critical issue is that the 11.3 $\mu$m feature lies on the edge of the silicate absorption. If this absorption is strong, the apparent equivalent width (EW) of the 11.3 $\mu$m feature may be underestimated. This problem is particularly acute in deconvolving a composite AGN and star forming galaxy SED, where the apparent depth of the silicate absorption is masked by the AGN emission. It becomes increasingly important at high IR luminosities (e.g., LIRG/ULIRG; Stierwalt et al. 2013). Not all of the SFG template libraries include silicate absorption (e.g., Chary & Elbaz 2001; Dale & Helou 2002; see the discussion in Appendix 1.3 of Rieke et al. 2009). Consequently, if SFG templates that omit the effect of silicate absorptions were used, the far-IR emission from the galaxy can be underestimated by adopting the wrong conversion factors from the aromatic feature flux.

With a consistent treatment of IR spectra, photometry, and theoretical models, Rieke et al. (2009) developed IR templates for local galaxies based on *Spitzer* data that include the accompanying increasing silicate absorption with increasing IR luminosity. The accuracy of the Rieke et al. (2009) templates has been demonstrated in a number of works (e.g., Willmer et al., 2009; Calzetti et al., 2010) and their validity to represent SFGs extends to redshifts up to 3 (e.g., Rex et al., 2010; Rujopakarn et al., 2013; Sklias et al., 2014; Lyu et al., 2016). In Appendix B, we derive the conversion factors for $\sim 100$ pure SFGs in the Great Observatories All-sky LIRG Survey (GOALS; Armus et al. 2009). As shown in Figure 3.3, it is very clear that the Dale & Helou (2002) templates do not match the

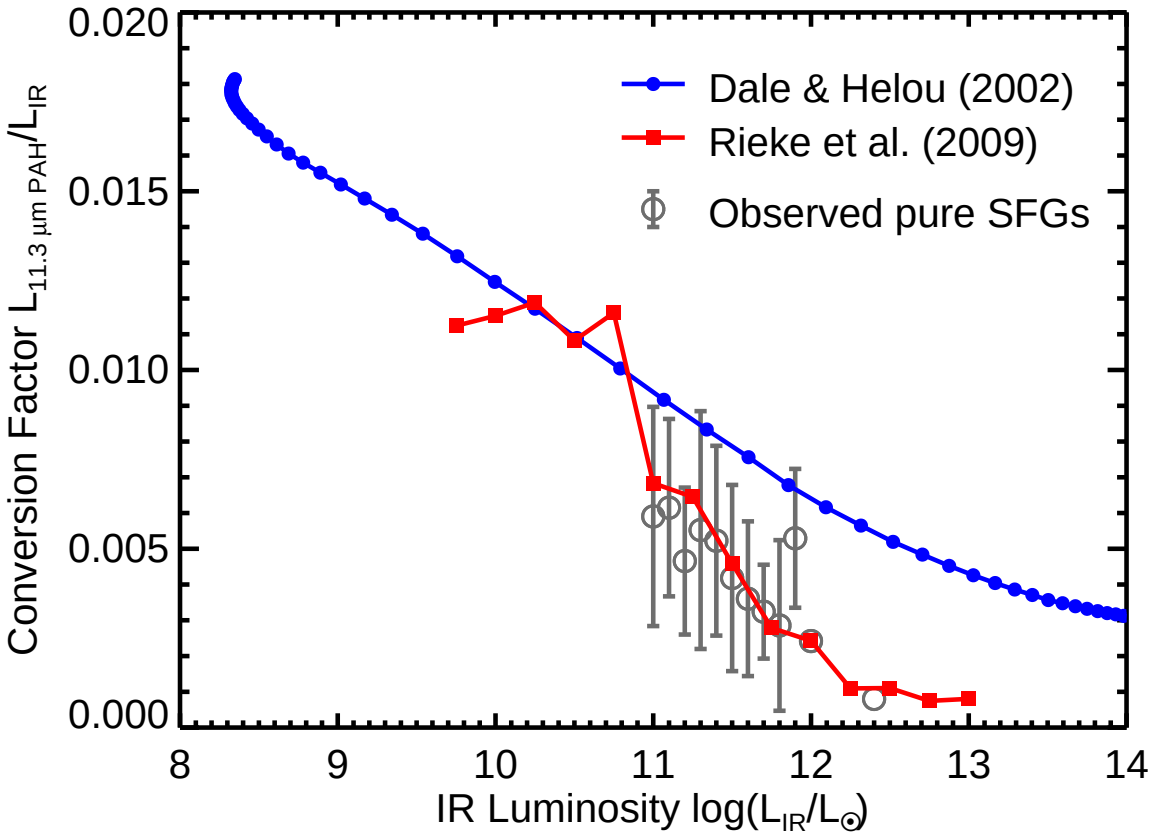


Figure 3.3 Comparisons of the luminosity conversion factors for the 11.3 $\mu$m aromatic feature to the 8–1000 $\mu$m IR emission in Dale & Helou (2002) templates and Rieke et al. (2009) templates. We also plot the observed correlation based on a study of ∼100 pure star-forming galaxies in the GOALS sample (see Appendix B).

observations.[1] In contrast, the Rieke et al. (2009) templates are in good agreement with the observed trend just as expected. Compared with Rieke et al. (2009), the Dale & Helou (2002) SFG templates would result in significantly lower estimates of the SFRs and resulting far-infrared luminosities for galaxies with star forming luminosities of $\sim 10^{11}\ L_{\odot}$ and higher.

For quasars, the discrepancy discussed here arises only if the host galaxy IR star forming luminosities are $10^{11}\ L_{\odot}$ or more. The SFRs of most PG quasar host galaxies were found to be ∼10–100 $M_{\odot}\mathrm{yr}^{-1}$ (see Shi et al. 2014), putting them into the (U)LIRG category. Moreover, studies that assume Elvis-like intrinsic AGN SEDs and that the far-IR

[1] We note that the Dale & Helou (2002) templates were not designed for use at the highest luminosities in the figure.

luminosity is dominated by star formation also suggest that many host galaxies are in this high-luminosity range (e.g., Xu et al., 2015b; Lyu et al., 2016).

The significance of the effects on the derivation of the intrinsic AGN far-IR SED due to the selection of SFG templates will be demonstrated in Section 3.3.3.

*The Luminosity Dependence of the Host Galaxy IR SEDs* According to the energy balance discussed in Section 3.2, it is not reasonable to assume the entire luminosities of far-IR-bright quasars are attributed to the central engine. A significant, perhaps dominant, part of the far-IR luminosity must arise from the host galaxy. To confirm that the Rieke et al. (2009) SFG templates can represent the quasar host galaxy IR emission and the aromatic emission observed in the quasar mid-IR spectra is indeed from the quasar host galaxy, in a statistical sense, (1) the fitted host galaxy IR luminosities should be consistent with the IR luminosities associated with the selected SFG templates from Rieke et al. (2009); (2) the 11.3 $\mu$m aromatic feature strengths observed in the mid-IR spectra should also agree with the values converted from the fitted galaxy template.

In Lyu et al. (2017), the mid- to far-IR SEDs of 87 $z < 0.5$ PG quasars were fitted with the SF-corrected Elvis AGN template (as well as the dust-deficient AGN templates) and SFG templates with $\log_{10}(L_{\rm IR}/L_{\odot})$=9.75–12.0 from Rieke et al. (2009). Besides the well-sampled IR broadband SEDs, high-quality *Spitzer*/IRS mid-IR spectra are also available for the whole sample, enabling simultaneous tests on the ability of both the far-IR SEDs and the mid-IR spectral features of the Rieke et al. (2009) templates to represent the quasar host galaxy emission. However, not all members in this sample were suitable for this purpose. Firstly, for each quasar, we should be able to reveal the differences among the Rieke et al. (2009) templates. Thus, we require the quasar to either have a substantial host galaxy contribution ($f_{\rm IR,\,host} > 33\%$), where the shape of the infrared galaxy template becomes important to change the $\chi^2$, or the Rieke et al. (2009) template with a similar luminosity as the observed value tends to a smaller $\chi^2$ at least by a factor of 1.5 compared with alternatives. 32 PG quasars meet this requirement. Additionally, there should be no nearby galaxy to pollute the *Herschel* photometry of the quasar far-IR emission, and two quasars failing this criteria have been dropped. Finally, poor fittings of the very far-IR

Table 3.2. Host Galaxy IR Properties of the 24 Palomar–Green Quasars

| ID (1) | Source (2) | $z$ (3) | $F_{\rm PAH,spec}$ (4) | $L_{\rm R09,PAH}$ (5) | $c_{\rm R09,PAH}$ (6) | $f_{\rm IR,AGN}$ (7) | $F_{\rm PAH,SED}$ (8) | $L_{\rm R09,temp}$ (9) | $L_{\rm host,obs.}$ (10) |
|---|---|---|---|---|---|---|---|---|---|
| 4 | PG 0043+039 | 0.38 | $0.10\pm0.04$ | 11.50 | 1.02 | 0.65 | 0.19 | 11.00 | 11.56 |
| 6 | PG 0050+124 | 0.06 | $4.60\pm0.18$ | 11.25 | 1.09 | 0.56 | 8.90 | 11.00 | 11.47 |
| 10 | PG 0838+770 | 0.13 | $0.25\pm0.05$ | 10.50 | 0.87 | 0.51 | 0.77 | 11.00 | 11.12 |
| 14 | PG 0923+129 | 0.03 | $1.82\pm0.06$ | 9.75 | 1.15 | 0.46 | 4.34 | 10.50 | 10.33 |
| 15 | PG 0934+013 | 0.05 | $0.58\pm0.04$ | 9.75 | 1.12 | 0.38 | 1.10 | 11.00 | 10.39 |
| 20 | PG 1011−040 | 0.06 | $0.56\pm0.04$ | 10.00 | 0.88 | 0.53 | 0.86 | 11.00 | 10.45 |
| 21 | PG 1012+008 | 0.19 | $<0.05$ | 10.00 | 0.92 | 0.76 | 0.23 | 11.00 | 10.96 |
| 22 | PG 1022+519 | 0.05 | $1.18\pm0.03$ | 10.00 | 1.03 | 0.35 | 0.87 | 11.00 | 10.29 |
| 25 | PG 1049−005 | 0.36 | $<0.04$ | 11.00 | 0.83 | 0.69 | 0.23 | 11.75 | 11.98 |
| 31 | PG 1119+120 | 0.05 | $0.72\pm0.10$ | 10.00 | 0.82 | 0.60 | 1.60 | 11.00 | 10.56 |
| 34 | PG 1149−110 | 0.05 | $0.14\pm0.04$ | 9.75 | 0.26 | 0.44 | 1.32 | 11.00 | 10.47 |
| 41 | PG 1244+026 | 0.05 | $0.52\pm0.04$ | 9.75 | 0.91 | 0.58 | 0.69 | 11.00 | 10.19 |
| 48 | PG 1341+258 | 0.09 | $0.21\pm0.04$ | 9.75 | 1.26 | 0.65 | 0.28 | 11.00 | 10.34 |
| 49 | PG 1351+236 | 0.05 | $2.02\pm0.03$ | 10.50 | 1.10 | 0.21 | 2.21 | 11.00 | 10.70 |
| 50 | PG 1351+640 | 0.09 | $1.77\pm0.09$ | 11.25 | 0.91 | 0.65 | 2.06 | 11.00 | 11.20 |
| 53 | PG 1402+261 | 0.16 | $0.31\pm0.11$ | 10.75 | 0.98 | 0.76 | 0.41 | 11.50 | 11.21 |
| 54 | PG 1404+226 | 0.10 | $0.27\pm0.03$ | 10.00 | 1.28 | 0.67 | 0.37 | 10.75 | 10.32 |
| 56 | PG 1415+451 | 0.11 | $0.78\pm0.03$ | 10.75 | 1.09 | 0.66 | 0.46 | 11.00 | 10.74 |
| 67 | PG 1519+226 | 0.14 | $0.20\pm0.04$ | 10.25 | 1.10 | 0.85 | 0.30 | 10.75 | 10.55 |
| 70 | PG 1543+489 | 0.40 | $<0.02$ | 10.50 | 0.87 | 0.55 | 0.35 | 11.75 | 12.27 |
| 73 | PG 1612+261 | 0.13 | $0.35\pm0.03$ | 10.50 | 1.19 | 0.60 | 0.77 | 11.25 | 11.14 |
| 77 | PG 1700+518 | 0.28 | $1.41\pm0.17$ | 13.00 | 0.88 | 0.74 | 0.38 | 11.75 | 11.95 |
| 78 | PG 1704+608 | 0.37 | $0.09\pm0.06$ | 11.25 | 1.09 | 0.81 | 0.12 | 12.00 | 11.78 |
| 81 | PG 2209+184 | 0.07 | $0.58\pm0.04$ | 10.00 | 1.33 | 0.57 | 0.58 | 09.75 | 10.20 |

Note. — Column (1): the object ID (see Table 2 in Lyu et al. 2017 for the list of the whole PG sample); Column (2): object name; Column (3): redshift; Column (4): the 11.3 $\mu$m aromatic feature flux (unit: $10^{-13}$erg s$^{-1}$ cm$^{-2}$) as measured by Shi et al. (2014); Column (5): the IR luminosity of the best-matched Rieke et al. (2009) template based on the 11.3 $\mu$m aromatic feature luminosity; Column (6): the scaling factor of the best-matched Rieke et al. (2009) template based on the 11.3 $\mu$m aromatic feature luminosity; Column (7): the AGN fractional contribution to the IR emission of each quasar; Column (8): the 11.3 $\mu$m aromatic feature flux (unit: $10^{-13}$erg s$^{-1}$ cm$^{-2}$) derived from the SED modeling; Column (9): the IR luminosity of the best-fitted Rieke et al. (2009) template from the SED modeling; Column (10): the observed IR luminosity of the host galaxy from the SED modeling.

SEDs may suggest dust heating by old stars, abnormal dust properties, confusion noise, or radio synchrotron emission contamination. In such cases, the radio-quiet AGN template combined with any selection of the SFG templates will be unreliable. Consequently, we dropped another six quasars due to their large fitting residuals ($\gtrsim 0.3$ dex) at $\lambda > 100$ $\mu$m. The final sample of the 24 PG quasars as well as their IR properties is listed in Table 3.2.

The far-infrared SEDs of star-forming galaxies show a consistent pattern of shapes as a function of the luminosity (e.g., Chary & Elbaz, 2001; Dale & Helou, 2002; Siebenmorgen & Krügel, 2007; Rieke et al., 2009). In Figure 3.4, we compare the derived host galaxy infrared luminosities from fitting the far-infrared SEDs with the luminosity of the template with the shape that gave the best fit for these 24 PG quasars. The luminosities of the optimally

shaped templates are roughly consistent with the quasar host galaxy luminosities derived by integrating the fitted fluxes. With a linear fit, we find a slope between these two groups of luminosities to be 1.05±0.20 and an intercept of 0.73±2.13, consistent with the expected 1:1 relation.

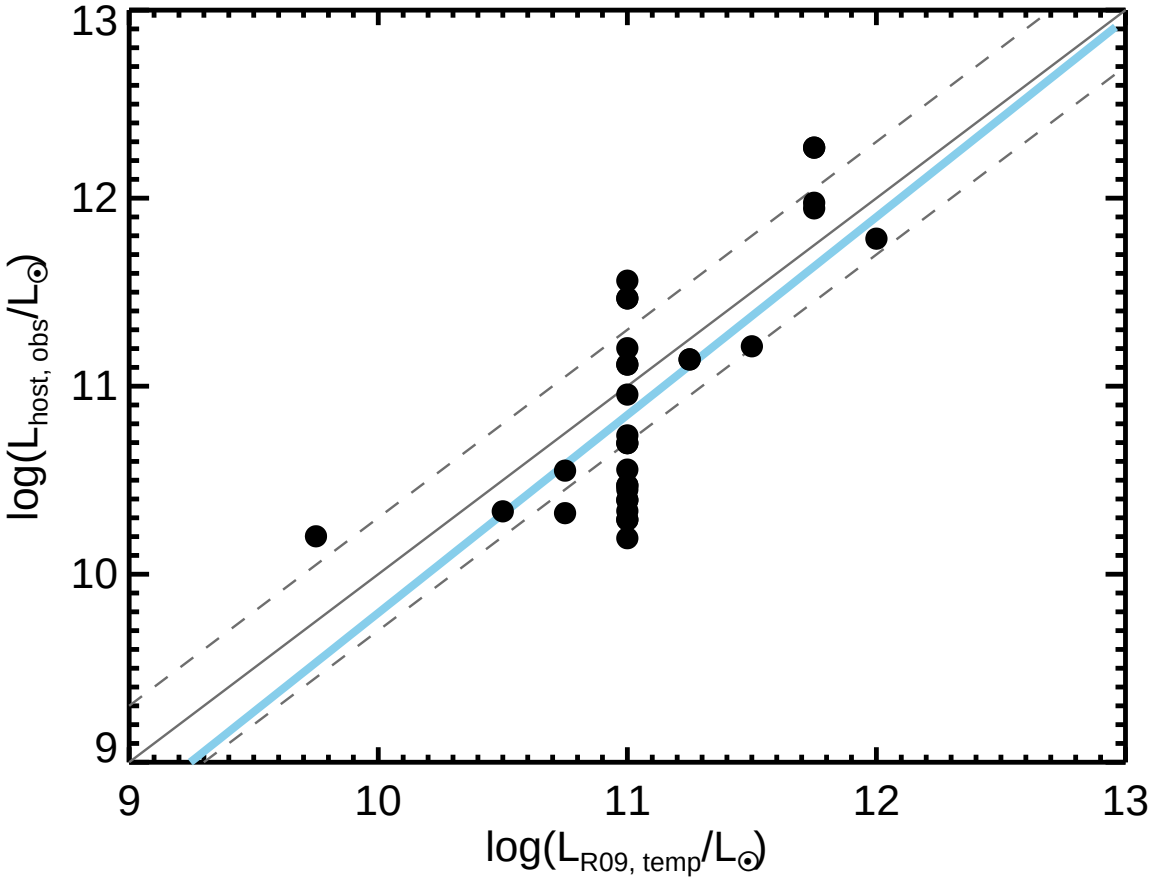


Figure 3.4 Relation between the derived host galaxy infrared luminosities with the $\chi^2$ selected Rieke et al. (2009) template luminosities. We show the 1:1 relation and a linear fitting of the data points as gray and blue solid lines separately.

*The 11.3 μm Aromatic Strength from the SED Model* If the excitation of the 11.3 μm feature is dominated by star formation as represented by the Rieke et al. (2009) templates, we should expect the observed mid-IR aromatic feature strength to be consistent with the aromatic flux converted from the SFG template fitted to the SED photometry. If the AGN plays an important role in exciting the aromatic feature, we would expect the feature strength to be greater than that predicted by the star-forming template.

To derive the aromatic feature strengths of the Rieke et al. (2009) templates, we decomposed the 5–40 $\mu$m portion of the templates using the IDL program *PAHFIT* (Smith et al., 2007b). In this code, the mid-IR dust continuum is fitted with multiple blackbody components with possible mid-IR extinction and the 11.3 $\mu$m aromatic feature is fitted with two Drude profiles centered at 11.23 and 11.33 $\mu$m. The 11.3 $\mu$m feature strength computed by *PAHFIT* was then compared with the 8.0–1000 $\mu$m integrated luminosity of each template. Finally, we ended up with the conversion factor for the 11.3 $\mu$m feature, varying from 0.011 at $\log_{10}(L_{\rm IR,SF}/L_{\odot}) = 9.75$ to 0.0024 at $\log_{10}(L_{\rm IR,SF}/L_{\odot}) = 12.0$.

Figure 3.5 compares the 11.3 aromatic feature flux converted from the fitted Rieke et al. (2009) templates in Lyu et al. (2017) with the values measured from *Spitzer/IRS* spectra by Shi et al. (2014). Considering the measurement uncertainties, the results are consistent within 0.3 dex for most objects and show a strong correlation. There is only one case above the correlation that might be a candidate for an additional contribution through excitation by the nucleus. The consistent results between the SED model predications and the mid-IR spectral measurements indicate that the excitation of the 11.3 $\mu$m aromatic feature is dominated by star formation in most of these systems.

### 3.3.3 Testing Alternative AGN "Intrinsic" IR Templates

Given the consistent SFRs estimated from the SED models with the values measured by the 11.3 $\mu$m aromatic bands (Figure 9 in Lyu et al. 2017) and the successful reproduction of the host galaxy mid-IR to far-IR properties by the Rieke et al. (2009) templates shown above, the argument that the intrinsic AGN IR emission of most quasars can be represented by the SF-corrected Elvis et al. (1994) template is also validated. Here we discuss whether the other versions of AGN "intrinsic" IR templates, e.g., as proposed by Netzer et al. (2007), Kirkpatrick et al. (2015), and Symeonidis et al. (2016), are good alternative choices to the SF-corrected Elvis et al. (1994) template.

*An Illustration of the Importance of SFG Template Selection* Recently, Symeonidis et al. (2016) derived an SF-corrected AGN template based on a sample of 47, radio-quiet PG quasars at $z < 0.18$. Even compared with the original Elvis et al. (1994) quasar template,

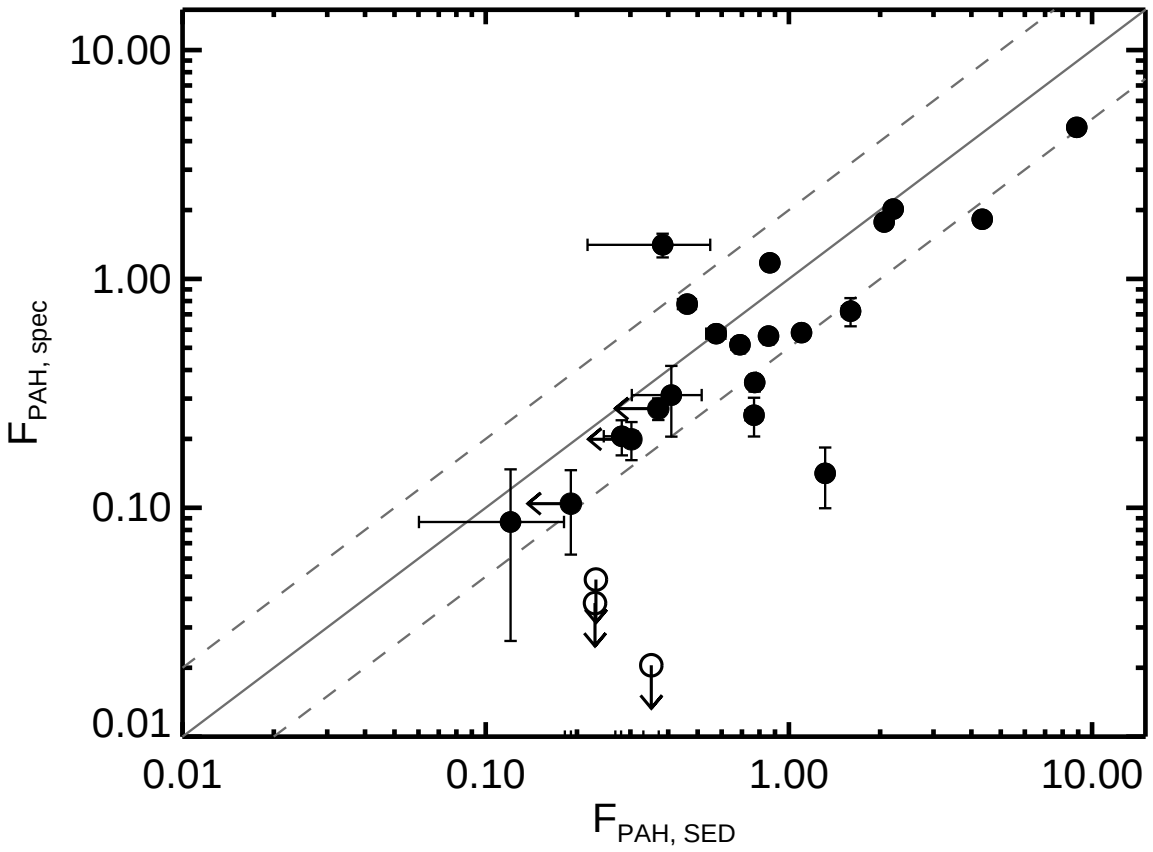


Figure 3.5 Comparison of the measured 11.3 $\mu$m aromatic feature flux (unit: $10^{-13}$ erg s$^{-1}$cm$^{-2}$) in Shi et al. (2014) from the mid-IR spectra ($f_{\rm PAH,\ spec}$) and that from the conversion of the fitted Rieke et al. (2009) templates ($f_{\rm PAH,\ SED}$) in Lyu et al. (2017).

the Symeonidis et al. (2016) template has much stronger far-IR emission. However, they used host galaxy luminosities derived from Shi et al. (2007), which were based on the Dale & Helou (2002) templates because replacements based on *Spitzer* data were not yet available. Recalling our comparisons of the Dale & Helou (2002) and the Rieke et al. (2009) SFG templates in Section 3.3.2, there is a risk that the cool SED component they found in the quasars is a result of underestimating the contribution of star formation to the quasar composite far-IR SED.

To test this possibility with the data described in Lyu et al. (2017), we made a similar derivation of the "intrinsic" AGN IR template based on the same sample as Symeonidis et al. (2016). To derive the quasar continuum, we interpolated the UV-to-IR photometry loga-

rithmically and smoothed the SED with a $\Delta\log(\nu) = 0.2$ boxcar.[2] With the Rieke et al. (2009) template that gave the closest 11.3 $\mu$m aromatic luminosity as measured by Shi et al. (2007), we derived a host galaxy luminosity with the matched and scaled SFG template for each quasar. This host galaxy IR luminosity was then compared to the observed quasar IR luminosity to derive a relative scaling of the selected Rieke et al. (2009) template, as shown in Figure 3.6. For quasars with only upper limits to the aromatic flux, we scaled the matched SFG template by adopting one-half of the IR host template luminosity corresponding to the upper limit, as in Symeonidis et al. (2016). Then the composite mean SEDs of the quasar sample and the relatively scaled Rieke et al. (2009) templates were computed. By subtracting the mean host galaxy SED from the observed mean quasar SED, we derived a final version of the "intrinsic" AGN SED template but with the Rieke et al. (2009) SFG templates to represent the host galaxy emission. As shown in Figure 3.6, this newly derived "intrinsic" AGN template, which is based on the Symeonidis et al. (2016) sample but with the Rieke et al. (2009) SFG library to convert the 11.3 $\mu$m aromatic strengths to the host IR luminosities, presents much weaker far-IR emission compared with the version from Symeonidis et al. (2016). We also derived another version of the "intrinsic" AGN SED template by subtracting the composite median host galaxy SED from the median quasar SED. Normalized at 20 $\mu$m, its far-IR part matches the SF-corrected Elvis et al. (1994) template reasonably well up to 100 $\mu$m. Beyond 100 $\mu$m, our mean (or median) SFG SED has similar emission strength with the mean (or median) quasar SED, suggesting that the AGN contribution in the composite quasar emission is weak. A more realistic replacement of these AGN templates at $\lambda > 100$ $\mu$m is a Rayleigh-Jeans tail with emissivity proportional to $\lambda^{-1.5}$, which would finally yield almost the same SED shape at 20–1000 $\mu$m as the SF-corrected Elvis et al. (1994) template.

Given this result, we suggest that the cooler "intrinsic" AGN IR SED derived by

[2]We note that Symeonidis et al. (2016) fitted the quasar IR SEDs at $\lambda > 22$ $\mu$m with a greybody for the far-IR and a power law for the mid-IR (see their Section 3.1). For some quasars with strong host far-IR emission, a local SED minimal can be seen between $\sim 20$ $\mu$m and $\sim 100$ $\mu$m (see the SEDs of, e.g., PG 0052+251, PG 0844+349, PG 1114+445, and PG 1416−129 in their Figure A3). In fact, this feature is common for many quasars but not always obvious due to the poorly constrained SEDs at these wavelengths (see our SED decompositions in Figure 5 of Lyu et al. 2017). The SED model used by Symeonidis et al. (2016) cannot reproduce such features due to the smoothly declining nature of their adopted function, leading to possible overestimations of the far-IR emission of many quasars.

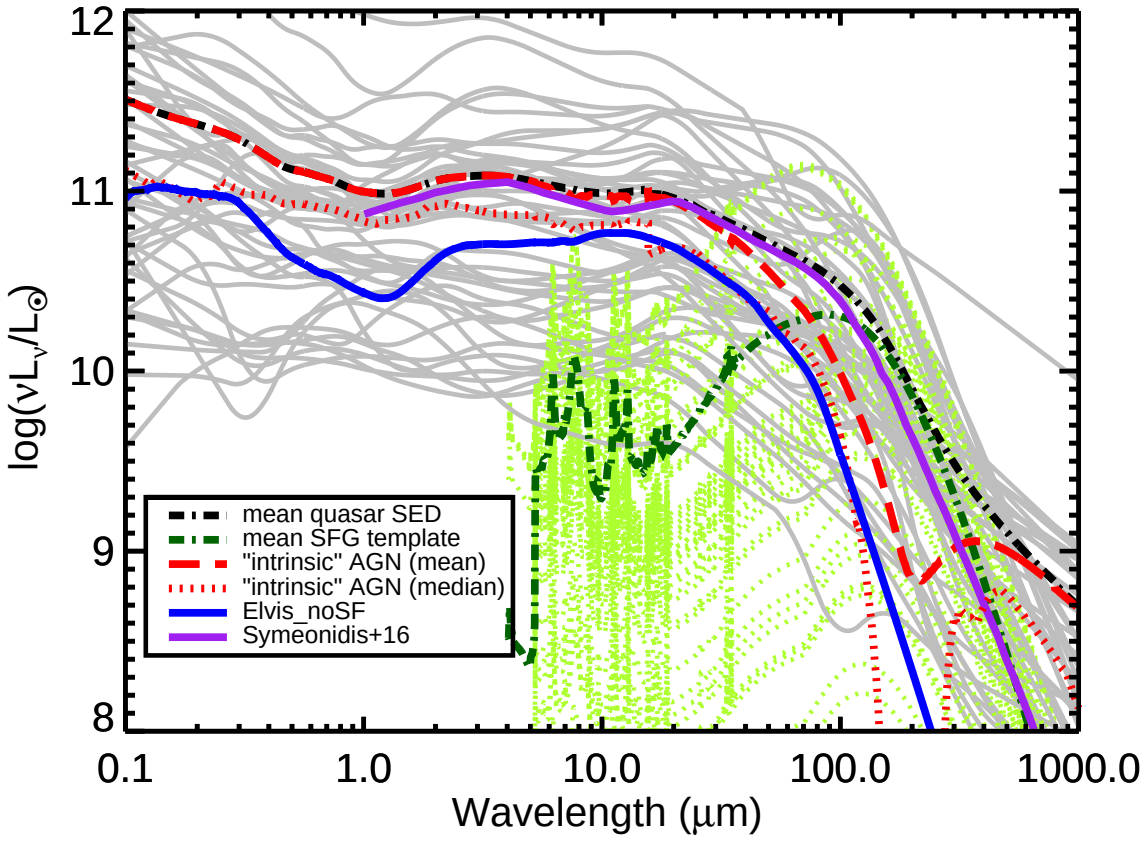


Figure 3.6 SEDs for the Symeonidis et al. (2016) PG quasar sample (gray solid curves) and their mean (thick black dashed–dotted curve), as well as the relatively scaled Rieke et al. (2009) SFG templates (light green dotted curves) and their mean (dark green dashed–dotted curve). We derive two "intrinsic" AGN SEDs, either by subtracting the mean SFG template from the mean quasar template (mean AGN SED; thick red dashed line) or by subtracting the median SFG template from the median quasar template (median AGN SED; thick red dotted line). The Symeonidis et al. (2016) cooler "intrinsic" AGN template and the SF-corrected Elvis et al. (1994) template (normalized at 20 $\mu$m to match the median AGN SED) are also plotted.

Symeonidis et al. (2016) is at the least a very uncertain conclusion and that a similar derivation using more appropriate star forming galaxy templates implies that this characteristic is not common. Consequently, it casts doubt on the argument of her following work (Symeonidis, 2017) that the AGN-heated dust emission would overwhelmingly contribute the far-IR emission of the most luminous quasars. Additionally, we further confirmed the validity of this SF-corrected Elvis et al. (1994) template by successfully reproducing a similar one with a different approach from Xu et al. (2015b).

*Tests Based on the Aromatic Band Behavior* As shown in Lyu et al. (2017), there is a range of intrinsic infrared SEDs for quasars. We limit this discussion to the confirmed 52 "normal" PG quasars as defined in that paper.

Since the EW reflects the relative strength of the emission feature, how the EW of the 11.3 $\mu$m aromatic feature changes with the AGN contribution to the quasar IR emission budget would provide a method to distinguish different AGN templates. In Figure 3.7, we compare the relations between the EW of the 11.3 $\mu$m feature and the relative AGN contribution in the total infrared emission derived from SED decomposition of the normal quasar sample and the relations derived from combining the AGN templates with the Rieke et al. (2009) $\log(L_{\rm IR}/L_{\odot})$=11.25 SFG template. The observation matches the SF-corrected Elvis et al. (1994) template reasonably well except for the cases where $f_{\rm AGN,TIR} > 0.8$. In these cases, the AGN contribution is so dominant that the measurement of the aromatic features becomes difficult, so we are unsure if this discrepancy is real. In addition, many quasars with $f_{\rm AGN,TIR} > 0.8$ have host galaxy IR luminosities $\sim 10^{10}\ L_{\odot}$, in which case the $\log(L_{\rm IR}/L_{\odot})$=11.25 SFG template adopted here would underestimate the EW of the aromatic features (see Figure 3.3).

As shown in Figure 3.7, combining the Kirkpatrick et al. (2015) AGN template with the SFG template to fit the far-IR underpredicts the 11.3 $\mu$m aromatic feature EWs, which supports the idea of that the (Kirkpatrick et al., 2015) templates have substantial host galaxy contamination in the IR. In comparison, using the Netzer et al. (2007) AGN template overpredicts the aromatic feature EWs, suggesting that the host galaxy is oversubtracted from their quasar average SEDs. As a result, we suggest the assumption in Netzer et al. (2007) that 50–100 $\mu$m emission of quasars is entirely due to star formation is too aggressive. Consequently, the SF-corrected Elvis et al. (1994) template is preferred over these two alternatives.

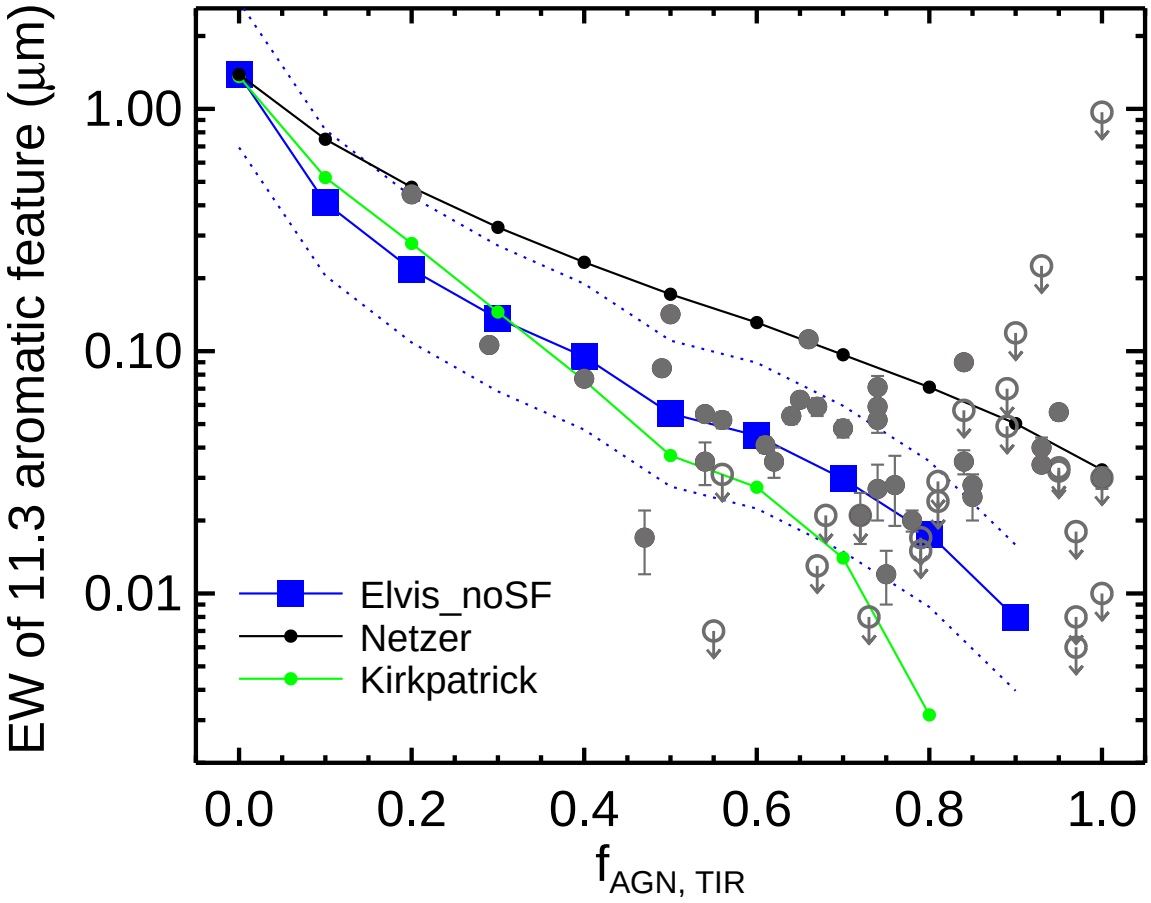


Figure 3.7 Equivalent width of the 11.3 $\mu$m feature as a function of AGN contribution to the total infrared luminosity, $f_{\rm AGN,TIR}$ for the 57 normal quasars in the PG sample (black filled dots for objects with aromatic feature detections, red open circles for upper limits). We also show the simulated curves by combining the Rieke et al. (2009) $\log(L_{\rm IR}/L_{\odot}))=$ 11.25 star-forming galaxy template with various AGN templates.

## 3.4 Discussion

### 3.4.1 Does the Normal Quasar IR Template Apply to Other Populations of Type-1 AGNs?

A natural question is whether most, if not all, AGNs have similar intrinsic IR SEDs. As shown by Lyu et al. (2017), among unobscured type-1 quasars, some 10% or more have a deficiency of the AGN intrinsic infrared emission, making their SEDs differ significantly from the normal cases. These dust-deficient quasars can be further grouped into the hot-dust-deficient (HDD) population and the warm-dust-deficient (WDD) population, possibly

connected with different AGN properties. In addition, it is established that the AGN SED, including the IR part, changes from the most luminous quasars to less luminous AGNs in nearby galaxies (Ho, 1999, 2008; Prieto et al., 2010). Hence the idea of one single IR template that applies for all kinds of AGNs, even just for quasars, is not correct.

Surprisingly, despite the variations in the near- and mid-IR, the intrinsic SEDs of many different types of AGNs are roughly similar in the far-IR. In Figure 3.8, we compare the empirical templates for normal quasars and dust-deficient quasars (Lyu et al., 2017), the sub-arcsec resolution average templates derived for nearby Seyfert 1 and Seyfert 2 galaxies (Prieto et al., 2010), the IR intrinsic template of moderate-luminosity AGNs derived by Mullaney et al. (2011), and the observed SEDs with the smallest beams[3] of the archetypal Seyfert galaxies: NGC 1068 (type 2) and NGC 4151 (type 1). Firstly, all three quasar templates have surprisingly similar 20–100 $\mu$m SEDs with mean deviations of less than 0.07 dex. For Seyfert galaxies, due to their low AGN luminosities, the host galaxy dust emission still contaminates the far-IR AGN emission. However, all of the Seyfert AGN templates and SEDs show a decreasing trend of the far-IR SED right after 20 microns, similar to the behavior of the quasars. In fact, based on subtraction of host galaxy contamination from the mid-IR continua of Seyfert galaxies, Deo et al. (2009) also reported a similar turn-over at$\sim$ 20 $\mu$m. Mullaney et al. (2011) derived their intrinsic AGN IR template by fitting both mid-IR spectral data and far-IR photometry of 11 nearby moderate-luminosity AGNs. We find it shares a similar far-IR SED as the quasar templates. For the Seyfert sample in Prieto et al. (2010), their 11.3 aromatic feature luminosities were found to be $\sim 10^{8-9}\ L_{\odot}$ (Sturm et al., 2000; Hernán-Caballero & Hatziminaoglou, 2011), corresponding to the host IR luminosities $\gtrsim 10^{11}\ L_{\odot}$. After subtracting a host galaxy template from the Prieto et al. (2010) Seyfert 1 and Seyfert 2 AGN templates in the far-IR, their $\gtrsim$70 $\mu$m SED can easily match that of Mullaney et al. (2011). As argued at the end of the next subsection, such an SED similarity in the far-IR might be inherently expected from

[3] Rieke & Low (1972, 1975a,b) presented the smallest photometric beam measurements of NGC 1068 and NGC 4151 at wavelengths longer than 20 $\mu$m (except for submillimeter and radio) so far at 21 and 34 $\mu$m (with a beam size $\sim$6$''$). For NGC 1068, we supplement the 14.3$''$aperture *Herschel* photometry at 70, 160, 250, 350, and 500 $\mu$m from (García-González et al., 2016) with a scaling factor of 5.7 to reduce the aperture effects with ground-based data. For NGC 4151, we plot the 10.2$''$aperture photometry at 70 and 160 $\mu$m from the same paper with a scaling factor of 1.44.

simple physics of dust grain emission in the optically thin limit.

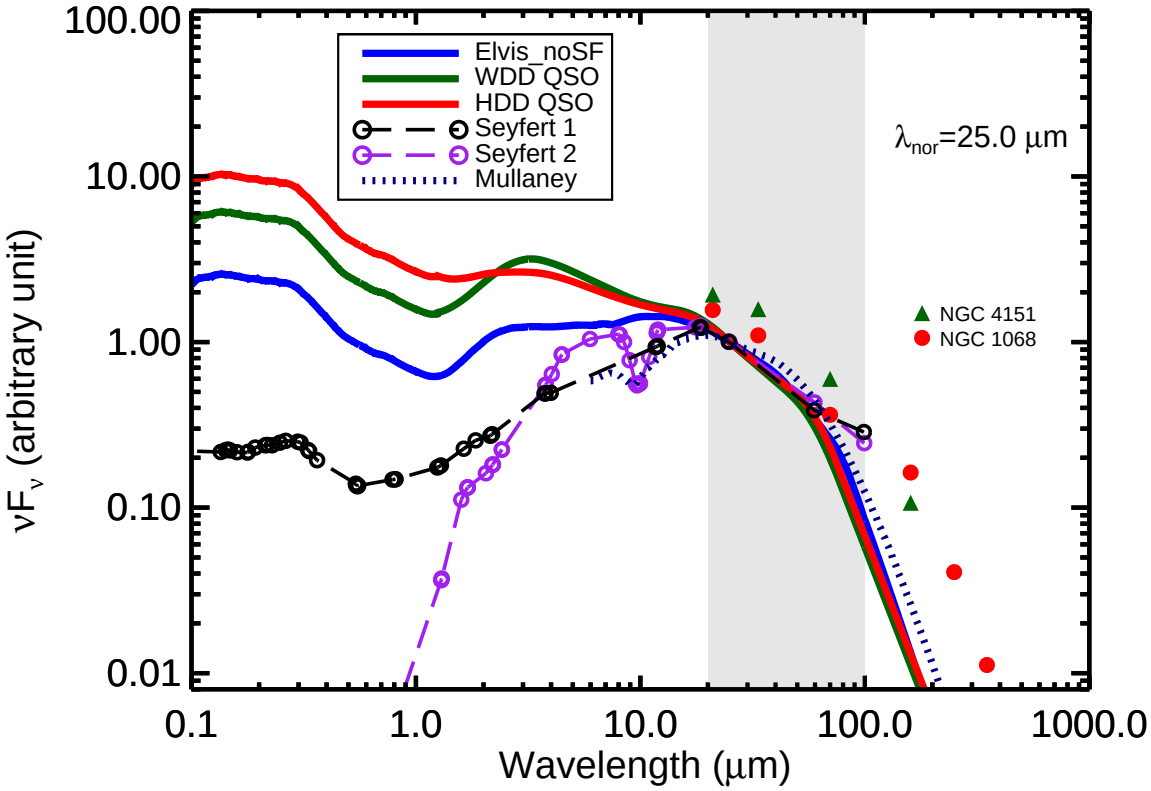


Figure 3.8 Comparison of the AGN templates for quasars and Seyfert galaxies. We highlight the far-IR 20–100 $\mu$m spectral region with a pink background. The normal quasar template is taken from Xu et al. (2015b), who removed the far-IR host galaxy contribution from the Elvis et al. (1994) template; the hot-dust-deficient (HDD) and warm-dust-deficient (WDD) quasar templates are from Lyu et al. (2017). The Seyfert 1 and Seyfert 2 AGN templates are taken from Prieto et al. (2010) (we only plot these templates at $\lesssim$ 100 $\mu$m, where there are photometry constraints). The intrinsic IR template for relatively low-luminosity AGNs from Mullaney et al. (2011) is also presented. We also show the small-beam SEDs of NGC 4151 and NGC 1068.

### 3.4.2 Implications for the Obscuring Structure

With the complete characterization of the intrinsic infrared SED templates for quasars (Xu et al., 2015b; Lyu et al., 2017) and the further confirmation as presented in this work, we can analyze the properties of the major dust components that determine the SED shape. Dust will sublimate at a temperature $T$ $\sim$1800 K in the innermost regions of the torus. Thus we use a blackbody with a fixed temperature at 1800 K to represent this hottest dust

component. Additionally, we add three dust components to represent the hot, warm, and cold dust contributions; the first two components are assumed to be black bodies and the cold dust component is assumed to be a modified blackbody with emissivity $\beta = 1.5$. Unlike the hottest dust component, the temperatures of the other three components can be varied freely. The relative fractions of all the dust components are free parameters. The emission from the accretion disk is represented with a power-law component, which can be described as $f_\nu \propto \nu^{0.3}$ with a break to the $f_\nu \propto \nu^2$ Rayleigh-Jeans slope at 3 $\mu$m (Hönig et al., 2010). We normalize this component to the template at 0.51 $\mu$m. After subtracting the contribution of this broken power-law component, the 1.0–1000 $\mu$m SED template is fitted by the four-component dust model with parameters determined by minimizing the $\chi^2$.

The template decomposition results are summarized in Figure 3.9 and Table 3.3. Our simple dust model fits reasonably well and confirms the deficiency of hot or warm dust emission in corresponding groups of AGNs. In Table 3.3, we quantify the emission strength of each dust component by its total luminosity, $L_{\rm dust}$, normalized by the emission coming from the accretion disk, $L_{\rm accr.\ disk} = L_{\rm AGN}[1\ {\rm keV}–1.3\ \mu{\rm m}]$. The WDD AGNs and normal AGNs have similar hot dust emission strength with $L_{\rm dust}/L_{\rm accr.\ disk} = 0.19 - 0.21$ but the warm dust emission strength of the former is only about half of the latter. The HDD AGNs have weaker hot dust emission ($\sim 50\%$) and warm dust emission ($\sim 26\%$) compared with the normal AGNs. While the relative contributions differ in these AGN templates, the temperatures of each dust component have narrow ranges with the hot dust component at $\sim$700–1000 K, the warm dust component at $\sim$200–300 K and the cold dust component at $\sim$60–80 K. This result suggests that we are seeing the infrared emission of a number of components of these AGNs that are nearly always present but in modestly different amounts.

Given the decomposition results, we can also make order-of-magnitude estimations of the physical sizes of these dust components. Assuming blackbody emission with temperature $T_{\rm d}$, the dust emission luminosity $L_{\rm d}$ can be approximated by the Stefan–Boltzmann law. Introducing a dust-covering factor $f_{\rm c}$ and a characteristic physical scale $r_{\rm d}$, then we

Table 3.3. Dust Components for the Quasar Intrinsic AGN IR Emission

| Dust Component (1) | $T$ (2) | $f_{\rm R}$ (3) |
|---|---|---|
| Normal AGN template | | |
| Sublimating dust | 1800 K | 0.05±0.01 |
| Hot dust | 883±49 K | 0.19±0.01 |
| Warm dust | 285±12 K | 0.23±0.01 |
| Cold dust | 77±5 K | 0.06±0.01 |
| All dust | – | 0.53 |
| WDD AGN template | | |
| Sublimating dust | 1800 K | 0.03±0.02 |
| Hot dust | 944±50 K | 0.21±0.01 |
| Warm dust | 276±31 K | 0.10±0.01 |
| Cold dust | 83±13 K | 0.02±0.01 |
| All dust | – | 0.36 |
| HDD AGN template | | |
| Subliminating dust | 1800 K | 0.03±0.01 |
| Hot dust | 752±77 K | 0.10±0.01 |
| Warm dust | 240±46 K | 0.06±0.01 |
| Cold dust | 66±30 K | 0.01±0.01 |
| All dust | – | 0.20 |

Note. — Column (1): the hottest dust component corresponds the dust close to the sublimation distance; Column (2): dust temperature from the decomposition model; Column (3): IR-processed light fraction of each dust component. $f_{\rm R} = L_{\rm dust}/L_{\rm accr.\ disk}$. We caculate the 1 keV–1.25 $\mu$m luminosity of the AGN template as $L_{\rm accr.\ disk}$ and the 1.25–1000 $\mu$m luminosity as $L_{\rm dust}$.

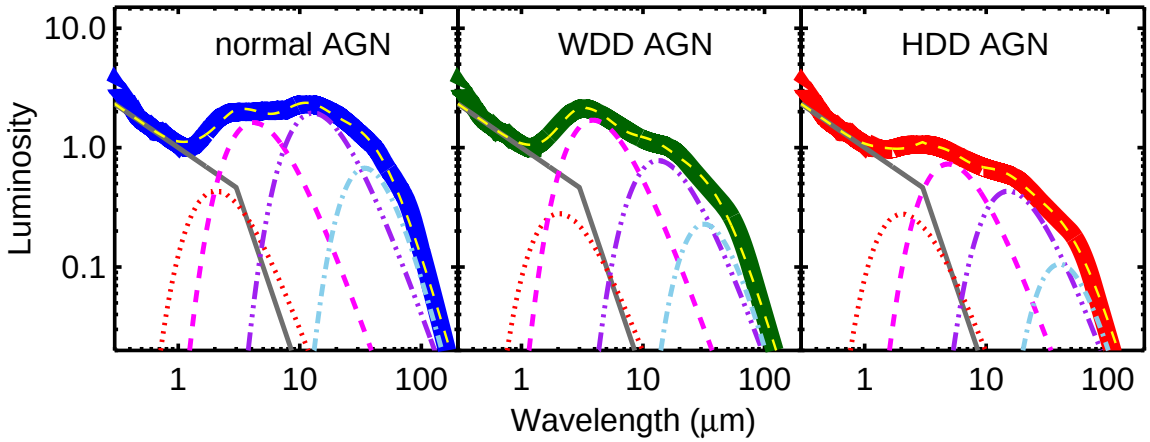


Figure 3.9 Dust component decomposition of the three empirical AGN templates (normal AGN: blue thick line; WDD AGN: green thick line; HDD AGN: red thick line). Each template is decomposed into a UV–optical broken power-law component (gray solid lines), a hottest dust component (red dotted lines), a hot dust component (magenta dotted line), a warm dust component (purple dashed–dotted–dotted–dotted lines), and a cold dust component (light blue dashed–dotted lines). The final model templates (yellow dashed lines) are shown against the corresponding empirical templates in each panel.

have

$$L_{\rm d} \sim 4\pi r_{\rm d}^2 \, f_{\rm c} \, \sigma T_{\rm d}^4 \quad , \tag{3.4.1}$$

where $\sigma$ is the Stefan–Boltzmann constant. The dust-covering factor of each component can be assumed to be $\lesssim 1$. Substituting typical dust temperatures and the IR-processed light fractions of various dust components, for an AGN with luminosity $L_{\rm AGN} = 10^{11}\ L_{\odot}$, the characteristic physical scales of the hot, warm, and cold dust emission are of the order of 0.01–0.1, 1, and 10 pc. All these values scale with the square-root of AGN Luminosity ($r_{\rm d} \propto L_{\rm AGN}^{0.5}$). The typical physical size of the hot dust emission estimated from the SED analysis is consistent with the estimation from dust sublimation (e.g., Laor & Draine, 1993), suggesting that the subliming dust and hot dust may be part of a continuous distribution. The relatively weak far-IR emission of quasars suggests a compact torus at sub-kiloparsec scales, which was originally suggested by Pier & Krolik (1992, 1993) from a theoretical analysis. Only for the most luminous quasars ($L_{\rm AGN} \gtrsim 10^{14}\ L_{\odot}$), the dust far-IR emission heated by the AGN could extend into kiloparsec scales, but maybe only marginally so if the relatively decreasing mid-IR and far-IR emission of the AGN is common in these systems (see Section 6.3 of Lyu et al. 2017).

The results from the simple SED analysis above show that the AGN-heated dusty structures have a wide temperature distribution with diverse physical scales. Although the AGN obscuration structures are often pictured as a doughnut-like ring (or a torus), we are actually unsure of the size and structure of their outer part. In the mid-IR, high-resolution observations support a compact geometry of the mid-IR emission region for local AGNs (see, e.g., Asmus et al. 2014 and references therein). However, as suggested by, e.g., Antonucci (2015), one should be cautious when referring to a size of the torus since it depends on the observed wavelength. The Atacama Large Millimeter Array (ALMA) has the resolution to possibly image the torus structures in nearby systems (García-Burillo et al., 2016; Imanishi et al., 2016). Nevertheless, whether these dusty molecular clouds are obscuring the nuclei and heated up in the submillimeter bands by absorbing AGN emission is not easy to tell. The similar intrinsic far-IR SEDs of AGNs discussed in this work provide some observational constraints on this topic.

In the far-IR, the dust emission is expected to be in the optically thin limit. As suggested by Ivezic & Elitzur (1997), the SED shape under this condition is not sensitive to the geometry but the temperature of the dust grains (see their Section 5). If similar grain properties can be assumed, the identical equilibrium temperatures of optically thin dust, which would result in similar intrinsic AGN far-IR SEDs, are naturally expected once the spectral shape of the incoming radiation is settled (e.g., Laor & Draine, 1993). In fact, the incoming light that is absorbed by these dust grains in quasars and Seyfert nuclei share comparable SEDs (dominated by the emission of, e.g., the thin-disk accretion; Yuan & Narayan 2014). Meanwhile, the geometric structures of the torus, whose outer part could be potentially mixed with the galactic ISM, are allowed to be somewhat diverse.

## 3.5 Summary

The discrepancies in determinations of the intrinsic far-IR SED of luminous AGNs have been evaluated in this paper. We found that the SF-corrected Elvis et al. (1994)-like AGN template is the most-likely correct selection for most type-1 quasars. This conclusion is supported by the following evidence.

1. *Energy balance*. We assumed the IR (1.3–1000 $\mu$m) emission of the AGN comes from the dust-reprocessed black hole accretion emission at 0.0012 (1 keV)–1.3 $\mu$m and the IR-processed light fraction, $f_{\rm R}$, should be consistent with the observed dust-covering factor $\lesssim 0.65$ for luminous quasars. Adopting the Elvis et al. (1994) template to represent the SED of the accretion disk emission with a proper scaling, we found only a small number of empirical IR templates yielded a matched $f_{\rm R}$ (e.g., 0.53-0.55 for Elvis et al. 1994 as well as its SF-corrected version, 0.56 for Symeonidis et al. 2016, 0.46 for Netzer et al. 2007). In comparison, the AGN templates proposed by Polletta et al. (2007), Hanish et al. (2013), and Kirkpatrick et al. (2015) have $f_{\rm R} \gtrsim 0.7$, suggesting that they are unlikely valid for luminous type-1 objects in general.

2. *SED decomposition of the PG quasars*. Based on the results of Lyu et al. (2017), we found that (1) the far-IR SEDs of PG quasars are fitted well by the SF-corrected Elvis et al. (1994) AGN template combined with a Rieke et al. (2009) SFG template; (2) the best-matched SFG templates preserve the luminosity-dependent SED shapes as seen in IR-luminous star-forming galaxies; (3) the predicted 11.3 $\mu$m aromatic strengths from the SFG templates match the measurements from the quasar mid-IR spectra; (4) the observed relation between the EWs of the 11.3 $\mu$m aromatic feature and the AGN contributions to the total quasar infrared luminosities is also matched by the mock SED simulation by the SF-corrected Elvis et al. (1994) and the Rieke et al. (2009) templates.

Compared with the observations, the mock composite SEDs with the Netzer et al. (2007) AGN template overestimate the EW of the 11.3 $\mu$m aromatic feature, suggesting the assumption that the far-IR emission of quasars is totally SF-dominated is not completely true. Meanwhile, the cooler IR emission nature of the Symeonidis et al. (2016) intrinsic AGN template is a result of the questionable adoption of the Dale & Helou (2002) galaxy templates to relate the strengths of the aromatic feature to the galaxy far-IR emission for (U)LIRGs. The correct conversion between the aromatic flux and the galaxy far-infrared luminosity, plus high-quality mid-IR spectra, are required to avoid an under-

estimation of host galaxy contribution to the far-IR emission of quasars.

There is no one single IR template that can be applied to all kinds of AGNs, even just for type-1 quasars. Nevertheless, normal quasars, dust-deficient quasars and Seyfert nuclei have similar intrinsic AGN far-IR SED shapes at $\lambda > 20$ $\mu$m, which may indicate a similar emitting character in the outer part of the AGN-heated dusty structures. In fact, the similar intrinsic AGN far-IR emission SEDs for these objects are naturally expected when the responsible dust grains are in the optically thin limit.

Based on the decomposition of the intrinsic AGN IR templates for the type-1 quasar population, we found that four dust components with similar temperatures ($T \sim$1800, 700–1000, 200–300, and 60–80 K) can explain the diversity of the intrinsic AGN IR emission properties by changing their relative contributions. The weak emission of the AGN-heated cold dust component suggests a compact torus at sub-kiloparsec scales in the far-IR for most quasars.

The intrinsic AGN templates for normal quasars (Xu et al., 2015b) and dust-deficient quasars (Lyu et al., 2017) are provided in the appendix.

This work was supported by NASA grants NNX13AD82G and 1255094. We thank Allison Kirkpatrick, Alexandra Pope, Anna Sajina, Richard Green, and Aigen Li for helpful discussions and/or comments on an early draft of this paper, and Yong Shi for sharing the measurements of the *Spitzer*/IRS spectra of the PG sample in Shi et al. (2014). We also appreciate the comments from the referee that have helped us to improve the clarity of our writing.

CHAPTER 4

# POLAR DUST, NUCLEAR OBSCURATION AND IR SED DIVERSITY IN TYPE-1 AGNS

Despite the hypothesized similar face-on viewing angles, the infrared emission of type-1 AGNs has diverse spectral energy distribution (SED) shapes that deviate substantially from the well-characterized quasar templates. Motivated by the commonly-seen UV-optical obscuration and the discovery of parsec-scale mid-IR polar dust emission in some nearby AGNs, we develop semi-empirical SED libraries for obscured type-1 AGNs built on the quasar intrinsic templates, assuming low-level extinction caused by an extended distribution of large dust grains. We demonstrate that this model can reproduce the nuclear UV-to-IR SED and the strong mid-IR polar dust emission of NGC 3783, the type-1 AGN with the most relevant and robust observational constraints. In addition, we compile 64 low-$z$ Seyfert-1 nuclei with negligible mid-IR star formation contamination and satisfactorily fit the individual IR SEDs as well as the composite UV to mid-IR composite SEDs. Given the success of these fits, we characterize the possible infrared SED of AGN polar dust emission and utilize a simple but effective strategy to infer its prevalence among type-1 AGNs. The SEDs of high-$z$ peculiar AGNs, including the extremely red quasars, mid-IR warm-excess AGNs, and hot dust-obscured galaxies, can be also reproduced by our model. These results indicate that the IR SEDs of most AGNs, regardless of redshift or luminosity, arise from similar circumnuclear torus properties but differ mainly due to the optical depths of extended obscuring dust components.[1]

## 4.1 Introduction

Accreting supermassive black holes (BHs) are surrounded by copious dust and generally emit strongly in the infrared (IR). Compared with star-forming or quiescent galaxies

[1] A version of this chapter originally appeared as a published paper in the Astrophysical Journal (Lyu & Rieke, 2018). All the works described here were carried out by me, with help from coauthor George Rieke.

whose emission is dominated by stars and H II regions, the active galactic nuclei (AGNs) have distinctive IR spectral energy distributions (SEDs), offering a unique window to look for obscured AGNs (e.g., Lacy et al., 2004, 2007; Stern et al., 2005, 2012; Donley et al., 2012), a critical means to explore the properties of dusty structures around their central engines (e.g., Fritz et al., 2006; Nenkova et al., 2008a,b; Stalevski et al., 2012, 2016), and a powerful tool to constrain their host galaxy properties by SED decompositions (e.g., Bongiorno et al., 2007, 2012; Xu et al., 2015b; Lyu et al., 2016; Collinson et al., 2017). More importantly, the dusty structures around the central engine, commonly termed as "torus", lay the foundation of AGN unification and have physical scales that bridge the BH accretion disk and the host galaxy (e.g., Antonucci, 1993; Urry & Padovani, 1995). The IR SEDs have become a crucial probe for the AGN phenomenon and the BH-galaxy co-evolution (e.g., Heckman & Best, 2014; Caputi, 2014; Netzer, 2015). Nevertheless, most studies are focused on individual objects or some particular narrowly defined AGN population. In this work, we propose and test a model to reconcile the various IR SEDs of type-1 AGNs over a broad range of luminosity and redshift.

The intrinsic SEDs of the most luminous AGNs, or quasars (bolometric luminosity $L_{\rm AGN,bol} \gtrsim 10^{11}\ L_{\odot}$), are observationally well-characterized (e.g., Elvis et al., 1994; Richards et al., 2006; Shang et al., 2011; Krawczyk et al., 2013; Scott & Stewart, 2014; Lyu et al., 2017; Lyu & Rieke, 2017; Lani et al., 2017). The average SEDs of unobscured quasars, whether the parent sample is (mainly) optically-selected (e.g., Elvis et al., 1994; Krawczyk et al., 2013), or combined with mid-IR selection (e.g., Richards et al., 2006), or X-ray-selected (e.g., Polletta et al., 2007; Elvis et al., 2012), have been found to be strikingly similar. The classical Elvis et al. (1994)-like template has proven to be a realistic representation of the infrared emission by hot dust in most quasars (Lyu et al., 2017). The exceptions, including hot-dust-free or hot-dust-poor objects (e.g., Jiang et al., 2010; Hao et al., 2010, 2011), are part of the quasar intrinsic IR SED diversity seen at all redshifts. For unobscured quasars at $z \sim$0–6, the AGN IR SEDs can be generally grouped into three basic types; besides the normal AGNs described by the Elvis-like template, there are also the warm-dust-deficient (WDD) AGNs and the hot-dust-deficient (HDD) AGNs (Lyu et al., 2017). Despite the variations in the near-IR or mid-IR, the shapes of

quasar far-IR intrinsic SEDs have an identical pattern in a statistical sense (Lyu & Rieke, 2017), which drops quickly at $\lambda \gtrsim 20$ $\mu$m (Xu et al. 2015b; Lyu & Rieke 2017; see also Lani et al. 2017).

By comparison, the behavior of the intrinsic emission from relatively faint AGNs ($L_{\rm AGN,bol} \sim 10^8$–$10^{11}$ $L_\odot$) is elusive because of the significant galaxy contamination as well as the possible line-of-sight (LOS) extinction. A frequent hypothesis is that the intrinsic SEDs of these Seyfert nuclei are identical to those of quasars, thus one single template for AGNs with a very broad luminosity range is assumed (e.g., Hopkins et al. 2007; Assef et al. 2010; Donley et al. 2012). However, notable differences seem to exist, particularly in the IR. The AGN emission of many Seyfert-1 galaxies is peaked at $\lambda \gtrsim 10$ $\mu$m and the near- to mid-IR broad-band SEDs are commonly described by a single power-law (e.g., Spinoglio et al., 1995; Alonso-Herrero et al., 2003; Prieto et al., 2010). On the other hand, normal quasars exhibit a prominent SED bump peaked in the UV and emit relatively less strongly in the IR with an obvious SED jump due to emission by hot dust starting at 1.3 $\mu$m and an almost flat ($\nu F_\nu \propto \nu^0$) mid-IR SED at $\sim$3–20 $\mu$m (e.g., Sanders et al., 1989; Elvis et al., 1994). As suggested by e.g., Prieto et al. (2010), such different behavior might be caused by obscuration. However, frequently only the reddening of the UV-optical SED is considered, while the accompanying effect on the IR emission is ignored.

In fact, an equatorial optically-thick torus is only a first-order approximation of the circumnuclear dust environment around AGN. Evidence for polar dust at $\sim 10^2$ pc scale has been suggested since the early 1990s (e.g., Braatz et al., 1993; Cameron et al., 1993; Bock et al., 2000) and the AGN obscuration is known to happen at a range of different scales (e.g., see review by Bianchi et al., 2012). In theory, the AGN torus could form during the gas accretion of the central black hole and have material exchanges with the ambient environment (e.g., Hopkins et al., 2012). Although it cannot survive very close to the central engine, dust is expected to be found in many other AGN components, e.g., narrow-line regions (e.g., Groves et al., 2006; Mor et al., 2009) and/or AGN-driven outflows (e.g., Fabian, 1999; Murray et al., 2005). As argued by many authors, the AGN infrared SED might be easily reshaped by these extended dusty structures (e.g., Sturm et al., 2005; Groves et al., 2006; Hönig et al., 2012, 2013; Hönig & Kishimoto, 2017).

Mid-IR interferometric observations have become available for some nearby Seyfert nuclei, allowing a direct investigation of the geometry of their nuclear IR structures at parsec scales. Interestingly, these studies show that the mid-IR warm dust emission in some systems is largely distributed along the AGN polar direction, instead of from an equatorial torus (e.g., Raban et al., 2009; Hönig et al., 2012, 2013; Tristram et al., 2014; López-Gonzaga et al., 2016; Leftley et al., 2018). These observations have motivated the developments of increasingly sophisticated dust models to explain the few best-studied cases (Hönig & Kishimoto, 2017; Stalevski et al., 2017). In the case of NGC 3783, it is proposed that both the torus and the polar dust are composed of optically thick clouds and that the polar dust is composed of large carbon grains (Hönig & Kishimoto, 2017). In comparison, the Circinus Galaxy is modeled with a parsec-scale optically-thick dusty disk and an IR optically-thin cone following the structure of the narrow-line region (NLR) out to a distance of $\sim 40$ pc (Stalevski et al., 2017). The success of these different approaches indicates that these complex models could be highly degenerate for most AGNs due to the lack of detailed observational constraints. We will address whether it is possible to develop a much simpler model that can be applied uniformly and is still of sufficient fidelity to provide useful insights.

With the success of our intrinsic templates to reproduce the AGN IR emission of bright quasars at different redshifts (Lyu et al., 2017), it is of considerable interest to explore whether they also apply to relatively low-luminosity AGNs. The possible existence of low-optical-depth dust in the vicinity of the AGN nucleus, as outlined above, motivates us to develop a new library of reddened AGN templates. We take the Lyu et al. (2017) empirical quasar templates as givens for polar-dust-free AGNs and investigate the extent to which the addition of a low-optical-depth but extended dust component with reasonable assumptions for the dust grain properties and their large-scale distribution can yield IR SED shapes consistent with those observed. In Section 5.3.2, we introduce this model and validate it by fitting the detailed observations of NGC 3783, the archetypical example of a type-1 AGN with its mid-IR emission dominated by polar dust.

Although the extended dust distribution may have a range of morphologies, any mid-infrared emission by low-optical-depth dust should be roughly isotropic and hence de-

tectable from any view angle. We therefore focus on whether the model trained for NGC 3783 can be generally applied to match the infrared SEDs of those AGNs where standard quasar templates fail, assuming the choice of intrinsic AGN template and the optical depth of the obscuration as the only free parameters for the SED shape. This analysis is carried out on 64 low-$z$ Seyfert nuclei with negligible mid-IR star formation contamination in Section 4.3. In addition, if the polar dust emission is a common phenomenon for all populations of moderate-luminosity AGNs, a consequence is that Seyfert-1 nuclei should be moderately obscured on a statistical basis. We build composite SEDs of Seyfert-1 SEDs and confirm this prediction.

We find that the deviations from the quasar-like SED templates can indeed be explained to first order by the combination of extinction and infrared emission by polar dust. In Section 4.4, we characterize the SED features of the polar dust emission and discuss the prevalence of polar dust in a sample of AGNs much larger than those that can currently be explored in any detail through mid-infrared interferometry. We also demonstrate that one single semi-empirical template can describe the influence on the AGN SED by the polar dust emission for most objects. A consistency check of the results from our SED analysis and those from morphology-based identification for AGN polar dust emission is also carried out.

Various AGN populations with peculiar SED features that cannot be easily matched by the classical AGN templates have been reported at high-$z$. Some notable examples are extremely red quasars (Ross et al., 2015; Hamann et al., 2017), AGNs with mid-IR warm-excess emission (e.g., Xu et al., 2015b) and the hot dust-obscured galaxies (e.g., Eisenhardt et al., 2012; Wu et al., 2012). The success of our model at low-$z$ encourages us to explore if these peculiar SED features can be explained in a similar way. These studies are presented in Section 4.5.

Section 4.6 provides discussions on the implications of these results for interpreting the AGN IR emission, the relation between X-ray obscuration and polar dust extinction, and the AGN unification scheme. We propose a tentative picture of the different circumnuclear dusty environments among AGNs that leads to their diverse IR properties. Section 6.6 is a final summary.

We adopt cosmology $\Omega_m = 0.27$, $\Omega_\Lambda = 0.73$ and $H_0 = 71 \mathrm{km\ s^{-1} Mpc^{-1}}$(Bennett et al., 2003) throughout this paper. We use the term *type-1* to describe AGNs showing broad emission lines without distinguishing if the LOS is dust-obscured or not. Since the word *obscured* is frequently reserved to describe type-2 (or narrow-line) AGNs, we adopt the name *reddened type-1 AGNs* to denote the broad-line AGNs with some extinction along the LOS (aka the polar direction), even if the real reddening might be insignificant because of a very flat extinction curve (e.g., Gaskell et al., 2004). Lastly, the word *unobscured* means no extinction, neither from the torus nor from any extended dust distribution, along the LOS to the central engine.

## 4.2 A Semi-empirical SED Model for Reddened Type-1 AGNs

We introduce a relatively simple framework to produce a library of reddened type-1 AGN templates, which will be used to fit the SEDs of Seyfert-1 nuclei in Section 4.3. This model is based on two major assumptions:

1. Seyfert nuclei have a circumnuclear optically-thick torus whose SED variations from a face-on viewpoint can be described by the intrinsic AGN templates of unobscured quasars;

2. Besides the torus, there could exist an extended dust component with some power-law density profile that is dominated by large dust grains heated by the AGN.

We describe the motivations as well as the details of these assumptions in Section 4.2.1–4.2.2. The model and its behavior are presented in Section 4.2.3. In Section 4.2.4, we test our approach by fitting the observations of NGC 3783.

### 4.2.1 Accretion Disk and Dusty Torus

The continuum SED of an AGN is contributed mostly by the UV-optical emission from the accretion disk around the black hole and the near-IR to mid-IR emission emerges from the surrounding dusty structures. To reduce the uncertainties, we adopt well-tested extinction-free empirical templates to represent this AGN intrinsic emission.

The UV to mid-IR SEDs of most luminous type-1 quasars are well described by the Elvis et al. (1994)-like AGN template, regardless of the redshift (e.g., see discussion in Lyu et al., 2017). An AGN-heated dusty structure in type-1 quasars is revealed by the broad IR emission bump at $\lambda \sim 1.3$–$40\ \mu$m. In addition, broad emission lines have been detected in the optical polarized spectra of type-2 quasars (Zakamska et al., 2005). Under the precepts of AGN unification (Antonucci, 1993; Urry & Padovani, 1995), these observations support the existence of some equatorial optically-thick dusty structures, which cause the nuclear photons to preferentially escape along the polar direction.

As demonstrated by Lyu et al. (2017), the diversity of intrinsic IR emission among type-1 quasars at $z \sim$0–6 can be characterized by three distinct templates derived for (1) normal AGNs, (2) warm-dust-deficient (WDD) AGNs, and (3) hot-dust-deficient (HDD) AGNs. These templates are unlikely to be affected significantly by dust extinction since their derivations are based on the study of optically-blue quasars that are not obscured. In other words, there should be no significant dust distribution along the polar direction. We suggest these AGN templates describe the emission from the unobscured accretion disk plus a face-on view of the dusty torus[2].

At $\lambda < 0.1\ \mu$m, current observations do not give good constraints. Following Stalevski et al. (2016), we assume a broken power-law, where

$$\nu F_\nu \propto \begin{cases} \lambda^{0} & 0.01\ \mu\text{m} < \lambda < 0.1\ \mu\text{m} \\ \lambda^{1.2} & 0.001\ \mu\text{m} < \lambda < 0.01\ \mu\text{m} \end{cases} \tag{4.2.1}$$

Nevertheless, our study will not be influenced by the assumed X-ray to UV SED shape. In fact, considering the likely dominance of large dust grains along the face-on direction (see Section 4.2.2), the extinction at these wavelengths is small and will not contribute to the IR SEDs.

### 4.2.2 Extended Polar Dust Component

Besides the torus component characterized by the intrinsic AGN templates discussed above, we introduce another dust component to provide relatively low-level obscuration for the

[2]We use the word *torus* to describe the polar-dust-free obscuration structures as in optically-blue quasars and do not make assumptions on the geometry or boundaries.

nucleus as well as the additional IR emission from the absorbed energy.

We suggest that the dust size distribution in this component is dominated by very large particles, which will be characterized by grain size cutoffs, $a_{\rm max}$ and $a_{\rm min}$. In real situations, different grain species sublimate at different temperatures and could have a broad range of dust sublimation zones. However, we find that the calculated SEDs do not change significantly between $T_{\rm sub} = 2000$ and $T_{\rm sub} = 1500$, indicating that the introduction of separate values appropriate for carbon and silicates would not change our results. For simplicity, we adopt the same dust sublimation temperature $T_{\rm sub}$ for all the grain compositions.

For the large scale structure, we assume a density profile parameterized as a power-law in radius with slope $\alpha$:

$$\rho(r) \propto r^{-\alpha}, \quad r_{\rm in} < r < r_{\rm out} \ , \tag{4.2.2}$$

where the inner radius $r_{\rm in}$ is equal to the dust sublimation radius $R_{\rm sub}$ set by $T_{\rm sub}$ as well as the light source luminosity, and the outer radius $r_{\rm out}$ is a free-parameter. We introduce another parameter, the outer-to-inner radius ratio $Y = r_{\rm out}/r_{\rm in}$, to describe $r_{\rm out}$. Given the nature of this model, the geometry will not influence the dust emission SED so that there is no need to introduce more free parameters.

In the following, we outline the motivations behind these configurations.

*Grain Properties* There are strong reasons to suggest the classical dust properties are altered by the harsh environment of the direct exposure to an AGN. As suggested by Aitken & Roche (1985), small grains ($a \sim 10^{-3}$ $\mu$m) can be easily destroyed out to several hundred parsecs in a typical Seyfert-1 nucleus, on a timescale of less than a few years. Physically, the majority of dust destruction mechanisms around AGN are relatively less significant for large dust grains (Laor & Draine, 1993). For example, large grains are expected to exist close to the torus inner part since they have smaller $R_{\rm sub}$ than small grains. The torus itself can be dynamically unstable and material exchanges with the surrounding environments through various mechanisms are expected from simulations (e.g., Hopkins et al., 2012). Baskin & Laor (2018) have analyzed the effects of sublimation on both carbon and silicate grains near an AGN. They find that only large ($a > 0.1$ $\mu$m) carbon grains can survive at the outer edge of the BLR out to about 20 times this radius. They

also conclude that the silicate grain size distribution will be skewed toward large sizes to significantly greater distances.

Conditions for grain growth may exist in the circumnuclear tori, where the densities are high and grains are shielded from the X-ray and UV output of the central engine (e.g., Maiolino et al., 2001a). As suggested by e.g., Hönig et al. (2012, 2013), some dust in the torus can be uplifted into the polar direction by AGN winds. It may also be possible for these large dust grains to form in situ. Elvis et al. (2002) suggested that dust can form in AGN-driven winds where conditions are similar to those in the winds of late-type stars. By these mechanisms, grains in the 0.1–1 $\mu$m range are plausible (Höfner, 2008). However, determining observational constraints on the grain sizes around AGN can be quite difficult. This can be seen from the diverse AGN UV-optical extinction curves reported that range from steeply rising SMC-like laws (e.g, Hall et al., 2002; Richards et al., 2003) to flat or gray laws (e.g., Gaskell et al., 2004; Czerny et al., 2004; Gaskell & Benker, 2007). As argued by e.g., Baskin & Laor (2018), it is possible the grain properties depend on the observing angle.

Nonetheless, despite various uncertainties, there are observational indications of relatively large dust grains around AGNs, including (1) the lower ratios $A_V/N_H$ and $E(B-V)/N_H$ in intermediate-type Seyfert galaxies (Maiolino et al. 2001b,a; but see Weingartner & Murray 2002); (2) the lower ratios between $A_V$ and the mid- IR silicate absorption strength, $\Delta\tau_{9.7}$, in type-2 AGNs (Lyu et al., 2014; Shao et al., 2017); (3) successful fittings of the silicate emission profile in quasars and Seyfert galaxies with micron-sized grain models (Xie et al., 2017); (4) the smaller observed torus inner radius from near-IR interferometry of nearby Seyfert nuclei compared with the expectations for classical dust grains (e.g.,Kishimoto et al. 2007, 2009a; Hönig et al. 2013; Burtscher et al. 2013; but see Kawaguchi & Mori 2010).

As shown in Appendix C, for classical ISM properties at low optical thickness, the mid-IR silicate emission feature at $\lambda \sim 10$ $\mu$m would be very prominent with a sharp peak (see also, e.g., Fritz et al. 2006; Nenkova et al. 2008a) that is not commonly seen among Seyfert nuclei (Hao et al., 2007). Instead, the lack of such detections could be an expected consequence of large grains. For example, dust grains with size $a \gtrsim 0.3$ $\mu$m would reduce

the strength of silicate features effectively (Laor & Draine, 1993).

Due to the difficulties for setting direct constraints on the dust properties around the AGN, we minimize departures from standard ISM grain models and assume only the grain sizes, as characterized by the grain size cuts, $a_{\rm max}$ and $a_{\rm min}$, are altered in the vicinity of an AGN.

*Large-scale Geometry* Currently we do not have strong observational constrains about the geometry of the dust responsible for the low-level obscuration in type-1 AGNs. Nevertheless, AGN outflows (e.g., Crenshaw et al., 2003; Piconcelli et al., 2005) could be a natural mechanism to distribute the dust around the nucleus. Physically, it has been found that the radiation pressure on resonant absorption lines alone can not explain the outflow rates. The radiation feedback on dust within the clouds could be an effective mechanism (e.g., Roth et al., 2012). Based on a study of $\sim$3000 type-1 AGNs, Zhang et al. (2013) found that the relative strength of the mid-IR to the optical flux of these objects is correlated with the strength of outflows.

Several teams have tried to explore the origin of the polar dust, showing the outflow scenario is a promising solution. For example, Hönig et al. (2012, 2013) proposed that the dusty outflows could be launched from the surface of the inner torus and the Hönig & Kishimoto (2017) model motivated by this picture successfully explained the behavior of NGC 3783, a Seyfert-1 nucleus with a firm detection of polar dust emission. From an analysis of high-spatial mid-IR images of 149 nearby Seyfert galaxies, Asmus et al. (2016) found that elongated polar dust emission is co-spatial with the direction of AGN outflows for 18 objects.

Little is known about the exact density profile of the gas outflows. As a result, analytic analyses of self-similar solutions are typically pursued. We introduce a power-law density profile, $\rho(r) \propto r^{-\alpha}$, to approximate the real situations.

Physically, we do not expect the outflow solution retains the memory of initial conditions on large scales. As suggested by Faucher-Giguère & Quataert (2012), to reach a finite free expansion radius, the gas density profile should have profiles with $\alpha \lesssim 2$. Observationally, various values of $\alpha$ have been derived for materials in the outflows. For

example, Behar (2009) derived $\alpha \sim$1.0–1.3 for five nearby Seyfert nuclei from analyzing the X-ray absorption spectra. Feruglio et al. (2015) suggested a $r^{-2}$ profile for the ultra-luminous IR galaxy Mrk 231. Revalski et al. (2018) derived the electron density of the narrow-line regions in the Seyfert-2 nucleus Mrk 573, finding $n_e \propto r^{-0.4}$–$r^{-0.6}$. Additionally, a constant density absorber ($\alpha$=0) is quite unlikely the real case. Assuming that the dust and gas are well mixed with a constant dust-to-gas ratio, we suggest the dust density profile should satisfy $0 < \alpha \lesssim 2$.

Based on mid-IR interferometry observations, the AGN polar dust emission is found to be elongated (e.g., Hönig et al., 2012, 2013; Tristram et al., 2014; López-Gonzaga et al., 2016) and possibly distributed along the edges of the ionization cone (Stalevski et al., 2017). In our model, however, the likely uneven distribution of the polar dust component will not influence its IR emission SED. This is a direct consequence of optically-thin dust emission in the IR, especially for large grains (e.g., Laor & Draine, 1993; Ivezic & Elitzur, 1997).

The modest levels of face-on extinction in type-1 AGNs correspond to a small value of $\tau_V$. Since the dust opacity is a strong function of wavelength that decreases rapidly towards the infrared, the extinction for such IR-reprocessed dust emission is likely to be close to zero. In other words, the IR emission of any dusty structures with a low $\tau_V$ is highly transparent: the emission from a single geometry element at some given location, where the included dust grains can be considered in local thermodynamic equilibrium (LTE), would share the same SED from different viewing angles and this SED would transit through other surrounding dusty structures without any notable changes. Consequently, the total integrated IR SED can be described as a summation of the dust emission from individual LTE geometry elements at all possible locations.

At the same distance $r$, the temperature of each LTE element would be the same as is the SED, $B_\lambda(r)$. The total emission from all the dust at the same distance is linearly scaled by the total numbers of LTE elements at the corresponding radius, $\rho(r)$, and has little to do with their possible uneven distribution. The total integrated SED, $F_\lambda$, can be

approximated by adding the contributions of all the elements at various radii, or

$$F_\lambda \simeq \int_{r_{\rm in}}^{r_{\rm out}} \rho(r) B_\lambda(r) dr \ . \tag{4.2.3}$$

Thus if the average radial profile, $\rho(r)$, is similar, the dust distribution at small scales, whether it is smooth, clumpy or filamentary, will not influence the SED.

As long as the integrated optical depth, $\tau_{\rm V}$, is low, the effects of asymmetries in the dust large-scale structure and/or illumination along the radial directions would proportionally change $\rho(r)$, only resulting in a scaling down of the output polar dust emission. Note that $\tau_{\rm V}$ is linearly scaled with $\rho(r)$ by

$$\tau_{\rm V} = \int_{r_{\rm in}}^{r_{\rm out}} \rho(r) C_{\rm ext,V} dr = C_{\rm ext,V} \int_{r_{\rm in}}^{r_{\rm out}} \rho(r) dr \ , \tag{4.2.4}$$

where $C_{\rm ext,V}$ is the optical V-band extinction of all the grains within a single LTE element. Thus these geometry effects can be modeled by simply changing $\tau_{\rm V}$. Figure 4.1 provides a simple illustration. In Appendix C, we provide some simple demonstrations of the lack of influence of the dust geometry on the derived SED with three-dimensional dust radiative transfer simulations. Although the distribution of polar dust realistically could be highly complicated, for the purpose of determining the resulting SED it is equivalent to assume spherical symmetry.

In summary, when the $\tau_{\rm V}$ of the extended dust component is not very high, its IR SED shape would be only dependent on the radial density profile. Since the nuclear dust morphology cannot be constrained for most AGNs, we will not introduce detailed geometry to match the very few observations.

### 4.2.3 Reddened Type-1 SEDs from the Model

We use the latest version of the radiative transfer code DUSTY (Ivezic et al., 2017)[3] to obscure the three AGN templates presented in Lyu et al. (2017). This code assumes a spherical symmetry and solves the one-dimensional radiation transfer equations as described in Ivezic & Elitzur (1997). Although a realistic model would place the emitting clouds preferentially in the polar direction, we have just shown that the output spectrum

[3] Accessible at https://github.com/ivezic/dusty.

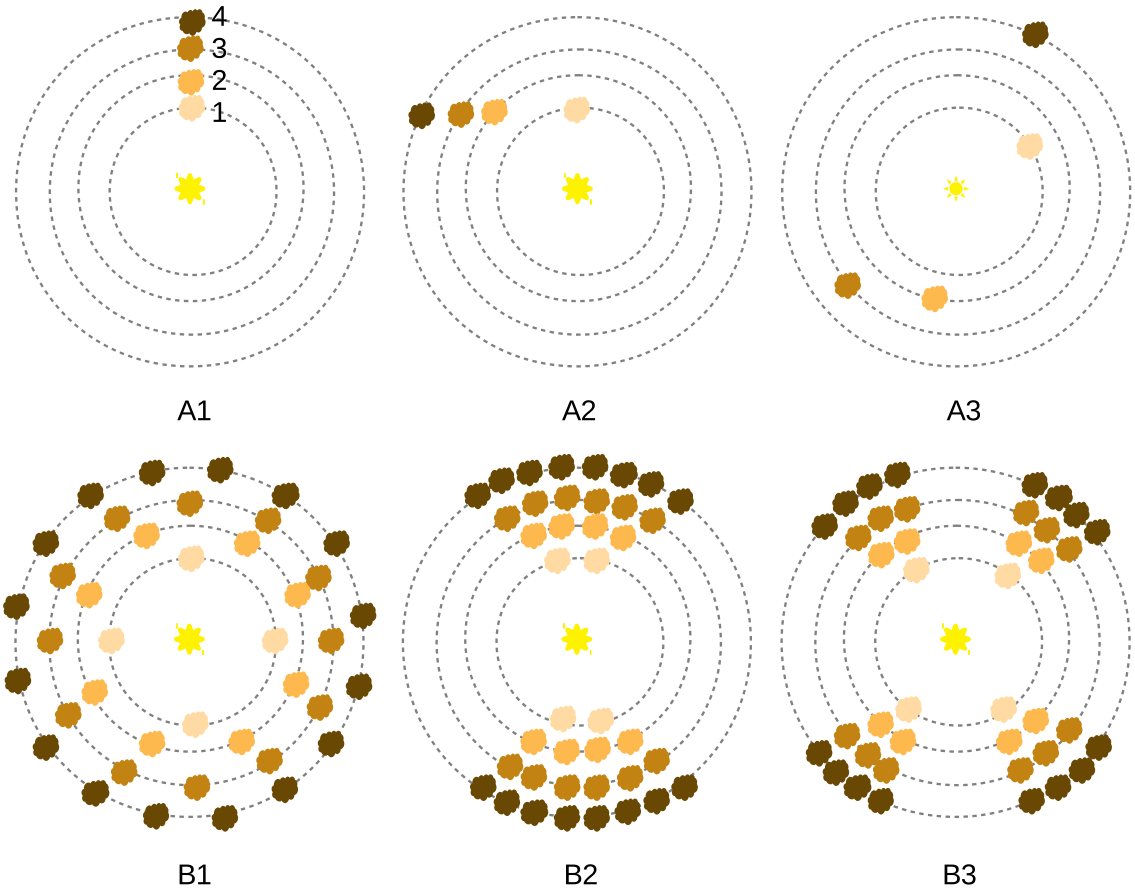


Figure 4.1 Cartoon illustrations of the optically-thin IR emission for different geometry configurations. Imagine that the dust structures are composed of similar small clouds at four different radii $r_1$, $r_2$, $r_3$, $r_4$ to the light source (the central yellow star in each panel). The total emission of all the clouds at a given $r_i$ would simply be $N_i F_i$, where $N_I$ is the number of clouds and $F_i = F_i(\nu)$ is the emission SED of one single cloud. Since the dust emission is assumed to be optically thin, the integrated emission of all the dust clouds with geometries described in panels A1, A2, A3 will be the same, $F_{\rm tot,A} = F_1 + F_2 + F_3 + F_4$. Similarly, since the number of clouds, $N_i$, in each radius, $r_i$, is the same, the integrated SEDs in panels B1, B2, B3 are also identical for optically-thin emission, and $F_{\rm tot,B} = N_1F_1 + N_2F_2 + N_3F_3 + N_4F_4 = 2F_1 + 4F_2 + 6F_3 + 8F_4$, which is not dependent on how the clouds are distributed.

for the optically thin case would be identical. For a centrally-heated spherical density distribution, the program needs the SED of the radiation source, a density profile of the dust distribution and information regarding the boundaries, the dust properties (chemical composition, grain size distribution and the sublimation temperature), and a range of required optical depths at some specific wavelength.

Table 4.1. DUSTY model setup

| Parameter | Label | Value |
|---|---|---|
| $r_{\rm in}$ temperature | $T_{\rm in}$ | 2000 K, 1500* K, 1000 K |
| density profile | $\alpha$ | 0, 0.5*, 1, 1.5, 2 |
| outer-to-inner radius | $Y$ | 50, 500*, 5000 |
| silicate:graphite mixture | | 0:1, 0.53:0.47*, 1:0 |
| maximum grain size | $a_{\rm max}$ | 0.25, 2.5, 10*, 100 |
| minimum grain size | $a_{\rm min}$ | 0.005, 0.01, 0.05*, 0.1 |
| input radiation SED | | norm, WDD*, HDD |
| optical depth | $\tau_{\rm V}$ | 0–10 with a step of 0.25 |

Note. — We use * to indicate the reference parameters that adopted to demonstrate the influence of the output SEDs in Figure 4.2.

We calculate three sets of reddened templates separately for normal, HDD, and WDD AGNs. The model parameters are summarized in Table 4.1. We adopted optical properties for graphite and silicate grains from Draine & Lee (1984) with the standard Mathis-Rumpl-Nordsieck (MRN) power-law grain size distribution distribution $dn/da \propto a^{-3.5}$ (Mathis et al., 1977) but left the boundaries, $a_{\rm max}$ and $a_{\rm min}$, to be varied.

Figure 4.2 presents the reddened WDD AGN SEDs as a function of the optical extinction level $\tau_{\rm V}$ for different values of model parameters. It is interesting that for large dust grains, the dust-reprocessed SEDs are not sensitive to the mixtures of silicates and graphites. For a given $\tau_{\rm V}$, the amount of UV-optical reddening is only sensitive to the smallest grain size $a_{\rm min}$ and has little to do with the dust geometry configurations. The strength of the mid-IR silicate emission feature is sensitive to the maximum grain size $a_{\rm max}$ and the geometry parameters $Y$ and $\alpha$. The relative strength of the hot dust emission is mainly determined by the compactness of the dust distribution ($\alpha$, $Y$). Finally, the shape of the broad-band IR continuum is mainly determined by the assumed geometry (as well as the input intrinsic SED).

Since the dust temperature at the inner radius ($T_{\rm in} = T_{\rm sub}$) and relative fraction between silicate and graphite grains have limited effects on the reddened SEDs, we decide to adopt $T_{\rm in} = 1500$ K, and a normal 0.53:0.47 mixture of silicate and graphite grains.

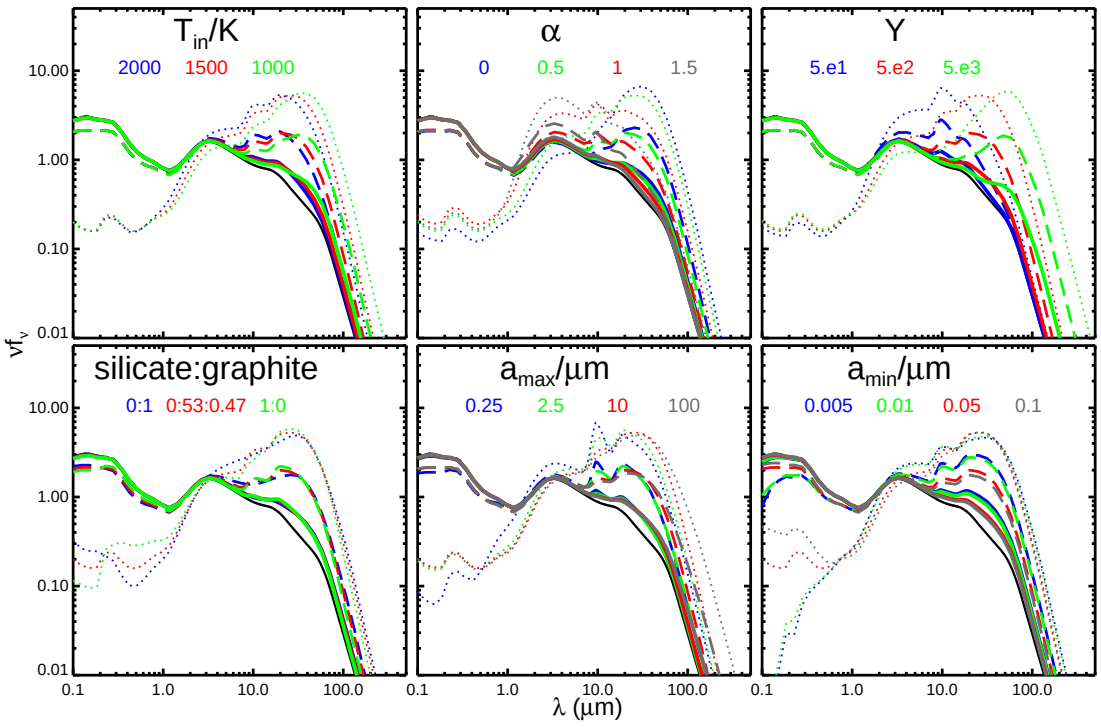


Figure 4.2 The influence of model parameters on the output SEDs. For each model setup, we computed the output SEDs with different levels of optical extinction $\tau_V$=0.1 (solid lines), 0.63 (dashed lines) and 3.98 (dotted lines).

### 4.2.4 Model Validation with Observations of NGC 3783

Our proposed simple model differs substantially from the approach of Hönig & Kishimoto (2017), who fitted the SED and interferometric data for NGC 3783 with a specific system of very optically thick ($\tau_V = 50$) small clouds. We show here that our model can fit the SED of this object equally well.

We adopted the X-ray to mid-IR subarcsecond high-spatial-resolution (HSR) nuclear photometry SED of NGC 3783 presented in Prieto et al. (2010). To improve the mid-IR continuum constraints, we collected its 2.5–5 $\mu$m *AKARI* spectrum (Kim et al., 2015) and 5.5–38 $\mu$m *Spitzer*/IRS spectrum (Lebouteiller et al., 2011a). Since the spectral flux is consistent with the HSR photometry at corresponding wavelengths (the *Spitzer*/IRS flux is also identical to the spectrum obtained through a $0.75'' \times 0.53''$ aperture; see Figure 3 in Hönig et al. 2013) and there is no obvious star-formation feature, we believe these data

apply to the AGN emission. To gauge the far-IR emission strength from the nucleus, we used the 1 kpc aperture *Herschel* 70 $\mu$m and 100 $\mu$m photometry of NGC 3783 from García-González et al. (2016). For the foreground extinction by the Milky Way (MW), we obtained $E(B-V) = 0.10$ from the SFD dust map (Schlegel et al., 1998; Schlafly & Finkbeiner, 2011) and used the Fitzpatrick (1999) extinction law to correct the UV-optical data.

For NGC 3783, the torus component is believed to dominate the near-IR emission but not the mid-IR (Hönig et al., 2013). After comparing the observed SED of this object with the Lyu et al. (2017) intrinsic AGN templates, we suggest its torus emission should be WDD-like. The 0.1–30 $\mu$m SED of NGC 3783 is then fitted by the reddened WDD AGN template with parameter ranges for the polar dust component in Table 4.1. We use Markov Chain Monte Carlo (MCMC) algorithms described by Johnson et al. (2013) to sample the large parameter space and find the most likely parameter combination. The values of the best-fit parameters and their 1-$\sigma$ uncertainties (68% confidence levels) are summarized in Table 4.2. The large fitted parameter errors suggest a strong degeneracy. After considering the possible contaminations by optical emission lines and the fact that the far-IR photometry provides an upper limit to the AGN-heated dust emission, we finally decide to adopt $\rho(r) \propto r^{-0.5}$, $Y = 500$ and $T_{\rm in}$=1500 K, and grain size cutoffs at $a_{\rm min} = 0.04$ $\mu$m and $a_{\rm max} = 10$ $\mu$m. Most of these values are picked near the mid-point of the fitted ranges for illustration.

As shown in the left panel of Figure 4.3, the UV-to-far-IR nuclear SED of NGC 3783 is reasonably matched by the WDD AGN template obscured by the suggested polar dust component with an optical depth $\tau_{\rm V} = 1.4$. In the right panel, we show the relative contributions of the attenuated and scattered WDD emission, as well as the polar dust emission in the best model. Besides the near-IR, the torus emission SED of the WDD AGN is not modified by the polar dust obscuration, so we can linearly separate the torus emission and the polar dust emission. At $\sim$10 $\mu$m, the optically-thin component would contribute about 75% of the total emission, which is in good agreement with the polar dust emission strength constrained by interferometry (Hönig et al., 2013; López-Gonzaga et al., 2016). Since the highly optically-thick torus can block the accretion disk emission along the equatorial direction and the dust along the polar direction is likely to be preferentially heated,

Table 4.2. Suggested model parameters for NGC 3783

| Parameter | Label | Adopted Value | MCMC output |
|---|---|---|---|
| $r_{\rm in}$ temperature | $T_{\rm in}$ | **1500** K | |
| density profile | $\alpha$ | 0.50 | $0.47^{+0.50}_{-0.44}$ |
| outer-to-inner radius | $Y$ | 500 | $475^{+513}_{-353}$ |
| silicate:graphite mixture | | **0.53:0.47** | |
| maximum grain size | $a_{\rm max}$ | 10 | $20^{+79}_{-18}$ |
| minimum grain size | $a_{\rm min}$ | 0.04 | $0.05^{+0.05}_{-0.04}$ |
| input radiation SED | | **WDD** | |
| optical depth | $\tau_{\rm V}$ | 1.4 | $1.44^{+0.55}_{-0.60}$ |

Note. — We use boldfaces to indicate assumed parameter values that do not go to MCMC parameter space sampling.

some elongated emission from the regions responsible for the low-level obscuration could be observable if the system has an appropriate viewing angle.

Although our goal does not include reproducing any detailed dust morphology, this model should yield similar sizes of the dusty structures to the observations. From fitting the mid-IR interferometry data of NGC 3783, Hönig et al. (2013) reported the nuclear dust is distributed over 20–70 $r_{\rm in}$, where $r_{\rm in} \sim 0.06$ pc is derived from near-IR reverberations. The model geometry $r_{\rm out}/r_{\rm in} \sim 500$ suggested from our SED fitting is much larger than this observation. However, at a given wavelength, we only observe dust with a narrow range of dust temperatures; the outer part of the extended dust component would be too cold to observe in the mid-IR. Based on the radial profile of dust temperature in our model, the observed geometry seen at 8–13 $\mu$m would have a size of 20–40 $r_{\rm in}$, which in fact qualitatively agrees with the Hönig et al. (2013) observations (see more discussion in Section 4.4.2).

### 4.2.5 The Degeneracy of Models Constrained Only by the AGN SED

The degeneracies of SED fitting - as shown here, equally good results from the Hönig & Kishimoto (2017) optically-thick clumpy dust model and our simple low-optical-depth obscuration model based on empirical AGN templates - indicate that the same observations can be ex-

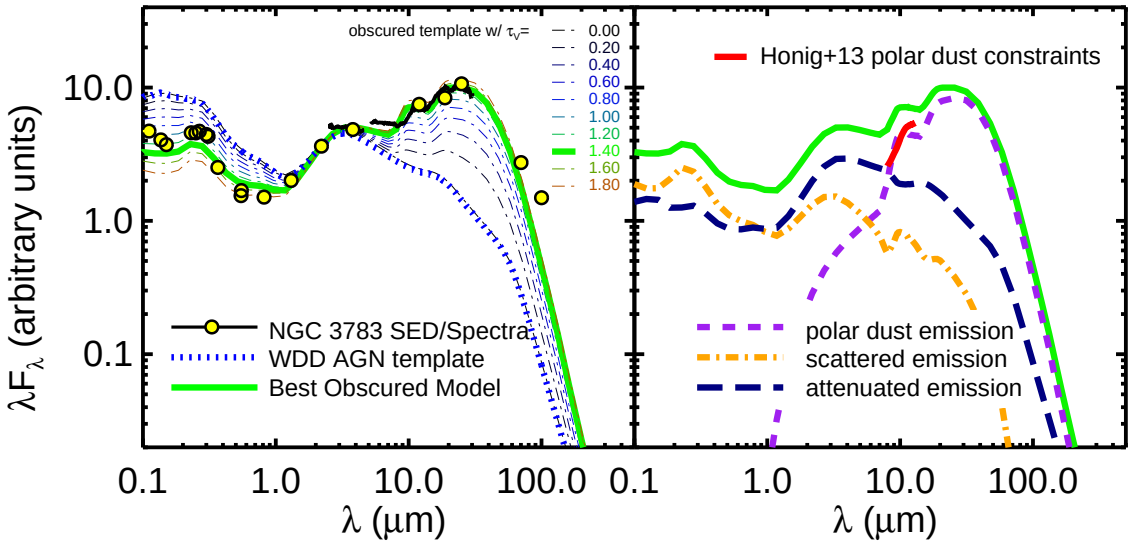


Figure 4.3 **Left**: simulated SEDs from the DUSTY model as a function of optical depth $\tau_V$ (thin lines). We assume the WDD AGN template (blue line) is obscured by a dust distribution with density profile $\rho(r) \propto r^{-0.5}$, outer-to-inner radius $Y = 500$, and dust temperature at inner radius $T_{in}$=1500 K. The dust grains have the standard ISM mixture (53% silicate and 47% graphite) with a standard distribution of grain sizes ($p$=3.5) but larger size cutoffs with $a_{min} = 0.04$ $\mu$m and $a_{max} = 10$ $\mu$m. The NGC 3783 SED is matched by the model with $\tau_V$=1.4 mag (thick green line). **Right**: the contributions of various components of the best-fit model as a function of wavelength. We also plot the 8–13 $\mu$m polar dust emission strength constrained by Hönig et al. (2013) for comparison.

plained through rather different descriptions about the AGN circumnuclear extended dust. In general, we lack any detailed structural information in the mid-infrared for most known AGNs. Consequently, additional parameters to characterize the geometry of this structure cannot be realistically constrained. As explained in Section 4.2.2, at low optical depth, the behavior of polar dust emission should not be sensitive to the shape of its large-scale distribution, nor the observing angle. Thus our reddened AGN SED model is consistent with the possible diverse polar dust morphologies.

## 4.3 Reproducing the SEDs of Low-$z$ Seyfert Nuclei

### 4.3.1 Sample and Data

In view of the success in reproducing the observations of NGC 3783, we will test if a similar model works for other Seyfert nuclei as well. To reduce the ambiguity in interpreting the SED, we have searched the literature and archives to find low-$z$ Seyfert-1 nuclei where the AGN mid-IR emission can be isolated from the host star-formation contamination or the contribution from the latter can be safely ignored. The details can be found in Appendix D. Below is a brief summary.

We first compiled AGNs with high spatial resolution (HSR) mid-IR SED constraints. About half of them are Seyfert 1-1.5 nuclei from Asmus et al. (2014); we required that the ground-based 12 $\mu$m flux measurements be consistent with the much larger beam WISE W3 band observations. We also included some very well-studied Seyfert-1 nuclei and all the type-1 objects with mid-IR interferometry observations. Due to these selections, the near-IR stellar contamination is not very significant in this HSR sample. In total, there are 32 nuclei selected. These objects span a redshift range of 0.002-0.16, with a median at $z = 0.02$. IR photometry from the literature and surveys like 2MASS, UKIDSS and WISE were collected to define the SEDs.

In addition, we looked for optically-selected broad-line AGNs from the Sloan Digital Sky Survey (SDSS; York et al. 2000b) that have *Spitzer*/IRS spectra allowing isolation of the nuclear emission in the mid-IR. The homogeneous datasets of this sample enable the derivation of composite SEDs that minimize the effects of different observing angles and variability, and can be used to test the complete range of reddened AGN SEDs predicted from our model. For this SDSS/*Spitzer* sample, we ended up with 33 type-1 AGNs with a redshift range of 0.008–0.20, with the median at $z = 0.06$. Except for NGC 4235, all of them are new objects with no duplication found in the HSR sample. Archival and literature X-ray, UV, optical and IR data from e.g., XMM-*Newton*, *Chandra*, *GALEX*, *Hubble*, *2MASS*, *WISE*, *Spitzer*, *AKARI*, *Herschel* and other ground-based optical and IR facilities are collected for these objects with a careful selection of photometry apertures if possible.

To have some crude idea on the influence of variabilities on the IR SEDs of these objects, we determined their mid-IR variability amplitudes in the WISE W1 and W2 bands using the archival data from the *WISE* (Wright et al., 2010) and the Near-Earth Object *WISE* Reactivation mission (*NEOWISE-R*; Mainzer et al. 2014) missions, covering a time period from 2010 to 2017.

Table 4.3 summarizes the information for the Seyfert-1 nuclei studied in this work.

Table 4.3. List of the Low-redshift Seyfert-1 Nuclei

| # | Name | $z$ | References for the IR SED data ($\lambda \sim$ 1-2.5 $\mu$m) | ($\lambda \sim$ 2.5-40 $\mu$m) | ($\lambda >$ 40 $\mu$m) | $F_g/F_s$ | $f_{MIR,SF}$ % | $EW_{PAH}$ $\mu$m | $\Delta$W1 mag. | $\Delta$W2 mag. | AGN type | $\tau_{V,ext.}$ | $f_{pol,10\ \mu m}$ |
|---|---|---|---|---|---|---|---|---|---|---|---|---|---|
| (1) | (2) | (3) | (4) | (5) | (6) | (7) | (8) | (9) | (10) | (11) | (12) | (13) | (14) |
| HSR AGN Sample | | | | | | | | | | | | | |
| 1 | PKS 1417-19 | 0.1195 | 2M | W | ... | 0.93 | ... | ... | 0.31 | 0.26 | WDD | 1.00 | 0.65 |
| 2 | ESO 141-55 | 0.0371 | 2M | W | 1, 2, 3 | 0.94 | ... | ... | 0.26 | 0.23 | WDD | 0.25 | 0.30 |
| 3 | Mrk 509 | 0.0344 | 2M | W | 2, 3 | 0.99 | ... | ... | 0.25 | 0.15 | WDD | 0.50 | 0.47 |
| 4 | Mrk 1239 | 0.0199 | 5,6 | 3,4,8,9,10,11,12 | 11 | 0.99 | ... | ... | 0.40 | 0.27 | NORM | 0.00 | 0.00 |
| 5 | 3C 382 | 0.0579 | 2M | W, 1 | 4 | 1.02 | ... | ... | 0.27 | 0.23 | WDD | 0.00 | 0.00 |
| 6 | IRAS 09149-6206 | 0.0573 | 2M | W, 2 | 5 | 1.09 | ... | ... | 0.28 | 0.20 | WDD | 0.25 | 0.30 |
| 7 | Ark 120 | 0.0327 | 2M | W | 2,3 | 1.13 | ... | ... | 0.38 | 0.37 | WDD | 0.00 | 0.00 |
| 8 | Fairall 51 | 0.0142 | 2M | W | 2,3 | 1.13 | ... | ... | 0.16 | 0.13 | WDD | 0.50 | 0.47 |
| 9 | IRAS 13349+2438 | 0.1076 | 2M | W | 1 | 1.14 | ... | ... | 0.09 | 0.05 | NORM | 2.50[a] | 0.83[a] |
| 10 | I Zw 1 | 0.0589 | 2M | W,13 | 12 | 1.16 | ... | ... | 0.29 | 0.20 | NORM | 0.50 | 0.33 |
| 11 | H 0557-385 | 0.0339 | 2M | W,1 | 2 | 1.18 | ... | ... | 0.24 | 0.15 | WDD | 0.25 | 0.30 |
| 12 | IC 4329A | 0.0161 | 2M | W,1 | 2,3 | 1.18 | ... | ... | 0.37 | 0.33 | WDD | 0.75 | 0.58 |
| 13 | 3C 120 | 0.0330 | 2M | W | 2,3 | 1.20 | ... | ... | 0.33 | 0.26 | WDD | 0.75 | 0.58 |
| 14 | 3C 390.3 | 0.0561 | 2M | W,1 | 8 | 1.20 | ... | ... | 0.35 | 0.29 | WDD | 0.50 | 0.47 |
| 15 | Pictor A | 0.0351 | 2M | W | 2,3 | 1.21 | ... | ... | 0.32 | 0.30 | WDD | 0.50 | 0.47 |
| 16 | MR 2251-178 | 0.0640 | 1 | W,1,3 | 9 | 1.21 | ... | ... | ?? | ?? | WDD | 0.25 | 0.30 |
| 17 | 3C 227 | 0.0858 | 2M | W,3,6 | 10 | 1.28 | ... | ... | 1.02 | 0.52 | WDD | 0.25 | 0.30 |
| 18 | Mrk 1014 | 0.1631 | 2M | W | 11,12,13 | 1.28 | ... | ... | 0.24 | 0.18 | NORM | 10.00 | 0.93 |
| 19 | 3C 445 | 0.0559 | 2M | W | 1 | 1.29 | ... | ... | 0.13 | 0.08 | NORM | 0.00 | 0.00 |
| 20 | 3C 93 | 0.3571 | 2M | W | ... | 1.54 | ... | ... | 0.33 | 0.41 | WDD | 0.50 | 0.47 |
| 21 | NGC 3783 | 0.0097 | P10 | P10 | 2,3, 19 | 1.03 | ... | ... | 1.91 | 2.37 | NORM | 1.00 | 0.51 |
| 22 | NGC 4507 | 0.0118 | 2M | W | 2, 3 | 1.15 | ... | ... | 0.16 | 0.18 | WDD | 1.75 | 0.78 |
| 23 | ESO 323-77 | 0.0150 | 2M | 1, 3, 7 | 2,3, 19 | 0.67 | ... | ... | 0.31 | 0.26 | WDD | 0.25 | 0.30 |
| 24 | NGC 4151 | 0.0033 | AH13 | AH13 | 19 | 0.78 | ... | ... | 1.15 | 0.78 | NORM | 0.75 | 0.44 |
| 25 | NGC 7469 | 0.0163 | P10, AH13 | P10, AH13 | 2,3 | 0.48 | ... | ... | 0.34 | 0.31 | NORM | 7.75 | 0.91 |
| 26 | NGC 1566 | 0.0050 | P10 | P10 | | 0.36 | ... | ... | 0.11 | 0.32 | NORM | 9.50 | 0.93 |
| 27 | NGC 4593 | 0.0090 | 2M | W, 3 | 11 | 0.85 | ... | ... | 0.35 | 0.52 | WDD | 0.75 | 0.58 |
| 28 | NGC 3227 | 0.0039 | F16 | F16 | 2,3 | 0.40 | ... | ... | 0.25 | 0.25 | HDD | 4.50 | 0.94 |
| 29 | NGC 4235 | 0.0080 | AH13 | AH13 | 2,14 | 0.78 | ... | ... | 0.23 | 0.26 | NORM | 0.00 | 0.00 |
| 30 | NGC 4015 | 0.0023 | 2M | W | 9 | ... | ... | ... | 0.41 | 0.43 | NORM? | 1.75? | 0.66? |
| 31 | Fairall 9 | 0.0470 | 2M | W | 2,3 | 1.11 | ... | ... | 0.09 | 0.04 | NORM | 0.00 | 0.00 |
| 32 | NGC 3516 | 0.0088 | AH13 | AH13 | 2,3 | ... | ... | ... | 0.66 | 0.79 | NORM | 1.00? | 0.51? |
| SDSS/*Spitzer* Sample | | | | | | | | | | | | | |
| 33 | Mrk 1393 | 0.0543 | 2M | W | 15 | ... | 0.2 | 0.01 | 0.22 | 0.23 | NORM | 0.75 | 0.44 |

### 4.3.2 SED Fitting Method

*Stellar Emission Template* While the galaxy star formation contribution to the mid-IR has been minimized by our sample selections, stellar contamination in the near-IR can be significant, especially for the SDSS/*Spitzer* AGNs. Luckily, the near-IR bands of low-$z$ galaxies are dominated by old stellar populations that share nearly identical broad-band SEDs. Despite the likely multiple stellar populations with different star formation histories, the stellar photospheric SEDs of these galaxies peak at $\sim$1 $\mu$m and drop quickly following a Rayleigh-Jeans tail toward the mid-IR (e.g., Polletta et al., 2007). It is known that dust around evolved stars could have additional emission that supplements the quickly dropping photospheric SED at $\lambda \gtrsim 7$ $\mu$m, particularly in early-type galaxies (e.g., Bressan et al., 2006; Rampazzo et al., 2013). For some low-luminosity AGNs, where the stellar contamination can even contribute to the mid-IR, we need more accurate templates.

There are several stellar population synthesis models that include the effect of circumstellar dust shells from evolved stars (e.g., Bressan et al., 1998; Silva et al., 1998; Piovan et al., 2003; González-Lópezlira et al., 2010; Cassarà et al., 2013; Villaume et al., 2015). However, due to the lack of constraints on the metallicity, mass loss rates or properties of the dust shells around the evolved stars in the AGN host galaxies, we decided to derive an empirical template. Following Hernán-Caballero et al. (2015), we used the *Spitzer*/IRS spectra of 18 local early-type galaxies with negligible indication of star formation activities[4] to derive a mean mid-IR stellar template at 6–20 $\mu$m with the normalization at 7 $\mu$m. Only a few of them have LL2 (19.9–39.9 $\mu$m) observations but the spectral slope can be roughly described by a power-law $f_\nu \propto \nu^{1.0}$ at $\lambda > 20$ $\mu$m. We continue this mid-IR stellar template as a power-law at longer wavelengths and join it to the 7 Gyr single stellar population (SSP) template from Bruzual & Charlot (2003) at 7.0 $\mu$m. The results can be seen in Figure 4.4, together with three elliptical galaxy templates generated with the GRASIL code (Silva et al., 1998) by Polletta et al. (2007). Compared with the original dust-free Bruzual & Charlot (2003) template, the star-heated dust features increase the flux

[4]This early-type galaxy sample includes: NGC 4474, NGC 4377, NGC 4564, NGC 4570, NGC 4660, M 85, NGC 4473, NGC 5812, NGC 1700, NGC 1374, NGC 0821, NGC 5831, NGC 1297, NGC 1366, NGC 3818, NGC 7332, NGC 1549, NGC 3904.

Table 4.3 (cont'd)

| # | Name | $z$ | References for the IR SED data ($\lambda \sim$ 1-2.5 $\mu$m) | ($\lambda \sim$ 2.5-40 $\mu$m) | ($\lambda >$ 40 $\mu$m) | $F_g/F_s$ | $f_{MIR,SF}$ % | $EW_{PAH}$ $\mu$m | $\Delta$W1 mag. | $\Delta$W2 mag. | AGN type | $\tau_{V,ext.}$ | $f_{pol,10\ \mu m}$ |
|---|---|---|---|---|---|---|---|---|---|---|---|---|---|
| (1) | (2) | (3) | (4) | (5) | (6) | (7) | (8) | (9) | (10) | (11) | (12) | (13) | (14) |
| 34 | Mrk 506 | 0.0431 | 2M | W | ... | ... | 2.2 | 0.03 | ?? | ?? | WDD | 0.25 | 0.30 |
| 35 | Mrk 926 | 0.0470 | 2M | W | 2,3 | ... | 4.6 | 0.01 | 0.73 | 0.61 | NORM | 0.25 | 0.20 |
| 36 | NGC 4074 | 0.0226 | 2M | W | 2,3 | ... | 7.3 | 0.02 | ?? | ?? | NORM | 1.50 | 0.62 |
| 37 | Mrk 1392 | 0.0359 | 2M | W | 2,3 | ... | 1.9 | 0.01 | ?? | ?? | NORM | 0.75 | 0.44 |
| 38 | [VV2006c] J020823.8-002000 | 0.0741 | 2M | W | ... | ... | 4.5 | 0.00 | 0.19 | 0.21 | NORM | 1.00 | 0.51 |
| 39 | NGC 2484 | 0.0408 | 2M | W | ... | ... | 1.7 | 0.00 | 0.08 | 0.15 | NORM? | 10.00? | 0.93? |
| 40 | 2MASX J14510879+2709272 | 0.0645 | 2M | W | 12 | ... | 1.3 | 0.05 | ?? | ?? | NORM | 0.50 | 0.33 |
| 41 | 2MASX J16164729+3716209 | 0.1518 | 2M | W | 16 | ... | 0.0 | 0.03 | 0.03 | 0.08 | NORM | 10.00 | 0.93 |
| 42 | NGC 863 | 0.0261 | 2M | W | 2,3 | 1.43 | 2.2 | 0.03 | 0.13 | 0.34 | NORM | 4.00 | 0.84 |
| 43 | Mrk 1018 | 0.0430 | 2M | W | 2,3 | ... | 4.4 | 0.00 | 0.77 | 1.11 | NORM | 0.00 | 0.00 |
| 44 | 3C 15 | 0.0735 | 2M | W | ... | ... | 1.2 | 0.06 | 0.13 | 0.20 | WDD | 0.25 | 0.30 |
| 45 | 2dFGRS TGN254Z050 | 0.0888 | 2M | W | 16 | ... | 0.0 | 0.04 | ?? | ?? | NORM | 10.00 | 0.93 |
| 46 | Ton 730 | 0.0864 | 2M | W | 12 | ... | 0.6 | 0.01 | ?? | ?? | HDD | 0.25 | 0.42 |
| 47 | Mrk 110 | 0.0355 | 2M | W | 12 | ... | 6.7 | 0.00 | ?? | ?? | NORM | 0.00 | 0.00 |
| 48 | 2MASX J09191322+5527552 | 0.0489 | 2M | W | 2,3 | ... | 6.1 | 0.00 | 0.22 | 0.20 | NORM | 1.00 | 0.51 |
| 49 | 2MASX J14492067+4221013 | 0.1786 | 2M | W | 16 | ... | 0.4 | 0.03 | 0.06 | 0.10 | NORM | 7.75[a] | 0.95[a] |
| 50 | NGC 5252 | 0.0229 | 2M | W | 2,3 | ... | 2.2 | 0.01 | 0.87 | 0.98 | WDD | 0.00 | 0.00 |
| 51 | 3C 219 | 0.1746 | 2M | W | ... | ... | 2.8 | 0.02 | 0.10 | 0.12 | WDD | 0.25 | 0.30 |
| 52 | SDSS J095504.55+170556.3 | 0.1378 | 2M | W | 12 | ... | 1.5 | 0.00 | 0.32 | 0.22 | NORM | 0.00 | 0.00 |
| 53 | Mrk 176 | 0.0265 | 2M | W | 17 | ... | 8.9 | 0.04 | 0.16 | 0.12 | NORM | 1.00 | 0.51 |
| 54 | 2MASX J14054117+4026326 | 0.0806 | 2M | W | 9 | ... | 0.2 | 0.08 | 0.06 | 0.09 | NORM | 10.00 | 0.93 |
| 55 | 2MASX J14482512+3559462 | 0.1133 | 2M | W | 16 | ... | 3.9 | 0.08 | ?? | ?? | HDD | 0.50 | 0.60 |
| 56 | [GH2004] 9 | 0.1952 | 2M | W | ... | ... | 0.0 | 0.00 | ?? | ?? | NORM | 2.50 | 0.75 |
| 57 | Mrk 417 | 0.0328 | 2M | W | 2,3 | ... | 6.7 | 0.01 | 0.36 | 0.30 | NORM | 1.00 | 0.51 |
| 58 | Mrk 668 | 0.0770 | 2M | W | 1 | ... | 2.8 | 0.08 | 0.78 | 0.95 | NORM | 0.50 | 0.33 |
| 59 | NGC 4235[b] | 0.0075 | 2M | W | 2,14 | ... | 7.1 | 0.10 | 0.23 | 0.26 | NORM? | 3.25? | 0.80? |
| 60 | 2MASX J12384342+0927362 | 0.0829 | 2M | W | ... | ... | 1.4 | 0.01 | 0.14 | 0.15 | HDD | 3.00 | 0.92 |
| 61 | 2MASS J10405880+5817034 | 0.0712 | 2M | W | 18 | ... | 7.0 | 0.07 | 0.16 | 0.15 | NORM | 1.25 | 0.58 |
| 62 | SDSS J164019.66+403744.4 | 0.1512 | 2M | W | 18 | ... | 3.3 | 0.10 | 0.38 | 0.49 | NORM | 1.50 | 0.62 |
| 63 | Mrk 50 | 0.0239 | 2M | W | 2,3 | ... | 3.2 | 0.04 | ?? | ?? | HDD | 0.00 | 0.00 |
| 64 | 2dFGRS TGN404Z026 | 0.0329 | 2M | W | 2,3 | ... | 5.1 | 0.00 | 0.44 | 0.35 | NORM | 0.50 | 0.33 |
| 65 | Mrk 771 | 0.0636 | 2M | W | 12 | ... | 5.5 | 0.00 | 0.45 | 0.34 | NORM | 0.75 | 0.44 |

Note. — Col. (4)-(6): references for the SED data, P10 - Prieto et al. (2010), AH03 - Alonso-Herrero et al. (2003), RA09-Ramos Almeida et al. (2009), F16 -Fuller et al. (2016), and the photometry data, NIR: 2M- 2MASS (Skrutskie et al., 2006), 1-Elvis et al. (1994), 2- Peng et al. (2006), 3- Abrahamyan et al. (2015), 4- Scoville et al. (2000), 5- Spinoglio et al. (1995), 6- Rudy et al. (1982); MIR: W- WISE (Wright et al., 2010), 1- Spitzer Science Center Source list (Teplitz et al., 2010), 2- Matsuta et al. (2012), 4- Gallimore et al. (2010), 3- Asmus et al. (2014), 5- Shi et al. (2010), 6- Dicken et al. (2008), 7- Hönig & Kishimoto (2010a), 8- Spinoglio et al. (1995), 9- Rudy et al. (1982), 10- Reunanen et al. (2010), 11- Haas et al. (2007), 12- Gorjian et al. (2004); 13 - Shi et al. (2014); FIR: 1- Hernán-Caballero & Hatziminaoglou (2011), 3-Shimizu et al. (2016), 2- Meléndez et al. (2014), 4-Dicken et al. (2010), 5- Matsuta et al. (2012), 6- Pollo et al. (2010), 7- Sargsyan et al. (2011), 8- Landt et al. (2010), 9- IRSA Faint Source Catalog (Moshir et al., 1990), 10- Dicken et al. (2008), 11- AKARI/FIS All-Sky Survey Point Source Catalogues (Yamamura et al., 2010), 12- Shi et al. (2014), 13- Ma & Yan (2015), 14- Auld et al. (2013), 15- Hanish et al. (2015), 16- Abrahamyan et al. (2015), 17- Bitsakis et al. (2014), 18- Oliver et al. (2012), 19- García-González et al. (2016) Col. (7): the 12-$\mu$m flux ratio between the ground-based observations from Asmus et al. (2014) and WISE band 3 data; Col. (8): the flux contribution of star-forming component in the *Spitzer*/IRS mid-IR spectra using the decomposition method proposed by Hernán-Caballero et al. (2015); Col. (9): the Equivalent Width of the aromatic feature at 11.3 $\mu$m; Col. (10)-(11): the maximum variations among different observing epochs for WISE W1 ($\sim$ 3.4 $\mu$m) and W2 ($\sim$ 4.6 $\mu$m) bands. Questions marks '??' indicate cases where there are not enough good single-epoch photometry data to establish a meaningful extinction curve; Col. (12): the intrinsic AGN template suggested from our best-fits, '?' indicates highly uncertain results; Col. (13)-(14): the derived V-band optical depth and relative 10 $\mu$m emission strength of the extended polar dust component, '?' indicates highly uncertain results.
[a] these values are based on the hot-dust-obscured AGN model introduced in Section 4.5.3; [b] the duplication of NGC 4235 serves as an example to demonstrate the uncertainties caused by strong host galaxy contamination on the SED fitting results.

by a factor of $\gtrsim 1.5-3$ at $\lambda > 10$ $\mu$m. At $\lambda \sim$1–8 $\mu$m, the SEDs of different templates are remarkably similar, so the choice of the Bruzual & Charlot (2003) templates has little effect for the IR SED modeling.

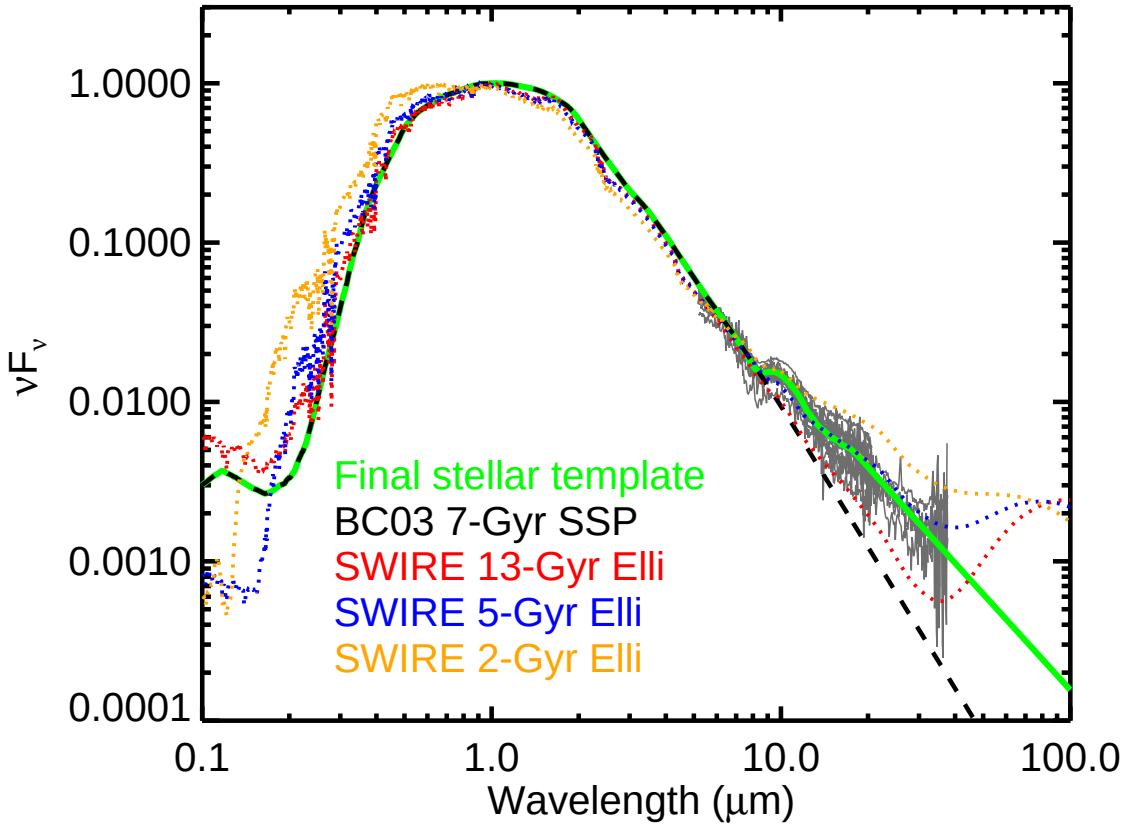


Figure 4.4 Comparisons of different stellar templates. We derive an empirical template by replacing a Bruzual & Charlot (2003) 7 Gyr SSP SED template with the mid-IR (6–20 $\mu$m) stellar template and a power-law SED ($\lambda >$20 $\mu$m). We plot the individual *Spitzer*/IRS spectra used to derived the mid-IR template as grey lines. The original Bruzual & Charlot (2003) and the elliptical galaxy templates with age 2, 5 and 13 Gyr from the SWIRE library (Polletta et al., 2007) are also presented.

*AGN Templates* For the AGN component, a series of semi-empirical SEDs is produced with the model introduced in Section 5.3.2. Because our major goal is to test if Seyfert nuclei behave similarly to NGC 3783, the radial density profile and dust grain properties of the extended dust component are fixed to the values in table 4.2. All three AGN intrinsic

templates presented in Lyu et al. (2017) are obscured with an increment of 0.25 in optical depth ($\tau_V$). We end up with 123 AGN templates that cover $\tau_V$=0–10.

*Other Far-infrared Components* More than 80% of our sample have constraints on the far-IR SEDs. We used Rieke et al. (2009) star-forming galaxy (SFG) templates to describe the host galaxy dust emission. This library was developed based on *Spitzer* observations of local galaxies and each template is parameterized by a different IR luminosity $\log(L_{\rm SF,temp}/L_\odot)$. We decide to adopt a default value of $\log(L_{\rm SF,temp}/L_\odot)$=10.75 for most objects.

Some radio-loud AGNs can have strong synchrotron radiation in the far-IR bands. We assume a broken power-law model (see, e.g., Pe'er, 2014) to represent this contribution

$$F_\nu \propto \begin{cases} \nu^{-0.7}: & \nu < 10^{13}\ \text{Hz, or } \lambda > 30\ \mu\text{m} \\ \nu^{-1.3}: & 10^{13}\ \text{Hz} < \nu < 10^{14}\ \text{Hz, or} \\ & \quad 3\ \mu\text{m} < \lambda < 30\ \mu\text{m} \\ 0: & \nu > 10^{14}\ \text{Hz, or } \lambda < 3\ \mu\text{m} \end{cases} \tag{4.3.1}$$

*SED Models* Our model would predict obscuration in the UV-optical band for many AGNs. However, this effect will be dependent on our line of sight (LOS); any clumpiness in the distribution of the polar dust will result in variations in the extinction. Indeed, it is possible to imagine a system where the polar dust covers 99% of the sky as seen by the central engine and hence provides an important infrared SED component, but where our LOS by chance falls along the 1% of directions without dust and hence the central engine appears to be unobscured. In light of this, we only focus on the IR SEDs for individual objects. To reduce the influence of host galaxy star-formation contamination, the fittings are limited to $\lambda \sim$1–30 $\mu$m.

We combined the (reddened) AGN templates with the stellar templates and used $\chi^2$ minimization to fit the SEDs. Since the data have a range of non-statistical errors, a uniform weight for all bands is assumed instead of using the quoted flux uncertainties. There are only four free parameters in our model: the normalizations of the stellar and the AGN templates, the type of the AGN template and its optical extinction $\tau_V$. The best AGN template is selected by searching the combination with the minimum $\chi^2$ value among all three sets of reddened AGN libraries (normal, WDD, HDD). However, if $\chi^2$ with the best

reddened normal AGN template is less than 1.5 times that with the best reddened dust-deficient template, the normal AGN template is selected.

For objects with at least two photometry data points at $\lambda > 50$ $\mu$m, a second-round SED fitting at $\lambda \sim$1–500 $\mu$m was carried out by combining the AGN template selected above, a stellar template and an SFG far-IR template. For eight objects, we changed the default SFG template to another (Rieke et al., 2009) template with a lower or higher $\log(L_{\rm SF,temp}/L_{\odot})$ in a range of 9.75–10.50 to improve the fitting of the far-IR SED peak. For two objects, Pictor A and 3C 120, the synchrotron emission template was added to reproduce their far-IR and submm SEDs.

### 4.3.3 Fitting the IR SEDs of Individual Objects

The best-fit results for type-1 nuclei can be seen in Figure 4.5. The SED shape of the AGN component is only determined by two free parameters: the type of the intrinsic template (normal, WDD, or HDD) and the optical depth, $\tau_{\rm V}$, of the polar dust component. Surprisingly, this simple model fits the broad-band IR SEDs of most objects reasonably well. The only notable exceptions are IRAS 13349+2438 and 2MASX J14492067+4221013, whose SEDs feature strong hot dust excess emission. As shown later (Section 4.5), similar characteristics can be found in the so-called hot dust-obscured galaxies, whose SEDs our model can fit by adjusting the density profile of the polar dust.

We want to mention several complications that could influence the quality of the SED fitting. First, AGNs show near- and mid-IR variability that could produce a gap between different datasets. In fact, $\gtrsim 40\%$ of the Seyfert sample have strong mid-IR variability with $\Delta W1 > 0.3$ mag during the available WISE epochs, in contrast with $\sim$13% for the PG quasar sample in our previous study (Lyu et al., 2017). Secondly, it is quite likely that the dust has different compositions or distributions among different objects. Indeed, we can improve the fittings by sampling more parameter space with similar MCMC methods used for NGC 3783 (see Section 4.2.4). However, the exact situations for these properties cannot be observationally constrained. Our goal is to reproduce a wide range of observations in a way that minimizes the uncertainties due to model degeneracy, not to produce another complicated model that may fit a few observations perfectly.

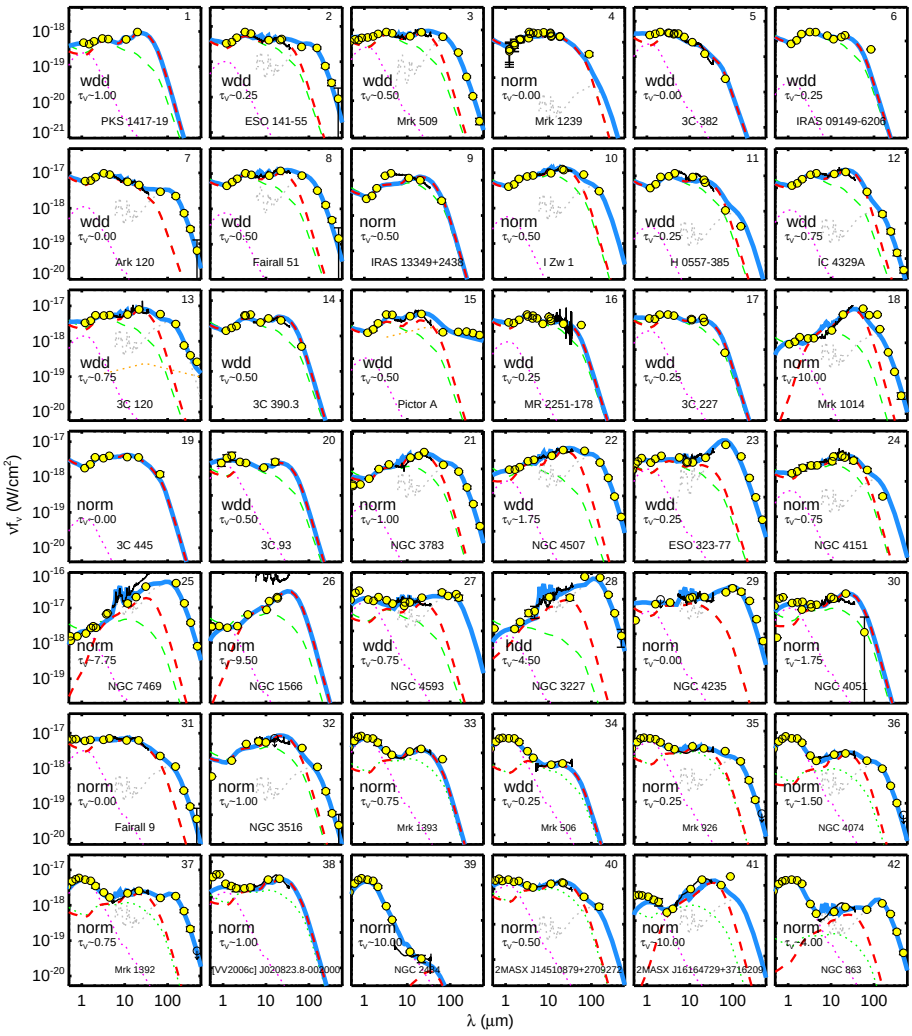


Figure 4.5 Best-fit results for low-$z$ Seyfert-1 nuclei with the reddened AGN model trained for NGC 3783. Photometric data points are shown as yellow dots and the *Spitzer/IRS* mid-IR spectra are plotted as black solid lines. The SED model (blue thick solid lines) is composed of the AGN component (red dashed lines), the stellar component (magenta dotted lines), and the far-IR star formation component (grey dotted lines). For 3C 120 and Pictor A, the sychrotrom emission component (orange dotted lines) is added into the fittings. We also plot the suggested intrinsic AGN template (green dashed lines) for each object from our SED fittings to compare the observed SED.

In summary, our four-free-parameter simple model provides reasonably good fits in the near-IR and mid-IR to nearly the entire sample of AGNs.

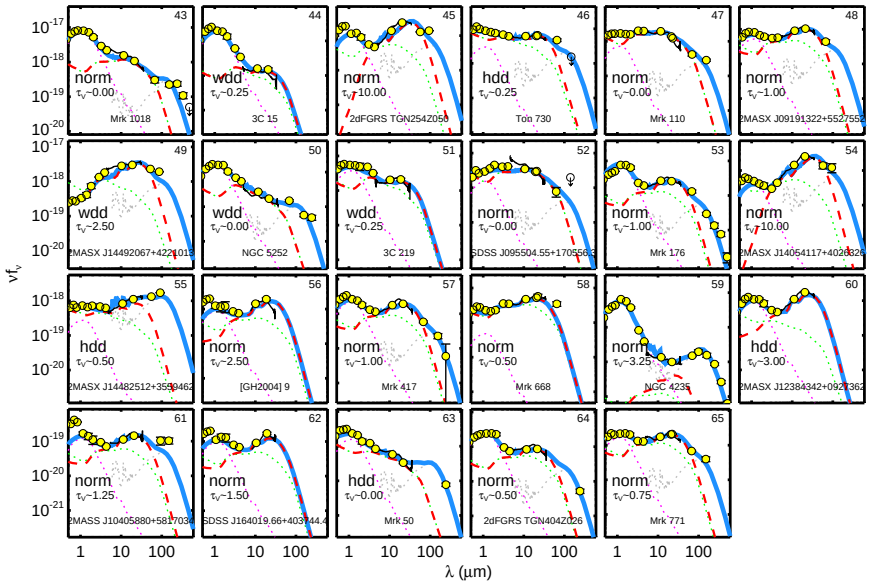


Figure 4.5 (continued.) Best-fit results for low-$z$ Seyfert-1 AGNs with the reddened AGN model trained for NGC 3783.

### 4.3.4 Testing the Reddened AGN Templates with Composite SEDs

We now work with SEDs averaged over the SDSS-*Spitzer*/IRS sample to test the prediction that objects with excess IR emission due to polar dust should have obscuration in some directions. By averaging over a sample of AGNs, evidence of such obscuration should be obvious even if it is very non-uniform for individual sources.

*Composite SEDs of the SDSS Seyfert-1 Nuclei* For each object, we corrected the flux for the foreground Galactic extinction in the UV-optical bands according to the SRD dust map (Schlegel et al., 1998; Schlafly & Finkbeiner, 2011). The observed flux is converted into luminosity and the SED is smoothed with a $\Delta\log(\nu) = 0.2$ boxcar in the $\lambda - \lambda L_\lambda$ space. The median of all these SEDs is then computed to produce a composite SED. To reduce the uncertainties in the mid-IR due to the low resolution of photometry data points, we also derive a median mid-IR spectrum of the sample using the *Spitzer*/IRS data in a similar fashion. In the last step, we replace the 6-35 $\mu$m low-resolution SED template based on photometric data with the median mid-IR spectrum of the sample.

Figure 4.6 presents the median SED for the whole SDSS-*Spitzer*/IRS Seyfert-1 sample.

Since we do not remove the near-IR host galaxy contamination, a near-IR SED bump due to emission from an old stellar population is expected. In the mid-IR, this Seyfert-1 median SED presents stronger emission at $\lambda \gtrsim 10$ $\mu$m compared with the near-IR normalized normal Elvis-like template. Since any objects with strong host galaxy contamination in the mid-IR have been dropped, such excess emission has to be AGN-dominated. On the other hand, the UV and soft X-ray (to $\sim 3$ keV) composite SED of this Seyfert-1 sample is suppressed relative to the quasar template. Beyond 3 keV, the two templates are similar. This UV-optical dip is the expected signature of obscuration in these Seyfert-1 nuclei. It is an indication that the Seyfert-1 mid-IR excess is from the reradiation of the absorbed energy by the dust that also provides the short-wavelength obscuration.

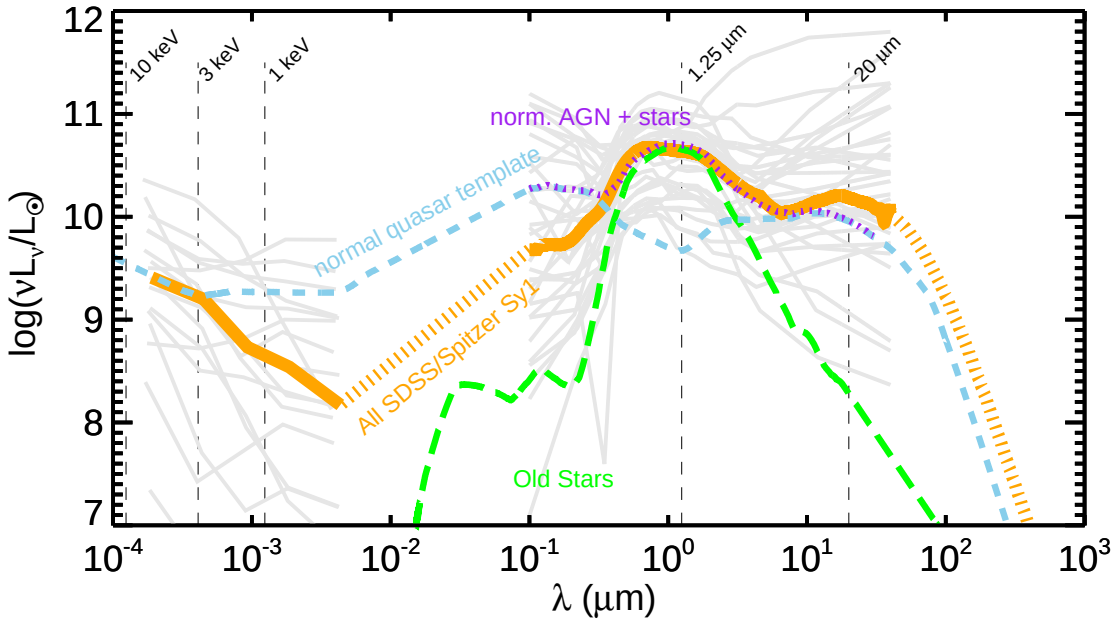


Figure 4.6 The individual SEDs (grey thin lines) and the median composite SEDs (orange thick line) of the SDSS-*Spitzer*/IRS Seyfert-1 AGN sample. As a comparison, we also plot the intrinsic AGN template for normal quasars (dashed blue line) from Xu et al. (2015b). We used the modified Bruzual & Charlot (2003) stellar template with age $\sim 7$ Gyr (green long-dashed line) and the normal AGN template (blue dashed line) to reproduce the composite SED at 0.5–3.0 $\mu$m with the model as a magenta dotted line.

With the SDSS/*Spitzer* sample, we also demonstrate that both normal AGNs and dust-deficient AGNs exist in the Seyfert-1 population, which supports the idea that similar intrinsic AGN templates are also valid for relatively low-luminosity AGNs. Based on the

mid-IR continuum shape, objects with similar IR SED characteristics are grouped together and a composite SED is derived similarly to the whole sample median SED. We classify these AGNs into three categories and show that their composite SEDs have the following characteristics compared with the Elvis et al. (1994)-like templates for normal AGNs:

- (C1, N=5) normal AGNs.

  These objects have SEDs well-reproduced by the normal AGN template with some stellar contribution in the near-IR. Some of them have a little far-IR excess emission, which might be associated with the host galaxy.

- (C2, N=7) dust-deficient AGNs.

  These objects present a deficiency of the dust emission at $\lambda \gtrsim 5$ $\mu$m. However, since the stellar contribution in the near-IR can not be calibrated, it is hard to argue this SED is hot-dust-deficient or warm-dust-deficient. It is likely a combination of both populations.

- (C3, N=20) warm-excess AGNs.

  These objects feature a mid-IR bump peaking around $\lambda \sim 20$ $\mu$m, in contrast with the flat $\sim$3–20 $\mu$m continuum of normal quasars. A similar mid-IR feature is also present in the SED of NGC 3783 as well as the composite SEDs of the whole sample.

These results are presented in Figure 4.7: (1) In the top panels we demonstrate using the *Spitzer*/IRS spectra to construct composite spectra in the 6–30 $\mu$m range. (2) In the middle panels we merge the mid-IR spectral templates with composite SEDs at the shorter wavelengths built primarily using photometry. The middle right panel shows the mid-IR bump clearly when compared with the left and center panels. (3) The bottom panels present our model fits (see below).

*Reproducing the Composite SEDs* For the composite templates (C1) and (C2), due to the relatively small sample sizes ($N < 10$), the UV-optical SEDs may not be representative of the overall extinction and suffer the possibility of variability. However, either the normal

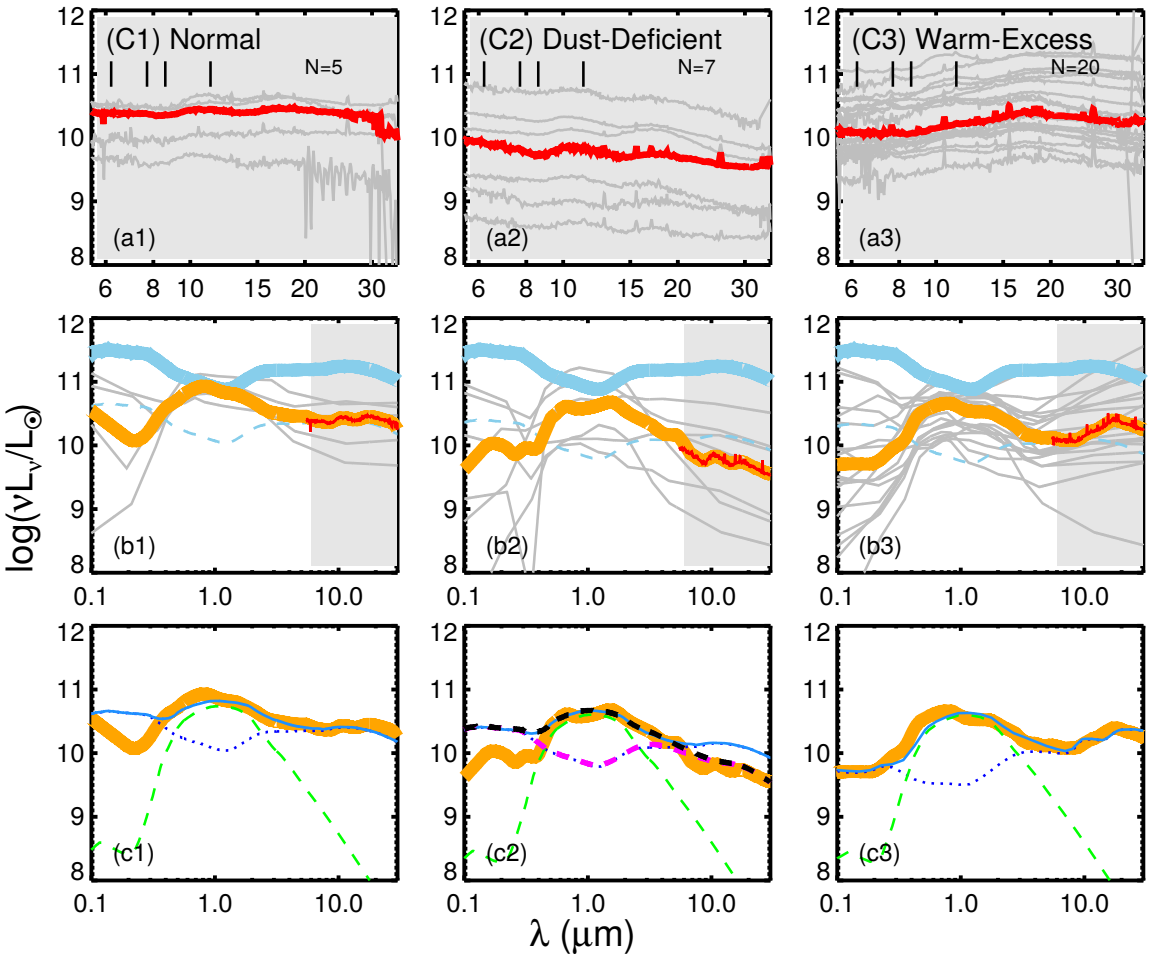


Figure 4.7 (a1-a3): Mid-IR spectra of the SDSS-*Spitzer*/IRS Seyfert-1 sample. Based on the continuum shape, we grouped them into normal AGNs, dust-deficient AGNs and warm-excess AGNs. Spectra of individual objects are plotted as grey lines and the composites are shown as red lines. The black vertical lines on the top panels label the location of the aromatic features at 6.2, 7.7, 8.6 and 11.3 $\mu$m. (b1-b3): Composite (orange) and individual UV-to-MIR SEDs (grey lines) for different groups of the SDSS-*Spitzer*/IRS Seyfert-1 sample. We also show templates of a normal AGN (blue lines) and the Seyfert-1 mid-IR spectral composites (red lines). (c1-c3): Reproductions of the composite SEDs of Seyfert-1 Nuclei. The model SED (blue solid lines) is composed of an AGN component (blue dotted lines) and a stellar component (green dashed lines). For (c2), we also present the fittings with the WDD intrinsic template (purple dashed line for the AGN component and black dashed line for the SED model).

AGN template or the dust-deficient AGN template plus the stellar template can reproduce the Seyfert IR SED.

For (C3), we apply the reddened AGN templates to fit the average composite SEDs

together with the stellar template. This UV-to-mid-IR composite SED is matched by the reddened WDD template with $\tau_V = 1.5$ and all other parameters of the polar dust component fixed the same for NGC 3783.

We conclude that the unobscured quasar templates can be directly applied to some Seyfert-1 nuclei ($\sim$37% in our case). Both normal AGNs and dust-deficient AGNs are seen among the Seyfert-1 population. Meanwhile, most Seyfert-1 nuclei present evidence for low- to moderate-level obscuration from the soft X-ray to the optical with some dust excess emission starting from the mid-IR, which can be reproduced by our polar-dust-obscured AGN template. These results support our model assumptions introduced in Section 5.3.2.

## 4.4 Characterizing the AGN Polar Dust Emission

In Section 4.2.4, the SED features and the polar dust emission strength of NGC 3783 were accurately reproduced by the reddened AGN model proposed in this study. With the same parameters used for this single object, our reddened AGN templates, combined with the host galaxy templates, successfully fit the IR SEDs of another 64 Seyfert-1 nuclei and the UV to mid-IR composite SEDs of the SDSS/*Spitzer* type-1 AGNs (Section 4.3.3). In Section 4.3.4, we found that on average Type-1 AGN SEDs show indications of extinction as predicted by our approach. These results support our proposal that the SED differences between quasars and Seyfert-1 nuclei are due to the IR reprocessed emission from the extended distribution of dust that is also responsible for the common low-level obscuration of the Seyfert nuclei.

Now we characterize the possible SED features of the polar dust emission and explore its prevalence among the Seyfert-1 nuclei studied in this work.

### 4.4.1 SED Features

In the top panels of Figure 4.8, we show the SEDs of the IR-reprocessed emission from the extended polar dust component as a function of $\tau_V$ for normal, WDD and HDD AGN. In the bottom panels, the relative contributions of the dust IR-reprocessed emission, dust

scattered emission and the attenuated emission of the intrinsic AGN templates are compared.

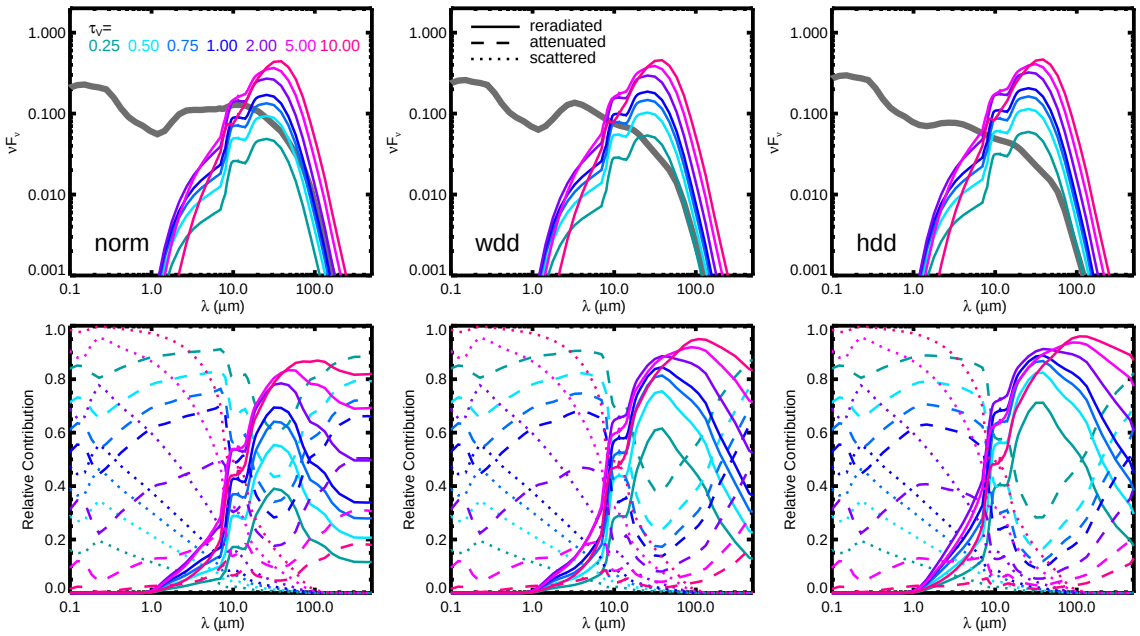


Figure 4.8 The IR emission SED of the polar dust component (top panels) and the relative contributions of the IR-reradiated emission from polar dust, the scattered emission of accretion disk plus torus (by the polar dust), and the attenuated emission of accretion disk plus torus by the polar dust obscuration, in our reddened AGN templates (bottom panels).

There are several interesting results. Firstly, at a given $\tau_V$, regardless of the intrinsic AGN template, the strength and the SED shape of the polar dust emission is almost identical. This is easily understood since the configurations of the dust obscuration properties and the UV to optical SED inputs, where the emission mostly heats the dust, are the same. This result also underlies the possibility to fit a broad variety of observed SEDs with $\tau_V$ as the only free parameter to characterize the contribution of the polar dust component.

In addition, at relatively low optical depth ($\tau_V < 5$), although the overall strength of the polar dust emission changes with $\tau_V$, its SED shape is identical at the wavelengths where this component matters. As discussed in Section 4.2.2, different dust covering factors would only change the relative scaling of the dust emission SED. Thus we can always change the value of $\tau_V$ to match the effect caused by the dust covering factor on the final SED shape, as long as $\tau_V$ is not so large that the polar dust emission becomes optically

thick in the mid-IR.

Thus, we can describe the AGN-heated polar dust emission with one single template when the integrated optical depth is modest ($\tau_V \lesssim 5$). In fact, ∼90% of our low-$z$ Seyfert-1 AGN sample are fitted by the reddened AGN templates with $\tau_V \leq 5$. We suggest that this polar dust template can be generally used to further reduce the number of free parameters in the SED fittings.

Figure 4.9 shows the SED template for the polar dust emission. Its emission is peaked at $\sim 25.6$ $\mu$m, corresponding to a characteristic dust temperature ∼113 K. In other words, most of the energy from the central engine absorbed by the polar dust will be radiatively transferred into the mid- to far-IR bands. As we discussed in Section 5.3.2, the polar dust should consist of large grains, e.g., $a_{\rm min} \sim 0.04$ $\mu$m and $a_{\rm max} \sim 10$ $\mu$m. We use the SKIRT code (Baes et al., 2003, 2011) to compute the optical properties of the polar dust by calculating the total extinction cross section averaged over such a standard grain size distribution with 20 bins for silicate and graphite with a mixture 0.53:0.47. Then an extinction is derived by normalizing the polar dust optical properties at V-band (0.55 $\mu$m) and shown in Figure 4.10. Due to the presence of $a \gtrsim 0.3\mu$m grains, the mid-IR extinction, e.g., $A_{10\mu{\rm m}}$, is at least two orders of magnitude lower relative to the optical extinction, $A_V$. Since the majority of our sample yields $A_V \lesssim 5$, the possible extinction at the wavelengths where the polar dust emits the most energy is extremely low. In this case, the shape of its emission SED would not be influenced by the geometry of the polar dust component but only depend on its radial density profile, as explained in Section 4.2.2.

### 4.4.2 Observed Size

Figure 4.11 presents the radial profiles of the temperature distribution for the extended polar dust component in our model. Similar to the IR-reprocessed emission SEDs, the temperature profiles also have little dependence on the optical depth ($\tau_V$). With the Wien displacement law, we relate some typical observed wavelengths to the dust temperature and estimate the corresponding physical size. In the near-IR ($\sim 2.2$ $\mu$m), we can only see the very inner part ($r_{\rm out,obs} \sim 1.3 r_{\rm in}$) of the extended dust component. In the mid-IR (∼8–13 $\mu$m), the observed size increases to $r_{\rm out,obs} \sim 20$–$41 r_{\rm in}$. At $\lambda \sim 26$ $\mu$m, the polar

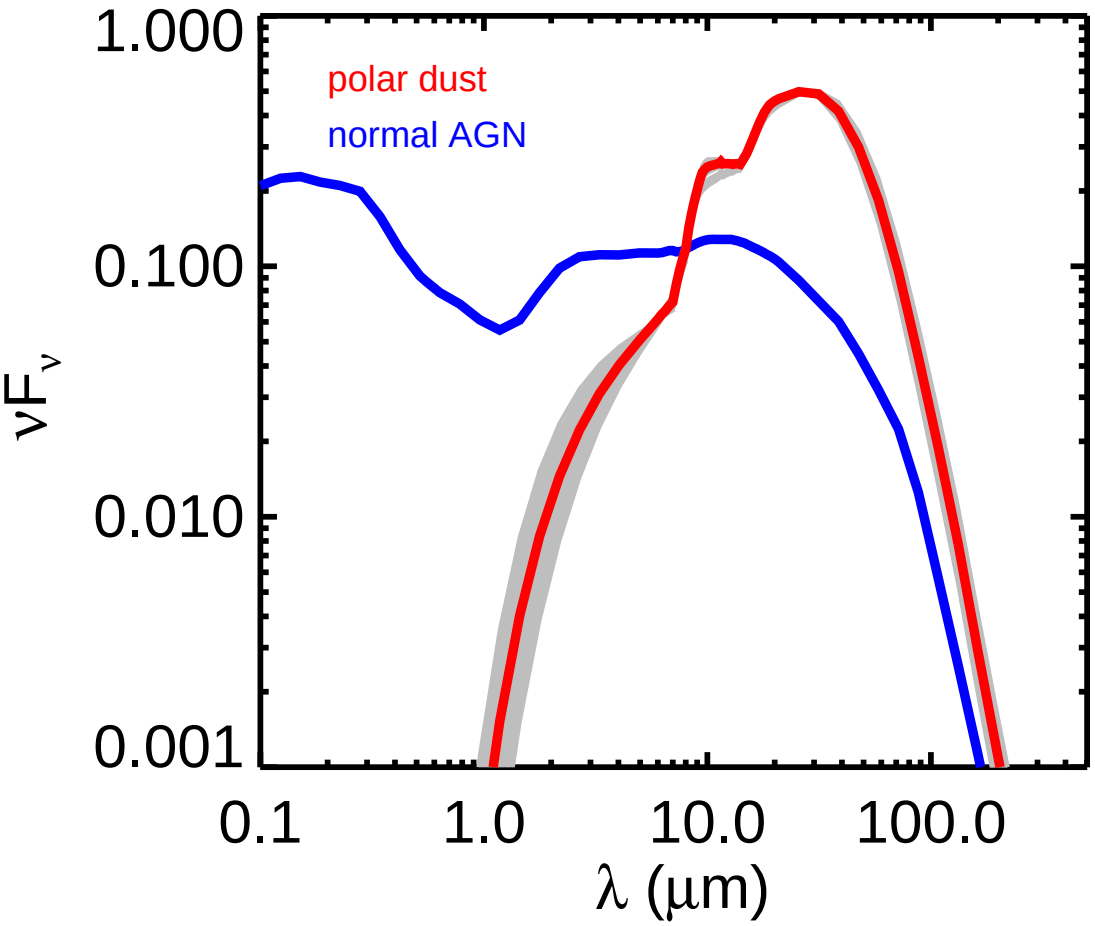


Figure 4.9 IR SED template for AGN polar dust emission (red). We also plot the intrinsic normal AGN template as a comparison (blue). The grey region represents the range of SED variations of polar dust emission with the normalizations at 26.5 $\mu$m and $\tau_V$ ~0–5.

dust emission reaches its peak, corresponding to an observed size $r_{\rm out,obs} \sim$ 200–300$r_{\rm in}$. At even longer wavelengths, the observed size of dust distribution is expected to change slowly. However, since its SED drops quickly as a power-law, the polar dust emission would be very faint and spreads out in a relatively extended area, making any detections challenging.

Considering the AGN polar dust distribution could have some dust-covering factor and its morphology will depend on the observing angle, the estimations provided here should be considered only as order-of-magnitude values.

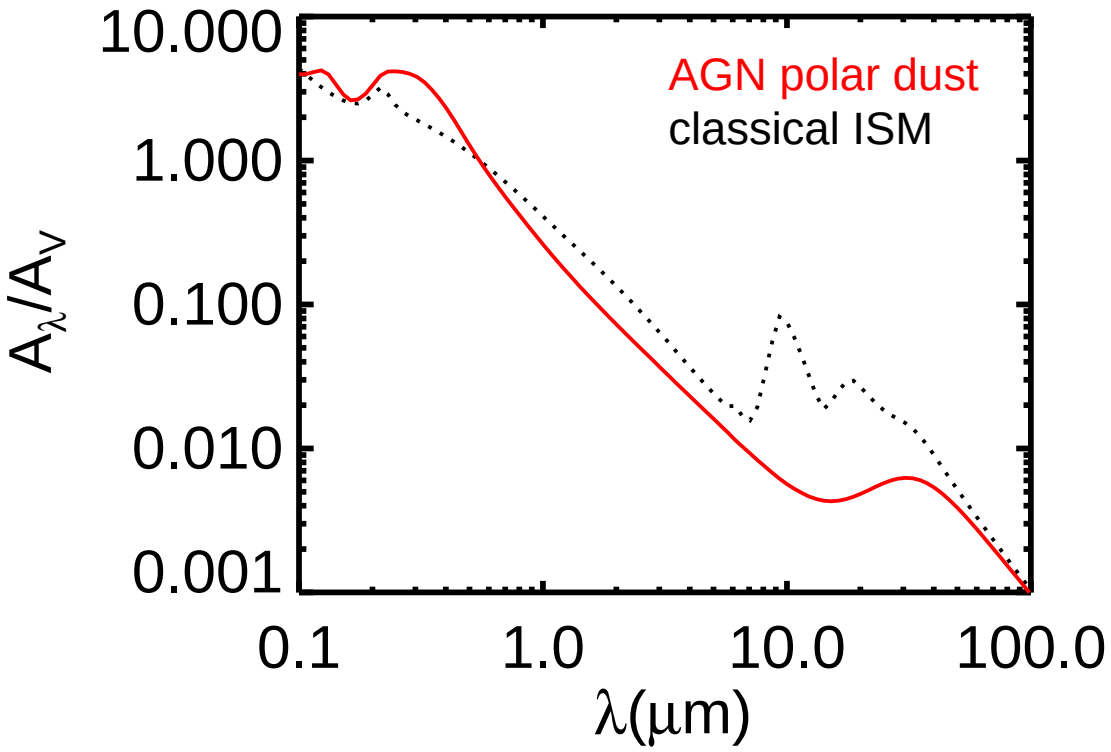


Figure 4.10 Extinction curves of suggested AGN polar dust (red solid line) and classical ISM dust (black dashed line).

### 4.4.3 The Prevalence of AGNs with Strong Polar Dust Emission

As presented in the bottom panels of Figure 4.8, the relative strength of the reprocessed and scattered emission by the polar dust is a function of the optical depth $\tau_V$. We take the relative contribution of the these two components at 10 $\mu$m, $f_{\rm pol,10\ \mu m} \gtrsim 0.5$ as the threshold for AGNs with significant polar dust emission. However, the exact values can not be definitive since there are several sources of uncertainties. First, the intrinsic IR emission of the AGNs presents variations and there could exist objects with intermediate SEDs that cannot be unambiguously grouped into normal, WDD or HDD AGNs (Lyu et al., 2017). In such cases, the SED model would not make a decisive selection of the intrinsic AGN type, making the value of $f_{pol,10\ \mu m}$ uncertain. In addition, despite the model simplicity, fitting degeneracy still exists. A good example is NGC 3783, where our SED fittings in Section 4.3.3 suggest the intrinsic AGN emission can be also represented by a normal AGN template with $f_{\rm pol,10\ \mu m} \sim 0.50$, which is much lower than the Hönig et al. (2013) mid-IR

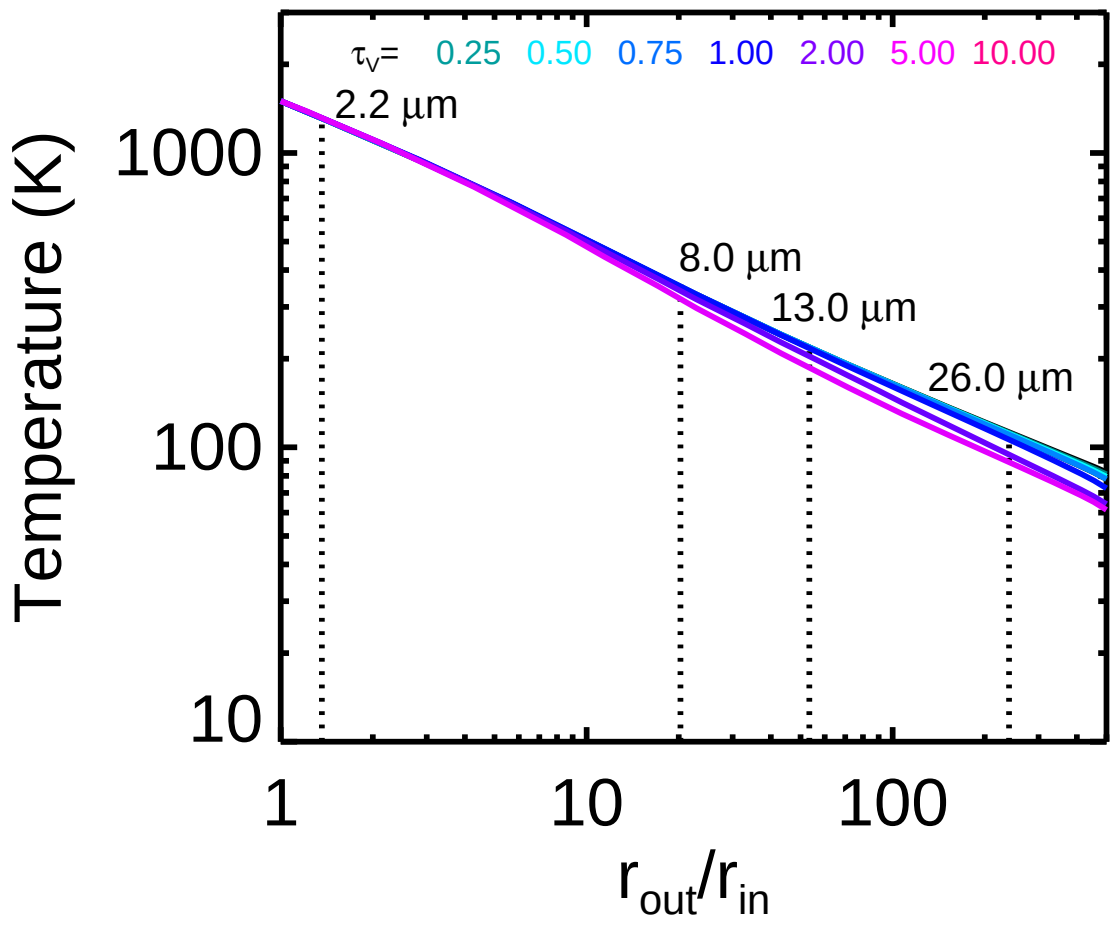


Figure 4.11 Radial profiles of the dust temperature of the extended dust component with $\tau_V$ = 0.25, 0.50, 0.75, 1.00, 2, 5, 9.75. The geometry structure and grain properties are the same as for NGC 3783 (see Table 4.2). We denote the radii that dominate the emission at four typical wavelengths by the vertical dotted lines.

interferometry measurements. Last but not the least, as shown by the example of NGC 4235 (see the fittings #29 and #59 in Figure 4.5), if the SED were strongly contaminated by the galaxy emission, the derived AGN component could be highly uncertain, making the identification of polar dust emission specious.

To get a conservative number of significant polar dust emitters, we remove objects with significant near-IR stellar contamination and count the fittings with the reddened normal AGN templates only. In this way, the fraction of objects with significant polar dust emission among the HSR Seyfert-1 sample is 13%–31%. For the SDSS/*Spitzer* sample, this value is 36%–45%. In Table 4.4, we list the candidate objects with significant polar

Table 4.4. Candidate AGNs with Significant Polar Dust Emission

| ID | Name | Type | $f_{pol,10\ \mu m}$ | Morph. |
|---|---|---|---|---|
| | HSR AGN sample | | | |
| 1 | PKS 1417-19 | WDD | 0.65 | p |
| 12 | IC 4329A | WDD | 0.58 | p, U |
| 13 | 3C 120 | WDD | 0.58 | u |
| 18 | Mrk 1014 | NORM | 0.93 | p |
| 21 | NGC 3783 | NORM | 0.51 | u, E |
| 22 | NGC 4507 | WDD | 0.78 | n, C |
| 25 | NGC 7469 | NORM | 0.91 | y, U |
| 26 | NGC 1566 | NORM | 0.93 | u |
| 27 | NGC 4593 | WDD | 0.58 | y, U |
| 28 | NGC 3227 | HDD | 0.94 | y |
| | SDSS/*Spitzer* AGN sample | | | |
| 36 | NGC 4074 | NORM | 0.62 | p |
| 38 | [VV2006c] J020823.8-002000 | NORM | 0.51 | ... |
| 41 | 2MASX J16164729+3716209 | NORM | 0.93 | ... |
| 42 | NGC 863 (aka Mrk 590) | NORM | 0.84 | n |
| 45 | 2dFGRS TGN254Z050 | NORM | 0.93 | ... |
| 48 | 2MASX J09191322+5527552 | NORM | 0.51 | ... |
| 49 | 2MASX J14492067+4221013 | WDD | 0.84 | ... |
| 53 | Mrk 176 | NORM | 0.51 | ... |
| 54 | 2MASX J14054117+4026326 | NORM | 0.93 | ... |
| 55 | 2MASX J14482512+3559462 | HDD | 0.60 | ... |
| 56 | [GH2004] 9 | NORM | 0.75 | ... |
| 57 | Mrk 417 | NORM | 0.51 | ... |
| 60 | 2MASX J12384342+0927362 | HDD | 0.92 | ... |
| 61 | 2MASS J10405880+5817034 | NORM | 0.58 | ... |
| 62 | SDSS J164019.66+403744.4 | NORM | 0.63 | ... |

Note. — These candiates are selected from our SED modelings. Morph. - nuclear mid-IR extension derived from single-disk images by Asmus et al. (2014): n - not resolved, p - possibly extended, u - unknown extension, y - extended, and interferometry observations by López-Gonzaga et al. (2016): C - circular, E - elongated, U - marginally resolved or unresolved 12 $\mu$m emission.

dust emission. This behavior appears to be characteristic for at least 25–38% of relatively low-luminosity type-1 AGNs in Seyfert galaxies.

Based on the SED analysis, we can also put an upper limit on the fraction of objects with polar dust emission. As argued in Section 4.2.1, an AGN whose SED can be directly matched by any of the Lyu et al. (2017) intrinsic templates (i.e., $\tau_{V,ext} \sim 0$) is unlikely to have strong polar dust emission. There are 11 such objects in our whole sample, mak-

ing the polar-dust-free sample fraction about $\sim 20\%$. There are another 11 objects with $\tau_{V,ext} \sim 0.25$, or $f_{pol,10\mu m} \lesssim 30\%$. Accordingly, the proportion in our Seyfert-1 sample with significant polar dust emission should be no more than $\sim 70\%$, assuming that the values of $f_{pol,10\ \mu m}$ were underestimated among half of the samples with moderate polar dust emission.

Lastly, note that our intrinsic AGN templates are the descriptions of common features and the IR SEDs of polar-dust-free AGNs are expected to have additional variations among individual objects (e.g., see Figure 10 in Lyu et al. 2017). Bearing this in mind, we may conclude that about 1/3 of the type-1 nuclei studied in this work show evidence for strong emission by polar dust, about 1/3 show no evidence, and the remaining 1/3 have weaker or absent emission - they are ambiguous.

### 4.4.4 Comparison with Mid-IR Morphology-based Polar Dust Identification

Among the type-1 AGNs studied in this work, there are thirteen objects whose mid-IR morphology has been studied via interferometry by López-Gonzaga et al. (2016). Ten of them, Mrk 1239, IRAS 09149-6206, IRAS 13349+2438, I Zw 1, H 0557-385, IC 4329A, ESO 323-77, NGC 4151, NGC 7469, NGC 4593, are marginally resolved or unresolved at $\sim$12 $\mu$m. For one object, NGC 1566, the result is uncertain. Conclusive arguments on the existence of their polar dust emission cannot be reached due to limited UV coverages and signal-to-noise ratios. From our SED analysis, NGC 7469 and NGC 1566 may present very preminant polar dust emission with $f_{pol,10\ \mu m} \gtrsim 0.9$; IC 4329 A, NGC 4151, NGC 4593, and I Zw 1 have $f_{pol,10\ \mu m}$ $\sim$0.4–0.6; IRAS 09149-6206 and ESO 323-77 could be moderate polar dust emitter with $f_{pol,10\ \mu m} \sim 0.3$; Mrk 1239 has an IR SED best-desribed by the intrinsic normal AGN template so it is unlikely to have much polar dust emission. Besides NGC 3783, López-Gonzaga et al. (2016) found another type-1 AGN, NGC 4507, has evidence for polar dust emission but with a nearly circular morphology. The strong polar dust emission of NGC 4507 is also identified by us with $f_{pol,10\ \mu m} \sim 78\%$.

Asmus et al. (2016) studied the mid-IR emission extension for a large number of low-$z$ Seyfert nuclei at subarcsecond scales. Among their objects with extended mid-IR emission that are likely associated with polar dust emission, four type-1 nuclei have been studied

with SED analysis in this work: NGC 3227, NGC 4593, NGC 7469 and ESO 323-77. The first three objects have been successfully identified by us in Table 4.4 with $f_{\mathrm{pol,10\ \mu m}} \gtrsim 0.6$. The SED of ESO 323-77 is best fitted by the reddened WDD AGN template with $\tau_V \sim 0.25$ and $f_{\mathrm{pol,10\ \mu m}} \sim 0.30$, suggesting the likelihood of moderate mid-IR polar dust emission. In fact, very recently, Leftley et al. (2018) reported interferometric observations of ESO 323-77, arguing that ∼35% of its flux at 8–13 $\mu$m is polar extended. This is in good agreement with our SED analysis.

These consistent results demonstrate that the infrared SED analysis could be a promising and low-budget method to look for AGNs with polar dust emission.

### 4.4.5 Type-2 AGNs

Since most AGNs with evidence for the extended polar dust emission are type-2 objects (e.g., López-Gonzaga et al., 2016; Asmus et al., 2016), it is ideal to carry out some similar SED analysis of such objects. However, we do not have a robust understanding of the SEDs of the circumnuclear tori for these sources. Although current radiative transfer models can produce a wide range of SED features, they have too many degeneracies to be tested robustly particularly given the likelihood of contamination by the emission of star forming regions and AGN-heated polar dust. Consequently, we have had to leave type-2 AGN out of our study.

## 4.5 High-$z$ Type-1 AGNs with Peculiar SED Features

Recent observations have identified some high-$z$ type-1 AGNs with peculiar SEDs that cannot be easily reproduced by the classical AGN template with simple UV-optical reddening. Although we lack the detailed understanding of these types of object that has been accumulated for Seyfert galaxies, we show in this section how their SEDs are consistent with being shaped by polar dust that can be fitted by our model.

### 4.5.1 Extremely Red Quasars

From the Baryon Oscillation Sky Survey, Ross et al. (2015) identified a population of extremely red quasars (ERQs), using SDSS and WISE photometry. These objects are very luminous with AGN bolometric luminosities $\gtrsim 10^{13}\ L_{\odot}$, so that any host galaxy contamination at longer wavelengths can be ignored. In addition, outflows are commonly revealed by the UV to optical emission line profiles in this type of objects (Zakamska et al., 2016; Hamann et al., 2017). These characteristics of ERQs match our model assumptions, offering a unique test for the validity of our reddened templates.

Hamann et al. (2017) built the median SEDs of Type-1 ERQs and showed that they were inconsistent with the simple reddening of the UV-optical SED of the normal quasar template, assuming a SMC-like extinction curve (see their Section 5.5). In Figure 4.12, we compare their median ERQ SED for the non-BAL core-sample with our model templates used for low-$z$ Seyfert-1 nuclei. Without any fine-tunings of the dust geometry and grain properties, this composite SED can be matched by the reddened normal AGN template with $\tau_{\rm V} = 3.0$.

The success of our model for these extremely red quasars indicates that similar dust obscuration structures as well as the grain properties of polar dust might be shared among AGNs with a very wide range of luminosities ($L_{\rm AGN,bol} \sim 10^{8}$–$10^{13}\ L_{\odot}$).

### 4.5.2 AGNs with Mid-IR Warm-excess Emission

From a study of 24 $\mu$m-selected AGNs in the Local Cluster Substructure Survey, Xu et al. (2015b) showed that the UV-to-IR SEDs of most Type-1 AGNs at $z \sim$0.3–2.5 can be reasonably reproduced by combining three empirical templates that describe AGN, stellar and star formation components. However, an additional warm dust emission component ($T \gtrsim$50 K) was found for eight type-1 AGNs whose SEDs can not be fitted by combining the Elvis-like intrinsic AGN template and any SFG galaxy template. Similar SED behavior has also been reported in other high-$z$ samples (e.g., Kirkpatrick et al., 2015) as well as a few quasars in the Palomar-Green sample (Lyu et al., 2017).

Figure 4.13 shows an example for high-$z$ warm-excess AGNs in Xu et al. (2015b).

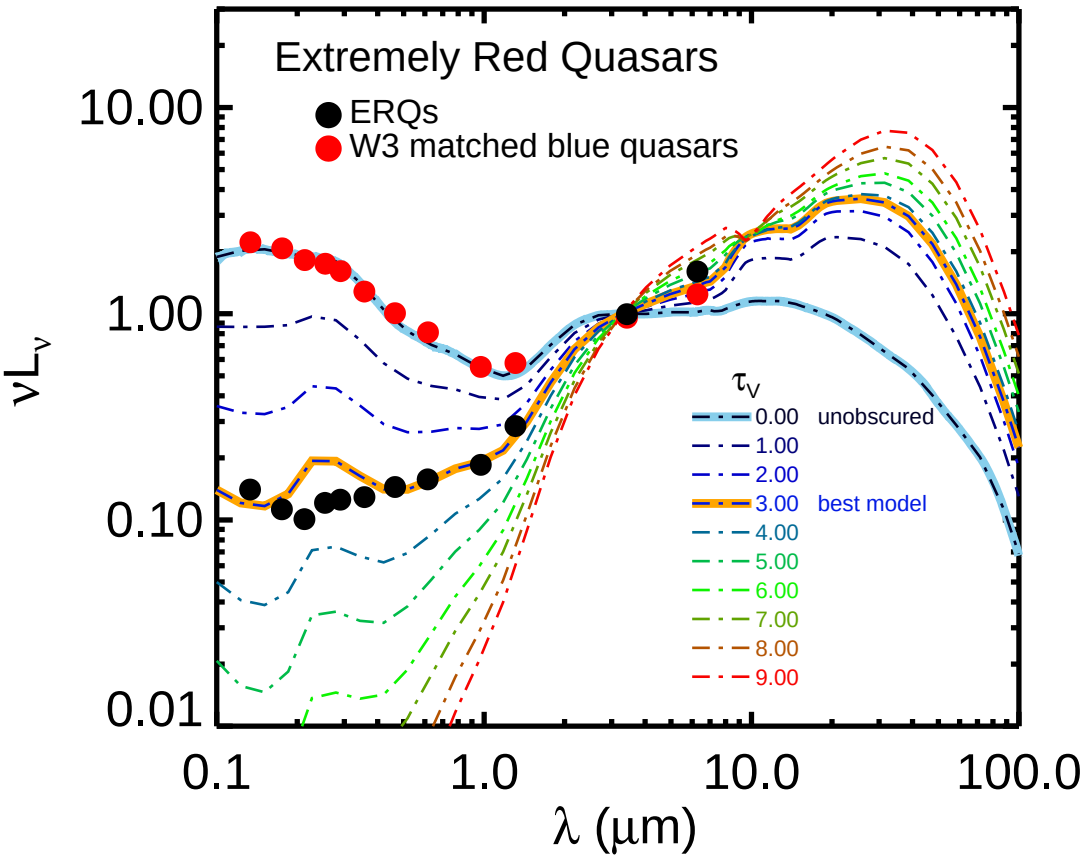


Figure 4.12 Reproduction of the median SEDs of extremely red quasars and blue quasars matched to the ERQ sample in the WISE W3 bands from Hamann et al. (2017). The polar dust component is configured with the same parameters as NGC 3783. The ERQ SED is best matched by the reddened normal AGN template with $\tau_V \sim 3.0$.

The contribution of the warm-excess emission to the total IR luminosity of this object is estimated to be 56% using the original Elvis-like AGN template (Xu et al., 2015b) and the Rieke et al. (2009) star-forming galaxy template. As demonstrated in this work, warm excess emission above the intrinsic AGN templates can be easily produced if there is polar dust around the nucleus. After allowing the AGN template to be obscured by our model, we made excellent fittings of the rest-frame 0.1–500 $\mu$m SEDs for all the warm-excess AGNs reported in Xu et al. (2015b).

The real origin of the warm-excess emission is not clear. Xu et al. (2015b) demon-

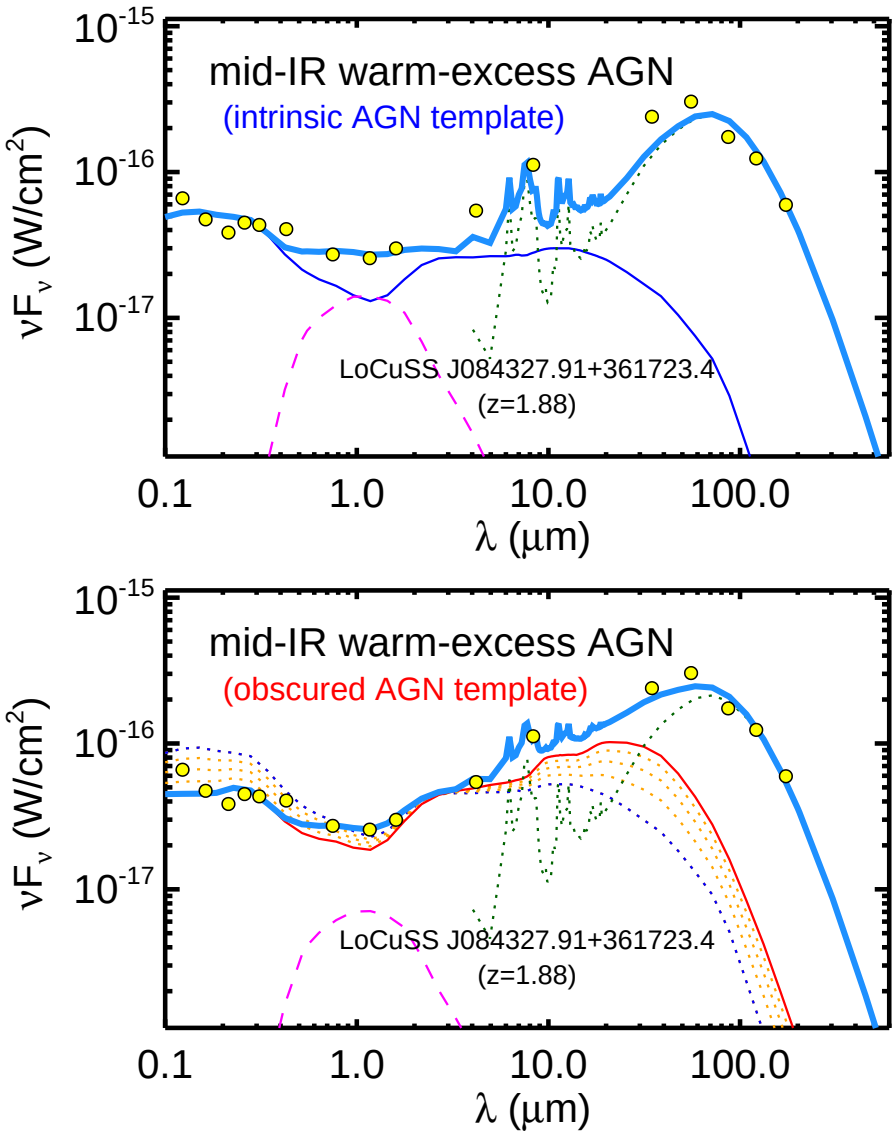


Figure 4.13 Best-fit results for a $z = 1.883$ type-1 AGN, LIRAS J084327.91+361723.4, in Xu et al. (2015b). Top: the results from fitting the SED with the intrinsic normal AGN template (blue solid thin line), the stellar template (magenta dashed line) and the star-forming template (green dotted line); the observed SED (yellow points) presents significant warm-excess emission in the mid-IR and far-IR compared with the final best-fit model (sky blue solid thick line). Bottom: the same fit as above, but with the addition of a standard template for emission by polar dust (red solid line).

strated that this warm component can be fitted by the spectrum of a parsec-scale starburst disk (Thompson et al., 2005; Ballantyne, 2008). In contrast, the success of our reddened AGN model suggests that this feature could be caused by the AGN heating of the sur-

rounding polar dust, a possibly common phenomenon in many objects.

### 4.5.3 Hot Dust-obscured Galaxies

An important discovery made by the *WISE* survey is the identification of very luminous hot dust-obscured galaxies, or hot DOGs (Eisenhardt et al., 2012; Wu et al., 2012). Compared with typical IR luminous galaxies, the SEDs of hot DOGs have very prominent hot dust emission with characteristic temperatures around 60–100K (e.g., Wu et al., 2012; Fan et al., 2016). From investigations of X-ray observations and rest-frame optical spectra, these objects are found to be powered by luminous but heavily reddened Type-1 AGNs (e.g., Stern et al., 2014; Ricci et al., 2017a; Wu et al., 2018).

Fan et al. (2016) presented the IR SEDs of 22 submm-detected Hot DOGs and suggested that they can be described by the CLUMPY torus model (Nenkova et al., 2008a,b) plus a cold dust component to represent the host galaxy star formation. Given the large number of free parameters of their models, we would like to see if our semi-empirical templates can provide an alternative solution.

Figure 4.14 presents a median IR SED of hot DOGs (Fan et al., 2016). To represent the galaxy far-IR emission, we adopted the empirical star-forming galaxy SED library derived by Rieke et al. (2009). Since the reddened AGN templates trained for NGC 3783 do not contain such strong hot dust emission, we allowed the geometry of the extended dust component to be variable but left the dust grain properties unchanged. Similar to the case for NGC 3783 (see Section 4.2.4), we used the MCMC algorithms to find the best-fit parameters. The results are summarized in Table 4.5. Reasonable fittings can be achieved with a broad range of parameters, such as a dust density profile $r^{-1.5}$, and outer-to-inner radius $Y = 5000$. Compared with most Seyfert nuclei, the fitted polar dust component for AGNs in hot-dust-obscured galaxies has a steeper density profile ($n \propto r^{-0.5} \rightarrow r^{-1.5}$) and more extended distribution ($Y \sim 500 \rightarrow 5000$).

Are the best-fit parameters of our model to match the Hot DOG SED physical? Assuming the central engine has $L_{\rm AGN,bol} = 10^{14} L_{\odot}$, the suggested extended dust would extend to kpc scales. Interestingly, ALMA observations of [CII] emission in the most luminous hot DOG W2246−0526 show a uniform and highly turbulent ISM, suggesting isotropic

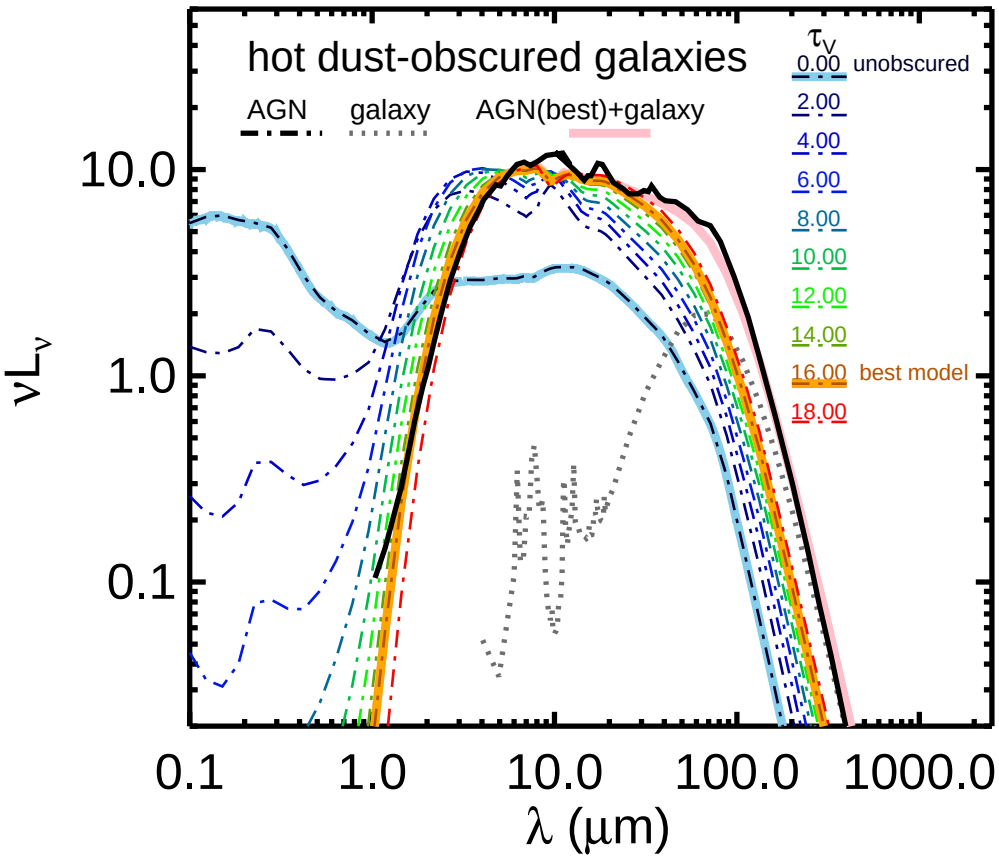


Figure 4.14 Reproduction of the median SED of hot dust-obscured AGNs from Fan et al. (2016). This SED is roughly matched with the reddened AGN template with $\tau_V \sim 16.0$ (orange thick line) plus a moderate star-formation template (grey dotted line) in the far-IR. Compared with other objects, the polar dust geometry to reproduced the Hot DOG SEDs features a steeply decreasing density profile ($n \sim r^{-1.5}$) and more extended structure ($Y \gtrsim 1000$).

galaxy-scale outflows (Díaz-Santos et al., 2016) which is consistent with our argument that the extended dust distribution might be related to AGN outflows. Hot DOGs are suggested to live in overdense environments based on submm (Jones et al., 2014, 2015) and near-IR observations (Assef et al., 2015). It is possible that these objects represent a special phase of galaxy evolution, e.g., galaxy mergers, that could change the gas and dust distribution around the AGNs compared with the relatively undisturbed environment for typical Seyfert nuclei. Indeed, complex velocity structures based on CO(4-3) emission lines are

Table 4.5. Suggested Model Parameters for Hot Dust-Obscured Galaxies

| Parameter | Label | Adopted Value | MCMC output |
|---|---|---|---|
| $r_{\rm in}$ temperature | $T_{\rm in}$ | **1500** K | |
| density profile | $\alpha$ | 0.50 | $1.49^{+0.46}_{-0.45}$ |
| outer-to-inner radius | $Y$ | 5000 | $4778^{+4762}_{-3323}$ |
| silicate:graphite mixture | | **0.53:0.47** | |
| maximum grain size | $a_{\rm max}$ | **10** $\mu$m | |
| minimum grain size | $a_{\rm min}$ | **0.04** $\mu$m | |
| input radiation SED | | **normal** | |
| optical depth | $\tau_{\rm V}$ | 16 | $17.16^{+1.64}_{-1.97}$ |
| $\log(L_{\rm SF,temp}/L_{\odot})$ | | 11.5 | $11.49^{+0.46}_{-0.44}$ |

Note. — We use boldfaces to indicate assumed parameter values that do not go to MCMC parameter space sampling.

reported in hot DOGs, suggesting a violent environment in such systems (Fan et al., 2018). Lastly, the SED model selected the Rieke et al. (2009) star-forming galaxy template with $\log(L_{\rm SF,temp}/L_{\odot}) \sim 11.5$, consistent with expectations for IR luminous galaxies at the hot DOG redshifts (Rujopakarn et al., 2013).

Although hot DOGs are claimed to exist only at high-$z$ (e.g., Eisenhardt et al., 2012; Wu et al., 2012), type-1 AGNs with similar SED features could exist at low-$z$. In Section 4.3.3, we note that two low-$z$ Seyfert-1 nuclei, IRAS 13349+2438 ($z = 0.11$), 2MASX J14492067+4221013 ($z = 0.18$), present strong hot dust emission for which our model with parameters set for NGC 3783 did not produce reasonable fits. In Figure 4.15, we present the SEDs of these objects and the best-fit model with the reddened AGN templates developed for hot DOGs. Due to their relatively low AGN luminosities, the stellar contamination in the near-IR cannot be ignored so that the apparent hot dust emission is not as strong as the case of high-$z$ hot DOGs. However, these objects have much stronger hot dust emission compared with the normal AGN template. Together with the stellar template, our hot dust-obscured AGN templates explain these SEDs well. Thus, we suggest AGNs with some extreme SEDs similar to high-$z$ hot DOGs do exist at low-$z$.

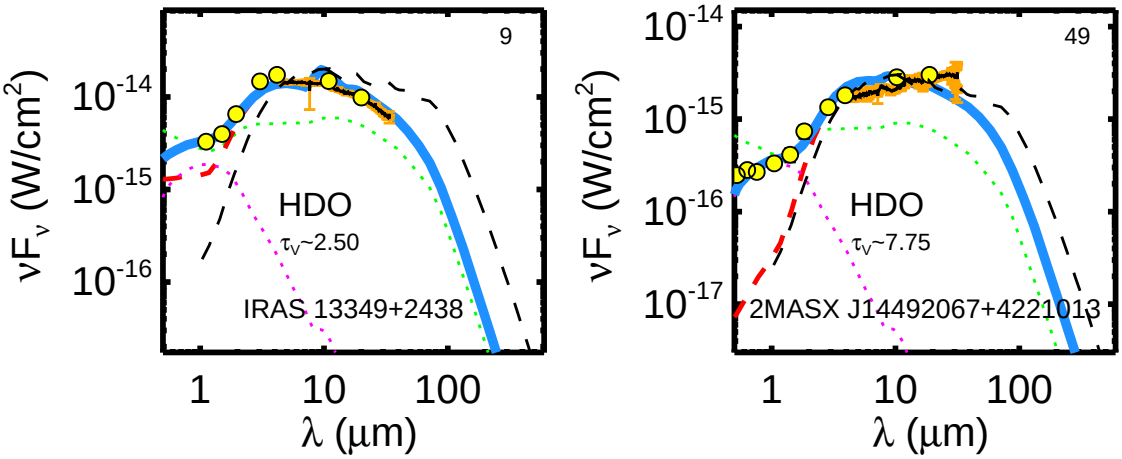


Figure 4.15 SEDs and the best-fit models of low-$z$ candidate hot dust-obscured (HDO) AGNs. The legend follows Figure 4.5. In each panel, we plot the composite SED template for hot DOGs from Fan et al. (2016) as a black dashed line.

## 4.6 Discussion

We have shown that the IR SEDs of most type-1 AGNs regardless of luminosity can be fitted by a small set of templates for the accretion disk and torus, supplemented by an extended component to represent emission by polar dust. This result indicates that the differences in the SEDs between Seyfert-1 nuclei and type-1 quasars are largely the result of the absorption of UV energy by polar dust and its reradiation in the IR. As argued by e.g., Stalevski et al. (2016), the IR SEDs of the optically-thick torus would stay almost the same for any lines of sight not blocked by the torus. Our intrinsic AGN templates should be faithful descriptions of the torus emission in type-1 systems with a range of possible observing angles. The suggested polar dust for most objects can be modeled with the similar density profiles and grain properties. Therefore, the diverse broad-band IR SED features of many type-1 AGNs are only determined by two free parameters: the AGN intrinsic IR SED type and the level of surrounding obscuration. These results have the following implications.

### 4.6.1 Interpreting the AGN Mid-IR Emission

Previous AGN-related studies mostly only consider the effects of the extinction in the UV-optical bands, leaving the IR SED unchanged (e.g., Assef et al., 2010; Xu et al., 2015b). An embedded assumption for such an approach is that the dust is distributed very far away from the AGN and the reprocessed emission is weak and possibly mixed with the host galaxy emission heated by stars. However, as suggested in this work, if the obscuration occurs in the vicinity of the AGN, it could naturally explain the polar dust emission in nearby AGNs as a result of energy balance and reconcile the diverse broad-band IR SED features of various AGN populations. This IR-reprocessed emission can be an important contributor to the AGN-heated IR features besides the torus.

Various radiative transfer models have been proposed to reproduce the AGN IR emission. For simplicity, the geometric structure of the nuclear dust is commonly assumed to be doughnut-like and numerous dusty torus radiative transfer models have been developed to produce the AGN-heated IR SEDs (e.g., Fritz et al., 2006; Nenkova et al., 2008a; Alonso-Herrero et al., 2011; Stalevski et al., 2012; Siebenmorgen et al., 2015). Although they have matched the SEDs or spectral observations (e.g., Fritz et al., 2006; Nenkova et al., 2008b; Alonso-Herrero et al., 2011; Siebenmorgen et al., 2015), most such comparisons are limited to the mid-IR bands and strong parameter degeneracy exists (e.g., see discussions in Hoenig 2013 and Netzer 2015). Additionally, some work found that the torus models alone are typically not enough to reproduce the complete AGN IR SEDs of bright quasars (e.g., Mor et al., 2009; Leipski et al., 2014).

An important support for the clumpy torus models comes from their ability to reproduce the behaviors of AGN mid-IR silicate features, especially the silicate emission seen in some type-2 AGNs (e.g., Nikutta et al. 2009, but see Feltre et al. 2012). However, the possible existence of AGN-heated polar dust makes the interpretation of the origin of the mid-IR spectral features ambiguous. In fact, as suggested by, e.g., Sturm et al. (2005), the silicate emission feature observed in Seyfert nuclei could come from low-optical-depth dust located in the AGN narrow-line regions. The success of our model supports this possibility (also see e.g., Efstathiou 2006, Schweitzer et al. 2008).

For a single object, the AGN-heated IR spectral features are a result of a mixture of intrinsic variations of the torus properties, possible IR-reprocessed emission by the polar dust and some specific observing angle. With these complications as well as the torus model degeneracies, the fittings of individual observations provide little information on the credibility of the model. Instead, we suggest that the best test is to see if the torus model can reproduce the empirical unobscured AGN templates, such as the three in Lyu et al. (2017). The objects used to derive the templates do not have evidence of obscuration, so that (1) the possibility of the polar dust emission is minimized and (2) these templates represent a face-on view of the system. In addition, by constructing average templates, variations of individual objects are smoothed out. In other words, the model degeneracies and observational uncertainties are greatly reduced.

### 4.6.2 Dust-covering Factor of Type-1 AGNs

A common tool to study the AGN dust environment is the so-called dust-covering factor, typically measured by the relative flux ratios between the near- to mid-IR band and the optical bands (e.g., Maiolino et al., 2007; Treister et al., 2008; Mor & Trakhtenbrot, 2011; Roseboom et al., 2013; Lusso et al., 2013). Many authors have tried to use this parameter to explore the possible evolution of the torus, assuming the AGN near- to mid-IR emission comes from the torus and the optical emission originates from the accretion disk (e.g., Lawrence, 1991; Simpson, 2005; Assef et al., 2013). Given the direct detections of the polar dust (Braatz et al., 1993; Cameron et al., 1993; Raban et al., 2009; Hönig et al., 2012, 2013) and its possibly frequent occurrence inferred in this work as well as e.g., Asmus et al. (2016), we should be cautious about the interpretations of the AGN IR-to-optical flux ratios.

We can obtain some rough idea on how significantly the AGN IR-to-optical flux ratio can be changed by the polar dust. Figure 4.16 presents some characteristic tracers of dust covering factors calculated from our reddened AGN model as a function of optical depth $\tau_V$. For the direct observed values, we divided the IR luminosity, $L_{IR}$, at $\lambda = 3$, 6.7, 15 $\mu$m by the apparent AGN optical luminosity, $L_{opt}$, at 5100 Å of reddened templates for normal, WDD and HDD AGNs. In all cases, the IR-to-optical flux is found to increase

exponentially with the optical depth. With moderate extinction ($\tau_V \lesssim$1–2), the change caused by polar-dust obscuration and emission would easily exceed the intrinsic variations of the torus in a type-1 AGN. Conversely, if we use the intrinsic (unobscured) luminosity at 5100 Å to represent the $L_{\rm opt}$, the integrated optical depth of the polar dust component would have limited influence on $L_{\rm IR}/L_{\rm opt}$, especially at shorter wavelengths. With $\tau_V$ ranges from 0 to 5, the values of $L_{3.4\ \mu{\rm m}}/L_{0.51\ \mu{\rm m}}$ are changed by a factor of 0.94, 0.91 and 1.26 for normal, WDD, HDD AGNs. For $L_{6.7\ \mu{\rm m}}/L_{0.51\ \mu{\rm m}}$, the changes are 1.53, 1.81, 2.67. For $L_{15\ \mu{\rm m}}/L_{0.51\ \mu{\rm m}}$, the corresponding values are 2.68, 4.67, 7.28. Since the SED of polar dust emission peaks at $\lambda \sim 26\ \mu$m (Section 4.4), its effects would be only important for the dust covering factors of warm and cold dust.

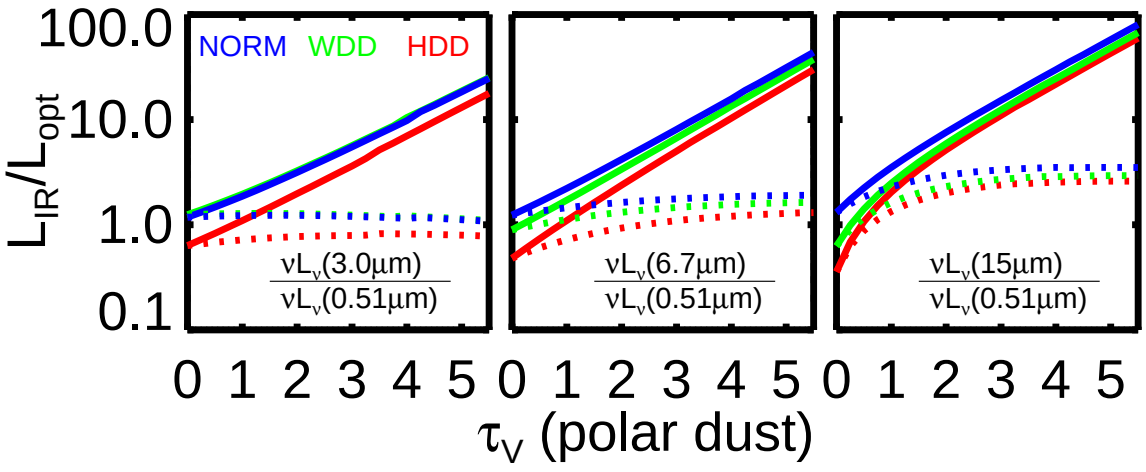


Figure 4.16 MIR-to-optical luminosity ratios ($L_{\rm IR}/L_{\rm opt}$) as a function of optical depth of the extended dust component ($\tau_V$) from our model for normal (blue), WDD (green) and HDD (red) AGNs. We compute these relations with the apparent (obscured) and intrinsic (unobscured) values of $L_{\rm opt}$ and show them separately as solid and dotted lines.

Nevertheless, as discussed in Section 4.2.2, the optically-thin IR emission from a dust component with different dust-covering factors can be easily reproduced by changing its overall optical depth $\tau_V$ with an assumption of a spherical dust distribution. Given this degeneracy, it is impossible to get a definite estimation of the dust geometry, like its covering factor, from the SED alone when the IR emission is not optically-thick.

Besides the possible existence of polar dust, there are many other factors that can change the value of $L_{\rm IR}/L_{\rm opt}$. In the optical band, the AGN emission can be modified

by the host galaxy contamination, dust obscuration at different physical scales with uncertain extinction curves, or even some short-term variability. Based on a 3D radiative transfer model, Stalevski et al. (2016) explored how the anisotropic emission of the dusty torus and the accretion disk could influence the estimation of real dust covering factor from $L_{\rm IR}/L_{\rm opt}$, showing that their relation could be non-linear and depend strongly on the assumed torus optical depth. Considering these complications, it is difficult to make conclusive arguments on the meaning of $L_{\rm IR}/L_{\rm opt}$ traced by the simple colors derived from a few photometric bands.

### 4.6.3 AGN X-ray Obscuration and Polar Dust Optical Depth

The extinction caused by the polar dust component in many AGNs is likely associated with the behavior of their X-ray obscuration. To explore this possibility, we collected the literature measurements of the absorbing column density, $N_{\rm H}$, and compared them to the derived integrated optical depth of the polar dust component (derived purely from IR SED fittings) in Figure 4.17. 41 out of 64 nearby Seyfert-1 nuclei in our sample are found to have good measurements. Among them, besides 3C 219 (taken from Comastri et al. 2003) and Mrk 1239 (taken from from Corral et al. 2011), the measurements of all others are collected from Ricci et al. (2017b).

First we check if the X-ray obscuration and the possible optical extinction caused by polar dust are consistent. As argued by Shimizu et al. (2018), most type-1 AGNs are unobscured in the X-ray, i.e., $N_{\rm H} \lesssim 10^{22}$ $\mathbf{cm^{-2}}$. If we adopt the AGN value of $N_{\rm H}/A_{\rm V}$ from Maiolino et al. (2001b), this means the corresponding optical extinction should satisfy $A_V \lesssim 1$. By this criteria, 28 out of the 41 objects ($\sim 68\%$) have low extinction both in the X-ray and optical. In addition, 9 out of 41 ($\sim 22\%$) are X-ray absorbed without much polar dust extinction. For most X-ray obscured Seyfert-1 nuclei for which the NGC 3783-like model works well, a value of $N_{\rm H}/A_{\rm V} \gtrsim 10^{23}$ $\mathbf{cm^{-2}/mag}$ seems favored, which is much higher than the typical values found for the Galactic ISM (e.g., $\sim 2.2 \times 10^{21}$ $\mathbf{cm^{-2}/mag}$; Güver & Özel 2009). This nicely fits the picture that small grains, which are most efficient carriers for the extinction in the optical band, can be easily destroyed by their direct exposures to the AGN radiation. The effect of large grains agrees with the behavior of

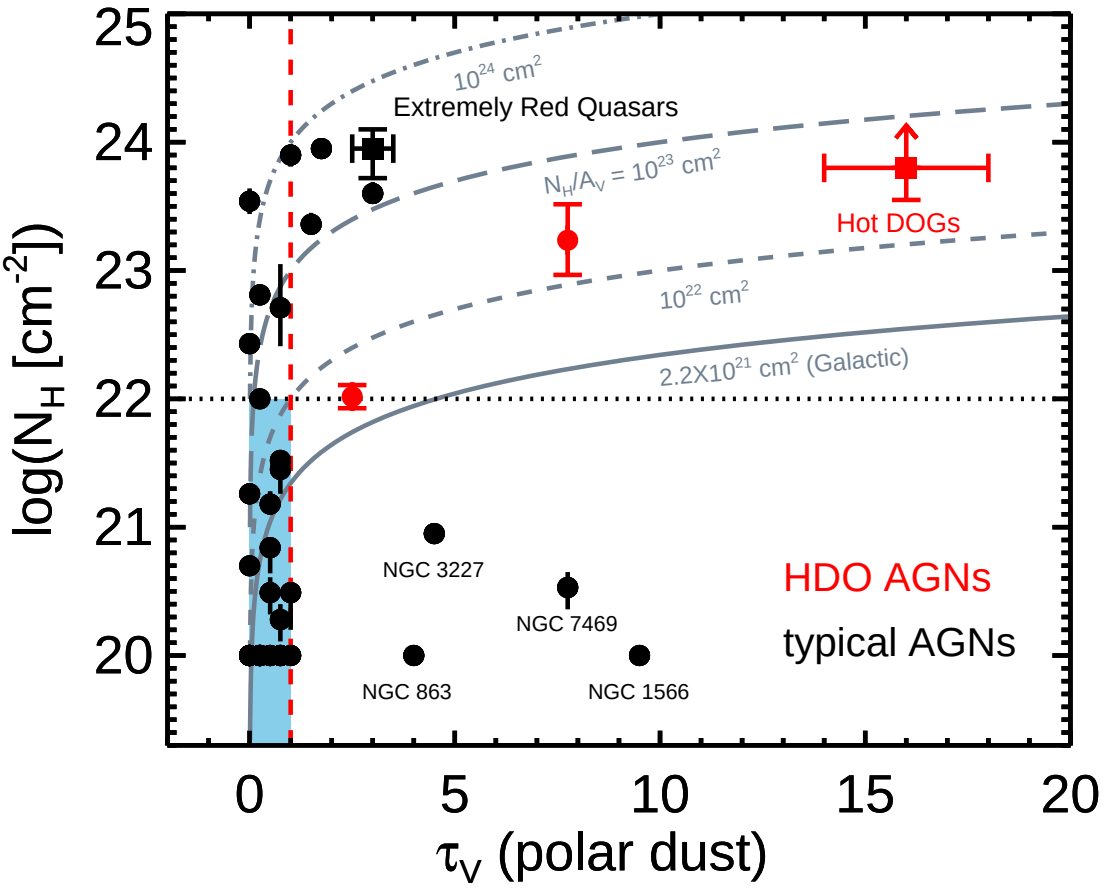


Figure 4.17 The distribution of gas column density and polar dust optical depth of the low-$z$ Seyfert-1 (dots) and the high-z reddened populations (squares). We use the black color to indicate objects whose IR SEDs are best described by the NGC 3783-like model and red colors to indicate the HDO AGNs. The blue shaded region represents low-extinction type-1 AGNs with $A_{\rm V} \lesssim 1$ mag and $N_{\rm H} \lesssim 10^{22}$ $cm^2$.

the nine X-ray-absorbed objects with small $A_{\mathbf{V}}$. Meanwhile, there are four outstanding outliers with high $\tau_{\mathbf{V}}$ but very low $N_{\mathbf{H}}$. However, this is also not a surprise since $\tau_{\mathbf{V}}$ describes the *average* polar dust optical depth along all possible LOSs. If the polar dusty clouds distribute close to the edge of the ionization core or are simply clumpy, the AGN X-ray corona could be unobscured along some lucky observing angles while the amount of polar dust is still significant. Consequently, we conclude that there is no obvious tension between the literature results on the X-ray obscuration and the optical depth of the polar dust component inferred by our SED model.

We can also compare the behaviors of the high-$z$ extremely red quasars and hot dust-

obscured galaxies discussed in Section 4.5 with these low-z Seyfert-1 nuclei to further check if they are also similar (or not) in the X-ray. Taking the gas column density measured for the stacked X-ray images from Goulding et al. (2018), a typical value of $N_{\mathbf{H}}/A_{\mathbf{V}}$ for extremely red quasars is $\sim 3 \times 10^{23}$ $\mathbf{cm^{-2}/mag}$, consistent with the trend of most X-ray obscured Seyfert-1 AGNs in our sample. In other words, besides a polar dust configuration resembling NGC 3783, these high-$z$ extremely red quasars also share the relation between X-ray gas obscuration and optical dust extinction of typical reddened Seyfert-1 nuclei.

In contrast, hot DOGs might be different. We computed an average $N_{\mathbf{H}} \gtrsim 6 \times 10^{23}$ $\mathbf{cm^{-2}}$ for high-$z$ hot DOGs with reported measurements from the literature (see Vito et al. 2018 and the references therein). Combined with the optical depth of polar dust component estimated from our SED modeling, this suggests a $N_{\mathbf{H}}/A_{\mathbf{V}} \gtrsim 4.0 \times 10^{22}$ $\mathbf{cm^{-2}}$. Together with the measurements of two low-$z$ candidates, these HDO objects have $N_{\mathbf{H}}/A_{\mathbf{V}}$ values of $\sim 10^{22}$–$10^{23}$ $\mathbf{cm^{-2}/mag}$, which are lower than those of typical Seyfert-1 nuclei (as well as the extremely red quasars) but still higher than the Galactic values. Perhaps the hot DOGs do represent a different phase of AGN-host evolution compared to typical Seyfert-1 nuclei (as well as extremely red quasars) so that their polar dust grains are not removed as significantly as the latter. For example, the host galaxies of HDO AGNs could be very obscured so that the AGN radiation is not efficient enough to destroy most dust distant from the nucleus. Alternatively, considering the large extent of the outflows in these cases, there could be some channels for dust production, e.g., (post-)AGB stars and/or supernovas, that mitigate the effects of dust destruction by the AGN.

### 4.6.4 AGN Structures and Unification

An anisotropic obscuration structure composed of optically-thick dust, typically pictured as a torus, provides a simple solution to unify the behaviors of different types of AGNs (Antonucci, 1993; Urry & Padovani, 1995). Besides the optically-thick torus, this work suggests the presence of an extended dust distribution that modifies both UV-optical and IR properties of the AGN. We can get some rough ideas on the physical scales associated with the extended dust distribution and discuss its relation with other known AGN components.

Based on our results, the observations of many type-1 AGNs can be reproduced by

assuming the same polar dust model configuration featuring a density profile $r^{-0.5}$ , outer-to-inner radius $Y = 500$ and temperature at the inner boundary $T \sim 1500$ K. For an $L_{\odot} = 10^{11}$ AGN, the dust responsible for the extended obscuration has a maximum size $r_{\rm out} \sim 0.1$ kpc, which is about one order of magnitude larger than the size of cold dust in the AGN torus ($r_{\rm torus,cold} \sim 10$ pc; see Section 4.2 in Lyu & Rieke 2017). AGN-driven winds or outflows can easily distribute dust around the torus to such scales.

One likely location for the polar dust grains is the narrow-line-region clouds. In fact, the required $A_{\rm V} \lesssim 5$ mag for most type-1 AGNs can be easily reproduced by combining the typical NLR column density ($N_{\rm H} \sim 10^{20}$–$10^{21}$ cm$^{-2}$) with the assumption of the classical value of $N_{\rm H}/A_V \sim 2.2 \times 10^{21}$ cm$^{-2}$/mag in the Galactic ISM (Güver & Özel, 2009). Alternatively, if we adopt $N_{\rm H}/A_V \gtrsim 10^{22}$ cm$^{-2}$/mag for Seyfert galaxies (Maiolino et al., 2001b) and assume the NLR cloud density $\sim 100$ cm$^{-3}$, the required physical scale of the line-of-sight dusty clouds would span $\sim$150 pc, which is also realistic and consistent with the value estimated above.

In Figure 4.18, we illustrate the various dust components surrounding a typical Seyfert nucleus. Very close to the accretion disk, dust could not survive due to evaporation at high temperatures. Since the accretion disk emission is not isotropic, some concave shape of dust-free regions is expected above and below the accretion disk. In the equatorial direction, we expect a torus-like component. Thanks to the shielding against the direct AGN emission by very optically-thick ($\tau_{\rm V} \gtrsim$20–50) clouds, a range of dust grain properties is expected within the torus. Along the polar direction, as discussed in Section 4.2.2, only large dust grains might survive. In other words, we would expect the dust properties are changing along different observing angles (see Baskin & Laor, 2018), which may lead to diverse AGN extinction curves as reported in the literature (e.g., Hall et al., 2002; Richards et al., 2003; Hopkins et al., 2004; Gaskell et al., 2004; Czerny et al., 2004; Gaskell & Benker, 2007). In regions far away from the nucleus, e.g., the galactic ISM at (sub-)kpc scales, the influence of the AGN is minimal so that classical dust properties are expected. Between the torus and the galactic ISM, there exists an extended dust component with low optical depth ($\tau_{\rm V} \lesssim$5) which causes the LOS obscuration and the polar dust emission seen in type-1 AGNs. In reality, there should no clear boundaries between these

components and they can exchange dust by various feedback mechanisms, e.g., inflows or outflows. Although our sketch shows a clumpy environment, the actual configuration could have other forms, such as filaments (Wada et al., 2009; Wada, 2012). In addition, the shape of the polar dust distribution could deviate strongly from isotropic symmetry, e.g., having some dust covering factor.

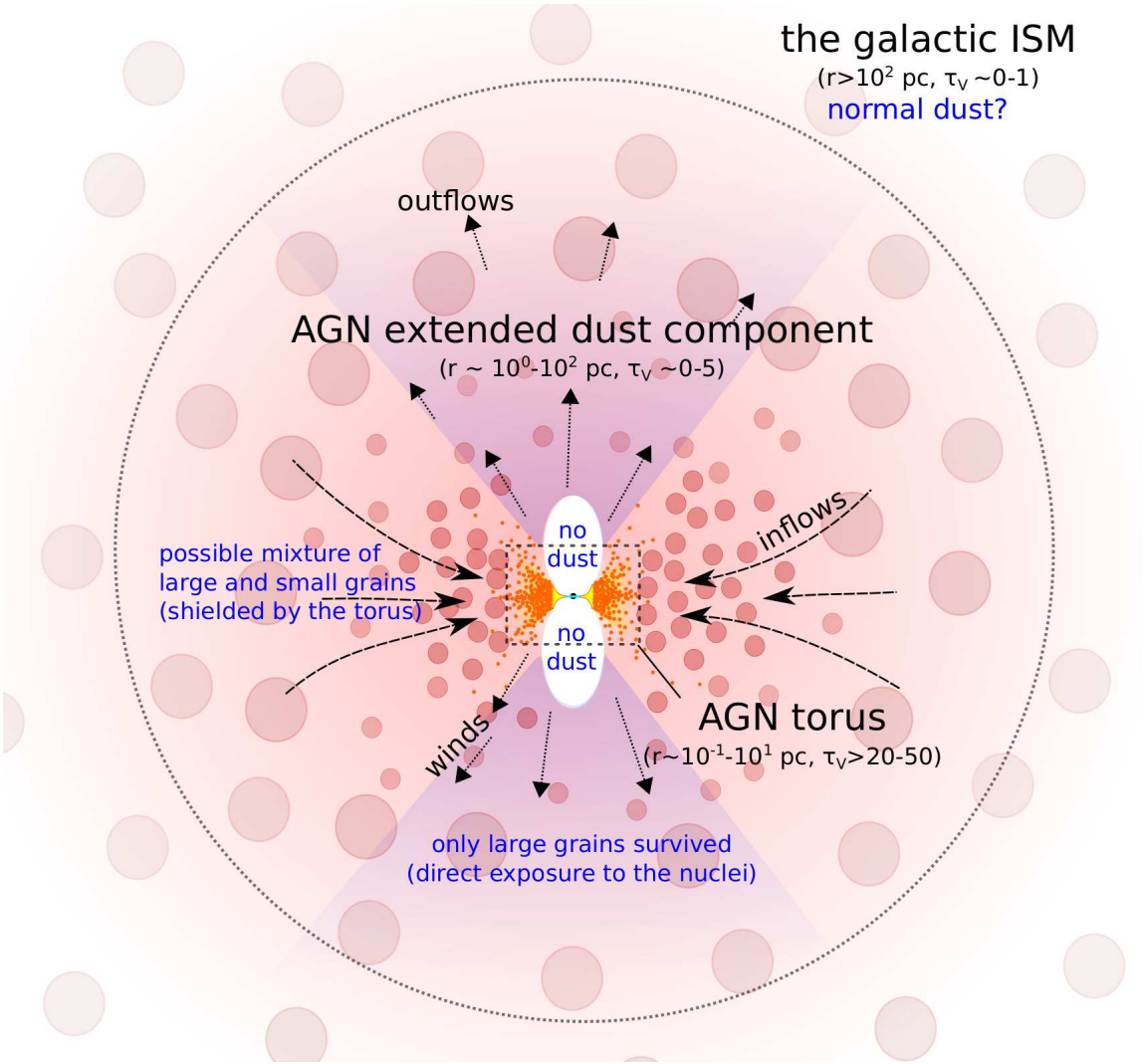


Figure 4.18 Schematic drawing for the dust environment around a typical Seyfert-like nuclei. See the text for details.

The intrinsic IR emission of AGNs at wide ranges of luminosity ($L_{\rm AGN,bol} \sim 10^8$–$10^{14}\ L_\odot$) and redshift ($z \sim$0–6) appears to be described well by a limited family of SED shapes. In Lyu et al. (2017), we demonstrated that the intrinsic IR emission of unobscured

quasars can be represented by a similar set of templates independent of redshift. Based on the low-$z$ Palomar-Green sample, complete IR SED templates have been built and tested for AGNs with $L_{\rm AGN,bol} \gtrsim 10^{11}\ L_{\odot}$. With the results obtained in this work, their validity is extended to Seyfert-1 nuclei and some peculiar AGN populations. Besides the torus SED variations, the IR SED differences are caused by an extended dust component that might reside in NLR clouds. Consequently, it is not necessary to invoke any new component that is only found in some special groups of AGNs.

### 4.6.5 The Diverse Dust Environments of AGNs

With our previous study of unobscured quasars (Lyu et al., 2017; Lyu & Rieke, 2017) and the results on other type-1 AGN populations obtained here, we have found that the IR properties of AGNs are not only determined by the observing angles, but also caused by the intrinsic variations of the torus and the different contributions of polar dust.

As illustrated in Figure 4.19, dust environments of AGNs can be grouped into three different scenarios, characterized by the obscuration along the face-on direction:

- unobscured AGNs:

  The IR properties of such systems are dominated by a torus-like structure without much dust distributed along the polar direction. It is likely that AGN activity is extremely strong, blowing out the dusty gas or simply destroying most dust along the polar direction. The photons from the central engine can be directly seen from a face-on observing angle. Typical examples are luminous blue quasars, where there is little extinction in the UV-optical bands.

  Due to its relatively compact size, the behavior of the torus is mainly determined by accretion parameters. As shown in Lyu et al. (2017), the intrinsic IR SEDs of unobscured quasars present clear variations and might be related to different AGN properties (e.g., luminosity and Eddington ratios). Among Seyfert nuclei, we have also seen the appearance of both normal and dust-deficient AGNs, suggesting the torus structures among Seyfert-1 populations are not exactly the same.

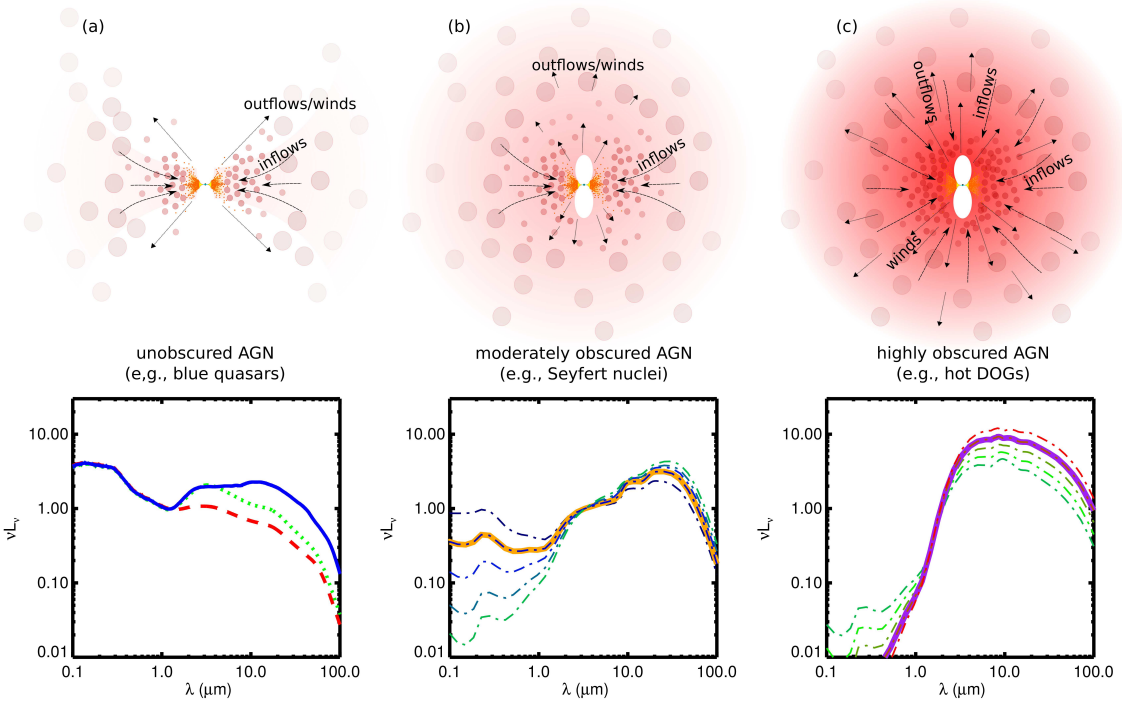


Figure 4.19 Schematic drawings for the dust environment around an AGN (upper panels) and typical SEDs (lower panels). In column (a), we present the suggested dust environment for an unobscured AGN and example SEDs for optically-blue quasars from Lyu et al. (2017) (blue solid line: normal AGN, green dotted line: WDD AGN, red dashed line: HDD AGN). Column (b) shows the corresponding picture and SEDs for a moderately obscured AGN. We present the model SEDs for typical Seyfert-1 nuclei with $\tau_V \sim$1–5. Column (c) is the description of a highly obscured AGN. The SEDs are from our model for the hot dust-obscured AGNs with $\tau_V \sim$5–20. See the text for details.

- moderately-obscured AGNs:

  Besides the torus, there exists an extended dust component ($r \sim 10^2$ pc) with low-optical depth ($\tau_V \gtrsim$0–5), which could be AGN dusty outflows, winds or dusty narrow line regions. Along the polar direction, the dust obscures the central engine, resulting in mid-IR excess emission and some moderate level of optical extinction if the observation is not made through some lucky dust-free LOS.

  Most AGNs, i.e., those in Seyfert galaxies, will fall into this category. In relation to unobscured quasars, our SED analysis suggested that Seyfert nuclei frequently have strong polar dust emission, indicating an extended dusty component that can be heated by the central engine. In fact, there are observational suggestions that

the AGN NLR could disappear at very high luminosities (Netzer et al., 2004). If we believe these NLR clouds are dusty, a decreasing frequency of AGNs with polar dust emission with increasing luminosity should be expected.

- highly-obscured AGNs:

  The AGN-heated dust in such systems can be very extended ($r \sim 10^3$ pc) with high optical depth ($\tau_V$ ~5–20), which might be a result of, e.g., galaxy mergers. The gravitational torque of large-scale interaction can bring a substantial amount of galactic ISM towards the nucleus which can be collide with the AGN outflows, resulting in a very turbulent environment that changes the circumnuclar dust density profile. These objects present clear evidence of UV-optical obscuration and strong near- to mid-IR dust emission. Typical examples are AGNs in hot DOGs.

In this picture, the torus is formed and maintained during the black hole accretion (e.g., Hopkins et al., 2012, and references therein). An extended dust component surrounding the AGN nucleus naturally bridges the torus and the host galaxy ISM. Both AGN and galaxy feedbacks may modify the properties of this component, resulting in the changing obscuration behaviors at different phases of galaxy evolution as suggested by many previous studies (e.g., Sanders et al., 1988b,c; King, 2003; Hopkins et al., 2010, 2016).

## 4.7 Summary and Conclusions

Motivated by the commonly seen UV-optical obscuration and the discoveries of polar dust emission in a few nearby Seyfert nuclei, we have proposed an empirically-driven model to produce the SEDs of reddened type-1 AGNs. The intrinsic AGN templates in Lyu et al. (2017) have been assumed as reasonable choices for polar-dust-free type-1 AGNs. With radiation transfer calculations, we obscured them by an extended dusty structure with a power-law density profile and large dust grains. This model naturally:

1. reproduced the nuclear UV to mid-IR SED (Prieto et al., 2010) and polar dust emission strength (Hönig et al., 2013) for the type-1 AGN in NGC 3783;

2. fitted the IR SEDs of a large sample of low-$z$ Seyfert-1 nuclei with the mid-IR emission dominated by the AGN;

3. reproduced the UV to mid-IR composite SEDs of the SDSS/*Spitzer* type-1 AGNs;

4. matched the composite SED of extremely red luminous quasars in Hamann et al. (2017);

5. explained the warm-excess dust emission seen in some high-$z$ type-1 AGNs, as first reported by Xu et al. (2015b);

6. reproduced the IR emission template of hot dust-obscured AGNs proposed by Fan et al. (2016).

Our main conclusions are as follows:

1. The broad-band IR SEDs of low-$z$ Seyfert-1 nuclei and some high-$z$ type-1 AGNs with peculiar SED features can be reconciled with the quasar intrinsic AGN templates by adding the IR-reprocessed emission of polar dust. It is possible that AGNs over a broad range of redshift and luminosity have a similar dust environment that features a circumnuclear torus plus an extended dust component.

2. The polar dust emission could be a natural result of the commonly-seen UV-optical obscuration among Seyfert-1 nuclei. This statement is supported by our detailed SED analysis of NGC 3783 and the our successful fitting of the composite SEDs of the SDSS/*Spitzer* Seyfert-1 AGN sample. Surprisingly, we found the same radial density profile ($n \propto r^{-0.5}$, $r_{\rm out}/r_{\rm in} \sim 500$) and dust grain properties ($a_{\rm max} = 10$ $\mu$m, $a_{\rm min} = 0.04$ $\mu$m) of the extended dust component works for most Seyfert-1 nuclei.

3. The primary factor to determine the behavior of the polar dust emission is the overall optical depth. The emission SED of the AGN polar dust component peaks around 26 $\mu$m with a characteristic temperature at $T \sim 113$ K, leaving strong mid- to far-IR warm-excess emission signatures above intrinsic AGN templates for some objects. The observed size of polar dust emission is a function of wavelength.

4. Our SED analysis provides an effective method to search for AGNs with polar dust emission. Among the 64 Seyfert-1 nuclei studied in this work, we found $\sim$1/3 of them have significant polar dust emission that contributes at least half of the AGN emission at $\sim 10$ $\mu$m, about another 1/3 show no evidence with IR SEDs matched by the intrinsic templates, and the remaining 1/3 have weaker or absent polar dust emission - they are ambiguous.

5. The reddened type-1 AGN model trained for NGC 3783 not only fitted the SEDs of most Seyfert-1 nuclei but also worked reasonably well to reproduce the SEDs for high-$z$ extremely red quasars and type-1 AGNs with mid-IR warm-excess. These results suggest that most AGNs could share similar properties of extended dust environment, which may indicate that AGN-driven outflows dominate the large-scale structure and grain properties of the nuclear extended dust environment.

6. The reddened type-1 AGN model can also reproduce the SEDs of hot dust-obscured galaxies when combined with a star-forming galaxy template. However, the best-fit parameters suggest a more extended AGN-heated dust distribution with a steeper density profile compared with objects like NGC 3782. This indicates the AGN dust environment in hot DOGs might be quite different from other systems. Objects with similar hot DOG SED features are also found at $z \sim 0.1$.

7. The general success of our reddened type-1 AGN model suggests the IR-reprocessed emission of the extended dust distribution in some objects can complicate the interpretation of the integrated AGN IR emission, such as the behavior of the torus radiative transfer models and constraints on their dust covering factors.

8. The SED shape of the AGN thermal IR emission might be a reflection of its dust environment. Depending on the obscuration level along the face-on direction, we propose three basic scenarios, in which the AGN and galaxy feedbacks may play different roles, that lead to the diverse IR SED properties among type-1 AGNs.

From a technical perspective, contrasting with other alternatives to fit the AGN-heated dust emission in the literature, the semi-empirical model proposed here is able to fit a wide range of AGN SEDs using relatively few free parameters. Combined with well-constrained

empirical templates of star-forming galaxies, we can get reasonably accurate separations of the AGNs and their host galaxies. Meanwhile, these observationally calibrated semi-empirical templates are a valuable tool to characterize the IR color space of AGNs, which could be useful to look for abnormal objects in the era of *JWST*.

We thank Dr. Aigen Li and Dr. Robert Nikutta for helpful discussions, Dr. Lei Hao for providing the spectral measurements of the SDSS DR7 Main Galaxy Sample, and Dr. Almudena Prieto for the clarification of NGC 3783 SED data. We are also grateful to the anonymous referee for a very constructive report and helpful comments.

This work was supported by NASA grants NNX13AD82G and 1255094.

This work is based in part on observations made with the Spitzer Space Telescope, which is operated by the Jet Propulsion Laboratory, California Institute of Technology under a contract with NASA. The Combined Atlas of Sources with Spitzer IRS Spectra (CASSIS) is a product of the IRS instrument team, supported by NASA and JPL.

This publication has made use of data products from the *Wide-field Infrared Survey Explorer*, which is a joint project of the University of California, Los Angeles, and the Jet Propulsion Laboratory/California Institute of Technology, funded by the National Aeronautics and Space Administration. This publication also makes use of data products from NEOWISE, which is a project of the Jet Propulsion Laboratory/California Institute of Technology, funded by the Planetary Science Division of the National Aeronautics and Space Administration. This publication makes use of data products from the Two Micron All Sky Survey, which is a joint project of the University of Massachusetts and the Infrared Processing and Analysis Center/California Institute of Technology, funded by the National Aeronautics and Space Administration and the National Science Foundation.

Funding for the SDSS and SDSS-II has been provided by the Alfred P. Sloan Foundation, the Participating Institutions, the National Science Foundation, the U.S. Department of Energy, the National Aeronautics and Space Administration, the Japanese Monbukagakusho, the Max Planck Society, and the Higher Education Funding Council for England. The SDSS Web Site is http://www.sdss.org/. The SDSS is managed by the Astrophysical Research Consortium for the Participating Institutions. The Participating

Institutions are the American Museum of Natural History, Astrophysical Institute Potsdam, University of Basel, University of Cambridge, Case Western Reserve University, University of Chicago, Drexel University, Fermilab, the Institute for Advanced Study, the Japan Participation Group, Johns Hopkins University, the Joint Institute for Nuclear Astrophysics, the Kavli Institute for Particle Astrophysics and Cosmology, the Korean Scientist Group, the Chinese Academy of Sciences (LAMOST), Los Alamos National Laboratory, the Max-Planck-Institute for Astronomy (MPIA), the Max-Planck-Institute for Astrophysics (MPA), New Mexico State University, Ohio State University, University of Pittsburgh, University of Portsmouth, Princeton University, the United States Naval Observatory, and the University of Washington.

We acknowledge the use of the NASA/IPAC Extragalactic Database (NED) which is operated by the Jet Propulsion Laboratory, California Institute of Technology, under contract with the National Aeronautics and Space Administration. This work has also made use of the VizieR catalogue access tool, CDS, Strasbourg, France.

*Software*: DUSTY (Ivezic et al., 2017), SKIRT (Baes et al., 2003, 2011)

CHAPTER 5

# MID-IR VARIABILITY AND DUST REVERBERATION MAPPING OF LOW-$z$ QUASARS

The continued operation of the *Wide-field Infrared Survey Explorer* (*WISE*) combined with several ground-based optical transient surveys (e.g., CRTS, ASAS-SN and PTF) offer an unprecedented opportunity to explore the dust structures in luminous AGNs. We use these data for a mid-IR dust reverberation mapping (RM) study of 87 archetypal Palomar–Green quasars at $z \lesssim 0.5$. To cope with various contaminations of the photometry data and the sparse time sampling of the light curves, procedures to combine these datasets and retrieve the dust RM signals have been developed. We find that $\sim$70% of the sample (with a completeness correction, up to 95%) has convincing mid-IR time lags in the *WISE* $W1$ ($\sim 3.4$ $\mu$m) and $W2$ ($\sim 4.5$ $\mu$m) bands and they are proportional to the square root of the AGN luminosity. Combined with previous $K$-band ($\sim 2.2$ $\mu$m) RM results in the literature, the inferred dust emission size ratios are $R_K : R_{W1} : R_{W2} = 0.6 : 1 : 1.2$. Under simple assumptions, we put preliminary constraints on the projected dust surface density at these bands and reveal the possibly different torus structures among hot-dust-deficient, warm-dust-deficient and normal quasars from the reverberation signals. With multi-epoch *Spitzer* data and later *WISE* photometry, we also explore AGN IR variability at 10–24 $\mu$m over a 5 yr time-scale. Except for blazars and flat-spectrum radio sources, the majority of AGNs have typical variation amplitudes at 24 $\mu$m of no more than 10% of that in the $W1$ band, indicating that the dust reverberation signals damp out quickly at longer wavelengths. In particular, steep-spectrum radio quasars also lack strong 24 $\mu$m variability, consistent with the unification picture of radio-loud AGNs.[1]

[1] A version of this chapter originally appeared as a published paper in the Astrophysical Journal (Lyu et al., 2019). Paul Smith and George Rieke contributed the study of AGN variability at 24 $\mu m$ and I was responsible for all the remaining work.

## 5.1 Introduction

The circumnuclear dusty structures in active galactic nuclei (AGNs) bridge the gap between the black hole (BH) accretion disk and the host galaxy interstellar medium (ISM) and lay the foundation for AGN unification proposals (Antonucci, 1993; Urry & Padovani, 1995; Netzer, 2015). However, due to their complex geometry and small sizes, it is very challenging to characterize torus structures as well as the properties of the constituent dust grains.

Infrard (IR) reverberation mapping (RM) opens a window to peek inside the so-called AGN dusty torus. When the UV/optical emission of the BH accretion disk changes, the varying signal travels at the speed of light to the torus, causing it to react as reprocessed emission in the IR but with a time lag. We can analyze the optical and IR light curves of AGNs to retrieve spatial information reflected in the response of the torus to changes in irradiation from the central engine. The procedure is similar to the RM originally proposed by Blandford & McKee (1982) and widely applied to study the broad-line regions (BLRs) and accretion disks (e.g., Peterson et al., 2004). The time lag of the IR emission was originally reported for the Seyfert 1 galaxy Fairall 9 by Clavel et al. (1989) and soon after analyzed in terms of RM to constrain the AGN dusty circumnuclear structure by Barvainis (1992). The behavior was subsequently observed for a number of AGNs; the most noteworthy work is the systematic study of time lags between the near-IR ($K$-band) and the optical of $\sim$30 Seyfert-1 nuclei through ground-based monitoring. The results follow an $R \propto L^{1/2}$ size-luminosity relation, as expected if there is a similar dust sublimation temperature in all the sources (e.g., Oknyanskij & Horne, 2001; Suganuma et al., 2006; Lira et al., 2011; Koshida et al., 2014; Pozo Nuñez et al., 2014; Mandal et al., 2018; Ramolla et al., 2018).

Glass (2004) conducted a *JHKL* (1.25–3.45 $\mu$m) long-term monitoring program of 41 Seyfert nuclei and reported tentative time-lag measurements between the $U$ ($\sim 0.36$ $\mu$m) and $L$ ($\sim 3.45$ $\mu$m) bands for five objects. Given the stable and cool space environment, high-precision photometry was made possible by the IRAC instrument on *Spitzer* and a mid-IR dust reverberation study was carried out at 3.6 and 4.5 $\mu$m and reported for the

reddened type-1 AGN in NGC 6418 (Vazquez et al. 2015). However, due to the limitations in observing at 3–5 $\mu$m from the ground and the difficulty and cost of carrying out long-term coordinated ground- and space-based targeted observations, no other detailed reverberation studies in this wavelength range are available.

Now there is a new possibility to conduct systematic dust RM at 3–5 $\mu$m for bright AGNs with the continued operation of the *Wide-field Infrared Survey Explorer* (*WISE*). Launched in 2009 December, this satellite performed a mid-IR all-sky survey, was put into hibernation, and then reactivated as the *Near-Earth Object WISE* (*NEOWISE*) mission for asteroid hunting (Mainzer et al., 2014). The telescope completes an all-sky map roughly every 6 months and had provided photometric data with 12–13 epochs that cover a time period of 8 yr by the end of 2018. The AGNs in Seyfert galaxies studied by Koshida et al. (2014) had typical luminosities up to about $3 \times 10^{11}$ $L_{\odot}$ and reverberation time delays at this luminosity are expected to be $\sim$ 100 days, i.e., too short to be sampled well at the *NEOWISE* cadence. However, the cadence is satisfactory for more luminous AGNs. When combined with ground-based wide-field optical transient surveys, these mid-IR multi-epoch data can be used to explore the dust reverberation signals close to the spectral energy distribution (SED) peak of the AGN hot dust emission at $\sim$ 3 $\mu$m for the first time. Given the depth, range, and sky coverage of these surveys, this approach has the potential to draw general conclusions about the structure of a typical AGN and the surrounding material in a statistically meaningful way. In this paper, we will demonstrate how to make the best use of these public datasets and present the results from an RM analysis at 3–5 $\mu$m of 87 $z < 0.5$ Palomar-Green (PG) quasars.

Despite the presence of terrestrial atmospheric windows at 10 and 20 $\mu$m, few studies of AGN IR variability are available there because of the sensitivity limitations of ground-based telescopes in the thermal IR. Nonetheless, studies of individual blazars have found large-amplitude coordinated variations from the visible through 10 $\mu$m (e.g., Rieke & Kinman, 1974). Neugebauer & Matthews (1999) reported a broader-based study based on coordinated data at $J(1.27\mu\text{m})$, $H(1.65\mu\text{m})$, $K(2.23\mu\text{m})$, $L'(3.69\mu\text{m})$, and $N(10.6\mu\text{m})$ of 25 PG quasars over several decades. They concluded that the blazar 3C 273 (PG 1226+023) was the only source that clearly varied at the $N$ band and another radio-quiet quasar,

PG 1535+547 might also be variable in this band, since its light curve mimicked the pattern seen at the shorter wavelengths. With the data collected for a large sample of AGNs repeatedly observed by *Spitzer* and *WISE*, we will provide an updated study of AGN variability behavior at 12 $\mu$m and 24 $\mu$m over a timescale of 4–5 yr and establish its relation with IR variability at shorter wavelengths.

This paper is organized as follows. We describe the data and the compilation of multiband light curves in Section D. To retrieve the dust reverberation signals rigorously, Section 5.3 introduces a new method for the cross-correlation analysis between the low-cadence optical and mid-IR light curves. We present the results from the 3–5 $\mu$m dust RM analysis, as well as the 10–24 $\mu$m variability study, in Section 5.4. Discussion about the origin of AGN mid-IR variability, the circumnuclear dust structure, and its relation to the BLR can be found in Section 6.5. Section 6.6 is the final summary.

Some technical details are left to appendices. Appendix E evaluates the quality of the photometric survey data used. We provide the derivations that relate time lag to torus size in Appendix F. In Appendix G, we reexamine the Seyfert 1 sample whose variability in the *K* band was studied by Koshida et al. (2014).

Throughout this paper, we adopt the cosmology $\Omega_m = 0.27$, $\Omega_\Lambda = 0.73$ and $H_0 = 71\mathrm{km\ s^{-1}Mpc^{-1}}$.

## 5.2 Photometric Data and Light Curves

### 5.2.1 Data Ensemble

The primary sample used for our mid-IR dust reverberation study is all 87 PG quasars at z $< 0.5$ (Schmidt & Green, 1983; Boroson & Green, 1992). For the 24 $\mu$m variability study, we also included 33 members of this PG sample plus another 106 quasars within the same redshift range to increase the statistical significance. Table 5.1 and Figure 5.1 provide an overview of the time-series datasets that have been used in this work. We present the details below.

*Optical Data from Ground-based Transient Surveys* We collected optical photometry of the PG quasars from the Catalina Real-Time Transient Survey (CRTS; Drake et al. 2009).

Table 5.1. Time-series datasets used in this work

| name | sky coverage | $\lambda$ | depth | time coverage | time gap | $N_{epoch}$ | $N_{object}$ |
|---|---|---|---|---|---|---|---|
| | | | Ground-based Optical Data | | | | |
| CRTS (DR2) | northern sky (survey) | unfiltered ($\sim$0.4–0.9 $\mu$m) | $M_V$ $\sim$13–19 mag | 2005–2013 | 1–30 days | $\sim$100–150 | 83(PG) |
| ASAS-SN | all sky (survey) | V ($\sim$ 0.55 $\mu$m) | $M_V$ $\sim$10–17 mag | 2012–2018 | 1-10 days | $\sim$200–300 | 87(PG) |
| PTF (DR3) | northern sky (survey) | g′ ($\sim$ 0.48 $\mu$m) | $M_{g'}$ $\sim$14–21.3 mag | 2009–2014[a] | | | 76(PG) |
| | | R ($\sim$ 0.66 $\mu$m) | $M_R$ $\sim$14–20.6 mag | 2009–2014[a] | | | |
| | | | Space-based Mid-IR Data | | | | |
| WISE/NEOWISE | all sky (survey) | W1 ($\sim$ 3.4 $\mu$m) | W1$\sim$8–16.6 mag | 2010–2018 | 6 months | 12–13 | 87(PG) |
| | | W2 ($\sim$ 4.6 $\mu$m) | W2$\sim$7–16.0 mag | 2010–2018 | 6 months | 12–13 | 87(PG) |
| | | W3 ($\sim$ 12 $\mu$m) | W3$\sim$3.8–10.8 mag | 2010 | – | 1–2 | 87(PG) |
| | | W4 ($\sim$ 22 $\mu$m) | W4$\sim$ $-$0.4–6.7 mag | 2010 | – | 1–2 | 87(PG)+106 |
| *Spitzer* | all sky (targeted) | MIPS 24 $\mu$m | – | 2004–2009 | 3–4 years | 2–3 | 33(PG)+106 |
| | | IRS spec. (5–35 $\mu$m) | – | 2003–2009 | – | 1 | 87(PG) |

[a]only selected g- and R-band data are available after Jan 1, 2013 (through Jan 28, 2015) in this data release

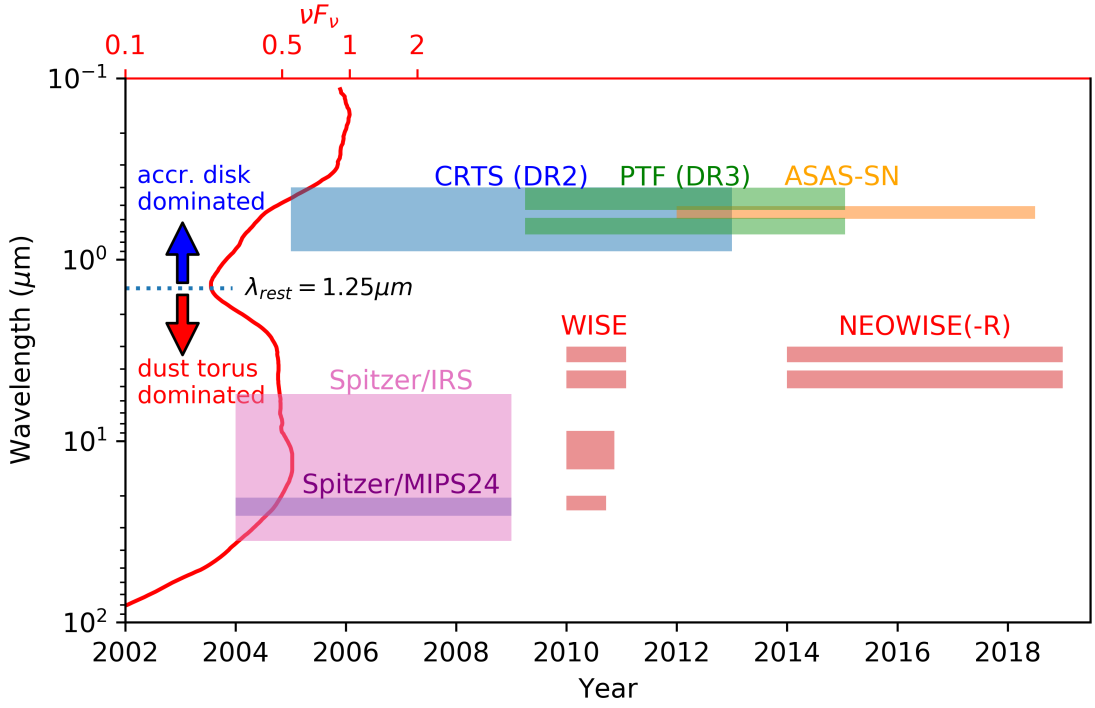


Figure 5.1 Time coverage and wavelength sampling of different time-series datasets used in this work. We also show the intrinsic SED shape of the normal AGN template at z=0.15 (mean redshift of the PG sample) along the $Y$-axis and highlight the separation between the UV-optical bump and the IR bump with dotted blue line.

This program utilizes two Steward Observatory telescopes, a 1.5 m telescope on Mt. Lemmon, Arizona, and a 0.68 m telescope on Mt. Bigelow, Arizona. Both survey the northern sky, covering timescales from minutes to years. All images are unfiltered and processed using the SExtractor package with the standard aperture photometry. With a sequence of 30 s exposures, the 1.5 m can reach as faint as $m_V \sim 21.5$ while the 0.68-m limit is $m_V \sim 19$. Photometry for sources brighter than $V = 13$ can be problematic due to source saturation and nonlinearity of the response. We gathered the 2005-2013 photometry values from the public archive of the second data release. According to Graham et al. (2017), the published error model of the CRTS archival photometry is problematic, and we follow their methodology to make the necessary corrections to these data.

We also utilized the $V$-band optical data from the All-Sky Automated Survey for Supernovae (ASAS-SN, Shappee et al. 2014), which are publicly available at the ASAS-SN

light-curve servers (Kochanek et al., 2017). The data were obtained through a global network of 20 14 cm diameter telescopes (camera lenses) with commercial-level CCD cameras that have observed nearly the entire sky continuously since 2012. The image FWHM is $\sim 16''$with an $\sim 8''$pixel size. The photometry is measured with a 2 pixel radius aperture, and the background is estimated with a 7 pixel radius annulus. Typical photometric uncertainties are less than 0.075 mag. The calibration is done by observing nearby APASS stars. Typically, ASAS-SN photometry saturates at 10-11 mag, and the depth is roughly $m_V \sim 17$ under good weather conditions.

Finally, we gathered the optical time-sequence photometry for the PG quasars from the Palomar Transient Factory (PTF; Law et al. 2009) Data Release 3 (DR3), which includes all data collected during the survey from 2009 March to 2012 December and some selected data obtained from 2013 to 2015 January. The PTF data nicely fill the time gap between the CRTS and ASAS-SN light curves. This survey was done with the Palomar 48 inch (1.2m) Samuel Oschin Telescope with a typical $2.''0$ FWHM imaging resolution. The photometry was taken mostly through two broadband filters, SDSS-$g'$ and Mould-$R$, reaching $4\sigma$ limiting AB magnitudes of $m_{g'} \sim 21.3$ and $m_R \sim 20.6$ in 60 second exposures. Both bands saturate at $\sim 14$ mag.

Since PG 1226+023 (also known as 3C 273) is saturated in CRTS and PTF, we have looked for alternative datasets to build its optical light curve. In fact, this object had been systematically monitored from late 2008 to the middle of 2018 as part of the Steward Observatory (SO) spectropolarmetric monitoring project (Smith, 2016).[2] These observations were carried out with the SPOL CCD spectropolarimeter (Schmidt et al., 1992) at either the SO 2.3 m Bok Telescope on Kitt Peak or the SO 1.54 m Kuiper Telescope on Mt. Bigelow. By convolving the spectra with a standard Johnson $V$-band filter, $\sim 300$ photometric measurements with high signal-to-noise (S/N) covering 10 yr are available. We also collected the $V$-band photometry of 3C 273 with the Light Curve Generator (LCG) on the AAVSO website[3], which archives photometry from various facilities of bright variable objects. We omitted measurements flagged as being discrepant or having measurement

[2] http://james.as.arizona.edu/~psmith/Fermi/
[3] https://www.aavso.org/lcg

uncertainties >0.1 mag. The AAVSO data provide an optical light curve for 3C 273 from 2005 to 2019.

*Multi-epoch Mid-IR Photometry from WISE and NEOWISE* The *WISE* mission performed an all-sky survey in four bands at 3.4, 4.6, 12, and 22 $\mu$m, from 2010 January through 2010 October. Then the telescope carried out a 4month *NEOWISE* program using the first two bands without cryogen before going into hibernation in 2011 February. In 2013 December, *WISE* was reactivated and began the post-hibernation survey (the *NEOWISE* reactivation mission, or *NEOWISE-R*). *WISE*/*NEOWISE-R* observes the entire sky roughly every 6 months. All of the single-epoch images have been processed, and profile-fit photometry of each detection has been carried out by a dedicated pipeline.[4]

We gathered all of the single-epoch profile-fit photometry measurements in the $W1$ ($\sim 3.4$ $\mu$m) and $W2$ ($\sim 4.6$ $\mu$m) bands from the *WISE* and *NEOWISE* missions, up to the *NEOWISE* 2019 Data Release, from the NASA/IPAC Infrared Science Archive. Typically, these data cover a time period from 2010 January to 2018 December with a 3 yr gap between 2011 and 2014. Each object was observed for 12–13 epochs, with 10–20 exposures acquired within each epoch. To construct the mid-IR light curves, we only used detections from good-quality frame sets, following the suggestions given in the online documentation.[5]

*10–25 $\mu$m Measurements from Spitzer and WISE* To test for variability at $\lambda > 20$ $\mu$m, we obtained MIPS 24 $\mu$m measurements (PID 40053 and PID 50099; PI: George Rieke) of a heterogeneous sample of quasars that had been measured at the same wavelength by *Spitzer* for various previous observing programs. All of the observations were conducted during the *Spitzer* cryogenic mission from 2004 to 2009 and sample a time interval of 3–4 yr. The entire sample was observed twice, while a subset of nearly 60 objects was observed during a third epoch roughly 1 yr after the second-epoch observation.To best utilize the instrumental stability and minimize subtle possible systematic effects, these

[4]See details in http://wise2.ipac.caltech.edu/docs/release/allwise/expsup/ and http://wise2.ipac.caltech.edu/docs/release/neowise/expsup/

[5]That is, frame quality score `qual_frame`>0, frame image quality score `qi_fact`>0, South Atlantic Anomaly separation `saa_sep`> 0, and Moon masking flag `moon_masked`=0, see http://wise2.ipac.caltech.edu/docs/release/neowise/expsup/sec2_3.html

AGNs were observed in exactly the same manner for all epochs. In this way, systematic effects associated with different durations for data collection events (DCEs) or a different total number of exposures are eliminated. In all cases, flux density measurements of the AGNs at 24 $\mu$m were obtained using the standard MIPS photometry-mode astronomical observation template (AOT) with either 3 or 10 s DCEs.

All observations were processed using the standard reduction algorithms of the MIPS Data Analysis Tool (DAT) with the same processing steps and calibrations on all targets for both observations (Gordon et al., 2005). This included subsampling the detector array pixels by a factor of 2 to produce final mosaicked images of 363 $\times$ 401 pixels$^2$ ($\sim$ 7.′5 $\times$ 8.′3). Aperture photometry using the DAOPHOT package (Stetson, 1987) within IRAF was performed on the calibrated mosaicked 24 $\mu$m images. The default parameters of the aperture photometry include an aperture of 24 pixels ($\sim$ 30″) and a sky annulus for background subtraction of 60–90″ from the center of the photometric aperture. In a few cases, smaller apertures were used to avoid contamination by nearby field objects. Flux densities were calculated using an aperture correction of 1.105 and a conversion factor of 0.0454 MJy sr$^{-1}$ (DN s$^{-1}$)$^{-1}$ (Engelbracht et al., 2007). No color corrections have been applied to the photometric results.

Because the reductions are identical for all the measurements of each object, the relative brightness is determined very accurately; i.e., for repeated measurements of standard stars, MIPS achieved repeatability of $\sim$ 0.4% (Engelbracht et al., 2007). Because the quasars are much fainter than the stars and hence less immune to faint background structures, we ascribe a systematic error of 0.7% (see Section 5.4.4) and combine it with the statistical errors by root sum square. We rejected a small number of sources detected at S/N $<$ 5, where the systematic errors may be larger. The measured fluxes and resulting errors for the remaining sample of 139 quasars are provided in Table 5.2.

Table 5.2. Quasar flux measurements at 24 $\mu$m and the variability results

| Name | z | JD -2,450,000 | f24 mJy | error mJy | stdev of change | comments |
|---|---|---|---|---|---|---|
| 2MASX J00070361+1554240 | 0.114 | 3194.8 | 63.5 | 0.7 | | RQ |
| | | 4676.2 | 62.9 | 0.7 | 0.6 | |
| | | 5376[a] | 63.3 | 2.6 | 0.2 | |
| PG0026+129 | 0.142 | 3747.4 | 43.2 | 0.7 | | RQ |
| | | 4677.8 | 43.2 | 0.7 | 0.0 | |
| | | 5382 | 44.1 | 3.8 | 0.2 | |
| 2MASS J00300421-2842259 | 0.278 | 3550.2 | 125.1 | 1.0 | | RQ, IRASF00275-2859 |
| | | 4675.4 | 124.7 | 1.0 | 0.3 | |
| | | 5362 | 122.7 | 3.9 | 0.5 | |
| 2MASS J00411870+2816408 | 0.194 | 3195.3 | 74.5 | 0.8 | | RQ |
| | | 4514.7 | 73.6 | 0.8 | 0.9 | |
| | | 5392 | 76.6 | 2.5 | 1.2 | |
| 2MASX J00505570+2933281 | 0.136 | 3218.3 | 58.0 | 0.6 | | |

To extend the time sampling to 2010, we collected *WISE* $W4$ measurements nominally at 22 $\mu$m for 136 of these objects from the ALLWISE Source Catalog. One *WISE* measurement was rejected because of confusion with a nearby source. The $W4$ and MIPS [24] photometric bands are similar, with a cut-on wavelength at 19.87 $\mu$m (half power) for the former and 20.80 $\mu$m for the latter, with the long wavelength response determined by the Si:As IBC detectors in both cases.

Low-resolution ($\lambda/\Delta\lambda$ ~60–130) mid-IR spectroscopic observations of all 87 PG quasars were obtained using the *Spitzer* IRS. By comparing them with the *WISE* $W3$ and $W4$ photometric measurements, we can study quasar variability at 10–22 $\mu$m. For the *Spitzer* mid-IR spectra, we adopted the optimal extraction products from the Combined Atlas of Sources with *Spitzer* IRS Spectra (CASSIS; Lebouteiller et al. 2011a). Besides PG 0003+199 (no Long-Low module observation at 14–38 $\mu$m) and PG 1352+183 (very poor Short-Low spectra at 5.2–14 $\mu$m), the mid-IR spectra cover ~5.2–24 $\mu$m for all objects and with good S/Ns. Compared with the *WISE* measurements in 2010, these *Spitzer*/IRS spectra were typically obtained 5 yr earlier. For PG 1226+023 (3C 273), multiple *Spitzer*/IRS observations were conducted between 2004 and 2009, making possible the construction of mid-IR light curves over a wide wavelength range. For the *WISE* $W3$ and $W4$ measurements of these PG quasars, since no convincing variability has been reported in these bands over the 9-month cryogenic mission by the *WISE* pipeline, we adopted the profile-fit photometry values from the ALLWISE source catalog.

### 5.2.2 Construction and Evaluation of the Light Curves

In the optical and mid-IR $W1$, $W2$ bands, we have sufficient data to sample light curves for many years. In this section, we discuss the procedures developed for this purpose.

*Optical* Typically, the CRTS data cover MJD~53500–56500, and the ASAS-SN data cover MJD~56000–58300, with an overlap of about 500 days. We rely on these datasets to construct the optical light curves for most objects. The CRTS data generally have smaller relative uncertainties. However, the absolute values of the unfiltered photometry are hard to interpret, so we scaled the CRTS data to match the ASAS-SN data in the region of over-

Table 5.2 (cont'd)

| Name | z | JD -2,450,000 | f24 mJy | error mJy | stdev of change | comments |
|---|---|---|---|---|---|---|
| | | 4514.7 | 57.3 | 0.7 | 0.8 | |
| | | 5394 | 57.3 | 2.3 | 0.0 | |
| PG0052+251 | 0.154 | 3217.8 | 68.7 | 0.7 | | RQ, W4 high due to strong 18 $\mu$m feature[b] |
| | | 4509.2 | 68.9 | 0.7 | 0.2 | |
| | | 5393 | 76.0 | 2.4 | 2.9 | |
| ... | ... | ... | ... | ... | ... | ... |

[a]For midpoint of the *WISE* observations

[b]The strong 18 $\mu$m feature in the spectrum of this source (Shi et al., 2014) combined with the $\sim$1 $\mu$m bluer bandpass of the W4 filter compared with the MIPS one can account for the higher signal seen by *WISE*.

[c]Steep-spectrum radio quasar (SSRQ) indicates that the spectral index between 1.4 and 5 GHz is $\leq -0.7$. Radio data obtained from summary in NASA Extragalactic Database (NED) and other sources. (see Section 5.4.4 for details.)

[d]Blazars are identified from Mao et al. (2016) and additional sources, see text.

[e]Flat-spectrum radio quasar (FSRQ) indicates that the spectral index between 1.4 and 5 GHz is $> -0.7$.

[f]This source is radio-intermediate by our criteria, but radio-loud using others (Laor et al., 2019); given its flat spectrum also, we classify it as radio-loud.

Note. — (This table is available in its entirety in machine-readable form. A portion is shown here for guidance regarding its form and content.)

lap; the latter have photometry measurements obtained through a standard V-band filter and calibrated by nearby standard stars. Since CRTS and ASAS-SN observations have different time samplings, we interpolated the observed values with the same time grid by fitting a Damped Random Walk (DRW) model to the CRTS and ASAS-SN light curves separately and computed an average scaling factor for the best-fit model light curves with the shared time periods.

To demonstrate the validity of using the combined unfiltered CRTS and V-band ASAS-SN light curves to trace the accretion disk variability, we compare the derived best-fit DRW parameters for these two datasets in Figure 5.2. We have used *JAVELIN* (Zu et al., 2013) to fit the slightly smoothed optical light curves[6] and the derived best-fit parameters using a MCMC analysis. They are in excellent agreement despite the large uncertainties of individual values, suggesting the CRTS and ASAS-SN light curves trace identical variability properties. In terms of the wavelength dependence of the AGN optical continuum variability, Jiang et al. (2017) found the average time delays between $g$ ($\sim 0.48$ $\mu$m) and $z$ ($\sim 0.91$ $\mu$m) are less than six days for quasars with $L_{\rm AGN,\,bol} \sim 10^{11}$–$10^{13}$ $L_{\odot}$. This is at least one order of magnitude smaller than the dust-reverberation lags our data can probe. Consequently, we do not need to make any corrections for the filter differences between the CRTS and ASAS-SN datasets. In fact, we have also visually checked the CRTS and ASAS-SN combined light curves of individual objects, finding that they have consistent features as revealed by the PTF light curves. Figure 5.3 gives some examples of how this model works on real data.

Among 87 PG quasars, four objects (PG 0804+761, PG 0838+761, PG 1100+772 and PG 1427+480) do not have CRTS observations. In these cases, we join the PTF data and ASAS-SN data together to extend the time coverage of their optical light curves. PG 1354+213 and PG 1416-129 are too faint for the ASAS-SN photometry to be useful. We have also dropped the CRTS light curve of PG 1226+023 since the photometry measurements are saturated.

For some objects, there are spike features in the optical light curves, which commonly

[6]A one-day smoothing window is introduced for both CRTS and ASAS-SN light curves to reduce the photometry uncertainties before the fittings.

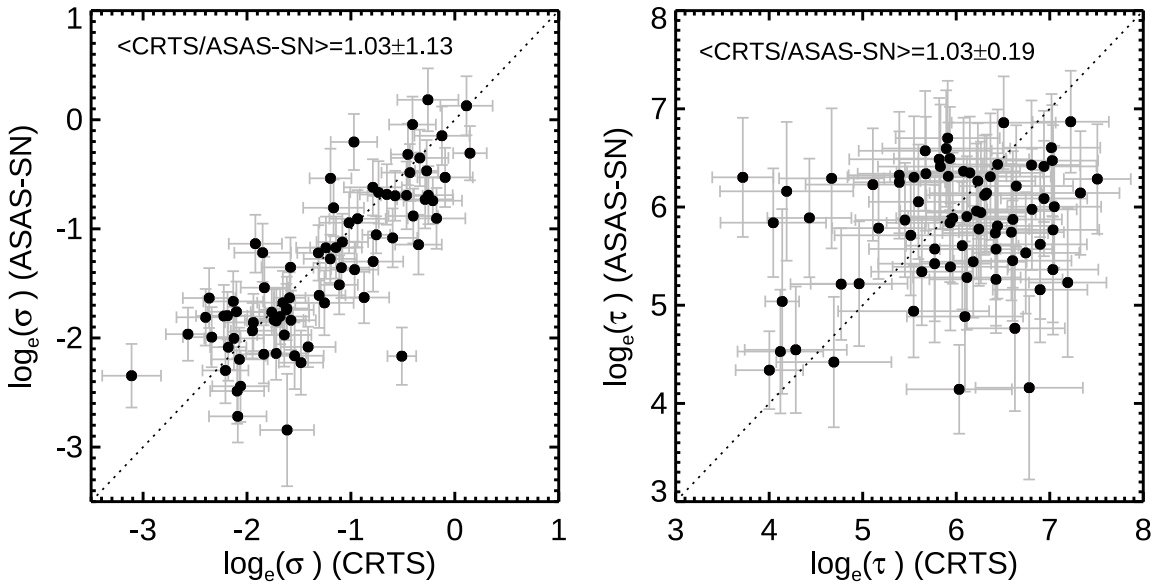


Figure 5.2 Comparisons of the best-fit DRW model parameters from fitting the ASAS-SN and CRTS light curves separately with the *JAVELIN* code. The left panel shows the amplitude $\sigma$ of the fitted covariance function and the left panel is the corresponding damping timescale. We denote the average parameter ratio with the corresponding standard deviation between CRTS and ASAS-SN light curves on the top of each panel.

turned out to be one single photometry measurement larger (or smaller) than the nearby average values by 1–2 mag. This is quite likely unrelated to the AGN itself, but caused by e.g., poor seeing conditions, calibration errors, or contamination such as cosmic rays. We rejected such data points by introducing 3-sigma clipping and smoothed the final optical light curve by averaging the remaining measurements taken within a single day to reduce the noise.

In the bottom-right panel of Figure 5.3, we compare the optical V-band light curves of PG 1226+023 from different sources. Although AAVSO and ASAS-SN measurements have larger dispersions than the data obtained from dedicated monitoring with the Steward Observatory (SO) telescopes, these light curves reveal the same variability patterns for this object. We decide to adopt the SO light curve for the correlation analysis between the optical and mid-IR variability and combine it with the AAVSO data to increase the time sampling range if required.

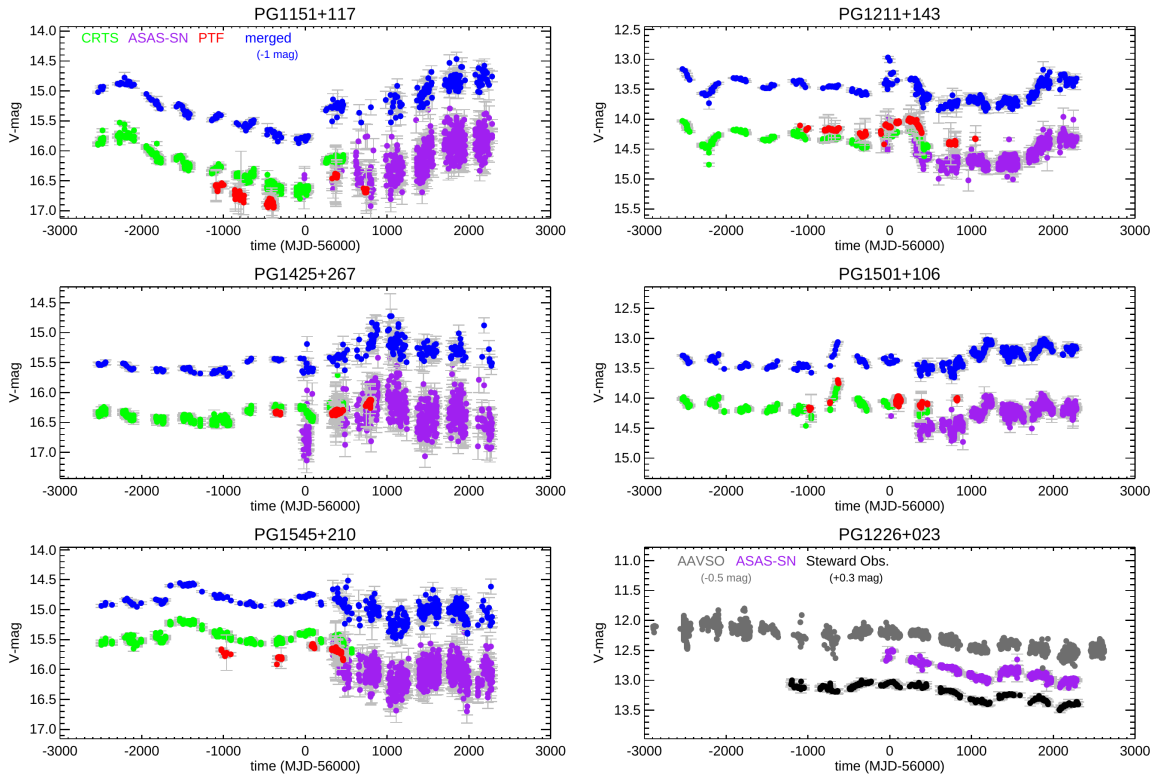


Figure 5.3 Example optical light curves of PG quasars. The magnitude measurements from ASAS-SN (purple), CRTS (green) and PTF (red) are shown with the original values in their catalog without any shifts. The final combined light curves (blue data points) are shifted by 1 mag for clarity. For PG 1226+023 (bottom-right panel), we compare its light curves from AAVSO (grey, shifted by $-0.5$ mag), ASAS-SN (purple, no shift) and observations obtained with two Steward Observatory telescopes (black, shifted by +0.3 mag).

*WISE W1 and W2* A single *WISE* epoch normally contains 10–20 7.7-second individual exposures with a total time coverage of about one day. For the mid-IR variability traced by the *WISE* data, we have first visually investigated the consistency of *WISE* W1 and W2 single-exposure photometry: they should have similar variability features given their small wavelength difference. This is confirmed for the available epochs of most objects. For PG 1259+593, PG 1534+580 and PG 1700+518, there are only 1–2 photometry spikes in the single-epoch light curves and they can be easily rejected. There are uncorrelated W1 and W2 variability signals in 1/3 of the epochs for PG 0923+129. Finally, PG 1617+175 has many abnormal W1-band photometry values in the two epochs observed in the cryogenic survey, whose variability features are not found in the W2 band. We have rejected these

problematic measurements.

We are interested in the response signal of the dust emission; the signal in the WISE bands will therefore arise near the inner radius of the torus around the central engine and any variations should be much slower than one light day. Therefore, we averaged the photometry values during each 1-day epoch to compile the mid-IR light curve, i.e.,

$$f_{epoch} = \frac{1}{N}\sum_{i=1}^{N} f_i \ . \tag{5.2.1}$$

Standard deviations of the single-exposure photometry were also derived to estimate the measurement uncertainties for each epoch. In addition, uncertainties in photometric measurements ($\sigma_{i,pho}$) as well as the system stability ($\sigma_{s.s.}$) need to be considered, so the total flux uncertainty for a given epoch is

$$\sigma^2_{epoch} = \frac{1}{N-1}\sum_{i=1}^{N}(f_i - \bar{f})^2 + \frac{1}{N^2}\sum_{i=1}^{N}\sigma^2_{i,pho} + \frac{1}{N}\sigma^2_{s.s.} \ . \tag{5.2.2}$$

In Appendix E, we study the photometric stability of WISE and NEOWISE using mid-IR calibration stars, finding $\sigma_{s.s.} \sim 0.029$ mag for *WISE* measurements and $\sigma_{s.s.} \sim 0.016$ mag for NEOWISE measurements.

For both optical and mid-IR light curves, we converted magnitudes into flux to better reflect the variability signals from the AGN, since various contaminations (e.g., AGN host galaxy, nearby objects) and photometry zero point uncertainties would only cause a constant flux shift.

In Table 5.3, we provide a summary of available light curve data and their basic properties for the PG sample. Interested readers may contact the authors directly to get a copy of these light curves.

Table 5.3. Summary of Available Data and Basic Variability Properties

| Name | Optical Sources | | | $\delta M_V$ | MJD(V) | $N_{\rm epoch}$ | V | $\Delta V$ | MJD(IR) | $N_{\rm epoch}$ | W1 | $\Delta W1$ | W2 | $\Delta W2$ |
|---|---|---|---|---|---|---|---|---|---|---|---|---|---|---|
| | CRTS | ASAS-SN | PTF | | | | | | | | | | | |
| (1) | (2) | (3) | (4) | (5) | (6) | (7) | (8) | (9) | (10) | (11) | (12) | (13) | (14) | (15) |
| PG0003+158 | I | I | II | 0.19 | 53648.3–58281.1 | 325 | 15.63 | 1.03 | 55376.1–58459.7 | 13 | 12.27 | 0.06 | 11.22 | 0.11 |
| PG0003+199 | I | I | II | 0.33 | 53648.3–58281.1 | 382 | 14.16 | 0.46 | 55377.8–58461.4 | 14 | 8.75 | 0.54 | 7.84 | 0.43 |
| PG0007+106 | I | I | III | 0.42 | 53520.5–58282.1 | 344 | 15.43 | 0.85 | 55375.0–58458.8 | 13 | 10.55 | 0.38 | 9.58 | 0.27 |
| PG0026+129 | I | I | III | 0.32 | 53520.5–58282.1 | 381 | 15.33 | 1.82 | 55379.5–58463.5 | 13 | 11.10 | 0.24 | 10.10 | 0.19 |
| PG0043+039 | I | I | III | 0.14 | 53563.4–58284.1 | 260 | 15.91 | 0.78 | 55559.1–58463.5 | 11 | 12.02 | 0.16 | 10.95 | 0.12 |
| PG0049+171 | I | I | N.A. | 0.28 | 53636.4–58281.1 | 369 | 15.57 | 1.20 | 55203.5–58311.3 | 13 | 11.79 | 0.24 | 10.84 | 0.19 |
| PG0050+124 | I | I | III | 0.41 | 53636.4–58273.1 | 380 | 14.12 | 0.54 | 55387.5–58309.8 | 12 | 8.77 | 0.30 | 7.77 | 0.21 |
| PG0052+251 | I | I | III | 0.26 | 53561.4–58138.7 | 378 | 15.40 | 1.00 | 55206.4–58314.9 | 16 | 11.08 | 0.20 | 10.09 | 0.18 |
| PG0157+001 | I | I | II | 0.22 | 53627.4–58158.5 | 315 | 15.46 | 0.82 | 55210.8–58319.8 | 13 | 10.80 | 0.43 | 9.81 | 0.31 |
| PG0804+761 | N.A. | I | I | 0.22 | 55312.3–58271.7 | 388 | 14.25 | 0.75 | 55284.5–58398.4 | 14 | 9.37 | 0.33 | 8.34 | 0.22 |
| PG0838+770 | N.A. | I | I | 0.22 | 55312.3–58257.8 | 180 | 15.95 | 1.00 | 55286.8–58400.7 | 15 | 11.58 | 0.31 | 10.66 | 0.27 |
| PG0844+349 | I | I | II | 0.24 | 53495.2–58254.8 | 385 | 14.36 | 0.82 | 55305.2–58418.5 | 11 | 10.49 | 0.29 | 9.63 | 0.22 |
| PG0921+525 | I | I | II | 0.27 | 53714.4–58260.8 | 383 | 14.36 | 0.93 | 55305.9–58422.9 | 18 | 10.24 | 0.55 | 9.30 | 0.41 |
| PG0923+201 | I | I | III | 0.29 | 53469.2–58228.6 | 352 | 15.24 | 0.95 | 55319.5–58432.8 | 12 | 10.48 | 0.16 | 9.55 | 0.11 |
| PG0923+129 | I | I | II | 0.45 | 53500.2–58264.5 | 421 | 14.26 | 0.56 | 55321.7–58434.8 | 12 | 10.16 | 0.36 | 9.27 | 0.31 |
| PG0934+013 | I | I | III | 0.30 | 53464.2–58223.7 | 347 | 15.56 | 0.76 | 55327.8–58440.6 | 13 | 11.34 | 0.82 | 10.41 | 0.77 |
| PG0947+396 | I | I | III | 0.24 | 53537.2–58252.8 | 168 | 16.41 | 1.02 | 55318.0–58431.2 | 15 | 11.75 | 0.44 | 10.59 | 0.43 |
| PG0953+414 | I | I | II | 0.09 | 53711.4–58261.4 | 337 | 14.88 | 0.84 | 55318.3–58431.6 | 14 | 10.74 | 0.27 | 9.76 | 0.17 |
| PG1001+054 | I | I | II | -0.08 | 53464.2–58246.6 | 298 | 16.17 | 1.82 | 55332.6–58445.1 | 12 | 11.42 | 0.24 | 10.41 | 0.25 |
| PG1004+130 | I | I | II | 0.19 | 53527.2–58264.5 | 256 | 15.33 | 0.60 | 55330.7–58443.3 | 13 | 11.58 | 0.18 | 10.48 | 0.13 |
| PG1011-040 | I | I | III | 0.31 | 53496.1–58230.6 | 364 | 14.93 | 0.78 | 55340.5–58453.2 | 13 | 11.08 | 0.25 | 10.21 | 0.24 |
| PG1012+008 | I | I | III | 0.27 | 53464.2–58228.6 | 335 | 15.62 | 1.02 | 55339.3–58448.9 | 12 | 11.36 | 0.35 | 10.37 | 0.23 |
| PG1022+519 | I | I | II | 0.21 | 53714.4–58271.8 | 263 | 15.41 | 0.81 | 55318.4–58431.8 | 15 | 11.35 | 0.42 | 10.53 | 0.42 |
| PG1048+342 | I | I | III | 0.22 | 53496.0–58275.8 | 227 | 16.52 | 0.71 | 55332.0–58444.6 | 15 | 12.36 | 0.24 | 11.34 | 0.27 |
| PG1048-090 | I | I | III | -0.51 | 53707.7–58233.5 | 345 | 15.44 | 0.62 | 55350.8–58462.9 | 14 | 11.98 | 0.06 | 10.97 | 0.06 |
| PG1049-005 | I | I | N.A. | 0.23 | 53464.3–58230.7 | 303 | 15.99 | 0.99 | 55347.7–58459.8 | 12 | 11.22 | 0.10 | 10.10 | 0.07 |
| PG1100+772 | N.A. | I | I | 0.23 | 55294.4–58281.8 | 338 | 15.26 | 0.64 | 55297.3–58410.9 | 14 | 11.29 | 0.17 | 10.23 | 0.17 |
| PG1103-006 | I | I | III | -0.07 | 53464.3–58231.9 | 310 | 16.05 | 1.11 | 55351.0–58462.9 | 13 | 12.21 | 0.08 | 11.09 | 0.10 |
| PG1114+445 | I | I | II | 0.18 | 53531.2–58280.8 | 261 | 15.83 | 0.86 | 55331.7–58451.9 | 18 | 10.88 | 0.10 | 9.73 | 0.11 |
| PG1115+407 | I | I | N.A. | 0.16 | 53527.2–58280.8 | 307 | 15.76 | 0.65 | 55334.1–58446.5 | 15 | 11.33 | 0.22 | 10.42 | 0.13 |
| PG1116+215 | I | I | III | 0.17 | 53469.3–58283.8 | 373 | 14.71 | 1.83 | 55345.2–58457.6 | 12 | 10.02 | 0.26 | 9.01 | 0.23 |
| PG1119+120 | I | I | III | 0.26 | 53498.2–58283.8 | 368 | 14.62 | 0.96 | 55349.6–58461.6 | 12 | 10.55 | 0.27 | 9.55 | 0.14 |
| PG1121+422 | I | I | N.A. | 0.14 | 53527.2–58280.8 | 261 | 16.25 | 1.17 | 55334.3–58452.1 | 17 | 12.13 | 0.38 | 11.15 | 0.38 |
| PG1126-041 | I | I | II | 0.19 | 53496.2–58230.5 | 375 | 14.48 | 0.63 | 55357.4–58263.6 | 13 | 9.70 | 0.30 | 8.78 | 0.27 |
| PG1149-110 | I | I | III | 0.54 | 53479.2–58275.8 | 360 | 15.11 | 3.18 | 55364.7–58271.2 | 12 | 11.06 | 0.55 | 10.34 | 0.57 |

Table 5.3 (cont'd)

| Name | Optical Sources | | | $\delta M_V$ | MJD(V) | $N_{\rm epoch}$ | V | $\Delta V$ | MJD(IR) | $N_{\rm epoch}$ | W1 | $\Delta W1$ | W2 | $\Delta W2$ |
|---|---|---|---|---|---|---|---|---|---|---|---|---|---|---|
| | CRTS | ASAS-SN | PTF | | | | | | | | | | | |
| (1) | (2) | (3) | (4) | (5) | (6) | (7) | (8) | (9) | (10) | (11) | (12) | (13) | (14) | (15) |
| PG1151+117 | I | I | II | 0.13 | 53466.2–58283.8 | 230 | 16.15 | 1.40 | 55356.8–58259.8 | 12 | 11.87 | 0.51 | 10.87 | 0.30 |
| PG1202+281 | I | I | II | 0.14 | 53470.3–58254.9 | 238 | 16.35 | 1.16 | 55352.1–58463.8 | 14 | 11.42 | 0.44 | 10.48 | 0.32 |
| PG1211+143 | I | I | II | 0.13 | 53466.3–58284.0 | 364 | 14.55 | 0.89 | 55360.1–58266.3 | 11 | 10.06 | 0.26 | 8.96 | 0.27 |
| PG1216+069 | I | I | I | 0.13 | 55270.4–58282.8 | 272 | 13.42 | 0.57 | 55364.1–58270.3 | 12 | 11.63 | 0.14 | 10.68 | 0.10 |
| PG1226+023 | III | I | N.A. | 0.00 | 55956.1–58283.8 | 299 | 12.87 | 0.61 | 55370.4–58274.3 | 12 | 8.41 | 0.16 | 7.45 | 0.11 |
| PG1229+204 | I | I | II | 0.29 | 53469.3–58282.8 | 424 | 14.89 | 0.66 | 55361.5–58267.6 | 15 | 10.64 | 0.48 | 9.73 | 0.42 |
| PG1244+026 | I | I | II | 0.31 | 53767.3–58283.8 | 276 | 15.82 | 0.74 | 55374.2–58277.9 | 12 | 11.63 | 0.08 | 10.58 | 0.06 |
| PG1259+593 | I | I | II | 0.06 | 53767.3–58279.8 | 309 | 15.44 | 0.62 | 55336.9–58452.8 | 16 | 11.25 | 0.18 | 10.22 | 0.13 |
| PG1302-102 | I | I | N.A. | 0.16 | 53496.2–58274.7 | 347 | 15.21 | 0.68 | 55208.7–58286.7 | 13 | 11.38 | 0.24 | 10.28 | 0.17 |
| PG1307+085 | I | I | N.A. | 0.14 | 53466.3–58283.8 | 315 | 15.62 | 0.74 | 55377.2–58280.7 | 12 | 11.41 | 0.28 | 10.36 | 0.23 |
| PG1309+355 | I | I | II | 0.15 | 53526.2–58284.9 | 360 | 15.36 | 0.64 | 55362.7–58268.9 | 17 | 11.14 | 0.13 | 10.07 | 0.08 |
| PG1310-108 | I | I | N.A. | 0.26 | 53496.2–58274.7 | 349 | 15.24 | 0.62 | 55210.2–58288.5 | 13 | 11.21 | 0.16 | 10.08 | 0.20 |
| PG1322+659 | I | I | II | -0.04 | 53860.4–58279.8 | 281 | 15.56 | 0.87 | 55330.8–58451.9 | 18 | 11.48 | 0.33 | 10.48 | 0.23 |
| PG1341+258 | I | I | II | 0.06 | 53470.3–58283.9 | 375 | 15.63 | 1.16 | 55204.0–58281.2 | 16 | 11.49 | 0.37 | 10.66 | 0.30 |
| PG1351+236 | I | I | III | 0.27 | 53470.3–58284.9 | 356 | 15.27 | 0.80 | 55207.3–58291.2 | 17 | 11.37 | 0.31 | 10.74 | 0.34 |
| PG1351+640 | I | I | II | 0.00 | 53767.5–58284.9 | 390 | 14.77 | 0.76 | 55337.1–58453.2 | 17 | 10.28 | 0.08 | 9.19 | 0.11 |
| PG1352+183 | I | I | II | 0.18 | 53469.4–58284.9 | 272 | 16.13 | 0.80 | 55208.9–58291.4 | 16 | 11.71 | 0.31 | 10.68 | 0.28 |
| PG1354+213 | I | III | II | 0.00 | 53469.4–56447.2 | 80 | 16.64 | 0.78 | 55208.4–58291.3 | 17 | 12.69 | 0.50 | 11.56 | 0.48 |
| PG1402+261 | I | I | II | 0.08 | 53470.3–58283.9 | 363 | 15.61 | 0.65 | 55208.4–58285.9 | 16 | 10.60 | 0.25 | 9.54 | 0.22 |
| PG1404+226 | I | I | N.A. | 0.13 | 53469.4–58284.9 | 298 | 15.80 | 0.77 | 55209.7–58287.8 | 15 | 11.81 | 0.24 | 10.89 | 0.19 |
| PG1411+442 | I | I | II | 0.22 | 53509.4–58284.8 | 355 | 14.73 | 0.67 | 55372.8–58276.5 | 15 | 10.11 | 0.16 | 9.07 | 0.16 |
| PG1415+451 | I | I | II | 0.17 | 53509.4–58284.8 | 317 | 15.79 | 0.74 | 55372.7–58276.5 | 15 | 11.33 | 0.44 | 10.44 | 0.33 |
| PG1416-129 | I | III | N.A. | 0.00 | 53498.3–56478.5 | 100 | 16.92 | 0.74 | 55222.9–58306.4 | 13 | 12.30 | 0.43 | 11.32 | 0.37 |
| PG1425+267 | I | I | II | 0.18 | 53470.3–58281.9 | 224 | 16.36 | 1.00 | 55212.5–58293.7 | 17 | 11.98 | 0.09 | 10.88 | 0.07 |
| PG1426+015 | I | I | II | 0.25 | 53464.4–58283.9 | 378 | 14.32 | 0.66 | 55221.0–58304.2 | 13 | 9.95 | 0.26 | 9.06 | 0.17 |
| PG1427+480 | N.A. | I | I | 0.25 | 54962.3–58284.8 | 402 | 16.39 | 2.28 | 55373.0–58276.8 | 15 | 12.25 | 0.15 | 11.18 | 0.11 |
| PG1435-067 | I | I | N.A. | 0.22 | 53497.3–58283.9 | 330 | 15.80 | 0.84 | 55225.1–58308.8 | 13 | 11.40 | 0.29 | 10.34 | 0.20 |
| PG1440+356 | I | I | II | 0.17 | 53480.3–58281.9 | 390 | 14.61 | 0.72 | 55211.4–58292.7 | 17 | 9.93 | 0.23 | 9.07 | 0.23 |
| PG1444+407 | I | I | III | 0.16 | 53509.4–58281.9 | 313 | 15.71 | 0.75 | 55209.3–58291.4 | 18 | 11.36 | 0.15 | 10.33 | 0.14 |
| PG1448+273 | I | I | II | 0.15 | 53470.4–58283.9 | 382 | 14.72 | 0.64 | 55217.2–58299.9 | 18 | 10.94 | 0.41 | 10.05 | 0.33 |
| PG1501+106 | I | I | II | 0.28 | 53466.4–58282.9 | 403 | 14.29 | 0.64 | 55225.8–58309.5 | 14 | 10.19 | 0.30 | 9.20 | 0.21 |
| PG1512+370 | I | I | II | 0.23 | 53480.3–58281.9 | 277 | 16.19 | 1.04 | 55217.9–58300.5 | 18 | 12.19 | 0.09 | 11.07 | 0.10 |
| PG1519+226 | I | I | II | 0.20 | 53506.3–58284.9 | 355 | 15.86 | 1.08 | 55225.9–58309.6 | 16 | 10.82 | 0.34 | 9.88 | 0.21 |
| PG1534+580 | I | I | II | 0.31 | 53856.4–58281.8 | 344 | 14.55 | 0.44 | 55203.3–58278.5 | 16 | 10.41 | 0.51 | 9.44 | 0.47 |
| PG1535+547 | I | I | II | 0.17 | 53880.5–58284.8 | 404 | 14.67 | 0.71 | 55203.1–58291.3 | 18 | 9.91 | 0.55 | 9.07 | 0.42 |

### 5.2.3 Converting the Mid-IR Measurements at $\lambda > 10$ $\mu$m for Comparison

We do not have sufficient data to construct light curves in the 10–25 $\mu$m range, but can assess variability by comparing the individual measurements. We describe here how we extended this comparison beyond just the MIPS 24 $\mu$m data.

*WISE W4 to MIPS [24]* To convert the *WISE* W4 measurements to the MIPS [24] system, we first eliminated all the quasars in our sample that we found to vary, plus those with W4 measurement errors $\geq 0.08$ magnitudes. These cuts left 95 quasars with high-weight measurements in both systems. We took the zero point for [24] to be 7.17 Jy and based the [24] magnitude on the weighted average of the two measurements of each quasar. A linear fit, which is specific to quasar SEDs, results in a transformation equation of

$$W4 - [24] = 0.014 \pm 0.036 + (0.024 \pm 0.015) \times (W3 - W4) \; . \tag{5.2.3}$$

We applied Equation 5.2.3 to the *WISE* data and assigned the date corresponding to the averaged modified Julian Date of the *WISE* single-exposures from the *WISE* All-Sky Data Release Source Catalog. To allow for uncertainties in the transformation as well as potential systematic uncertainties in the WISE measurements, we augmented the quoted errors by 0.02 magnitudes (see Appendix E), as the root sum square with the nominal error. We then calculated the change between the weighted average of the first *Spitzer* measurements and the *WISE* one. Table 5.2 shows the transformed *WISE* measurement, its estimated uncertainty, and the number of standard deviations difference between it and the *Spitzer* measurements. Sources with changes $> 3\sigma$ between the *Spitzer* and *WISE* measurements and among *Spitzer* measurements themselves are indicated as variable in the comments column.

The slope coefficient in Equation 5.2.3 is consistent with zero, so we have tested the reliability of the results by simply averaging the ratios of the two measurements to derive a color-independent transformation. Using these results slightly increased the apparent significance level of the changes, typically by about 0.1 sigma. In general, there would be no change in the designation of variable sources with this alternative transformation with the exception of Cygnus A, which is changed from being marginally not variable (2.5

Table 5.3 (cont'd)

| Name | Optical Sources | | | $\delta M_V$ | MJD(V) | $N_{\rm epoch}$ | V | $\Delta V$ | MJD(IR) | $N_{\rm epoch}$ | W1 | $\Delta W1$ | W2 | $\Delta W2$ |
|---|---|---|---|---|---|---|---|---|---|---|---|---|---|---|
| | CRTS | ASAS-SN | PTF | | | | | | | | | | | |
| (1) | (2) | (3) | (4) | (5) | (6) | (7) | (8) | (9) | (10) | (11) | (12) | (13) | (14) | (15) |
| PG1543+489 | I | I | II | 0.06 | 53531.3–58277.9 | 202 | 16.24 | 0.82 | 55216.8–58299.2 | 19 | 11.52 | 0.13 | 10.40 | 0.13 |
| PG1545+210 | I | I | II | 0.37 | 53506.4–58284.9 | 324 | 15.98 | 0.96 | 55232.7–58320.9 | 17 | 11.62 | 0.24 | 10.56 | 0.23 |
| PG1552+085 | I | I | III | 0.12 | 53466.4–58284.9 | 379 | 15.59 | 0.81 | 55241.0–58325.8 | 15 | 11.58 | 0.37 | 10.66 | 0.31 |
| PG1612+261 | I | I | II | 0.06 | 53470.4–58281.9 | 413 | 15.42 | 0.99 | 55241.2–58325.9 | 16 | 11.01 | 0.15 | 10.10 | 0.15 |
| PG1613+658 | I | I | II | 0.15 | 53856.4–58281.9 | 330 | 14.65 | 0.57 | 55355.0–58464.9 | 18 | 10.16 | 0.14 | 9.15 | 0.09 |
| PG1617+175 | I | I | II | 0.12 | 53469.4–58283.8 | 420 | 15.16 | 0.88 | 55245.4–58330.4 | 16 | 10.40 | 0.30 | 9.48 | 0.27 |
| PG1626+554 | I | I | II | 0.19 | 53505.4–58281.8 | 341 | 15.65 | 1.03 | 55221.1–58304.2 | 17 | 11.39 | 0.24 | 10.47 | 0.18 |
| PG1700+518 | I | I | II | 0.18 | 53505.4–58281.2 | 374 | 14.89 | 0.49 | 55242.8–58327.9 | 17 | 10.26 | 0.04 | 9.20 | 0.04 |
| PG1704+608 | I | I | II | 0.18 | 53856.4–58284.9 | 347 | 15.34 | 0.91 | 55223.3–58306.5 | 16 | 10.79 | 0.06 | 9.73 | 0.06 |
| PG2112+059 | I | I | III | 0.19 | 53466.5–58284.0 | 415 | 15.42 | 0.77 | 55330.9–58416.8 | 13 | 10.99 | 0.12 | 9.83 | 0.07 |
| PG2130+099 | I | I | II | 0.31 | 53466.5–58284.0 | 419 | 14.54 | 0.76 | 55336.4–58422.1 | 14 | 9.56 | 0.34 | 8.59 | 0.25 |
| PG2209+184 | I | I | II | 0.41 | 53480.5–58284.0 | 385 | 15.54 | 0.87 | 55348.9–58439.7 | 15 | 11.40 | 0.50 | 10.61 | 0.62 |
| PG2214+139 | I | I | II | 0.31 | 53554.4–58282.1 | 396 | 14.42 | 0.49 | 55348.5–58439.6 | 13 | 9.77 | 0.12 | 8.88 | 0.07 |
| PG2233+134 | I | I | II | 0.19 | 53531.4–58284.0 | 276 | 16.34 | 0.96 | 55355.1–58440.4 | 15 | 12.04 | 0.19 | 10.88 | 0.16 |
| PG2251+113 | I | I | II | 0.33 | 53531.4–58282.0 | 340 | 15.67 | 0.63 | 55358.4–58443.3 | 12 | 10.98 | 0.03 | 10.07 | 0.04 |
| PG2304+042 | I | I | II | 0.51 | 53553.4–58281.6 | 362 | 15.14 | 2.28 | 55358.5–58443.5 | 12 | 11.04 | 1.01 | 10.42 | 1.05 |
| PG2308+098 | I | I | II | 0.17 | 53506.5–58282.0 | 283 | 16.06 | 1.11 | 55361.6–58446.5 | 11 | 12.02 | 0.24 | 10.93 | 0.23 |

Note. — Col. (2)-(5): the optical data status: I – used to build the light curve, II – used to check the data consistency, III – not useful either due to limited time samplings or poor data quality, N.A. – data is not available; col. (6), (10): the range of Modified Julian Date that the final optical and IR light curve covers; col. (7), (11): number of data points in the light curves; col. (8), (12), (14): the average magnitude of the light curves; col. (9), (13), (15): the variation amplitude of the light curves.

$\sigma$) to marginally variable (3.4 $\sigma$). That is, the results are relatively robust against modest errors in the transformation. This is not surprising, given how closely the W4 and MIPS [24] bands resemble each other.

The MIPS-measured sample includes 33 of the 87 z $<$ 0.5 PG quasars (plus 106 additional AGN). To investigate the longer wavelength AGN IR variability for the complete PG sample, we compared their *WISE* W3 ($\sim$ 12 $\mu$m) and W4 ($\sim$ 22 $\mu$m) measurements and *Spitzer*/IRS spectra (Houck et al., 2004). We adopted the profile-fit photometry from the ALLWISE Source Catalog, whose measurements were carried out on the co-added image atlas since little variability was detected in PG quasars at these wavelengths. Due to the wide passbands of W3 and W4 as well as the calibration uncertainty of the W4 Relative Spectral Response (**?**), we introduced flux corrections by increasing the W3 band by 17% and decreasing the W4 band by 10%, based on the typical $f_\nu \sim \nu^{-1}$ SED shape of unobscured quasars at these wavelengths, as suggested by the Explanatory Supplement to the WISE All-Sky Data Release Products.[7]

*Synthesis Photometry from Spitzer/IRS Spectra* To be compared with the measurements in *WISE* W3 and W4 bands, we stitched the *Spitzer*/IRS spectra from different module observations together and computed synthetic photometry by convolving the spectral flux with the corresponding photometry Relative Spectral Response curves. For the synthesis photometry uncertainty, we convolved the total error spectra, which include statistical and systematic errors[8], with the relative photometry curves.

## 5.3 Reverberation Analysis Methods

In contrast to the reverberation mapping analysis of the optical emission lines, the transfer functions of the dust mid-IR response are greatly complicated by the radiation transfer of an IR optically-thick torus, whose structures, density profile, grain properties and the inclination angle to the observer are poorly known (e.g., Kawaguchi & Mori, 2011; Almeyda et al., 2017). With the sparse cadence of the infrared light curves, it is not very

[7] See details in http://wise2.ipac.caltech.edu/docs/release/allsky/expsup/sec4_4h.html.

[8] See http://irs.sirtf.com/Smart/CassisProducts

meaningful to fit these data with the simulated reverberation response of any specific torus model. Instead, we develop a "minimalist" method to retrieve the most important properties of the torus by comparing the IR and optical light curves.

### 5.3.1 Constraining the Optical Continuum Variability

The optical continuum variability of bright AGNs is well described by a damped random walk (DRW) (e.g., Kelly et al., 2009; Kozłowski et al., 2010; MacLeod et al., 2010; Zu et al., 2011). In this model, the quasar optical light curves can be reproduced as a stochastic process and the covariance function follows $S(\Delta t) = \sigma^2 \exp(-|\Delta t/\tau_{\rm DRW}|)$, where $\sigma$ is the amplitude and $\tau_{\rm DRW}$ is the damping timescale. We use *JAVELIN* (Zu et al., 2013) to fit the optical light curves with the DRW model and fill the time gaps with the model values.[9]

The damping timescale $\tau_{DRW}$ is known to have correlations with AGN luminosity (Kelly et al., 2009; Zu et al., 2011). In Figure 5.4, we confirm such a correlation also exists by modeling our stitched optical light curves; the trend extends the work by Zu et al. (2011) to higher luminosity. The consistency demonstrated in Figure 5.4 shows that, despite their relatively low quality, the optical light curves compiled from these ground transient surveys should be good enough to produce meaningful results. In addition, the characteristic variability timescales, as traced by $\tau_{\rm DRW}$, are so long that averaging flux measurements and smoothing light curves (introduced later) would not introduce much in the way of systematic uncertainty. Finally, the optical variability timescales are typically larger than the $\sim$200 days per epoch cadences of the mid-IR light curves, thus the dust reverberation signals should be detected with the sparsely sampled *WISE* data.

[9]The DRW model is also known as the simplest of the continuous-time autoregressive moving average process models (CARMA(1,0) or CAR(1)). Despite its wide use, evidence for deviations from the CAR(1) model for AGN optical light curves has been found (e.g., Mushotzky et al., 2011; Graham et al., 2014) and some authors have suggested that higher order CARMA models should be adopted (e.g., Kelly et al., 2014; Kasliwal et al., 2017). However, as demonstrated in Kasliwal et al. (2017), the behavior of the DRW model and more sophisticated CARMA models are identical for time-scales longer than $\sim$10 days. Our optical light curve data typically have significant flux uncertainties and their average time-samplings are $\sim$5–10 days. To be compared with the IR light curves (with time-sampling intervals $\sim$ 200 days), the fitted optical light curves need be further smoothed (see later). As a result, it is not necessary to use higher-order CARMA models to describe the optical light curves.

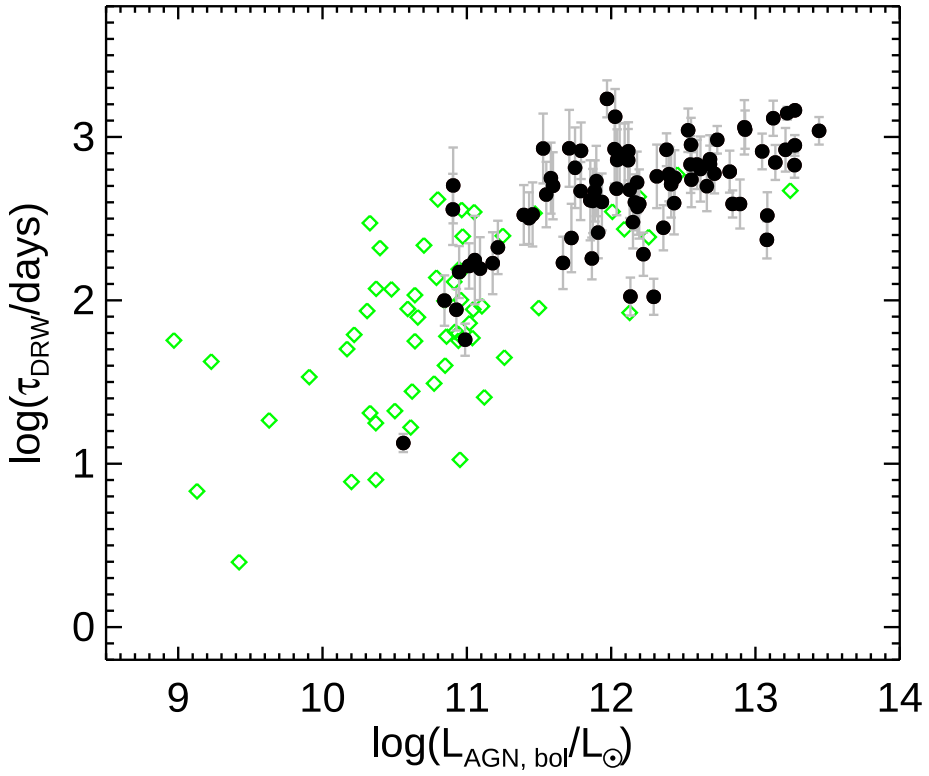


Figure 5.4 Rest-frame DRW damping timescale, $\tau_{\rm DRM}$, of the optical light curves as a function of AGN bolometric luminosity, $L_{\rm AGN,\,bol}$, for PG quasars (filled black dots) and the AGN sample studied by Zu et al. (2011) (open green dots).

### 5.3.2 Retrieving Dust Reverberation Signals

Traditional analyses of the dust reverberation signals were focused on calculating time lags between two light curves by cross-correlation. Although we use this method later to confirm the results, the low cadence of our data led us to develop an alternative method. In addition to the dust time lag, the scaling factor between the IR and optical variability amplitudes gives another important piece of information regarding the AGN torus. We therefore decided to introduce a simple model based only on single-value time lags and amplitudes to retrieve useful reverberation signals and mitigate the influences of many data quality issues.

As discussed in Appendix F, if the viewing angle is not perfectly face-on, the dust response lags on the same radius will have a range, resulting in a smoothing response to the optical variation features in the IR light curve (see also Kawaguchi & Mori 2011).

Therefore, for simplicity, we apply a top-hat function, $b(\tau)$, to smooth the optical DRW model fitting curve, $F(t)_{\rm OPT}$, so

$$< F(t)_{\rm OPT} >_{\tau_W} = \int_{-\tau_{\rm W}/2}^{+\tau_{\rm W}/2} F(t-\tau)_{\rm OPT} b(\tau) d\tau \ , \tag{5.3.1}$$

where $\tau_{\rm W}$ is the width of the boxcar. On average, the smoothing window size should be correlated with the size of the dust emission structure, $R$, which is traced by the average time lag, $\Delta t$, between the IR and optical light curves. By default, the fitted optical DRW model is smoothed on-the-fly with $\tau_{\rm W} = \Delta t/2$ and a maximum value of $\tau_{\rm W} = 200$ days. This upper limit is set to be similar to the time gaps among the NEOWISE epochs as well as in the optical light curve to avoid over-smoothing.

We assume that, to first order, the IR dust emission light curve $F(t)_{\rm IR}$ can be described as a scaled version of the smoothed optical light curve $< F(t')_{\rm OPT} >$ with a constant time lag $\Delta t = t' - t$:

$$F(t)_{\rm IR,\,dust} = AMP \times < F(t-\Delta t)_{\rm OPT} >_{\tau_{\rm W}} + F_{\rm const.} \ , \tag{5.3.2}$$

where $AMP$ is the ratio between the optical and IR flux variation amplitudes, and $F_{\rm const}$ is the systematic, time-insensitive flux shift between the optical and IR bands. Physically, $AMP$ reflects the efficiency of the dust IR energy transfer from the optical variation signal, which is related to the amount of dust; $\Delta t$ is the light travel time from the accretion disk to the dust torus at the studied wavelength. The constant, $F_{\rm const}$, is determined by (1) the AGN SED averaged over a long period of time, (2) systemic uncertainties between the optical and mid-IR flux zero-points, and (3) contamination from the host galaxy emission or nearby sources.

The AGN accretion disk could also produce some variability in the mid-IR light curves. With spectropolarimetry observations of a small sample of bright quasars, Kishimoto et al. (2008) showed that the quasar accretion disk power-law continuum extends into the near-IR ($\lambda \sim 2\ \mu$m) and is consistent with a $F_\nu \propto \nu^{1/3}$ shape. It is not clear at what wavelength the accretion disk emission would transfer to a Rayleigh-Jeans slope; typically a value of 3–5 $\mu$m is suggested in the literature (e.g., Hönig et al., 2010; Stalevski et al., 2016). Considering the lack of constraints, we assume the same $F_\nu \propto \nu^{1/3}$ spectral shape is valid

to describe the accretion disk emission from the optical to the mid-IR bands. Due to the weak wavelength dependence of the accretion disk variability (e.g., Jiang et al., 2017), the accretion disk emission in the mid-IR can be assumed to change simultaneously with the optical. As a result, we have

$$F(t)_{\rm IR,\ accr.\ disk} = F(t)_{\rm OPT}\left(\frac{\nu_{\rm IR}}{\nu_{\rm OPT}}\right)^{1/3} , \tag{5.3.3}$$

and $\nu_{\rm IR}/\nu_{\rm OPT}$ ~0.16 and ~0.12 for the *WISE* W1 and W2 bands, respectively. To recover the dust reverberation signals, the contribution of IR variability by the accretion disk itself needs to be removed according to

$$F(t)_{\rm IR,\ dust} = F(t)_{\rm IR} - F(t)_{\rm IR,\ accr.\ disk} , \tag{5.3.4}$$

where $F(t)_{\rm IR}$ is the observed *WISE* light curve. As pointed out at the very end of Section 5.2.2, various time-insensitive contaminations and uncertainties in the optical light curves would only cause a flux offset. With our linear models to relate the optical and IR variability, these factors are included in $F_{\rm const}$ and should not influence the measurements of $\Delta t$ and $AMP$.

Based on the model described above, we fitted the smoothed and delayed optical light curves (interpolated by the DRW model) to the *WISE* W1 and W2 ones separately with the Levenberg-Marquardt least-squares fitting procedure as implemented in the IDL MPFIT (Markwardt, 2009) package. Figure 5.5 provides some examples of how this approach applies to real data.

### 5.3.3 Detecting the Time Lags

Two methods have been adopted to find the most likely time lags. We first use the classical $\chi^2$ minimization technique to get best-fit values of AMP, $\Delta t$ and $F_{\rm const}$ by fitting the rescaled and shifted optical DRW light curve model to the *WISE* W1 and W2 light curves separately. To explore the influences of different initial values on the final results, we change initial guesses of $\Delta t$/day from 0 to 3000 with an increment of 10. For objects with multiple local minimized $\chi^2$ values, the parameter values with the smallest $\chi^2$ were usually adopted in the end. For the time lag uncertainty, the error provided by MPFIT

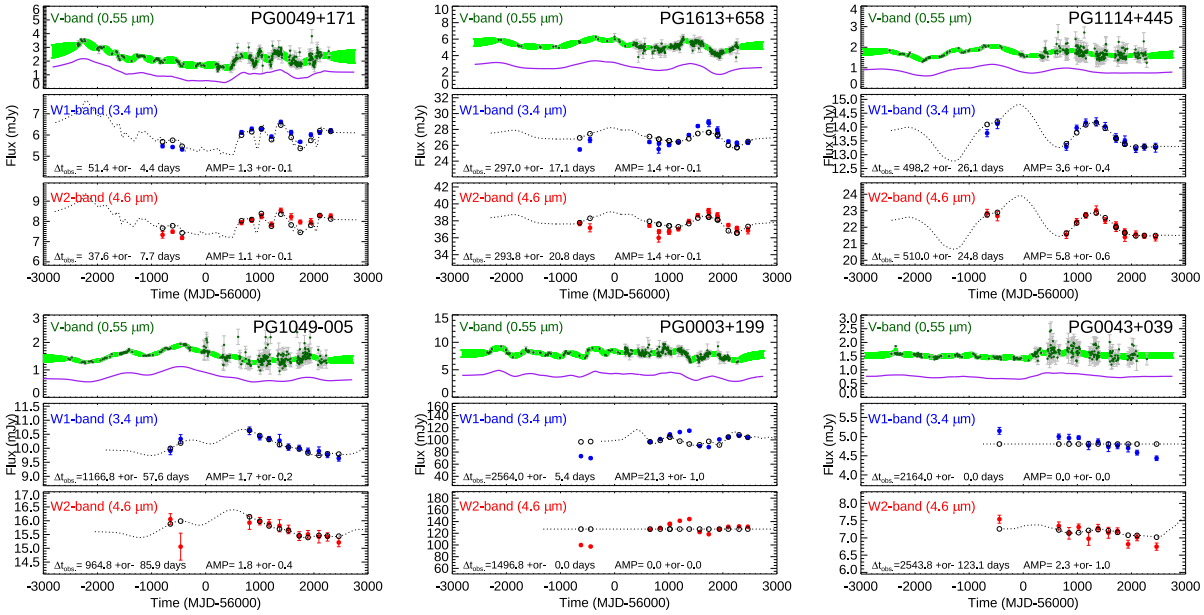


Figure 5.5 Representative optical and mid-IR light curves and corresponding DRW and time-lag fits of PG quasars. Objects in Panels (a)-(d) have convincing dust reveration signals with different mid-IR time lags from $\sim$ 60 to $\sim$ 1400 days; Panel (e) gives an example whose IR light curves are uncorrelated with the optical ones; Panel (f) is a case where the mid-IR and/or the optical light curves do not contain enough features to get any convincing time lag measurement. All measurements are presented in the observed frame. The optical (green), 3.4 $\mu$m (blue) and 4.6 $\mu$m (red) data are presented in the top, middle and bottom sub-panels, respectively. The thick green line in the top sub-panel is a DRW model constrained by the optical light curve, with the solid purple line representing a smoothed version of the model scaled down for clarity. The dashed lines in the middle and bottom sub-panels are the model based on the optical light curve to fit the IR, as described in Section 5.3.2. The model mid-IR fluxes at the observed epochs are shown as open circles. We denote the best-fit parameters with their errors for the mid-IR reverberation signals on the bottom of the corresponding sub-panels.
(The complete figure set (87 images) for all PG quasars is available in the online journal)

only accounts for the measurement uncertainties of the mid-IR fluxes. To estimate the uncertainty introduced by the DRW interpolation of the optical light curve and the optical data itself, we compute 1000 (optical) DRW models with the Monte Carlo (MC) method around the best-fit parameters of the optical light curves within the observing constraints from *JAVELIN*. Adopting the same initial values of the model parameters for the MPFIT code, the same observed mid-IR light curve is then repeatedly fitted by all the 1000 mock optical DRW light curves with the same RM model using *MPFIT*. For the majority of objects, the distribution of the best-fit time lags with these optical mock light curves is symmetric and can be approximated by a Gaussian. We trim away outliers with 3-$\sigma$ clipping and compute the standard deviation to represent the 1-$\sigma$ uncertainty caused by the optical data and DRW model. The final time-lag uncertainty is a combination of this optical uncertainty based on MC simulation and the IR uncertainty reported by *MPFIT*.

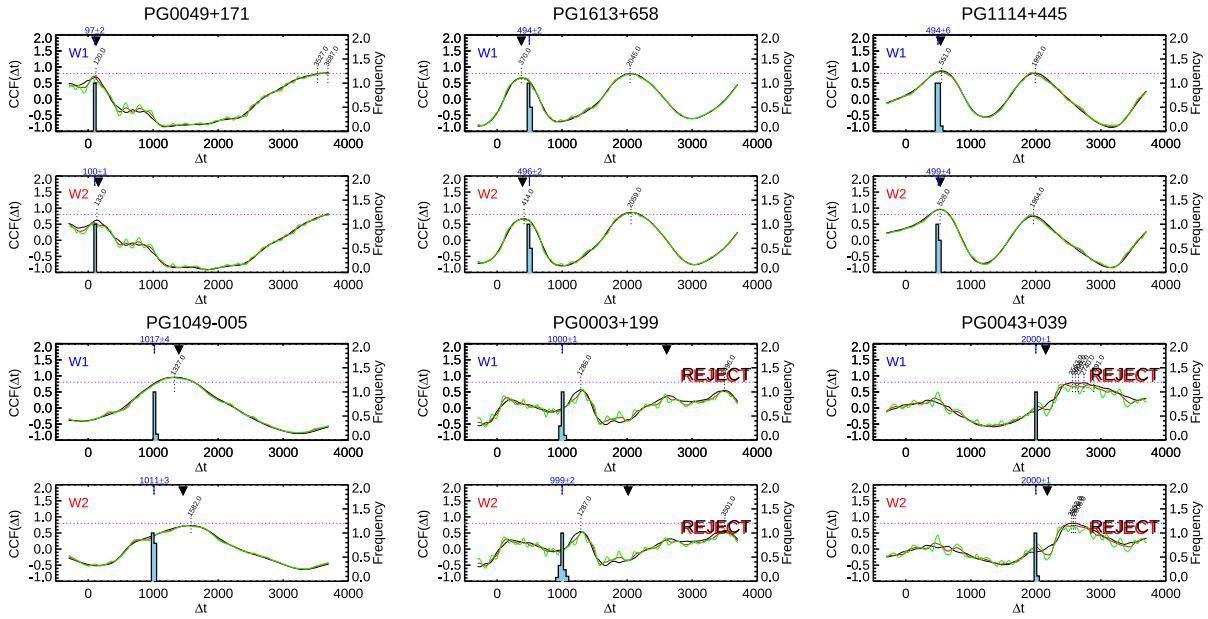


Figure 5.6 Cross-correlation functions between the optical and IR light curves of example PG quasars. The plots here are matched to the objects in Figure 5.5 with the same panel IDs. Panels (a)-(d) are the cases where we think the time lag measurements are reasonable and Panels (e)-(f) are objects whose fittings should be rejected. In each sub-panel, we calculate the $CCF(t)$ with different smoothing windows: $\tau_W$ (black curves), $\tau_W/2$ (red curves), $\tau_W/10$(green curves) where $\tau_W$ is assumed to be 200 days. The histograms show the best-fit time lag distribution by MC modeling of the optical light curve (blue regions). (The complete figure set (87 images) for all PG quasars is available in the online journal)

After removing the accretion disk variability in the AGN IR emission following Equa-

tions 5.3.3 and 5.3.4, we also performed a cross-correlation analysis to constrain the time lags between the optical and the mid-IR light curves. For each object, the interpolated optical light curve based on the DRW model was shifted with $\Delta t = -300$–$3500$ days and the cross-correlation functions $CCF(\Delta t)$ to the *WISE* mid-IR light curves were calculated. We provide several examples in Figure 5.6. In general, we adopt $CCF(\Delta t) > 0.8$ as the criterion for a strong correlation signal. Due to the limited time sampling, multiple $CCF(\Delta)$ peaks for the optical-MIR light curve pair can be found in many objects. In such cases, we inspect the peak locations sorted by the correlation values with the following steps: (1) we first reject any peaks close to the maximum of the explored $\Delta t$ range, which are nonphysical given the possible torus sizes for the AGN luminosity range; (2) we compare the other peak locations to the time lag derived from the $\chi^2$ fitting and adopt the one with the smallest discrepancy. For the vast majority of the sample, such a peak location has the maximum $CCF$ value. In Figure 5.7, we compare the time lags from light-curve fitting with the maximum $CCF(\Delta t)$ from cross-correlation analysis. In general, these two methods yield consistent $\Delta t$, particularly for the W1 band.

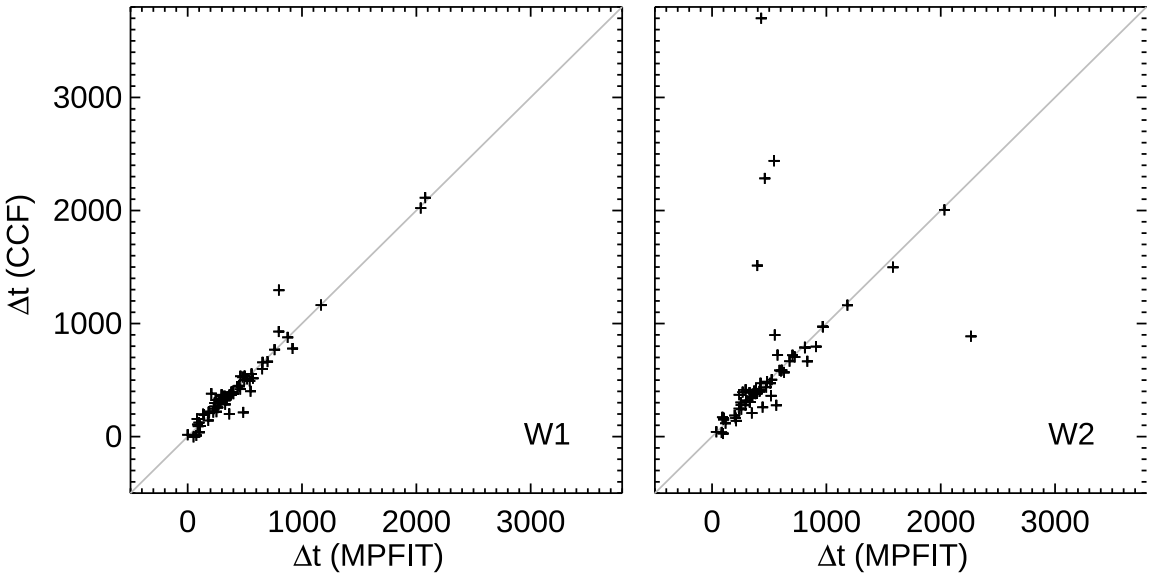


Figure 5.7 Comparison of mid-IR time lags between the results from $\chi^2$ fittings and cross-correlation analysis. The grey diagonal lines are the 1:1 relation.

By default, the final time lags reported in Table 5.4 are adopted from the light-curve fitting method. However, in cases like PG 0049+171 where the MPFIT code returns sus-

picious results, e.g., $\Delta_{W1} > \Delta_{W2}$, we choose to adopt the time lags inferred from the cross-correlation analysis. The reasons for doing this is that model fittings with MPFIT are sensitive to the initial values and the fittings can be stopped at some local minimum of the parameter space. In addition, given the sparse sampling of the light curves, the solution is also not unique. We have inspected each object carefully to check if the fitting results make sense.

We can have a more intuitive idea on how the dust reverberation signals are retrieved by looking at representative objects individually in Figures 5.5 and 5.6. In both figures, Panels (a)-(d) present four examples with convincing measurements of time lags over a broad range and Panels (e)-(f) are two cases whose dust RM fittings are rejected. For objects with convincing time lags, both optical and mid-IR light curves have clear features like small dents (Panel (a)), bumps (Panel (b), (c)) or sometimes just a simple slope (Panel (d)). For these objects, typically there are clear peaks in their cross-correlation curve with CCF$\gtrsim 0.8$ and the corresponding time lag is identical to that obtained by RM model fitting. Objects like the one in Panel (e) are rejected because their optical and mid-IR light curves seem uncorrelated. As shown in Panel (e) of Figure 5.5, both optical and mid-IR light curves have strong features but the RM model fitting poorly reproduces the mid-IR data. For such objects, the peak of the CCF values are typically smaller than 0.6, suggesting a weak, if non-zero, correlation. As will be argued in Section 5.5.1, there could be other explanations for the IR variability of such objects. Objects like Panel (f) do not have enough features in the mid-IR light curves and their optical light curves are also typically of very low variability amplitude. Thus, the data itself cannot allow the model to determine the fitting parameters. In Figure 5.6, it can be seen that the cross-correlation analysis does not show any peaks for this source with CCF$\gtrsim 0.5$ for any reasonable time lags (the W1-band dust time lags for quasars are very unlikely to have $\Delta t > 2000$ days, see Section 5.4.2). We will reject such objects for the reverberation analysis.

## 5.4 Results

### 5.4.1 Mid-IR Variability and Dust Reverberation Signals

Table 5.4 summarizes the derived parameters from fitting the optical and *WISE* W1 and W2 mid-IR light curves with the reverberation mapping model introduced above. Among the 87 PG quasars, we detect convincing dust time lag signals in 67 objects. For those objects without time-lag measurements, eight have data completeness or quality issues, eight lack clear variability features (e.g., very smooth light curves) to pin down a best-fit model (e.g., PG 0043+039, as shown in Figure 5.5), and the remaining four objects have uncorrelated optical and mid-IR temporal variations (e.g., PG 0003+199, as shown in Figure 5.5). In addition, there are nine quasars whose *WISE* flux during the first two or three epochs falls well above or below the time-shifted DRW model prediction in both bands and we rely on the later NEOWISE epochs to extract the dust RM signals.

For the study of the time lag – AGN luminosity relation, we will focus on the 67 PG quasars ($\sim$77% of the sample) with convincing time lag measurements and assume the torus properties are stable over timescales of several years or more.

Table 5.4. Summary of the Mid-IR Reverberation Properties

| name (1) | $z$ (2) | type (3) | $L_{\rm AGN,\,bol}$ (4) | $\log_e(\sigma)$ (5) | $\log_e(\tau)$ (6) | $\Delta t_{\rm W1,\,\chi^2}$ (7) | $AMP_{\rm W1}$ (8) | $\Delta t_{\rm W1,\,CCF}$ (9) | $\Delta t_{\rm W2,\,\chi^2}$ (10) | $AMP_{\rm W2}$ (11) | $\Delta t_{\rm W2,\,CCF}$ (12) | tag$_{W1}$ (13) | tag$_{W2}$ (14) |
|---|---|---|---|---|---|---|---|---|---|---|---|---|---|
| PG 0003+158 | 0.45 | HDD | 13.3 | −1.64 | 6.95 | 1084.1±402.0 | 0.2±0.1 | 3700 (0.55) | 1057.5±462.0 | 0.1±0.2 | 3700 (0.34) | 0 | 0 |
| PG 0003+199 | 0.03 | Norm | 11.2 | −0.42 | 5.43 | 2607.5±288.3 | 20.0±1.0 | 1287 (0.57) | 2014.3±332.7 | 0.0±0.0 | 3501 (0.58) | 0 | 0 |
| PG 0007+106 | 0.09 | Norm | 11.9 | −1.02 | 5.70 | 280.0± 41.0 | 4.7±0.2 | 316 (0.96) | 313.6± 34.5 | 4.5±0.2 | 332 (0.92) | 1 | 1 |
| PG 0026+129 | 0.14 | HDD | 12.4 | −1.04 | 6.53 | 557.2± 41.4 | 1.7±0.2 | 503 (0.91) | 624.9± 33.7 | 2.1±0.2 | 1488 (0.90) | 1 | 1 |
| PG 0043+039 | 0.38 | HDD? | 13.0 | −2.30 | 4.60 | 2152.8±187.5 | 0.0±0.0 | 2564 (0.79) | 2176.2±264.7 | 0.0±0.0 | 2553 (0.80) | 0 | 0 |
| PG 0049+171 | 0.06 | HDD | 11.6 | −0.60 | 6.45 | 120.0± 11.4 | 0.8±0.1 | 3688 (0.82) | 157.0± 28.7 | 0.6±0.1 | 3700 (0.83) | 1 | 1 |
| PG 0050+124 | 0.06 | Norm | 12.3 | −0.32 | 4.76 | 290.4± 42.8 | 14.9±0.4 | 325 (0.95) | 348.0± 43.8 | 15.2±0.5 | 354 (0.95) | 1 | 1 |
| PG 0052+251 | 0.16 | HDD | 12.6 | −0.94 | 6.52 | 400.5± 42.9 | 1.1±0.1 | 2569 (0.77) | 463.4± 60.7 | 0.9±0.1 | 2555 (0.81) | 1 | 1 |
| PG 0157+001 | 0.16 | Norm | 12.6 | −1.51 | 6.67 | 916.5± 0.4 | 17.8±0.5 | 244 (0.96) | 910.8± 0.4 | 17.3±0.7 | 252 (0.95) | 1 | 1 |
| PG 0804+761 | 0.10 | WDD | 12.6 | 0.11 | 6.68 | 659.9± 22.7 | 5.2±0.1 | 665 (0.92) | 661.2± 23.8 | 5.2±0.2 | 676 (0.92) | 1 | 1 |
| PG 0838+770 | 0.13 | Norm | 11.9 | −1.71 | 6.20 | 347.7± 5.1 | 5.0±0.1 | 339 (0.97) | 362.1± 52.8 | 5.8±0.2 | 364 (0.98) | 1 | 1 |
| PG 0844+349 | 0.06 | HDD? | 11.9 | −0.32 | 5.31 | 230.8± 31.2 | 1.5±0.1 | 255 (0.93) | 288.0± 31.5 | 1.3±0.1 | 287 (0.92) | 1 | 1 |
| PG 0921+525 | 0.04 | Norm | 11.0 | −0.00 | 5.18 | 101.8± 3.0 | 3.4±0.1 | 159 (0.85) | 104.0± 3.3 | 2.7±0.1 | 187 (0.82) | 1 | 1 |
| PG 0923+201 | 0.19 | WDD | 12.6 | −1.23 | 7.04 | 1200.8± 92.4 | 4.9±0.4 | 1155 (0.62) | 1327.8±151.5 | 4.9±0.5 | 1305 (0.87) | 0 | 0 |
| PG 0923+129 | 0.03 | Norm | 11.0 | −1.06 | 4.12 | 306.1± 11.9 | 8.0±0.4 | 86 (0.81) | 298.8± 16.5 | 7.5±0.6 | 1272 (0.76) | 0 | 0 |
| PG 0934+013 | 0.05 | Norm | 10.9 | −1.48 | 6.34 | 330.4± 10.3 | 9.3±0.2 | 291 (0.97) | 367.9± 68.8 | 11.9±0.3 | 482 (0.96) | 1 | 1 |
| PG 0947+396 | 0.21 | Norm | 12.4 | −1.68 | 6.64 | 1963.5± 28.2 | 7.3±0.3 | 1915 (0.89) | 2021.3±100.4 | 11.9±0.5 | 1915 (0.84) | 0 | 0 |
| PG 0953+414 | 0.24 | WDD | 12.9 | −0.42 | 7.30 | 913.0± 35.6 | 2.8±0.1 | 911 (0.97) | 1153.6± 49.9 | 2.1±0.2 | 1134 (0.98) | 1 | 1 |
| PG 1001+054 | 0.16 | Norm | 12.0 | −1.60 | 6.39 | 256.0± 47.9 | 6.3±0.4 | 715 (0.86) | 255.0± 91.4 | 9.4±0.8 | 370 (0.92) | 1 | 1 |
| PG 1004+130 | 0.24 | Norm | 12.6 | −1.30 | 6.80 | 796.0± 93.7 | 1.6±0.2 | 707 (0.83) | 532.0±107.8 | 0.9±0.1 | 692 (0.68) | 1 | 1 |
| PG 1011−040 | 0.06 | HDD | 11.7 | −1.26 | 6.87 | 424.8± 35.9 | 3.0±0.2 | 415 (0.96) | 510.8± 47.7 | 3.0±0.2 | 480 (0.95) | 1 | 1 |
| PG 1012+008 | 0.19 | Norm | 12.2 | −1.67 | 6.51 | 519.8± 20.1 | 5.8±0.2 | 536 (0.98) | 570.5± 94.3 | 5.4±0.3 | 2463 (0.97) | 1 | 1 |
| PG 1022+519 | 0.05 | HDD? | 11.2 | −1.78 | 5.23 | 94.0± 47.5 | 6.6±0.2 | 94 (0.93) | 118.0± 43.5 | 7.2±0.3 | 125 (0.94) | 1 | 1 |
| PG 1048+342 | 0.17 | Norm | 11.8 | −2.14 | 6.94 | 276.0± 61.5 | 2.1±0.1 | 241 (0.87) | 565.8±115.5 | 2.9±0.2 | 572 (0.85) | 1 | 1 |
| PG 1048−090 | 0.34 | WDD | 12.8 | −1.29 | 6.78 | 589.0±155.2 | 0.0±0.0 | 2632 (0.54) | 549.7± 55.3 | 0.0±0.0 | 2488 (0.71) | 0 | 0 |
| PG 1049−005 | 0.36 | Norm | 13.0 | −1.71 | 7.08 | 1284.6±108.3 | 1.6±0.2 | 1327 (0.96) | 1059.3±130.8 | 1.7±0.4 | 1583 (0.73) | 1 | 0 |
| PG 1100+772 | 0.31 | HDD | 13.1 | −1.38 | 6.13 | 720.8± 88.1 | 1.3±0.1 | 722 (0.59) | 724.4±144.8 | 1.6±0.2 | 725 (0.58) | 0 | 0 |
| PG 1103−006 | 0.43 | Norm | 12.8 | −1.80 | 6.38 | 593.9± 51.1 | 0.6±0.2 | 2223 (0.46) | 823.0±273.4 | 0.8±0.3 | 2371 (0.31) | 0 | 0 |
| PG 1114+445 | 0.14 | Norm | 12.3 | −1.73 | 6.55 | 534.8± 21.7 | 3.3±0.4 | 551 (0.88) | 527.9± 37.0 | 5.4±0.6 | 528 (0.96) | 1 | 1 |
| PG 1115+407 | 0.15 | HDD | 12.4 | −1.93 | 5.83 | 465.9± 18.3 | 5.0±0.3 | 422 (0.83) | 455.4± 30.7 | 4.3±0.5 | 273 (0.74) | 1 | 1 |
| PG 1116+215 | 0.18 | WDD | 12.9 | −0.40 | 7.28 | 819.6± 98.6 | 4.6±0.2 | 1895 (0.85) | 967.4± 90.0 | 4.9±0.3 | 1139 (0.83) | 1 | 1 |
| PG 1119+120 | 0.05 | Norm | 11.5 | −0.69 | 5.92 | 108.0± 6.7 | 3.1±0.2 | 42 (0.94) | 101.0± 6.7 | 2.7±0.2 | 29 (0.91) | 1 | 1 |
| PG 1121+422 | 0.23 | HDD | 12.5 | −1.48 | 7.28 | 912.1±116.1 | 2.8±0.1 | 497 (0.94) | 515.2± 82.4 | 3.2±0.2 | 2277 (0.88) | 1 | 1 |
| PG 1126−041 | 0.06 | Norm | 11.8 | −0.41 | 6.27 | 554.1± 28.3 | 7.0±0.3 | 566 (0.87) | 661.1± 25.4 | 7.3±0.4 | 731 (0.88) | 1 | 1 |
| PG 1149−110 | 0.05 | Norm | 11.1 | −1.38 | 5.15 | 86.9± 23.1 | 7.6±0.2 | 110 (0.85) | 211.6± 23.2 | 7.6±0.2 | 143 (0.79) | 1 | 1 |
| PG 1151+117 | 0.18 | Norm | 12.0 | −1.25 | 7.69 | 295.9± 27.3 | 2.4±0.1 | 341 (0.96) | 414.0± 63.5 | 2.3±0.2 | 414 (0.87) | 1 | 1 |

Table 5.4 (cont'd)

| name (1) | $z$ (2) | type (3) | $L_{\rm AGN,\,bol}$ (4) | $\log_e(\sigma)$ (5) | $\log_e(\tau)$ (6) | $\Delta t_{\rm W1,\,\chi^2}$ (7) | $AMP_{\rm W1}$ (8) | $\Delta t_{\rm W1,\,CCF}$ (9) | $\Delta t_{\rm W2,\,\chi^2}$ (10) | $AMP_{\rm W2}$ (11) | $\Delta t_{\rm W2,\,CCF}$ (12) | tag$_{W1}$ (13) | tag$_{W2}$ (14) |
|---|---|---|---|---|---|---|---|---|---|---|---|---|---|
| PG 1202+281 | 0.17 | Norm | 12.1 | −1.69 | 6.93 | 361.0± 39.3 | 7.8±0.4 | 358 (0.96) | 439.1± 44.5 | 7.9±0.5 | 429 (0.95) | 1 | 1 |
| PG 1211+143 | 0.09 | Norm | 12.1 | −0.07 | 4.79 | 365.6± 90.2 | 2.7±0.2 | 358 (0.88) | 557.5± 47.6 | 3.3±0.3 | 2015 (0.77) | 1 | 1 |
| PG 1216+069 | 0.33 | HDD | 13.0 | −0.10 | 3.23 | 1016.9± 23.9 | 0.3±0.1 | 985 (0.30) | 1012.9± 76.3 | 0.2±0.1 | 703 (0.34) | 0 | 0 |
| PG 1226+023 | 0.16 | WDD | 13.4 | 1.09 | 7.21 | 1918.4± 67.9 | 0.0±0.0 | 933 (0.75) | 1684.4±280.6 | 0.0±0.0 | 951 (0.59) | 0 | 0 |
| PG 1229+204 | 0.06 | Norm | 11.5 | −0.70 | 6.87 | 266.3± 71.2 | 5.3±0.1 | 261 (0.98) | 328.0± 8.5 | 5.2±0.1 | 305 (0.97) | 1 | 1 |
| PG 1244+026 | 0.05 | Norm | 11.1 | −2.36 | 5.27 | 118.9± 70.3 | 0.8±0.3 | 1101 (0.60) | 180.0±177.3 | 0.7±0.5 | 1205 (0.46) | 0 | 0 |
| PG 1259+593 | 0.47 | WDD | 13.3 | −1.54 | 7.25 | 746.2± 55.9 | 2.3±0.1 | 732 (0.98) | 784.4± 70.3 | 2.2±0.2 | 794 (0.93) | 1 | 1 |
| PG 1302−102 | 0.29 | HDD | 13.2 | −1.18 | 7.05 | 643.8± 33.2 | 1.6±0.1 | 619 (0.90) | 681.0± 82.6 | 1.8±0.2 | 662 (0.91) | 1 | 1 |
| PG 1307+085 | 0.16 | Norm | 12.2 | −1.51 | 6.20 | 357.6± 46.1 | 2.8±0.2 | 334 (0.91) | 505.9± 57.7 | 3.1±0.2 | 368 (0.87) | 1 | 1 |
| PG 1309+355 | 0.18 | Norm | 12.4 | −1.74 | 6.59 | 404.6± 62.0 | 2.5±0.3 | 419 (0.78) | 531.8± 92.0 | 1.6±0.5 | 1453 (0.58) | 1 | 1 |
| PG 1310−108 | 0.04 | Norm | 10.9 | −1.68 | 4.56 | 152.0± 30.2 | 2.0±0.3 | 208 (0.76) | 363.9± 26.5 | 4.4±0.4 | 391 (0.83) | 1 | 1 |
| PG 1322+659 | 0.17 | Norm | 12.1 | −1.29 | 6.38 | 524.2± 54.3 | 2.8±0.1 | 657 (0.89) | 745.0±115.0 | 3.0±0.1 | 748 (0.86) | 1 | 1 |
| PG 1341+258 | 0.09 | HDD? | 11.7 | −2.25 | 5.27 | 351.1±246.1 | 5.8±0.3 | 356 (0.71) | 383.9± 18.5 | 6.9±0.4 | 383 (0.71) | 1 | 1 |
| PG 1351+236 | 0.05 | Norm | 10.8 | −2.08 | 4.70 | 79.6± 48.9 | 7.9±0.4 | 11 (0.70) | 83.8± 32.9 | 5.1±0.4 | 38 (0.60) | 1 | 1 |
| PG 1351+640 | 0.09 | Norm | 12.2 | −0.37 | 6.11 | 631.2± 29.5 | 1.1±0.1 | 1509 (0.87) | 808.6± 51.8 | 1.5±0.2 | 953 (0.88) | 1 | 1 |
| PG 1352+183 | 0.16 | Norm | 11.9 | −1.70 | 6.20 | 272.0± 10.1 | 3.1±0.2 | 247 (0.91) | 316.0± 78.4 | 3.5±0.3 | 329 (0.94) | 1 | 1 |
| PG 1354+213 | 0.30 | Norm | 12.4 | −2.04 | 7.06 | 911.5±124.1 | 4.4±0.2 | 897 (0.91) | 1061.4±169.3 | 5.2±0.3 | 1066 (0.88) | 0 | 0 |
| PG 1402+261 | 0.16 | Norm | 12.4 | −1.44 | 6.18 | 368.1± 54.6 | 5.6±0.4 | 1972 (0.91) | 414.6± 82.4 | 8.8±0.6 | 2011 (0.88) | 1 | 1 |
| PG 1404+226 | 0.10 | HDD? | 11.7 | −2.16 | 5.63 | 214.7± 13.2 | 2.4±0.2 | 1893 (0.86) | 272.0± 30.7 | 2.9±0.4 | 1977 (0.89) | 1 | 1 |
| PG 1411+442 | 0.09 | Norm | 12.0 | −0.55 | 6.89 | 441.7± 46.2 | 2.3±0.1 | 704 (0.88) | 445.2± 77.6 | 2.5±0.2 | 1000 (0.84) | 1 | 1 |
| PG 1415+451 | 0.11 | Norm | 11.7 | −1.79 | 6.64 | 300.0±232.3 | 4.3±0.1 | 350 (0.95) | 677.4±245.2 | 0.0±0.0 | 433 (0.91) | 1 | 1 |
| PG 1416−129 | 0.13 | Norm | 11.6 | −2.32 | 6.41 | 424.8±426.7 | 2.8±0.3 | −162 (0.53) | 511.0±113.4 | 1.9±0.3 | 530 (0.44) | 0 | 0 |
| PG 1425+267 | 0.37 | Norm | 12.7 | −2.00 | 7.25 | 744.1± 99.5 | 0.8±0.1 | 749 (0.88) | 760.5±321.7 | 0.6±0.2 | 738 (0.70) | 1 | 1 |
| PG 1426+015 | 0.09 | Norm | 12.0 | −0.11 | 6.77 | 264.0± 24.7 | 3.9±0.2 | 314 (0.95) | 352.0± 64.5 | 3.3±0.2 | 359 (0.92) | 1 | 1 |
| PG 1427+480 | 0.22 | Norm | 12.2 | −2.19 | 5.97 | 342.6± 46.7 | 1.4±0.1 | 332 (0.86) | 356.0± 52.0 | 1.1±0.2 | 352 (0.78) | 1 | 1 |
| PG 1435−067 | 0.13 | HDD | 12.2 | −1.88 | 5.43 | 244.0± 42.1 | 4.8±0.2 | 314 (0.86) | 356.1± 63.6 | 4.5±0.4 | 362 (0.82) | 1 | 1 |
| PG 1440+356 | 0.08 | Norm | 11.9 | −0.35 | 6.29 | 255.3± 40.0 | 4.3±0.2 | 290 (0.95) | 264.9± 30.4 | 4.7±0.2 | 296 (0.92) | 1 | 1 |
| PG 1444+407 | 0.27 | Norm | 12.7 | −1.95 | 6.52 | 399.5± 16.4 | 2.6±0.2 | 405 (0.93) | 448.1± 61.1 | 2.6±0.3 | 505 (0.74) | 1 | 1 |
| PG 1448+273 | 0.06 | Norm | 11.4 | −0.75 | 5.88 | 280.0± 31.7 | 2.8±0.1 | 289 (0.98) | 371.3± 49.0 | 2.6±0.1 | 378 (0.97) | 1 | 1 |
| PG 1501+106 | 0.04 | Norm | 11.4 | −0.05 | 5.91 | 113.9± 16.4 | 2.1±0.1 | 151 (0.85) | 112.0± 11.9 | 2.0±0.1 | 2703 (0.77) | 1 | 1 |
| PG 1512+370 | 0.37 | Norm | 12.7 | −1.95 | 6.91 | 1352.4±257.2 | 0.5±0.1 | 3152 (0.82) | 2122.8±478.4 | 1.2±0.3 | 3383 (0.68) | 0 | 0 |
| PG 1519+226 | 0.14 | Norm | 12.0 | −1.68 | 7.40 | 193.8±113.1 | 7.4±0.2 | 228 (0.99) | 356.5±105.0 | 6.2±0.3 | 365 (0.98) | 1 | 1 |
| PG 1534+580 | 0.03 | Norm | 10.9 | −0.67 | 5.08 | 128.0± 2.9 | 3.2±0.2 | 240 (0.67) | 139.3± 12.7 | 4.1±0.1 | 376 (0.75) | 0 | 0 |
| PG 1535+547 | 0.04 | Norm | 10.9 | −0.54 | 5.99 | 180.0± 1.4 | 8.5±0.1 | 157 (0.92) | 207.7± 0.2 | 7.7±0.2 | 219 (0.92) | 1 | 1 |
| PG 1543+489 | 0.40 | Norm | 13.1 | −2.88 | 5.85 | 2052.2±606.7 | 8.9±0.9 | 2002 (0.74) | 2066.0±276.3 | 13.4±1.3 | 1974 (0.72) | 1 | 1 |
| PG 1545+210 | 0.27 | WDD | 12.7 | −1.37 | 6.90 | 774.8± 51.3 | 1.8±0.1 | 794 (0.94) | 835.3± 74.3 | 2.1±0.1 | 804 (0.94) | 1 | 1 |

### 5.4.2 The IR Time Lag – AGN Luminosity Correlation

The inner size of the dust torus is physically determined by grain sublimation. Since carbon and silicate dust are the dominant species of interstellar grains, a similar grain mixture is also commonly assumed for the AGN torus. The sublimation temperatures, $T_{\rm sub}$, of grains are estimated to be 1500–1800 K for graphite and 800-1000 K for silicates. Consequently, only graphite grains would survive at the innermost regions and silicate grains would be distributed at larger radii. Assuming an optically-thin environment, Barvainis (1987) provided an estimate of the graphite sublimation radius

$$\frac{R_{\rm sub,C}}{\rm pc} = 1.3 \left( \frac{L_{\rm UV}}{10^{46} {\rm erg\ s^{-1}}} \right)^{0.5} \left( \frac{T_{\rm sub}}{1500K} \right)^{-2.8} \left( \frac{a}{0.05\ \mu{\rm m}} \right)^{-0.5} , \tag{5.4.1}$$

where $L_{\rm UV}$ is the AGN UV luminosity. Following Kishimoto et al. (2007), we also introduce a $a^{-1/2}$ term to approximate the $R_{\rm sub}$ dependence on the grain size $a$. For silicate dust grains, adopting the absorption efficiency of astronomical silicate (Draine & Lee, 1984; Laor & Draine, 1993) and repeating the derivations in Barvainis (1987), we have

$$\frac{R_{\rm sub,S}}{\rm pc} = 2.7 \left( \frac{L_{\rm UV}}{10^{46} {\rm erg\ s^{-1}}} \right)^{0.5} \left( \frac{T_{\rm sub}}{1000K} \right)^{-2.8} \left( \frac{a}{0.05\ \mu{\rm m}} \right)^{-0.5} . \tag{5.4.2}$$

If we take $L_{\rm UV} = 0.165\ L_{\rm AGN,bol}$ (Risaliti & Elvis, 2004) and assume $T_{\rm sub}$ =1500 K and $T_{\rm sub}$ =1000 K for graphite and silicate dust grains, for an AGN with $L_{\rm AGN,bol} = 10^{12}\ L_{\odot}$, $R_{\rm sub,C} \sim 0.33$ pc and $R_{\rm sub,S} \sim 0.69$ pc.

For an infinitely thin ring viewed from a perfect face-on observing angle, the time lag is directly related to the dust radius as $\Delta t = R_{\rm d}/c$. In real situations, the relation would be dependent on the observing angle as well as the dust distribution (some additional discussion is provided in Appendix F). However, for a large sample of type-1 AGNs, these effects would be smeared out. To first order, we adopt the following linear equation to fit the data:

$$\log(\Delta t) = \alpha + \beta \log(L_{\rm AGN}) . \tag{5.4.3}$$

In the following analysis and discussion, we have applied the dilation factor $(1+z)$ for the time lag (i.e., $\Delta t = \Delta t_{\rm \mathbf{int.}} = \Delta t_{\rm \mathbf{obs.}}/(1+z)$). Due to the lack of constraints on the wavelength-dependent torus size, we will not make K corrections for individual quasars but treat the sample as a whole and compute the correction with an averaged redshift.

Table 5.4 (cont'd)

| name (1) | $z$ (2) | type (3) | $L_{\rm AGN,\,bol}$ (4) | $\log_e(\sigma)$ (5) | $\log_e(\tau)$ (6) | $\Delta t_{\rm W1,\,\chi^2}$ (7) | $AMP_{\rm W1}$ (8) | $\Delta t_{\rm W1,\,CCF}$ (9) | $\Delta t_{\rm W2,\,\chi^2}$ (10) | $AMP_{\rm W2}$ (11) | $\Delta t_{\rm W2,\,CCF}$ (12) | tag$_{W1}$ (13) | tag$_{W2}$ (14) |
|---|---|---|---|---|---|---|---|---|---|---|---|---|---|
| PG 1552+085 | 0.12 | HDD? | 12.1 | −1.37 | 6.85 | 212.0± 30.2 | 3.3±0.1 | 243 (0.98) | 264.0± 22.9 | 3.5±0.1 | 261 (0.98) | 1 | 1 |
| PG 1612+261 | 0.13 | Norm | 12.0 | −0.98 | 6.77 | 627.3± 39.7 | 1.2±0.2 | 624 (0.41) | 664.2± 62.0 | 2.0±0.3 | 1262 (0.71) | 0 | 0 |
| PG 1613+658 | 0.13 | Norm | 12.4 | −0.65 | 6.43 | 371.9± 63.3 | 1.6±0.2 | 2046 (0.80) | 390.4± 37.1 | 1.8±0.2 | 2059 (0.87) | 1 | 1 |
| PG 1617+175 | 0.11 | WDD | 12.1 | −0.71 | 6.75 | 472.4± 34.7 | 3.3±0.1 | 1187 (0.97) | 575.8± 26.7 | 4.4±0.2 | 1183 (0.97) | 1 | 1 |
| PG 1626+554 | 0.13 | HDD | 12.2 | −1.14 | 6.10 | 346.8± 7.4 | 1.6±0.1 | 381 (0.90) | 414.5± 9.2 | 1.4±0.1 | 416 (0.81) | 1 | 1 |
| PG 1700+518 | 0.28 | Norm | 13.1 | −1.69 | 7.49 | 292.4±669.7 | 1.4±0.3 | −300 (0.80) | 967.9±216.2 | 0.0±0.0 | 3700 (0.68) | 0 | 0 |
| PG 1704+608 | 0.37 | Norm | 13.1 | −1.15 | 6.93 | 1650.3±744.1 | 0.7±0.1 | 3700 (0.60) | 1689.5±815.7 | 0.8±0.1 | 1660 (0.70) | 0 | 0 |
| PG 2112+059 | 0.47 | Norm | 13.3 | −1.44 | 7.74 | 2265.0±105.9 | 0.9±0.2 | 646 (0.95) | 2614.9±413.5 | 1.1±1.0 | 883 (0.67) | 1 | 1 |
| PG 2130+099 | 0.06 | Norm | 11.9 | −0.27 | 6.41 | 525.3± 44.7 | 5.8±0.2 | 521 (0.89) | 801.3± 46.6 | 5.5±0.2 | 1075 (0.89) | 1 | 1 |
| PG 2209+184 | 0.07 | HDD? | 11.6 | −1.02 | 6.23 | 108.0± 10.4 | 5.3±0.1 | 19 (0.95) | 187.0± 13.3 | 7.7±0.2 | 189 (0.97) | 1 | 1 |
| PG 2214+139 | 0.07 | WDD | 11.9 | −0.59 | 6.13 | 324.6±165.6 | 4.2±0.4 | 2545 (0.86) | 378.4±622.9 | 3.0±0.4 | 2622 (0.85) | 1 | 0 |
| PG 2233+134 | 0.32 | Norm | 12.7 | −2.30 | 6.73 | 455.1± 39.0 | 2.2±0.2 | 449 (0.90) | 426.9± 47.7 | 2.7±0.4 | 420 (0.83) | 1 | 1 |
| PG 2251+113 | 0.32 | WDD | 12.9 | −2.40 | 6.30 | 579.7±116.8 | 2.7±0.8 | 576 (0.85) | 598.0±101.8 | 3.5±1.0 | 591 (0.91) | 0 | 0 |
| PG 2304+042 | 0.04 | Norm | 10.6 | 0.11 | 2.66 | 86.0± 3.6 | 3.7±0.0 | 156 (0.97) | 98.2± 1.5 | 3.8±0.1 | 171 (0.97) | 1 | 1 |
| PG 2308+098 | 0.43 | HDD | 13.2 | −1.11 | 7.68 | 703.1± 50.7 | 1.3±0.1 | 548 (0.88) | 1418.8±129.5 | 1.2±0.1 | 1493 (0.83) | 0 | 0 |

Note. — Col. (1): object name; Col. (2): redshift; Col. (3): IR SED type from Lyu et al. (2017); Col. (4): AGN bolometric luminosity estimated from IR SED decompositions (Lyu et al., 2017) with bolometric corrections described in Section 5.4.2; Col. (5)-(6): DRW model amplitude ($\sigma$) and timescale ($\tau$) from the fitting the combined V-band light curve with the *Javelin* code, both in natural logs; Col. (7)-(8): IR dust time lag (obsered frame) and IR-optical variability amplitude factor from fitting the *WISE* W1-band light curves with our model; Col. (9): W1-band dust time lag suggested by cross-correlation analysis with the peak CCF value in brackts; Col. (10)–Col. (12): similar to Col. (6)–(8) but for *WISE* W2-band; Col. (13), (14): if the results are used for reverberation analysis, 1–yes, 0–no.

**Comments on individual objects**: the results of PG 0003+129, PG 1048-090 and PG 1244+026 are dropped since their IR light curves contain large uncertainties. The mid-IR photometry of several epochs of PG 1226+069 are saturated, making the mid-IR light curve unuseful. The optical light curves of PG 0923+129, PG 1216+069, PG 1354+213 and PG 1416-129 have limited time (only good CRTS or ASAS-SN data are available). PG 0043+039, PG 0947+396, PG 1100+772, PG 1103+006, PG 1512+370, PG 1700+518, PG 1704+608 and PG 2308+098 do not show enough variability features so that meaningful time lags cannot be constrained. The optical and IR light curves of PG 0003+199, PG 0923+201, PG 1534+580 and PG 1612+261 seem uncorrelated with peak CCF$<$0.7, so their results have been also dropped.

*AGN Luminosity Estimation* To make a comparison of the AGN bolometric luminosity $L_{\rm AGN,\,bol}$ in the literature, we use the integrated AGN IR emission of PG quasars as the best estimator. As demonstrated in Lyu et al. (2017), despite their identical UV-optical SED shape, unobscured type-1 quasars present intrinsic SED variations in the IR that can be grouped into normal, warm-dust-deficient (WDD) and hot-dust-deficient (HDD) types (see the comparison in Figure 5.8). After building the intrinsic AGN templates, Lyu et al. (2017) fit the observed SEDs of PG quasars with an empirical SED model. The AGN intrinsic SED types were determined by comparing the fitted $\chi^2$ of the model. We convert the AGN-heated IR luminosity derived from the optical-to-IR SED fittings in Lyu et al. (2017) to the monochromatic luminosity at 5100 Å with the following scaling factors:

$$\lambda L_\lambda(0.51\ \mu{\rm m}) = 0.47 L_{\rm NORM,\ 8\text{-}1000\ \mu m} \tag{5.4.4}$$

$$= 1.02 L_{\rm WDD,\ 8\text{-}1000\ \mu m} \tag{5.4.5}$$

$$= 1.75 L_{\rm HDD,\ 8\text{-}1000\ \mu m} \tag{5.4.6}$$

where NORM, WDD, HDD represent the normal Elvis et al. (1994)-like, warm-dust-deficient, and hot-dust-deficient AGN templates as characterized in Lyu et al. (2017); Lyu & Rieke (2017). We then convert $L_\lambda(0.51\ \mu{\rm m})$ to $L_{\rm AGN,\,bol}$ with the updated quasar bolometric correction from Runnoe et al. (2012c):

$$\log\left(\frac{L_{\rm AGN,bol}}{\rm erg\ s^{-1}}\right) = 4.89 + 0.91\log\left(\frac{\lambda L_\lambda(0.51\mu{\rm m})}{\rm erg\ s^{-1}}\right) \tag{5.4.7}$$

We realize that there are several alternative tracers for $L_{\rm AGN,bol}$ widely used in the literature, such as hard X-ray luminosity, mid-IR AGN continuum luminosity, and the mid-IR [O IV]$\lambda$25.89 $\mu$m emission line luminosity (Meléndez et al., 2008; Diamond-Stanic et al., 2009; Rigby et al., 2009). Although these tracers could be less affected by dust obscuration and might be isotropic, whether they can be applied over a wide AGN luminosity range that covers the quasar population is a question. For example, the application of [O IV] emission line has been only discussed for the Seyfert population ($L_{\rm AGN,\,bol} \lesssim 10^{11} L_\odot$) and there is evidence suggesting the structures of AGN narrow-line regions could evolve at high luminosity (e.g., Netzer et al., 2004). Using the single-band mid-IR continuum is also complicated: (1) the fraction of the AGN luminosity that is reprocessed in the mid-IR (7–15 $\mu$m) can vary intrinsically by 0.3–0.9 dex (Lyu et al., 2017); (2) the possible addition

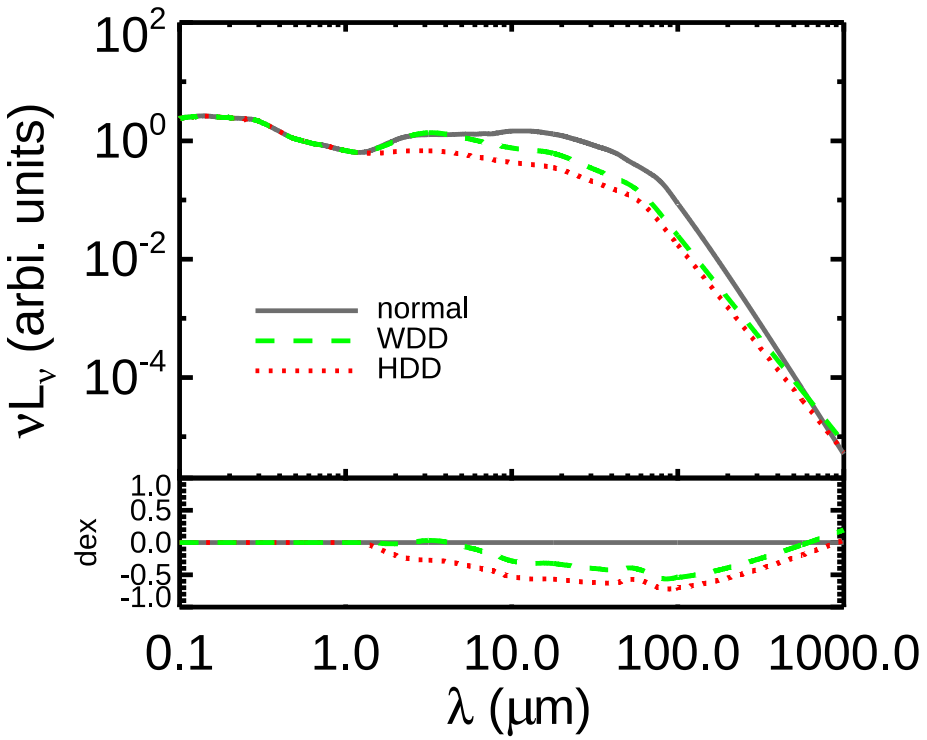


Figure 5.8 Comparison of the normal, WDD and HDD AGN templates developed in Lyu et al. (2017). The bottom panel highlights the infrared flux differences in dex of these templates by normalizing their SEDs by the normal AGN template.

of reprocessed emission from AGN-heated polar dust can easily lead to scatter exceeding 1 dex for the same $L_{\rm AGN,\,bol}$ (Lyu & Rieke, 2018). Given these uncertainties, we opt to use the V-band bolometric correlation throughout this work.

The ambiguities in calculating AGN bolometric luminosity have contributions from both measured qualities (e.g., the photometric errors) and bolometric correction factors. In many cases, the latter can dominate. Given the likely variation from source to source, we adopt 0.3 dex as the relative $L_{\rm AGN}$ uncertainty for all objects.

*Correlation between Mid-IR Time Lag and AGN Luminosity* In Figure 5.9, we present the time lags of the mid-IR emission in the *WISE* W1 and W2 bands of PG quasars as a function of their AGN bolometric luminosities. It is clear that these two quantities are strongly correlated. From fitting these measurements with equation 5.4.3 with the IDL

program FITEXY, we have

$$\Delta t_{\rm torus,W1}/{\rm day} = 10^{2.10\pm0.06}(L_{\rm AGN,SED}/10^{11}L_{\odot})^{0.47\pm0.06} \tag{5.4.8}$$

for the W1 band, and

$$\Delta t_{\rm torus,W2}/{\rm day} = 10^{2.20\pm0.06}(L_{\rm AGN,SED}/10^{11}L_{\odot})^{0.45\pm0.05} \tag{5.4.9}$$

for the W2 band. These correlations closely follow the expected $\Delta t \propto L_{\rm AGN}^{0.5}$ relation. At a given $L_{\rm AGN}$, the time lag differences in the W1 and W2 bands are small with the mean value of $\Delta t_{\rm torus,W2}/\Delta t_{\rm torus,W1} \sim 1.21 \pm 0.36$, and a median value at 1.15. A linear fit to both W1 and W2 time lags yields

$$\Delta t_{\rm torus,W2} = (1.17 \pm 0.11)\Delta t_{\rm torus,W1} + (0.21 \pm 54.3)\ . \tag{5.4.10}$$

Despite the large uncertainty, the fitted intercept is very close to zero, indicating that the time lag in W2 is always statistically larger than in W1 by a constant factor.

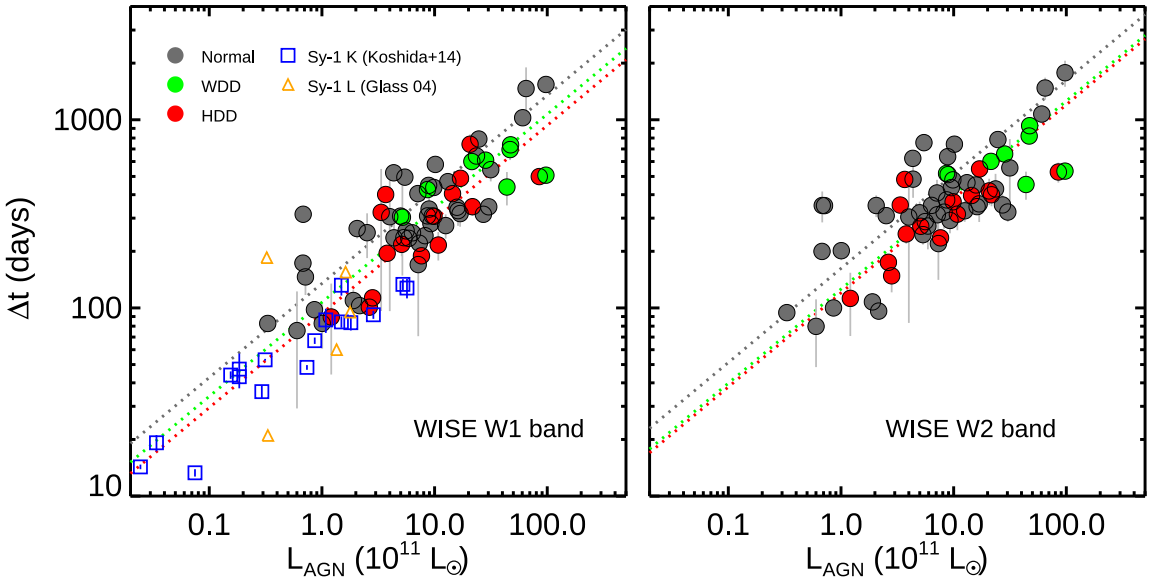


Figure 5.9 Dust time lags between the *WISE* mid-IR band and optical band light curves plotted against the AGN luminosity for PG quasars. The dotted lines are the fitted correlations for normal (grey), WDD (green) and HDD (red) quasars assuming $\Delta t \propto L_{\rm AGN}^{0.5}$. We also show the K-band time-lag measurements of the 17 Seyfert-1 nuclei studied in Koshida et al. (2014) and the L-band time-lag measurements of the 5 Seyfert-1 nuclei in Glass (2004) with our estimation of their AGN bolometric luminosities in the left panel.

The average redshift of the 67 fitted PG quasars is 0.15±0.10. Assuming a normal AGN template, the corresponding intrinsic wavelengths of the *WISE* W1 and W2 band filters are $2.94^{+0.28}_{-0.24}$ $\mu$m and $4.03^{+0.38}_{-0.33}$ $\mu$m. For an AGN with $L_{\rm AGN,\,bol} = 10^{12}\ L_{\odot}$, these results correspond to a dust emission region size at $\lambda_{\rm rest} \sim 3$ $\mu$m of ∼0.31 pc for the W1 band and at $\lambda_{\rm rest} \sim 4$ $\mu$m of $\sim 0.37$ pc for the W2 band. The similar sizes at the W1 and W2 bands strongly support a compact torus, where the emission at the rest frame ∼3–5 $\mu$m is dominated by dust grains with similar temperatures.

*Comparison with Previous Dust Reverberation Studies* Previous ground-based K-band reverberation mapping has been only focused on relatively low-luminosity AGNs ($L_{\rm AGN} \lesssim 10^{11}\ L_{\odot}$) in Seyfert galaxies. However, given the SED analysis in Lyu & Rieke (2018), it is likely that Seyfert-1 nuclei and quasars share similar torus properties. For the 17 Seyfert-1 objects in Koshida et al. (2014), we adopted the average K-band time lags estimated with the CCF methods and the $\alpha_{\nu} = 1/3$ accretion-disk component model, and converted the weighted averaged V-band absolute magnitude to $L_{\rm AGN,\,bol}$ following Equation 5.4.7. (See Appendix G for further discussion of the consistency of their and our measurements of time lags and AGN luminosities.) Applying the same correlation analysis to Seyfert-1 K-band time lag and AGN bolometric luminosity yields

$$\Delta t_{\rm torus,K}/{\rm day} = 10^{1.86\pm0.06}(L_{\rm AGN,SED}/10^{11}L_{\odot})^{0.45\pm0.07}\ . \tag{5.4.11}$$

For $L_{\rm AGN,bol} = 10^{12}\ L_{\odot}$, the corresponding K-band torus size ($\lambda_{\rm rest} \sim 2.1$ $\mu$m) is 0.17 pc, which is about half of the WISE W1 size. Such a difference could provide important insights to the properties of the AGN innermost torus, which will be discussed in detail in another paper. Both the K-band and W1 behavior are consistent with a general scaling as $L^{0.5}$ over a range of 10, 000 in luminosity, demonstrating that similar circumnuclear torus structures are common to AGNs in general.

Glass (2004) provided preliminary time lag measurements between the U ($\sim 0.36$ $\mu$m) and L ($\sim 3.4$ $\mu$m) bands of five Seyfert-1 nuclei: Fairall 9, Akn 120, NGC 3783, ESO141-G55 and NGC7469. We have analyzed the IR SEDs of all these AGNs with our empirical templates in Lyu & Rieke (2018). Following Section 5.4.2, we estimate their $L_{\rm AGN}$ and plot their locations in Figure 5.9. These objects have a very limited luminosity range

($L_{\rm AGN} = 10^{10.5} \sim 10^{11.2}\ L_{\odot}$), so it is not possible to pin down a meaningful lag-luminosity relation given the uncertain time lag measurements and small sample. Nevertheless, they distribute around the prediction of our time-lag correlations based on the *WISE* W1 and W2 band data of PG quasars.

The optically reddened type-1 AGN NGC 6418 is the only object with published robust mid-IR dust reverberation results. With high cadence *Spitzer*/IRAC monitoring, Vazquez et al. (2015) found this object had time lags of 37.2 days at 3.6 $\mu$m and 47 days at 4.5 $\mu$m. Based on the $H\alpha$ luminosity of NGC 6418, they determined a lower limit to the AGN bolometric luminosity, $L_{\rm AGN,\ bol} \geq 5 \times 10^9\ L_{\odot}$. With our previous developed AGN templates (Lyu et al., 2017; Lyu & Rieke, 2017), we can estimate an upper limit on its AGN bolometric luminosity to be $\lesssim$6.3–20 $\times 10^9 L_{\odot}$ (depending on if the AGN is normal, WDD or HDD) based on its *WISE* W4 flux and SED shape. If NGC 6418 shares similar torus properties as PG quasars, given the similar bandpasses of *WISE* and *Spitzer/IRAC*, its AGN bolometric luminosity should be about 8-9$\times 10^9 L_{\odot}$ based on equations 5.4.8 and 5.4.9 for the reported time lags. This value is well above the lower limit constrained by Vazquez et al. (2015) and below the upper limit given by its mid-IR emission. As a result, we conclude that there is no evidence for strong differences in the torus structures between this low-luminosity AGN and quasars in the mid-IR.

### 5.4.3 PG Quasar Variability at 10–25 $\mu$m

Among the 87 PG quasars at $z \lesssim 0.5$, 33 have repeated MIPS measurements at 24 $\mu$m. In Table 5.2, we present the flux change significance, $S_{i,j}$, between (1) the first two MIPS measurements, (2) the third measurement (if acquired) and the previous measurement that shows the greatest difference, and (3) the average of the MIPS measurements and the WISE measurement if the latter is available. The significance of a change in flux is given by

$$S_{i,j} = \frac{|f_i - f_j|}{\sqrt{\sigma_i^2 + \sigma_j^2}}\ , \tag{5.4.12}$$

where $f_i$, $f_j$ are the two flux measurements and $\sigma_i$, $\sigma_j$ are the corresponding uncertainties. We identify variability when one of these values satisfies $S_{i,j} \geq 3$ (similar to the three-

sigma criterion given its definition). Among 26 radio-quiet PG objects, only one, PG 1535+547, was found to vary at 24 $\mu$m. For the remaining seven radio-loud quasars, two out of three flat-spectrum ($\alpha > -0.7$)[10] but none of the four steep-spectrum ($\alpha < -0.7$) objects were found to vary. It appears that AGN 24 $\mu$m variability is related with the radio-band classification. In the upcoming section, we will expand the statistics with a larger sample of 139 quasars with similar observations.

We also explore the 12 $\mu$m and 22 $\mu$m variability of the 87 PG quasars by comparing *Spitzer*/IRS synthetic photometry to the *WISE* measurements (see Table 5.5). Only nine objects (10% of the sample) have 12 $\mu$m flux variations larger than 3-$\sigma$ and two objects (2% of the sample) at 22 $\mu$m. Because there may be systematic errors of a few percent between data obtained from different observatories (Carey, 2010; Sloan et al., 2015) in addition to the statistical uncertainties, a 5$\sigma$ significance level is more convincing for variability detection. With this requirement, only two quasars, PG 1226+023 (3C273) and PG 0007+106 (a flat-spectrum radio source and blazar at z=0.089; Mao et al. 2016), are left. This is not surprising, since previous studies of blazars and flat-spectrum radio sources have found them to vary substantially at 10$\mu$m (e.g., **?**Rieke & Kinman, 1974; **?**; Neugebauer & Matthews, 1999). In particular, 3C 273 is a well-known IR variable object (e.g., Neugebauer & Matthews, 1999; Soldi et al., 2008). It seems that most, if not all, significant AGN IR variability at $\lambda \gtrsim 10$ $\mu$m can be associated with non-thermal processes.

### 5.4.4 AGN Variability at 22–24 $\mu$m in a Larger Sample

*General Variability Behavior* With the multi-epoch MIPS and *WISE* measurements of 139 objects, we now further probe AGN variability at 22–24 $\mu$m with a much larger sample. The measurements and results are also listed in Table 5.2 and shown graphically in Figure 5.10. We use $q_{24} = \log[f_\nu(24\ \mu\mathrm{m})/f_\nu(1.4\ GHz)]$ to determine radio loudness and tag radio-loud (RL) for $q_{24} < -0.5$, radio-intermediate (RI) for $-0.5 < q_{24} < 0.5$ and radio-quiet (RQ) for $q_{24} > 0.5$. The radio data were taken from the NASA Extragalactic

[10]We assume a radio spectrum with $f_\nu \propto \nu^\alpha$ where $f_\nu$ is the observed flux density and $\nu$ is the observed frequency.

Table 5.5. PG quasar variability at 12 and 22 $\mu$m

| name | MJD | $f_{12\mu m}$ mJy | error mJy | stdev | $\Delta M_{W3}$ | MJD | $f_{22\mu m}$ mJy | error mJy | stdev of change | $\Delta M_{W4}$ | comment |
|---|---|---|---|---|---|---|---|---|---|---|---|
| PG 0003+158 | 53721.5 | 13.62 | 0.88 | | | 53721.5 | 24.41 | 2.06 | | | |
| | 55376.1 | 13.96 | 0.34 | -0.36 | 0.03 | 55376.1 | 25.02 | 1.24 | -0.25 | 0.03 | |
| PG 0003+199 | 53559.2 | 175.20 | 3.62 | | | ... | ... | ... | | | |
| | 55377.8 | 191.29 | 2.53 | -3.65 | 0.10 | 55377.8 | 280.42 | 5.60 | | | |
| PG 0007+106 | 53721.3 | 74.01 | 2.75 | | | 53721.3 | 153.34 | 3.90 | | | |
| | 55375.0 | 64.94 | 1.00 | 3.10 | 0.15 | 55375.0 | 126.65 | 2.79 | 5.56 | 0.23 | variable, FSRQ |
| PG 0026+129 | 53592.9 | 30.56 | 1.50 | | | 53725.8 | 45.84 | 2.34 | | | |
| | 55379.5 | 32.70 | 0.96 | -1.20 | 0.08 | 55379.5 | 43.63 | 3.55 | 0.52 | 0.05 | |
| PG 0043+039 | 53381.3 | 14.28 | 1.55 | | | 53381.3 | 22.14 | 2.03 | | | |
| | 55383.0 | 16.03 | 0.55 | -1.06 | 0.13 | 55382.0 | 25.22 | 2.12 | -1.05 | 0.15 | |
| PG 0049+171 | 53750.4 | 13.60 | 0.99 | | | 53750.4 | 19.02 | 2.40 | | | |
| | 55342.6 | 15.76 | 0.34 | -2.07 | 0.17 | 55342.6 | 17.96 | 1.17 | 0.40 | 0.06 | |
| ... | ... | ... | ... | ... | ... | ... | ... | ... | ... | ... | ... |

Note. — (This table is available in its entirety in machine-readable form. A portion is shown here for guidance regarding its form and content.)

Database (NED), the *FIRST* survey, Kellermann et al. (1989, 2016, both corrected to 1.4 GHz assuming a slope of $-0.7$) , Hodge et al. (2011), and the Molonglo Galactic Plane Survey (Murphy et al., 2007). There is one anomalous case, PG 1309+355, which has a flat radio spectrum but is radio-intermediate by our definition; by other criteria, however, it is radio-loud (Laor et al., 2019). We have counted it among the radio-loud flat-spectrum radio quasars (FSRQs). Sources lacking radio data are by default included with the radio-quiet sample. Because there was no difference in variability behavior, we have also combined the radio-intermediate sources with this sample. Hereafter this mixed sample is referred as "radio-quiet" for brevity.

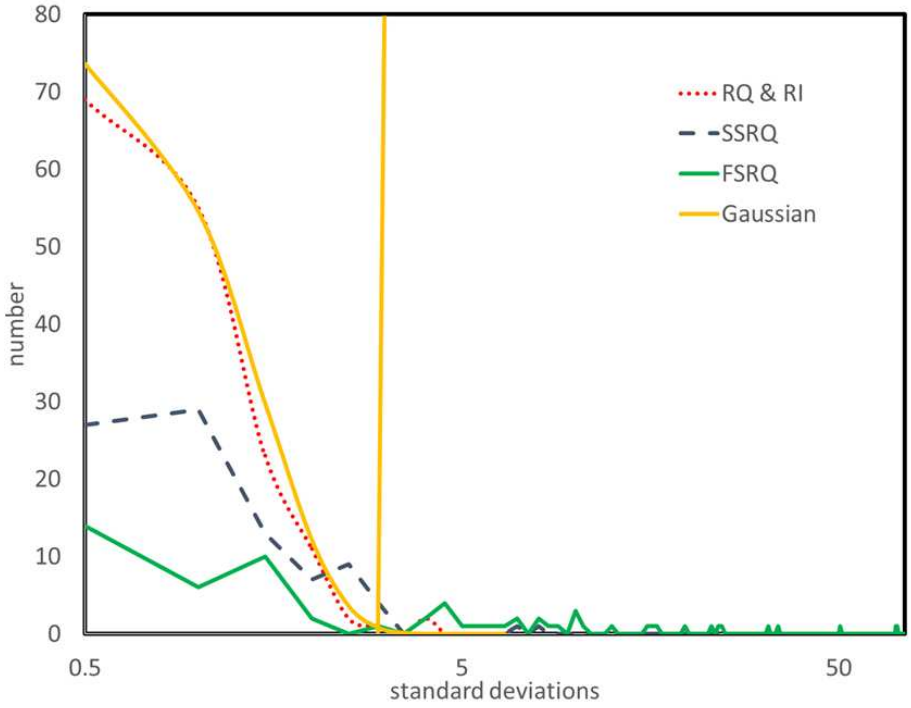


Figure 5.10 Distribution of variability significance $S_{i,j}$ between different 24 $\mu$m measurements in all 139 quasars. The calculated $S_{i,j}$ have been linearly binned from 0 with a bin size of 0.5. A Gaussian with $\sigma = 0.9$ has been binned similarly. The vertical orange line indicates $S_{i,j} = 3$ used to identify variability. Two objects, 2MASSi J0918486+211717 and PG 1535+547 stand out as having larger changes and appear to be exceptional radio-quiet variables. Although only one steep-spectrum quasar is identified as being probably variable, their distribution of variability significances is broader than that for the radio-quiet sources suggestive of low level variability in some of them. Compared with step-spectrum radio quasars, the distribution for the flat-spectrum radio quasars is even broader and indicates a strong link between this radio characteristic and variability at 24 $\mu$m.

As shown in Figure 5.10, the flux change significance distribution of radio-quiet AGNs is best fitted with a Gaussian of width of 0.9 — that is, this fit indicates that the estimates of individual standard deviations are high (conservative) by about 10% under the assumption that the sample is not variable[11]. This result confirms that our criterion for identifying variations is conservative and furthermore emphasizes how rare 24 $\mu$m variability is for these objects. As indicated by the 10% smaller width of the Gaussian fit to the radio-quiet population, the real systematic error might be smaller than 0.7% as introduced in Section 5.2.1. However, we decided not to change it since a uniform correction would not apply across the entire sample (e.g., faint sources probably have larger errors). Given these uncertainties, two sources, the FSRQ NGC 1275 and the SSRQ 3C 270, are identified as possibly being variable because they are detected at very high signal to noise and show flux changes at 2.7–2.8$\sigma$. Overall, we detect 24 $\mu$m variations in 22 (including the two probable variables) out of 139 targets and set tight constraints on possible variations for the rest of the sample within the limits of our observational cadence.

The steep-spectrum radio-loud sources show a distribution of the 24 $\mu$m flux change significance that is somewhat broader than that for the radio-quiet sample, suggesting that low levels of infrared variability may apply for some of them even if it is not detected individually. However, their overall pattern is not very different from the radio-quiet sample. In contrast, the distribution of flat-spectrum sources is very broad, showing that variability is common among them. In fact, we detect variations in 14 out of 19 FSRQs — a very high fraction given our small number of observations.

*Other variability studies* It seems possible that the measurements by IRAS at 25 $\mu$m could extend the time scale of our survey. However, the IRAS photometry is of relatively low accuracy. There are variations at the 5% level (up to 10%) in the response along a pixel, and the simple bulk photoconductors used are susceptible to responsivity shifts due to exposure to ionizing radiation (bei, 1988). Evidence for a significant ($> 3\sigma$) flux change after applying these systematic errors is found for only three objects: 3C 273, 3C 274, and PKS 2005-189. The increased brightness of 3C 274 as seen by IRAS can be explained by

[11] Since PG 1309+355 has not varied in our observations, classifying it as radio-intermediate would have no effect on this result.

its resolved nature evident in the Spitzer images. **?** have shown that the extended 24 $\mu$m emission is the IR synchrotron radiation from the outer jet and inner radio lobes of this nearby FR I-type radio galaxy. All of the extended emission would be included within the IRAS beam and photometry of the Spitzer images using a $1'$ aperture completely recovers the excess flux measured by IRAS. However, the IRAS data do demonstrate that 3C273 was nearly twice as bright and PKS 2005-189 about three times as bright when measured in 1983 compared with our measurements. Both of these sources are FSRQ blazars, so these results help document the extent of their variability but do not qualitatively change the findings above.

Neugebauer & Matthews (1999) presented a multi-year photometry monitoring for 25 PG quasars from 1 through 10 $\mu$m (J through N band) and reported 10 $\mu$m variability in 3C 273. They also deduced possible variations at 10 $\mu$m for PG 1535+547 on the basis that its mid-IR light curve tended to follow the variations seen at shorter wavelengths even if by itself the measurements did not have enough signal to noise to make a persuasive detection. They also used a statistical argument to make a case for variations in other radio-loud objects.

*Lack of 24 $\mu$m Variations in Radio-quiet Quasars* Our study therefore represents a substantial advance over previous work on variability of AGNs at 10 and 20 $\mu$m. We now use it to evaluate the overall variability of the radio-quiet sample by computing the weighted average of the absolute changes in flux between the initial two MIPS measurements.[12] Although we have only two measurements per object, the large sample size lets us put interesting limits on variability using a statistical approach.

The repeatability of the MIPS 24 $\mu$m photometry in the absence of any photon noise can be as good as 0.4% (Engelbracht et al., 2007). If we remove 2MASSi J0918486+211717 and PG 1535+547, plus all of the blazars and flat-spectrum radio sources, the rms scatter in our quasar measurements is $0.0085 \pm 0.0006$ magnitudes ($0.79 \pm 0.06\%$); if we further remove all radio-loud objects, the rms scatter reduces to $0.0076 \pm 0.0006$ magnitudes

[12]We focus on the initial two MIPS 24 $\mu$m measurements instead of the *WISE* results since they are generally of higher signal-to-noise ratio and use a smaller beam that reduces contamination issues. Also, the first two epochs of observations encompassed the entire sample, whereas the third MIPS observational epoch only includes radio-loud AGNs.

(0.70±0.06%). That is, outside of 2MASSi J0918486+211717 and PG 1535+547, plus the flat-spectrum radio sources and blazars, the rms scatter in the measurements is consistent with virtually no variability over the ∼ 3 year period spanned by the MIPS observations.

Now we compare these 24 $\mu$m upper limits to the variability in *WISE* W1 and W2 bands, i.e., at 3–5 $\mu$m. For the entire PG sample, the rms scatter is 0.086 mag and 0.071 mag at W1 and W2, respectively. For the subset for which we have 24 $\mu$m measurements, the values are the same. That is, variability at 3.4 $\mu$m is a factor of ten larger than the upper limits set for 24 $\mu$m. As deduced by Neugebauer & Matthews (1999), the variability damps out dramatically going from the near infrared to the mid infrared. The *Spitzer* measurements put this result on much sounder ground than previously: to illustrate the gain, at 73 mJy, PG 1535+547 is close to the median brightness of the sample, 86 mJy, yet its variations were just at the detection limit with the previous ground-based data.

*Behavior of Variable Radio-quiet Quasars* PG 1535+547 and 2MASSi J0918486+211717 are of interest as apparently normal, radio-quiet, optically-selected quasars that have exceptional mid-infrared variability signals at 10 and 24 $\mu$m. PG 1535+547 (Mrk 486) is of particular interest because it is very thoroughly studied. Lyu et al. (2017) find its infrared SED to be fitted very well by their warm dust deficient template, which makes the assumption that the nuclear non-thermal continuum has dropped to a negligible level by 24 $\mu$m and that the mid-IR flux comes mostly from the circumnuclear torus with very little contribution from polar dust. Xie et al. (2017) show it to have weak silicate emission features, requiring that some, if not all, of its 24 $\mu$m emission is from heated dust. In the optical band, PG 1535+547 is moderately obscured with a red continuum and it has the strongest polarization signals reported in the PG sample ($p \sim 2.5\%$; Berriman et al. 1990). Indeed, Hubble Space Telescope ultraviolet and ground-based spectropolarimetry show that the polarization rises to nearly 8% in the UV and that there are complex polarization changes across the H$\alpha$ and H$\beta$ emission-line profiles (Smith et al., 1997). The presence of strong emission lines in the polarized flux spectrum and the strong rise of the polarization into the UV suggests that dust scattering of the AGN nuclear continuum and emission from the BLR is the polarizing mechanism. Despite the fact that the polarization is from scattering,

Smith et al. (1997) found evidence that the optical polarization varies on time scales as short as a year. In total, these observations indicate that PG 1535+547 cannot be face-on, but must be partially-obscured by its circumnuclear torus. In this case, even if a jet is present, its apparent emission would not be strongly amplified by relativistic beaming and hence would be weak due to its misalignment with our line of sight and it would not contribute significantly to the observed flux at 10 and 24 $\mu$m (see more discussion in Section 5.5.1). Instead, we suggest the IR variations of PG 1535+547 at longer wavelengths are dust reverberation signals.

To illustrate the different mid-IR variable behaviors between radio-quiet and radio-loud quasars, we compare the IR light curves of PG 1535+547 and 3C 273 in Figure 5.11. For the blazar 3C 273, there is no obvious similarity between its optical and mid-IR light curves, especially given the large variations seen between the neighbouring epochs in *WISE* W2. The brightness of 3C 273 at W3 and W4 varied by $\sim$0.3 mag, about 0.15 mag larger than the variations observed in W1 and W2. Such behavior is not expected from the dust emission, since its energy output at longer wavelengths must correspond to larger physical scales where the amplitude of variability is expected to decrease.

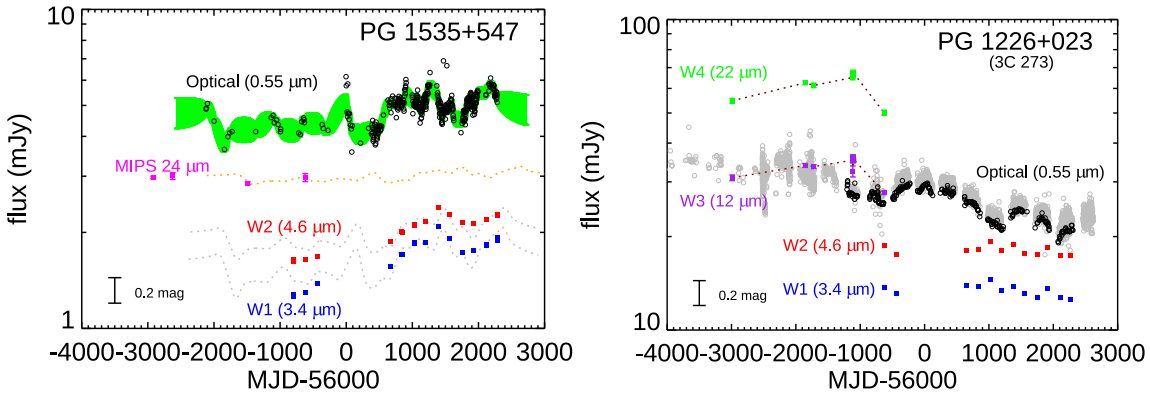


Figure 5.11 Multi-band IR and optical light curves of the radio-quiet PG 1535+547 (left) and the blazar PG 1226+023 (right). See text for details.

In contrast, the W1 and W2-band light curves of PG 1535+547 can be reproduced by shifting and scaling its optical light curve, as expected for dust reverberation signals with time lags of $\sim$ 180 days for W1 and $\sim$ 205 days for W2. Assuming a time lag of 2.5 times larger (i.e. $\sim$ 450 days) than W1 and an amplitude factor of 0.6, the 24 $\mu$m light curve can

be matched by dust reverberation mapping. The variability amplitude of PG 1535+547 in W1 is $\gtrsim 0.5$ mag, among the 10% largest W1-band variables in the PG sample. In comparison, the 24 $\mu$m variability amplitude of PG 1535+547 is about ten times smaller at only $\sim$0.06 mag. The observed behavior of this object suggests that a detectable level of mid-IR variability caused by dust reverberation is plausible given a highly variable quasar, high signal-to-noise-ratio data, and fortunate time sampling.

## 5.5 Discussion

### 5.5.1 The Origin of AGN Mid-IR Variability

*Synchrotron Emission* The *Spitzer* 24 $\mu$m results reaffirm the generally accepted picture that the smooth UV-millimeter continua of blazars is dominated by the variable, optically thin synchrotron radiation produced in the core and inner relativistic jet that also gives rise to the self-absorbed, flat-spectrum radio emission at centimeter wavelengths (see e.g., Kellermann & Pauliny-Toth 1981). According to the classical unification scheme (Urry & Padovani, 1995), this type of object corresponds to an AGN with a powerful jet pointed toward the observer and its broad-band X-ray to IR SED is dominated by synchrotron emission that is enhanced by relativistic beaming.

As shown in Section 5.4.3, among the radio-loud AGNs, steep-spectrum radio quasars (SSRQ) seem to lack strong variability at 24 $\mu$m, in contrast to flat-spectrum radio quasars. As suggested by Urry & Padovani (1995), FSRQ are believed to be oriented at relatively small angles to the line of sight ($\theta \lesssim 15$, where SSRQ have intermediate angles between FSRQ and FR II radio galaxies. For an ideal relativistic beam, the apparent luminosity can be calculated as $L = L_0/[\gamma(1-\beta\cos\theta)]^2$, where $\gamma$ is the Lorentz factor, $L_0$ is the intrinsic luminosity, and $\beta = (1-\gamma^{-2})^{1/2}$ is the beam speed in the AGN frame in units of light speed $c$ (Cohen et al., 2007). For blazars, Lorenz factors up to 10–20 are common for parsec-scale jets (Homan, 2012). Assuming $\gamma = 20$, the jet variability signal can be boosted by a factor of 2–1600 for FSRQs (see Figure 5.12), while the apparent variability for SSQRs decreases quickly to a few percent or smaller when $\theta > 15$ In other words, given the same level of intrinsic jet variability, FSRQs are expected to have much higher

(synchrotron) IR variability detection rates compared with SSQRs. In addition, it is possible that the infrared emission of the SSRQs is no longer dominated by the relativistic jet but by the emission of a circumnuclear torus. In that case, their behavior would resemble that of radio-quiet quasars, which do not vary significantly within our 24 $\mu$m observations.

Given the arguments above, the different mid-IR variability behavior among SSRQs, FSRQs, and blazars can be ascribed to first order to different angles of the radio jets relative to the observer. This result is consistent with the unification picture for radio-loud AGN (Urry & Padovani, 1995).

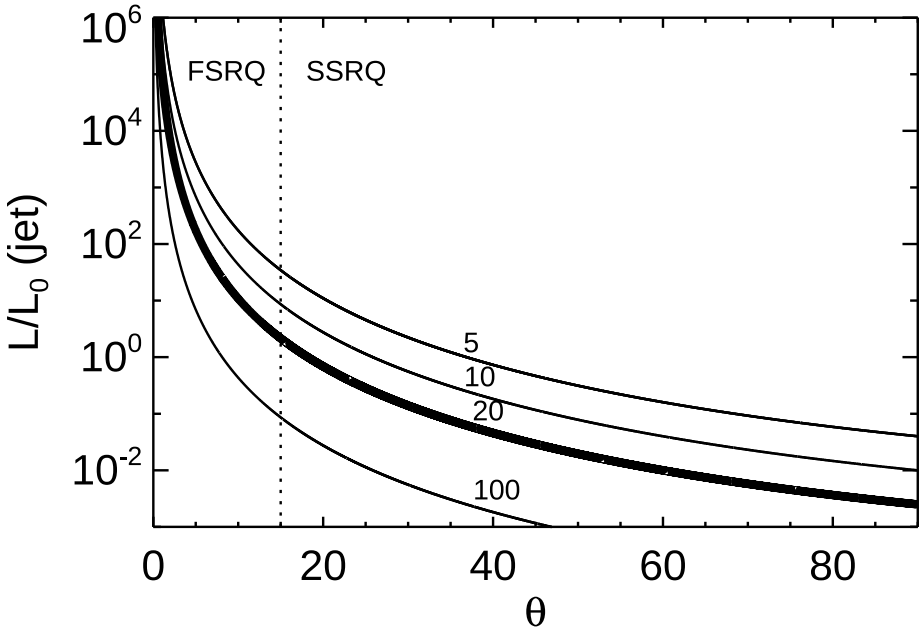


Figure 5.12 The flux boosting factor as a function of observing angle for different Lorentz factors ($\gamma$=5, 10, 20, 100).

*Dust Infrared Reverberation Signals* The mid-IR variations of the radio-quiet quasars show little evidence for any synchrotron component, but are dominated by the dust response to the UV-optical variations of the central engine. As summarized in Section 5.4.1, the 3–5 $\mu$m IR emission of $\sim 77\%$ of the PG quasars at $z < 0.5$ show such dust reverberation signals. If we set aside the 16 sources where the data were inadequate to look for time lags, 95% of the remaining objects behave in this way, with only four objects (5%) showing an alternative pattern of variations. This is a strong evidence for the common

existence of circumnuclear dust outside the black hole accretion disk.

The near infrared SEDs of quasars with normal or warm-dust-deficient (WDD) behavior (Lyu & Rieke, 2017) show direct evidence for this circumnuclear dust heated by the accretion disk, in the form of a spectral bump at $\sim$3 $\mu$m that matches the expected emission of dust heated to sublimation temperatures. Although hot-dust-deficient (HDD) quasars do not show a similar near-IR bump, as shown in Figure 5.9, they still follow the $R \propto L^{1/2}$ size-luminosity relation and their dust time lags increase with wavelength. This is true even for the most HDD quasar — PG 0049+171, where we detect time lags $\sim$120 days for its W1 variations and $\sim$157 days for W2. This behavior is evidence that the emission near 3 $\mu$m is dominated by the emission of the circumnuclear torus and not by the accretion disk/central engine. Furthermore, since the IR SEDs of unobscured quasars at $z \sim$0–6 have similar forms as the PG sample (Lyu et al., 2017), the result implies that there are few, if any, completely dust-free quasars.

For radio-quiet quasars, the average RMS variability amplitudes at V, W1 and W2 bands are 0.145 mag, 0.093 mag, 0.076 mag. In other words, the W1 and W2 dust variation signals are typically only $\sim$ 60% and $\sim$ 50% of those in the optical band. As presented in Section 5.4.3, the possible flux change at 24 $\mu$m is less than 10% of that at $\sim$ 3 $\mu$m (corresponding to 6% of the variability at V-band). The decrease in variability with increasing wavelength is likely to be the result of averaging over the variations due to light travel time to various parts of the extended circumnuclear torus. Diminished variability at 24 $\mu$m then results from the emission originating in a substantially larger region, i.e. at a significantly larger radius than the emission at 3–4 $\mu$m.

*AGN Mid-IR Variability under the Unification Scheme* Our reverberation mapping study has focused on the PG quasars because their selection criteria strongly favor cases where we can see the central engine, accretion disk, and circumnuclear torus all relatively unobscured. We discuss here the complexities that can be expected where this simple situation is not the case.

In general, both synchrotron emission and torus-reprocessed emission will contribute to the mid-IR variability of a radio-loud AGN; their relative importance depends on the

inclination angle and radio-loudness. In addition, the obscuration of the central engine will substantially affect the apparent optical variability, making the interpretation of the mid-IR light curves difficult. Figure 5.13 provides an illustration of the classical unification model (Antonucci, 1993; Urry & Padovani, 1995) and shows the optical and mid-IR continuum light curves of various AGN components.

In the radio-loud case, the integrated optical continuum emission of the AGN is a combination of the jet component ($f_{\rm jet,opt}(t)$) and the accretion disk ($f_{\rm AD,opt}(t)$),

$$F_{\rm radio-loud,opt} \approx C_{\rm torus}(\theta) f_{\rm AD,opt}(t) + C_{\rm beam}(\theta) f_{\rm jet,opt}(t) \ , \tag{5.5.1}$$

where $C_{\rm torus}(\theta)$ reflects the obscuration level of the accretion disk light by the torus ($C_{\rm torus} \sim 1$ for type-1 AGNs and $\sim 0$ for type-2 AGNs) and $C_{\rm beam}(\theta)$ is the flux boosting factor due to realistic beaming. As the presumed inclination angle of the jet to our line of sight increases from BL Lac, FSRQ to SSRQ, the relative contribution of $f_{\rm AD,opt}$ increases quickly. For Narrow-Line Radio Galaxies (NLRG), although the absolute strength of the jet variability is weaker than for the SSRQ case, the optical light curve is dominated by the jet since the accretion disk is obscured ($C_{\rm torus} \sim 0$). In principle, both the jet component and the accretion disk can provide UV-optical energy to heat the torus and produce the mid-IR emission. As they locate in different regions, the mid-IR dust reverberation signals of the torus might be mixed with the two separated time lags ($\Delta t_{\rm jet(opt)}$ and $\Delta t_{\rm AD}$). The relativistic beaming effects also apply to the jet IR emission, so the observed integrated mid-IR emission can be written as

$$\begin{aligned} F_{\rm radio-loud,IR} \approx\ & f_{\rm AD,IR}(t) + C_{\rm beam}(\theta) f_{\rm jet,IR}(t) + \\ & \mathscr{F}_{\rm AD,opt}(t-\Delta t_{\rm AD}) + \mathscr{F}_{\rm jet,opt}(t-\Delta t_{\rm jet(opt)}), \end{aligned} \tag{5.5.2}$$

where we use $\mathscr{F}(t-\Delta t)$ to denote the dust-reprocessed emission of the optical light $f(t)$ with a time lag $\Delta t$. Since the jet is highly beamed and perpendicularly distributed, its illumination to the torus could often be ignored. As a result, the observed total IR emission can be further simplied into

$$F_{\rm radio-loud,IR} \approx f_{\rm AD,IR}(t) + C_{\rm beam}(\theta) f_{\rm jet,IR}(t) + \mathscr{F}_{\rm AD,opt}(t-\Delta t_{\rm AD}) \ . \tag{5.5.3}$$

Comparing it with the form of $F_{\rm radio-loud,opt}$, if dominated by different components, the optical and mid-IR light curves could be uncorrelated (the jet component and accretion

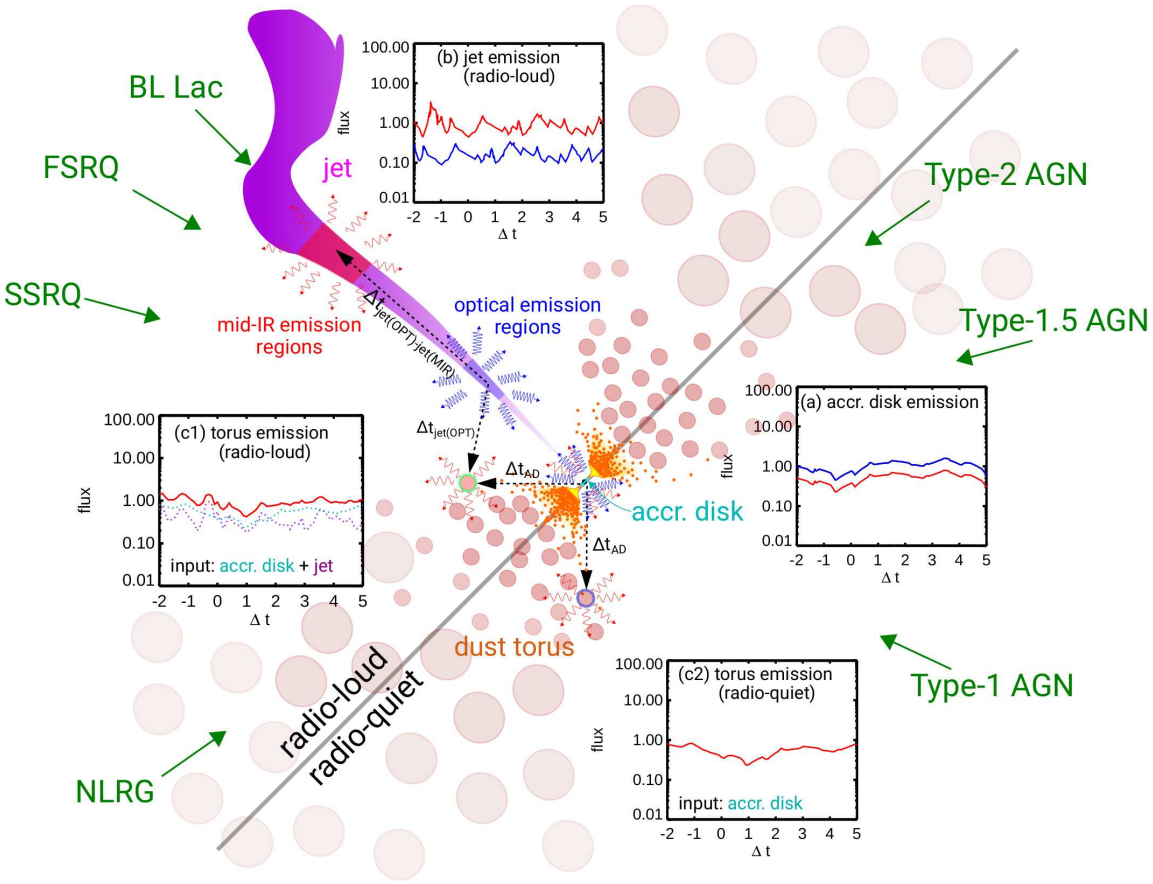


Figure 5.13 Sketch of the main AGN structures related to the AGN optical and mid-IR continuum variabilities. At the very center is the BH and its accretion disk (cyan). The dust torus is assumed to be clumpy and the yellow, orange, red colors represent a decreasing dust temperature. A strong jet (purple) exists for the radio-loud case and we highlight its optical emission (blue) and mid-IR emission (red) regions. For the accretion disk and the jet component, we plot their optical (blue solid line) and mid-IR (red solid line) light curves in panels (a) and (b). The mid-IR light curves (red solid line) of the torus in the radio-loud and radio-quiet cases are plotted in panels (c1) and (c2). For the radio-loud case, we show the contribution from the dust reverberation signals to the accretion disk and the jet in dashed cyan and purple lines. According to the AGN unification model (Antonucci, 1993; Urry & Padovani, 1995), we denote different AGN types at different inclination angles for radio-loud and radio-quite cases with green arrows. See text for detailed explanations.

disk have different variability patterns). This could explain the behavior of 3C 273 (as seen in Figure 5.11).

The situation for radio-quiet AGNs is much simpler; their optical light curve is $F_{\rm radio-quiet,opt} \approx C_{\rm torus}(\theta) f_{\rm AD,opt}(t)$ and their mid-IR light curve $F_{\rm radio-quiet,IR} \approx f_{\rm AD,IR}(t) + \mathscr{F}_{\rm AD,opt}(t -$

$\Delta t_{AD}$). When the nucleus is unobscured ($C_{\rm torus} \sim 1$), we readily observe the time lag $\Delta t_{AD}$, which reflects the light travel time from the accretion disk to the torus, as demonstrated by our dust reverberation mapping. However, if the nucleus is obscured, the optical band could have a significant contribution from the host galaxy. Given the large beams used for much of our visible data, in this situation it would be difficult to extract the nuclear component accurately. To illustrate this issue, consider the full sample observed at 24 $\mu$m, excluding the radio loud sources. 50% of the remaining sources are 2MASS quasars, which show varying amounts of AGN obscuration (e.g., Cutri et al. 2002). Of the remaining sources, 40% are of types 1.8, 1.9, or 2 (from the NED database), again indicating substantial obscuration.

*Other Causes of IR Variations* Besides the radio-loud PG 1226+023 (3C 273), four other PG objects — PG 0003+199, PG 0923+201, PG 1534+580, and PG 1612+261 — have uncorrelated optical and mid-IR variability. None of these objects are blazars or even radio-loud, so it is unlikely that non-thermal emission contributes to their IR variations. In addition, since all of these four objects show blue optical continua and strong broad Balmer emission lines, the optical light curve should delineate the variations of the accretion disk. Consequently, their IR variations cannot be the dust reverberation signals from a classical torus. We cannot rule out the possibility that these objects have very complicated dust structures (e.g., there are several polar dust clouds or filaments) that cause reverberation signals with a wide range of time lags with diverse luminosity weights — for some configurations, the integrated IR light curve might not show any variation pattern similar to the input optical signals. Nevertheless, there is no new mechanism involved in this possibility – it still belongs to the dust reverberation signals.

Dynamical motion of the torus material could be another possibility to cause AGN IR variability. Assuming the dusty environment of an AGN can be described as a radiation-driven fountain, Schartmann et al. (2014) explored the time-resolved IR SEDs and argued for possible variations, but over a timescale of 0.1 Myr. As their simulation indicates, there could be significant but temporary dust in the line-of-sight that is heated by the AGN, causing changes in the IR (by dust emission) and optical flux (by dust extinction). On

yearly timescales, however, the turbulence/fountain argument cannot explain the observed mid-IR variations of these four quasars by merely moving dust clouds. Taking the typical velocities of order 300–400 km/sec, the moving dusty clouds/filaments could only travel a few $10^{-4}$ parsec, which would not change the exposed solid angle significantly at a distance of a parsec from the heating source.

However, there is a chance that dust grains could be evaporated when the dusty clouds/filaments move to an environment with strong radiation heating by the AGN or where an outburst (which could be at a non-visible wavelength, e.g., X-rays) by the central engine evaporates dust in a formerly 'safe' environment. As a result, their IR emission could be quickly reduced. In fact, the dust destruction timescale around the sublimation region is estimated to be order of 10 days (Kishimoto et al., 2013), quick enough to produce the mid-IR variation we see. Observed optical polarization variability seen in objects like PG0050+124, PG1535+547 (Smith et al., 1997), and Mrk231 (Gallagher et al., 2005) on timescales of less than a year may also be related to rapid sublimation events. In another paper, we will provide a detailed study on how to explain these peculiar mid-IR variability features with this possibility and discuss its broad implications.

In conclusion, (1) observed mid-IR variability on monthly to yearly time-scales of most quasars is caused by dust reverberation signals that are correlated with the variations of the accretion disk emission. The amplitude of the dust IR variability decreases quickly with increasing wavelength. (2) If a jet is present and the system is viewed close to the line of sight to the jet axis (e.g., FSRQ or blazar), non-thermal processes dominate the IR variations with larger variation amplitudes over shorter timescales. (3) Only a small subset of quasars appears to have IR variability that does not fall into these two categories, which might be explained by reverberation signals off structures other than the circumnuclear torus, or by the motions of dusty clumps combined with the heating and destruction of the constituent dust grains.

### 5.5.2 Constraints on the Torus Properties

*Wavelength-dependent Torus Size and Issues with the Classical Clumpy Model* To compare the torus sizes constrained through dust reverberation signals at different wavelengths, we fix the slope of the time-lag vs. AGN luminosity relation to be 0.5, and repeat the fitting for W1 and W2-band measurements of the PG quasars. The results can be found in Table 5.6. For the 67 objects with convincing dust time lags, we find that the dust emission size ratios follow $R_{W1} : R_{W2} = 1 : 1.2$. As suggested by Lyu et al. (2017), quasars having different intrinsic IR SED variations may be a reflection of different torus structures. Therefore, we also compute separately the corresponding $\Delta t$—$L_{AGN}$ relations for normal, warm-dust-deficient (WDD) and hot-dust-deficient (HDD) populations. Discussion of how the torus size depends on SED type will be expanded in Section 5.5.2. Here we simply assume all AGNs have a similar torus structure.

We also make a similar correlation analysis for the K-band reverberation signals of the 17 Seyfert-1 sample in Koshida et al. (2014), finding a size ratio between K band and W1 band of $R_K : R_{W1} = 0.6 : 1$. In Appendix G.1, we present the SED decomposition results of these Seyfert-1 nuclei and estimate that half of the sample should have intrinsic IR SEDs best-described by the normal AGN template. This value is similar to the $60-70\%$ normal AGN fraction in the PG quasar sample (Lyu et al., 2017). As a result, the AGN dust emission size differences at K and W1 bands are unlikely to be related to the different AGN IR SED types. To test whether the results depend strongly on the uncertainties in the AGN luminosity estimate, we changed the uncertainty of $L_{\rm AGN}$ from 0.3 dex to 0.025 dex (the latter value corresponds to the typical V-band magnitude uncertainty of Seyfert-1 nuclei in Koshida et al. 2014) and repeated the fits. The $\Delta t - L_{\rm AGN}$ correlations shift by 0.05-0.1 dex, but the size ratios between K, W1 and W2 are not significantly affected, i.e., $R_K : R_{W1} : R_{W2} = 0.6 : 1 : 1.2$.

The poor time sampling of the 24 $\mu$m observations prevents us from deriving any torus size through reverberation mapping. On the other hand, the lack of variability at this wavelength is most readily explained if the torus zone dominating the 24 $\mu$m emission is much larger than the zone producing the bulk of the flux observed at W1 and W2. In this

Table 5.6. Results of Linear Regression of Lag-Luminosity Relation

| Sample | Observed Band | ¡z¿ | $\lambda_{rest}$ ($\mu$m) | Sample Size | $\alpha$ ($\Delta L_{\rm AGN} = 0.3$ dex) | $\alpha$ ($\Delta L_{\rm AGN} = 0.025$ dex) | $\beta$ |
|---|---|---|---|---|---|---|---|
| (1) | (2) | (3) | (4) | (5) | (6) | (7) | (8) |
| Normal QSOs | W1 | 0.145 | 2.95 | 44 | 2.13±0.04 | 2.21±0.01 | 0.5 |
| | W2 | 0.145 | 4.04 | 44 | 2.21±0.04 | 2.28±0.01 | 0.5 |
| WDD QSOs | W1 | 0.220 | 2.78 | 8 | 2.03±0.09 | 2.04±0.05 | 0.5 |
| | W2 | 0.241 | 3.72 | 7 | 2.10±0.09 | 2.12±0.05 | 0.5 |
| HDD QSOs | W1 | 0.122 | 3.01 | 15 | 1.97±0.07 | 1.98±0.04 | 0.5 |
| | W2 | 0.122 | 4.12 | 15 | 2.08±0.07 | 2.08±0.04 | 0.5 |
| All QSOs | W1 | 0.149 | 2.94 | 67 | 2.08±0.03 | 2.19±0.01 | 0.5 |
| | W2 | 0.149 | 4.03 | 66 | 2.16±0.03 | 2.27±0.01 | 0.5 |
| Seyfert-1 | K | 0.038 | 2.11 | 17 | 1.88±0.05 | 1.93±0.02 | 0.5 |

Note. — The fitted model is $\log(\Delta t) = \alpha + \beta \log(L_{\rm AGN})$. Col. (1): sample information; Col. (2): the studied photometry band; Col. (3): the average redshift of the sample; Col. (4): the effecive rest-frame wavelength that the observations are probing; (5): number of sample objects; Col. (6): derived $\alpha$ assuming the same 0.025 dex uncertainty of $L_{\rm AGN}$ for all objects; Col. (7): similar to Col. (5) but the uncertainty is assumed to be 0.3 dex; Col. (8): $\beta$ is fixed to 0.5.

case, the time lags have a large range so that the variability is smoothed out.

These observational results provide some challenges to the predictions based on the classical "clumpy" torus picture. Almeyda et al. (2017) simulated the IR reverberation response of such a torus model and suggested that the dust time lags at 3–5 $\mu$m have very limited wavelength dependence (see their section 4.1). In addition, their model also predicted substantial reverberation signals at 10 and 30 $\mu$m (see their Figure 5). These conclusions are expected with their basic model assumption: from the illuminated face to the dark side, the same optically-thick clouds can have a broad temperature distribution that results in IR emission over a wide wavelength range. However, this picture is not favored by our observations. Given the typical redshift of the sources we have observed at 24 $\mu$m, the rest wavelength is $\sim$ 20 $\mu$m. Interpolating their results at 10 and 30 $\mu$m for an extended clumpy torus, the same model would predict a peak response at the wavelength of our observations of about 35% of the response at rest 3.6 and 4.5 $\mu$m. In contrast, we have found that the response at 24 $\mu$m is an order of magnitude smaller than that at (observed) 3.4 and 4.5 $\mu$m.

Rather than being purely clumpy, the torus is likely to be a mixture of optically-thick dusty clouds and some diffuse distribution of low-density dust. Such a structure is likely because clumps at the inner edge of the torus are not likely to be completely stable against gravitational shearing and hence must be sustained as a result of turbulence or similar effects. In fact, it is known that the clumpy torus model (e.g., Nenkova et al., 2008a) alone can not reasonably fit the $\sim$ 3 $\mu$m hot dust emission peak among quasars and another blackbody with $T \sim$ 1300K needs to be added (e.g., Mor et al., 2009; Leipski et al., 2013). In contrast, the two-phase (clumps + diffuse dust) torus model developed by Stalevski et al. (2012, 2016) does not have this problem and appears to reproduce the AGN hot dust emission features.

Previous work has often argued that a single black body plus a power-law SED is enough to reproduce the quasar continuum at $\lambda \sim$0.5–3 $\mu$m (e.g., Glikman et al., 2006; Kim et al., 2015; Hernán-Caballero et al., 2016). Since dust temperature is a strong function of distance, the dust grains responsible for the $\lambda \sim$1–3 $\mu$m emission should be located at similar radii. However, our study finds contradictory evidence with $R_K : R_{W1} = 0.6 : 1$

and indicates a complicated picture. Interestingly, under the assumption of similar grain sizes, the sublimation radii for graphite and silicate dust grains have $R_{\rm sub,C}/R_{\rm sub,\,S} \sim 0.5$ (see Section 5.4.2), very close to the reported $R_K : R_{W1} \sim 0.6$. Future work should address whether this possibility can be supported by other evidence, as well as folding in the constraints on torus structure provided by the relative lack of variability at 24 $\mu$m.

*Surface Density Profiles of the Hot Dust Emission* Previously, the radial structures of AGN tori have been explored at 8–13 $\mu$m only by long-baseline infrared interferometry observations of $< 10$ Seyfert nuclei (Kishimoto et al., 2009b, 2011b). Assuming a power-law radial surface density distribution of heated dust, the profile ranges from $\sim r^0$ to $\sim r^{-1}$, and might be dependent on AGN luminosity (Kishimoto et al., 2011b). However, it is likely that most of these objects have some contribution of extended polar dust emission in the mid-IR ($f_{\rm pol,10\mu m}/f_{\rm total,10\mu m} \sim 0.3-0.8$ estimated from SED analysis in Lyu & Rieke 2018), so the real density profile of the compact torus at these wavelengths is still highly uncertain.

With the measurements of variability amplitude differences between the optical and IR light curves, crude constraints on the dust surface density profile can be calculated with some simple approximations.

For simplicity, we assume the dust sublimation zone is smooth (i.e., not clumpy) and that its surface density profile can be described by a power-law $\Sigma(r) \propto r^{\alpha}$. In addition, the dust grains in the sublimation zone will have only a modest range of temperature given that the AGN hot dust emission feature is well-matched by a single black body spectrum (e.g., Mor et al., 2009). Furthermore, the dust grains will be hot enough that the temperature-dependence of their emission will be modest (i.e., they approach the Rayleigh-Jeans regime). Therefore, we can ignore the radial dependence of the temperature and express the IR emission as:

$$f_{\rm IR} \propto \int \Sigma(r) r dr \propto r^{\alpha+2} \,. \tag{5.5.4}$$

Since the hot dust time lag has been found to be linearly correlated with the square root of AGN luminosity, we can argue that the dust distance $r$ is correlated to the AGN optical

luminosity by the inverse square law, $r \propto L_{\rm opt}^{0.5}$, so

$$f_{\rm IR} \propto f_{\rm opt}^{(\alpha+2)/2} \ . \tag{5.5.5}$$

When the optical flux $f_{\rm opt}$ is changed to $f'_{\rm opt}$ by a factor of $\xi$, the corresponding IR flux changes from $f_{\rm IR}$ to $f'_{\rm IR}$ and

$$\frac{f'_{\rm IR}}{f_{\rm IR}} = \left(\frac{f'_{\rm opt}}{f_{\rm opt}}\right)^{(\alpha+2)/2} = \xi^{(\alpha+2)/2} \ . \tag{5.5.6}$$

With our RM model, the absolute flux change in the IR is correlated with that in the optical according to Equation 5.3.1,

$$\Delta f_{\rm IR} = f'_{\rm IR} - f_{\rm IR} = AMP \times (\xi - 1) f_{\rm opt} \ . \tag{5.5.7}$$

We can rewrite Equation 5.5.6 as

$$1 + AMP(\xi - 1)\frac{f_{\rm opt}}{f_{\rm IR}} = \xi^{(\alpha+2)/2} \ . \tag{5.5.8}$$

The IR variability can be characterized by magnitude change $\Delta M_{\rm IR}$,

$$\Delta M_{\rm IR} = -2.5 \log\left(\frac{f'_{\rm IR}}{f_{\rm IR}}\right) \ . \tag{5.5.9}$$

Finally we have

$$\alpha = 2\left(\frac{\log\left(10^{-\Delta M_{\rm IR}/2.5}\right)}{\log\left(1 + (10^{-\Delta M_{\rm IR}/2.5} - 1)(f_{\rm IR}/f_{\rm opt})AMP^{-1}\right)} - 1\right) \ , \tag{5.5.10}$$

where $f_{\rm IR}/f_{\rm opt}$ is the infrared to optical color of the AGN SED.

We summarize the mean values of $\Delta M$ and $AMP$ of Seyfert-1 AGN and PG quasar samples in Table 5.7. Assuming a normal AGN template, the characteristic dust surface density profiles are found to be $r^{0.3}$ in K, $r^{-0.7}$ in W1 and $r^{-1.0}$ in W2. Such a result suggests that the surface density gradient of sublimating dust increases gradually with radius at 2.0 $\mu$m, reaches a peak after that, and drops quickly at longer wavelengths.

*Normal Quasars versus Dust-deficient Quasars* Lyu et al. (2017) showed that the intrinsic IR SEDs of PG quasars can be grouped into normal, WDD and HDD populations that

Table 5.7. Parameters related to the torus radial density profiles

| Parameter | K | W1 | W2 |
|---|---|---|---|
| $<\lambda_{\rm rest}>/\mu$m | 2.1 | 3.0 | 4.1 |
| $\Delta M_{\rm IR}$ | 0.48±0.33 | 0.19±0.11 | 0.16±0.09 |
| $AMP$ | 4.65±3.07 | 4.65±3.51 | 4.68±3.47 |
| $f_{\rm IR}/f_{\rm opt}$ | 4.16 | 6.90 | 9.49 |
| $\alpha$ | 0.3 | -0.7 | -1 |

are likely associated with different torus structures. Now we discuss if such arguments are supported by the dust reverberation results. Considering the relatively small numbers of dust-deficient quasars in our PG sample, we reduce the number of free parameters by assuming that the time lag goes exactly as the square root of the luminosity (i.e., $\beta = 0.5$) to facilitate comparisons of the time lag - AGN luminosity relations for the different quasar types. The fitted parameters can be found in Table 5.6. At the same AGN luminosity, WDD and HDD quasars appear to have smaller time lags (see also Figure 5.9), suggesting a more compact hot dust emission zone.

In Figure 5.14, we compare the variation amplitudes and time lags for different populations of quasars. First, there is no strong correlation between these two properties. The HDD quasars have relatively smaller variation amplitudes compared with normal quasar population, as expected from their different SED features. However, the WDD quasars do not show much of a difference. This is possibly related to their similar SEDs to normal quasars at these wavelengths.

We have carried out Kolmogorov-Smirnov (K-S) tests to check if the distribution of the variation amplitudes and time lags among dust-deficient quasars and normal quasars are different at a significant level. The K-S probabilities that describe the likelihood that the two samples do not differ significantly can be found in Table 5.8. As demonstrated in Lyu et al. (2017), the distribution of AGN luminosities among HDD quasars is not significantly different from that for normal quasars. For the mid-IR time lags, the K-S probabilities of the HDD against normal quasars are close to unity ($p \sim 0.95$). In other words, the time lag distributions of the W1 and W2 bands between the HDD population and the

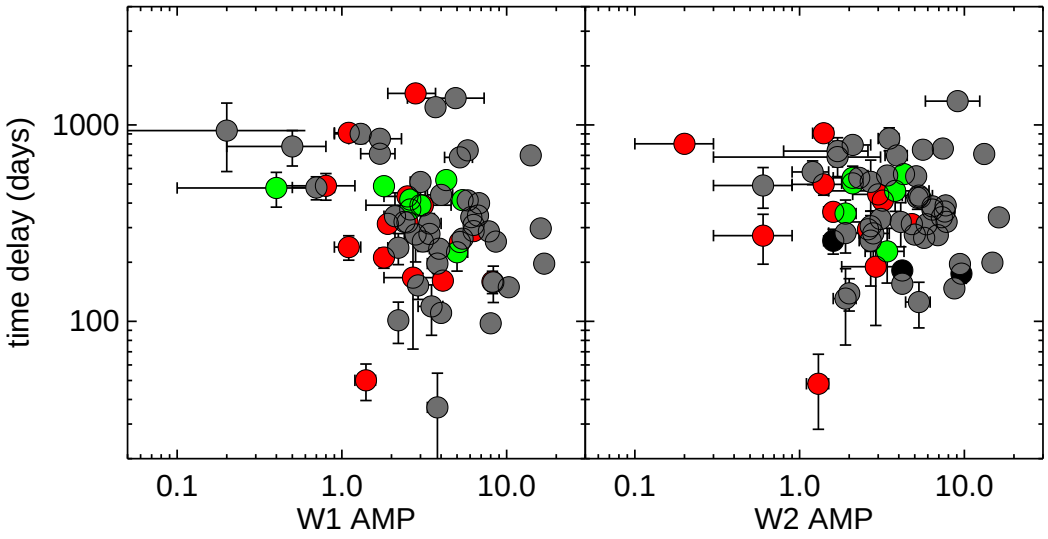


Figure 5.14 The distribution of variation amplitudes and time lags for normal (grey), WDD (green) and HDD (red) quasars.

normal population are similar (but their dependences on AGN luminosity are different, as shown in Table 5.6). However, the variation amplitude distribution between HDD and normal quasars are significantly different ($p \sim 0.009$ for W1 and $p \sim 0.005$ for W2), which can be expected if HDD quasars have fewer hot dust grains heated by the AGN, as previously proposed based on SED features in Lyu et al. (2017). For WDD quasars, although the K-S test results do not support any significant differences with normal quasars, the situation is uncertain since WDD quasars have higher redshifts and higher luminosities. These two features would impact the observed torus size in the opposite directions, hindering meaningful comparisons.

### 5.5.3 Relation between Dusty Torus and Broad-line Regions

In the classical AGN unification scheme, the broad-line region (BLR) is dust-free and relatively small, well-separated from the outer dusty torus (Antonucci, 1993; Urry & Padovani, 1995). In recent years, proposals have been made that the BLR is a failed dusty wind from the outer accretion disc (Czerny & Hryniewicz, 2011). Under this picture, Baskin & Laor (2018) explored the expected dust properties and corresponding BLR structure, and ar-

Table 5.8. K-S probabilities of the HDD and WDD quasars against normal quasars

| Measurement | HDD | WDD | HDD+WDD |
|---|---|---|---|
| W1 AMP | **0.009*** | 0.315 | 0.014 |
| W1 lag | 0.947 | 0.046 | 0.439 |
| W2 AMP | **0.005** | 0.227 | **0.005** |
| W2 lag | 0.949 | 0.351 | 0.847 |

*We indicate significant differences ($p < 0.01$) in bold.

gued for the presence of large graphite grains ($a \gtrsim 0.3\mu$m) down to the observed size of the BLR. By comparing the reverberation mapping analysis of the BLR and dusty torus sizes, these statements can be tested.

Previous comparisons of K-band and the UV-optical emission-line time lags relative to the optical continuum have suggested the torus inner radius is larger than the BLR region, with $R_{\rm BLR} \sim 0.5 R_{\rm TOR,\,K}$ for Seyfert-1 nuclei (Suganuma et al., 2006; Koshida et al., 2014). This result was obtained by comparing the time lag - AGN luminosity correlation for the BLR and torus from different samples. A very small number of objects have size estimates of both the torus (in the near-IR band) and the BLR from dust and emission line reverberation mappings at similar observing epochs. Clavel et al. (1989) reported $R_{\rm BLR,MgII}/R_{\rm TOR,\,K} \sim 0.4$ for Fairall 9, a bright quasar with $L_{\rm AGN,\,bol} \sim 3 \times 10^{12} L_{\odot}$. Pozo Nuñez et al. (2015) found $R_{\rm BLR,H\alpha}/R_{\rm TOR,\,K} \sim 0.4$ for PGC 50424, a Seyfert-1 nucleus with $L_{\rm AGN,\,bol} \sim 3 \times 10^{10}\ L_{\odot}$. Ramolla et al. (2018) studied the optical and near-IR time lags of 3C 120, a type-1 AGN with $L_{\rm AGN,\,bol} \sim 4 \times 10^{11}\ L_{\odot}$, and argued for $R_{\rm BLR,H\alpha}/R_{\rm TOR,\,K} \sim 0.7$.

With our mid-IR reverberation analysis and previous BLR size measurements of the PG sample, we can explore the BLR and torus relation in a large sample of bright quasars. Kaspi et al. (2000) studied the variations in the optical Balmer emission lines and the continuum emission of 28 PG quasars, and reported time lag measurements for 17 objects. Among these 17 objects, we have detected mid-IR time lags in 15. The results are sum-

Table 5.9. Time lag comparison of BLR and mid-IR dust for 12 PG quasars

| Name | Type | $\log(L_{\rm AGN,\,bol}/L_{\odot})$ | $\Delta t_{H\alpha}$ | $\Delta t_{H\beta}$ | $\Delta t_{\rm W1}$ | $\Delta t_{\rm BLR}/\Delta t_{\rm TOR,\,W1}$ |
|---|---|---|---|---|---|---|
| PG 0026+129 | HDD | 12.44 | $132^{+29}_{-31}$ | $125^{+29}_{-31}$ | 577.0±20.4 | 0.47 |
| PG 0052+251 | HDD | 12.56 | $211^{+66}_{-44}$ | $99^{+30}_{-31}$ | 360.0±75.1 | 0.58 |
| PG 0804+761 | WDD | 12.55 | $193^{+20}_{-17}$ | $151^{+26}_{-24}$ | 659.9±40.4 | 0.30 |
| PG 8444+349 | HDD? | 11.87 | $39^{+16}_{-16}$ | $13^{+14}_{-11}$ | 224.0±26.4 | 0.17 |
| PG 0953+414 | WDD | 12.93 | | $187^{+27}_{-33}$ | 913.0±68.7 | 0.20 |
| PG 1211+143 | NORM | 12.13 | $116^{+38}_{-46}$ | $103^{+32}_{-44}$ | 365.6±22.4 | 0.32 |
| PG 1229+204 | NORM | 11.53 | $71^{+39}_{-46}$ | $36^{+32}_{-18}$ | 266.3±2.3 | 0.27 |
| PG 1307+085 | HDD | 12.16 | $179^{+94}_{-145}$ | $108^{+46}_{-115}$ | 357.6±25.2 | 0.50 |
| PG 1411+442 | NORM | 12.02 | $103^{+40}_{-37}$ | $118^{+72}_{-71}$ | 441.7±26.2 | 0.27 |
| PG 1426+015 | NORM | 12.09 | $90^{+46}_{-68}$ | $115^{+49}_{-68}$ | 264.0±34.3 | 0.44 |
| PG 1613+658 | NORM | 12.42 | $43^{+40}_{-22}$ | $44^{+20}_{-23}$ | 371.9±86.3 | 0.12 |
| PG 2130+099 | NORM | 11.90 | $237^{+53}_{-28}$ | | 525.3±18.5 | 0.45 |

marized in Table 5.9. The mean value of $\Delta t_{\rm BLR}/\Delta t_{\rm TOR,3.0\ \mu m} \sim 0.23 \pm 0.10$, with the maximum value 0.44, minimum value at 0.06 and the median at 0.23.

In Figure 5.15, we explore if there are correlations between $\Delta t_{\rm BLR}$ and $\Delta t_{\rm TOR,\ W1}$. Linear fits result in:

$$\Delta t_{\rm BLR,H\alpha} = (0.37 \pm 0.06)\Delta t_{\rm TOR,W1} + (-43.00 \pm 26.49)\ , \tag{5.5.11}$$

and

$$\Delta t_{\rm BLR,H\beta} = (0.28 \pm 0.05)\Delta t_{\rm TOR,W1} + (-44.18 \pm 21.98)\ . \tag{5.5.12}$$

In log-log space, we find

$$\Delta t_{\rm BLR,H\alpha} = 10^{-2.64\pm0.29}(\Delta t_{\rm TOR,W1})^{1.77\pm0.11}\ , \tag{5.5.13}$$

and

$$\Delta t_{\rm BLR,H\beta} = 10^{-4.12\pm0.26}(\Delta t_{\rm TOR,W1})^{2.27\pm0.09} \tag{5.5.14}$$

.

Given the mean value of $\Delta t_{\rm BLR}/\Delta t_{\rm TOR,3\mu m} \sim 0.23$ for the PG quasars and $\Delta t_{\rm TOR,K}/\Delta t_{\rm TOR,W1} \sim 0.6$ from our fits of Koshida et al. (2014) measurements (Section 5.4.2), we find $R_{\rm BLR}/R_{\rm TOR,\ K} \sim 0.4$. This result statistically confirms the values obtained in the three cases discussed above. It suggests that the BLR region is only slightly smaller than the size of the K-band dust emission, providing strong support for the picture proposed by Baskin & Laor (2018) that large graphite dust grains might survive down to $R_{\rm BLR}$ and that the very hot dust emission comes from regions very close to the BLR.

## 5.6 Summary

We present the first statistical mid-IR dust reverberation mapping study of the quasar torus with an innovative usage of the long-term time-series data from the mid-IR *WISE*/*NEOWISE* mission and several optical transient surveys (CRTS, ASAS-SN and PTF) over a timescale of about 8 yr. Compared with previous dedicated targeted observations, the data in these public archives have various complications and uncertainties. We have developed procedures to maximize the usefulness of these data and characterize the dust reverberation

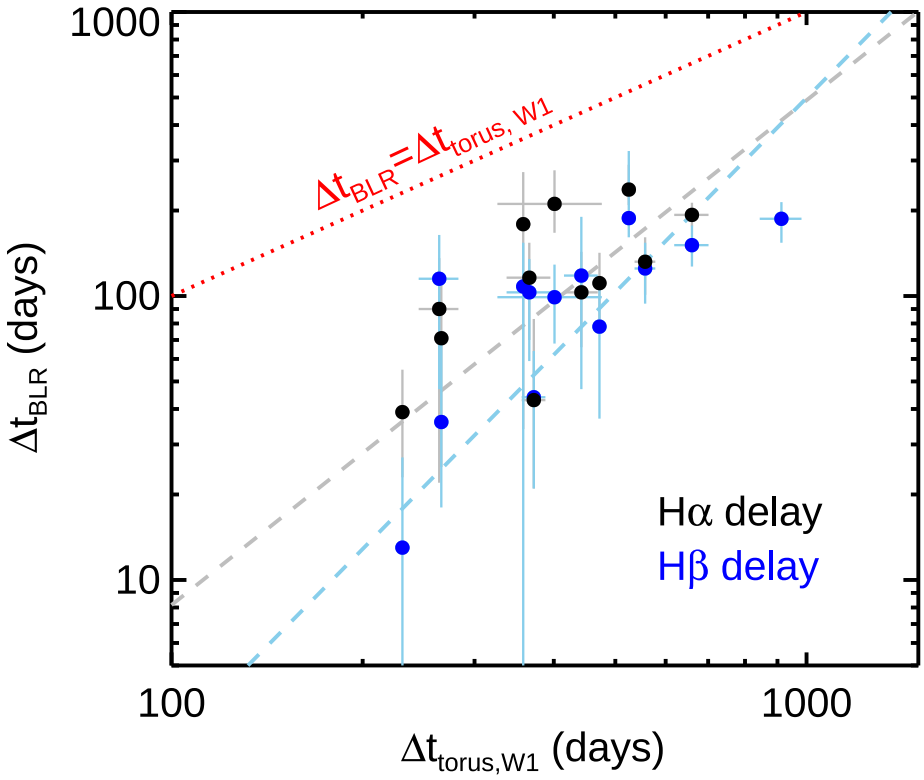


Figure 5.15 Comparison of the infrared light lags in the *WISE* W1 band ($\sim 3.4\ \mu$m) from this work and the broad emission line lags of 17 PG quasars from Kaspi et al. (2000). We fit linear functions for H$\beta$ lag vs. W1 lag (blue dots) and H$\alpha$ lag vs. W1 lag (black dots) separately, shown as blue and black dashed lines (see text for details). The red dotted line represents where the torus IR time lags equal the BLR time lags.

signals by comparing the mid-IR and optical light curves with a simple linear model. The success of this approach has been demonstrated by our detection of mid-IR time dust lags to the optical variation signals in 67 out of 87 $z < 0.5$ PG quasars. Most of the remaining quasars have data quality issues or featureless mid-IR light curves, making analysis ambiguous. Our key results for AGN variability at 1–3 $\mu$m are as follows.

1. The majority of PG quasars ($\sim 77\%$) have convincing dust reverberation signals with time-lags that follow the expected $\Delta t \propto L_{\rm AGN}^{0.5}$ relation. For the *WISE* W1 and W2 filter bandpasses, we find

$$\Delta t_{\rm torus,W1}/{\rm day} = 10^{2.10\pm0.06}(L_{\rm AGN,SED}/10^{11}L_{\odot})^{0.47\pm0.06}$$

and

$$\Delta t_{\rm torus,W2}/{\rm day} = 10^{2.20\pm0.06}(L_{\rm AGN,SED}/10^{11}L_{\odot})^{0.45\pm0.05} .$$

Combined with previous studies in the near-IR, the AGN IR time lags share the same scaling relation with AGN luminosity over four orders of magnitude, indicating that similar circumnuclear dust structures are common to AGNs;

2. By combining our mid-IR results of PG quasars and previous K-band analysis of Seyfert-1 nuclei by Koshida et al. (2014), we provide the first multiwavelength torus size constraints. Assuming the same $\Delta t \propto L_{\rm AGN}^{0.5}$ relation for different bands, we find average time lag ratios of $\Delta t_{\rm K} : \Delta t_{\rm W1} : \Delta t_{\rm W2} \sim 0.6 : 1.0 : 1.2$ ($\lambda_{\rm rest} \sim$2.1, 2.9, 4.0 $\mu$m);

3. With the variability amplitudes derived from reverberation model fitting, it is possible to put some crude constraints on surface density profiles of AGN-heated hot dust grains. We find $\Sigma(r) \propto r^{0.3}$ at K-band, $\Sigma(r) \propto r^{-0.7}$ at *WISE* W1-band and $\Sigma(r) \propto r^{-1.0}$ at W2-band, indicating the concentration of the hottest dust grains in the innermost regions of the torus;

4. For the same AGN luminosity, the mid-IR emission region sizes of dust-deficient quasars are only 60–70% of those found for normal quasars. In addition, their relative size differences in the *WISE* W1 and W2 bands are smaller, possibly indicating compact dust structures. Meanwhile, the difference between the optical and mid-IR variability amplitudes are smaller for hot-dust-deficient quasars than for normal quasars, indicating a smaller amount of dust reprocessing the accretion disk emission. On the other hand, there is no difference in the ratio of mid-IR to optical variability amplitude between warm-dust-deficient and normal quasars. These results are roughly consistent with their SED features and support their different torus structures as argued by Lyu et al. (2017);

5. Using previous measurements of BLR size measurements in the literature, the mean value of $R_{\rm BLR}/R_{\rm torus,W1} \sim 0.23 \pm 0.10$. Given that the relative IR time lags between W1 and K bands, $R_{\rm BLR}/R_{\rm torus,K} \sim 0.4$, indicating that the dust torus is located just outside of AGN BLRs.

With the multi-epoch infrared data from *Spitzer* and WISE, we also studied the AGN variability behavior at 10–24 $\mu$m and explored its relationship to that at 3–5$\mu$m. The most important results are:

6. With very few exceptions, significant AGN IR variability at $\lambda \gtrsim 10$ $\mu$m is only found among blazars and/or flat-spectrum radio sources (FSRQs). Considering the limited number of 24 $\mu$m observations, it is likely that all of these sources vary in the mid-IR. In contrast with blazars and FSRQ, we have found only one steep-spectrum radio quasar (SSRQ) to probably be variable at 24 $\mu$m. Such a difference can be explained under the radio-loud AGN unification scheme. Since SSRQs have larger inclination angles to our line of sight compared with FSRQs, realistic beaming effects greatly enhance the variability of the latter population.

7. Besides blazars and FSRQs, the vast majority of AGNs do not show variability at 24$\mu$m. That is the IR variability amplitude decreases quickly as a function of wavelength. Compared with W1 band, the W2 band variability is reduced to 90% and the 24$\mu$m is less than 10%. Given the fact that typical W1-band variation RMS$\lesssim$0.1 mag for most quasars, the corresponding flux change at $\sim 24$ $\mu$m is no more than 0.01 mag. Only in very rare cases is a possible dust reverberation signal detected (e.g., PG 1535+547).

We thank the referee, Makoto Kishimoto, for his constructive report.

This work was supported by NASA grants NNX13AD82G and 1255094.

This publication has made use of data products from the *Wide-field Infrared Survey Explorer*, which is a joint project of the University of California, Los Angeles, and the Jet Propulsion Laboratory/California Institute of Technology, funded by the National Aeronautics and Space Administration. This publication also makes use of data products from NEOWISE, which is a project of the Jet Propulsion Laboratory/California Institute of Technology, funded by the Planetary Science Division of the National Aeronautics and Space Administration. This work is based in part on archival data obtained with the Spitzer Space Telescope, which is operated by the Jet Propulsion Laboratory, California Institute

of Technology under a contract with NASA. Support for this work was provided by an award issued by JPL/Caltech.

The CSS survey is funded by the National Aeronautics and Space Administration under Grant No. NNG05GF22G issued through the Science Mission Directorate Near-Earth Objects Observations Program. The CRTS survey is supported by the U.S. National Science Foundation under grants AST-0909182 and AST-1313422. ASAS-SN is supported by the Gordon and Betty Moore Foundation through grant GBMF5490 to the Ohio State University and NSF grant AST-1515927. Development of ASAS-SN has been supported by NSF grant AST-0908816, the Mt. Cuba Astronomical Foundation, the Center for Cosmology and Astro Particle Physics at the Ohio State University, the Chinese Academy of Sciences South America Center for Astronomy (CASSACA), the Villum Foundation, and George Skestos. Data from the Steward Observatory spectro-polarimetric monitoring project were used. This program is supported by Fermi Guest Investigator grants NNX08AW56G, NNX09AU10G, NNX12AO93G, and NNX15AU81G. We also acknowledge with thanks the 3C 273 observations from the *AAVSO International Database* contributed by observers worldwide and used in this research.

This work is based in part on observations made with the Spitzer Space Telescope, which is operated by the Jet Propulsion Laboratory, California Institute of Technology under a contract with NASA. The Combined Atlas of Sources with Spitzer IRS Spectra (CASSIS) is a product of the IRS instrument team, supported by NASA and JPL.

*Software*: SExtractor (Bertin & Arnouts, 1996), DAOPHOT package (Stetson, 1987), IRAF (Tody, 1986, 1993), MPFIT (Markwardt, 2009), JAVELIN (Zu et al., 2013), Matplotlib (Hunter, 2007)

CHAPTER 6

# THE CONTRIBUTION OF HOST GALAXIES TO THE INFRARED ENERGY OUTPUT OF $z \gtrsim 5.0$ QUASARS

The infrared spectral energy distributions (SEDs) of $z \gtrsim 5$ quasars can be reproduced by combining a low-metallicity galaxy template with a standard AGN template. The host galaxy is represented by Haro 11, a compact, moderately low metallicity, star-bursting galaxy that shares typical features of high-$z$ galaxies. For the vast majority of $z \gtrsim 5$ quasars, the AGN contribution is well modeled by a standard empirical template with the contamination of star formation in the infrared subtracted. Together, these two templates can separate the contributions from the host galaxy and the AGN even in the case of limited data points, given that this model has only two free parameters. Using this method, we re-analyze 69 $z \gtrsim 5$ quasars with extensive *Herschel* observations, and derive their AGN luminosities $L_{\rm AGN}$ in a range $\sim (0.78-27.4)\times10^{13}\,L_{\odot}$, the infrared luminosities from star formation $L_{\rm SF,IR} \sim (<1.5-25.7)\times10^{12}\,L_{\odot}$, and the corresponding star formation rates SFR $\sim (<290-2650)\,M_{\odot}$/yr. The average infrared luminosity from star formation and the average total AGN luminosity of the $z \gtrsim 5$ quasar sample follows the correlation defined by quasars at $z<2.6$. We assume these quasar host galaxies maintain a constant average SFR ($\sim 620\,M_{\odot}$/yr) during their mass assembly and estimate the stellar mass that could form till $z\sim5-6$ to be $\langle M_{*}\rangle \sim (3-5)\times10^{11}M_{\odot}$. Combining with the black hole (BH) mass measurements, this stellar mass is adequate to establish a BH-galaxy mass ratio $M_{\rm BH}/M_{*}$ at 0.1-1%, consistent with the local relation. [1]

## 6.1 Introduction

Over 150 quasars with black hole masses of the order of $10^{8}-10^{9}\,M_{\odot}$ have been discovered beyond $z\sim5$, less than a billion years after the Big Bang (e.g., Fan et al., 2006;

[1] A version of this chapter originally appeared as a published paper in the Astrophysical Journal (Lyu et al., 2016). All the works described here was carried out by me, with help from coauthor George Rieke and Stacey Alberts.

Jiang et al., 2008; Mortlock et al., 2009; Willott et al., 2010a; Morganson et al., 2012; McGreer et al., 2013; Bañados et al., 2014). In the local Universe, the masses of supermassive black holes (SMBHs) are correlated with the properties of their host galaxies, suggesting galaxies and SMBHs possibly coevolve (Kormendy & Ho, 2013, and references therein). Since star formation (SF) enables the buildup of galaxies and active galactic nuclei (AGN) trace the growth of SMBHs, the so-called SF-AGN relation has come under intense scrutiny for decades (Heckman & Best, 2014, and references therein). With the use of ground- and space-based facilities, similar research can be extended to $z > 5$, allowing the preliminary examination of both the stellar and SMBH growth at very early stages in galaxy evolution (e.g., Walter et al., 2004, 2009; Maiolino et al., 2005; Riechers et al., 2006; Jahnke et al., 2009; Wang et al., 2010b, 2013; Willott et al., 2013, 2015).

However, observing the AGN host galaxy in a quasar is challenging, since the bright continuum emission from the active nucleus overpowers the light from the galaxy from the UV through the near-infrared (near-IR or NIR). At $z > 5$, the situation is even more extreme: the AGN tend to be the most luminous because of the evolution of the quasar luminosity function and selection effects (e.g., Fan et al., 2004; Jiang et al., 2008; Willott et al., 2010b; McGreer et al., 2013); the host galaxies are found to be compact and small (e.g., Jiang et al., 2013; Wang et al., 2013); and the presence of copious amounts of dust (e.g., Wang et al., 2008b; Leipski et al., 2014) may also obscure the galaxy light. To study these very distant AGN host galaxies, attention has turned to the emission in longer wavelengths (e.g., Wang et al., 2010b, 2011b, 2013; Leipski et al., 2013, 2014), where the AGN is less dominant.

A promising tool to probe the stellar activity in a quasar is analyzing its infrared (IR) spectral energy distribution (SED). For galaxies, most of the radiation from the recently formed stars is absorbed and re-emitted at IR wavelengths. However, in quasars, the central AGN may also heat the dust (e.g., Haas et al., 2003; Netzer et al., 2007). Since spatially resolving the IR emission at high-redshift is impossible with current facilities, we have to rely on SED models to distinguish star formation and nuclear activity (e.g., Marshall et al. 2007; Mullaney et al. 2011; Mor & Netzer 2012b; Magdis et al. 2013; Netzer et al. 2014; Xu et al. 2015b,a).

The UV-to-NIR SEDs of AGN seem to have little evolution with redshift and Eddington-ratio (e.g., Hao et al. 2014; Wang et al. 2008b). However, at $z > 5$, the far-IR SEDs of quasars seem to include a warm (40-60 K) dust component (e.g., Beelen et al., 2006; Wang et al., 2008a; Leipski et al., 2014), which is not commonly found in the local quasars. It is intriguing to check if such behavior is due to the evolution of the AGN host galaxies, since the IR SEDs of galaxies do change at high-$z$ (see Lutz 2014 for a review). Compared with local nuclear-concentrated ULIRGs, intermediate redshift ($z \sim 2-3$) dusty star-forming galaxies (DSFGs) are more extended, resulting in cooler SEDs than those locally with similar IR luminosities (Rujopakarn et al., 2011). Meanwhile, galaxies at higher redshifts have more gas (e.g., Carilli & Walter, 2013) to supply the star formation, boosting their IR luminosities (e.g., Daddi et al., 2005, 2007; Rodighiero et al., 2011; Magnelli et al., 2014; Schreiber et al., 2015). Moreover, both observations and theories suggest galaxies in the early Universe are generally metal poor (e.g., Madau & Dickinson, 2014, and references therein), which could also have detectable effects on their SEDs, such as weak aromatic features, featureless mid-IR (MIR) continuum, and higher dust temperatures (e.g., Galliano et al., 2005; Rémy-Ruyer et al., 2013). At extremely high redshift (e.g., $z > 4$), direct constraints on metallicity in galaxies are rare; however, indirect evidence supporting low-metallicity comes from the failed detection of the dust continuum for nearly all $z > 6$ galaxies (e.g., Ouchi et al. 2013; Maiolino et al. 2015, but see Watson et al. 2015). It is likely that galaxies, in general, including those quasar host galaxies, are of relatively low-metallicity when the Universe age is within $\sim 1$ Gyr.

Because of these issues, fits to the SEDs of high redshift quasars are unsuccessful using conventional quasar templates plus those for typical normal (e.g., $\sim$ solar metallicity) SF galaxies, a method that works well for low-to-intermediate redshift quasars (e.g., Mullaney et al. 2011; Magdis et al. 2013; Xu et al. 2015b). In this paper, we demonstrate that the SEDs of $z \gtrsim 5$ quasars can be modeled using a moderately low-metallicity galaxy template to represent the AGN host galaxy. We combine a galaxy template derived from Haro 11 and a modified AGN template based on Elvis et al. (1994) to provide physically-motivated fits that successfully reproduce these $z \gtrsim 5$ quasar infrared SEDs. This simple model can be used to probe the relation between the AGN activity and host star formation

in quasars with very limited observations.

Throughout this paper, we adopt cosmology $\Omega_m = 0.27$, $\Omega_\Lambda = 0.73$ and $H_0 = 71 \mathrm{km\ s^{-1} Mpc^{-1}}$.

## 6.2 Selection of SED Templates

In modeling the SEDs of quasars at $z \gtrsim 5.0$, the dearth of data points at long wavelengths requires minimizing the number of free parameters in SED fitting. While more precise fittings may be achieved by adding more free parameters, the scientific interpretation is then more subject to model degeneracy. To first order, the SED of a quasar should consist of an AGN component, and a host galaxy component. If suitable SED templates can be found, we only need two free parameters to normalize their contributions. Such a two-parameter model can be used to retrieve information from sources with less complete observations and make the interpretation less ambiguous.

### 6.2.1 Host Galaxy Template: Why Haro 11?

Galaxies at $z \sim 2-3$ are of relatively low-metallicity (e.g., Cullen et al., 2014; Maier et al., 2014). Confirming the trend toward lower metallicity to $z \gtrsim 5$ is difficult with current capabilities. Recently, some groups have tried to detect the dust continua of $z > 6$ normal galaxies using the Atacama Large Millimeter/Sub-millimeter Array (ALMA). The unexpected failures of almost all of these efforts have led to the interpretation that these $z > 6$ galaxies may be scaled-up versions of local very metal-poor dwarf galaxies (e.g., Ouchi et al., 2013; Maiolino et al., 2015). As Fisher et al. (2014) pointed out, it would be almost impossible to observe the dust emission of any $z > 6$ galaxies with extreme low metallicity like the local dwarf galaxy 1 Zw 18. For the most luminous systems, however, the change in metallicity seems to be modest (e.g., Rawle et al., 2014). As a result, the ideal sample to draw a representative template for IR observable high-$z$ galaxies is the moderately low-metallicity galaxies in the local Universe.

In addition, AGN host galaxies at $z > 4$ are found to be compact with typical sizes $\sim$ 1-3 kpc, from observations at rest-frame UV (Jiang et al., 2013), deep $K_s$-band images (Targett et al., 2012), dust continuum maps (Wang et al., 2013), submm fine structure line

maps (e.g., Wang et al., 2013; Willott et al., 2013, 2015), molecular gas distributions (e.g., Walter et al., 2004, 2009; Wang et al., 2013), and from SED analysis (Greve et al., 2012). Compared with extended galaxies of the same infrared luminosity, they are expected to have hotter far-IR SEDs due to compact star forming regions (Groves et al., 2008). Thus, we are motivated to search for a moderately low-metallicity galaxy with a high surface density of star formation to provide a SED analogous to that we expect for the star formation in the host galaxies of high-$z$ quasars.

Appendix H presents the procedure to derive low-metallicity galaxy templates. To summarize briefly, we began with the sample of the Dwarf Galaxy Survey (DGS; Madden et al. 2013), which includes the largest metallicity range observable in the local Universe, with 12+log(O/H) ranging from 7.14 to 8.43, and spans four orders of magnitude in star formation rates. Combining their *Herschel* far-IR data (Rémy-Ruyer et al., 2013) and archival WISE mid-IR photometry, we fit the broad-band SEDs with a far-IR modified blackbody plus a mid-IR power-law component, and replaced the mid-IR fit SEDs with the corresponding *Spitzer* spectra. Among the 19 dwarf galaxies studied in detail, Haro 11 is the best candidate analog for high-z galaxies. Haro 11 is a moderately low-metallicity ($Z = 1/3\,Z_{\odot}$, James et al. 2013) dwarf ($M_{*} = 10^{10}\,M_{\odot}$, Östlin et al. 2001) galaxy in the nearby Universe ($D = 92.1$ Mpc, Bergvall et al. 2006). It shows substantial star formation activity (SFR $\approx 20 - 30\,M_{\odot}/\mathrm{yr}$, Grimes et al. 2007, see also Appendix I.1.1) and emits strongly in the infrared ($L_{\mathrm{IR}} \approx 2.0 \times 10^{11}\,L_{\odot}$, Adamo et al. 2010). Haro 11 also contains an extremely young stellar population with age $< 40$ Myr (Adamo et al., 2010). Some authors suggest it is a local analogue of the high-$z$ Lyman break galaxies (LBGs) or Lyman-$\alpha$ emitters (Hayes et al., 2007; Leitet et al., 2011).

Besides low metallicity, the most important two features of Haro 11 are its high star formation rate and compact size, indicating a very high star formation surface density. From our estimation, the star formation rate of Haro 11 can be as high as $\sim 32\,M_{\odot}/\mathrm{yr}$ (based on $L_{\mathrm{IR}}$ and $L_{\mathrm{FUV}}$, see Appendix I.1.1), which is significantly higher than the vast majority of dwarf galaxies in the literature (Hopkins et al., 2002). Meanwhile, Haro 11 has a compact size. Its MIPS 24$\mu$m image is perfectly diffraction-limited (see Figure 6.1), which puts an upper-limit on its IR emitting region size ($< 3.4''$ or 1.2 kpc). The size of the star forma-

tion region of Haro 11 constrained from high-resolution H$\alpha$ images (Östlin et al., 2009) is also small ($\sim$ 1.3 kpc from measuring 50% total flux, and $\sim$2.7 kpc from measuring 90% total flux). The IR luminosity surface density, $\Sigma_{L(\mathrm{IR})}$, of Haro 11 is $\sim 10^{11}\,L_{\odot}/\mathrm{kpc}^2$, which approaches the values in galaxies at $z \gtrsim 4$ (e.g., GN20 has $\Sigma_{L(\mathrm{IR})} \sim 10^{12}\,L_{\odot}/\mathrm{kpc}^2$, Hodge et al. 2015). The high star formation rate surface density and infrared luminosity surface density of Haro 11 are exceptional among dwarf galaxies, making it the most suitable local analog to high-$z$ quasar host galaxies.

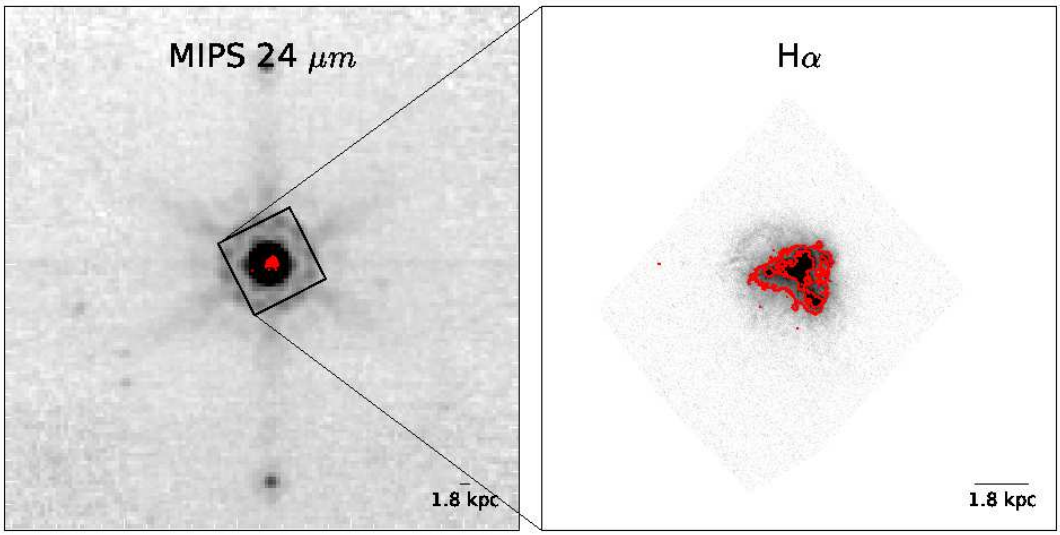


Figure 6.1 The *Spitzer* MIPS 24$\mu$m (left; Program ID: 59, PI: G. H. Rieke) and the HST H$\alpha$ (right; Östlin et al. 2009) images of Haro 11. The H$\alpha$ image is zoomed to view the central square region on the 24$\mu$m image. We also overplot the same H$\alpha$ contours (red lines) on both images.

In Figure 6.2, we compare the derived Haro 11 template with a number of normal solar-metallicity star-forming (SF) templates in Rieke et al. (2009). Haro 11 has a larger mid-IR slope with $\alpha = 3.63$ ($f_{\nu} \propto \lambda^{\alpha}$), in contrast with normal galaxies with $\alpha \sim 2.0$ (e.g., Blain et al., 2003; Casey, 2012). The derived dust temperature is T = 46.5 K with emissivity index $\beta = 1.9$. Haro 11 also presents very weak aromatic features compared with normal galaxies. All these characteristics are commonly seen for other dwarf galaxies (see Appendix H.3). Compared with the Rieke et al. (2009) SED templates with $\log L_{\mathrm{IR}} <$ 11.50, which are representative for $z \sim 2$ galaxies (see Section 6.3.1), Haro 11 has similar

$L_{IR}$ surface densities but higher dust temperature. We suggest the low-metallicity of Haro 11 is the most likely reason for its warmer SED.

### 6.2.2 AGN Continuum Template

Candidate AGN templates can be derived from either numerical models (e.g., Fritz et al., 2006; Hönig & Kishimoto, 2010b) or semi-analytic models (e.g., Mullaney et al., 2011; Sajina et al., 2012). However, such models always have many free parameters, which need to be optimized to fit real AGN behavior. Hence the starting point for determining AGN templates needs to be an accurate empirical version.

Elvis et al. (1994) built an X-ray to radio SED template for a sample of 47 well-defined optically selected quasars and subtracted the host galaxy emission in the UV/optical and near-IR bands. This template has become the classic representation of Type 1 AGN SEDs in the ultraviolet, visible, near, and mid-infrared. Many studies based on larger samples and modern data have closely reproduced the Elvis template (e.g., Richards et al., 2006; Shang et al., 2011; Runnoe et al., 2012a; Elvis et al., 2012; Hanish et al., 2013; Scott & Stewart, 2014). The remarkable similarity of these results to the Elvis template is demonstrated by the comparisons in Scott & Stewart (2014) (their Figure 5). The success of the Elvis template is also demonstrated by its broad application, for example, to study the SEDs of type-1 AGN in XMM-COSMOS (Elvis et al., 2012) and decompose the SEDs of intermediate-redshift quasars in Xu et al. (2015b). The template shape appears to vary little with cosmic evolution or other characteristics such as the Eddington ratio (e.g., Hao et al., 2011, 2014). In particular, this template appears to work equally well to $z \sim 6$. Jiang et al. (2006) demonstrated that the rest-frame $0.15 - 3.5\mu$m SEDs of 13 $z \sim 6$ quasars can be matched with the Elvis et al. (1994) template. Wang et al. (2008b) demonstrated that the average optical-to-near-IR SED of 33 $z \sim 6$ quasars is consistent with the Elvis template. Jiang et al. (2010) find that the near infrared and optical-to-NIR colors of hundreds of quasars are virtually the same from the local epoch to $z \geq 6$, i.e., they are consistent with a common SED shape, which must therefore be consistent with the Elvis template. Therefore, the Elvis template is a useful metric for testing more complex models and is currently the most suitable approach for SED decompositions involving UV-luminous

Type-1 AGNs.

There are two issues in applying the Elvis template. The first is that it is likely to have a residual contribution in the far infrared from dust heated by star formation, a possibility that has hindered its application in using the far infrared to measure star formation rates in quasar host galaxies (e.g., Barnett et al., 2015). However, a version of the template corrected for this effect is now available (Xu et al., 2015b). Based on the analysis of the Spitzer and IRAS data of the Elvis et al. (1994) sample, these authors found a tight correlation between the strength of the 11.3 $\mu$m aromatic feature and the infrared 60 to 25 $\mu$m flux ratio. They concluded that star formation, as traced by the aromatic feature, boosted the infrared flux ratio in the template by a factor of 1.27. A scaled Rieke et al. (2009) star-forming galaxy template (log $L_{\rm IR}$ = 11.0) was subtracted from the Elvis et al. (1994) template to remove this contribution. The second issue is that of order 10% of quasars have SEDs similar to the Elvis template in the UV and optical, but are relatively weak in the near and mid-infrared, a behavior attributed to a relative lack of hot dust (Hao et al., 2010, 2011). The exact SED shape of these dust-poor quasars requires future work to address.

Leipski et al. (2013) used three components to represent the AGN SEDs for their high redshift quasar sample: a UV/optical power-law, a NIR dust emission component, and a torus model. They adjusted the relative contributions of these components to optimize their SED fits. However, all three components are implicitly embedded in the Elvis template. Any adjustments in relative strengths should only be made after it has been demonstrated that the Elvis template (or similar ones) gives an unsatisfactory fit. In this work, we use the Elvis template for our SED decomposition. When combined with the Haro 11 template, we find that its fits are of comparable quality to the relatively unconstrained fits used by Leipski et al. (2013, 2014) in the sense of chi-square tests. There is thus no advantage for our study in using those more complex and less constrained models for the quasar SEDs - they introduce additional free parameters without improving the fits correspondingly (see Section 6.3.3).

### 6.2.3 Fitting Procedure

To compare the templates described above to observations, we used a fitting procedure that takes into account upper-limit data points where available. For $n$ measurements of $x_i$ with uncertainties $\sigma_i$ and $m$ non-detections with $x_j < n\sigma_j$ ($n^{\text{th}}$ confidence level), we define the fitting chi-square as (Isobe et al., 1986):

$$\chi^2_{\text{total}} = \sum_i^n z_i^2 - \sum_j^m 2\ln\frac{1+\text{erf}(z_j/\sqrt{2})}{2} , \tag{6.2.1}$$

where

$$z_i = \frac{x_i - \hat{x}_i(\theta)}{\sigma_i} , \tag{6.2.2}$$

$$\text{erf}(x) = \frac{2}{\sqrt{\pi}}\int_0^x e^{-t^2}dt , \tag{6.2.3}$$

which is the error function, and $\hat{x}_i(\theta)$ is the modeled value. In Equation 6.2.1, the first term on the right-hand side is the classical definition of chi-square, and the second term introduces the error function to quantify the fitting of upper-limits. We use Markov Chain Monte Carlo (MCMC) methods to find the parameter set $\theta$ to minimize $\chi^2_{\text{total}}$. $3\sigma$ upper limits are adopted for all non-detections. To compare the fitting quality of different fitting methods, the total $\chi^2_{\text{total}}$ should be normalized by the degrees of freedom, $\nu$. In our case, $\nu = n+m-k$, where $k$ is the number of free parameters in the model. We will use $\chi^2_\nu$ to represent the reduced chi-square, i.e., $\chi^2_\nu = \chi^2_{\text{total}}/\nu$.

To deal with the trade-off between the goodness of fit and the complexity of the model, we use the corrected Akaike Information Criterion (AICc) test (Sugiura, 1978), which is defined by

$$\text{AICc} = -2\ln\mathscr{L}_{\max} + 2k + \frac{2k(k+1)}{N-k-1} , \tag{6.2.4}$$

where $\mathscr{L}_{\max}$ is the maximum likelihood achievable by the model, and $N$ is the number of data points used in the fit, $N = n+m$. The likelihood of a model to fit data satisfies

$$-2\ln\mathscr{L}_{\max} = \chi^2_{\text{total}} + C , \tag{6.2.5}$$

where the constant $C$ is related to the errors, $\sigma_i$, and the binning, $\Delta x_i$, of the data points, which are fixed at the time of observations. We can ignore $C$ when comparing different

models to fit the same observations, and finally have

$$\mathrm{AICc} = \chi^2_{\mathrm{total}} + 2k + \frac{2k(k+1)}{n+m-k-1} \,. \tag{6.2.6}$$

## 6.3 Tests of the Templates

### 6.3.1 Template Fits for High-$z$ Galaxies

We now discuss alternative SF template candidates to be used at high-$z$. Rieke et al. (2009) derived templates for local normal star-forming galaxies with different infrared luminosities ($L_{\mathrm{IR}}$). Although carefully calibrated in the local Universe, these templates may not apply at high redshift. The star formation in luminous galaxies at high-$z$ has been found to be more physically extended than that in local galaxies with similar $L_{\mathrm{IR}}$ (local LIRGs and ULIRGs are sub-kpc, whereas high-$z$ DSFGs are kpc in size, see Rujopakarn et al. 2011). Rujopakarn et al. (2011, 2013) found that the Rieke et al. (2009) $\log L_{\mathrm{IR}}$=11.00-11.50 SED templates are representative of galaxies found at $0.4 < z < 2.7$ due to their similar $L_{\mathrm{IR}}$ surface densities. This argument is supported by the consistency between the empirical average SED of $z \sim 2$ galaxies derived in Kirkpatrick et al. (2012) and the $\log L_{\mathrm{IR}}$=11.00-11.50 SED templates from Rieke et al. (2009) (Figure 6.3). In fact, Figure 6.3 shows the progressively poorer correspondence of the Rieke et al. (2009) templates with the empirical one with increasing $L_{\mathrm{IR}}$. It is also consistent with the finding of a shift toward colder FIR SEDs at high redshift by Symeonidis et al. (2009, 2013). Greve et al. (2012) found evidence of extended structures in DSFGs out to redshift $z \sim 4.0$, based on analysis of their infrared SEDs. With this evidence, we focus on Rieke et al. (2009) SED templates with luminosity $\log L_{\mathrm{IR}} < 11.50$ in the following comparisons. These normal SF templates represent galaxies that are almost certainly more metal-rich than is appropriate for $z > 4$. We will therefore compare them with fits using a template derived from Haro 11.

We test the Rieke et al. (2009) and Haro 11 template fittings to extremely high-$z$ galaxies, as examples of potential host galaxies for high redshift quasars. Due to the lack of data available for star-forming galaxies at $z > 5$, we extend our redshift range down to $z = 4$. We find 8 galaxies (see Table 6.1) with multiple constraints on their rest-frame infrared SEDs, suitable for comparison with these templates. By selection, these highest-$z$ DSFGs

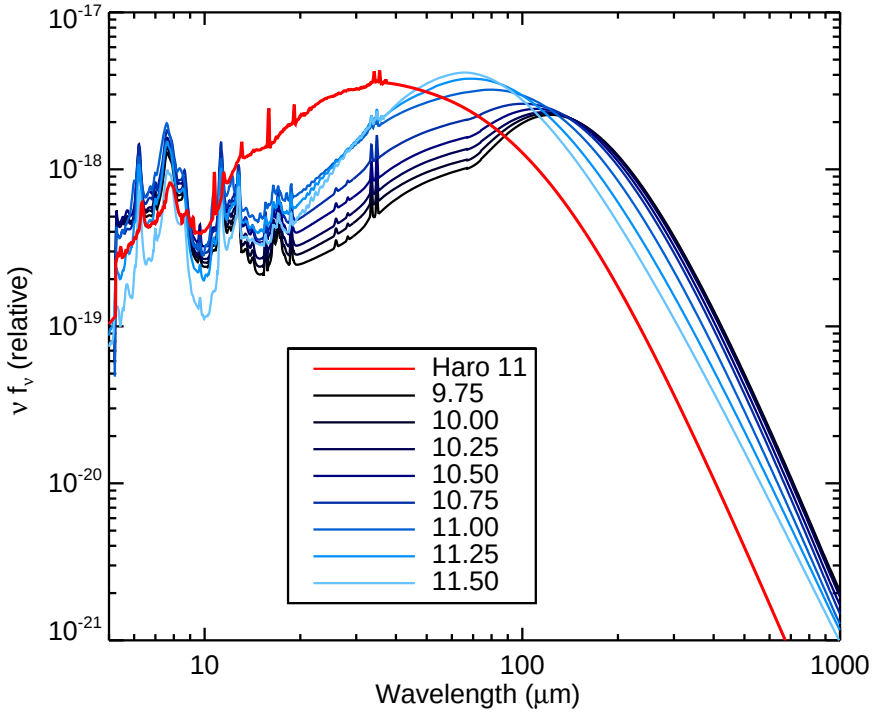


Figure 6.2 Comparison of Haro 11 template (red line) and the normal star-forming galaxy templates with $\log L_{\rm IR} = 9.75 \sim 11.50$ in Rieke et al. (2009) (blue lines). All the templates are normalized to have the same $L_{\rm IR,template}$

are limited to a handful of submillimeter galaxies (SMGs), which were originally discovered in the submm and relatively bright in the far-IR. The identification technique of SMGs could bias their SEDs to be relatively cold compared with high-$z$ galaxies selected in other ways (Le Floc'h et al., 2004), whereas the SEDs of low-metallicity galaxies tend to be relatively hot (e.g., Rémy-Ruyer et al., 2013). As a result, the high-$z$ galaxy examples studied here might be biased against typical low metallicity galaxies, which, as in the case of Haro 11, tend to have SEDs dropping rapidly toward the submm.

Table 6.1 summarizes the fitting results for the $z > 4$ galaxies. We limit the fits to rest-frame 8-1000 $\mu$m, where the emission is purely from dust. Although a few examples, e.g., GN20, have a cold far infrared SED matched better by the Rieke et al. (2009) templates, in general the fits with the Haro 11 SED are at least as good. We conclude that it is as good as the local higher metallicity templates in fitting the SEDs of these extreme $z > 4$ SMGs.

That is, even given the selection bias against it, the Haro-11-based template can be used without a substantial loss of accuracy.

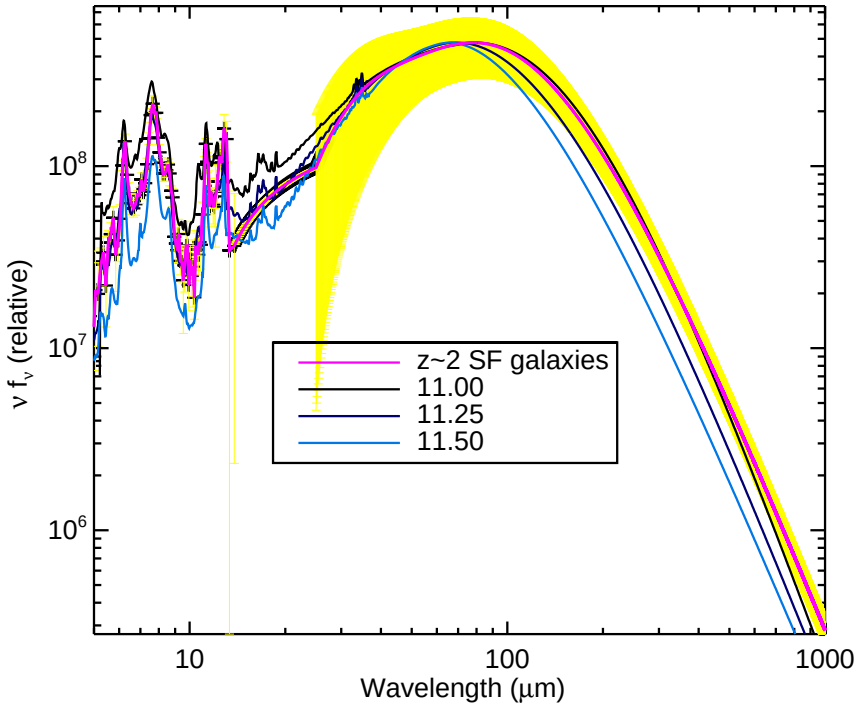


Figure 6.3 Comparison of the $z \sim 2$ galaxy SED in Kirkpatrick et al. (2012) (magenta line with template errors in yellow) and the normal star-forming galaxy templates with $\log L_{\rm IR} = 11.00, 11.25, 11.50$ in Rieke et al. (2009) (black, navy, blue lines). All the templates are normalized to have the same $L_{\rm IR,template}$

### 6.3.2 Template Fits for High-$z$ Quasars

The Elvis et al. (1994) template has been shown to match type-1 quasar SEDs for redshifts up to $z \sim 3$ and for wavelengths $\lambda \lesssim 24\mu$m (Hao et al. 2014; Xu et al. 2015b). An issue in applying it, or the similar template of Richards et al. (2006), in the far-IR is the uncertain contribution of host galaxy star formation (e.g., Barnett et al., 2015). However, Xu et al. (2015b) were able to correct for this effect. In Figure 6.4, we compare this corrected template with the stacked SEDs from Leipski et al. (2014). While the UV-to-optical parts of all three SEDs are well matched with the AGN continuum template, differences emerge

Table 6.1. Comparisons of galaxy templates used to fit $z > 4$ galaxies

| Source (1) | $z$ (2) | $\chi^2_{\nu,\mathrm{Haro11}}$ (3) | R09 best (4) | $\chi^2_{\nu,\mathrm{R09}}$ (5) | Ref. (6) |
|---|---|---|---|---|---|
| HFLS 3 | 6.34 | 13.1 | 11.50 | 30.9 | 1 |
| AzTEC 3 | 5.30 | 1.5 | 11.50 | 2.3 | 2, 3 |
| HLS J0918+5142 | 5.24 | 18.1 | 11.50 | 18.4 | 3 |
| AzTEC 1 | 4.64 | 6.9 | 11.50 | 2.0 | 3 |
| Capak4.55 | 4.55 | 0.6 | 11.50 | 2.1 | 3 |
| ID 141 | 4.24 | 5.7 | 11.50 | 17.9 | 5 |
| GN10 | 4.05 | 3.2 | 11.50 | 1.5 | 3 |
| GN20 | 4.05 | 23.1 | 11.25 | 0.2 | 3 |

Note. — Col. (1): Source names sorted by their redshifts; Col. (3): $\chi^2_\nu$ of Haro 11 template fitting; Col. (4): the Rieke et al. (2009) template which has the minimum $\chi^2_\nu$; Col. (5): minimum $\chi^2_\nu$ among tested Rieke et al. (2009) templates; Col. (6): references for photometric data. **References.** (1) Riechers et al. (2013); (2) Dwek et al. (2011); (3) Huang et al. (2014); (4) Rawle et al. (2014); (5) Cox et al. (2011)

in the infrared. The stacked SED of quasars detected in at least 3 *Herschel* bands has a substantial excess over the AGN template in the far-IR, which we attribute to host galaxy star formation (see Section 6.5.1). The stacked SED of quasars not detected with *Herschel* is not matched as well in the infrared although the reduced chi-square is still acceptable. This behavior could be due to the unsuitability of a classical AGN template to represent the hot-dust-free (Jiang et al., 2010) or hot-dust-poor (Hao et al., 2010, 2011) quasars (hereafter hot-dust-deficient quasars, or HDD quasars) as pointed out by Leipski et al. (2014). The fit to the *Herschel* partly-detected (detected in only 1-2 *Herschel* bands) stacked SED is virtually perfect over the entire wavelength range. The agreement of the template with both the *Herschel*-undetected and *Herschel* partly-detected stacked SEDs suggests that the star-formation corrected Elvis SED is a good choice to fit the high-redshift AGN continua. More discussion will be provided in Section 6.5

### 6.3.3 SED Fitting with Well-measured High-$z$ Quasars

To test further whether the Haro 11 template as well as the AGN (modified Elvis et al. (1994)) template are reasonable choices to decompose $z \gtrsim 5$ quasar SEDs, we focus on 5 quasars with the most complete infrared SEDs. Besides SDSS J1204−0021, the SEDs

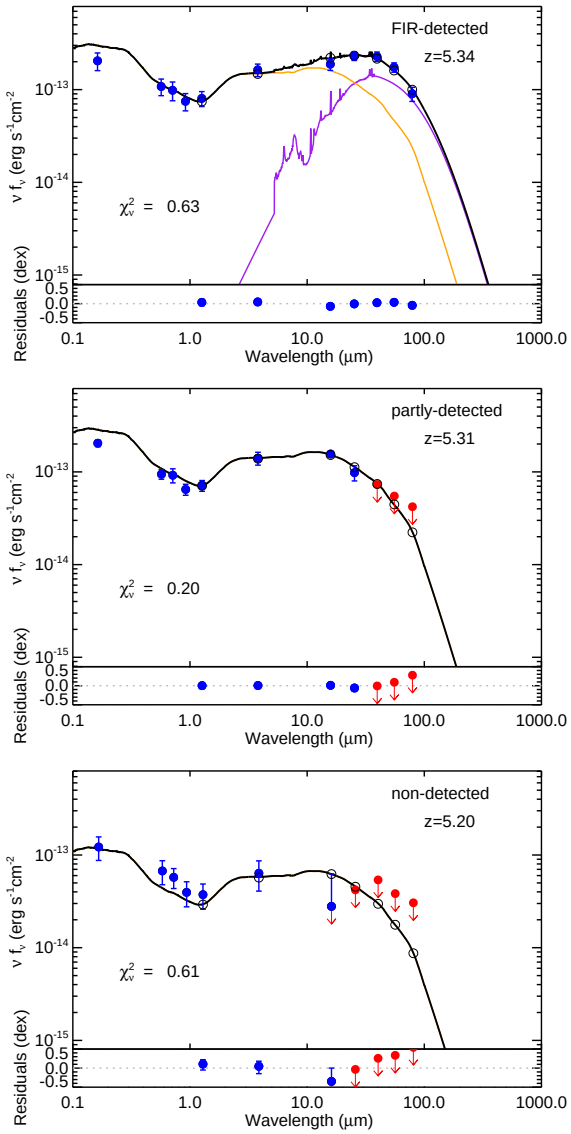


Figure 6.4 Three stacked SEDs in Leipski et al. (2014) and our fitting results. We limit the fitting to rest-frame wavelengths 1-1000$\mu$m. The black solid line is the modelled SED, the black circles are the modelled points (convolved with the corresponding photometric filters). The AGN component and galaxy component are shown as gray and purple solid lines, respectively. The blue dots are for detections with 1$\sigma$ error bars and red dots are for upper limits at 3$\sigma$. The reduced chi-square of the fit is shown on the bottom left of each plot.

of all the other quasars were studied in Leipski et al. (2013)[2]. We model the observed

[2]Among the five millimeter-detected quasars with at least two *Herschel* observations in Leipski et al. (2013), SDSS J1044−0125 is excluded since the number of detected data points at rest-frame $1-1000\mu$m is smaller than the number of free parameters of the Leipski et al. (2013) model. This hinders the computation of a reduced chi-square of the Leipski et al. (2013) model for only the IR data points to be compared with

rest-frame 1-1000$\mu$m SED as a linear combination of the Haro 11 template and the AGN template with two free normalizing factors. These two templates are taken to be independent. To compare the Haro 11 template with the normal SF templates, we replace the Haro 11 template by the normal SF templates in Rieke et al. (2009), and redo the fit. We also apply the Leipski et al. (2013) model to the UV-to-IR SED of these quasars and compare the fits of the IR SED with those from our two-component models.

In Figure 6.5, we present the SED decomposition results. In general, the Haro 11 template fits have smaller residuals ($\lesssim$ 0.3 dex) compared with the best-fit[3] normal SF template. In particular, the Haro 11 template yields much better fits in representing the warm dust component from the two-component decomposition. We comment on the two-component fits (left and middle columns of Figure 6.5) for each SED below:

**J0338+0021** (or SDSS J033829.31+002156.3; we use JHHMM $\pm$ DDMM for brevity). The Haro 11 template is better than the best normal SF template in decomposing the SED. Fitting the mid-IR at $< 10\mu$m and the far-IR drop beyond 100$\mu$m results in the normal SF template model underestimating the flux at $10-100\mu$m. We note an excess between $\sim$ 10 $\mu$m and $\sim$ 40 $\mu$m over the normal SF template fitting model SED, which could be the warm excess seen in relatively low-$z$ AGN SEDs reported by Xu et al. (2015b). In contrast, such an excess is not strong in the Haro 11 template fits.

**J0756+4104**. Judging from the fit $\chi^2_\nu$, the normal SF template seems better. However, $\sim$ 50% of the $\chi^2_\nu$ of the Haro 11 template fit is contributed by the data point at the longest wavelength ($\lambda_{\rm rest} = 139\mu$m), whereas the $\chi^2_\nu$ contribution of the same data point in the normal SF template fitting is minimal. Again, the normal SF template fitting underestimates the SED at $\sim 10-40\mu$m. We conclude the normal SF template and the Haro 11 template yield fits of similar quality.

**J0927+2001**. The Haro 11 template is much better than the normal SF template in reproducing the observed SED. The maximum deviation of the dwarf galaxy model and observed SEDs is less than 0.3 dex. In the case of this quasar, the normal SF template

the two-component fits.

[3]We fit these quasars with normal SF templates in Rieke et al. (2009) with $\log L_{\rm IR} \leq 11.50$, and pick the one that has the lowest $\chi^2_\nu$ as the best. The $\log L_{\rm IR} > 11.50$ normal SF templates do not yield any better results, especially in the mid-IR, as shown in Figure 6.5.

underestimates the SED at $\sim 10-100\mu$m.

**J1148+5251**. For this well-studied quasar, the Haro 11 template fitting is almost the same as the best normal SF template fitting when comparing $\chi^2_\nu$. Interestingly, our estimation of the host contribution of this quasar is consistent with result based on the theoretical analysis by Schneider et al. (2015) .

**J1204−0021**. This is the only case where the Haro 11 template fitting has one data point with fitting residual (slightly) greater than 0.3 dex. Both two-component fits underestimate the observed $10-100\mu$m flux. However, the residual from the Haro 11 template fitting is much smaller than the normal SF one.

For the Leipski et al. (2013) model (right column of Figure 6.5), we only apply the fit to the detected data points in the UV-to-IR, in the same fashion as Leipski et al. (2013), and compute the $\chi^2_\nu$ for the detected data points at rest-frame 1-1000$\mu$m. Since it has more components, especially a torus component selected from a large model library, small details of the observed SED can be reproduced. Thus, the residuals are generally smaller. However, our two-parameter fit has similar reduced chi-square compared with the Leipski et al. (2013) model, despite its simplicity. To judge which fit is preferred, we have used the AICc test (see Section 6.2.3). Since the slope of the power law component is not useful in fitting the infrared data, we have assumed that the Leipski et al. (2013) fits had six free parameters over 1-1000 $\mu$m. As shown in Table 6.2, the value of AICc is lower in all five cases for the 2-parameter fits, indicating that they are indeed preferred. That is, even for these quasars with the maximum number of measurements, the Leipski et al. (2013) model over-fits the data compared with our two-parameter one.

In summary, we find that the Haro 11 galaxy template and the modified Elvis AGN template are at least as good at fitting the overall high-$z$ quasar SEDs as the fits using templates for local star forming galaxies of solar metallicity. The Haro 11 template fits better in the rest-frame mid-IR, but may be slightly worse in the far-IR range. Though the Leipski et al. (2013) model could reproduce more details of the observed SED, our two-component model yields fits of comparable overall quality and is preferred in model selection due to its simplicity.

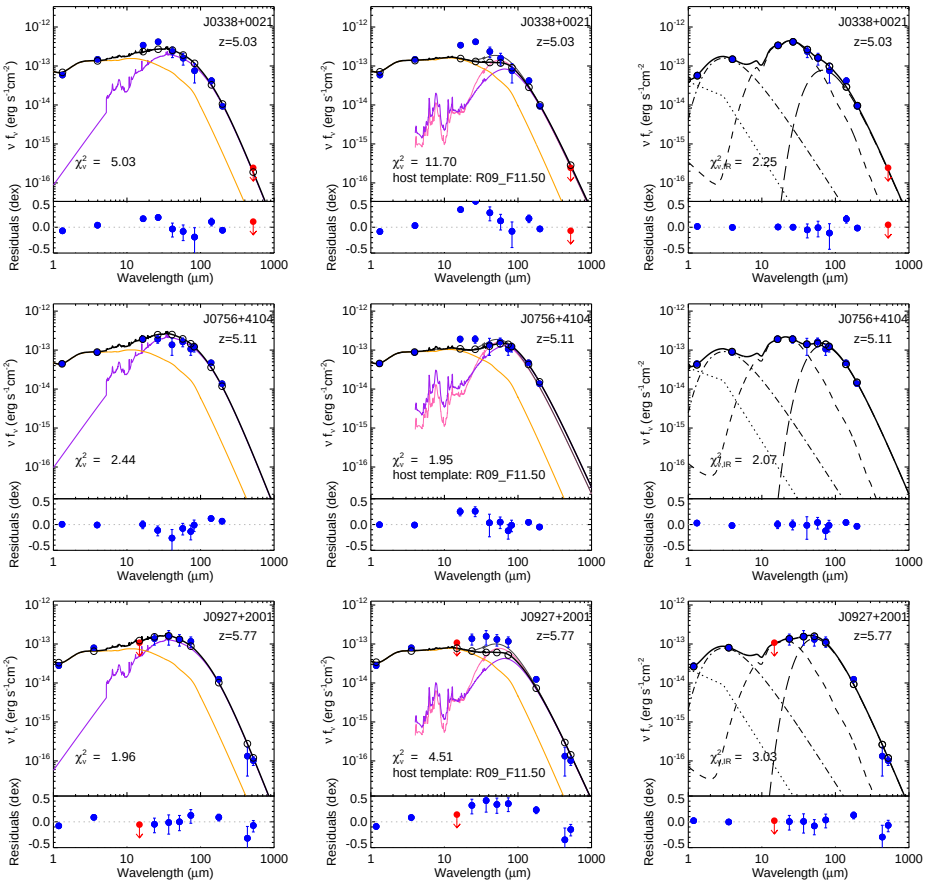


Figure 6.5 SEDs and their decompositions for 5 quasars with strong far-IR SED constraints. The plots show $\nu F_\nu$ in units of erg/s/cm$^2$ over the rest-frame wavelengths. We show the results from "Haro 11 + AGN" decomposition (left column), "normal SF galaxy + AGN" decomposition (middle column), and the Leipski et al. (2013) model (right column). In each plot, the blue dots are for detections with $1\sigma$ error bars and red dots are for upper limits at $3\sigma$. The bottom panel of each plot presents the residuals from the fit. In the left and middle columns, the colored lines show the results of a two-component SED fit as described in Section 6.2: the SF-subtracted type-1 AGN template in orange, and a galaxy template in purple. The black line is the total of these two components. The black circles are the synthetic photometry points from the model. To demonstrate that Rieke et al. (2009) templates with $\log L_{\rm IR} > 11.50$ do not yield better results, we make another fitting with Rieke et al. (2009) $\log L_{\rm IR}$=12.50 template, and plot the fitted galaxy component (pink thin line) and the total model SED (gray thin line) in the middle column. In the right column, we use the Leipski et al. (2013) model, which is a combination of a UV/optical power-law (dotted line), a 1200 K near-IR dust component (dot-dashed line), a near-/mid-IR torus model (short-dashed line), and a modified black-body far-IR component with $\beta = 1.6$ (long-dashed line).

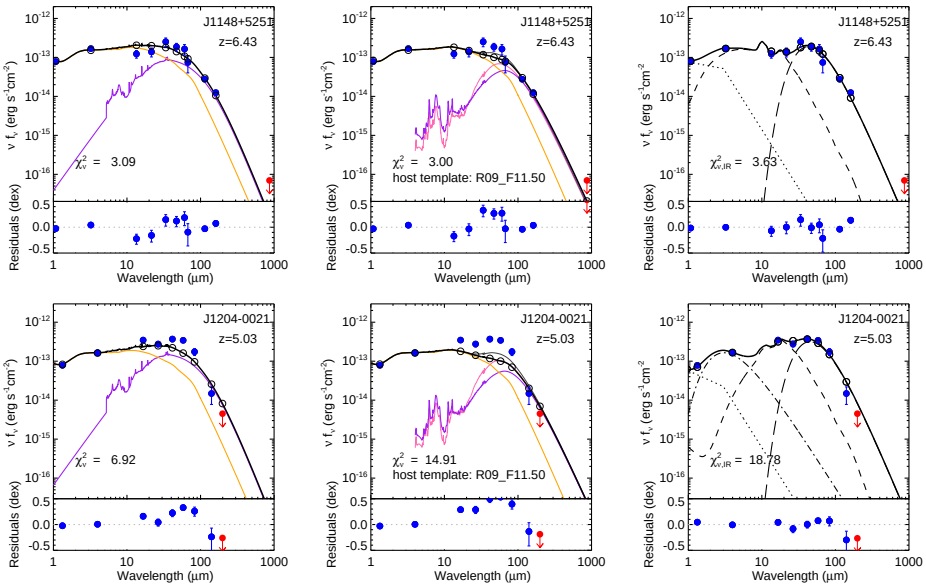


Figure 6.5 continued. SEDs and their decompositions of 5 quasars with strong far-IR SED constraints.

Table 6.2. SED decomposition results for $z \gtrsim 5$ 5 quasars with well-measured SEDs

| Source (1) | Redshift (2) | $L_{IR}/10^{13}L_\odot$ (3) | $f_{host,IR}$ (4) | $\chi^2_\nu$ (5) | AICc (6) | R09 best (7) | $\chi^2_{\nu,R09}$ (8) | $\chi^2_{\nu,L13,IR}$ (9) | $AICc_{L13}$ (10) |
|---|---|---|---|---|---|---|---|---|---|
| SDSS J0338+0021 | 5.03 | 4.01 | 0.57 | 5.03 | 45.95 | 11.50 | 11.70 | 2.25 | 49.00 |
| SDSS J0756+4104 | 5.11 | 3.77 | 0.69 | 2.44 | 25.26 | 11.50 | 1.95 | 2.07 | 48.28 |
| SDSS J0927+2001 | 5.77 | 3.21 | 0.64 | 1.96 | 21.39 | 11.50 | 4.51 | 3.03 | 52.12 |
| SDSS J1148+5251 | 6.43 | 5.31 | 0.34 | 3.09 | 33.31 | 11.50 | 3.00 | 3.63 | 51.10 |
| SDSS J1204−0021 | 5.03 | 3.79 | 0.46 | 6.92 | 54.44 | 11.50 | 14.91 | 18.78 | 110.34 |

Note. — Results of full IR fits. Upper-limit data points are included in the evaluation process. Col. (3): the total infrared luminosity (8-1000 $\mu$m) estimated from the "Haro 11 + AGN" two-component SED fit; Col. (4): the fraction of luminosity of host template contribution to the whole fit SED, based on result from the "Haro 11 + AGN" decomposition; Col. (5): reduced chi-square from the "Haro 11 + AGN" decomposition; Col. (6): the AICc test value of the "Haro 11 + AGN" two-component model; Col. (7): log$L_{IR}$ of the Rieke et al. (2009) template which has the minimum $\chi^2_\nu$; Col. (8): the minimum $\chi^2_\nu$ of the "normal SF galaxy + AGN" decomposition with all tested Rieke et al. (2009) templates; Col. (9): reduced chi-square from the Leipski et al. (2013) model, only counting data points at rest-frame 1-1000 $\mu$m; Col. (10): the AICc test value of the Leipski et al. (2013) model, assuming 6 free parameters.

## 6.4 AGN and Host Galaxy Decomposition for Quasars at $z \gtrsim 5$

Combining *Herschel*, *Spitzer* and ground-based 250 GHz observations, we apply the "Haro 11 + AGN" two-component fit to the observed SEDs of all 69 quasars in Leipski et al. (2014) (hereafter, *sample-A*). Since our interest is the infrared output, we again limit the fit to rest-frame $1.0 - 1000\mu$m. The fits are presented in Figure 6.6. We can confirm

again the suitability of the modified Elvis et al. (1994) AGN template: the near-IR to mid-IR SEDs of these $z \gtrsim 5$ quasars are well-matched with our empirical AGN template in 58 cases. Combining with the Haro 11 template, this modified Elvis et al. (1994) AGN template provides reasonably good fittings to all these $z \gtrsim 5$ quasars, which suggests the Elvis et al. (1994) AGN template derived on local quasars is suitable for vast majority of $z \gtrsim 5$ quasars. There are 11 cases where the Elvis template overestimates the mid-infrared, which is the signature of HDD quasars: the incidence of this behavior ($\sim 16\%$) is similar to that observed at lower redshift (Mor & Trakhtenbrot, 2011). The $\chi^2_\nu$, derived total infrared luminosities ($L(\mathrm{IR})$), and host component contributions from the fits are listed in Table 6.3. We also calculate the star formation rates using the method described in Section 6.5.3

We can compare the results of the host galaxy far-IR luminosity with other works. It is frequently assumed that the far-IR SED of high-$z$ quasars can be described as a $T = 47$ K and $\beta = 1.6$ modified black body (Beelen et al., 2006) and the infrared luminosity of this component is used to estimate their star formation rates (e.g., Omont et al., 2013; Leipski et al., 2013, 2014; Calura et al., 2014; Willott et al., 2015). However, real galaxies have strong mid-infrared emission that is under-represented by a single (modified) black body SED (e.g., Dunne & Eales, 2001; Willmer et al., 2009; Galametz et al., 2012; Kirkpatrick et al., 2012). With the inclusion of the mid-IR energy contribution from star formation, the Haro 11 template yields an infrared luminosity $L_{\mathrm{SF,IR}}$ 1.5-2.0 times larger than the infrared luminosity of the Beelen et al. (2006) modified back body template $L_{\mathrm{FIR}}$, depending on the exact far-IR constraints to the galaxy component. Compared with the Leipski et al. (2014) results from the four-component decomposition on 19 quasars with most complete IR SED observations, our results are different, especially for the host galaxy far-IR luminosity. For a quasar with strong host galaxy far-IR emission, its mid-IR emission will be dominated by star formation. Since the modified black body misses significant luminosity at shorter wavelengths, the Leipski et al. (2013) model has to scale up the torus component to fit the rest-frame mid-IR data, ending with an overestimated fraction of the far-IR emission due to the AGN (the torus) and an underestimated host galaxy contribution. Consequently, the star formation rates derived by the Leipski et al. (2013) model

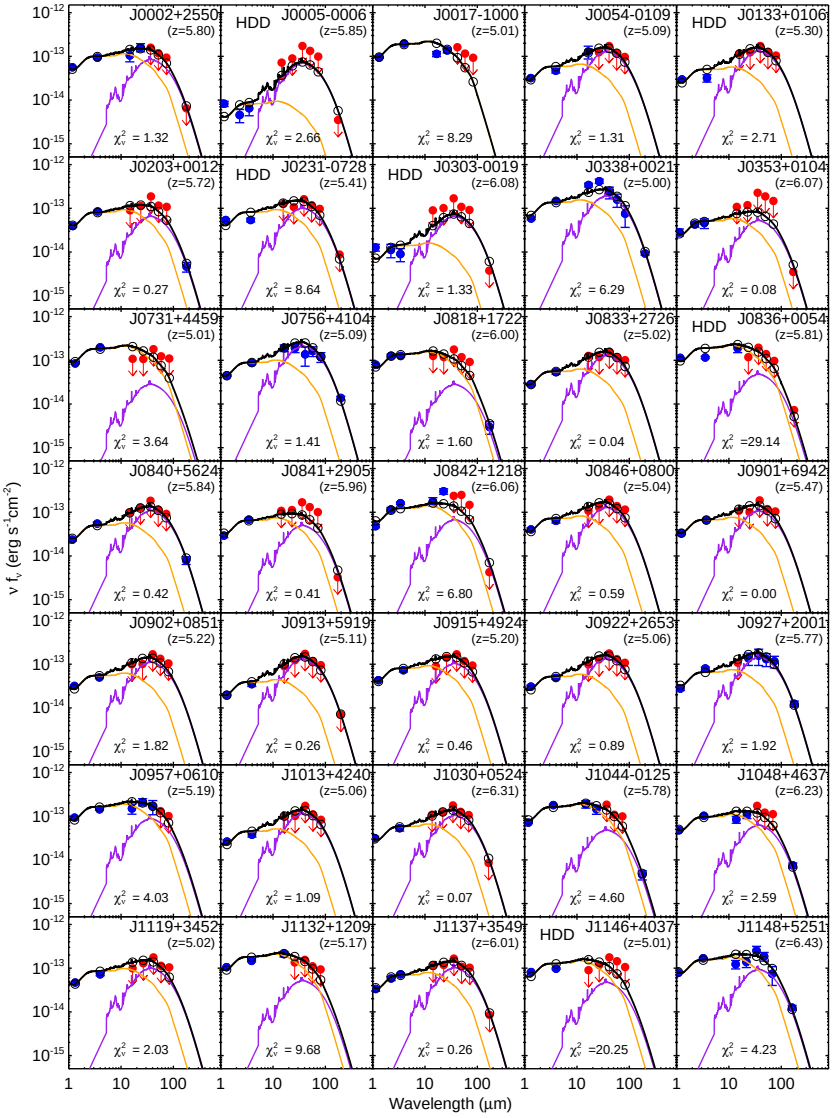


Figure 6.6 Two-component SED decompositions of 69 quasars (*sample-A*) in Leipski et al. (2014). The plots show $\nu F_\nu$ in unit of erg/s/cm$^2$ over the rest-frame wavelength. The black solid line is the modelled SED, the black circles are the modelled points. The AGN component and galaxy component are shown as gray and purple solid lines, respectively. The blue dots are for detections with $1\sigma$ error bars and red dots are for upper limits at $3\sigma$. The reduced chi-square of the fit is shown on the bottom of each plot. We put a tag 'HDD' near the top-left corner of the panel if the corresponding quasar is identified as hot-dust-deficient (HDD).

in such cases (like SDSS J0756+4104, J0927+2001, J1202+3235, J1340+2813, which have $L_{\rm SF,IR} \sim 2.2-2.9 L_{\rm FIR}$) are much lower than our values. For a quasar without strong host galaxy far-IR emission, however, the Leipski et al. (2013) model gives a higher $L_{\rm FIR}$

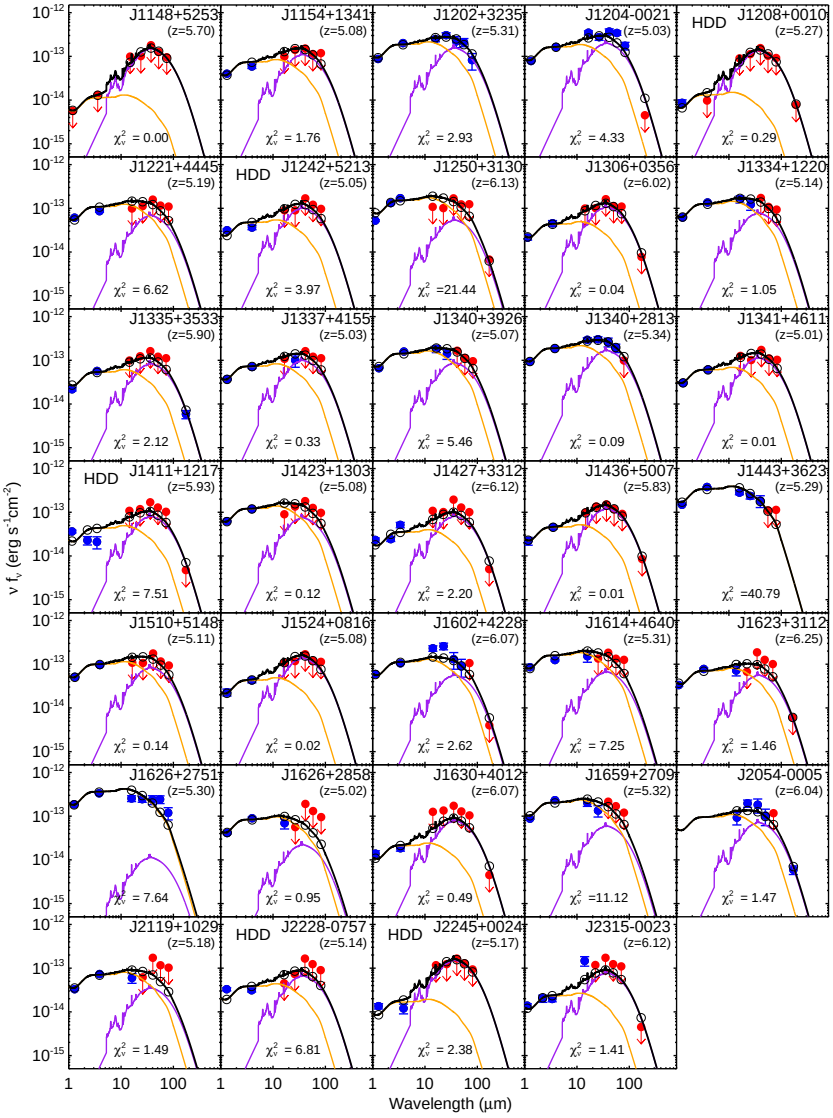


Figure 6.6 continued. Two-component SED decomposition of 69 quasars (*sample-A*) in Leipski et al. (2014).

than our $L_{\rm SF,IR}$. Examples are SDSS J0842+1218, J1044-0125, J1048+4637, J1148+5251, J1659+2709, with $L_{\rm SF,IR} \sim 0.5 - 1.0 L_{\rm FIR}$. This discrepancy is still due to the template differences. The torus templates used in Leipski et al. (2013, 2014) by themselves generally underpredict the far-IR emission compared with our AGN template. As a result, the far-IR modified black body has to be scaled up to match the far-IR observations. We believe the star formation rate based on the $L_{\rm SF,IR}$ from our model is more reliable, since 1) the host galaxy template is based on a real galaxy that includes the mid-IR star formation contri-

bution; 2) the relative contributions of the torus and near-IR component are fixed in our AGN template that is based on real observations. In addition, thanks to the simplicity of the two-component model, we can place constraints on the host galaxy star formation for the other 50 $z \gtrsim 5$ quasars in Leipski et al. (2014), which only have upper-limits for the MIR-FIR SEDs and the Leipski et al. (2013) model can not fit. We will discuss our model results in Section 6.5.

Table 6.3. SED decomposition results for $z \gtrsim 5.0$ 69 quasars (*sample-A*)

| Source (1) | $z$ (2) | $m_{1450\text{Å}}$ (3) | $\chi^2_\nu$ (4) | $L_{\rm IR}(10^{13}L_\odot)$ (5) | $f_{\rm host,IR}$ (6) | $c_{\rm SFR}$ (7) | SFR($M_\odot$/yr) (8) |
|---|---|---|---|---|---|---|---|
| SDSS J000239.39+255034.8 | 5.80 | 19.0 | 1.32 | ≤3.18 | ≤0.44 | 0.88 | ≤2394 |
| SDSS J000552.34−000655.8* | 5.85 | 20.8 | 2.66 | ≤1.34 | ≤0.89 | 0.61 | ≤1408 |
| SDSS J001714.67−100055.4 | 5.01 | 19.4 | 8.29 | ≤2.39 | ≤0.00 | 1.00 | ≤0.20(?) |
| SDSS J005421.42−010921.6 | 5.09 | 20.5 | 1.31 | ≤2.32 | ≤0.68 | 1.00 | ≤3006 |
| SDSS J013326.84+010637.7* | 5.30 | 20.7 | 2.71 | ≤2.49 | ≤0.72 | 1.00 | ≤3425 |
| SDSS J020332.35+001228.6 | 5.72 | 20.9 | 0.27 | 2.44 | 0.43 | 1.00 | 2028 |
| SDSS J023137.65−072854.5* | 5.41 | 19.5 | 8.64 | ≤2.66 | ≤0.54 | 1.00 | ≤2750 |
| SDSS J030331.40−001912.9* | 6.08 | 21.3 | 1.33 | ≤1.51 | ≤0.82 | 0.62 | ≤1467 |
| SDSS J033829.31+002156.3 | 5.00 | 20.0 | 6.29 | 3.93 | 0.57 | 1.00 | 4305 |
| SDSS J035349.72+010404.4 | 6.07 | 20.2 | 0.08 | ≤1.97 | ≤0.49 | 0.69 | ≤1281 |
| SDSS J073103.12+445949.4 | 5.01 | 19.1 | 3.64 | ≤2.63 | ≤0.13 | 1.00 | ≤643 |
| SDSS J075618.14+410408.6 | 5.09 | 20.1 | 1.41 | 3.73 | 0.69 | 1.00 | 4964 |
| SDSS J081827.40+172251.8 | 6.00 | 19.3 | 1.60 | 3.13 | 0.16 | 1.00 | 971 |
| SDSS J083317.66+272629.0 | 5.02 | 20.3 | 0.04 | ≤2.20 | ≤0.69 | 1.00 | ≤2901 |
| SDSS J083643.85+005453.3* | 5.81 | 18.8 | 29.14 | ≤4.19 | ≤0.19 | 1.00 | ≤1544 |
| SDSS J084035.09+562419.9 | 5.84 | 20.0 | 0.42 | 2.72 | 0.67 | 1.00 | 3504 |
| SDSS J084119.52+290504.4 | 5.96 | 19.6 | 0.41 | ≤2.10 | ≤0.42 | 0.69 | ≤1167 |
| SDSS J084229.23+121848.2 | 6.06 | 19.9 | 6.80 | ≤3.66 | ≤0.34 | 0.61 | ≤1448 |
| SDSS J084627.85+080051.8 | 5.04 | 19.6 | 0.59 | ≤2.44 | ≤0.63 | 1.00 | ≤2938 |
| BWE 910901+6942 | 5.47 | 19.8 | 0.00 | ≤2.58 | ≤0.60 | 1.00 | ≤2979 |
| SDSS J090245.77+085115.8 | 5.22 | 20.6 | 1.82 | ≤2.20 | ≤0.66 | 1.00 | ≤2785 |
| SDSS J091316.56+591921.5 | 5.11 | 21.5 | 0.26 | ≤2.12 | ≤0.76 | 0.97 | ≤2996 |
| SDSS J091543.64+492416.7 | 5.20 | 19.3 | 0.46 | ≤2.43 | ≤0.55 | 1.00 | ≤2557 |
| SDSS J092216.82+265359.1 | 5.06 | 20.4 | 0.89 | ≤2.27 | ≤0.71 | 1.00 | ≤3099 |
| SDSS J092721.82+200123.7 | 5.77 | 19.9 | 1.92 | 3.51 | 0.68 | 1.00 | 4561 |
| SDSS J095707.67+061059.5 | 5.19 | 19.0 | 4.03 | ≤3.35 | ≤0.33 | 1.00 | ≤2151 |
| SDSS J101336.33+424026.5 | 5.06 | 19.4 | 1.09 | ≤1.95 | ≤0.71 | 1.00 | ≤2647 |
| SDSS J103027.10+052455.0 | 6.31 | 19.7 | 0.07 | ≤3.35 | ≤0.63 | 0.78 | ≤3165 |
| SDSS J104433.04−012502.2 | 5.78 | 19.2 | 4.60 | 3.64 | 0.22 | 1.00 | 1530 |
| SDSS J104845.05+463718.3 | 6.23 | 19.2 | 2.59 | 3.23 | 0.38 | 1.00 | 2360 |
| SDSS J111920.64+345248.2 | 5.02 | 20.2 | 2.03 | ≤2.26 | ≤0.53 | 1.00 | ≤2278 |
| SDSS J113246.50+120901.7 | 5.17 | 19.4 | 9.68 | ≤3.10 | ≤0.21 | 1.00 | ≤1262 |
| SDSS J113717.73+354956.9 | 6.01 | 19.6 | 0.26 | ≤3.18 | ≤0.58 | 0.90 | ≤3207 |
| SDSS J114657.79+403708.7* | 5.01 | 19.7 | 20.25 | ≤2.16 | ≤0.26 | 1.00 | ≤1072 |
| SDSS J114816.64+525150.3 | 6.43 | 19.0 | 4.23 | 5.48 | 0.36 | 1.00 | 3801 |
| RD J1148+5253 | 5.70 | 23.1 | 0.00 | ≤2.58 | ≤0.93 | 0.96 | ≤4406 |
| SDSS J115424.74+134145.8 | 5.08 | 20.9 | 1.76 | ≤2.29 | ≤0.59 | 1.00 | ≤2571 |
| SDSS J120207.78+323538.8 | 5.31 | 18.6 | 2.93 | 4.79 | 0.44 | 1.00 | 4046 |
| SDSS J120441.73−002149.6 | 5.03 | 19.1 | 4.33 | 4.42 | 0.54 | 1.00 | 4547 |
| SDSSp J120823.82+001027.7* | 5.27 | 20.5 | 0.29 | ≤1.99 | ≤0.91 | 0.90 | ≤3125 |
| SDSS J122146.42+444528.0 | 5.19 | 20.4 | 6.62 | ≤2.35 | ≤0.37 | 1.00 | ≤1683 |
| SDSS J124247.91+521306.8* | 5.05 | 20.6 | 3.97 | ≤1.82 | ≤0.67 | 1.00 | ≤2344 |
| SDSS J125051.93+313021.9 | 6.13 | 19.6 | 21.44 | ≤4.08 | ≤0.25 | 1.00 | ≤1954 |
| SDSS J130608.26+035626.3 | 6.02 | 19.6 | 0.04 | ≤2.76 | ≤0.70 | 0.81 | ≤2992 |
| SDSS J133412.56+122020.7 | 5.14 | 19.5 | 1.05 | ≤2.65 | ≤0.37 | 1.00 | ≤1869 |
| SDSS J133550.81+353315.8 | 5.90 | 19.9 | 2.12 | 2.41 | 0.60 | 1.00 | 2762 |
| SDSS J133728.81+415539.9 | 5.03 | 19.7 | 0.33 | ≤2.09 | ≤0.56 | 1.00 | ≤2261 |
| SDSS J134015.04+392630.8 | 5.07 | 19.6 | 5.46 | ≤2.89 | ≤0.37 | 1.00 | ≤2031 |
| SDSS J134040.24+281328.2 | 5.34 | 19.9 | 0.09 | 5.03 | 0.46 | 1.00 | 4404 |
| SDSS J134141.46+461110.3 | 5.01 | 21.3 | 0.01 | ≤2.08 | ≤0.64 | 1.00 | ≤2558 |
| SDSS J141111.29+121737.4* | 5.93 | 20.0 | 7.51 | ≤2.21 | ≤0.64 | 0.68 | ≤1827 |
| SDSS J142325.92+130300.7 | 5.08 | 19.6 | 0.12 | ≤2.47 | ≤0.37 | 1.00 | ≤1740 |
| FIRST J142738.5+331241 | 6.12 | 20.3 | 2.20 | ≤2.22 | ≤0.69 | 0.65 | ≤1910 |
| SDSS J143611.74+500706.9 | 5.83 | 20.2 | 0.01 | ≤2.83 | ≤0.72 | 0.86 | ≤3346 |
| SDSS J144350.67+362315.2 | 5.29 | 20.3 | 40.79 | ≤4.85 | ≤0.00 | 1.00 | ≤1.6(?) |
| SDSS J151035.29+514841.0 | 5.11 | 20.1 | 0.14 | ≤2.34 | ≤0.44 | 1.00 | ≤1976 |
| SDSS J152404.10+081639.3 | 5.08 | 20.6 | 0.02 | ≤2.22 | ≤0.75 | 1.00 | ≤3196 |

Table 6.3 (cont'd)

| Source (1) | $z$ (2) | $m_{1450\text{Å}}$ (3) | $\chi^2_\nu$ (4) | $L_{\rm IR}(10^{13}L_\odot)$ (5) | $f_{\rm host,IR}$ (6) | $c_{\rm SFR}$ (7) | SFR($M_\odot$/yr) (8) |
|---|---|---|---|---|---|---|---|
| SDSS J160254.18+422822.9 | 6.07 | 19.9 | 2.62 | $\leq$3.25 | $\leq$0.32 | 0.68 | $\leq$1341 |
| SDSS J161425.13+464028.9 | 5.31 | 20.3 | 7.25 | $\leq$3.20 | $\leq$0.28 | 1.00 | $\leq$1729 |
| SDSS J162331.81+311200.5 | 6.25 | 20.1 | 1.46 | $\leq$2.59 | $\leq$0.43 | 0.99 | $\leq$2107 |
| SDSS J162626.50+275132.4 | 5.30 | 18.7 | 7.64 | 5.35 | 0.03 | 1.00 | 292 |
| SDSS J162629.19+285857.6 | 5.02 | 19.9 | 0.95 | $\leq$1.32 | $\leq$0.20 | 1.00 | $\leq$503 |
| SDSS J163033.90+401209.6 | 6.07 | 20.6 | 0.49 | $\leq$1.87 | $\leq$0.78 | 0.63 | $\leq$1752 |
| SDSS J165902.12+270935.1 | 5.32 | 18.8 | 11.12 | $\leq$3.76 | $\leq$0.21 | 1.00 | $\leq$1547 |
| SDSS J205406.49−000514.8 | 6.04 | 20.6 | 1.47 | 3.15 | 0.41 | 1.00 | 2501 |
| SDSS J211928.32+102906.6 | 5.18 | 20.6 | 1.49 | $\leq$1.40 | $\leq$0.32 | 1.00 | $\leq$857 |
| SDSS J222845.14−075755.2* | 5.14 | 20.2 | 6.81 | $\leq$1.34 | $\leq$0.62 | 1.00 | $\leq$1593 |
| WFS J2245+0024* | 5.17 | 21.8 | 2.38 | $\leq$2.15 | $\leq$0.89 | 1.00 | $\leq$3685 |
| SDSS J231546.57−002358.1 | 6.12 | 21.3 | 1.41 | $\leq$1.94 | $\leq$0.76 | 0.61 | $\leq$1741 |

Note. — Col. (1): Object name with a * is identified as a hot dust deficient (HDD) quasar; Col. (2): Redshift; Col. (3): Rest-frame 1450Å apparent magnitudes, or mag(1450Å); Col. (4): Reduced chi-square, as defined in 6.2.3; Col. (5): The integrated infrared luminosity (8-1000 $\mu$m) from the fitted two-component SED models; if there are no any detections with $\lambda_{\rm rest} < 10\mu$m, the derived AGN contribution is put as an upper limit; the host galaxy contribution is treated as an upper limit if there is no detection at $\lambda_{\rm rest} > 50\mu$m; Col. (6): Relative contribution of the galaxy component to $L_{\rm IR}$. Col. (7): Correction of the host IR luminosity for the derivation of SFR; Col. (8): Star formation rate estimated from the galaxy component luminosity, assuming the Haro 11 star formation law; a question mark indicates the quasar has a minimal host contribution in the IR, in which case the derived SFR is dubious and not used in the analysis.

We also searched for other $z \gtrsim 5.0$ quasars with rest-frame far-IR observations in the literature and found 33 more quasars not included in Leipski et al. (2014) (hereafter *sample B*). The majority of them have been listed in Calura et al. (2014), except for RD J0301+0020 and TN J0924-2201. We collected all available observations on dust continuum as well as the UV/optical continuum (Bertoldi & Cox, 2002; Petric et al., 2003; Wang et al., 2008b, 2011b,c, 2013; Omont et al., 2013; Willott et al., 2013, 2015; Barnett et al., 2015). Because of the lack of constraints on the near-IR and mid-IR bands, we did not make full fits as for the cases in *sample-A*, but scaled the templates to some specific data points. For the AGN component, considering the potential extinction effect and possible lack of hot dust emission (to be discussed in Section 6.5), we scale the template to the data point at $\lambda_{\rm rest} = 0.1450 - 1.0\mu$m, which yields a maximum AGN luminosity. For the host component, we scale the Haro 11 template to the data point at $\lambda_{\rm rest} > 50\mu$m, which yields a minimum IR luminosity. Then we calculated their total infrared luminosities, the fraction of host contribution, and star formation rates, as summarized in Table 6.4. Compared with *sample-A*, *sample-B* contains less-luminous quasars (mainly contributed by the

Table 6.4. SED decomposition results for $z \gtrsim 5.0$ 33 quasars (*sample-B*)

| Source (1) | $z$ (2) | $m_{1450\text{Å}}$ (3) | $L_{\rm IR}(10^{13}L_{\odot})$ (4) | $f_{\rm host,IR}$ (5) | SFR($M_{\odot}$/yr) (6) |
|---|---|---|---|---|---|
| SDSS J003311.40-012524.9 | 6.13 | 21.53 | 0.81 | 0.69 | 1079 |
| CFHQS J005006+344522 | 6.25 | 19.84 | $\leq$ 2.99 | $\leq$0.46 | $\leq$2643 |
| CFHQS J005502+014618 | 6.02 | 21.82 | 0.28 | 0.33 | 179 |
| CFHQS J010250-021809 | 5.95 | 22.02 | $\leq$ 1.27 | $\leq$0.88 | $\leq$2141 |
| SDSS J012958.51-003539.7 | 5.78 | 22.28 | 1.16 | 0.90 | 2013 |
| CFHQS J013603+022605 | 6.21 | 22.04 | $\leq$ 3.09 | $\leq$0.65 | $\leq$3852 |
| CFHQS J021013-045620 | 6.44 | 22.25 | 0.19 | 0.25 | 92 |
| CFHQS J021627-045534 | 6.01 | 24.15 | $\leq$ 1.11 | $\leq$0.98 | $\leq$2082 |
| CFHQS J022122-080251 | 6.16 | 21.98 | $\leq$ 2.26 | $\leq$0.93 | $\leq$4016 |
| CFHQS J022743-060530 | 6.20 | 21.41 | $\leq$ 1.08 | $\leq$0.73 | $\leq$1522 |
| SDSS J023930.24-004505.4 | 5.82 | 22.28 | $\leq$ 1.66 | $\leq$0.93 | $\leq$2945 |
| RD J0301+0020 | 5.50 | 23.40 | 0.52 | 0.91 | 906 |
| CFHQS J031649-134032 | 5.99 | 21.72 | $\leq$ 3.89 | $\leq$0.95 | $\leq$7077 |
| TN J0924-2201 | 5.20 | – | $\leq$ 1.04 | $\leq$0.84 | $\leq$1659.35 |
| CFHQS J105928-090620 | 5.92 | 20.75 | $\leq$ 2.06 | $\leq$0.60 | $\leq$2377 |
| ULAS J1120+0641 | 7.08 | – | 0.42 | 0.63 | 513 |
| ULAS J131911.29+095051.4 | 6.13 | 19.65 | 3.47 | 0.59 | 3927 |
| SDSS J142516.30+325409.0 | 5.85 | 20.62 | $\leq$ 1.89 | $\leq$0.50 | $\leq$1810 |
| CFHQS J142952+544717 | 6.21 | 20.59 | 2.68 | 0.63 | 3246 |
| SDSS J150941.78-174926.8 | 6.12 | 19.63 | $\leq$ 2.52 | $\leq$0.43 | $\leq$2057 |
| SDSS J162100.70+515544.8 | 5.71 | 19.89 | $\leq$ 4.21 | $\leq$0.18 | $\leq$1438 |
| SDSS J164121.64+375520.5 | 6.04 | 21.19 | $\leq$ 1.17 | $\leq$0.71 | $\leq$1603 |
| SDSS J205321.77+004706.8 | 5.92 | 21.20 | $\leq$ 1.34 | $\leq$0.76 | $\leq$1946 |
| CFHQS J210054-171522 | 6.09 | 21.37 | $\leq$ 3.46 | $\leq$0.24 | $\leq$1604 |
| SDSS J214755.40+010755.0 | 5.81 | 21.65 | $\leq$ 1.44 | $\leq$0.65 | $\leq$1782 |
| CFHQS J222901+145709 | 6.15 | 21.90 | 0.19 | 0.06 | 22 |
| CFHQS J224237+033421 | 5.88 | 22.09 | $\leq$ 1.48 | $\leq$0.90 | $\leq$2561 |
| SDSS J230735.35+003149.4 | 5.87 | 21.73 | $\leq$ 1.68 | $\leq$0.45 | $\leq$1460 |
| SDSS J231038.88+185519.7 | 6.00 | 19.30 | 6.07 | 0.69 | 7996 |
| CFHQS J231802-024634 | 6.05 | 21.55 | $\leq$ 1.38 | $\leq$0.82 | $\leq$2178 |
| SDSS J232908.28-030158.8 | 6.43 | 21.53 | $\leq$ 1.38 | $\leq$0.00 | $\leq$ 0.0(?) |
| CFHQS J232914-040324 | 5.90 | 21.96 | $\leq$ 1.14 | $\leq$0.86 | $\leq$1886 |
| SDSS J235651.58+002333.3 | 6.00 | 21.77 | $\leq$ 1.06 | $\leq$0.81 | $\leq$1653 |

Note. — Col. (1): Quasar name; Col. (2): Redshift; Col. (3): Rest-frame 1450Å AB apparent magnitudes, or mag(1450Å); Col. (4): The integrated infrared luminosity (8-1000 $\mu$m) from the fit two-component SED models; if there is no detection with $\lambda_{\rm rest} < 10\mu$m, the derived AGN contribution is put as an upper limit; the host contribution is treated as an upper limit if the quasar is not detected at $\lambda_{\rm rest} > 50\mu$m; Col. (5): Relative contribution of the galaxy component to $L_{\rm IR}$; Col. (6): Star formation rate estimated from the galaxy component luminosity, assuming the Haro 11 star formation law; a question mark indicates the quasar has a minimal host contribution in the IR, in which case the derived SFR is dubious and not used in the analysis.

Canada-France High-z Quasar Survey, see Omont et al. 2013 and references therein), and consists almost entirely of quasars at $z > 5.7$.

In the following discussion, we will mainly focus on *sample-A*, whose data points are more uniformly collected and have the same detection limits. We will discuss *sample-B* only as a complement to conclusions based on *sample-A*.

## 6.5 Discussion

### 6.5.1 Heating Sources for the Infrared Energy Output

To study the host galaxies of high-$z$ quasars from infrared SEDs, the heating sources of the infrared-emitting dust and the contribution from the host star formation should be examined first. Previously, a number of papers made the assumption that the heating process for the FIR-emitting warm dust is dominated by host star formation (e.g., Leipski et al., 2014), or assumed some conservative fraction of host star formation heating (e.g., Wang et al., 2011c). From a theoretical point of view, Li et al. (2008b) and Schneider et al. (2015) studied the heating of the observed SED of J1148+5251, an archetypal high-luminosity high-redshift quasar. They argued that the heating of the dust in the host galaxy could be dominated by processes related to the central engine, rather than the host star formation. This field is quite controversial.

As shown in Figure 6.6, the AGN template from Xu et al. (2015b) is not sufficient to reproduce the far-IR SED of many $z \gtrsim 5$ quasars with rest-frame far-IR detections. To investigate the average infrared properties of these quasars, we fit the three stacked SEDs in Leipski et al. (2014), shown in Figure 6.4. For the FIR-detected SED (from objects detected at least three *Herschel* bands), we can see a clear contribution in the far-IR from the host galaxy. For the partly detected SED (from objects with significant PACS 100 $\mu$m and/or 160$\mu$m flux), the AGN template alone is enough to reproduce the SED. For the objects without any *Herschel* detections, there are some HDD quasars with SEDs deviating from normal AGNs, as indicated by the low ratio of rest 24 $\mu$m to optical. The stacked SEDs for the 14 partly *Herschel* detected and the 33 non-detected systems show no evidence for significant far-IR output over that of typical quasar templates. It would be difficult to understand why just 10 of this sample had strong heating of the host galaxy ISM by the quasar. A plausible explanation is that these 10 *Herschel*-detected systems have high levels of star formation, while for the other quasars the star formation is weak.

At very high redshift, cosmic microwave background (CMB) is also a source for dust heating (da Cunha et al., 2013). However, since the dust temperatures in high-$z$ quasar host galaxies are typically $\sim$ 35-50K (e.g., Xu et al. 2015b; Leipski et al. 2014), at least

Table 6.5. SED decomposition results for the stacked quasar SEDs

| Source (1) | N (2) | Redshift (3) | $L_{IR}/10^{13}L_{\odot}$ (4) | $f_{host,IR}$ (5) | $\chi^2_\nu$ (6) | SFR($M_{\odot}$/yr) (7) |
|---|---|---|---|---|---|---|
| FIR-detected | 10 | 5.34 | 4.08 | 0.47 | 0.63 | 3666 |
| partly-detected | 14 | 5.31 | 2.04 | 0.00 | 0.20 | $\lesssim 1.5$ (?) |
| non-detected | 33 | 5.20 | 0.87 | 0.00 | 0.61 | $\sim 0$ (?) |

Note. — Results of full IR fits. Upper-limit data points are included in the evaluation process.
Col. (1): Type of stacked SED; Col. (2): The number of stacked quasars; Col. (3): Average redshift; Col. (4): The total infrared luminosity (8-1000 $\mu$m) estimated from the "Haro 11 + AGN" two-component SED fit; Col. (5): The fraction of luminosity of host template contribution to the whole fit SED, based on result from the "Haro 11 + AGN" decomposition; Col. (6): Reduced chi-square from the "Haro 11 + AGN" decomposition; Col. (7): Estimation of the star formation rate.

twice the CMB temperature for the relevant redshift range ($T_{\rm CMB} \sim 18$K at $z \sim 5.5$), a correction is not significant compared with the other uncertainties in our derivations.

### 6.5.2 Are AGN Host Galaxies at $z \gtrsim 5$ Low-metallicity?

For quasars at $z \sim 1-6$, emission line ratios are found to trace (super-)solar gas metallicities (up to $\sim 10 Z_{\odot}$) in broad line regions (BLRs) without any strong indication of redshift evolution (Nagao et al., 2006, 2012; Jiang et al., 2007; Juarez et al., 2009). However, the mass of the BLRs is small ($10^2 - 10^4 M_{\odot}$), and might not be representative of the overall formation history of the galaxy. Wang et al. (2010a, 2011a) showed that the star formation can be enhanced in the accretion flow of the AGN, possibly resulting in locally increased metallicity. The narrow-line regions (NLRs) of quasars at $z \sim 1-4$ are also found to be around solar-metallicity without strong evolution (Matsuoka et al., 2009). In contrast with the BLRs, the typical size of the NLRs ($\sim 10^{1-4}$ pc, Bennert et al. 2006b,a) is comparable to the size of the host galaxies. The only quasar beyond $z \gtrsim 5$ with a NLR metallicity constraint is TN J0924−2201, a type-2 radio galaxy at $z = 5.19$ (Matsuoka et al., 2011).

Considering the small sample size and uncertainty of the metallicity calibration, the result for TN J0924−2201 does not provide much knowledge of the metallicity in the $z \gtrsim 5$ quasars. We do not have observational constraints on the metallicity of these quasar hosts from emission line analysis.

Another possible approach to get metallicity constraints on (or near) distant quasar hosts is from analyzing the absorbers with high H I content ($N_{\rm H\,I} \gtrsim 10^{20}{\rm cm}^{-2}$), or so-called damped Lyman-alpha (DLA) systems, at the redshift of the quasar (Hennawi et al., 2009; Zafar et al., 2011). Hennawi et al. (2009) reported the discovery of a bright Lyman-$\alpha$ blob associated with the $z = 3$ quasar SDSS J124020.91+145535.6 and gave a lower limit to the gas metallicity $Z \gtrsim 1/10 Z_{\odot}$. Zafar et al. (2011) studied a physical quasar pair Q0151+048 ($z \sim 1.9$) and suggested an overall metallicity of $0.01\,Z_{\odot}$ for a DLA associated with one member. The redshifts of these two quasars are relatively low. It is also not clear if they are representative of the general population. As argued by Finley et al. (2013), statistical study shows the absorption of the associated DLAs is more likely to happen in the galaxies neighboring the quasar, rather than in the AGN host galaxy. Further detailed studies on larger samples are needed to make any conclusive argument.

Several works argued that some massive galaxies at high-$z$ have solar metallicity (e.g., Maiolino et al., 2008; Mannucci et al., 2009; Rawle et al., 2014). It is possible that these objects are mature and highly evolved. However, we should be cautious about the derived metallicity with very limited data points for individual sources. Convincing measurements of metallicity at high-$z$ require more understanding of the ISM in these systems. For $2.0 < z < 2.5$ galaxies, statistical studies based on multiple metallicity tracers show that their metallicities drop at large masses (Maier et al., 2014; Cullen et al., 2014). For the very early Universe, simulations suggest population III stars contribute little to the chemical enrichment of the ISM (Valiante et al., 2009). The existence of a huge population of low-metallicity systems between the cosmic reionization and $z > 2.5$ should be expected. Since high-$z$ quasars are originally identified by their AGN features, the properties of their host galaxies should not be much biased by the selection. It is therefore plausible that the high-$z$ quasar host galaxies have metallicities moderately, if not substantially, below solar.

In this work, hints for the low-metallicity of the AGN host galaxies at $z \gtrsim 5$ are from

the successful reproduction of the observed SEDs based on two-component fits, as shown in Section 6.3.3. The high dust temperature and boosted mid-IR emission are two major features of the IR SED of Haro 11, a dwarf galaxy with metallicity $Z \sim 1/3 Z_{\odot}$. For the IR SED of these quasars, the low-metallicity Haro 11 template works significantly better than the normal SF templates.

Xu et al. (2015b) discovered a warm mid-IR component of some type-1 quasars at $z \sim 0.7 - 2.5$, which can not be reproduced by the combination of the AGN template and normal SF template. This warm excess is found to be more prominent at higher redshifts in their sample. As shown in Section 6.3.3, a strong mid-IR SED excess also does exist when fitting the host galaxy with normal SF templates for the $z \gtrsim 5$ quasars. In contrast, by introducing the Haro 11 template, the mid-IR part of the SED of the $z \gtrsim 5.0$ quasars is reproduced better: there is no strong hint of the warm excess for the majority of the quasars. The low-metallicity of the host galaxy is a possible explanation for many such warm excesses at high-$z$: the dust population in the low-metallicity environment tends to be dominated by small-size grains, which would result in substantial emission in the mid-infrared. Due to the increase of the mid-IR emission, the effective dust temperature fit from the whole infrared SED is also boosted. Nonetheless, a small number of $z \gtrsim 5$ quasars still show a mid-IR warm excess, such as J0338+0021 and J1602+4228, even with the Haro 11 template fitting. We suggest that such additional warm excess not reproduced by the "Haro 11 + AGN" SED model could be due to an extreme circumnuclear starburst or that the host galaxy has a much lower metallicity.

### 6.5.3 The Star Formation Rates of Quasars at $z \gtrsim 5$

In estimating a SFR, the largest uncertainty comes from the assumed star formation calibration. In Appendix I, the star formation determination for the low-metallicity dwarf galaxies is discussed. We show that the Kennicutt (1998) IR star formation law is still valid to roughly estimate the obscured star formation rates for the low-metallicity dwarf galaxies, including Haro 11. Besides the obscured star formation, we also consider the unobscured star formation as revealed by the UV emission. As shown in Appendix I.1.1, Haro 11 has a low UV star formation rate estimate, which is only $\sim$10% of that deduced from the

far-IR. For a $2000\,M_\odot$/yr infrared SFR, the corresponding UV SFR would be $200\,M_\odot$/yr, consistent with the upper limit given for the archetypal $z\sim6$ quasar J1148+5251 (Mechtley et al., 2012). The UV star formation of high-luminosity quasar host galaxies at $z\sim2.6$ is also found to be quite weak (Cai et al., 2014). These examples indicate that a low contribution to the estimated SFR from the UV is appropriate for quasar host galaxies identical to those for J1148+5251 and the Cai et al. (2014) quasar sample. However, we can not rule out the possibility that some of the host galaxies at the epoch of reionization have larger escape fractions than Haro 11 and hence a large fraction of UV emission, causing us to underestimate their total SFRs.

Many censored data points also make the SFR estimation difficult. For the quasars with at least two detections in the far-IR, the host galaxies are reasonably well fit. The derived star formation rates are on the order of $10^3\,M_\odot$/yr, a typical value also found by other authors (e.g., Wang et al., 2008b; Leipski et al., 2014). For quasars without any far-IR detections, we could only determine the upper-limits of their SFRs. As described in Section 6.2.3, we consider all the censored data points during the fitting process. For sources without far-IR detections, the fitted upper limits on the SFRs are based on templates constrained by multiple 3-$\sigma$ non-detections and result in overestimated SFR constraints. To solve this problem, we scale the host template to each non-detected $3\sigma$-limit observation, derive the respective SFR, and pick the lowest one as the final constraint on the quasar host SFR. During this process, the contribution of the fitted AGN component is fixed and subtracted when deriving the SFR.

For the HDD quasars, the AGN template fails at $\lambda\gtrsim1.0\mu$m. In addition, none of them are detected in the far-IR. To derive conservative upper limits for their SFRs, we assume that all their far-IR emission comes from the host galaxy. Consequently, we ignore the fitted AGN component when we scale the host template to the observations.

We ignore the results for J0017−1000 and J1443+3623 of *sample-A*, whose host contribution is too minimal to be evaluated. From Kaplan-Meier analysis[4], the mean infrared host galaxy luminosity of the *sample-A* is

$$\langle\log(L_{\rm SF,IR}/L_\odot)\rangle = 12.51\pm0.10\,, \qquad \text{(sample A)}$$

[4] As implemented in the Astronomy Survival Analysis Package (ASURV, Lavalley et al. 1992)

which corresponds to an average star formation rate

$$\langle \mathrm{SFR} \rangle = 621^{+161}_{-128} M_{\odot}/\mathrm{yr} \, . \qquad \text{(sample A)}$$

Another approach to compute the average star formation rate is to analyze the stacked SEDs. As shown in Figure 6.4 and Table 6.5, the fraction of the host contribution is too small to give any physical constraints on the SFR of the stacked SEDs of *Herschel* partly- and non-detected quasars. We simply conclude substantial star formation only happens in the *Herschel* FIR-detected stacked SED, whereas the star formation in other stacked SEDs is minimal and set to be zero. Then an arithmetic mean of *sample-A* is

$$\langle \mathrm{SFR} \rangle = 643 M_{\odot}/\mathrm{yr} \, . \qquad \text{(A-stacked)}$$

This result is almost the same as that from the Kaplan-Meier analysis for individual sources, confirming the validity of the result from the Kaplan-Meier estimator.

For *sample-B*, after rejecting SDSS J2329-0301 due to its minimal host contribution, we use the Kaplan-Meier approach to derive a mean infrared luminosity for 32 quasars

$$\langle \log(L_{\mathrm{SF,IR}}/L_{\odot}) \rangle = 12.27 \pm 0.22 \, , \qquad \text{(sample B)}$$

which corresponds to an average star formation rate

$$\langle \mathrm{SFR} \rangle = 357^{+236}_{-142} M_{\odot}/\mathrm{yr} \, . \qquad \text{(sample B)}$$

This estimate is subject to systematic errors because the majority of the *sample-B* members only have submillimeter measurements at 1.2 mm, and these fall well beyond the peaks of their far-IR SEDs. Therefore, any deviation of the SED from the template will result in significant errors in the estimate of infrared luminosity. Nonetheless, within the errors, this $\langle \mathrm{SFR} \rangle$ is similar to that from *sample-A*. In fact, we will show in Section 6.5.5 that the indicated slightly lower SFRs for *sample-B* is as might be expected from the generally lower luminosities of their AGNs.

We believe that the average SFR estimated above is robust even if Haro 11 is not representative for some quasar host galaxies. As shown in Section 6.3.1, the results from the Haro 11 template are not substantially different from the normal SF templates

in Rieke et al. (2009). In fact, the AGN template is principally fixed by data points at $\sim 1-5$ $\mu$m, leaving the SF template to be matched to the mid-IR to far-IR SED. The large range between the maximum star formation rates and the averages suggests that star formation is very "bursty" in the host galaxies, and that the averages can be considered to represent the rates integrated over time. These issues are discussed in Section 6.5.5.

### 6.5.4 AGN Luminosity

The total AGN luminosity can be estimated from integrating the Elvis template (e.g., Hao et al. 2014, Xu et al. 2015b. Since our fits are limited to the infrared (1-1000 $\mu$m), the total AGN luminosity can be derived by scaling an infrared-to-bolometric correction of 5.28 (Xu et al., 2015b) to the AGN total infrared luminosity $L_{\rm IR,AGN}$[5]. Before that, we check the validity of the Elvis template in the UV/optical bands. As shown in Figure 6.4, the Elvis et al. (1994) template reproduces the UV to mid-IR stacked SED of these quasars well. For individual sources, although there are some detailed offsets, the Elvis template generally matches the observations. The monochromatic flux at rest frame 1450Å is a frequently used indicator of AGN UV continuum brightness in the literature. By applying a scaling factor of 4.65[6] on the $\nu L_\nu$(1450Å), the AGN bolometric luminosity can be estimated. Taking mag(1450Å) in the literature as a crude but independent tracer of AGN bolometric luminosity, in Figure 6.7, we plot the mag(1450Å)-based AGN bolometric luminosities against the $L_{FIR}$-based ones. There is a small offset from 1:1 on the correlation between the AGN luminosities from mag(1450Å) and from the infrared bolometric correction, which can be explained by possible UV extinction. In summary, though the normalization of the AGN template is constrained by the rest-frame near-IR to mid-IR data points, the residuals of observed UV/optical SEDs from the IR fit to the Elvis template are generally small.

Leipski et al. (2014) pointed out 11 quasars with a dearth of very hot dust. We confirm their peculiarity by comparing their observed SEDs with the Elvis template. If normalized at UV/optical wavelengths, the Elvis template clearly overestimates the observed SED

[5]For quasars with $L_{\rm IR}$ upper limits in Table 6.3, we can still get their AGN total infrared luminosities: $L_{\rm IR,AGN} = L_{\rm IR}(1-f_{\rm host,IR})$, where $f_{\rm host,IR}$ is the host galaxy contribution upper limit.

[6]This value is derived based on the Richards et al. (2006) template.

beyond rest frame 1 $\mu$m. Since we do not have a clear picture of the full wavelength SED of these HDD objects, their luminosities are hard to derive. We still rely on the $L_{\rm FIR}$-based luminosity, rather than UV-based luminosity, for two reasons: (1) the UV-optical SED could suffer extinction, thus underestimating the total bolometric luminosity; (2) the UV emission is not isotropic while the sources are optically thin in the near- and mid-IR (Marconi et al., 2004). Judging by the UV/optical observation, we do not expect the template-derived luminosity has more than one order of magnitude deviation from the observed one. In Figure 6.7, it is interesting to note the HDD quasars in this work generally follow the same trend as normal quasars.

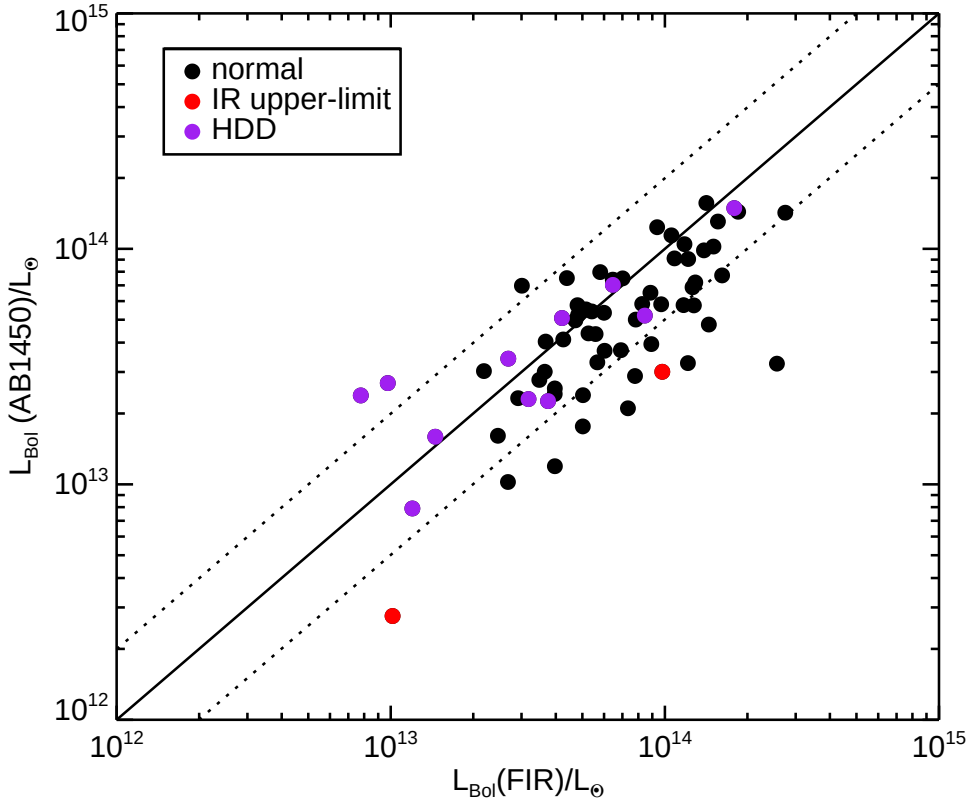


Figure 6.7 Comparison of AGN luminosities derived from mag(1450Å) and infrared SED fits. 0.3 dex offsets are shown as dotted lines. Purple dots are for the 11 HDD quasars, red dots for two quasars with upper-limit of $L_{\rm AGN,IR}$, black dots for other quasars.

Finally, we can derive the average AGN bolometric luminosity of *sample-A* with stan-

dard error to be:

$$\langle L_{\rm AGN}\rangle = 5.287 \times \langle L_{\rm AGN,IR}\rangle \approx (7.48 \pm 0.62) \times 10^{13} L_{\odot}\ . \qquad \text{(sample A)}$$

Similarly, *sample-B* has

$$\langle L_{\rm AGN}\rangle \approx (2.63 \pm 0.14) \times 10^{13} L_{\odot}\ . \qquad \text{(sample B)}$$

This value is $\sim 36\%$ of *sample-A*

### 6.5.5 Implications for BH-galaxy Evolution

We now compare the relative strength between SF activities and AGN luminosities of $z \gtrsim 5$ quasars with that of relatively low-$z$ and intermediate-$z$ quasars. In Figure 6.8, we put the average values for $z \gtrsim 5$ quasars on the relation between SF IR luminosity, $L_{\rm SF,IR}$, and AGN luminosity, $L_{\rm AGN}$, for the Xu et al. (2015b) type-1 quasar sample. The average properties of the $z \gtrsim 5$ quasars fall along the fit relation. This is unexpected, however, since quasars at $z \gtrsim 5$ and those at $z < 3$ should be in different star formation phases. From a theoretical perspective, there should be no star formation main sequence as is the case in the $z < 3$ Universe, but bursts of star formation and periods of near-zero star formation rates, likely due to the dynamically disturbed gas within the galaxy halo (e.g., Muratov et al., 2015). Current observations suggest the star formation in some $z > 5$ quasars is extremely vigorous with SFRs at levels of $\gtrsim 10^3\ M_{\odot}$/yr (e.g., Wang et al., 2008b) or relatively mild with SFRs $\lesssim 50\ M_{\odot}$/yr (e.g., Willott et al., 2013). Despite this large dispersion, an underlying relation between the average host star formation and AGN luminosity, which has been suggested for very luminous AGNs at $z \lesssim 2.5$ (e.g., Netzer, 2009; Rosario et al., 2012), seems to already exist at $z \sim 5-6$.

By taking an average of the star formation rates of quasar host galaxies in the largest sample at $z \sim 5-7$, we can retrieve a rough time-averaged star formation rate during the lifetime of these quasar host galaxies. In other words, we assume that the relative number of host galaxies with very active star formation (SFR$\sim 10^3\ M_{\odot}$/yr) to those without significant star formation (SFR$\lesssim 10\ M_{\odot}$/yr) reflects the relative time duration of the star-bursting phase to the quiescent phase of the galaxies. Since stars lose mass quickly

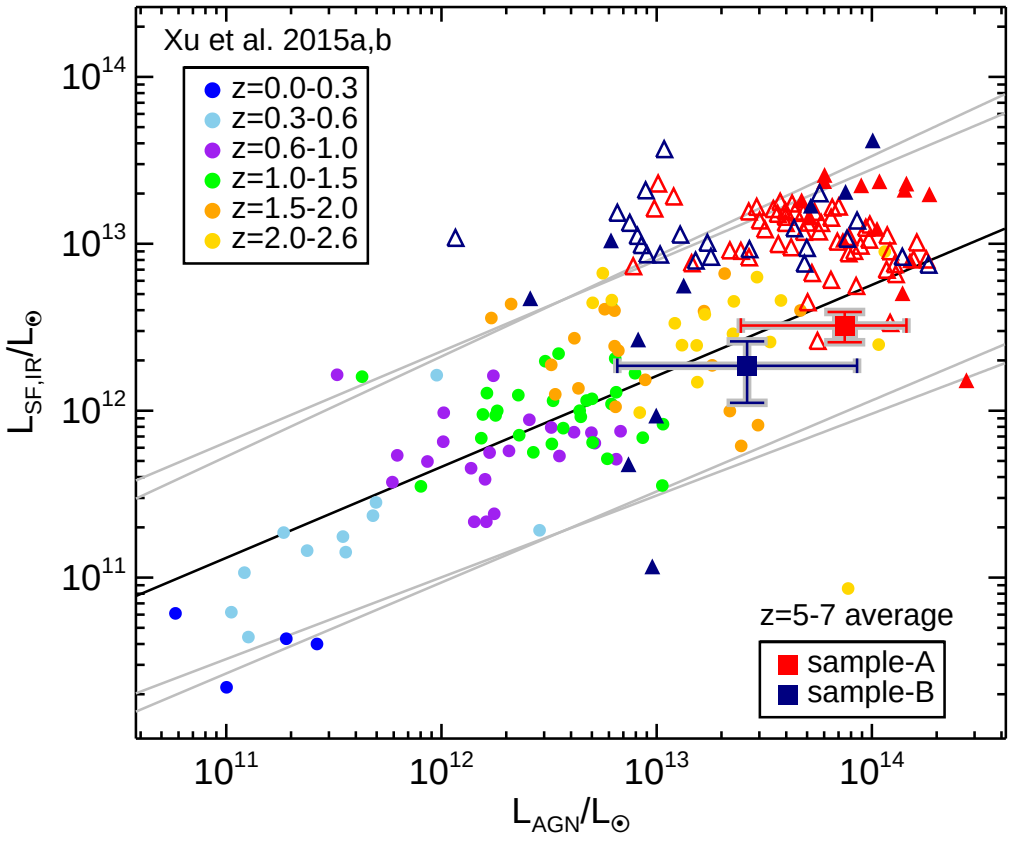


Figure 6.8 The IR luminosity of the star-formation component $L_{\rm SF,IR}$ versus the total AGN luminosity $L_{\rm AGN}$ for quasars at different redshifts. Only type-1 AGNs in Xu et al. (2015b) are plotted (small dots). The solid back line is the best-fit unweighted relationship for all type-1 AGN in Xu et al. (2015b) with a slope of 0.55, with shifted relation by 1-$\sigma$ error of either slope or intercept shown as grey solid lines. Our measurements for individual $z \gtrsim 5$ quasars are also shown as red (*sample-A*) and blue (*sample-B*) triangles, with filled for detections and open for upper-limits. We also plot the Kaplan-Meier mean of $z \gtrsim 5$ AGN host galaxy IR luminosities at mean AGN luminosities for *sample-A* (red square) and *sample-B* (blue square), with horizontal error bars showing the range including 80% of the sample's sources.

after leaving the main sequence, we can ignore their contribution to the stellar mass of the galaxy. The main sequence lifetime of a star with mass $M$ is

$$\tau_{\rm MS} = 10 \times (M/M_\odot)^{-2.5} \ \ {\rm Gyr} \ . \tag{6.5.1}$$

Then we have a simple model relating the stellar mass $M_*$ to the galaxy growth time $\Delta t$

and the initial mass function $\xi(m)$ as:

$$\langle M_* \rangle \sim \int_0^{\Delta t} \int_{M_{\rm low}}^{M_\odot (t/10)^{-0.4}} \xi(m) \langle {\rm SFR} \rangle {\rm d}m{\rm d}t \ , \tag{6.5.2}$$

where $M_{\rm low}$ is the minimum stellar mass, which is assumed to be $0.1\,M_\odot$; $M_\odot (t/10)^{-0.4}$ is the maximum stellar mass of stars that are still on the main sequence at time $t$ (unit: Gyr); $\Delta t$ is the epoch of galaxy mass assembly.

To start, we simply assume a standard Salpeter IMF (Salpeter, 1955), and estimate the increase in host galaxy stellar mass since the start of the cosmic reionization, i.e., $z = 8.8^{+1.7}_{-1.4}$ (Planck Collaboration et al., 2015), corresponding to a Universe age $0.573^{-0.122}_{+0.150}$ Gyr. Then the time duration $\Delta t$ from reionization to the average age of the quasars in our sample ($\langle z \rangle$=5.5) is $\Delta t = 0.489^{+0.122}_{-0.150}$ Gyr. Taking the average star formation rate for *sample-A* and solving the integration in Equation 6.5.2, we derive the stellar mass that could form in a $z \sim 5.5$ quasar to be

$$\langle M_* \rangle \approx 3.0^{+0.7}_{-0.9} \times 10^{11}\,M_\odot \ . \tag{6.5.3}$$

This rough estimate is not highly sensitive to the starting redshift, nor to the form of the standard IMF (see Table 6.6). For example, if we assume a start at $z = 20$, the total stellar mass increases by less than a factor of two. We can also change the power-law Salpeter IMF to a more realistic Kroupa & Weidner (2003) IMF with a turnover below $\sim 1\ M_\odot$ and use the updated IR star formation calibration in Kennicutt & Evans (2012). The derived $M_*$ is lower by up to 10%. As a result, we estimate that the SFRs we deduce for the host galaxies are likely to result in formation of a net mass $(3-5) \times 10^{11} M_\odot$ during the major assembly phases for these quasar host galaxies. Although this result was derived for *sample-A*, the high average SFR also exhibited for *sample-B* indicates it is generally true for high-redshift quasars.

We compare this mass with typical masses for the central black holes in these galaxies, $\sim 10^8 - 10^9\ M_\odot$ (e.g., Jiang et al. 2007; Kurk et al. 2007, 2009; Willott et al. 2010a; De Rosa et al. 2011; Jun et al. 2015). It appears that the formation of stellar mass is adequate to establish $M_{\rm BH}/M_{*,total}$ at 0.1 - 1%, which is in good agreement with estimates of this parameter locally (e.g., Kormendy & Ho 2013 and references therein), and with the

Table 6.6. Estimation of a typical host galaxy mass

| IMF | SFR $(M_\odot/\mathrm{yr})^a$ | $M_*$ $(M_\odot)^b$ $z_0 = 8.8$ | $M_*$ $(M_\odot)^b$ $z_0 = 20$ |
|---|---|---|---|
| Salpeter | 621 | $3.02 \times 10^{11}$ | $5.42 \times 10^{11}$ |
| Kroupa | 534[c] | $3.00 \times 10^{11}$ | $4.80 \times 10^{11}$ |

Note. — [a] Values derived from *sample-A*; [b] Stellar masses derived based on Equation 6.5.2, $z_0$ is the redshift when the first galaxies begin to assembly their masses; [c] Kennicutt & Evans (2012) updated their original IR star formation calibration (Kennicutt, 1998) with the Kroupa & Weidner (2003) IMF. The SFR should be reduced to ∼86%.

evidence at $z \lesssim 2$ that the ratio does not evolve substantially with redshift. If some of the $z \gtrsim 5$ host galaxies have a larger escape fraction than Haro 11 and hence their SFRs are under-represented by our approach, this conclusion is strengthened. Our conclusion agrees with the measurement of the dynamical masses of these systems (Willott et al., 2015) that also indicates very little evolution of this ratio with redshift up to z∼6.

## 6.6 Summary

In this work, we describe an effective strategy to analyze the infrared output of high-$z$ quasars. A two-component SED model to quantify and distinguish star formation and nuclear activity is proposed: the host galaxy component can be represented by the SED of Haro 11, a low-metallicity dwarf galaxy with extreme compact star-forming regions; the AGN component can be represented by the Elvis et al. (1994) AGN template with the IR star formation contribution subtracted. Such a simple model can help us have a better idea of the AGN and star formation contribution for these high-$z$ objects when only limited observations are available. Using this method, we have analyzed the AGN contribution and host galaxy contribution to the infrared SEDs of 69 quasars with *Herschel* observations in

Leipski et al. (2014) and another 33 quasars in the literature. Our major conclusions are as follows:

1. Haro 11 is a faithful representation for the host galaxies of $z \gtrsim 5$ quasars. Besides its moderately low-metallicity, Haro 11 has a very high star formation surface density, which is common for high-redshift galaxies as well as quasar hosts.

2. The AGN contribution to the UV-to-IR SEDs of $z \gtrsim 5$ quasars can be well-represented by the Elvis et al. (1994) AGN template with the star formation contribution to the IR subtracted. For the infrared, except for the HDD quasars, there is no detectable over-prediction of the observed flux from the modified AGN template. After subtracting the AGN contribution in the IR, the residual flux can be interpreted as the IR contribution from host galaxy star formation, which is well-fit by the Haro 11 template.

3. The warm excess found for some high-$z$ quasars (see, e.g., Xu et al. 2015b) can be produced by the introduction of the Haro 11 template, suggesting this feature may reflect the low-metallicity of the quasar host. The Haro 11 template also shares the high dust temperature found in the far-IR measurements of high-$z$ quasars. That is, these two features can be explained by the dust properties and distribution in the low-metallicity environment.

4. The average SFR of the $z \sim 5-6.5$ quasars observed by *Herschel* is $\sim 620 M_{\odot}/\mathrm{yr}$, considering both far-IR detected and non-detected observations.

5. For the overall population of $z \gtrsim 5$ quasars, the total AGN luminosity $\langle L_{\mathrm{AGN}} \rangle$ and average infrared luminosity from star formation $\langle L_{\mathrm{SF,IR}} \rangle$ fall along the relation defined by $z < 2.6$ quasars. This is unexpected since the star formation at $z \gtrsim 5$ and that at $z \lesssim 3$ should experience different phases (e.g., bursty vs. relatively steady).

6. Assuming the sample averaged SFR is a rough time-averaged SFR estimate during the lifetime of the quasar host galaxies, we found the $z \sim 5-6$ quasar host galaxies could form $\sim (3-5) \times 10^{11} M_{\odot}$ of stars. With the black hole mass measurements of these quasars, such massive host galaxies make possible a local BH-galaxy mass relation $M_{\mathrm{BH}}/M_{*} \sim 0.1-1\%$ at $z \sim 6$, suggesting there may not be strong redshift evolution of the BH-galaxy mass ratio.

We are grateful to the referee for comments and suggestions that improved the clarity of this paper. We thank Eiichi Egami, Richard Green, Daniel Stark and Xiaohui Fan for helpful suggestions. This work was supported by NASA grants NNX13AD82G and 1255094. This publication has made use of data products from the *Wide-field Infrared Survey Explorer*, which is a joint project of the University of California, Los Angeles, and the Jet Propulsion Laboratory/California Institute of Technology, funded by the National Aeronautics and Space Administration. This research has also benefited from the use of the NASA/IPAC Extragalactic Database (NED) which is operated by the Jet Propulsion Laboratory, California Institute of Technology, under contract with the National Aeronautics and Space Administration.

# CHAPTER 7
# SUMMARY AND OUTLOOK

## 7.1 Summary of Key Results

In this thesis, I present a comprehensive investigation of the IR emission of Type-1 AGNs from $z \sim 0$ to $z \sim 6$, aiming to infer the physical reasons behind the IR SED variations and to obtain insights into the AGN dusty environment.

The key conclusions are summarized in the following five sentences:

- **The existence of circumnuclear torus-like dust is common for type-1 AGNs over a range of 10,000 in luminosity and $z \sim 0$–6, and they have intrinsic IR SED variations that might be a reflection of different torus structures linked with AGN properties;**

  In Chapter 2, we have demonstrated the quasar intrinsic SEDs have similar variations that can be grouped into HDD, WDD and normal types from $z \sim 0$ to $z \sim 6$. By adding polar dust obscuration of these intrinsic SED templates, Chapter 4 has successfully explained the SED variations of other type-1 AGN populations at different redshifts, indicating their intrinsic IR emission could be similar. The dust reverberation mapping study in Chapter 5 has demonstrated similar dust lag vs AGN luminosity relations for both quasars and Seyfert-1 nuclei, strongly supporting the existence of tori over a wide luminosity range. We have provided evidence that the appearance of WDD and HDD SEDs could be related to higher AGN luminosity and lower Eddington ratio, respectively, and propose their SED behaviors can be reflected by a change of torus structures in Chapter 2. The different structures among WDD, HDD and normal quasars are tentatively supported with the geometry constraints from the dust reverberation analysis in Chapter 5;

- **Besides the relatively compact torus, AGN-heated polar dust emission extends to 0.1–1 kpc scales exists in some type-1 AGNs and contributes significantly to**

**most of their SED variations; the behavior of this component is likely controlled by feedback from AGN and/or host galaxy;**

Chapter 4 has developed a semi-empirical SED model for reddened type-1 AGNs motivated by the recent discoveries of mid-IR polar dust. By simply changing the optical depth of the extended obscuring component, we were able to reproduce the properties of all three type-1 AGNs with polar dust constraints from mid-IR interferometry observations, demonstrating the validity of our assumptions on the behaviors of the polar dust. With this model, we have successfully reconciled the IR SED variations of type-1 AGNs at different redshifts and found the strong polar emission was frequently associated with evidence for AGN outflows (and also a turbulent host ISM for hot-dust obscured galaxies).

- **Regardless of luminosity and redshift, the IR SEDs of most type-1 AGNs can be reproduced with a simple two-free parameter model by changing the intrinsic AGN types and the integrated optical depth of the extended polar dust component;**

  Chapter 2 and Chapter 6 have demonstrated the lack of strong evolution on the AGN intrinsic IR SEDs of type-1 quasars at $z \sim$0–6. The success of the reddened type-1 AGN model in Chapter 4 has supported this argument.

- **Most, if not all, high-$z$ AGNs with claimed abnormal SED features have counterparts at $z \lesssim 0.1$, indicating that the AGN-heated dust environment is generally composed of the torus component ($\sim$1–10 pc) and the extended polar dust component ($\sim$0.1–1 kpc);**

  This conclusion is obtained by combining the results from Chapters 2, 4, 5 and 6.

- **In contrast with the non/little-cosmic-evolving nature of the AGN-heated emission, the quasar host galaxies at $z \gtrsim 5$ present a warm far-IR SED evolution compared to those at $z \lesssim 0.5$, which could be explained a cosmic evolution of the ISM properties in these systems.**

  Chapter 3 has investigated the intrinsic far-IR SED of type-1 quasars and suggested

the Elvis-like version with a minor modification is the best description. Chapter 2 has combined such AGN intrinsic far-IR template with empirical templates of normal star-forming galaxies to fit the IR SEDs of $z \lesssim 0.5$ PG quasars and reproduced the observations very well. Similar analysis have been also applied for quasars at $z \gtrsim 5$ in Chapter 3, however, the SED fitting results were very poor as the model under-predicted the warm dust emission. Instead, after subtracting the AGN contribution, the host far-IR SEDs of these $z \sim 5$–6 quasars are better described by the relatively warm SED of the metal-poor starbursting galaxy Haro 11, who shares many expected ISM properties for galaxies at these redshifts. Later work by De Rossi et al. (2018) reported a transition from cold to warm far-IR SEDs of galaxies between $z \lesssim 4$ and $z \gtrsim 5$ and showed the Haro-11 like SED is a consequence of the high energy densities and silicate-rich dust composition in first massive population II galaxies.

## 7.2 Ongoing and Future Work

Below is a list of some example projects motivated by this thesis:

(1) **Robust Constraints on the Properties of AGN Circumnuclear Torus**: I am currently combining the dust reverberation mapping results (Chapter 5), the intrinsic IR SED constraints (Chapters 2 and 3), and literature IR interferometry analysis to develop a robust model that simultaneously matches these observations. As demonstrated by Lyu et al. (2019), by a cross-correlation analysis of the long time-baseline WISE/NEOWISE IR light curves and ground-based optical time-domain data, torus spatial information down to $\sim 10^{-2}$ can be retrieved. In the future, I will greatly expand this study to a much larger sample with higher redshifts, aiming to produce a continuous dust-reverberation mapping at $\lambda \sim$1–5 $\mu$m. This program will not only enable detailed study of AGN torus but also provide a chance to measure the cosmology constant through the IR time-lag vs AGN luminosity relation.

(2) **Resolved Study of the Extended Polar Dust in Nearest AGNs**: To confirm if the AGN SED shape can effectively trace the different dust environments around an AGN, as proposed in Chapter 4, I am currently leading an observing program to use the *Mag-*

*ellan*/IMACS-IFU to study the ISM properties of representative low-$z$ type-1 AGNs with AGN-dominated IR emission that cover dust-deficient, normal, warm-excess and hot-dust-obscured types. In the near future, I will also propose ALMA observations to study the morphology and dynamics of the cold gas component. With the launch of the *James Webb Space Telescope* (JWST), we will be able to obtain IFU maps from the near-IR and mid-IR wavelengths, which can directly explore the properties of the polar dust component. For example, based on our SED analysis in Lyu & Rieke (2018), the surface brightness and observed size of the AGN-heated polar dust component should be a strong function of wavelength (Figure 7.1). I will use JWST MIRI and NIRSpec IFU observations at 2–28 $\mu m$ to confirm this prediction and further constrain the possible interaction between the AGN torus and the host galaxy ISM in different SED types.

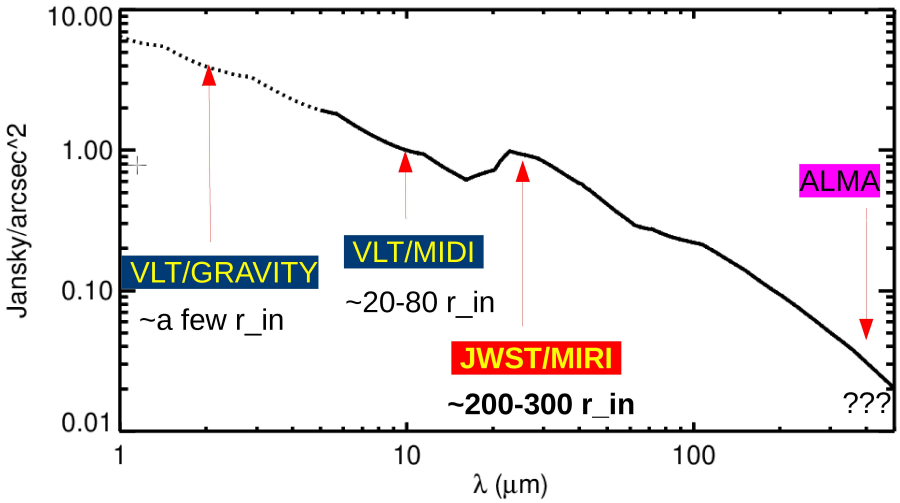


Figure 7.1 Flux density profile of the AGN polar dust emission based on Lyu & Rieke (2018) model, normalized at $\sim$10 $\mu m$. We denote some related telescopes/instruments and the expected physical scales of the polar dust component at different wavelengths. The polar dust component is expected to have a local peak at $\sim$20–30 $\mu$m, where JWST/MIRI would provide the crucial test.

(3) **The Obscured Star Formation Activities in AGN Host Galaxies**: To constrain the star formation rate of AGN host galaxies, many astronomers have assumed the far-IR/sub-mm bands are dominated by the galaxy emission. However, there are concerns that if the AGN can heat the whole galactic ISM (e.g., Roebuck et al., 2016) and current SED

models have not robustly tested in the far-IR. I am building a large sample of low-$z$ AGNs with *Spitzer*/IRS observations, good far-IR SED constraints and optical spectra that cover a wide range of star formation activities. I will gauge the differences and uncertainties of star formation rates measured via our empirical SED analysis, mid-IR aromatic features and SF-driven ionization lines and investigate the possible contribution of the AGN-heated polar dust emission in the far-IR for the first time. The results of this project will provide some general guidelines for related studies for JWST and future IR missions.

(4) **Searching Obscured AGNs through mid-IR variabilities**: A complete census of AGN activity is crucial for our understanding of the build-up of SMBHs and its relations with the host galaxies. However, obscured AGNs are hard to find. As shown in the left panel of Figure 7.2, although the simple color-color cut can effectively identify most unobscured AGNs, about half of the Compton-thick AGNs are missed. Interestingly, from my preliminary study, $>90\%$ of the Compton-thick AGNs are variable in the mid-IR bands, similar to unobscured quasars (right panel of Figure 7.2), which offers a promising approach to search them. I am now developing pipelines to conduct difference photometry on the time-resolved co-added WISE/NEOWISE images to select variable objects. Combined with the knowledge of AGN mid-IR variability patterns (e.g., Lyu et al. 2019) and the range of their SED mid-IR SED variations (e.g., Lyu et al. 2017; Lyu & Rieke 2018), large number of high-$z$ obscured quasars are expected to be identified. Possible future follow-up observations of these candidates with deep X-ray (e.g., Chandra) and mid-IR observations (e.g., JWST) will reveal the nature of this largely unexplored quasar population.

(5). **Direct Investigation of the Host Stellar Properties of Quasars at** $z\sim6$: Lyu et al. (2016) have provided a crude estimation on the properties of quasar host galaxies at $z\sim$5–6 (i.e., a massive galaxy with $\sim10^{11}\,M_{\odot}$ stellar mass and relatively low metallicity ISM, dominated by young stellar populations). With JWST, we can obtain a rest-frame optical spectrum for such a quasar directly (see the simulation in Figure 7.3). Based on detailed analysis of the continuum shape and absorption features, we will be able to put limits on the stellar mass and explore if the Magorrian relation has any cosmic evolution when the Universe is only $\sim$1 Gyr. It is also possible to reveal the galaxy ISM dynamics with our

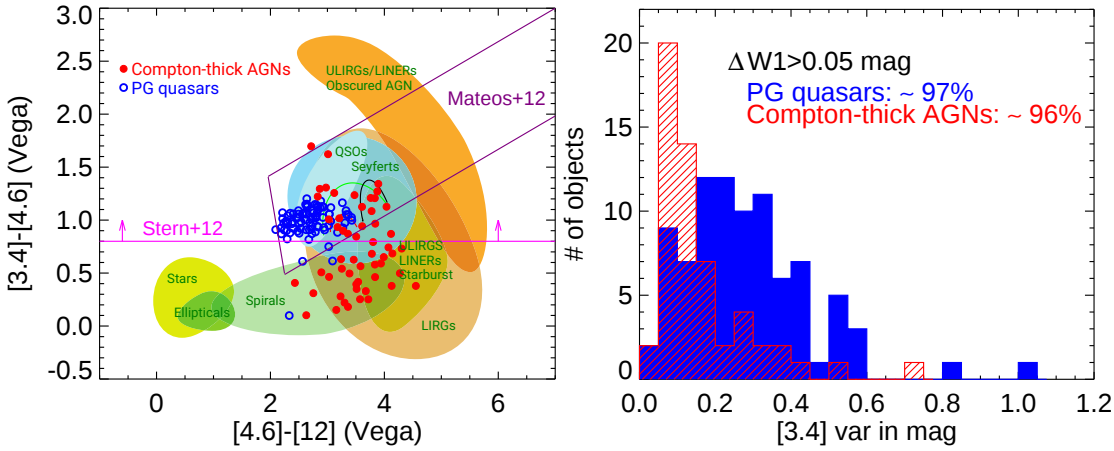


Figure 7.2 Left: The WISE color-color diagram for extragalactic sources. Half of the Compton-thick AGNs cannot be identified by the mid-IR color selection criteria. Right: The WISE W1 band ($\sim$3.4 $\mu$m) variability amplitude distribution of PG quasars and Compton-thick AGNs. As the WISE flux measurement uncertainty is $\sim$0.02–0.03 mag, over 90% AGNs can be identified as variable in the mid-IR, regardless of whether they are obscured or not.

proposed IFU observations.

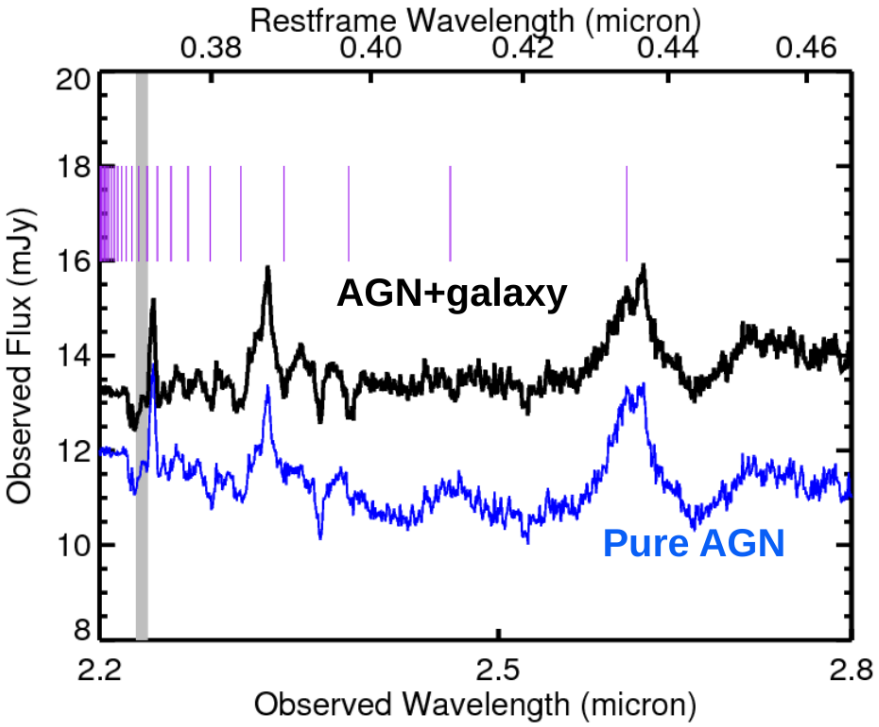


Figure 7.3 Simulated JWST/NIRSpec spectrum for a typical quasar at $z \sim 6$.

# APPENDIX A

# THE AGN INTRINSIC SED TEMPLATES

Xu et al. (2015b) derived the intrinsic AGN template for normal quasars based on the Elvis et al. (1994) template. The validity of this template has been demonstrated for the most luminous quasars at $z \gtrsim 5$ (Lyu et al., 2016), type-1 AGNs at $z \sim$0.7–2.5 (Xu et al., 2015b), and PG quasars at $z < 0.5$ (Lyu et al., 2017). In Lyu et al. (2017), we have derived the intrinsic AGN templates for WDD and HDD quasars and shown that these dust-deficient AGNs can be found at $z \sim$0–6. In Table A.1, we provide the 0.1–1000 $\mu$m SEDs of these three templates.

Table A.1. AGN Intrinsic Templates

| $\log(\lambda/\mu\mathrm{m})$ (1) | $\log(\nu/\mathrm{Hz})$ (2) | $\log(\nu F_{\nu,\mathrm{normal}})$ (3) | $\log(\nu F_{\nu,\mathrm{HDD}})$ (4) | $\log(\nu F_{\nu,\mathrm{WDD}})$ (5) |
|---|---|---|---|---|
| -1.00 | 15.48 | 0.575 | 0.574 | 0.571 |
| -0.99 | 15.47 | 0.578 | 0.576 | 0.574 |
| -0.98 | 15.46 | 0.579 | 0.578 | 0.576 |
| -0.97 | 15.45 | 0.588 | 0.587 | 0.585 |
| -0.96 | 15.44 | 0.595 | 0.594 | 0.591 |
| ... | | | | |

Note. — The template luminosities are normalized at 1.25 $\mu$m. For all of the templates at $\lambda > 100$ $\mu$m, a modified blackbody with temperature at 118 K and dust emissivity 1.5 is scaled to match the observed SED. The 0.1–1.25 $\mu$m SEDs of the HDD and WDD templates are assumed to be the same as Elvis et al. (1994).
(This table is available in its entirety in machine-readable form. A portion is shown here for guidance regarding its form and content.)

# APPENDIX B
# PURE STAR-FORMING GALAXIES IN THE GOALS SAMPLE

The Great Observatories All-sky LIRG Survey (GOALS; Armus et al. 2009) provided the community a comprehensive dataset for over 200 (U)LIRGs in the local Universe. We selected 101 pure star-forming galaxies from this sample by removing any objects with an X-ray cross-identification according to the NASA/IPAC Extragalactic Database (NED), identified as AGN in the literature, or presenting mid-IR [Ne v] emission lines. We obtained the *Spitzer*/IRS low-resolution spectra for all these objects from the *Combined Atlas of Sources with Spitzer IRS Spectra* (CASSIS; Lebouteiller et al. 2011a). If necessary, we scaled the Short-Low (SL) module spectra to match the Long-Low (LL) module spectra to make a continuous mid-IR continuum. The final combined spectra were then analyzed by the IDL program *PAHFIT* (Smith et al., 2007b). Finally, the flux of the 11.3 aromatic feature complex was derived for each object. Adopting the 8–1000 $\mu$m IR luminosities in Armus et al. (2009), we calculated the luminosity conversion factor from the 11.3 aromatic feature complex to the total IR emission for each star-forming galaxy and binned individual measurements as a function of the IR luminosity. The standard deviations are used to show the dispersions of the observed conversion factors in Figure 3.3. Our sample of pure SFGs in GOALS as well as corresponding measurements are presented in Table B.1.

Table B.1. Properties of 101 SFGs in the GOALS sample

| Name (1) | $z$ (2) | $\log(L_{\rm PAH}/L_{\odot})$ (3) | $\log(L_{\rm IR}/L_{\odot})$ (4) | $f_{\rm conv.}$ (5) |
|---|---|---|---|---|
| RAS F19297-0406 | 0.0857 | 9.30 | 12.40 | 0.0008 |
| IRAS 19542+1110 | 0.0650 | 9.38 | 12.00 | 0.0024 |
| IRAS 17132+5313 | 0.0509 | 9.72 | 11.90 | 0.0066 |
| CGCG 448-020 | 0.0361 | 9.39 | 11.90 | 0.0031 |
| ESO 593-IG008 | 0.0487 | 9.70 | 11.90 | 0.0062 |
| ... | | | | |

Note. — Column (1): the object name; Column (2): redshift from NED; Column (3): the luminosity of the 11.3 aromatic emission as measured from the mid-IR spectrum; Column (4): the IR luminosity of the object in Armus et al. (2009); Column (5): the luminosity conversion factor between the 11.3 aromatic emission and the total IR emission. $f_{\rm conv.} = L_{\rm PAH}/L_{\rm IR}$.
(This table is available in its entirety in machine-readable form. A portion is shown here for guidance regarding its form and content.)

# APPENDIX C
# THE EFFECTS OF OPTICAL THICKNESS

We use 3D radiative transfer simulations to demonstrate how the optical thickness of the dusty medium can affect its SED. Detailed simulation and analysis of the IR emission from clumpy clouds is described in the literature (e.g., Nenkova et al. 2008a; Stalevski et al. 2012). We illustrate several key concepts focusing on a single dusty cloud heated by the emission from an accretion disk at some distance.

For simplicity, the cloud is assumed to be a sphere with a radius $r = 1$ pc and a homogeneous density distribution of typical ISM dust grains. The accretion disk is approximated as a point source with a broken power-law SED following Stalevski et al. (2016), and located at a distance of 5 pc to the cloud. We use the radiative transfer code SKIRT (Baes et al., 2003, 2011) to compute the output SEDs as well as the images observed from different angles as a function of the optical thickness of the cloud ($\tau_{\rm cl}$). The results can be found in Figure C.1. If the cloud is optically thin ($\tau_{\rm cl} \lesssim 1$), the IR SEDs would be identical for any viewing angles. In fact, if the V-band optical thickness is not very large ($\tau_{\rm cl} \lesssim 10$), the cloud would be almost transparent for its own emission, given the rapidly decreasing extinction at longer wavelengths. These conclusions can be seen from the differential images between the front view of the bright side of the cloud and the back view of the dark side of the cloud. In the case of blocking, the dust emission SED will not change once the optical depths at the corresponding wavelength are low (e.g., $\lambda \sim 100\ \mu$m).

The optically-thin assumption also makes the effects of the dust-covering factor relatively easy to be accounted. In Figure C.2, we symmetrically distribute spherical dusty spheres at the same distance and calculate the output SEDs. The shape of the dust-processed SED is the same as the case of a single cloud, and the intensity can be matched by linearly scaling the emission from the single cloud.

For a low-optical-depth dust component, the output SEDs are not sensitive to the clumpiness of the dusty clouds. We demonstrate the effect of clumpiness in Figure C.3.

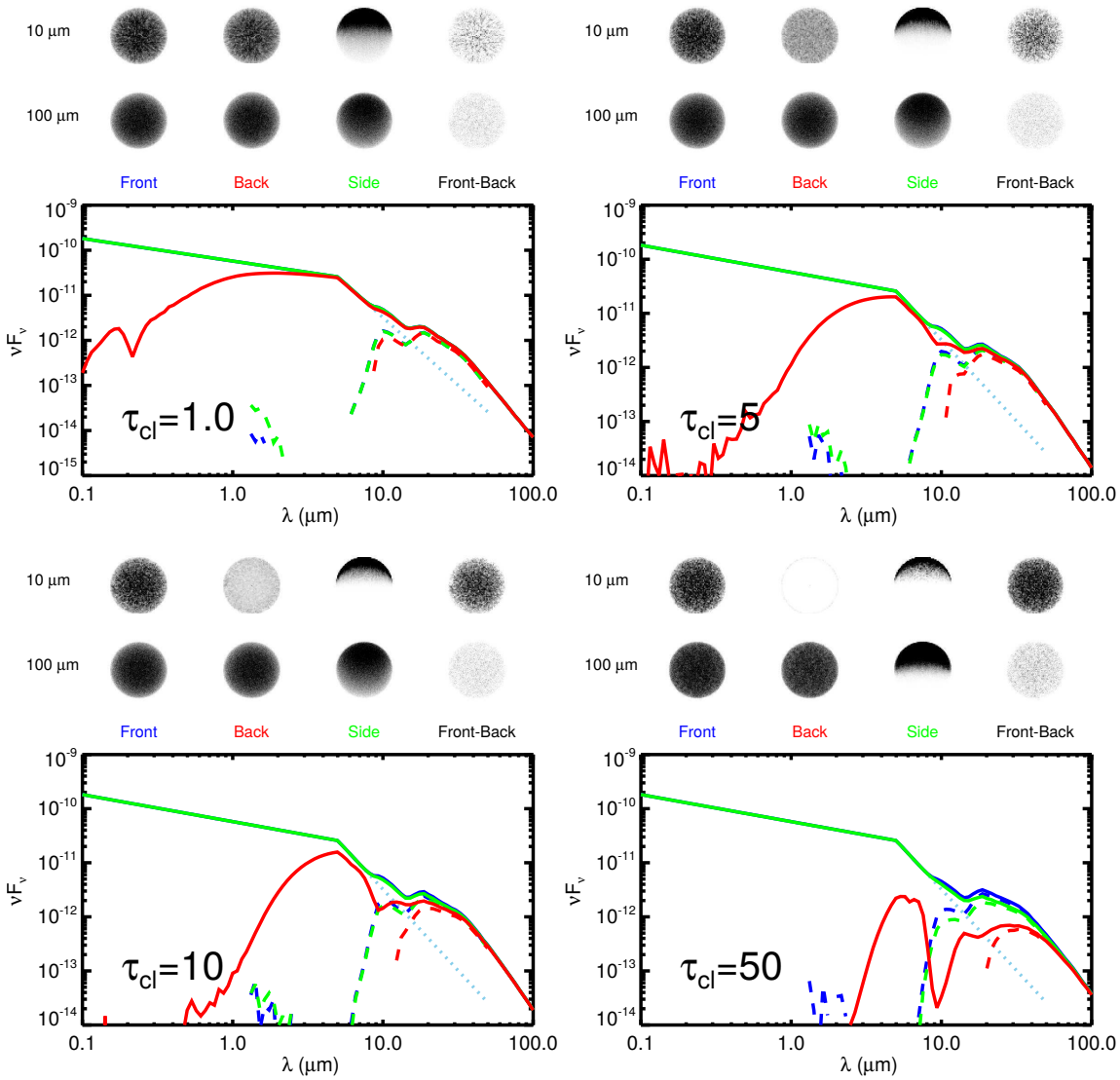


Figure C.1 The output SEDs and images of a single dusty cloud plus the accretion disk emission viewing from different angles. The integrated SEDs are plotted as solid lines. The accretion disk emission is represented as the blue dotted line. We also show the pseudo IR emission SEDs (dashed lines) of the cloud by subtracting the accretion disk SED from the total SED. We show the model images of the dusty cloud at 10 $\mu$m and 100 $\mu$m. The brightness is linearly scaled with the darkness of the pixel. To demonstrate the transparency of the dust cloud, a differential image 'Front-Back' is also made by subtracting the 'Back' emission from the 'Front' emission at corresponding pixels.

We first use the SKIRT code to produce the output SED of a $\tau_V = 1.5$ dusty sphere with density profile $n \sim r^{-0.5}$, $r_{in} = 0.6\ pc$ and $r_{out} = 300\ pc$, assuming the large dust grain distribution $a_{max} = 10\ \mu$m, $a_{min} = 0.04\ \mu$m. With the same total dust grain mass, we break

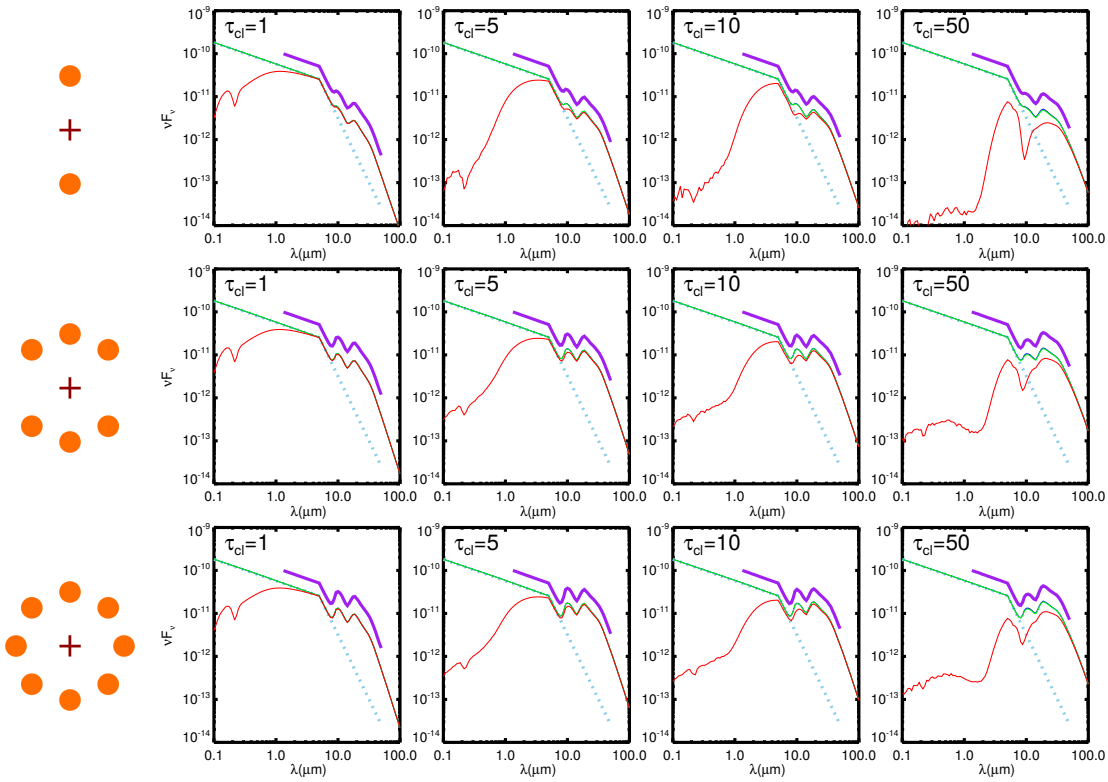


Figure C.2 The output SEDs of systems with different numbers of dusty clumps with optical depth $\tau_V = 1, 5, 10, 50$, heated by the accretion disk emission observed from different lines of sight (blue: face-on, red: edge-on, green: 45-degree inclination angle). The intrinsic accretion disk emission is represented by a broken power and shown as the dashed blue line. The purple line is the SED of the accretion disk emission linearly combined with the emission from a single cloud but multiplied by N times, where N is the number of the clouds in the corresponding system. We arbitrarily scaled the purple by 2 times for clarity.

the smooth geometry into 1000 randomly distributed spherical clumps with different size $R_{cl}$, but following the same density profile. Depending on whether the line-of-sight is blocked by the dust, the UV-optical SEDs present large variations for different viewing angles. However, the dust-reprocessed IR SEDs are nearly identical. We conclude the clumpiness would not influence the IR SED shapes.

In summary, we have demonstrated that optical depth up to $\tau_V \lesssim 5$ does not strongly modify the infrared output of a cloud composed of classical ISM dust and directly heated by an AGN. For larger grains suggested for polar dust, such effects would be further minimized. At the same radius, the integrated IR SED of $N$ identical clouds, whatever their

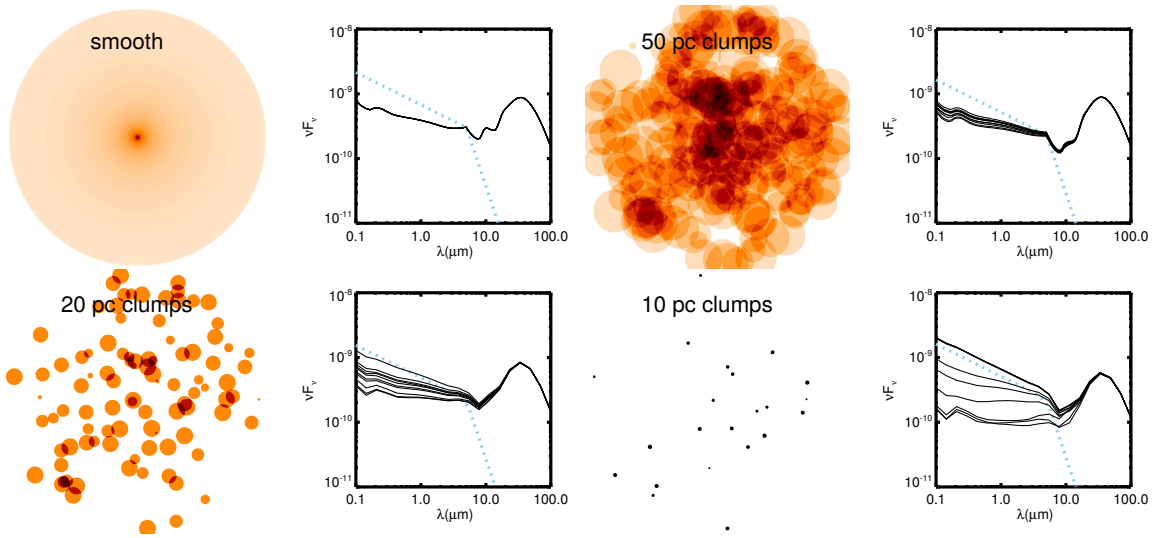


Figure C.3 Demonstration on the effect of clumpiness. The top-left panel shows the projected dust density distribution and the SEDs at different line-of-sights (inclination angle 0–90), assuming a $n \propto r^{-0.5}$ dusty sphere with $R_{\rm in} = 0.6pc$, $R_{\rm out} = 300pc$ and radial optical depth $\tau_{\rm V} = 1.5$, heated by a point source in the center with luminosity $L_{\rm AGN} = 10^{11}\ L_{\odot}$. We adopt a broken power-law SED for the intrinsic accretion disk emission, following e.g, Stalevski et al. (2012) (blue dotted line). In all these simulations, large dust grains in AGN environment are assumed (see text for details). In the other panels, we redistribute the dust in the sphere into 1000 clumps with different sizes (50 pc, 20 pc and 10 pc), following the same large geometry distribution with the same total dust mass. The simulations are run with a $100 \times 100 \times 100$ bin linear mesh of a box size $600 \times 600 \times 600$ pc.

placement, can be matched by linearly scaling the emission SED of single cloud by a factor of $N$. Assuming modest optical depths, the output SED is also insensitive to the clumpiness of the dusty medium. Thus, the primary determination of the infrared SED is the placement of the polar dust clouds along the radial direction, i.e., the radial density profile.

APPENDIX D

# SAMPLE AND DATA COMPILATION FOR LOW-$z$ SEYFERT-1 NUCLEI

## D.1 AGNs with HSR SED Observations

We first constructed a sample of AGN with high spatial resolution (HSR) measurements as follows. Asmus et al. (2014) presented a comprehensive mid-IR imaging atlas of 253 nearby AGNs with publicly available data from sub-arcsec-resolution observations carried out by ground-based 8-m class telescopes. We adopted this atlas as the parent sample and selected all type 1, 1.2, 1.5 and 1n objects. To reduce the possibility of mid-IR host galaxy contamination, we cross-matched this sample with the ALLWISE source catalog (Wright et al., 2010) and compared the 12 $\mu m$ flux from ground-based subarcsec resolution observation, $F_g(12\ \mu\mathrm{m})$, and that from space-based 6.5″ resolution WISE band 3 observation, $F_s(12\ \mu\mathrm{m})$. The W3 flux is known to have a systematic bias that is color-dependent (Section 2.2 in Wright et al. 2010). Our objects have $f_\nu \propto \nu^{-\beta}$ with $\beta$ ∼0–3, which corresponds to a flux correction factor of 0.92–1.10. Considering this and other uncertainties from e.g., flux zeropoints and filter differences, we selected objects that satisfy $F(12\ \mu\mathrm{m})_g/F(12\ \mu\mathrm{m})_s > 0.9$. In addition, we required that the source shape is consistent with a point-source in all four WISE bands. Any objects falling within the extrapolated isophotal footprint of a 2MASS extended source have been removed to avoid strong stellar contamination in the near-IR. [1] Since the SEDs of Palomar-Green (PG) quasars whose SEDs have been studied in our previous work (Lyu et al., 2017), we remove them from this study.

Since we are also interested in the AGN polar dust emission, we included all the type-1 objects with mid-IR interferometry observations in López-Gonzaga et al. (2016) besides 3C 273 (PG 1226+023). Finally, some well-known nearby Seyfert-1 nuclei with high-spatial-resolution IR SEDs in the literature (e.g., Alonso-Herrero et al., 2003; Ramos Almeida et al.,

[1] We removed any ALLWISE sources with ext_flg=1,2,3,5.

2009; Prieto et al., 2010; Fuller et al., 2016) are also included in this study. This sample is summarized in Table 4.3.

For the above sample selected from Asmus et al. (2014), we adopted the 2MASS profile-fit photometry and the WISE profile-fit photometry to sample the near-IR to mid-IR SED. The FWHM of a typical 2MASS point-spread-function (PSF) is about 2.5 arcsec and the FWHM of the WISE band 1–3 is about 6 arcsec. We replace them with the higher spatial resolution data from, e.g., *Spitzer*/IRAC or HST/NICMOS if available. It is known that the ground-based mid-IR imaging could have unstable PSF (e.g., Radomski et al., 2008), thus we retained the WISE band-3 (12 $\mu$m) flux. The FWHM of the WISE W4 band is about 12 arcsec, we replace that with *Spitzer*/MIPS 24 micron data wherever possible. Most of the other objects have (sub)arcsec resolution SEDs presented in the literature. We complemented the incomplete SEDs with either WISE or 2MASS photometry.

To further constrain the SED shape of the dust emission, we collected the mid-IR spectra for objects observed by *Spitzer*/IRS. For the staring mode observations, we adopt the *CASSIS* products (Lebouteiller et al., 2011a). For the mapping mode, we used *CUBISM* (Smith et al., 2007a) to reprocess the data, following the standard pipeline given in the software document.

## D.2 The SDSS-*Spitzer*/IRS Type-1 AGNs

We adopted the spectral decomposition results of the Main Galaxy Sample (Strauss et al., 2002) in the SDSS Seventh Data Release (DR7; Abazajian et al. 2009) processed with the optical spectral data reduction pipeline developed by Hao et al. (2005a). After subtracting the host galaxy continuum and the power-law AGN components, type-1 AGNs were selected as objects with the H$\alpha$ broad component with full width at half maximum (FWHM) $>$ 1200 km/s from multi-Gaussian line-profile fit with a rest-frame H$\alpha$ equivalent width (EW)$>$ 3 $\AA$. Due to the requirement of a direction of H$\alpha$ information, the sample was limited to $z < 0.33$ by the SDSS spectral coverage.

After compiling the SDSS Seyfert-1 sample, we cross-matched their SDSS coordinates with the *Combined Atlas of Sources with Spitzer IRS Spectra* (CASSIS, Lebouteiller et al. 2011a) within a 3$''$ search radius to get the mid-IR data. The CASSIS contains all *Spitzer*/IRS

staring mode observations with enough signal for a useful spectrum. Since a strong host galaxy contamination in the mid-IR would make the interpretations ambiguous, only objects without evidence for strong aromatic features or silicate absorption(s) were selected. All of the sample have 11.3 $\mu$m aromatic features with equivalent width (EQW) less than 0.1 $\mu$m from *Spitzer*/IRS spectral decomposition with a modified version of *PAHFIT* (Smith et al., 2007b), following Gallimore et al. (2010) to add an optically-thin, warm dust component to reproduce the AGN silicate emission features (see their Section 4.1). Finally, we ended up with 33 SDSS-*Spitzer*/IRS type-1 AGNs. We used the IDL routine *DeblendIRS* (Hernán-Caballero et al., 2015) to double check the level of star formation; the average luminosity contribution at 5.5–15 $\mu$m is about 3% with the maximum value $< 9\%$.

To cover the full SED, we collected other multi-band photometry data for this sample. Seventeen objects ($\sim$52%) have X-ray observations from XMM-*Newton* or *Chandra*. We searched the *GALEX*, *SDSS*, *2MASS* and *WISE* archives for the corresponding UV/optical/IR photometric data. Over 80% of these objects are resolved in the 2MASS images; for them, we adopted the Standard Photometry with isophotal apertures based on the $K_s$ 20 mag arcsec$^{-2}$ elliptical isophote from the 2MASS extended source catalog. For the WISE W1 ($\sim 3.4$ $\mu$m)and W2 ($\sim 4.6$ $\mu$m) bands, we used the scaled-2MASS-aperture photometry with the largest aperture as long as no other sources was included if the object was in the 2MASS extended source catalog and the WISE aperture photometry is larger than the default profile-fit photometry. We adopted the profile-fit photometry of the J, H, K, W1 and W2 band in other cases.

## D.3 IR Light Curves from WISE/NEOWISE

To address the infrared variabilities of these AGNs, we derive light curves based on the W1 and W2 band observations from the *WISE* (Wright et al., 2010) and the Near-Earth Object *WISE* Reactivation (*NEOWISE-R*; Mainzer et al. 2014) missions, following similar procedures in our previous work (Lyu et al., 2017). For most objects, the light curves cover seven to nine different epochs with 10–20 individual exposures for each epoch. We computed the mean photometry for each epoch and derived the maximum variability

amplitudes. These results are included in Table 4.3.

APPENDIX E

# PHOTOMETRIC STABILITY OF OPTICAL TRANSIENT SURVEYS AND *WISE*/*NEOWISE* MISSION

None of the CRTS, ASAS-SN and *WISE*/NEOWISE missions has put AGN variability study as its main science objective, thus we need to assess the noise characteristics of their photometric measurements. For our time-series analysis, a clear idea of the instrument photometric stability is of paramount importance. With careful selections of photometric standard stars in the optical and mid-IR bands, we construct the light curves of non-variable sources and explore the systematics and noise characteristics in this appendix.

## E.1 Optical Data from CRTS and ASAS-SN

From the Optical and UV Spectrophotometric Standard Stars web page at ESO,[1] we have selected 15 stars to study the optical photometric stability of the CRTS and ASAS-SN data. Besides GD 108, a sub-dwarf, all of these stars are white dwarfs. We have compiled their optical measurements from the CRTS and ASAS-SN archives and constructed the corresponding optical light curves. Since the CRTS data were taken without a photometric filter, we matched the CRTS light curve to those derived from ASAS-SN by introducing a constant offset. We also rejected photometry outliers that showed a discrepancy of $> 0.5$ mag from the average values. The final light curves are plotted in Figure E.1.

We calculate the mean magnitudes and the root-mean-square (RMS) offsets of the CRTS and ASAS-SN light curves separately and summarize the results in Table E.1. Besides the uncertainties caused by standard photometry measurements, any issues with system stability can further increase the observed magnitude RMS offset, and these values could be related as

$$RMS^2_{M-\bar{M}} = RMS^2_{\Delta M} + \sigma^2_{s.s.} \quad . \tag{E.1.1}$$

[1] http://www.eso.org/sci/observing/tools/standards/spectra/stanlis.html

Table E.1. Measurements of Optical Standard Stars

| Name | $M_V$ | CRTS | | | ASAS-SN | | |
|---|---|---|---|---|---|---|---|
| | | $\bar{M}$ | $\mathrm{RMS}_{M-\bar{M}}$ | $\mathrm{RMS}_{\Delta M}$ | $\bar{M}$ | $\mathrm{RMS}_{M-\bar{M}}$ | $\mathrm{RMS}_{\Delta M}$ |
| (1) | (2) | (3) | (4) | (5) | (6) | (7) | (8) |
| HZ43 | 12.91 | 12.577 | 0.092 | 0.009 | 12.687 | 0.023 | 0.015 |
| GD153 | 13.35 | 13.371 | 0.036 | 0.011 | 13.384 | 0.041 | 0.022 |
| NGC7293 | 13.51 | 13.527 | 0.065 | 0.013 | 13.534 | 0.035 | 0.030 |
| GD108 | 13.56 | 13.551 | 0.034 | 0.012 | 13.548 | 0.039 | 0.027 |
| HZ2 | 13.86 | 13.902 | 0.051 | 0.012 | 13.882 | 0.053 | 0.034 |
| GD50 | 14.06 | 14.070 | 0.021 | 0.013 | 14.068 | 0.052 | 0.038 |
| BPM16274 | 14.20 | 14.285 | 0.040 | 0.018 | 14.257 | 0.051 | 0.047 |
| HZ4 | 14.52 | 14.555 | 0.016 | 0.017 | 14.568 | 0.066 | 0.048 |
| HZ21 | 14.68 | 14.646 | 0.022 | 0.019 | 14.670 | 0.077 | 0.054 |
| G158-100 | 14.89 | 14.968 | 0.022 | 0.018 | 14.980 | 0.109 | 0.076 |
| GD248 | 15.09 | 15.170 | 0.025 | 0.020 | 15.146 | 0.102 | 0.083 |
| LB227 | 15.34 | 15.326 | 0.038 | 0.019 | 15.324 | 0.101 | 0.083 |
| SA95-42 | 15.61 | 15.567 | 0.040 | 0.023 | 15.581 | 0.156 | 0.123 |
| G193-74 | 15.70 | 15.732 | 0.019 | 0.023 | 15.743 | 0.156 | 0.130 |
| G138-31 | 16.14 | 16.461 | 0.297 | 0.245 | 16.594 | 0.195 | 0.177 |

Note. — Col. (1): star name; Col. (2): V-band magnitude given in the ESO standard star list; Col. (3): mean magnitude of all CRTS measurements, an offset is included to match the CRTS light curve; Col. (4): RMS value for all the magnitude deviations relative to the mean magnitude for CRTS data; Col. (5): RMS value for all magnitude errors reported in the CRTS catalog; Col. (6)-(8): similar to Col. (3)-(5) but for ASAS-SN data.

On average, we get $\sigma_{s.s.} \sim 0.018$ mag for ASA-SN data and $\sigma_{s.s.} \sim 0.023$ mag for CRTS data.

## E.2 Mid-IR from *WISE*/NEOWISE

With the *WISE*/NEOWISE catalogs, we examined the photometric stability of W1 and W2 bands as a function of time. Fourteen mid-IR standard stars from the *Spitzer*/IRAC

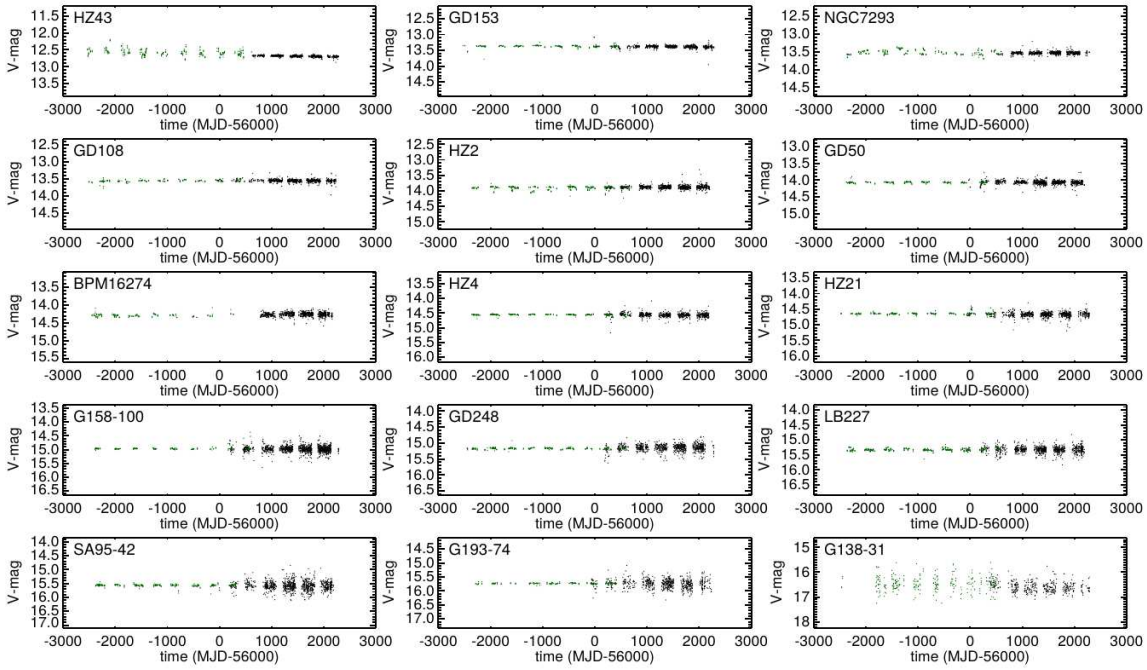


Figure E.1 Optical light curves of 15 optical spectrophotometric standard stars. The CRTS data are in green and the ASAS-SN data are in black.

primary calibrators[2] and *WISE* (W1, W2) Calibration stars[3] were chosen for this purpose. The constructed mid-IR light curves can be seen in Figure E.2. We summarize the RMS magnitude offsets and RMS errors of W1 and W2 bands during the *WISE* and NEOWISE mission in Table E.2.

With equation E.1.1, we get $\sigma_{s.s.} \sim 0.029$ mag for *WISE* and 0.016 mag for NEOWISE. Since we have averaged the 10∼20 observations for the mid-IR light curve construction (Section 5.2.2), the contribution to the measurement uncertainties from the system instability is expected to be $<$0.009 mag for *WISE* and $<$ 0.005 mag for NEOWISE.

[2] https://irsa.ipac.caltech.edu/data/SPITZER/docs/irac/iracinstrumenthandbook/17/

[3] http://wise2.ipac.caltech.edu/docs/release/allsky/expsup/sec4_4ht7.html

Table E.2. Measurements of Mid-IR Standard Stars

| Name | W1 band | | | | | W2 band | | | | |
|---|---|---|---|---|---|---|---|---|---|---|
| | | ALLWISE | | NEOWISE | | | ALLWISE | | NEOWISE | |
| | $\bar{M}$ | $\mathrm{RMS}_{M-\bar{M}}$ | $\mathrm{RMS}_{\Delta M}$ | $\mathrm{RMS}_{M-\bar{M}}$ | $\mathrm{RMS}_{\Delta M}$ | $\bar{M}$ | $\mathrm{RMS}_{M-\bar{M}}$ | $\mathrm{RMS}_{\Delta M}$ | $\mathrm{RMS}_{M-\bar{M}}$ | $\mathrm{RMS}_{\Delta M}$ |
| (1) | (2) | (3) | (4) | (5) | (6) | (7) | (8) | (9) | (10) | (11) |
| KF09T1 | 8.055 | 0.038 | 0.024 | 0.022 | 0.016 | 8.123 | 0.037 | 0.021 | 0.022 | 0.016 |
| NPM1+66.0578 | 8.237 | 0.041 | 0.024 | 0.020 | 0.016 | 8.323 | 0.032 | 0.021 | 0.020 | 0.016 |
| KF05T1 | 8.767 | 0.035 | 0.024 | 0.019 | 0.016 | 8.863 | 0.027 | 0.022 | 0.019 | 0.016 |
| KF03T2 | 8.891 | 0.029 | 0.024 | 0.020 | 0.016 | 9.007 | 0.033 | 0.022 | 0.020 | 0.016 |
| HD271776 | 9.647 | 0.032 | 0.024 | 0.023 | 0.016 | 9.671 | 0.034 | 0.022 | 0.023 | 0.016 |
| WOH_G642 | 9.229 | 0.042 | 0.024 | 0.021 | 0.016 | 9.319 | 0.036 | 0.022 | 0.021 | 0.016 |
| HD270485 | 9.248 | 0.030 | 0.025 | 0.031 | 0.016 | 9.277 | 0.052 | 0.022 | 0.031 | 0.016 |
| KF03T1 | 9.858 | 0.033 | 0.025 | 0.022 | 0.016 | 9.952 | 0.049 | 0.023 | 0.022 | 0.016 |
| KF03T4 | 10.019 | 0.034 | 0.025 | 0.021 | 0.016 | 10.155 | 0.035 | 0.023 | 0.021 | 0.016 |
| KF02T3 | 10.223 | 0.037 | 0.025 | 0.028 | 0.017 | 10.332 | 0.035 | 0.025 | 0.028 | 0.017 |
| KF06T3 | 10.298 | 0.030 | 0.025 | 0.022 | 0.017 | 10.410 | 0.032 | 0.025 | 0.022 | 0.017 |

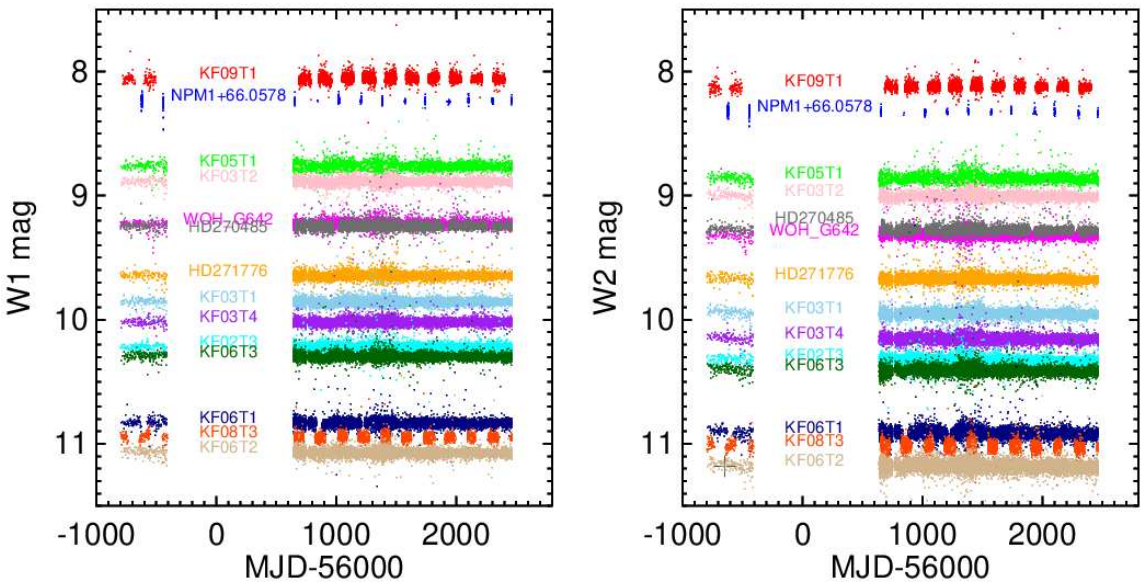


Figure E.2 *WISE* W1 (left) and W2 (right) light curves of 14 IR calibration standard stars

Table E.2 (cont'd)

| Name | W1 band | | | | | W2 band | | | | |
|---|---|---|---|---|---|---|---|---|---|---|
| | | ALLWISE | | NEOWISE | | | ALLWISE | | NEOWISE | |
| | $\bar{M}$ | $RMS_{M-\bar{M}}$ | $RMS_{\Delta M}$ | $RMS_{M-\bar{M}}$ | $RMS_{\Delta M}$ | $\bar{M}$ | $RMS_{M-\bar{M}}$ | $RMS_{\Delta M}$ | $RMS_{M-\bar{M}}$ | $RMS_{\Delta M}$ |
| (1) | (2) | (3) | (4) | (5) | (6) | (7) | (8) | (9) | (10) | (11) |
| KF06T1 | 10.832 | 0.036 | 0.026 | 0.023 | 0.018 | 10.912 | 0.039 | 0.027 | 0.023 | 0.018 |
| KF08T3 | 10.946 | 0.033 | 0.027 | 0.021 | 0.018 | 11.020 | 0.039 | 0.028 | 0.021 | 0.018 |
| KF06T2 | 11.072 | 0.031 | 0.026 | 0.031 | 0.018 | 11.179 | 0.042 | 0.029 | 0.031 | 0.018 |

Note. — Col. (1): star name; Col. (2): average W1 magnitude of all *WISE*/NEOWISE measurements; Col. (3): RMS magnitude offset relatively to the mean W1 magnitude for measurements taken during the ALLWISE mission; Col. (4): RMS value of all the W1 magnitude errors reported in the ALLWISE Multiepoch Photometry Table; Col. (5)-(6): similar to Col. (3)-(4) but for W1 measurements taken during the NEOWISE mission; Col. (7)-(11): similar to Col. (2)-(6), but for W2 band measurements.

APPENDIX F

# A SIMPLE MODEL FOR RELATING TIME LAGS TO THE TORUS STRUCTURES

As shown in Figure F.1, we consider a thin dust shell with a half opening angle $\Omega_{\rm TOR}$ that surrounds the accretion disk. We also assume that a single *WISE* band traces the IR emission from dust at some similar distance, $R$, to the accretion disk. Placing the axis of symmetry along the z-axis, we have a dusty layer with $r = R$, $\theta = [\Omega_{\rm TOR}, \pi - \Omega_{\rm TOR}]$ and $\phi = [0, 2\pi)$. The observer is located at an observing angle of $\Omega_{\rm LOS}$ to the z-axis and parallel to the $z$-$y$ plane.

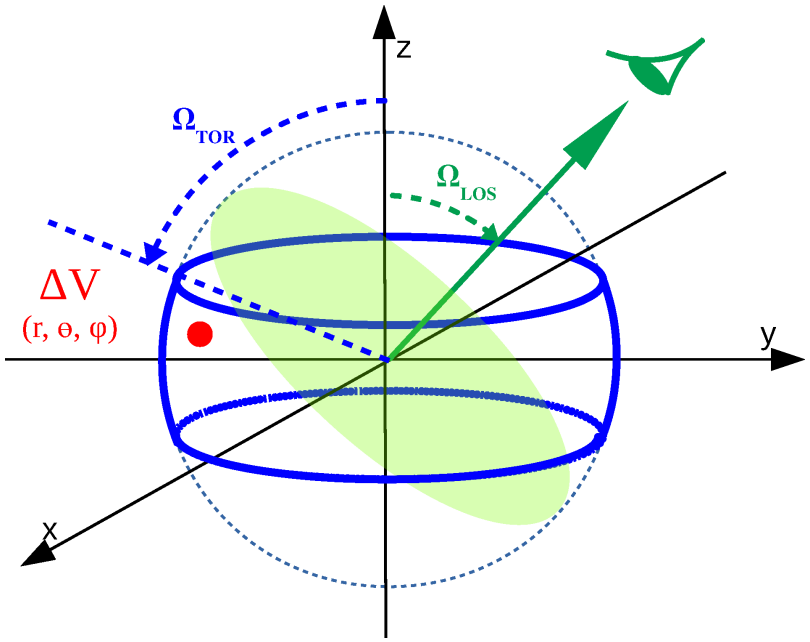


Figure F.1 The geometry of a dusty shell with a radius $r$ from the origin (accretion disk) and a half opening angle $\Omega_{\rm TOR}$. The observer has a viewing angle $\Omega_{\rm LOS}$.

Now imagine a plane that is perpendicular to the observing angle and also tangent to the dusty sphere, which can be described by the function

$$[\sin\Omega_{\rm LOS}]y + [\cos\Omega_{\rm LOS}]z - R = 0\ . \tag{F.0.1}$$

It takes time, $R/c$ for emission from the accretion disk to reach this plane.

For a point on the dusty sphere with coordinates $(x,y,z) = R(\sin\theta\cos\phi, \sin\theta\sin\phi, \cos\theta)$, the light travel distance would be

$$l = R + |R[\sin\Omega_{\rm LOS}\sin\theta\sin\phi + \cos\Omega_{\rm LOS}\cos\theta - 1]| \tag{F.0.2}$$

$$= R[2 - \sin\Omega_{\rm LOS}\sin\theta\sin\phi - \cos\Omega_{\rm LOS}\cos\theta] \ . \tag{F.0.3}$$

An average time lag of all elements on that sphere is given by

$$< t > = \frac{\int wlds}{c\int ds} \tag{F.0.4}$$

$$= \frac{\int_0^{2\pi}\int_{\Omega_{\rm TOR}}^{\pi-\Omega_{\rm TOR}} wlR\sin\theta d\theta d\phi}{c\int_0^{2\pi}\int_{\Omega_{\rm TOR}}^{\pi-\Omega_{\rm TOR}} R\sin\theta d\theta d\phi} \ , \tag{F.0.5}$$

where $w$ is the weight of each element, which is dependent on the dust optical depth in the IR band along the LOS and the local strength of dust emission. If the emission is optically thin and homogeneously distributed, we have $w = 1$, so

$$< t > = \frac{\int_0^{2\pi}\int_{\Omega_{\rm TOR}}^{\pi-\Omega_{\rm TOR}} R[2 - \sin\Omega_{\rm LOS}\sin\theta\sin\phi - \cos\Omega_{\rm LOS}\cos\theta]R\sin\theta d\theta d\phi}{c\int_0^{2\pi}\int_{\Omega_{\rm TOR}}^{\pi-\Omega_{\rm TOR}} R\sin\theta d\theta d\phi} \tag{F.0.6}$$

$$= \frac{2R}{c}. \tag{F.0.7}$$

Consequently, the average time lag between the surrounding dusty torus shell and the accretion disk is

$$\Delta t = \frac{R}{c} \ , \tag{F.0.8}$$

This means the time lag is not dependent on the viewing angle in the optically thin case.

If the dusty torus is extremely optically thick, we can only see flux from the edge of the structure that is exposed to the observer. When the observer is looking through the torus opening angle (type-1; $\Omega_{\rm LOS} < \Omega_{\rm TOR}$), the time lag can be easily calculated to be

$$\Delta t = \frac{R}{c}(1 - \cos\Omega_{\rm LOS}\cos\Omega_{\rm TOR}). \tag{F.0.9}$$

It is straightforward to prove the time lag in this situation will always be shorter than the optically-thin case for the same $R$.

In true physical situations where the torus dust is not perfectly optically thin or optically thick in the mid-IR, we should have

$$\frac{R}{c} > \Delta t > \frac{R}{c}(1 - \cos\Omega_{\rm LOS}\cos\Omega_{\rm TOR}) \tag{F.0.10}$$

Knowing the fraction of type-2 objects in the quasar population ($\sim$0.5–0.6; Reyes et al. (2008)), we have roughly $\Omega_{\rm TOR} = \pi/3$ and

$$\frac{R}{c} > \Delta t \gtrsim 0.5\frac{R}{c} \tag{F.0.11}$$

In other words, a naive size estimation from $c\Delta t$ could slightly underestimate the true physical size up to a factor of two. For a single ring with $\theta = \theta_0$, the range of time lags, $\Delta t$, is given by

$$max(\Delta t) - min(\Delta t) = \frac{2R}{c}\sin\Omega_{\rm LOS}\sin\theta_0 \ . \tag{F.0.12}$$

For a complete shell,

$$max(\Delta t) - min(\Delta t) = \frac{2R}{c}\cos(\Omega_{\rm TOR} - \Omega_{\rm LOS}) \ . \tag{F.0.13}$$

Finally, the standard deviation of the time lag $\Delta t$ for a dusty shell

$$\sigma(\Delta t) = \frac{R}{c}\sqrt{\frac{1}{3}\cos^2\Omega_{\rm TOR} + \frac{1}{2}\sin^2\Omega_{\rm LOS}\sin^2\Omega_{\rm TOR}} \ . \tag{F.0.14}$$

This can introduce a smoothing effect on the integrated IR reverberation light curves, whose strength is proportional to the torus size (or time lag $\Delta t$).

APPENDIX G

# A REVISIT OF THE KOSHIDA ET AL. SAMPLE

## G.1 SED Analysis

For consistency with the luminosity estimates for the PG sample, we examined the broad-band IR SEDs of the Seyfert-1 sample presented by Koshida et al. (2014) with the decomposition model introduced in Lyu & Rieke (2018). The total IR emission is assumed to be a linear combination of the contributions from three components: AGN-heated dust, near-IR starlight and mid-to-far IR emission from HII regions within the host galaxy. To reduce the ambiguity of interpretation, we have used well-tested empirical templates to describe each component. For the AGN templates, we first used the three types of intrinsic AGN SEDs proposed in Lyu et al. (2017) to represent the intrinsic variations of the torus. We also allow obscuration by an IR optically-thin extended dust distribution of large grains and the corresponding IR reprocessed emission. The latter component has been shown to be a valid explanation for the AGN polar dust emission seen by mid-IR interferometry analysis (see details in Lyu & Rieke 2018). We used $\chi^2$ minimization to determine the final best-fit model. The dust-deficient AGN template was selected only when it improved the $\chi^2$ value by a factor greater than two compared with the normal AGN template.

The results can be seen in Figure G.1. About half of the Koshida et al. (2014) sample have been identified as WDD AGNs and the other half are normal AGNs. With the derived intrinsic AGN SEDs, we calculated the AGN bolometric luminosities following Section 5.4.2 and summarized the results in Table G.1. As shown in Figure G.2, the results are consistent with those converted from the observed $V$-band measurements provided in Koshida et al. (2014), yielding an average $L_{\mathrm{AGN\ bol,\ SED}}/L_{\mathrm{AGN\ bol,\ V}} = 0.98 \pm 0.03$.

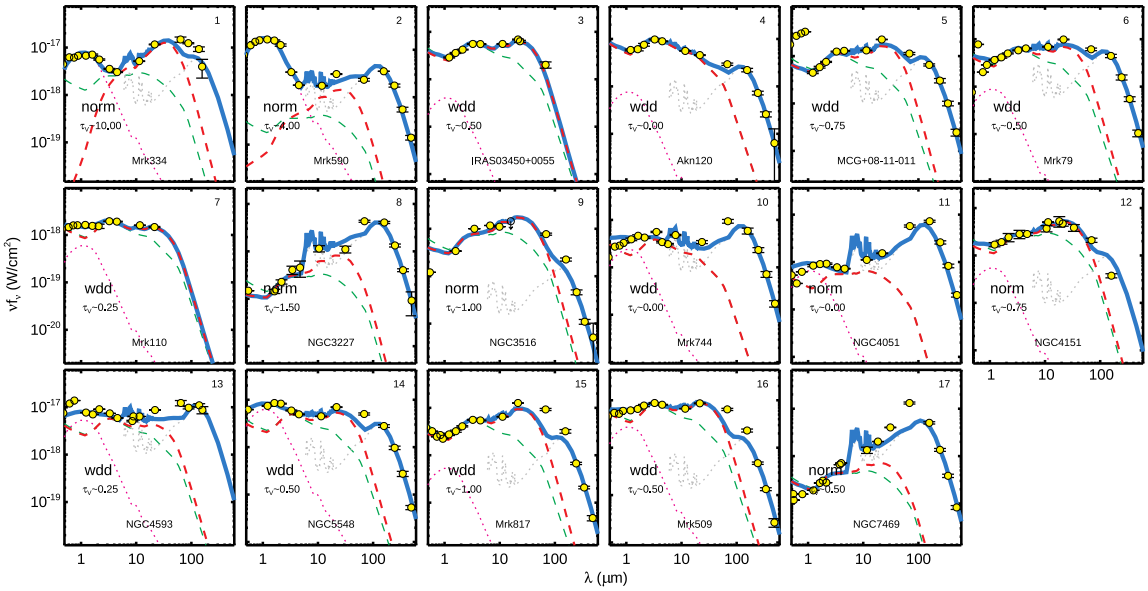


Figure G.1 Best-fit results for the Seyfert-1 nuclei studied in Koshida et al. (2014). Photometric data points are shown as yellow dots. The SED model (blue thick solid lines) is composed of the AGN component (red dashed lines), the stellar component (magenta dotted lines), and the far-IR star formation component (grey dotted lines). We also plot the suggested intrinsic AGN template (green dashed line) for each object from our SED fittings to compare with the observed SED.

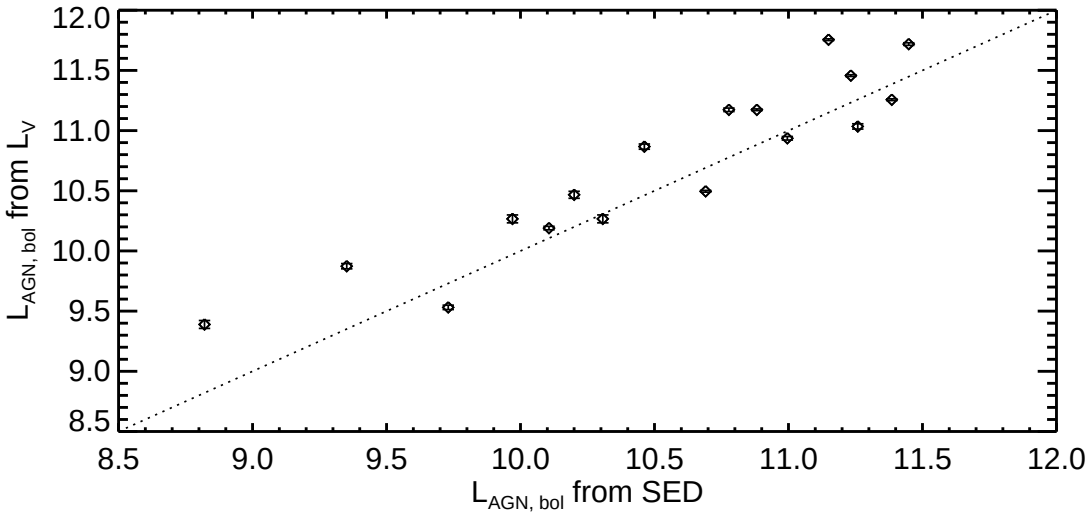


Figure G.2 AGN luminosity estimation comparison between SED fitting and V-band photometry from Koshida et al. (2014). The dotted line is the 1:1 relation.

## G.2 Time Lag Measurements

To determine if our time-lag measurements are significantly different from those determined by traditional CCF analysis, we apply the model introduced in Section 5.3.2 to fit the high-cadence light curves of 17 Seyfert-1 nuclei in Koshida et al. (2014) and present our measurements of the $K$-band time lags in Table G.1. In Figure G.3, we compare the results from these two approaches. Except for Mrk 590 and Akn 120, most measurements are consistent with each other, and the average difference is $< 10\%$. This suggests that the $R_{\rm K}/R_{\rm W1} \sim 0.6$ is not caused by the systematics from the different measurement approaches.

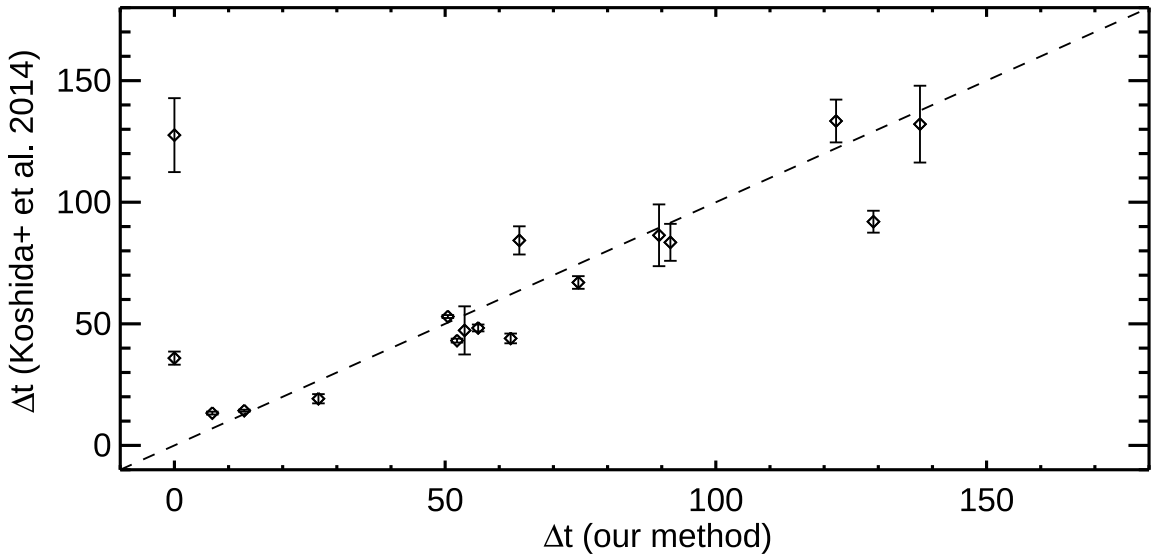


Figure G.3 K-band time lag comparison between our model and the Koshida et al. (2014) method. The dotted line is the 1:1 relation.

Table G.1. New Time Lag Measurements of the Koshida et al. (2014) Seyfert-1 Sample

| Name | Type | $\log(L_{\rm AGN,\,bol}/L_{\odot})$ (V-band) | (SED) | $\Delta t$/day | AMP |
|---|---|---|---|---|---|
| Mrk 334 | Norm | 11.17 | 10.88 | 137.7 | 5.1 |
| Mrk 590 | Norm | 10.46 | 10.20 | 0 | 6.2 |
| IRAS 03450+0055 | WDD | 11.46 | 11.23 | 129.1 | 6.2 |
| Akn 120 | WDD | 11.87 | 11.14 | 0 | 4.0 |
| MCG+08-11-011 | WDD | 11.76 | 11.25 | 89.5 | 9.5 |
| Mrk 79 | WDD | 10.93 | 10.99 | 74.6 | 2.1 |
| Mrk 110 | Norm | 11.17 | 10.77 | 63.7 | 2.8 |
| NGC 3227 | Norm | 9.85 | 9.35 | 7.0 | 5.3 |
| NGC 3516 | Norm | 10.26 | 10.30 | 53.6 | 6.8 |
| Mrk 744 | WDD | 9.48 | 9.73 | 26.6 | 19.9 |
| NGC 4051 | NORM | 9.30 | 8.82 | 12.9 | 6.4 |
| NGC 4151 | NORM | 10.26 | 9.97 | 52.2 | 4.2 |
| NGC 4593 | WDD | 10.17 | 10.10 | 62.1 | 6.9 |
| NGC 5548 | WDD | 10.49 | 10.69 | 50.5 | 4.9 |
| Mrk 817 | NORM | 11.26 | 11.38 | 91.6 | 6.7 |
| Mrk 590 | WDD | 11.71 | 11.44 | 122.2 | 2.4 |
| NGC 7469 | NORM | 10.87 | 10.46 | 56.1 | 5.1 |

APPENDIX H

# TEMPLATES FOR DWARF GALAXIES

## H.1 Sample and Infrared Data

The sample used to compute the SEDs of low-metallicity galaxies is from the Dwarf Galaxy Survey (DGS; Madden et al., 2013). This sample covers the full metallicity range observable in the local Universe with 12+log(O/H) ranging from 7.14 to 8.43, and spans four orders of magnitude in star formation rates.

The far-IR data adopted here is mainly from Rémy-Ruyer et al. (2013) [1]. A total of 48 dwarf galaxies were observed with PACS and SPIRE on board of the *Herschel Space Observatory* at 70, 100, 160, 250, 350, and 500 $\mu$m. For I Zw 18, we update with the *Herschel* data from Fisher et al. (2014). We also collect the near-IR to mid-IR photometry data for the whole sample from the *Wide-field Infrared Survey Explorer* (WISE ,Wright et al. 2010) at 3.4, 4.6, 12 and 22 $\mu$m. 47 of these galaxies were found to have low-resolution mid-IR spectroscopic observations from the *Spitzer* archive. We collect the staring-mode *Spitzer*/IRS spectra from the Cornell Atlas of *Spitzer*/IRS Sources (CASSIS; Lebouteiller et al., 2011b)[2] and adopt the post-BCD products from the *Spitzer* Heritage Archive (SHA) for mapping-mode observations, which were reduced in the SSC Pipeline Version S18.18. The latter spectral maps are combined into a single spectrum to represent the mid-IR emission continuum of the galaxy. However, since the surface brightnesses of dwarf galaxies are typically low, only a few *Spitzer* spectra have high enough signal-to-noise ratio (S/N) continuum to be useful for our derivation of the full IR SEDs. Finally, we focus on 19 DGS galaxies to study their IR SEDs.

[1] Rémy-Ruyer et al. (2015b) corrected the PACS photometry for three galaxies, HS 0822+3542, HS 1442+4250 and Tol 0618. However, none of our arguments made in the appendix would be changed.

[2] The Cornell Atlas of Spitzer/IRS Sources (CASSIS) is a product of the Infrared Science Center at Cornell University, supported by NASA and JPL.

## H.2 SED Modeling and Template Construction

[3]

In Rémy-Ruyer et al. (2013), a simple modified blackbody is fit to the far-IR photometry of the DGS sample to derive dust properties like temperature, mass, and emissivity index. After introducing the WISE mid-IR data at 12 and 22 $\mu$m, the far-IR SED peak shifts towards a shorter wavelength for the majority of sources, leading to a higher dust temperature. One single (modified) blackbody is not enough to represent the full IR SED, since galaxies always have a range of dust temperatures (e.g., Dunne & Eales, 2001; Willmer et al., 2009; Galametz et al., 2012; Kirkpatrick et al., 2012)

Here we utilize the Casey (2012) procedure (hereafter CMC fits) to address the mid-IR excess. Casey (2012) developed a fitting routine to fit the IR data points with a modified blackbody plus a power-law component. The mid-IR component is described as an analytical function

$$S(\lambda)_{\rm MIR} = N_{\rm MIR}\lambda^{\alpha}e^{-(\lambda/\lambda_{\rm c})^2}\ , \tag{H.2.1}$$

where $\alpha$ is the mid-IR power-law slope, and $\lambda_{\rm c}$ the power-law turnover wavelength. The normalizing factor $N_{\rm mid-IR}$ and turnover wavelength $\lambda_c$ are bounded with other parameters. We relax the bounding condition of $\lambda_c$ to fit the diverse SEDs of the DGS sample, leaving other configurations unchanged (see Casey, 2012). Since the light from old stellar populations may contribute to the SED (mainly at short wavelengths), we assume the emission in the WISE W1 band is completely stellar and scale a Rayleigh-Jeans tail to estimate the stellar contribution to other bands. The final SED fit is done for $\lambda > 8\mu$m data points after subtracting the possible old population stellar contribution from the observed fluxes.

In Table H.1, we list the basic information and fit parameter values. In Figure H.1, we show the SED continuum fits for the 19 DGS galaxies. We also present the results of single modified blackbody fits (only on *Herschel* data) for comparison.

Figure H.2 shows the full infrared SEDs (after adding the *Spitzer* spectra) for the 19

[3] After the submission of this paper, a comprehensive study of the physical basis of the infrared SEDs of the DGS sample of galaxies was published by Rémy-Ruyer et al. (2015a). Their conclusions about the general shape of the SEDs are similar to ours.

DGS galaxies. The mid-IR continua derived from the photometry fitting and those directly obtained from the mid-IR spectra are consistent. The mid-infrared regions of these low-metallicity objects present substantial forbidden line emissions and weak or no PAH emission (e.g., Wu et al., 2006, 2007), which contribute little to the continuum. For the final model SEDs of the 19 DGS galaxies, we discard the mid-IR portion of the fit SED continua based on WISE and *Herschel* photometry, and replace it with scaled *Spitzer* spectra.

## H.3 Features of Low-metallicity Galaxy Templates

Figure H.3 compares the 19 low-metallicity templates with the normal SF galaxy templates in Rieke et al. (2009). The SEDs of these dwarf galaxies show a lot of variation. Compared with the solar-metallicity galaxies, the low-metallicity infrared SEDs derived in this work tend to have the following features:

- Higher far-IR dust temperature. For the low-metallicity galaxies, the typical dust temperature is $T_{\rm dust} = 34 \pm 7.7$. Our value is similar to the result by Rémy-Ruyer et al. (2013) ($T_{\rm dust} \sim 32$K). Compared with the *Herschel* KINGFISH sample ($T_{\rm dust} \sim 23$K, Rémy-Ruyer et al. 2013), which contains more metal-rich environments, the dust in these low-metallicity systems is generally warmer;

- Steeply rising mid-IR continua. For low-metallicity galaxies in this work, the mid-IR continua slope $\alpha = 3.8 \pm 0.8$, which is much larger than typical values in normal galaxies ($\alpha = 2.0 \pm 0.5$ in Casey 2012; 1.7-2.2 in Blain et al. 2003);

- Weaker aromatic features. The contribution of aromatic features to the infrared SED of low-metallicity galaxies is substantially lower than normal galaxies. The weaker aromatic features with decreasing metallicity have been reported by many authors (e.g., Engelbracht et al., 2005, 2008; Madden et al., 2006).

All of these features can be explained by a rich population of small (and/or hot) grains in the low-metallicity environments (e.g., Madden et al. 2006). In addition, some authors also report mm excess emission in these dwarf systems (e.g., Galliano et al. 2003, 2005;

Table H.1. Low-metallicity Galaxies Used to Derive the Templates

| Source (1) | 12+log(O/H) (2) | $T_{dust}$ (K) (3) | $\beta$ (4) | $\alpha$ (5) | Mid-IR Spectrum? (6) |
|---|---|---|---|---|---|
| Haro 11 | 8.36±0.01 | 46.5±1.0 | 1.89 | 3.63 | good |
| Haro 3 | 8.28±0.01 | 32.3±0.9 | 1.66 | 3.20 | limited |
| He 2-10 | 8.43±0.01 | 36.1±0.7 | 1.62 | 3.32 | good |
| HS 0017+1055 | 7.63±0.10 | 50.9±8.2 | 1.03 | 2.50 | good |
| HS 0052+2536 | 8.04±0.10 | 33.4±2.1 | 1.19 | 3.50 | good |
| HS 1304+3529 | 7.93±0.10 | 33.9±2.6 | 1.60 | 3.92 | good |
| IC 10 | 8.17±0.03 | 34.3±0.8 | 1.57 | 6.23 | poor |
| Mrk 1089 | 8.10±0.08 | 29.5±1.0 | 1.65 | 3.26 | good |
| Mrk 1450 | 7.84±0.01 | 40.6±1.5 | 1.39 | 3.91 | good |
| Mrk 153 | 7.86±0.04 | 33.3±2.3 | 1.90 | 3.82 | good |
| Mrk 209 | 7.74±0.01 | 38.4±1.2 | 1.63 | 4.14 | limited |
| Mrk 930 | 8.03±0.01 | 29.2±1.7 | 1.93 | 3.70 | good |
| NGC 1140 | 8.38±0.01 | 27.4±1.0 | 1.77 | 3.01 | good |
| NGC 4214 | 8.26±0.01 | 23.3±0.7 | 1.41 | 3.75 | limited |
| SBS 1415+437 | 7.55±0.01 | 38.9±3.2 | 1.23 | 4.14 | limited |
| UM 311 | 8.36±0.01 | 20.4±0.7 | 1.78 | 4.41 | limited |
| UM 448 | 8.32±0.01 | 31.3±1.0 | 2.03 | 3.30 | good |
| UM 461 | 7.73±0.01 | 40.0±2.0 | 0.90 | 3.40 | good |
| VII Zw 403 | 7.66±0.01 | 27.6±1.8 | 1.91 | 4.49 | good |

Note. — Col. (1): The galaxy name; Col. (2) The metallicity 12+log(O/H); Col. (3): The dust temperature derived from the CMC fit (see text); Col. (4): The far-IR emission index; Col. (5): The mid-IR power-law index; Col. (6): The existence of the mid-IR *Spitzer* spectrum: *good* – the galaxy has full range $5-35\mu$m mid-IR spectrum; *limited* – the galaxy has mid-IR spectrum with limited coverage; *poor* – IC 10 is quite extended, as judged from its MIPS $24\mu$m image, making the *Spitzer* spectrum a poor reflection of the overall mid-IR continuum.

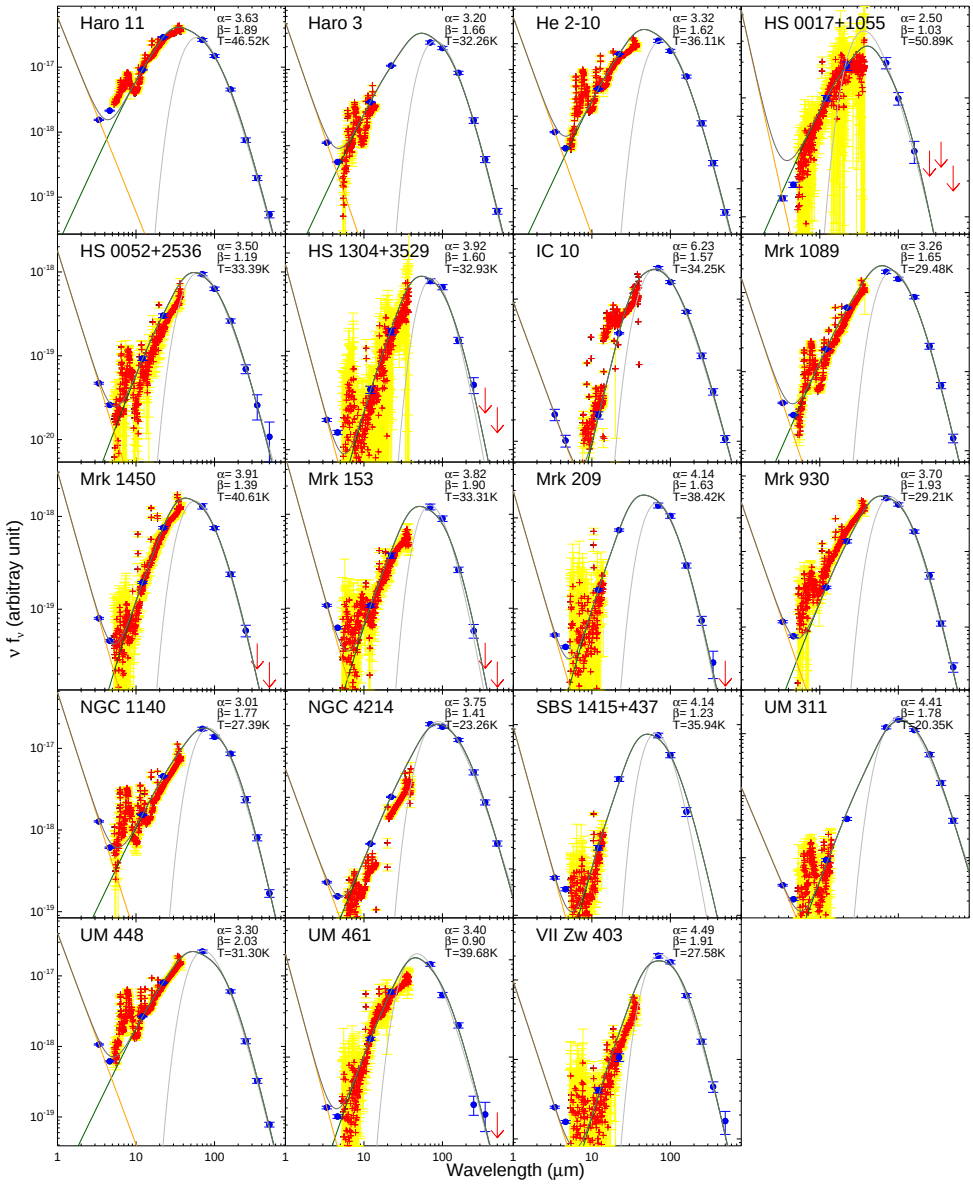


Figure H.1 IR SEDs of the 19 DGS galaxies. Blue circles are for detections and red down arrows are for upper limits. The available *Spitzer*/IRS spectrum for each source (red crosses for the flux, yellow shadows for the flux error) is also plotted. We first subtract the stellar light in the SED by assuming a Rayleigh-Jeans tail scaled by the WISE W1 band data point, then fit the data points at 8-1000$\mu$m with the modified blackbody + mid-IR power-law model (namely, CMC fits, green lines). The final model SED is shown as dark grey lines. The $T$, $\alpha$, and $\beta$ parameters derived from the CMC fits are indicated on the right up corner of each panel. In a similar fashion as Rémy-Ruyer et al. (2013), a single modified blackbody is also fit to the *Herschel* data points for comparison (light grey line).

Galametz et al. 2009). Since the origin of this excess is not clear and its contribution to the infrared luminosity is tiny, we do not consider it in this work.

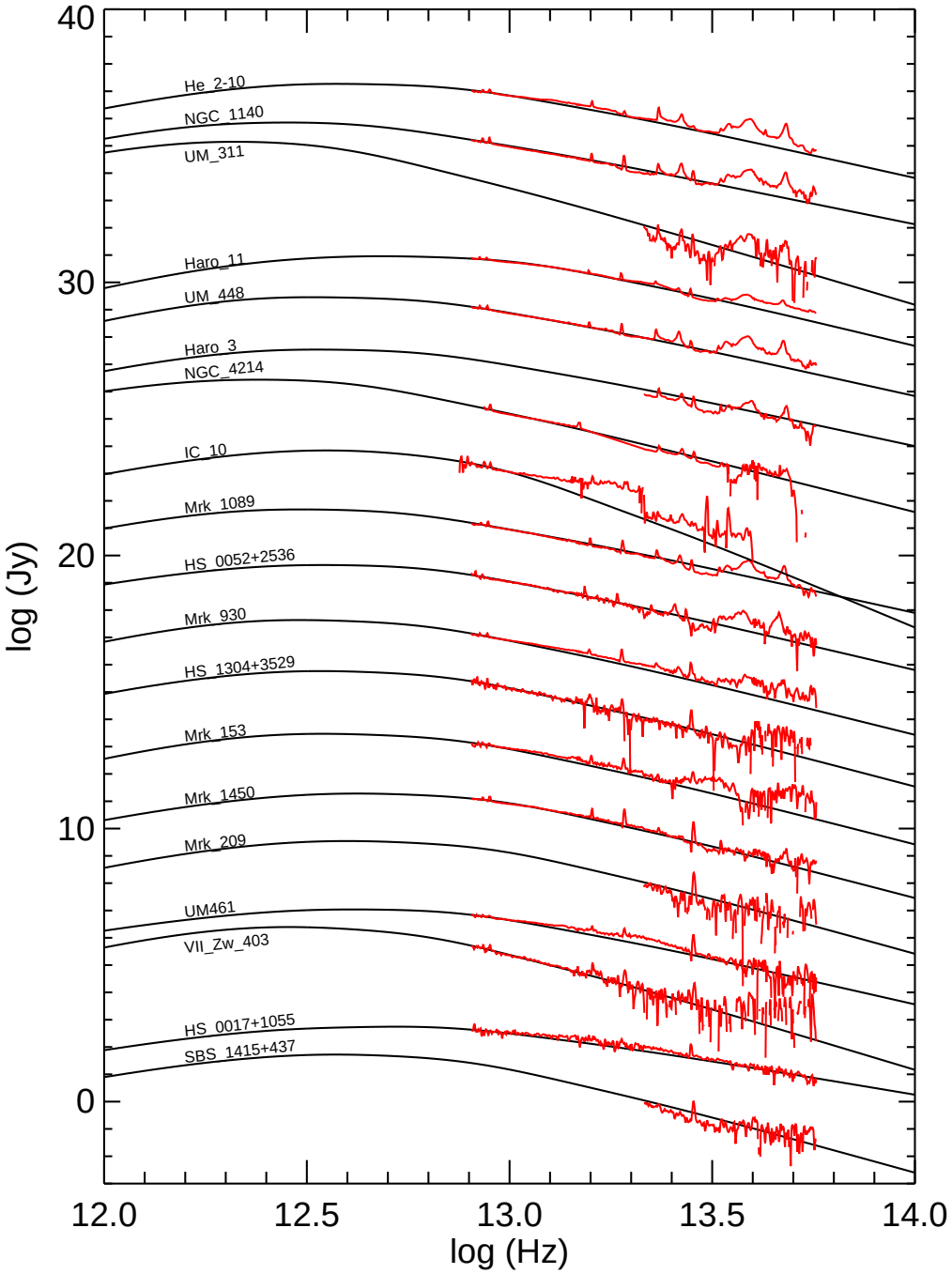


Figure H.2 Full IR SEDs of the 19 DGS galaxies that have *Spitzer*/IRS low-resolution spectra with high enough S/N, sequenced by their metallicity with the lowest at the bottom. The *Spitzer* spectra are scaled to match the continuum SEDs.

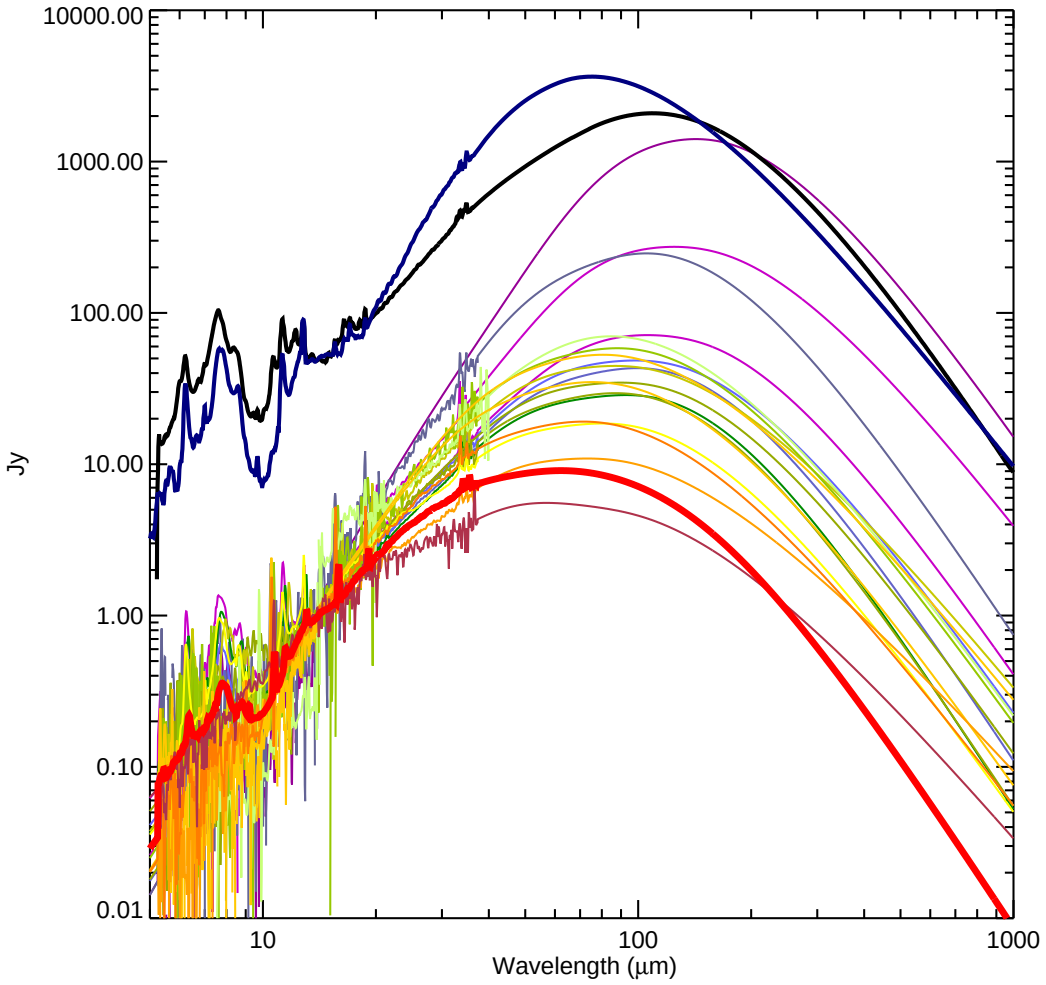


Figure H.3 Family of full IR SEDs of the 19 DGS galaxies, normalized at rest-frame 14 $\mu$m (bottom group). We use thick red line to highlight the SED of Haro 11. For comparison, we present two normal SF SED templates in Rieke et al. (2009): $\log(L/L_{\odot})$= 12 (thick blue line), 11 (thick black line).

APPENDIX I

# STAR FORMATION IN DWARF GALAXIES

## I.1 Star Formation Determination

The star formation rate can be estimated by the 8-1000 $\mu$m infrared emission, following the Kennicutt (1998) star formation law,

$$\mathrm{SFR}(\mathrm{IR}, M_\odot/\mathrm{yr}) = 4.5 \times 10^{-44} L(\mathrm{IR}, \mathrm{erg/s}) \ . \tag{I.1.1}$$

This relation is widely used for high-$z$ galaxies though it was originally established for star-bursting galaxies. However, it is not clear if and how it is valid for low-metallicity dwarf galaxies.

In general, the star formation in a galaxy can be both dust-obscured and dust-unobscured. For unobscured star formation, tracers that probe direct stellar light (e.g., the GALEX FUV at 0.153$\mu$m) or ionized gas tracers (e.g., H$\alpha$, Pa$\alpha$) are used. For dwarf galaxies, Lee et al. (2009) find FUV has a better performance than $H\alpha$ to trace the star formation, since the latter tends to underpredict the total SFR relative to the FUV for low luminosity systems. Therefore we use the FUV star formation law derived in Salim et al. (2007), a study that includes dwarf galaxies, to calculate the dust-unobscured star formation rate:

$$\mathrm{SFR}(\mathrm{FUV}, M_\odot/\mathrm{yr}) = 1.08 \times 10^{-28} L_\nu(\mathrm{FUV}, \mathrm{erg/s/hz}) \ . \tag{I.1.2}$$

The dust-obscured star formation can be determined from the dust-processed light at wavelengths where dust emission dominates (e.g., the 24 $\mu$m emission, the total infrared emission). We use MIPS 24$\mu$m star formation law in Rieke et al. (2009):

$$\mathrm{SFR}(24\mu\mathrm{m}, M_\odot/\mathrm{yr}) = 2.02 \times 10^{-43} L(24\mu\mathrm{m}, \mathrm{erg/s}) \ . \tag{I.1.3}$$

The final star formation rates of these dwarf galaxies are assumed to be a sum of these two components, which will be compared with that derived from the total infrared luminosity (Equation I.1.1).

We collect GALEX FUV and MIPS 24$\mu$m data to derive the star formation. All of the 19 dwarf galaxies above have MIPS 24 $\mu$m observations, and 14/19 have GALEX FUV observations. We retrieve their photometry from the catalog of Spitzer Enhanced Imaging Products[1] and the GALEX offical online catalog[2]. IC10, NGC 4214, UM 311, VII Zw 403 are either too extended or have a close companion in their MIPS 24 $\mu$m images, thus they were removed from the comparison. GALEX FUV photometry can be found for all sources with MIPS observations.

In Figure I.1, we compare the star formation rates derived from the 8-1000$\mu$m infrared emission and those derived from the combined GALEX FUV and MIPS 24$\mu$m emission. Within a three order-of-magnitude dynamical range, the star formation rates from these two approaches are generally consistent, without any obvious offset due to metallicity effect. Thus, we conclude the behavior of Kennicutt (1998) $L_{\rm TIR}$ star formation law is similar to other star formation indicators for the population of dwarf galaxies, at least for those studied in this work, and not very sensitive to metallicity.

[1] http://irsa.ipac.caltech.edu/data/SPITZER/Enhanced/SEIP/overview.html
[2] http://galex.stsci.edu/GalexView/

Table I.1. The star formation rates of the dwarf galaxies

| Source | 12+(O/H) | $L_{\rm IR}$ ($10^{11}L_{\odot}$) | $\rm SFR_{IR}$ ($M_{\odot}$/yr) | $\rm SFR_{FUV}$ ($M_{\odot}$/yr) | $\rm SFR_{24\mu m}$ ($M_{\odot}$/yr) | $\rm SFR_{FUV+24\mu m}$ ($M_{\odot}$/yr) |
|---|---|---|---|---|---|---|
| (1) | (2) | (3) | (4) | (5) | (6) | (7) |
| Haro 11 | 8.36±0.01 | 1.77 | 30.60 | 3.37 | 56.06 | 59.43 |
| Haro 3 | 8.28±0.01 | 0.057 | 0.99 | 0.22 | 0.82 | 1.04 |
| He 2-10 | 8.43±0.01 | 0.061 | 1.05 | – | 1.13 | – |
| HS 0017+1055 | 7.63±0.10 | 0.0095 | 0.16 | – | 0.26 | – |
| HS 0052+2536 | 8.04±0.10 | 0.18 | 3.07 | 1.57 | 1.88 | 3.45 |
| HS 1304+3529 | 7.93±0.01 | 0.017 | 0.30 | – | 0.18 | – |
| IC 10 | 8.17±0.03 | 0.000055 | 0.00095 | – | – | – |
| Mrk 1089 | 8.10±0.08 | 0.35 | 6.10 | 2.40 | 3.49 | 5.89 |
| Mrk 1450 | 7.84±0.01 | 0.0030 | 0.053 | – | 0.064 | – |
| Mrk 153 | 7.86±0.04 | 0.0098 | 0.17 | 0.67 | 0.12 | 0.79 |
| Mrk 209 | 7.74±0.01 | 0.00029 | 0.0051 | 0.012 | 0.0046 | 0.017 |
| Mrk 930 | 8.03±0.01 | 0.16 | 2.78 | 1.13 | 2.70 | 3.83 |

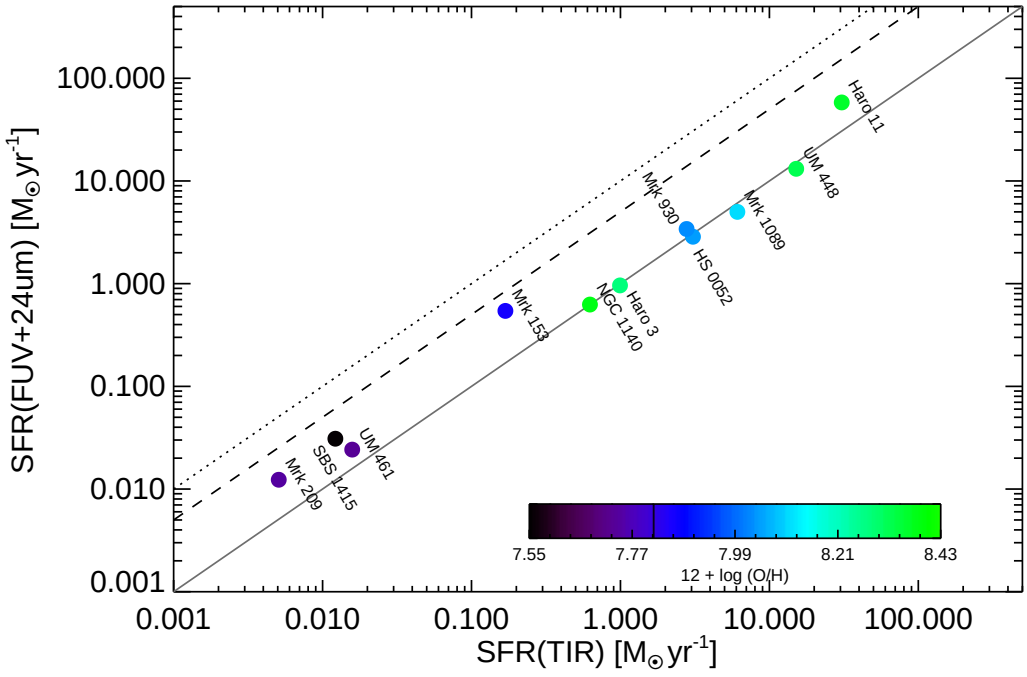


Figure I.1 Comparison of star formation rates (SFRs) from the total infrared luminosity (8-1000 $\mu$m) and those from GALEX FUV + MIPS 24 $\mu$m. The colors code the metallicity 12+log(O/H). As a guide to the eye, we also show the one-to-one (gray solid line), one-to-five (gray dashed line), and one-to-ten (gray dotted line) lines.

### I.1.1 Star Formation Law of Haro 11

As discussed in Section 6.2, Haro 11 was selected as the candidate galaxy template for high-$z$ galaxies. With ample observations presented in the literature, its star formation rate can be estimated using various star-formation indicators, including the 8-1000 $\mu$m infrared luminosity, MIPS 24 $\mu$m emission, H$\alpha$ emission-line luminosity, and FUSE/GALEX FUV luminosity. Following the calibrations listed above, we estimate its star formation rates and summarize these results in Table I.2.

The SFR determined from the 24 $\mu$m emission is $\sim$ 1.8 times higher than that from either $L_{\rm IR}$ or $L(H\alpha)$. This discrepancy is a direct consequence of its hot SED (Engelbracht et al., 2008) and the resulting large fraction of its $L_{\rm IR}$ emitted at 24 $\mu$m (see Figure I.2)[3]. Given

[3]Another galaxy with SFR(24$\mu$m)/SFR(FIR)$>$ 1.25 in our low-metallicty galaxy sample is Mrk 153, which hosts an AGN that boosts the mid-IR emission.

Table I.1 (cont'd)

| Source | 12+(O/H) | $L_{\rm IR}$ ($10^{11} L_\odot$) | $\rm SFR_{IR}$ ($M_\odot$/yr) | $\rm SFR_{FUV}$ ($M_\odot$/yr) | $\rm SFR_{24\mu m}$ ($M_\odot$/yr) | $\rm SFR_{FUV+24\mu m}$ ($M_\odot$/yr) |
|---|---|---|---|---|---|---|
| (1) | (2) | (3) | (4) | (5) | (6) | (7) |
| NGC 1140 | 8.38±0.01 | 0.036 | 0.62 | 0.49 | 0.32 | 0.81 |
| NGC 4214 | 8.26±0.01 | 0.0040 | 0.070 | 0.076 | – | – |
| SBS 1415+437 | 7.25±0.01 | 0.00070 | 0.012 | 0.033 | 0.0094 | 0.042 |
| UM 311 | 8.36±0.01 | 0.037 | 0.65 | 0.21 | – | – |
| UM 448 | 8.32±0.01 | 0.88 | 15.15 | 2.19 | 11.76 | 13.95 |
| UM 461 | 7.73±0.01 | 0.00091 | 0.016 | 0.0010 | 0.017 | 0.028 |
| VII Zw 403 | 7.66±0.01 | 0.00016 | 0.0028 | 0.0065 | – | – |

Note. — Objects with '–' in Column (5), (6) do not have corresponding observations or are not point-sources to be included in the catalogs (see text).

Table I.2. Star Formation Rate of Haro 11

| Method | Luminosity ($L_\odot$)[a] | SFR ($M_\odot$/yr) | SFR Law | Reference |
|---|---|---|---|---|
| $L_{\rm IR}$ | $1.8 \times 10^{11}$ | 30.6 | Kennicutt (1998) | this work |
| MIPS 24 $\mu$m | $6.7 \times 10^{10}$ | 56.1 | Rieke et al. (2009) | this work |
| H$\alpha$ (Fabry-Perot)[b] | $1.3 \times 10^{9}$ | 39.1 | Kennicutt et al. (1994) | Östlin et al. (1999) |
| H$\alpha$ (HST image)[b] | $8.7 \times 10^{8}$ | 25.7 | Kennicutt et al. (1994) | Östlin et al. (2009) |
| GALEX FUV (0.153$\mu$m)[c] | $1.6 \times 10^{10}$ | 3.4 | Salim et al. (2007) | this work |
| FUSE FUV (0.115$\mu$m)[c] | $2.2 \times 10^{10}$ | 4.5 | Kennicutt (1998) | Grimes et al. (2007) |

Note. — [a] All luminosities are scaled to the distance 92.1 Mpc (Bergvall et al., 2006). [b] We corrected the $H\alpha$ extinction based on the observed Balmer decrement $H\alpha/H\beta = 4.08$ (Bergvall & Östlin, 2002) with the assumption of an intrinsic ratio 2.85 and a Calzetti (2001) extinction law. The attenuation at V-band is estimated to be $A_V = 0.95$, suggesting the intrinsic H$\alpha$ flux would be a factor of 1.34 larger than the observed. [c] For the UV band, since we do not make extinction corrections, the SFR(FUV) listed here are only for unobscured star formation.

the close agreement in the SFRs from H$\alpha$ and $L_{\rm IR}$, we conclude that Haro 11 falls above the trend line in Figure I.1 because FUV+24 $\mu$m overestimates the SFR and $L_{\rm IR}$ gives a valid estimate. Moreover, since Haro 11 presents very young stellar populations (Adamo et al., 2010), the contamination of emission from old stars to the far infrared emission is negligible, which makes the $L_{\rm IR}$, following the Kennicutt (1998) SF law, a robust tracer of the obscured star formation

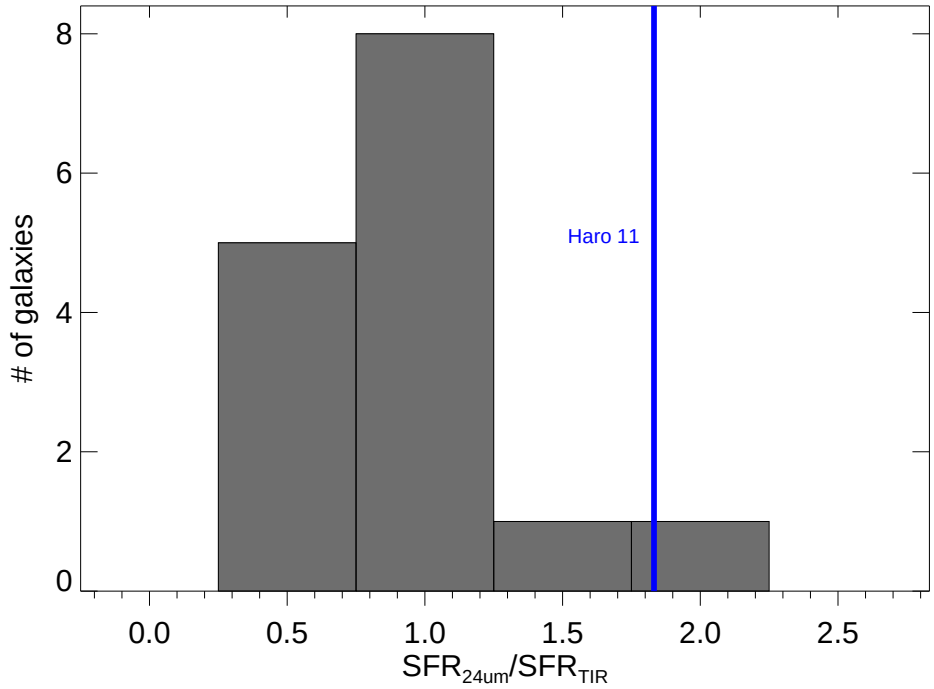


Figure I.2 Histogram of the ratio between the 24$\mu$m-based SFR and $L_{\rm IR}$-based SFR of dwarf galaxies. Haro 11 has a SFR(24$\mu$m)/SFR(TIR) 1.82 as denoted in the blue line.

We use the FUV luminosity based on GALEX observation and assume the star formation law in Salim et al. (2007) to estimate the unobscured star formation. The final adopted star formation rate of Haro 11, which is 34.0 $M_{\odot}$/yr, is based on a combination of GALEX FUV emission and the 8-1000 $\mu$m infrared emission. We can finally relate the infrared luminosity and FUV luminosity of Haro 11 to its total star formation rate, which includes both the obscured and the unobscured, as

$$\mathrm{SFR}_{\mathrm{Haro\ 11}}(M_{\odot}/\mathrm{yr}) = 5.00 \times 10^{-44} L(\mathrm{IR}, \mathrm{erg/s}) \tag{I.1.4}$$

$$= 1.92 \times 10^{-10} L(\mathrm{IR}, \mathrm{L}_{\odot}) \tag{I.1.5}$$

This is the star formation law used for the Haro 11 template in the main part of this paper.

# REFERENCES

1988, Infrared Astronomical Satellite (IRAS) Catalogs and Atlases.Volume 1: Explanatory Supplement., Vol. 1

Abazajian, K. N., Adelman-McCarthy, J. K., Agüeros, M. A., et al. 2009, ApJS, 182, 543

Abrahamyan, H. V., Mickaelian, A. M., & Knyazyan, A. V. 2015, Astronomy and Computing, 10, 99

Adamo, A., Östlin, G., Zackrisson, E., et al. 2010, MNRAS, 407, 870

Aitken, D. K., & Roche, P. F. 1985, MNRAS, 213, 777

Akylas, A., Georgantopoulos, I., Georgakakis, A., Kitsionas, S., & Hatziminaoglou, E. 2006, A&A, 459, 693

Alam, S., Albareti, F. D., Allende Prieto, C., et al. 2015, ApJS, 219, 12

Alexander, D. M., & Hickox, R. C. 2012, New A Rev., 56, 93

Alexander, T., Sturm, E., Lutz, D., et al. 1999, ApJ, 512, 204

Almeyda, T., Robinson, A., Richmond, M., Vazquez, B., & Nikutta, R. 2017, ApJ, 843, 3

Alonso-Herrero, A., Quillen, A. C., Rieke, G. H., Ivanov, V. D., & Efstathiou, A. 2003, AJ, 126, 81

Alonso-Herrero, A., Pérez-González, P. G., Alexand er, D. M., et al. 2006, ApJ, 640, 167

Alonso-Herrero, A., Ramos Almeida, C., Mason, R., et al. 2011, ApJ, 736, 82

Alonso-Herrero, A., Ramos Almeida, C., Esquej, P., et al. 2014, MNRAS, 443, 2766

Alonso-Herrero, A., Pereira-Santaella, M., García-Burillo, S., et al. 2018, ApJ, 859, 144

Alonso-Herrero, A., García-Burillo, S., Pereira-Santaella, M., et al. 2019, A&A, 628, A65

Antonucci, R. 1993, ARA&A, 31, 473

—. 2015, ArXiv e-prints

Armus, L., Mazzarella, J. M., Evans, A. S., et al. 2009, PASP, 121, 559

Asmus, D., Gandhi, P., Hönig, S. F., Smette, A., & Duschl, W. J. 2015, MNRAS, 454, 766

Asmus, D., Hönig, S. F., & Gandhi, P. 2016, ApJ, 822, 109

Asmus, D., Hönig, S. F., Gandhi, P., Smette, A., & Duschl, W. J. 2014, MNRAS, 439, 1648

Assef, R. J., Stern, D., Noirot, G., et al. 2018, ApJS, 234, 23

Assef, R. J., Kochanek, C. S., Brodwin, M., et al. 2010, ApJ, 713, 970

Assef, R. J., Stern, D., Kochanek, C. S., et al. 2013, ApJ, 772, 26

Assef, R. J., Eisenhardt, P. R. M., Stern, D., et al. 2015, ApJ, 804, 27

Auld, R., Bianchi, S., Smith, M. W. L., et al. 2013, MNRAS, 428, 1880

Bañados, E., Venemans, B. P., Morganson, E., et al. 2014, AJ, 148, 14

Baes, M., Verstappen, J., De Looze, I., et al. 2011, ApJS, 196, 22

Baes, M., Davies, J. I., Dejonghe, H., et al. 2003, MNRAS, 343, 1081

Ballantyne, D. R. 2008, ApJ, 685, 787

Ballo, L., Giustini, M., Schartel, N., et al. 2008, A&A, 483, 137

Barger, A. J., Cowie, L. L., Mushotzky, R. F., et al. 2005, AJ, 129, 578

Barnett, R., Warren, S. J., Banerji, M., et al. 2015, A&A, 575, A31

Barvainis, R. 1987, ApJ, 320, 537

—. 1990, ApJ, 353, 419

—. 1992, ApJ, 400, 502

Baskin, A., & Laor, A. 2005, MNRAS, 356, 1029

—. 2018, MNRAS, 474, 1970

Beckert, T., & Duschl, W. J. 2004, A&A, 426, 445

Beelen, A., Cox, P., Benford, D. J., et al. 2006, ApJ, 642, 694

Behar, E. 2009, ApJ, 703, 1346

Bell, E. F., McIntosh, D. H., Katz, N., & Weinberg, M. D. 2003, ApJS, 149, 289

Bennert, N., Jungwiert, B., Komossa, S., Haas, M., & Chini, R. 2006a, A&A, 459, 55

—. 2006b, A&A, 456, 953

Bennett, C. L., Halpern, M., Hinshaw, G., et al. 2003, ApJS, 148, 1

Bergvall, N., & Östlin, G. 2002, A&A, 390, 891

Bergvall, N., Zackrisson, E., Andersson, B.-G., et al. 2006, A&A, 448, 513

Berriman, G., Schmidt, G. D., West, S. C., & Stockman, H. S. 1990, ApJS, 74, 869

Berta, S., Lutz, D., Santini, P., et al. 2013, A&A, 551, A100

Bertin, E., & Arnouts, S. 1996, A&AS, 117, 393

Bertoldi, F., & Cox, P. 2002, A&A, 384, L11

Bianchi, L., Conti, A., & Shiao, B. 2014, Advances in Space Research, 53, 900

Bianchi, S., Maiolino, R., & Risaliti, G. 2012, Advances in Astronomy, 2012, 782030

Bitsakis, T., Charmandaris, V., Appleton, P. N., et al. 2014, A&A, 565, A25

Blain, A. W., Barnard, V. E., & Chapman, S. C. 2003, MNRAS, 338, 733

Blandford, R. D., & McKee, C. F. 1982, ApJ, 255, 419

Bock, J. J., Neugebauer, G., Matthews, K., et al. 2000, AJ, 120, 2904

Bongiorno, A., Zamorani, G., Gavignaud, I., et al. 2007, A&A, 472, 443

Bongiorno, A., Merloni, A., Brusa, M., et al. 2012, MNRAS, 427, 3103

Bongiorno, A., Schulze, A., Merloni, A., et al. 2016, A&A, 588, A78

Boquien, M., Burgarella, D., Roehlly, Y., et al. 2019, A&A, 622, A103

Boroson, T. A., & Green, R. F. 1992, ApJS, 80, 109

Braatz, J. A., Wilson, A. S., Gezari, D. Y., Varosi, F., & Beichman, C. A. 1993, ApJ, 409, L5

Bressan, A., Granato, G. L., & Silva, L. 1998, A&A, 332, 135

Bressan, A., Panuzzo, P., Buson, L., et al. 2006, ApJ, 639, L55

Brocksopp, C., Starling, R. L. C., Schady, P., et al. 2006, MNRAS, 366, 953

Bruzual, G., & Charlot, S. 2003, MNRAS, 344, 1000

Burtscher, L., Meisenheimer, K., Tristram, K. R. W., et al. 2013, A&A, 558, A149

Cai, Z., Fan, X., Noterdaeme, P., et al. 2014, ApJ, 793, 139

Calderone, G., Sbarrato, T., & Ghisellini, G. 2012, MNRAS, 425, L41

Calistro Rivera, G., Lusso, E., Hennawi, J. F., & Hogg, D. W. 2016, ApJ, 833, 98

Calura, F., Gilli, R., Vignali, C., et al. 2014, MNRAS, 438, 2765

Calzetti, D. 2001, PASP, 113, 1449

Calzetti, D., Wu, S.-Y., Hong, S., et al. 2010, ApJ, 714, 1256

Cameron, M., Storey, J. W. V., Rotaciuc, V., et al. 1993, ApJ, 419, 136

Cao, X. 2009, MNRAS, 394, 207

Caputi, K. I. 2014, International Journal of Modern Physics D, 23, 1430015

Carey, S. J. 2010, in Hubble after SM4. Preparing JWST, 37

Carilli, C. L., & Walter, F. 2013, ARA&A, 51, 105

Carini, M. T., Noble, J. C., Taylor, R., & Culler, R. 2007, AJ, 133, 303

Casey, C. M. 2012, MNRAS, 425, 3094

Casey, C. M., Narayanan, D., & Cooray, A. 2014, Phys. Rep., 541, 45

Cassarà, L. P., Piovan, L., Weiss, A., Salaris, M., & Chiosi, C. 2013, MNRAS, 436, 2824

Chary, R., & Elbaz, D. 2001, ApJ, 556, 562

Ciesla, L., Boquien, M., Boselli, A., et al. 2014, A&A, 565, A128

Ciesla, L., Charmandaris, V., Georgakakis, A., et al. 2015, A&A, 576, A10

Clavel, J., Wamsteker, W., & Glass, I. S. 1989, ApJ, 337, 236

Cohen, M. H., Lister, M. L., Homan, D. C., et al. 2007, ApJ, 658, 232

Collinson, J. S., Ward, M. J., Landt, H., et al. 2017, MNRAS, 465, 358

Comastri, A., Brunetti, G., Dallacasa, D., et al. 2003, MNRAS, 340, L52

Combes, F., García-Burillo, S., Audibert, A., et al. 2019, A&A, 623, A79

Corral, A., Della Ceca, R., Caccianiga, A., et al. 2011, A&A, 530, A42

Corrales, L. R., García, J., Wilms, J., & Baganoff, F. 2016, MNRAS, 458, 1345

Cox, P., Krips, M., Neri, R., et al. 2011, ApJ, 740, 63

Crenshaw, D. M., Kraemer, S. B., & George, I. M. 2003, ARA&A, 41, 117

Cullen, F., Cirasuolo, M., McLure, R. J., Dunlop, J. S., & Bowler, R. A. A. 2014, MNRAS, 440, 2300

Cutri, R. M., Nelson, B. O., Francis, P. J., & Smith, P. S. 2002, in Astronomical Society of the Pacific Conference Series, Vol. 284, IAU Colloq. 184: AGN Surveys, ed. R. F. Green, E. Y. Khachikian, & D. B. Sanders, 127

Cutri, R. M., Nelson, B. O., Kirkpatrick, J. D., Huchra, J. P., & Smith, P. S. 2001, in Astronomical Society of the Pacific Conference Series, Vol. 232, The New Era of Wide Field Astronomy, ed. R. Clowes, A. Adamson, & G. Bromage, 78

Cutri, R. M., Wisniewski, W. Z., Rieke, G. H., & Lebofsky, M. J. 1985, ApJ, 296, 423

Czerny, B., & Hryniewicz, K. 2011, A&A, 525, L8

Czerny, B., Li, J., Loska, Z., & Szczerba, R. 2004, MNRAS, 348, L54

da Cunha, E., Groves, B., Walter, F., et al. 2013, ApJ, 766, 13

Daddi, E., Dickinson, M., Chary, R., et al. 2005, ApJ, 631, L13

Daddi, E., Dickinson, M., Morrison, G., et al. 2007, ApJ, 670, 156

Dale, D. A., & Helou, G. 2002, ApJ, 576, 159

Dale, D. A., Helou, G., Magdis, G. E., et al. 2014, ApJ, 784, 83

De Rosa, G., Decarli, R., Walter, F., et al. 2011, ApJ, 739, 56

De Rossi, M. E., Rieke, G. H., Shivaei, I., Bromm, V., & Lyu, J. 2018, ApJ, 869, 4

de Vries, W. H., Becker, R. H., White, R. L., & Loomis, C. 2005, AJ, 129, 615

Del Moro, A., Alexander, D. M., Bauer, F. E., et al. 2016, MNRAS, 456, 2105

Delvecchio, I., Gruppioni, C., Pozzi, F., et al. 2014, MNRAS, 439, 2736

Denney, K. D., Peterson, B. M., Pogge, R. W., et al. 2010, ApJ, 721, 715

Deo, R. P., Richards, G. T., Crenshaw, D. M., & Kraemer, S. B. 2009, ApJ, 705, 14

Devereux, N. A., & Eales, S. A. 1989, ApJ, 340, 708

di Clemente, A., Giallongo, E., Natali, G., Trevese, D., & Vagnetti, F. 1996, ApJ, 463, 466

Di Matteo, T., Springel, V., & Hernquist, L. 2005, Nature, 433, 604

Diamond-Stanic, A. M., & Rieke, G. H. 2010, ApJ, 724, 140

—. 2012, ApJ, 746, 168

Diamond-Stanic, A. M., Rieke, G. H., & Rigby, J. R. 2009, ApJ, 698, 623

Díaz-Santos, T., Assef, R. J., Blain, A. W., et al. 2016, ApJ, 816, L6

Dicken, D., Tadhunter, C., Axon, D., et al. 2010, ApJ, 722, 1333

Dicken, D., Tadhunter, C., Morganti, R., et al. 2008, ApJ, 678, 712

Dong, X. Y., & Wu, X.-B. 2016, ApJ, 824, 70

Donley, J. L., Koekemoer, A. M., Brusa, M., et al. 2012, ApJ, 748, 142

Doroshenko, V. T., Lyuty, V. M., Bochkarev, N. G., et al. 2001, Astronomy Letters, 27, 65

Draine, B. T., & Lee, H. M. 1984, ApJ, 285, 89

Drake, A. J., Djorgovski, S. G., Mahabal, A., et al. 2009, ApJ, 696, 870

Dullemond, C. P., & van Bemmel, I. M. 2005, A&A, 436, 47

Dunne, L., & Eales, S. A. 2001, MNRAS, 327, 697

Dwek, E., Staguhn, J. G., Arendt, R. G., et al. 2011, ApJ, 738, 36

Dye, S., Warren, S. J., Hambly, N. C., et al. 2006, MNRAS, 372, 1227

Edelson, R. A., & Malkan, M. A. 1986, ApJ, 308, 59

Efstathiou, A. 2006, MNRAS, 371, L70

Efstathiou, A., & Rowan-Robinson, M. 1995, MNRAS, 273, 649

Eisenhardt, P. R. M., Wu, J., Tsai, C.-W., et al. 2012, ApJ, 755, 173

Elvis, M., Marengo, M., & Karovska, M. 2002, ApJ, 567, L107

Elvis, M., Wilkes, B. J., McDowell, J. C., et al. 1994, ApJS, 95, 1

Elvis, M., Hao, H., Civano, F., et al. 2012, ApJ, 759, 6

Engelbracht, C. W., Gordon, K. D., Rieke, G. H., et al. 2005, ApJ, 628, L29

Engelbracht, C. W., Rieke, G. H., Gordon, K. D., et al. 2008, ApJ, 678, 804

Engelbracht, C. W., Blaylock, M., Su, K. Y. L., et al. 2007, PASP, 119, 994

Enya, K., Yoshii, Y., Kobayashi, Y., et al. 2002a, ApJS, 141, 31

—. 2002b, ApJS, 141, 45

Esquej, P., Alonso-Herrero, A., González-Martín, O., et al. 2014, ApJ, 780, 86

Fabian, A. C. 1999, MNRAS, 308, L39

Fan, L., Han, Y., Nikutta, R., Drouart, G., & Knudsen, K. K. 2016, ApJ, 823, 107

Fan, L., Knudsen, K. K., Fogasy, J., & Drouart, G. 2018, ApJ, 856, L5

Fan, X., Hennawi, J. F., Richards, G. T., et al. 2004, AJ, 128, 515

Fan, X., Strauss, M. A., Becker, R. H., et al. 2006, AJ, 132, 117

Faucher-Giguère, C.-A., & Quataert, E. 2012, MNRAS, 425, 605

Feltre, A., Hatziminaoglou, E., Fritz, J., & Franceschini, A. 2012, MNRAS, 426, 120

Feruglio, C., Fiore, F., Carniani, S., et al. 2015, A&A, 583, A99

Finley, H., Petitjean, P., Pâris, I., et al. 2013, A&A, 558, A111

Fisher, D. B., Bolatto, A. D., Herrera-Camus, R., et al. 2014, Nature, 505, 186

Fitzpatrick, E. L. 1999, PASP, 111, 63

Fritz, J., Franceschini, A., & Hatziminaoglou, E. 2006, MNRAS, 366, 767

Fuller, L., Lopez-Rodriguez, E., Packham, C., et al. 2016, MNRAS, 462, 2618

Galametz, M., Madden, S., Galliano, F., et al. 2009, A&A, 508, 645

Galametz, M., Kennicutt, R. C., Albrecht, M., et al. 2012, MNRAS, 425, 763

Gallagher, S. C., Schmidt, G. D., Smith, P. S., et al. 2005, ApJ, 633, 71

Galliano, F., Madden, S. C., Jones, A. P., Wilson, C. D., & Bernard, J.-P. 2005, A&A, 434, 867

Galliano, F., Madden, S. C., Jones, A. P., et al. 2003, A&A, 407, 159

Gallimore, J. F., Yzaguirre, A., Jakoboski, J., et al. 2010, ApJS, 187, 172

Gallimore, J. F., Elitzur, M., Maiolino, R., et al. 2016, ApJ, 829, L7

Gallo, L. C., Grupe, D., Schartel, N., et al. 2011, MNRAS, 412, 161

Gandhi, P., Hönig, S. F., & Kishimoto, M. 2015, ApJ, 812, 113

García-Burillo, S., Combes, F., Usero, A., et al. 2014, A&A, 567, A125

García-Burillo, S., Combes, F., Ramos Almeida, C., et al. 2016, ApJ, 823, L12

García-González, J., Alonso-Herrero, A., Hernán-Caballero, A., et al. 2016, MNRAS, 458, 4512

Gaskell, C. M., & Benker, A. J. 2007, ArXiv e-prints

Gaskell, C. M., Goosmann, R. W., Antonucci, R. R. J., & Whysong, D. H. 2004, ApJ, 616, 147

Giustini, M., Cappi, M., Chartas, G., et al. 2011, A&A, 536, A49

Giveon, U., Maoz, D., Kaspi, S., Netzer, H., & Smith, P. S. 1999, MNRAS, 306, 637

Glass, I. S. 2004, MNRAS, 350, 1049

Glikman, E., Helfand, D. J., & White, R. L. 2006, ApJ, 640, 579

González-Lópezlira, R. A., Bruzual-A., G., Charlot, S., Ballesteros-Paredes, J., & Loinard, L. 2010, MNRAS, 403, 1213

González-Martín, O., Masegosa, J., García-Bernete, I., et al. 2019a, ApJ, 884, 10

—. 2019b, ApJ, 884, 11

Gordon, K. D., Rieke, G. H., Engelbracht, C. W., et al. 2005, PASP, 117, 503

Gorjian, V., Werner, M. W., Jarrett, T. H., Cole, D. M., & Ressler, M. E. 2004, ApJ, 605, 156

Goulding, A. D., Alexander, D. M., Bauer, F. E., et al. 2012, ApJ, 755, 5

Goulding, A. D., Zakamska, N. L., Alexandroff, R. M., et al. 2018, ApJ, 856, 4

Graham, M. J., Djorgovski, S. G., Drake, A. J., et al. 2014, MNRAS, 439, 703

—. 2017, MNRAS, 470, 4112

Granato, G. L., & Danese, L. 1994, MNRAS, 268, 235

GRAVITY Collaboration, Dexter, J., Shangguan, J., et al. 2019, arXiv e-prints, arXiv:1910.00593

Green, R. F., Schmidt, M., & Liebert, J. 1986, ApJS, 61, 305

Greve, T. R., Vieira, J. D., Weiß, A., et al. 2012, ApJ, 756, 101

Grimes, J. P., Heckman, T., Strickland, D., et al. 2007, ApJ, 668, 891

Groves, B., Dopita, M., & Sutherland, R. 2006, A&A, 458, 405

Groves, B., Dopita, M. A., Sutherland, R. S., et al. 2008, ApJS, 176, 438

Gu, M. 2013, ApJ, 773, 176

Güver, T., & Özel, F. 2009, MNRAS, 400, 2050

Guyon, O., Sanders, D. B., & Stockton, A. 2006, ApJS, 166, 89

Haas, M., Müller, S. A. H., Chini, R., et al. 2000, A&A, 354, 453

Haas, M., Siebenmorgen, R., Pantin, E., et al. 2007, A&A, 473, 369

Haas, M., Klaas, U., Müller, S. A. H., et al. 2003, A&A, 402, 87

Hall, P. B., Anderson, S. F., Strauss, M. A., et al. 2002, ApJS, 141, 267

Hamann, F., Zakamska, N. L., Ross, N., et al. 2017, MNRAS, 464, 3431

Hamilton, T. S., Casertano, S., & Turnshek, D. A. 2002, ApJ, 576, 61

—. 2008, ApJ, 678, 22

Hanish, D. J., Teplitz, H. I., Capak, P., et al. 2013, ApJ, 768, 13

Hanish, D. J., Capak, P., Teplitz, H. I., et al. 2015, ApJS, 217, 17

Hao, H., Elvis, M., Civano, F., & Lawrence, A. 2011, ApJ, 733, 108

Hao, H., Elvis, M., Civano, F., et al. 2010, ApJ, 724, L59

—. 2014, MNRAS, 438, 1288

Hao, L., Weedman, D. W., Spoon, H. W. W., et al. 2007, ApJ, 655, L77

Hao, L., Strauss, M. A., Tremonti, C. A., et al. 2005a, AJ, 129, 1783

Hao, L., Strauss, M. A., Fan, X., et al. 2005b, AJ, 129, 1795

Hatziminaoglou, E., Hernán-Caballero, A., Feltre, A., & Piñol Ferrer, N. 2015, ApJ, 803, 110

Hayes, M., Östlin, G., Atek, H., et al. 2007, MNRAS, 382, 1465

Heckman, T. M., & Best, P. N. 2014, ARA&A, 52, 589

Henden, A. A., Templeton, M., Terrell, D., et al. 2016, VizieR Online Data Catalog, II/336

Hennawi, J. F., Prochaska, J. X., Kollmeier, J., & Zheng, Z. 2009, ApJ, 693, L49

Hernán-Caballero, A., & Hatziminaoglou, E. 2011, MNRAS, 414, 500

Hernán-Caballero, A., Hatziminaoglou, E., Alonso-Herrero, A., & Mateos, S. 2016, ArXiv e-prints

Hernán-Caballero, A., Alonso-Herrero, A., Hatziminaoglou, E., et al. 2015, ApJ, 803, 109

Heymann, F., & Siebenmorgen, R. 2012, ApJ, 751, 27

Hickox, R. C., & Alexander, D. M. 2018, ARA&A, 56, 625

Ho, L. C. 1999, ApJ, 516, 672

—. 2008, ARA&A, 46, 475

Hodge, J. A., Becker, R. H., White, R. L., Richards, G. T., & Zeimann, G. R. 2011, AJ, 142, 3

Hodge, J. A., Riechers, D., Decarli, R., et al. 2015, ApJ, 798, L18

Hoenig, S. F. 2013, ArXiv e-prints

Höfner, S. 2008, A&A, 491, L1

Homan, D. C. 2012, in International Journal of Modern Physics Conference Series, Vol. 8, International Journal of Modern Physics Conference Series, 163–171

Hönig, S. F. 2019, ApJ, 884, 171

Hönig, S. F., & Beckert, T. 2007, MNRAS, 380, 1172

Hönig, S. F., Beckert, T., Ohnaka, K., & Weigelt, G. 2006, A&A, 452, 459

Hönig, S. F., & Kishimoto, M. 2010a, A&A, 523, A27

—. 2010b, A&A, 523, A27

—. 2017, ApJ, 838, L20

Hönig, S. F., Kishimoto, M., Antonucci, R., et al. 2012, ApJ, 755, 149

Hönig, S. F., Kishimoto, M., Gandhi, P., et al. 2010, A&A, 515, A23

Hönig, S. F., Kishimoto, M., Tristram, K. R. W., et al. 2013, ApJ, 771, 87

Hopkins, A. M., Schulte-Ladbeck, R. E., & Drozdovsky, I. O. 2002, AJ, 124, 862

Hopkins, P. F., Hayward, C. C., Narayanan, D., & Hernquist, L. 2012, MNRAS, 420, 320

Hopkins, P. F., Hernquist, L., Cox, T. J., & Kereš, D. 2008, ApJS, 175, 356

Hopkins, P. F., Hernquist, L., Martini, P., et al. 2005, ApJ, 625, L71

Hopkins, P. F., Richards, G. T., & Hernquist, L. 2007, ApJ, 654, 731

Hopkins, P. F., Torrey, P., Faucher-Giguère, C.-A., Quataert, E., & Murray, N. 2016, MNRAS, 458, 816

Hopkins, P. F., Younger, J. D., Hayward, C. C., Narayanan, D., & Hernquist, L. 2010, MNRAS, 402, 1693

Hopkins, P. F., Strauss, M. A., Hall, P. B., et al. 2004, AJ, 128, 1112

Horst, H., Smette, A., Gandhi, P., & Duschl, W. J. 2006, A&A, 457, L17

Houck, J. R., Roellig, T. L., van Cleve, J., et al. 2004, ApJS, 154, 18

Huang, J.-S., Rigopoulou, D., Magdis, G., et al. 2014, ApJ, 784, 52

Hunter, J. D. 2007, Computing in Science and Engineering, 9, 90

Imanishi, M., Nakanishi, K., & Izumi, T. 2016, ApJ, 822, L10

Imanishi, M., Nakanishi, K., Izumi, T., & Wada, K. 2018, ApJ, 853, L25

Isobe, T., Feigelson, E. D., & Nelson, P. I. 1986, ApJ, 306, 490

Ivezic, Z., & Elitzur, M. 1997, MNRAS, 287, 799

Ivezic, Z., Nenkova, M., Heymann, F., & Elitzur, M. 2017, User Manual for DUSTY (V4)

Izumi, T., Wada, K., Fukushige, R., Hamamura, S., & Kohno, K. 2018, ApJ, 867, 48

Jahnke, K., Bongiorno, A., Brusa, M., et al. 2009, ApJ, 706, L215

James, B. L., Tsamis, Y. G., Walsh, J. R., Barlow, M. J., & Westmoquette, M. S. 2013, MNRAS, 430, 2097

Jester, S., Schneider, D. P., Richards, G. T., et al. 2005, AJ, 130, 873

Jiang, L., Fan, X., Vestergaard, M., et al. 2007, AJ, 134, 1150

Jiang, L., Fan, X., Hines, D. C., et al. 2006, AJ, 132, 2127

Jiang, L., Fan, X., Annis, J., et al. 2008, AJ, 135, 1057

Jiang, L., Fan, X., Brandt, W. N., et al. 2010, Nature, 464, 380

Jiang, L., Egami, E., Fan, X., et al. 2013, ApJ, 773, 153

Jiang, N., Zhou, H.-Y., Ho, L. C., et al. 2012, ApJ, 759, L31

Jiang, Y.-F., Green, P. J., Greene, J. E., et al. 2017, ApJ, 836, 186

Johnson, H. L. 1964, ApJ, 139, 1022

Johnson, S. P., Wilson, G. W., Tang, Y., & Scott, K. S. 2013, MNRAS, 436, 2535

Jones, S. F., Blain, A. W., Stern, D., et al. 2014, MNRAS, 443, 146

Jones, S. F., Blain, A. W., Lonsdale, C., et al. 2015, MNRAS, 448, 3325

Juarez, Y., Maiolino, R., Mujica, R., et al. 2009, A&A, 494, L25

Jud, H., Schartmann, M., Mould, J., Burtscher, L., & Tristram, K. R. W. 2017, MNRAS, 465, 248

Jun, H. D., & Im, M. 2013, ApJ, 779, 104

Jun, H. D., Im, M., Lee, H. M., et al. 2015, ApJ, 806, 109

Kasliwal, V. P., Vogeley, M. S., & Richards, G. T. 2017, MNRAS, 470, 3027

Kaspi, S., Maoz, D., Netzer, H., et al. 2005, ApJ, 629, 61

Kaspi, S., Smith, P. S., Netzer, H., et al. 2000, ApJ, 533, 631

Kawaguchi, T., & Mori, M. 2010, ApJ, 724, L183

—. 2011, ApJ, 737, 105

Kawaguchi, T., Shimura, T., & Mineshige, S. 2001, ApJ, 546, 966

Kawakatu, N., & Ohsuga, K. 2011, MNRAS, 417, 2562

Kellermann, K. I., Condon, J. J., Kimball, A. E., Perley, R. A., & Ivezić, Ž. 2016, ApJ, 831, 168

Kellermann, K. I., & Pauliny-Toth, I. I. K. 1981, ARA&A, 19, 373

Kellermann, K. I., Sramek, R., Schmidt, M., Shaffer, D. B., & Green, R. 1989, AJ, 98, 1195

Kelly, B. C., Bechtold, J., & Siemiginowska, A. 2009, ApJ, 698, 895

Kelly, B. C., Becker, A. C., Sobolewska, M., Siemiginowska, A., & Uttley, P. 2014, ApJ, 788, 33

Kennicutt, R. C., & Evans, N. J. 2012, ARA&A, 50, 531

Kennicutt, Jr., R. C. 1998, ARA&A, 36, 189

Kennicutt, Jr., R. C., Tamblyn, P., & Congdon, C. E. 1994, ApJ, 435, 22

Kim, D., Im, M., Kim, J. H., et al. 2015, ApJS, 216, 17

Kim, M., Ho, L. C., Peng, C. Y., Barth, A. J., & Im, M. 2008, ApJS, 179, 283

King, A. 2003, ApJ, 596, L27

Kirkpatrick, A., Pope, A., Sajina, A., et al. 2015, ApJ, 814, 9

Kirkpatrick, A., Pope, A., Alexander, D. M., et al. 2012, ApJ, 759, 139

Kishimoto, M., Antonucci, R., Blaes, O., et al. 2008, Nature, 454, 492

Kishimoto, M., Hönig, S. F., Antonucci, R., et al. 2011a, A&A, 527, A121

—. 2009a, A&A, 507, L57

—. 2011b, A&A, 536, A78

Kishimoto, M., Hönig, S. F., Beckert, T., & Weigelt, G. 2007, A&A, 476, 713

Kishimoto, M., Hönig, S. F., Tristram, K. R. W., & Weigelt, G. 2009b, A&A, 493, L57

Kishimoto, M., Hönig, S. F., Antonucci, R., et al. 2013, ApJ, 775, L36

Kochanek, C. S., Shappee, B. J., Stanek, K. Z., et al. 2017, PASP, 129, 104502

Kokubo, M., & Minezaki, T. 2019, arXiv e-prints, arXiv:1904.08946

Kormendy, J., & Ho, L. C. 2013, ARA&A, 51, 511

Koshida, S., Yoshii, Y., Kobayashi, Y., et al. 2009, ApJ, 700, L109

Koshida, S., Minezaki, T., Yoshii, Y., et al. 2014, ApJ, 788, 159

Kozłowski, S., Kochanek, C. S., Ashby, M. L. N., et al. 2016, ApJ, 817, 119

Kozłowski, S., Kochanek, C. S., Udalski, A., et al. 2010, ApJ, 708, 927

Krawczyk, C. M., Richards, G. T., Mehta, S. S., et al. 2013, ApJS, 206, 4

Krolik, J. H. 1999, Active galactic nuclei : from the central black hole to the galactic environment

Krolik, J. H., & Begelman, M. C. 1988, ApJ, 329, 702

Kroupa, P., & Weidner, C. 2003, ApJ, 598, 1076

Kurk, J. D., Walter, F., Fan, X., et al. 2009, ApJ, 702, 833

—. 2007, ApJ, 669, 32

La Franca, F., Fiore, F., Comastri, A., et al. 2005, ApJ, 635, 864

Labita, M., Treves, A., Falomo, R., & Uslenghi, M. 2006, MNRAS, 373, 551

Lacy, M., Petric, A. O., Sajina, A., et al. 2007, AJ, 133, 186

Lacy, M., Storrie-Lombardi, L. J., Sajina, A., et al. 2004, ApJS, 154, 166

Lagache, G., Dole, H., & Puget, J.-L. 2003, MNRAS, 338, 555

Lagache, G., Dole, H., Puget, J.-L., et al. 2004, ApJS, 154, 112

Landt, H., Buchanan, C. L., & Barmby, P. 2010, MNRAS, 408, 1982

Landt, H., Ward, M. J., Kynoch, D., et al. 2019, MNRAS, 489, 1572

Lani, C., Netzer, H., & Lutz, D. 2017, MNRAS, 471, 59

Laor, A., Baldi, R. D., & Behar, E. 2019, MNRAS, 482, 5513

Laor, A., & Draine, B. T. 1993, ApJ, 402, 441

Lavalley, M., Isobe, T., & Feigelson, E. 1992, in Astronomical Society of the Pacific Conference Series, Vol. 25, Astronomical Data Analysis Software and Systems I, ed. D. M. Worrall, C. Biemesderfer, & J. Barnes, 245

Law, N. M., Kulkarni, S. R., Dekany, R. G., et al. 2009, PASP, 121, 1395

Lawrence, A. 1991, MNRAS, 252, 586

Lawrence, A., Warren, S. J., Almaini, O., et al. 2007, MNRAS, 379, 1599

Le Floc'h, E., Pérez-González, P. G., Rieke, G. H., et al. 2004, ApJS, 154, 170

Lebofsky, M. J., & Rieke, G. H. 1980, Nature, 284, 410

Lebouteiller, V., Barry, D. J., Spoon, H. W. W., et al. 2011a, ApJS, 196, 8

—. 2011b, ApJS, 196, 8

Lee, J. C., Gil de Paz, A., Tremonti, C., et al. 2009, ApJ, 706, 599

Leftley, J. H., Tristram, K. R. W., Hönig, S. F., et al. 2018, ApJ, 862, 17

Leipski, C., Falcke, H., Bennert, N., & Hüttemeister, S. 2006, A&A, 455, 161

Leipski, C., Meisenheimer, K., Walter, F., et al. 2013, ApJ, 772, 103

—. 2014, ApJ, 785, 154

Leitet, E., Bergvall, N., Piskunov, N., & Andersson, B.-G. 2011, A&A, 532, A107

Leja, J., Johnson, B. D., Conroy, C., & van Dokkum, P. 2018, ApJ, 854, 62

Li, M. P., Shi, Q. J., & Li, A. 2008a, MNRAS, 391, L49

Li, Y., Hopkins, P. F., Hernquist, L., et al. 2008b, ApJ, 678, 41

Lira, P., Arévalo, P., Uttley, P., McHardy, I., & Breedt, E. 2011, MNRAS, 415, 1290

Lira, P., Arévalo, P., Uttley, P., McHardy, I. M. M., & Videla, L. 2015, MNRAS, 454, 368

Liu, J. Y., Liu, B. F., Qiao, E. L., & Mineshige, S. 2012, ApJ, 754, 81

López-Gonzaga, N., Burtscher, L., Tristram, K. R. W., Meisenheimer, K., & Schartmann, M. 2016, A&A, 591, A47

Low, F. J., & Johnson, H. L. 1965, ApJ, 141, 336

Lusso, E., Comastri, A., Vignali, C., et al. 2011, A&A, 534, A110

Lusso, E., Comastri, A., Simmons, B. D., et al. 2012, MNRAS, 425, 623

Lusso, E., Hennawi, J. F., Comastri, A., et al. 2013, ApJ, 777, 86

Lutz, D. 2014, ARA&A, 52, 373

Lutz, D., Maiolino, R., Spoon, H. W. W., & Moorwood, A. F. M. 2004, A&A, 418, 465

Lutz, D., Berta, S., Contursi, A., et al. 2016, A&A, 591, A136

Lynden-Bell, D. 1969, Nature, 223, 690

Lyu, J., Hao, L., & Li, A. 2014, ApJ, 792, L9

Lyu, J., & Rieke, G. H. 2017, ApJ, 841, 76

—. 2018, ApJ, 866, 92

Lyu, J., Rieke, G. H., & Alberts, S. 2016, ApJ, 816, 85

Lyu, J., Rieke, G. H., & Shi, Y. 2017, ApJ, 835, 257

Lyu, J., Rieke, G. H., & Smith, P. S. 2019, arXiv e-prints, arXiv:1909.11101

Lyuty, V. M., & Doroshenko, V. T. 1999, Astronomy Letters, 25, 341

Ma, X.-C., & Wang, T.-G. 2013, MNRAS, 430, 3445

Ma, Z., & Yan, H. 2015, ApJ, 811, 58

MacLeod, C. L., Ivezić, Ž., Kochanek, C. S., et al. 2010, ApJ, 721, 1014

Madau, P., & Dickinson, M. 2014, ARA&A, 52, 415

Madden, S. C., Galliano, F., Jones, A. P., & Sauvage, M. 2006, A&A, 446, 877

Madden, S. C., Rémy-Ruyer, A., Galametz, M., et al. 2013, PASP, 125, 600

Magdis, G. E., Rigopoulou, D., Helou, G., et al. 2013, A&A, 558, A136

Magnelli, B., Lutz, D., Saintonge, A., et al. 2014, A&A, 561, A86

Maier, C., Lilly, S. J., Ziegler, B. L., et al. 2014, ApJ, 792, 3

Mainzer, A., Bauer, J., Cutri, R. M., et al. 2014, ApJ, 792, 30

Maiolino, R., Marconi, A., & Oliva, E. 2001a, A&A, 365, 37

Maiolino, R., Marconi, A., Salvati, M., et al. 2001b, A&A, 365, 28

Maiolino, R., Shemmer, O., Imanishi, M., et al. 2007, A&A, 468, 979

Maiolino, R., Cox, P., Caselli, P., et al. 2005, A&A, 440, L51

Maiolino, R., Nagao, T., Grazian, A., et al. 2008, A&A, 488, 463

Maiolino, R., Carniani, S., Fontana, A., et al. 2015, MNRAS, 452, 54

Mandal, A. K., Rakshit, S., Kurian, K. S., et al. 2018, MNRAS, 475, 5330

Mannucci, F., Cresci, G., Maiolino, R., et al. 2009, MNRAS, 398, 1915

Mao, P., Urry, C. M., Massaro, F., et al. 2016, ApJS, 224, 26

Marble, A. R., Hines, D. C., Schmidt, G. D., et al. 2003, ApJ, 590, 707

Marconi, A., Risaliti, G., Gilli, R., et al. 2004, MNRAS, 351, 169

Markwardt, C. B. 2009, in Astronomical Society of the Pacific Conference Series, Vol. 411, Astronomical Data Analysis Software and Systems XVIII, ed. D. A. Bohlender, D. Durand, & P. Dowler, 251

Marshall, J. A., Herter, T. L., Armus, L., et al. 2007, ApJ, 670, 129

Martin, D. C., Fanson, J., Schiminovich, D., et al. 2005, ApJ, 619, L1

Massaro, E., Maselli, A., Leto, C., et al. 2015, Ap&SS, 357, 75

Mateos, S., Alonso-Herrero, A., Carrera, F. J., et al. 2012, MNRAS, 426, 3271

Mateos, S., Carrera, F. J., Alonso-Herrero, A., et al. 2015, MNRAS, 449, 1422

—. 2016, ApJ, 819, 166

Mathis, J. S., Rumpl, W., & Nordsieck, K. H. 1977, ApJ, 217, 425

Matsuoka, K., Nagao, T., Maiolino, R., Marconi, A., & Taniguchi, Y. 2009, A&A, 503, 721

—. 2011, A&A, 532, L10

Matsuta, K., Gandhi, P., Dotani, T., et al. 2012, ApJ, 753, 104

McAlary, C. W., McLaren, R. A., McGonegal, R. J., & Maza, J. 1983, ApJS, 52, 341

McDowell, J. C., Elvis, M., & Wilkes, B. J. 1992, in American Institute of Physics Conference Series, Vol. 254, American Institute of Physics Conference Series, ed. S. S. Holt, S. G. Neff, & C. M. Urry, 532–535

McGreer, I. D., Jiang, L., Fan, X., et al. 2013, ApJ, 768, 105

McLeod, K. K., & McLeod, B. A. 2001, ApJ, 546, 782

McLeod, K. K., & Rieke, G. H. 1994, ApJ, 431, 137

Mechtley, M., Windhorst, R. A., Ryan, R. E., et al. 2012, ApJ, 756, L38

Meléndez, M., Mushotzky, R. F., Shimizu, T. T., Barger, A. J., & Cowie, L. L. 2014, ApJ, 794, 152

Meléndez, M., Kraemer, S. B., Armentrout, B. K., et al. 2008, ApJ, 682, 94

Minezaki, T., Yoshii, Y., Kobayashi, Y., et al. 2019, arXiv e-prints, arXiv:1910.08722

Mor, R., & Netzer, H. 2012a, MNRAS, 420, 526

—. 2012b, MNRAS, 420, 526

Mor, R., Netzer, H., & Elitzur, M. 2009, ApJ, 705, 298

Mor, R., & Trakhtenbrot, B. 2011, ApJ, 737, L36

Morganson, E., De Rosa, G., Decarli, R., et al. 2012, AJ, 143, 142

Mortlock, D. J., Patel, M., Warren, S. J., et al. 2009, A&A, 505, 97

Moshir, M., Kopan, G., Conrow, T., et al. 1990, in BAAS, Vol. 22, Bulletin of the American Astronomical Society, 1325

Mullaney, J. R., Alexander, D. M., Goulding, A. D., & Hickox, R. C. 2011, MNRAS, 414, 1082

Muratov, A. L., Kereš, D., Faucher-Giguère, C.-A., et al. 2015, MNRAS, 454, 2691

Murphy, T., Mauch, T., Green, A., et al. 2007, MNRAS, 382, 382

Murray, N., Quataert, E., & Thompson, T. A. 2005, ApJ, 618, 569

Mushotzky, R. F., Edelson, R., Baumgartner, W., & Gand hi, P. 2011, ApJ, 743, L12

Nagao, T., Maiolino, R., De Breuck, C., et al. 2012, A&A, 542, L34

Nagao, T., Maiolino, R., & Marconi, A. 2006, A&A, 447, 863

Nenkova, M., Sirocky, M. M., Ivezić, Ž., & Elitzur, M. 2008a, ApJ, 685, 147

Nenkova, M., Sirocky, M. M., Nikutta, R., Ivezić, Ž., & Elitzur, M. 2008b, ApJ, 685, 160

Netzer, H. 1987, MNRAS, 225, 55

—. 2009, MNRAS, 399, 1907

—. 2015, ARA&A, 53, 365

Netzer, H., Lani, C., Nordon, R., et al. 2016, ApJ, 819, 123

Netzer, H., Mor, R., Trakhtenbrot, B., Shemmer, O., & Lira, P. 2014, ApJ, 791, 34

Netzer, H., Shemmer, O., Maiolino, R., et al. 2004, ApJ, 614, 558

Netzer, H., Lutz, D., Schweitzer, M., et al. 2007, ApJ, 666, 806

Neugebauer, G., Green, R. F., Matthews, K., et al. 1987, ApJS, 63, 615

Neugebauer, G., & Matthews, K. 1999, AJ, 118, 35

Neugebauer, G., Miley, G. K., Soifer, B. T., & Clegg, P. E. 1986, ApJ, 308, 815

Neugebauer, G., Soifer, B. T., Matthews, K., & Elias, J. H. 1989, AJ, 97, 957

Nguyen, H. T., Schulz, B., Levenson, L., et al. 2010, A&A, 518, L5

Nikutta, R., Elitzur, M., & Lacy, M. 2009, ApJ, 707, 1550

Ochsenbein, F., Bauer, P., & Marcout, J. 2000, A&AS, 143, 23

O'Dell, S. L., Puschell, J. J., Stein, W. A., & Warner, J. W. 1978, ApJS, 38, 267

Ojha, R., Zacharias, N., Hennessy, G. S., Gaume, R. A., & Johnston, K. J. 2009, AJ, 138, 845

Oknyanskij, V. L., & Horne, K. 2001, in Astronomical Society of the Pacific Conference Series, Vol. 224, Probing the Physics of Active Galactic Nuclei, ed. B. M. Peterson, R. W. Pogge, & R. S. Polidan, 149

Oliver, S. J., Bock, J., Altieri, B., et al. 2012, MNRAS, 424, 1614

Omont, A., Willott, C. J., Beelen, A., et al. 2013, A&A, 552, A43

Östlin, G., Amram, P., Bergvall, N., et al. 2001, A&A, 374, 800

Östlin, G., Amram, P., Masegosa, J., Bergvall, N., & Boulesteix, J. 1999, A&AS, 137, 419

Östlin, G., Hayes, M., Kunth, D., et al. 2009, AJ, 138, 923

Ouchi, M., Ellis, R., Ono, Y., et al. 2013, ApJ, 778, 102

Pacholczyk, A. G. 1971, ApJ, 163, 449

Packham, C., Radomski, J. T., Roche, P. F., et al. 2005, ApJ, 618, L17

Page, M. J., Brindle, C., Talavera, A., et al. 2012, MNRAS, 426, 903

Paltani, S., & Courvoisier, T. J.-L. 1994, A&A, 291, 74

Pasetto, A., González-Martín, O., Esparza-Arredondo, D., et al. 2019, ApJ, 872, 69

Paturel, G., Petit, C., Rousseau, J., & Vauglin, I. 2003, A&A, 405, 1

Pe'er, A. 2014, Space Sci. Rev., 183, 371

Peng, Z., Gu, Q., Melnick, J., & Zhao, Y. 2006, A&A, 453, 863

Penston, M. V. 1973, MNRAS, 162, 359

Penston, M. V., Penston, M. J., Neugebauer, G., et al. 1971, MNRAS, 153, 29

Peterson, B. M., Ferrarese, L., Gilbert, K. M., et al. 2004, ApJ, 613, 682

Petric, A. O., Carilli, C. L., Bertoldi, F., et al. 2003, AJ, 126, 15

Petric, A. O., Ho, L. C., Flagey, N. J. M., & Scoville, N. Z. 2015, ApJS, 219, 22

Piconcelli, E., Jimenez-Bailón, E., Guainazzi, M., et al. 2005, A&A, 432, 15

Pier, E. A., & Krolik, J. H. 1992, ApJ, 401, 99

—. 1993, ApJ, 418, 673

Piovan, L., Tantalo, R., & Chiosi, C. 2003, A&A, 408, 559

Planck Collaboration, Adam, R., Ade, P. A. R., et al. 2015, ArXiv e-prints

Polletta, M., Courvoisier, T. J.-L., Hooper, E. J., & Wilkes, B. J. 2000, A&A, 362, 75

Polletta, M., Tajer, M., Maraschi, L., et al. 2007, ApJ, 663, 81

Pollo, A., Rybka, P., & Takeuchi, T. T. 2010, A&A, 514, A3

Popescu, C. C., Tuffs, R. J., Völk, H. J., Pierini, D., & Madore, B. F. 2002, ApJ, 567, 221

Pott, J.-U., Malkan, M. A., Elitzur, M., et al. 2010, ApJ, 715, 736

Pozo Nuñez, F., Haas, M., Chini, R., et al. 2014, A&A, 561, L8

Pozo Nuñez, F., Ramolla, M., Westhues, C., et al. 2015, A&A, 576, A73

Pozzi, F., Vignali, C., Comastri, A., et al. 2010, A&A, 517, A11

Prieto, M. A., Maciejewski, W., & Reunanen, J. 2005, AJ, 130, 1472

Prieto, M. A., Mezcua, M., Fernández-Ontiveros, J. A., & Schartmann, M. 2014, MNRAS, 442, 2145

Prieto, M. A., Reunanen, J., Tristram, K. R. W., et al. 2010, MNRAS, 402, 724

Raban, D., Jaffe, W., Röttgering, H., Meisenheimer, K., & Tristram, K. R. W. 2009, MNRAS, 394, 1325

Radomski, J. T., Piña, R. K., Packham, C., et al. 2003, ApJ, 587, 117

Radomski, J. T., Piña, R. K., Packham, C., Telesco, C. M., & Tadhunter, C. N. 2002, ApJ, 566, 675

Radomski, J. T., Packham, C., Levenson, N. A., et al. 2008, ApJ, 681, 141

Ramolla, M., Haas, M., Westhues, C., et al. 2018, A&A, 620, A137

Ramos Almeida, C., & Ricci, C. 2017, Nature Astronomy, 1, 679

Ramos Almeida, C., Levenson, N. A., Rodríguez Espinosa, J. M., et al. 2009, ApJ, 702, 1127

Ramos Almeida, C., Levenson, N. A., Alonso-Herrero, A., et al. 2011, ApJ, 731, 92

Rampazzo, R., Panuzzo, P., Vega, O., et al. 2013, MNRAS, 432, 374

Rawle, T. D., Egami, E., Bussmann, R. S., et al. 2014, ApJ, 783, 59

Reines, A. E., & Volonteri, M. 2015, ApJ, 813, 82

Rémy-Ruyer, A., Madden, S. C., Galliano, F., et al. 2013, A&A, 557, A95

—. 2015a, A&A, 582, A121

—. 2015b, A&A, 573, C1

Reunanen, J., Prieto, M. A., & Siebenmorgen, R. 2010, MNRAS, 402, 879

Revalski, M., Crenshaw, D. M., Kraemer, S. B., et al. 2018, ApJ, 856, 46

Rex, M., Rawle, T. D., Egami, E., et al. 2010, A&A, 518, L13

Reyes, R., Zakamska, N. L., Strauss, M. A., et al. 2008, AJ, 136, 2373

Ricci, C., Assef, R. J., Stern, D., et al. 2017a, ApJ, 835, 105

Ricci, C., Trakhtenbrot, B., Koss, M. J., et al. 2017b, Nature, 549, 488

Richards, G. T., Hall, P. B., Vanden Berk, D. E., et al. 2003, AJ, 126, 1131

Richards, G. T., Lacy, M., Storrie-Lombardi, L. J., et al. 2006, ApJS, 166, 470

Richards, G. T., Deo, R. P., Lacy, M., et al. 2009, AJ, 137, 3884

Riechers, D. A., Walter, F., Carilli, C. L., et al. 2006, ApJ, 650, 604

Riechers, D. A., Bradford, C. M., Clements, D. L., et al. 2013, Nature, 496, 329

Rieke, G. H. 1978, ApJ, 226, 550

Rieke, G. H., Alonso-Herrero, A., Weiner, B. J., et al. 2009, ApJ, 692, 556

Rieke, G. H., & Kinman, T. D. 1974, ApJ, 192, L115

Rieke, G. H., & Lebofsky, M. J. 1981, ApJ, 250, 87

Rieke, G. H., & Low, F. J. 1972, ApJ, 176, L95

—. 1975a, ApJ, 200, L67

—. 1975b, ApJ, 199, L13

Rigby, J. R., Diamond-Stanic, A. M., & Aniano, G. 2009, ApJ, 700, 1878

Risaliti, G., & Elvis, M. 2004, in Astrophysics and Space Science Library, Vol. 308, Supermassive Black Holes in the Distant Universe, ed. A. J. Barger, 187

Rodighiero, G., Daddi, E., Baronchelli, I., et al. 2011, ApJ, 739, L40

Roebuck, E., Sajina, A., Hayward, C. C., et al. 2016, ApJ, 833, 60

Rosario, D. J., Santini, P., Lutz, D., et al. 2012, A&A, 545, A45

Roseboom, I. G., Lawrence, A., Elvis, M., et al. 2013, MNRAS, 429, 1494

Ross, N. P., Hamann, F., Zakamska, N. L., et al. 2015, MNRAS, 453, 3932

Roth, N., Kasen, D., Hopkins, P. F., & Quataert, E. 2012, ApJ, 759, 36

Rowan-Robinson, M. 1995, MNRAS, 272, 737

Rudy, R. J., Levan, P. D., & Rodriguez-Espinosa, J. M. 1982, AJ, 87, 598

Rujopakarn, W., Rieke, G. H., Eisenstein, D. J., & Juneau, S. 2011, ApJ, 726, 93

Rujopakarn, W., Rieke, G. H., Weiner, B. J., et al. 2013, ApJ, 767, 73

Runnoe, J. C., Brotherton, M. S., & Shang, Z. 2012a, MNRAS, 422, 478

—. 2012b, MNRAS, 426, 2677

—. 2012c, MNRAS, 426, 2677

Runnoe, J. C., Shang, Z., & Brotherton, M. S. 2013, MNRAS, 435, 3251

Sajina, A., Yan, L., Fadda, D., Dasyra, K., & Huynh, M. 2012, ApJ, 757, 13

Salim, S., Rich, R. M., Charlot, S., et al. 2007, ApJS, 173, 267

Salpeter, E. E. 1955, ApJ, 121, 161

—. 1964, ApJ, 140, 796

Sanders, D. B., Phinney, E. S., Neugebauer, G., Soifer, B. T., & Matthews, K. 1989, ApJ, 347, 29

Sanders, D. B., Soifer, B. T., Elias, J. H., et al. 1988a, ApJ, 325, 74

—. 1988b, ApJ, 325, 74

Sanders, D. B., Soifer, B. T., Elias, J. H., Neugebauer, G., & Matthews, K. 1988c, ApJ, 328, L35

Sargsyan, L., Weedman, D., Lebouteiller, V., et al. 2011, ApJ, 730, 19

Schartmann, M., Meisenheimer, K., Camenzind, M., et al. 2008, A&A, 482, 67

Schartmann, M., Wada, K., Prieto, M. A., Burkert, A., & Tristram, K. R. W. 2014, MNRAS, 445, 3878

Schlafly, E. F., & Finkbeiner, D. P. 2011, ApJ, 737, 103

Schlegel, D. J., Finkbeiner, D. P., & Davis, M. 1998, ApJ, 500, 525

Schmidt, G. D., Stockman, H. S., & Smith, P. S. 1992, ApJ, 398, L57

Schmidt, M., & Green, R. F. 1983, ApJ, 269, 352

Schmitt, H. R., Antonucci, R. R. J., Ulvestad, J. S., et al. 2001, ApJ, 555, 663

Schneider, R., Bianchi, S., Valiante, R., Risaliti, G., & Salvadori, S. 2015, A&A, 579, A60

Schnülle, K., Pott, J.-U., Rix, H.-W., et al. 2015, A&A, 578, A57

Schreiber, C., Pannella, M., Elbaz, D., et al. 2015, A&A, 575, A74

Schweitzer, M., Groves, B., Netzer, H., et al. 2008, ApJ, 679, 101

Scott, A. E., & Stewart, G. C. 2014, MNRAS, 438, 2253

Scoville, N. Z., Evans, A. S., Thompson, R., et al. 2000, AJ, 119, 991

Shang, Z., Brotherton, M. S., Wills, B. J., et al. 2011, ApJS, 196, 2

Shangguan, J., Ho, L. C., & Xie, Y. 2018, ApJ, 854, 158

Shao, Z., Jiang, B. W., & Li, A. 2017, ApJ, 840, 27

Shappee, B. J., Prieto, J. L., Grupe, D., et al. 2014, ApJ, 788, 48

Shen, Y. 2013, Bulletin of the Astronomical Society of India, 41, 61

Sheng, Z., Wang, T., Jiang, N., et al. 2017, ApJ, 846, L7

Shi, Y., Rieke, G. H., Ogle, P. M., Su, K. Y. L., & Balog, Z. 2014, ApJS, 214, 23

Shi, Y., Rieke, G. H., Smith, P., et al. 2010, ApJ, 714, 115

Shi, Y., Rieke, G. H., Hines, D. C., et al. 2006, ApJ, 653, 127

Shi, Y., Ogle, P., Rieke, G. H., et al. 2007, ApJ, 669, 841

Shields, G. A. 1978, Nature, 272, 706

Shimizu, T. T., Meléndez, M., Mushotzky, R. F., et al. 2016, MNRAS, 456, 3335

Shimizu, T. T., Davies, R. I., Koss, M., et al. 2018, ApJ, 856, 154

Siebenmorgen, R., Heymann, F., & Efstathiou, A. 2015, A&A, 583, A120

Siebenmorgen, R., & Krügel, E. 2007, A&A, 461, 445

Silva, L., Granato, G. L., Bressan, A., & Danese, L. 1998, ApJ, 509, 103

Simpson, C. 2005, MNRAS, 360, 565

Sklias, P., Zamojski, M., Schaerer, D., et al. 2014, A&A, 561, A149

Skrutskie, M. F., Cutri, R. M., Stiening, R., et al. 2006, AJ, 131, 1163

Sloan, G. C., Herter, T. L., Charmandaris, V., et al. 2015, AJ, 149, 11

Smith, E. P., Heckman, T. M., Bothun, G. D., Romanishin, W., & Balick, B. 1986, ApJ, 306, 64

Smith, J. D. T., Armus, L., Dale, D. A., et al. 2007a, PASP, 119, 1133

Smith, J. D. T., Draine, B. T., Dale, D. A., et al. 2007b, ApJ, 656, 770

Smith, P. 2016, Galaxies, 4, 27

Smith, P. S., Schmidt, G. D., Allen, R. G., & Hines, D. C. 1997, ApJ, 488, 202

Smith, P. S., Schmidt, G. D., Hines, D. C., Cutri, R. M., & Nelson, B. O. 2002, ApJ, 569, 23

Soldi, S., Türler, M., Paltani, S., et al. 2008, A&A, 486, 411

Spinoglio, L., Malkan, M. A., Rush, B., Carrasco, L., & Recillas-Cruz, E. 1995, ApJ, 453, 616

Stalevski, M., Asmus, D., & Tristram, K. R. W. 2017, MNRAS, 472, 3854

Stalevski, M., Fritz, J., Baes, M., Nakos, T., & Popović, L. Č. 2012, MNRAS, 420, 2756

Stalevski, M., Ricci, C., Ueda, Y., et al. 2016, MNRAS, 458, 2288

Stalevski, M., Tristram, K. R. W., & Asmus, D. 2019, MNRAS, 484, 3334

Steffen, A. T., Strateva, I., Brandt, W. N., et al. 2006, AJ, 131, 2826

Stern, D., Eisenhardt, P., Gorjian, V., et al. 2005, ApJ, 631, 163

Stern, D., Assef, R. J., Benford, D. J., et al. 2012, ApJ, 753, 30

Stern, D., Lansbury, G. B., Assef, R. J., et al. 2014, ApJ, 794, 102

Stetson, P. B. 1987, PASP, 99, 191

Stierwalt, S., Armus, L., Surace, J. A., et al. 2013, ApJS, 206, 1

Strauss, M. A., Weinberg, D. H., Lupton, R. H., et al. 2002, AJ, 124, 1810

Sturm, E., Lutz, D., Tran, D., et al. 2000, A&A, 358, 481

Sturm, E., Schweitzer, M., Lutz, D., et al. 2005, ApJ, 629, L21

Suganuma, M., Yoshii, Y., Kobayashi, Y., et al. 2006, ApJ, 639, 46

Sugiura, N. 1978, Communications in Statistics-Theory and Methods, 7, 13

Surace, J. A., Sanders, D. B., & Evans, A. S. 2001, AJ, 122, 2791

Swain, M., Vasisht, G., Akeson, R., et al. 2003, ApJ, 596, L163

Symeonidis, M. 2017, MNRAS, 465, 1401

Symeonidis, M., Giblin, B. M., Page, M. J., et al. 2016, MNRAS

Symeonidis, M., Page, M. J., Seymour, N., et al. 2009, MNRAS, 397, 1728

Symeonidis, M., Vaccari, M., Berta, S., et al. 2013, MNRAS, 431, 2317

Targett, T. A., Dunlop, J. S., & McLure, R. J. 2012, MNRAS, 420, 3621

Teplitz, H. I., Capak, P., Brooke, T., et al. 2010, in Astronomical Society of the Pacific Conference Series, Vol. 434, Astronomical Data Analysis Software and Systems XIX, ed. Y. Mizumoto, K.-I. Morita, & M. Ohishi, 437

Thompson, T. A., Quataert, E., & Murray, N. 2005, ApJ, 630, 167

Tody, D. 1986, Society of Photo-Optical Instrumentation Engineers (SPIE) Conference Series, Vol. 627, The IRAF Data Reduction and Analysis System, ed. D. L. Crawford, 733

Tody, D. 1993, in Astronomical Society of the Pacific Conference Series, Vol. 52, Astronomical Data Analysis Software and Systems II, ed. R. J. Hanisch, R. J. V. Brissenden, & J. Barnes, 173

Trebitsch, M., Volonteri, M., & Dubois, Y. 2019, MNRAS, 487, 819

Treister, E., Krolik, J. H., & Dullemond, C. 2008, ApJ, 679, 140

Tristram, K. R. W., Burtscher, L., Jaffe, W., et al. 2014, A&A, 563, A82

Tsai, C.-W., Eisenhardt, P. R. M., Wu, J., et al. 2015, ApJ, 805, 90

Ueda, Y., Akiyama, M., Ohta, K., & Miyaji, T. 2003, ApJ, 598, 886

Urry, C. M., & Padovani, P. 1995, PASP, 107, 803

Valiante, R., Schneider, R., Bianchi, S., & Andersen, A. C. 2009, MNRAS, 397, 1661

Vazquez, B., Galianni, P., Richmond, M., et al. 2015, ApJ, 801, 127

Veilleux, S., Rupke, D. S. N., Kim, D.-C., et al. 2009, ApJS, 182, 628

Venemans, B. P., Walter, F., Decarli, R., et al. 2017, ApJ, 851, L8

Vestergaard, M., & Peterson, B. M. 2006, ApJ, 641, 689

Villaume, A., Conroy, C., & Johnson, B. D. 2015, ApJ, 806, 82

Vito, F., Brandt, W. N., Stern, D., et al. 2018, MNRAS, 474, 4528

Vollmer, B., Beckert, T., & Davies, R. I. 2008, A&A, 491, 441

Wada, K. 2012, ApJ, 758, 66

Wada, K., Papadopoulos, P. P., & Spaans, M. 2009, ApJ, 702, 63

Wada, K., Schartmann, M., & Meijerink, R. 2016, ApJ, 828, L19

Walter, F., Carilli, C., Bertoldi, F., et al. 2004, ApJ, 615, L17

Walter, F., Riechers, D., Cox, P., et al. 2009, Nature, 457, 699

Wang, J.-M., Yan, C.-S., Gao, H.-Q., et al. 2010a, ApJ, 719, L148

Wang, J.-M., Ge, J.-Q., Hu, C., et al. 2011a, ApJ, 739, 3

Wang, R., Wagg, J., Carilli, C. L., et al. 2008a, AJ, 135, 1201

Wang, R., Carilli, C. L., Wagg, J., et al. 2008b, ApJ, 687, 848

Wang, R., Carilli, C. L., Neri, R., et al. 2010b, ApJ, 714, 699

Wang, R., Wagg, J., Carilli, C. L., et al. 2011b, ApJ, 739, L34

—. 2011c, AJ, 142, 101

—. 2013, ApJ, 773, 44

Watson, D., Christensen, L., Knudsen, K. K., et al. 2015, Nature, 519, 327

Weigelt, G., Hofmann, K.-H., Kishimoto, M., et al. 2012, A&A, 541, L9

Weingartner, J. C., & Murray, N. 2002, ApJ, 580, 88

Welsh, B. Y., Wheatley, J. M., & Neil, J. D. 2011, A&A, 527, A15

Wheatley, J. M., Welsh, B. Y., & Browne, S. E. 2008, AJ, 136, 259

Willmer, C. N. A., Rieke, G. H., Le Floc'h, E., et al. 2009, AJ, 138, 146

Willott, C. J., Bergeron, J., & Omont, A. 2015, ApJ, 801, 123

Willott, C. J., Omont, A., & Bergeron, J. 2013, ApJ, 770, 13

Willott, C. J., Albert, L., Arzoumanian, D., et al. 2010a, AJ, 140, 546

Willott, C. J., Delorme, P., Reylé, C., et al. 2010b, AJ, 139, 906

Woo, J.-H., Treu, T., Barth, A. J., et al. 2010, ApJ, 716, 269

Wright, E. L., Eisenhardt, P. R. M., Mainzer, A. K., et al. 2010, AJ, 140, 1868

Wu, J., Tsai, C.-W., Sayers, J., et al. 2012, ApJ, 756, 96

Wu, J., Jun, H. D., Assef, R. J., et al. 2018, ApJ, 852, 96

Wu, Y., Charmandaris, V., Hao, L., et al. 2006, ApJ, 639, 157

Wu, Y., Charmandaris, V., Hunt, L. K., et al. 2007, ApJ, 662, 952

Xie, Y., Hao, L., & Li, A. 2014, ApJ, 794, L19

Xie, Y., Li, A., & Hao, L. 2017, ApJS, 228, 6

Xu, L., Rieke, G. H., Egami, E., et al. 2015a, ApJ, 808, 159

—. 2015b, ApJS, 219, 18

Yamamura, I., Makiuti, S., Ikeda, N., et al. 2010, VizieR Online Data Catalog, 2298

Yang, Q., Wu, X.-B., Fan, X., et al. 2018, ApJ, 862, 109

York, D. G., Adelman, J., Anderson, John E., J., et al. 2000a, AJ, 120, 1579

York, D. G., Adelman, J., Anderson, Jr., J. E., et al. 2000b, AJ, 120, 1579

Yoshii, Y., Kobayashi, Y., Minezaki, T., Koshida, S., & Peterson, B. A. 2014, ApJ, 784, L11

Yuan, F., & Narayan, R. 2014, ARA&A, 52, 529

Zafar, T., Møller, P., Ledoux, C., et al. 2011, A&A, 532, A51

Zakamska, N. L., Schmidt, G. D., Smith, P. S., et al. 2005, AJ, 129, 1212

Zakamska, N. L., Hamann, F., Pâris, I., et al. 2016, MNRAS, 459, 3144

Zhang, K., Wang, T.-G., Yan, L., & Dong, X.-B. 2013, ApJ, 768, 22

Zhang, Z., Shi, Y., Rieke, G. H., et al. 2016, ApJ, 819, L27

Zu, Y., Kochanek, C. S., Kozłowski, S., & Udalski, A. 2013, ApJ, 765, 106

Zu, Y., Kochanek, C. S., & Peterson, B. M. 2011, ApJ, 735, 80